INTERPLAY BETWEEN MECHANICS AND CHEMISTRY ACROSS DIFFERENT SCALES
From Protein to Cell Dynamics and Morphogenesis

Andriy Goychuk

Munich 2021

Interplay Between Mechanics and Chemistry Across Different Scales

From Protein to Cell Dynamics and Morphogenesis

Andriy Goychuk

Dissertation submitted
to the Faculty of Physics at the
Ludwig–Maximilians–Universität München
for the degree of
Doctor rerum naturalium

Munich, May 25, 2021

ZUSAMMENFASSUNG (GERMAN SUMMARY)

Lebende Organismen reagieren aktiv auf ihre Umwelt, sei es auf der Suche nach Nahrung oder auf der Flucht vor Fressfeinden. Dazu müssen sie Signale aus der Umgebung wahrnehmen und verarbeiten. Mikroorganismen, wie Bakterien oder eukaryotische Zellen, nutzen dafür biochemische Signalnetzwerke aus molekularen Schaltern. Einige dieser Signalnetzwerke müssen daher mechanische Signale erkennen und mechanische Antworten liefern können. Die vorliegende Arbeit veranschaulicht in mehreren Kapiteln die Konsequenzen einer Kopplung zwischen Mechanik und Chemie. Nach einer allgemeinen Einführung, die einige Hauptergebnisse herausgreift und in einen breiteren Kontext einordnet, werden in einer separaten mathematischen Einleitung nützliche analytische Werkzeuge erläutert. Dieser gemeinsame Rahmen der Differentialgeometrie verbindet drei übergreifende Themen dieser Arbeit, wobei jedes Thema zwei Unterprojekte hat.

Mechanochemische Kopplung auf der Mikroskala. Beim Binden an eine elastische Membran können Proteine diese über reziproke Kräfte verformen. Wie wirkt sich dieser Effekt auf eine Reaktionskinetik aus, die das Zytosol mit der Membran koppelt? Der Abschnitt II.1 "Mechanochemical Coupling between Proteins and Membranes" zeigt, wie generische Wechselwirkungen zwischen Proteinen und einer Membran letztere nicht nur verformen, sondern auch zu einer nichtlinearen Selbstrekrutierung von Proteinen aus dem Zytosol auf die Membran führen. Da nichtlineare Reaktionen ein zentrales Thema musterbildender Systeme sind, könnten externe Stimuli über mechanische Kooperativität zu einer Änderung der intrazellulären Signalmuster führen.

Durch Reaktionen angetriebene intrazelluläre Muster implizieren wiederum Teilchenflüsse, welche im Fokus von Abschnitt II.2 "Protein Fluxes Induce Generic Transport of Cargo" liegen. In einer dichten Umgebung, wie auf der Zellmembran, koppeln Teilchenflüsse über eine effektive Reibung, die durch hydrodynamische oder direkte Wechselwirkungen vermittelt wird. Dies führt zu einem generischen diffusiophoretischen Effekt, bei dem Proteinmuster völlig unbeteiligte Moleküle transportieren und sogar sortieren können. Diese Ergebnisse legen nahe, dass Proteine mechanische Arbeit verrichten können, ohne auf eine spezialisierte molekulare Maschinerie wie das Aktomyosin-Zytoskelett zurückzugreifen.

Signaltransfer bei der Zellwanderung. Das Aktomyosin-Zytoskelett ist jedoch unverzichtbar für die Zellwanderung. Zum Steuern dieser Maschinerie verarbeiten Zellen externe Stimuli über mehrere Signalwege, sowohl mit positiven als auch mit negativen Rückkopplungen. In Abschnitt III.1 "Collective

Cell Dynamics in Rigid Environments" werden diese komplexen Signalwege auf nur zwei Rückkopplungen herunter gebrochen, die eine Polarisierung der (simulierten) Zellen ermöglichen. Dieses Projekt zeigt, wie unter bestimmten Bedingungen eine Zellbewegung mit der Benetzung einer Oberfläche durch ein aktives Tröpfchen gleichbedeutend ist.

Wenn einzelne Proteine Membranen durch Binden verformen können, dann sollten Zellen entsprechend in der Lage sein, ein Substrat an dem sie haften zu verformen. In der Tat dehnen und untersuchen Zellen aktiv ihre Umgebung, indem sie aktiv an ihr ziehen. In Abschnitt III.2 "Cell Migration and Shape in Soft Environments" wird unter der Prämisse dieser Zugkräfte untersucht, welchen Einfluss Substratverformungen auf die Dynamik von Zellen haben. Substratdeformationen implizieren lokale Änderungen des Abstands zwischen den Oberflächenliganden, an die eine Zelle binden kann, wodurch Gradienten an Adhäsivität erzeugt werden. Infolgedessen können sich Zellen auf sehr weichen Substraten festsetzen, indem sie adhäsive Inseln bilden, und können auf noch weicheren Substraten sogar durch drastische Elongation die Rotationssymmetrie brechen. Wenn sich viele Zellen auf demselben Substrat aufhalten, dann können sie diese Effekte ausnutzen um Netzwerke zu bilden.

Wie Anisotropie die Morphogenese beeinflusst. Das Brechen der Rotationssymmetrie bedeutet, dass Zellen eine anisotrope Spannung ausüben und eine besonders starke Kontraktilität in eine bestimmte Richtung zeigen. Folglich können zelluläre Neuausrichtungen die Spannung auf Gewebeebene und damit auch die Gewebeform regulieren. Der Abschnitt IV.1 "Collective Cell Migration Affects Morphogenesis" zeigt, wie eine solche Neuorientierung von Zellen eine Formveränderung von miniaturisierten Organen bewirken kann. Anschließend werden in Abschnitt IV.2 "Between Morphogenesis and Hydrodynamic Flows" die Konsequenzen der zellulären Anisotropie und der Mechanik für die Hydrodynamik von Geweben untersucht. Eines der wichtigsten Ergebnisse ist, dass sich eine Spannungsmodulation aufgrund von Zellneuausrichtung qualitativ von einer isotropen Spannungsmodulation unterscheidet, und zwar durch die Richtung, in die sich ein Gewebe bewegt. Interessanterweise können isotrope Kontraktilitätsgradienten durch den Marangoni-Effekt und den resultierenden hydraulischen Druck zu einer Ausbeulung des Gewebes in den kontraktilsten Regionen führen. Dies könnte auch ein minimales Modell für eine aktive, vom Zytoskelett einer Zelle angetriebene Exozytose darstellen. Ein weiteres Ergebnis ist, dass elastische röhrenförmige Schalen die Zeitumkehrsymmetrie durch Hystereseeffekte brechen können, was gerichteten Transport ermöglichen könnte. Es gibt also noch viel mehr zu entdecken!

Summary

Living organisms actively respond to their surroundings, be it searching for food or escaping from predators. These actions require detecting and processing environmental signals. Microorganisms, such as bacteria or eukaryotic cells, do so via biochemical signaling networks of molecular switches. Then, some of these signaling networks must be capable of detecting mechanical signals and facilitating mechanical responses. This thesis, structured into several chapters, illustrates the consequences of coupling mechanics and chemistry. After giving a general introduction that outlines some of the main results and places them into a broader context, a separate mathematical introduction explains useful analytical tools and methods. This common framework of differential geometry ties together three overarching themes of this thesis, each having two subprojects.

Mechanochemical coupling on the microscale. When binding to an elastic membrane, proteins can induce deformations thereof by exerting reciprocal forces. Then, what are the consequences of this effect for reaction kinetics that couple the cytosol to the membrane? Section II.1 "Mechanochemical Coupling between Proteins and Membranes" illustrates how generic interactions between proteins and a membrane not only deform the latter but also lead to nonlinear self-recruitment of proteins from the cytosol to the membrane. With nonlinear reactions being a central theme of pattern-forming systems, external stimuli could, via mechanical cooperativity, drastically change intracellular signaling patterns.

In turn, intracellular pattern formation, via protein turnover and reactions, implies particle fluxes—the center of attention in Section II.2 "Protein Fluxes Induce Generic Transport of Cargo". In particular, in any dense environment such as on the cell membrane, particle fluxes will couple via effective friction, mediated by hydrodynamic interactions or direct interactions among proteins. This leads to a generic diffusiophoretic effect, where protein patterns can transport and even spatially sort entirely unrelated molecules. Taken together, these results suggest that proteins can perform mechanical work without relying on specialized molecular machinery like the actomyosin cytoskeleton.

Integrating signals during cell migration. The actomyosin cytoskeleton is, however, indispensable for the migration of cells. To control this machinery, cells integrate external stimuli via several regulatory pathways that involve positive and negative feedback loops. In Section III.1 "Collective Cell Dynamics in Rigid Environments", these complex regulatory networks are represented in terms of only two feedback loops that allow the (simulated) cells to polarize. Furthermore, this project shows how, under certain conditions, cell motion is

equivalent to an entirely different problem: active surface wetting by a liquid droplet.

If proteins can deform membranes by binding, then the much larger cells should do the same to a substrate to which they adhere. In fact, cells induce strains and probe their environment by actively pulling and generating traction forces. Section III.2 "Cell Migration and Shape in Soft Environments" takes these traction forces as a premise for studying how substrate deformations affect cell dynamics. In particular, substrate deformations imply local changes in the distance between the surface ligands that a cell can adhere to, thus generating gradients of adhesiveness. Then, cells can trap themselves on very soft substrates by creating adhesive islands and even break rotational symmetry via profound elongation. When present on the same substrate, large populations of cells can exploit these effects to form networks.

How anisotropy affects morphogenesis. Breaking rotational symmetry means that cells exert anisotropic tension, showing particularly strong contractility in some chosen direction. Consequently, cellular reorientations can regulate the tension on a tissue level and thereby control tissue shape. Section IV.1 "Collective Cell Migration Affects Morphogenesis" shows how such a reorientation of cells can induce a shape transformation in miniaturized organs. Then, Section IV.2 "Between Morphogenesis and Hydrodynamic Flows" further studies the consequences of cellular anisotropy and mechanics for the hydrodynamics of tissues. One of the main results is that a tension modulation due to cell reorientation is qualitatively different from an isotropic tension modulation by the very direction in which the tissue will move. Interestingly, isotropic contractility gradients can, through the Marangoni effect and hydraulic pressure, lead to a bulging out of the tissue in the most contractile regions. Such effects could also provide a minimal model for active cell cytoskeleton-driven exocytosis. Another result is that elastic tubular shells can break time-reversal symmetry by exhibiting different hysteresis effects, possibly enabling directed transport. Thus, there is much more to discover!

Acknowledgements

Before we discuss science, I would like to thank all people that supported me on my academic journey so far. Foremost, I am thankful to Erwin Frey for providing a great environment to do independent research and be creative. He was always open for discussions, even regarding some of the more daring ideas, and provided fantastic feedback as a mentor. What helped me grow the most, I believe, is the breadth of different topics that I could research in your group. Furthermore, I would like to thank you for the support, enabling me to participate in several conferences at the beginning of my studies. It was a pleasure to work with you, and I enjoyed great discussions with all members of both your and Chase Broedersz's groups. The group retreats were always productive and a lot of fun.

I would also like to thank Chase Broedersz, with whom I collaborated and had many interesting discussions on cell dynamics. It was a pleasure to hear your feedback and working on a joint project with you. It was also fun to discuss and join forces with David Brückner, who has a splendid intuition for cell behavior. On the experimental side, I am thankful for the support by Andrew Holle, who did many experiments for me to analyze, and who was always keen to discuss science. Our collaboration started slightly before Erwin and I made a short visit to the laboratory of Joachim Spatz, where you worked at the time. During my studies, I also had a great collaboration with Joachim Rädler and the members of his group, whom I also accompanied on their group retreat. While studying the migratory dynamics of cells, I closely worked with Sophia Schaffer from the Rädler laboratory and with Felix Kempf from the Frey group. One of the tools that I used and further developed while studying cell dynamics, the extended Cellular Potts model, was first conceived by Florian Thüroff. He also co-advised me during my bachelor's thesis in the Frey group, where my scientific journey began in a collaboration with the laboratory of Stefan Zahler. In particular, Kerstin Kick and later Daniel Rüdiger did many experiments that showed how cells use their environment to organize into networks. Cell organization was also a central theme of my collaboration with the laboratory of Andreas Bausch, who provided excellent feedback. Here, I benefitted by working together and gathering ideas with Pablo Fernández, Benedikt Buchmann, and Samuel Randriamanantsoa, who know a lot about mammary gland organoids and pancreatic organoids. Thank you for the great collaboration!

Apart from cell and tissue dynamics, a significant part of my studies focused on pattern formation in cells and in reconstituted *in vitro* experiments. Here, I would like to thank Manon Wigbers, with whom I discussed possible mechanochemical modeling of lipid vesicles and the starfish oocyte. I am also thankful to Laeschkir Würthner, who was always keen on discussing

RESEARCH ARTICLES

During my doctoral studies, I pursued several research projects that culminated in publications. The following listing gives an account of the research projects that influenced my thesis the most. The corresponding publications are reprinted on the indicated pages under the indicated license. Projects that are not yet published in an academic journal but already under review or in preparation are listed separately on the next page.

The asterisk symbol (*) indicates shared first authorship.

PUBLISHED

[M1]   **Andriy Goychuk** and Erwin Frey. *Protein Recruitment through Indirect Mechanochemical Interactions.* Published in Physical Review Letters **123**, 178101 (2019). Reprinted on pages 61–73 under the terms of the ⓒⓘ Creative Commons Attribution 4.0 International License.

[M2]   Beatrice Ramm*, **Andriy Goychuk***, Alena Khmelinskaia, Philipp Blumhardt, Hiromune Eto, Kristina A. Ganzinger, Erwin Frey and Petra Schwille. *A diffusiophoretic mechanism for ATP-driven transport without motor proteins.* Published in Nature Physics **17**, 850–858 (2021). Reprinted on pages 83–197 under the terms of the ⓒⓘ Creative Commons Attribution 4.0 International License.

[M3]   Florian Thüroff*, **Andriy Goychuk***, Matthias Reiter and Erwin Frey. *Bridging the gap between single-cell migration and collective dynamics.* Published in eLife **8**, e46842 (2019). Reprinted on pages 209–264 under the terms of the ⓒⓘ Creative Commons Attribution 4.0 International License.

Under Review

[M4]   **Andriy Goychuk**, David B. Brückner, Andrew W. Holle, Joachim P. Spatz, Chase P. Broedersz and Erwin Frey. *Morphology and Motility of Endothelial Cells on Soft Substrates.* Preprint included on pages 273–324.

[M5]   Pablo Fernández*, Benedikt Buchmann*, **Andriy Goychuk***, Lisa K. Engelbrecht, Marion Raich, Christina H. Scheel, Erwin Frey and Andreas R. Bausch. *Surface tension induced budding drives alveologenesis in human mammary gland organoids.* Accepted for publication in Nature Physics (2021). Accepted manuscript reprinted on pages 341–394.

In Preparation

[M6]   Laeschkir Würthner*, **Andriy Goychuk*** and Erwin Frey. *Geometry-induced instabilities in reaction-diffusion systems on deforming boundaries.*

[M7]   **Review: Andriy Goychuk**, Laeschkir Würthner, Manon Wigbers and Erwin Frey. *Mechanics shapes chemical patterns.*

CONTENTS

Contents

I | NON-EQUILIBRIUM DYNAMICS IN BIOLOGY

I.1 | ACTIVITY IS A MATTER OF LIFE AND DEATH

> What is our life? The play of passion. Our mirth? The music of division: Our mothers' wombs the tiring-houses be, where we are dressed for life's short comedy. The earth the stage; Heaven the spectator is, who sits and views whosoe'er doth act amiss. The graves which hide us from the scorching sun are like drawn curtains when the play is done. Thus playing post we to our latest rest, and then we die in earnest, not in jest.
>
> Sir Walter Raleigh

Life is dynamic. All living beings self-organize, adapt, and autonomously respond to external stimuli by performing work. To accomplish these tasks, akin to complex machines, biological organisms rely on many smaller functional subunits that act in concert. Their continued operation requires a steady supply of energy through biological fuel and only stops at death. Higher forms of life such as animals and plants have a hierarchical structure. They are subdivided into different *organs* such as the brain, heart and skin (Reece et al., 2014; Carlson, 2019). These organs are complex biological composites of several macroscopic tissues, in turn consisting of many smaller cells (Reece et al., 2014). Each cell has a life of its own that depends on the operation of even smaller subunits, like the cell cytoskeleton, and *organelles* such as the cell core (Reece et al., 2014; Phillips, Kondev, et al., 2012; Alberts, Bray, et al., 2014; Alberts, A. Johnson, et al., 2014; Steven et al., 2016). The building blocks for these intracellular structures are macromolecules such as proteins and lipids (Reece et al., 2014; Phillips, Kondev, et al., 2012; Alberts, Bray, et al., 2014; Alberts, A. Johnson, et al., 2014). When studying the various aspects of life, one therefore encounters a plethora of systems that each have their own function. Figure I.1 depicts this cascade of coupled systems across disparate length scales. In the following, I intend to take the reader on a short expedition, starting at the macroscopic behavior of an organism and then diving further into the depths of microscopic dynamics. Along this journey, I give a concise and non-exhaustive overview of several re-
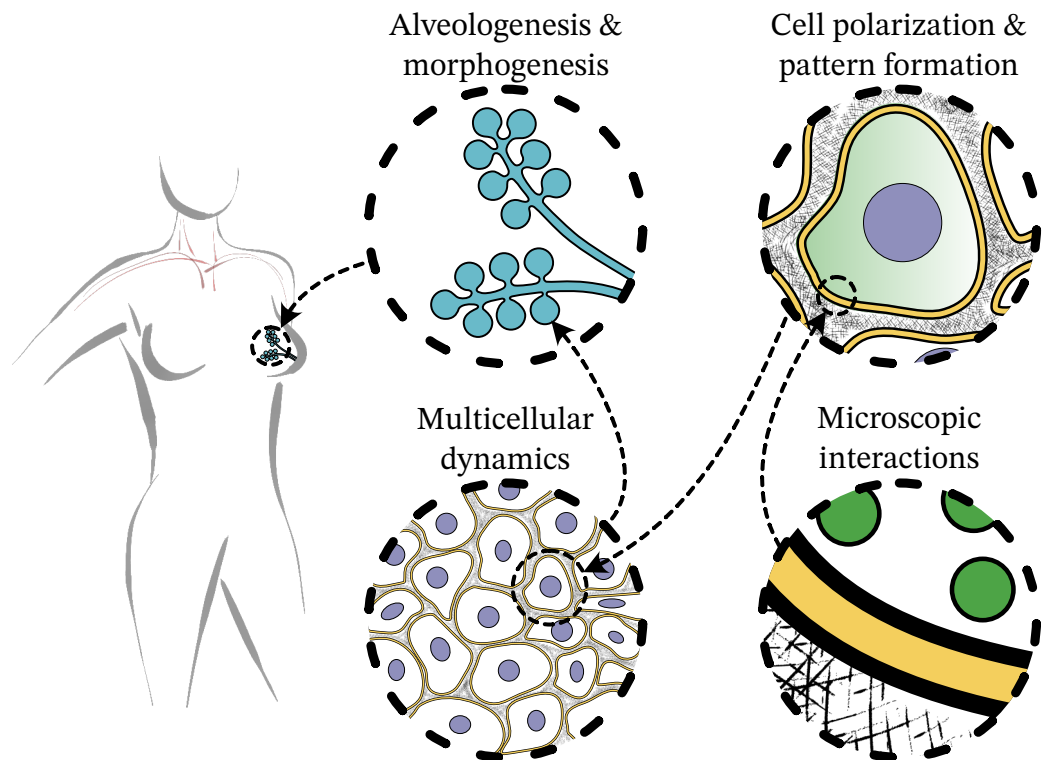
Figure I.1: A living being consists of several coupled subsystems that form a hierarchy across different length scales. The top left view shows the mammary gland organ, which has a tree-like ductal structure terminating in alveolar buds. This organ consists of many cells (top right view) that form a confluent tissue (bottom left view). Each cell has a life of its own that is determined by the microscopic dynamics of proteins (green, bottom right view). All of these different components, and many others, contribute to the function of the whole organism.

lated topics. Finally, we will slowly resurface while taking a closer look at several phenomena that arise across different scales.

The seemingly endless complexity of life raises an important question: *If two subjects look and act differently, then are they really distinct or could both simply be played by the same agent disguised with another mask?* In this thesis, as we study the macroscopic behavior of cells and the microscopic dynamics of proteins, we find striking conceptual analogies. This suggests that there must exist some generic principles that underlie the dynamics of distinct organisms.

I.1.1 MULTICELLULAR DYNAMICS

Form begets function...   One common point of all living beings is that they clearly distinguish themselves from their surroundings through a sharp physical boundary. An example of such a boundary is the skin, a multicellular epithelium that protects animals from environmental hazards (Reece et al., 2014; Carlson, 2019). In the case of individual cells, this pivotal role is played by their membrane or a cell wall (Reece et al., 2014; Phillips, Kondev, et al., 2012; Alberts, Bray, et al., 2014; Alberts, A. Johnson, et al., 2014). Analogously, both organs and organelles have well-defined boundaries that set them apart from other functional subunits of the enclosing organism. Within this confinement, the constituents that make up an organ or organelle can move and interact with minimal outside interference. We summarize these points as follows: *A biophysical boundary localizes and groups different yet related components into a larger functional entity such as an organ or an organelle.*

There are also cases where the boundary defines the very purpose of the organ or organelle. For example, the shell-like vascular system of blood vessels and the lymphatic system both have only one dedicated function: to facilitate efficient advective transport lest the surrounding porous tissue would only allow slow diffusive transport. This function tightly relates to the tubular morphology of the vessels, making them pipelines for blood and lymphatic fluid (Reece et al., 2014; Carlson, 2019), respectively. The blood itself, however, is a viscous fluid whose diverse functions are not explicitly tied to its shape but rather to its composition. In particular, blood transports biological fuel in the form of sugar to maintain a steady power supply throughout the organism, as well as several different cell types in suspension—erythrocytes, platelets and immune cells (Reece et al., 2014; Carlson, 2019). Thus, it might seem that some biological functions can be independent from morphology. But when looking at the bigger picture, blood cannot fulfill its role without a vasculature that has a specialized shape. Defects in this shape that can arise due to physical instabilities, such as bulges of the vasculature, so-called aneurysms, can endanger the entire organism by locally jeopardizing its power supply (Herman, 2016). We therefore arrive at the following conclusion: *The ability of a functional entity to perform a task crucially depends both on its composition and on the biophysical properties of its boundary.*

...while functional activity begets form.   In our examples so far, the different biological components can behave like fluids such as blood or solids such as blood vessels. Then, how does this distinction between fluid and solid affect the dynamics and function of a tissue? In Section IV.1 "Collective Cell Migration Affects Morphogenesis", we further investigate these concepts in the context of mammary gland morphogenesis. Mammary glands are organs that also

have a ductal structure (Wang et al., 2017). Their function is to provide milk for the nourishment of mammal offspring (Reece et al., 2014; Carlson, 2019). To study the dynamics of mammary gland development, we employ a miniaturized and simplified version of the full organ, which we refer to as *organoid* (Linnemann et al., 2015). Such a mammary gland organoid, grown in a collagen gel inside a Petri dish, has the following architecture. Active cells form a fluid-like tubular epithelial shell at the interface between a passive fluid in the lumen and a passive elastic solid in the surroundings (Fernández et al., 2021). Thus, the entire dynamics of the organ are driven by the activity of cells. These cells behave like anisotropic force dipoles that migrate due to an additional polar motile force. As a consequence of cell motility, the epithelium switches from collective oscillatory motion along the tube axis to collective rotations along the tube circumference. We find that this switch in motile behavior and the corresponding reorientation of the anisotropic cells leads to a shape transformation, where spherical buds form at the end of the tubular organoid ducts (Fernández et al., 2021). Such an active rearrangement of cells and the resulting shape transformations could also be at play during embryogenesis of the fruit fly *Drosophila melanogaster* (Streichan et al., 2018; Martin, 2020; Gheisari et al., 2020) or other organisms (Wozniak and Chen, 2009; Münster et al., 2019). Finally, in Section IV.2 "Between Morphogenesis and Hydrodynamic Flows", we explicitly study the hydrodynamics of a boundary-driven fluid such as in the case of mammary gland morphogenesis. Our results show that surface tension gradients and cell motility can lead to a hydraulic pressure, which overcomes the Laplace pressure, and drives outwards motion of the boundary in regions of high tension. These counterintuitive findings could pose a mechanism for a robust control of endocytosis and exocytosis in cells, through the contractility of the actomyosin cytoskeleton.

From cellular activity and tissue dynamics… These findings raise the following question: *How does collective cell behavior depend on the motility of individual cells and their coupling via intercellular adhesions?* We begin our investigation of these questions in Section III.1 "Collective Cell Dynamics in Rigid Environments", where we discuss a mesoscopic *Cellular Potts* model (Graner and Glazier, 1992) for the collective migration of actively polarizing cells on a rigid two-dimensional surface (Segerer et al., 2015; F. Thüroff et al., 2019). First, we apply our model in the context of single cell motility, collective rotations of cells in circular geometries, and wound healing (F. Thüroff et al., 2019). We find that single cells first break symmetry by polarizing, followed by a persistent random walk with ballistic motion on short timescales and diffusive motion on long timescales (F. Thüroff et al., 2019). In circular geometries, the polar cells minimize viscous shear by migrating in cohesive groups, leading to collec-

tive rotations (Doxzen et al., 2013; Segerer et al., 2015; F. Thüroff et al., 2019). Conceptually, this observation resembles the flocking of polar particles that one observes in the Vicsek model (Vicsek et al., 1995). The tendency to minimize viscous shear also explains why collective rotations of polar cells emerge in the mammary gland organoid, see Section IV.1 "Collective Cell Migration Affects Morphogenesis". Studying large extended tissues in the context of wound healing, we then find that the polarizing cells actively invade the cell-free region and pull on the trailing cells (F. Thüroff et al., 2019).

…in soft deformable environments…   However, cells in an organism migrate in a soft environment as opposed to a rigid surface, and can also respond to its mechanical properties (Discher et al., 2005). Therefore, in Section III.2 "Cell Migration and Shape in Soft Environments", we further generalize our *Cellular Potts* model by accounting for the traction stresses that cells exert on a soft substrate, and the resulting deformation thereof. Then, we investigate the impact of substrate stiffness on both single cell motility and shape. Depending on the mechanical properties of the substrate, we find qualitative differences in phenomenology, where cells behave more like persistently migrating force monopoles, self-trapping isotropic force dipoles, or elongating anisotropic force dipoles (A. Goychuk, Brückner, et al., 2018). In our *Cellular Potts* model, these effects do not rely on a control of gene expression or metabolism through extracellular matrix rigidity (Bissell and Barcellos-Hoff, 1987; C. M. Nelson and Bissell, 2006; Ge et al., 2021; Pandamooz et al., 2020; Jang et al., 2021) but arise purely as a consequence of mechanical interactions.

…to self-organization of cells.   Finally, using our *Cellular Potts* model, we test how a large population of cells should interact via the elastic substrate that they adhere to. For soft substrates, where cells behave like anisotropic force dipoles, we find that cells organize themselves into networks. Interestingly, similar networks also emerge during the *in vitro* study of angiogenesis (that is, the formation of vasculature) in tube-formation assays (Vailhé et al., 2001). Furthermore, like in our simulations, *in vitro* tube formation depends on the mechanical properties of the substrate (Saunders and Hammer, 2010; Rüdiger et al., 2020). Thus, we conclude that the cells can use the deformable substrate for long-ranged mechanical communication (Reinhart-King et al., 2008; Winer et al., 2009; Sopher et al., 2018; van Oers et al., 2014). From a purely theoretical point of view, one can understand these results via the generic tendency of anisotropic force dipoles in elastic environments to align into stringlike structures (Bischofs and Schwarz, 2003; Bischofs, S. A. Safran, et al., 2004).

In this thesis, we focus on mechanical interactions during physiological pro-

cesses. However, mechanics can also have important implications for pathological conditions such as microbial infections. For example, bacterial biofilm growth on elastic surfaces such as epithelia can lead to wrinkling (Fei et al., 2020) or even mechanical disruption (Cont et al., 2020) of the infected surface. Such morphological changes then facilitate further invasion of the bacteria into the host. To summarize, it seems evident that cell activity and mechanics play a crucial role for the dynamics of macroscopic multicellular tissues, both in development (Wozniak and Chen, 2009) and disease. In the following, we broaden this perspective by discussing how biochemical self-organization can control cellular dynamics, and thus shape. This lends to a general interplay between biochemical patterns and mechanics (Vining and Mooney, 2017; Gross et al., 2017; Hannezo and Heisenberg, 2019).

I.1.2 INTRACELLULAR SELF-ORGANIZATION

Cell activity requires biochemical signaling. So far, we have entirely focused on the macroscopic dynamics of tissues, in turn driven by the activity of cells. But what is the microscopic origin of cell activity? To answer this question, one has to take a closer look at the physiological processes that take place in cells. For example, the cell cytoskeleton plays a central role in cell migration, division, and intercellular adhesion (Théry and Bornens, 2006; Kunda and Baum, 2009; Salbreux et al., 2012; Alberts, Bray, et al., 2014; Alberts, A. Johnson, et al., 2014; Steven et al., 2016; Chugh and Paluch, 2018). Like a machine assembled from many molecular building blocks, the cytoskeleton turns chemical energy into mechanical work. The corresponding cytoskeletal forces are generated via actin polymerization and actomyosin contractility—the latter is also involved in muscle contraction hence the name (Alberts, Bray, et al., 2014; Alberts, A. Johnson, et al., 2014; Steven et al., 2016). Thus, microscopic intracellular processes not only affect tissue dynamics via cell motility, as we discuss in Chapter III "From Cellular Dynamics to Self-Organization", but can also directly lead to motion of the whole organism.

In analogy to artificial machines with an on-off switch, cytoskeletal assembly and actomyosin contractility are controlled by a myriad of regulatory proteins. For example, the Rho family of small GTPases effectively controls cell migration and shape through the cytoskeleton (Lauffenburger and Horwitz, 1996; Ridley, 2001; Ridley et al., 2003; Ridley, 2015; Lawson and Ridley, 2018). Through feedback mechanisms that involve complex reaction networks of these regulatory proteins (Hodge and Ridley, 2016), the cytoskeleton responds to extracellular mechanical stimuli (Marée, Jilkine, et al., 2006; Marée, Grieneisen, et al., 2012). In Section III.1 "Collective Cell Dynamics in Rigid Environments", we prune these regulatory networks into two prototypic feedback loops to study both sin-

gle and collective cell migration.

Apart from cell migration, small GTPases also partake in many other intracellular processes such as cell division (Théry and Bornens, 2006; Alberts, A. Johnson, et al., 2014; Alberts, Bray, et al., 2014; Steven et al., 2016). As their name suggests, GTPases catalyze the hydrolysis of high-energy guanosine triphosphate (GTP), a biochemical fuel similar to adenosine triphosphate (ATP), into low-energy guanosine diphosphate (GDP). In particular, small GTPases have two conformations, one active GTP-bound state and one inactive GDP-bound state[1] (Alberts, A. Johnson, et al., 2014). Guanine nucleotide exchange factors (GEFs) catalyze GDP release and replacement by GTP, thus switching GTPases into their active conformation (Halatek, Brauns, et al., 2018). In contrast, GTPase activating proteins (GAPs) increase the intrinsic GTP hydrolysis rate of GTPases, thus switching them into their inactive conformation (Halatek, Brauns, et al., 2018). The conformational changes of GTPases that occur during activation (effective phosphorylation via replacement of GDP by GTP) and deactivation (effective dephosphorylation via GTP hydrolysis to GDP) constitute a *molecular switch*, which is a recurrent concept in biology (Phillips, 2020). This can lead to signaling cascades, where one molecular switch "flips" another molecular switch by activating or deactivating it via phosphorylation, similar to a network of stochastic transistors. To that end, protein kinases mediate protein phosphorylation, while protein phosphatases induce protein dephosphorylation (Alberts, A. Johnson, et al., 2014). These interactions can lead to complex reaction networks such as for the Rho family of small GTPases (Hodge and Ridley, 2016).

Having two conformations enables molecular switches not only to present a *key* for turning parts of the intracellular machinery on or off, but also to transmit the required energy to do so. To maintain extended reaction networks between such molecular switches under constant protein turnover, one has to provide a constant supply of energy—but that alone is not enough. In addition, each component has to operate with efficiency close to unity to minimize the energy losses during each "flip" of the active switch state. Interestingly, in stark contrast to artificial engines, for molecular machines it is indeed possible to achieve efficiency close to unity under large thermal fluctuations (I. Goychuk, 2016). Then, however, molecular machines have to operate close to thermal equilibrium so that it is not easy to determine the axis of time for their irreversible dynamics.

Of biochemical patterns and particle fluxes. Several different types of proteins can act as a molecular switch with two conformations, and interact

---

[1] For some molecules, the GTP-bound conformation is inactive and the GDP-bound conformation is active (Alberts, A. Johnson, et al., 2014).

with other proteins to form reaction networks. Non-trivial reaction dynamics, together with protein diffusion, then leads to the formation of intracellular patterns (Halatek, Brauns, et al., 2018) as was first recognized by Alan Turing (Turing, 1952). In the past decades, several prominent examples of biological pattern formation have spurred research. For example, the Rho family of GTPases is involved in the regulation of the eukaryotic cytoskeleton, as mentioned above (Lauffenburger and Horwitz, 1996; Ridley, 2001; Ridley et al., 2003; Ridley, 2015; Lawson and Ridley, 2018). In particular, the Cdc42 family of GTPases, a subfamily of the Rho GTPases, plays a role in determining the position of a new growth zone or bud site in *Saccharomyces cerevisiae* (D. I. Johnson, 1999). Likewise, PAR proteins are key players for defining the anteroposterior axis of the embryo in *Caenorhabditis elegans* (Goldstein and Macara, 2007; Lang and Munro, 2017).

But intracellular regulation is not a special property that is reserved for eukaryotic cells. Rather, regulation is a signature of life in general, and thus also takes place in prokaryotes. In this context, the bacterium *Escherichia coli* is a paradigmatic model organism where Min protein oscillations were linked to the correct placement of the bacterial division axis (de Boer et al., 1989; Hu and Lutkenhaus, 1999; Raskin and de Boer, 1999; Lutkenhaus, 2007; Ramm, Heermann, et al., 2019). At its heart, the Min system consists of only two proteins, the ATPase MinD and the ATPase activating protein MinE (Raskin and de Boer, 1999; Loose, Fischer-Friedrich, Ries, et al., 2008). The ATPase MinD, in analogy to GTPases, has an active ATP-bound state and an inactive ADP-bound state (Huang et al., 2003; Halatek and Frey, 2012). In the cytosol, MinD is activated by binding ATP. Then, active MinD cooperatively binds to the bacterial membrane, where it forms a positive feedback loop by recruiting even more MinD from the cytosol (Huang et al., 2003; Halatek and Frey, 2012). Furthermore, membrane-bound MinD also recruits the ATPase activating protein MinE from the cytosol, thereby forming a MinDE complex with a high rate of ATP hydrolysis (Huang et al., 2003; Halatek and Frey, 2012). Finally, this ATP hydrolysis leads to the inactivation of MinD via the loss of a phosphate group, and the inactivated MinDE complex detaches from the bacterial membrane (Huang et al., 2003; Halatek and Frey, 2012). Interestingly, MinE itself also has two conformations that regulate its activity (Park, W. Wu, et al., 2011; Park, Villar, et al., 2017; Denk et al., 2018), thus making it a molecular switch. This property of MinE is crucial for the robustness of MinDE patterns across a wide regime of MinE to MinD concentration ratios (Denk et al., 2018).

To summarize, the different interactions between MinD, MinE, and the membrane lead to reactive fluxes with a continuous particle exchange between active membrane-bound proteins and inactive cytosolic proteins. These reactive fluxes then build up protein density gradients on the membrane and in the cytosol. In

turn, protein density gradients correspond to diffusive fluxes, thus leading to a closed cycle of fluxes that is driven by particle exchange. These relatively simple microscopic dynamics lead to a broad range of phenomena. In the bacillus (that is, rod-shaped bacterium) *Escherichia Coli*, one observes pole to pole oscillations (Hu and Lutkenhaus, 1999; Raskin and de Boer, 1999; Hale et al., 2001; F. Wu et al., 2015). When reconstituting the Min system *in vitro*, one observes traveling waves or stationary patterns on planar membranes (Loose, Fischer-Friedrich, Ries, et al., 2008; Vecchiarelli et al., 2016; Glock et al., 2019). In geometric confinement *in vitro* that is similar to the shape of the bacterium *Escherichia Coli*, one finds oscillations and striped patterns (Zieske and Schwille, 2014; Caspi and Dekker, 2016).

Yet there is more to these non-equilibrium protein dynamics than initially met the eye, as they were shown to regulate the localization of passive and unrelated molecules (Ramm, Glock, et al., 2018; Shih et al., 2019). In Section II.2 "Protein Fluxes Induce Generic Transport of Cargo", we trace this observation back to a diffusiophoretic effect: the diffusive fluxes of membrane-bound proteins confer an effective mesoscopic friction that acts on other membrane-bound molecules, thus inducing their directed molecular transport (Ramm, A. Goychuk, et al., 2021). It would be interesting to see whether such an unspecific mechanical coupling between proteins can lead to alignment or synchronization of biochemically distinct pattern-forming systems when placed in the same geometry.

Of activity and form, yet again.   Interestingly, the Min system was also shown to induce deformations in giant unilamellar vesicles (Litschel et al., 2018; Fu et al., 2021). Together with the transport of passive and unrelated molecules, these findings suggest that pattern-forming systems of molecular switches such as Min proteins can perform mechanical work without relying on specialized proteins. Similarly, several polymers and proteins can induce membrane bending (Ford et al., 2002; Tsafrir et al., 2003; Lee et al., 2005; Gov and Gopinathan, 2006; Zimmerberg and Kozlov, 2006; Prinz and Hinshaw, 2009; Stachowiak et al., 2012; McMahon and Boucrot, 2015; Jarsch et al., 2016; Gov, 2018; Yuan et al., 2021), including proteins that contain Bin/Amphiphysin/Rvs (BAR) domains (Zimmerberg and McLaughlin, 2004; Peter et al., 2004; Bhatia et al., 2009; Mim and Unger, 2012; Zhu et al., 2012; Prévost et al., 2015; Simunovic et al., 2015). Taking a closer look at the mechanochemical coupling between proteins and a membrane, in Section II.1 "Mechanochemical Coupling between Proteins and Membranes" we find that membrane-bending proteins have the capacity to induce self-recruitment, by cooperatively deforming the membrane into a binding-favorable configuration. However, cell shape and membrane deformations are not only induced by membrane-binding proteins but also driven by the

actin cortex (Salbreux et al., 2012; Chugh and Paluch, 2018), which can generate intracellular flows by contracting. The actin cortex and its ability to generate active cytoskeletal forces is in turn regulated by the Rho family of GTPases, which can for example result in cell migration (Lauffenburger and Horwitz, 1996; Ridley, 2001; Ridley et al., 2003; Ridley, 2015; Lawson and Ridley, 2018). Taken together, this leads to a general coupling between mechanics, hydrodynamics and chemistry on the microscale (Goehring, Trong, et al., 2011; Goehring and Grill, 2013; Schiffhauer and Robinson, 2017; Mietke, Jemseena, et al., 2019; Mietke, Jülicher, et al., 2019), analogous to mechanochemical interactions during morphogenesis (Vining and Mooney, 2017; Gross et al., 2017; Petridou, Spiró, et al., 2017; Brinkmann et al., 2018; Recho et al., 2019; Hannezo and Heisenberg, 2019).

On a final note, reaction-diffusion systems typically sense the geometry that they are placed in (Halatek and Frey, 2012; F. Wu et al., 2015; Thalmeier et al., 2016; Eroumé et al., 2021). Then, any mechanochemical coupling also directly implies feedback mechanisms between biochemical patterns and geometry. Such feedback mechanisms could occur during the surface contraction waves that starfish oocytes of the species *Patiria miniata* exhibit, which are guided by geometry (Wigbers et al., 2021). In Section I.3 "A Foundation for Patterns in Adapting Organisms", we recapitulate important concepts from differential geometry for describing such a coupling between geometry and biochemical pattern formation. These concepts also prove useful in the context of mammary gland morphogenesis in Section IV.1 "Collective Cell Migration Affects Morphogenesis" and Section IV.2 "Between Morphogenesis and Hydrodynamic Flows".

I.1.3   AN APPROACH TO RECONCILE DISPARATE SCALES

In the introduction so far, we have seen that living beings consist of smaller subunits, each with its own dynamics. These constituents can be as tiny as single ions, much larger molecules such as proteins or can even be as large as whole cells or clusters of cells. The human body, for example, is a dynamic assembly of roughly 4×10^{14} cells (Milo and Phillips, 2015), each containing up to 1×10^9 proteins (Milo and Phillips, 2015) and many more other particles such as water molecules. In turn, these small subunits then interact and form complex biological patterns across vastly different orders of magnitude in both space and time. It is this cascade of different patterns and intertwining machineries that gives rise to the complexity of life (Fig. I.1). Looking at the broader concepts, one finds that there is some degree of recursion in life—both function-wise and structure-wise.

Recursion in function. As our introduction illustrates, mechanochemical interactions are an example of a common theme both for microscopic self-organization and for macroscopic morphogenesis. To further investigate the role of mechanochemical interactions in biology, we take a two-fold approach of descriptive and complementary methods: (i) starting from experimental observations, we seek a minimal theoretical explanation thereof, and (ii) by combining different theoretical concepts, we make predictions that can be tested against experiments. Our goal is to explore different biological processes, which give life its amazing ability to self-organize by consuming energy.

Recursion in structure. Biological organisms are subdivided into different functional subunits, organs and tissues, which consist of smaller organisms, cells. In turn, these cells are subdivided into organelles and other intracellular structures, which consist of proteins and lipids. Then, one can draw some parallels when comparing naturally occurring life to artificial machines. Both require a power supply to maintain their operation and both are similarly made up of smaller subsystems like gears, springs, hydraulics, levers, motors, and controllers. But there are also striking differences between artificial machines and living beings, as the latter actively adapt to their environment by reorganizing their functional subunits. Moreover, in contrast to artificial machines, an extended interruption of operation means permanent death[2].

In the following, we use these similarities to cast different pattern-forming systems into a common language. We make no explicit distinction between living organisms and artificial machines, and instead refer to both as "active matter" or "active systems". A single active system is then simply an "active agent". We begin by discussing in Section I.2 "The Fuel for Self-Organization" how an active system is driven out of equilibrium, from a thermodynamic point of view. This makes active matter fundamentally different from "passive matter", which is inanimate or dead. We then illustrate these concepts on a rudimentary pattern that occurs in biology, a density difference between two membrane-separated compartments. To provide a specific biological example, we finally consider how plants generate biochemical fuel from electromagnetic energy.

---

[2] Some organisms can survive or even thrive in extreme conditions, such as extremophiles (Rothschild and Mancinelli, 2001). This includes multicellular organisms, as tardigrades can even survive in space (Jönsson et al., 2008).

I.2 THE FUEL FOR SELF-ORGANIZATION

I.2.1 A THERMODYNAMIC PERSPECTIVE ON ACTIVITY

To illustrate how active matter is driven out of equilibrium, we consider a semi-closed active system with a selectively permeable boundary, in an environment at constant temperature T. The active system takes up chemical energy from its environment via particle exchange δN_i and converts this chemical energy into mechanical work[3] δW. In turn, mechanical work ultimately dissipates into the environment via friction and the generation of heat δQ. All of these processes correspond to fluxes of physical quantities across the selectively permeable boundary and can change the internal energy of the active system by δU. The active system must then obey the following energy conservation equation (Landau and Lifshitz, 1980):

$$\delta U + \delta W = \sum_i \mu_i \, \delta N_i + \delta Q \,, \tag{I.1}$$

where μ_i is the chemical potential of a fuel or waste product. Here, we have flipped the conventional sign in front of δW to clarify that the system performs work on the environment and not the other way around. According to the Clausius inequality, $\delta Q \leq T \, \delta S$, the heat production is bounded from above by the entropy production δS weighted with the system temperature T. Note that individual molecular motors and proteins that partake in signaling events can in principle operate with efficiency close to unity (I. Goychuk, 2016). This indicates that the corresponding processes occur close to thermal equilibrium, so that $\delta Q \simeq T \, \delta S$. However, if we do not have a grasp on the entropy of the system and its environment, then this Eq. (I.1) leaves us little further insight.

The story is different if we perform a Legendre transformation of the internal energy U with the two conjugated variables of entropy S and temperature T. Then, the activity of the system corresponds to changes in the Helmholtz free energy $F = U - TS$, given by (Landau and Lifshitz, 1980):

$$\delta F + \delta W \leq \sum_i \mu_i \, \delta N_i - S \, \delta T \,. \tag{I.2}$$

We assume that the active system is in homeostasis, and that it maintains a constant temperature[4], so that $\delta T = 0$. Thus, one finds *a posteriori* that the Helmholtz free energy corresponds to the maximal amount of energy that the

---

[3] Such an active system could be an animal, for example. Note that plants also take up electromagnetic energy and convert it into chemical energy.

[4] In a more general setting, one should also account for the heat generation due to biological processes. Then, one would have to explicitly model the flow of heat.

system can transform into mechanical work. However, Eq. (I.2) still accounts for many processes that seemingly take place at the same time, where the active system (i) stores free energy δF, for example through mechanical deformations, (ii) performs mechanical work δW against some either passive or active material, (iii) exchanges particles δN_i with chemical potential μ_i with the environment, and (iv) possibly interconverts different particle species via metabolic reactions.

Now, we disentangle Eq. (I.2) by defining pairs of *conjugated processes*. As we have seen in the introduction so far, a living being is not an unstructured soup where various possibly unrelated processes occur at the same time. Instead, an organism is a well-organized soft machine, which is assembled of different coupled functional components. These components are in turn regulated by cascades of signaling networks. Because of this modular structure and temporal order of events, we split the organism into several subsystems that can be either active or passive, each with one task only. For example, the active actomyosin cytoskeleton converts chemical energy in the form of fuel (that is, ATP) into work and depleted fuel (that is, ADP), $\delta W = (\mu_{ATP} - \mu_{ADP})\,\delta N_{ATP}$. This work can be dissipated via molecular friction. Analogously, the passive elastic membrane can store mechanical work in elastic deformations, $\delta F + \delta W = 0$. Many proteins such as ATP have an active configuration P_i^* and an inactive configuration P_i° and are thus molecular switches (Phillips, 2020). Then, signaling events between different molecular switches correspond to molecular work δW that one switch performs to activate or inactivate a different switch. Such a change of state is equivalent to a chemical potential change of the molecule.

Finally, we note that defining such conjugated processes is analogous to having only pairwise interactions on a molecular scale. Different conjugated processes can then interact via (imaginary) spatial boundaries or reactive boundaries, where the latter differentiates between two systems at the same position. Next, we apply these ideas to a rudimentary biological pattern, crucial for the fuel supply that powers living organisms.

I.2.2 CONJUGATED PROCESSES DURING FUEL GENERATION

Density differences of solute particles between two sides of a membrane (Fig. I.2a) are as crucial for life on Earth as they are ubiquitous. For a semipermeable membrane, such density differences correspond to an osmotic pressure drop that gradually equilibrates via osmotic solute and solvent fluxes (Marbach and Bocquet, 2019), thereby dissipating energy through friction. In contrast, cells have a tight grip on these fluxes and use them in various physiological processes, tightly regulating their volume as well as the concentration differences across their membranes (Kay, 2017).

In this section, we illustrate how living organisms can make use of such density differences to generate biochemical fuel. In spirit of the discussion in the previous section, we consider the solutions on each side of the membrane as ideal and well-mixed lattice gases where each particle has the same size. The compartments on each side of the membrane, which we denote with the index "$\pm$", have $N_\pm$ available lattice sites of molecular volume v, respectively. The solute occupies a fraction $\theta_\pm$ of the available space in each compartment, which corresponds to $N_\pm^* \equiv \theta_\pm N_\pm$ lattice sites. The solvent fills the remainder of the available space, $1 - \theta_\pm$, which corresponds to $N - N_\pm^*$ lattice sites. Then, each compartment has the following free energy[5]:

$$F_\pm = N_\pm\, k_B T\left[\theta_\pm \ln(\theta_\pm) + (1 - \theta_\pm)\ln(1 - \theta_\pm)\right]. \qquad \text{(I.3)}$$

Now suppose that we take one solute particle from compartment "$-$" and put it in compartment "$+$". With the density of solutes given by $c_\pm := \theta_\pm/v$, this would change the free energy of each compartment by

$$\pm\mu_\pm = \pm\frac{\partial F_\pm}{\partial N_\pm^*} = \pm\frac{\partial}{\partial c_\pm}\left(\frac{F_\pm}{N_\pm v}\right) = \pm k_B T\left[\ln(c_\pm v) - \ln(1 - c_\pm v)\right], \qquad \text{(I.4)}$$

which corresponds to the chemical potential of the solute particle. One can simplify Eq. (I.4) if the density of solutes is sufficiently small, so that their occupied volume fraction is negligible, $c_\pm v \ll 1$. To that end, we define the density in each compartment as the deviation from a mean value, $c_\pm = c_0 \pm \Delta c/2$. Then, we perform a Taylor expansion up to first order in small concentration differences, $\Delta c \ll c_0$, to obtain an approximate chemical potential difference of $\Delta\mu = \mu_+ - \mu_- = -k_B T \Delta c/c_0$ between the two compartments. Thus, by exchanging particles between the two compartments, we can either store or extract energy in the system by increasing or decreasing its free energy, respectively. Note that for charged particles such as protons, moving the particles against an electrostatic potential difference also stores additional energy proportional to their charge.

Cells do precisely this. For example, plants and cyanobacteria use proton pumps to build up an electrochemical potential difference between the two sides of the thylakoid membranes (Reece et al., 2014; Phillips, Kondev, et al., 2012; Alberts, Bray, et al., 2014; Alberts, A. Johnson, et al., 2014; Steven et al., 2016). This process is fueled by the absorption of sunlight (electromagnetic energy) at photosystems I and II (Reece et al., 2014; Phillips, Kondev, et al., 2012; Alberts, Bray, et al., 2014; Alberts, A. Johnson, et al., 2014; Steven et al., 2016). The latter also splits water into protons, which further contribute to the electrochemical potential difference, and oxygen as a byproduct (Reece et al., 2014; Phillips, Kondev,

---

[5] For polymer solutions, one would formulate a Flory-Huggins theory with an appropriate polymer size factor (Huggins, 1941; Flory, 1942; de Gennes, 1979).
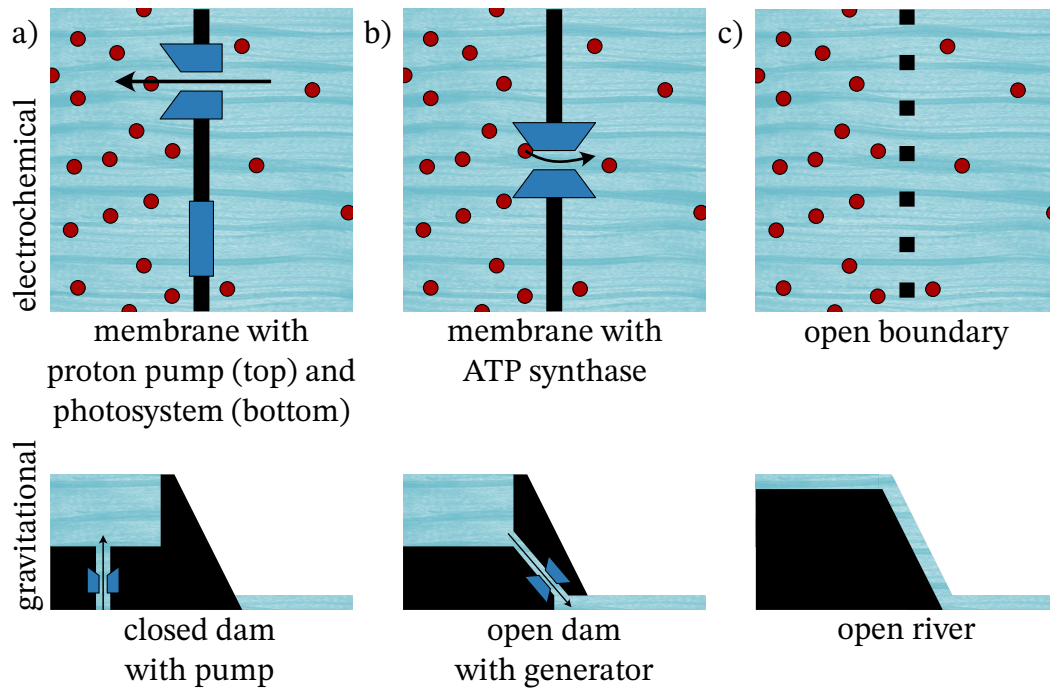
Figure I.2: Exemplary uses of potential differences. Top row: Microscopic intracellular systems. a) Cells build up an electrochemical potential difference between two compartments separated by a membrane. b) By permitting particles (that is, protons; oversized depiction in red) to pass through ATP synthase proteins (depicted in blue), cells exploit the electrochemical potential difference to convert ADP into ATP. c) Without a membrane, particle density gradients relax via diffusion. Bottom row: Analogous macroscopic systems, where energy is not stored in electrochemical potential differences but in gravitational potential differences.

et al., 2012; Alberts, Bray, et al., 2014; Alberts, A. Johnson, et al., 2014; Steven et al., 2016). However, proton pumps can also be driven directly by light, such as bacteriorhodopsin[6] in archaea (Phillips, Kondev, et al., 2012; Alberts, Bray, et al., 2014; Alberts, A. Johnson, et al., 2014), or by chemical reactions such as in mitochondria (Reece et al., 2014; Phillips, Kondev, et al., 2012; Alberts, Bray, et al., 2014; Alberts, A. Johnson, et al., 2014; Steven et al., 2016). Thus, the two conjugated processes in this case correspond to (i) taking up chemical or electrodynamic energy from the environment, and (ii) storing it in the free energy of the system. This is analogous to a dam (or, more precisely, a pumped-storage power plant), where one can store energy by increasing the amount of accumu-

---

[6] Like many biomolecules, bacteriorhodopsin is also a molecular switch (Phillips, 2020), which takes on an excited configuration after photon absorption.

lated water against the gravitational potential (Fig. I.2, bottom row).

Conversely, in a hydroelectric dam one can also extract the stored energy by permitting water flow through a turbine connected to a generator (Fig. I.2b). Cells do precisely this. After building up an electrochemical potential difference between two sides of a membrane, cells harvest this potential difference by allowing proton fluxes through a biomolecule called ATP synthase. Across the channel length of the ATP synthase, L, there is then an average chemical potential gradient $\Delta\mu/L$, which corresponds to a thermodynamic force. Similar arguments apply for the electrostatic potential difference, which we here neglect for simplicity. According to Onsager's theory of non-equilibrium thermodynamics (Balian, 2007), these thermodynamic forces induce a particle flux, $j = -c_0\,\Delta\mu/(\xi L)$, against the resistance of the ATP synthase, ξ. The ATP synthase is an all-in-one turbine and generator, which draws on the proton fluxes to power the phosphorylation of ADP to ATP, thereby storing chemical energy (Reece et al., 2014; Phillips, Kondev, et al., 2012; Alberts, Bray, et al., 2014; Alberts, A. Johnson, et al., 2014; Steven et al., 2016). Conceptually, this corresponds to an inversion of the two conjugated processes that we have sketched in the previous paragraph: (i) take free energy from the system, and (ii) store it as chemical energy in a biochemical fuel.

The biomolecule ATP then serves as the fuel for the formation of all biological patterns. Therefore, one can conceptually represent the biomolecule ATP as an activated fuel F^* and the biomolecule ADP as a depleted fuel F°. Cells use activated fuel to phosphorylate inactive proteins P° into an activated configuration P^* (or vice versa), which we can represent with the following simplified exchange reaction scheme:

$$P^\circ + F^* \longrightarrow P^* + F^\circ\,.$$
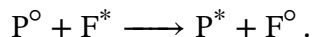
The difference between activated fuel (ATP) and depleted fuel (ADP) is that the former has one phosphate group more than the latter.

I.2.3 FROM OSMOTIC PRESSURE DIFFERENCES TO DIFFUSION

In the previous section, we have considered a density difference between two membrane-separated compartments. We have linked this density difference with a chemical potential gradient, across a channel that connects these two compartments. Then, we have calculated the resulting solute fluxes through this channel. Now, we remove the membrane and instead consider density gradients in solution (Fig. I.2c). We tessellate the solution into infinitesimal compartments with imaginary boundaries. In each compartment, the chemical potential

of a solute particle is given by Eq. (I.4). Adjacent compartments can have different compositions, which leads to chemical potential gradients (that is, thermodynamic forces). As before, thermodynamic forces induce particle fluxes according to Onsager's theory of non-equilibrium thermodynamics (Balian, 2007):

$$j = -c\frac{\nabla\mu}{\xi} = -\frac{k_B T}{\xi}\frac{1}{1 - vc}\nabla c\,, \tag{I.5}$$

where ξ is now the (Stokes) friction of a particle with the embedding fluid, and v is the molecular volume. If the solute particles are present at small density and occupy a negligible volume fraction, $c_{\pm}v \ll 1$, then one recovers Fick's first law of diffusion, $j = -D\nabla c$, by taking into account the Einstein relation, $D = k_B T/\xi$.

I.2.4 A Primer on the Calculus of Variations

Finally, as a last warm-up exercise, we give a short primer on the calculus of variations. These concepts frequently recur in the remainder of the thesis and are crucial for its understanding. For a more extensive treatise, we refer to (Gelfand and Fomin, 2000; Courant and Hilbert, 2004).

In the previous two sections, we have considered the mixing free energy of a (locally) well-mixed ideal fluid, to derive its local chemical potential. Specifically, suppose that we spatially arrange different infinitesimal compartments, each possibly having a different local density of solute particles, $c(\boldsymbol{x})$. The total free energy of the system is then given by the functional $F[c] = \int d^3\boldsymbol{x}\, f(c(\boldsymbol{x}))$, where $f \equiv F_{comp}/V_{comp}$ is the free energy density of a compartment. Since the free energy only depends on the local values of the density variable, $c(\boldsymbol{x})$, in Paragraph "Conjugated Processes During Fuel Generation" we were easily able to calculate the independent chemical potential in each infinitesimal compartment, Eq. (I.4). This chemical potential indicates how a local addition or removal of one particle will affect the free energy of the whole system.

Now, let us switch to different state variables, say, $u(\boldsymbol{x})$, for which the free energy functional has a more complicated form[7]:

$$F[u] = \int d^3\boldsymbol{x}\, f(u(\boldsymbol{x}), \nabla u(\boldsymbol{x}), \nabla^2 u(\boldsymbol{x}), \dots)\,. \tag{I.6}$$

Such a free energy functional naturally arises in elasticity theory, for example. Variational calculus then amounts to asking the following question: *How will a*

---

[7] The following discussion remains fully valid if the free energy functional also depends on other state variables. Then, one would consider changes in one state variable at a time independently of all other state variables. Constraints on the variables, such as conservation laws, can then be imposed *a posteriori*. In this way, one can also extend the discussion to vector-valued or tensor-valued state variables.

slight change (that is, a variation) in the position-dependent state variable affect the free energy functional of the whole system? To answer this question, one has to first formalize what a variation means. Specifically, we consider a *smooth localized* change of the state variable,

$$u(\boldsymbol{x}) \to u(\boldsymbol{x}) + \delta u(\boldsymbol{x}), \tag{I.7}$$

where $\delta u(\boldsymbol{x})$ is maximal at some position $\boldsymbol{x}_0$ and decays to zero at some infinitesimal distance ε away from this position:

$$\delta u(\boldsymbol{x}) = 0 \quad \forall \boldsymbol{x} : \ \|\boldsymbol{x} - \boldsymbol{x}_0\| \geq \varepsilon. \tag{I.8}$$

With its smoothness property, we imply that the variation $\delta u(\boldsymbol{x})$ is infinitely differentiable, and that its derivatives also vanish at the distance ε. Now, we can determine how the functional, Eq. (I.6), changes upon such a variation. To that end, we perform a Taylor expansion of the integrand[8] in Eq. (I.6), and find:

$$\delta F = \int d^3\boldsymbol{x} \left[\frac{\partial f}{\partial u}\bigg|_{\boldsymbol{x}_0} \delta u + \frac{\partial f}{\partial(\boldsymbol{\nabla} u)}\bigg|_{\boldsymbol{x}_0} \cdot \boldsymbol{\nabla}(\delta u) + \frac{\partial f}{\partial(\boldsymbol{\nabla}^2 u)}\bigg|_{\boldsymbol{x}_0} \boldsymbol{\nabla}^2(\delta u) + \dots \right]. \tag{I.9}$$

Here, we have defined $\delta F[u] := F[u+\delta u] - F[u]$. After integrating by parts twice, and then using the localization Eq. (I.8) as well as the smoothness property of the variation δu, one arrives at (Gelfand and Fomin, 2000; Courant and Hilbert, 2004):

$$\delta F = \int d^3\boldsymbol{x} \left[\frac{\partial f}{\partial u} - \boldsymbol{\nabla} \cdot \frac{\partial f}{\partial(\boldsymbol{\nabla} u)} + \boldsymbol{\nabla}^2 \frac{\partial f}{\partial(\boldsymbol{\nabla}^2 u)} - \dots \right]_{\boldsymbol{x}_0} \delta u. \tag{I.10}$$

Then, one defines the term in the square brackets as the *functional derivative* $\delta F/\delta u$. Functional derivatives and calculus of variations will be our faithful companions in the following chapters, which allow us to ask: *What happens if we poke an organism?*

---

[8] Note that we here imply $\frac{\partial f}{\partial(\nabla u)} \cdot \boldsymbol{\nabla}(\delta u) \equiv \sum_i \frac{\partial f}{\partial(\partial_i u)} \partial_i(\delta u)$.

I.3 A FOUNDATION FOR PATTERNS IN ADAPTING ORGANISMS

In this technical section, we review several key concepts of differential geometry and tensor calculus. We frequently apply these concepts to three-dimensional bodies and two-dimensional surfaces in the remainder of the thesis. With these tools in hand, in the main part of the thesis we then go on to discuss several problems involving elasticity theory and fluid mechanics, in a geometric context. There are several books (Kreyszig, 1959; Lebedev and Cloud, 2003; Pressley, 2010; Frankel, 2011; Grinfeld, 2013; Tu, 2017) and reviews (Kamien, 2002; Deserno, 2015) that give an extensive treatment of differential geometry and tensor calculus. Analogously, there is also extensive literature on elasticity theory (Timoshenko and Gere, 1961; Amenzade, 1979; Landau, Pitaevskii, et al., 1986; Lai et al., 2010; Murea, 2018), fluid mechanics (Landau and Lifshitz, 1987; Lai et al., 2010; Murea, 2018), and membrane mechanics (Seifert, 1997; Kamien, 2002; S. Safran, 2003; D. Nelson et al., 2004; Deserno, 2015; Guckenberger and Gekle, 2017). Here, our main goal is to establish a self-contained mathematical common ground that will accompany us through the remaining chapters. As our second goal, we aim to give an intuitive understanding of the underlying mathematical and physical concepts. To that end, we use index notation only where necessary, and give all important results in index-free notation where possible.

We first set up a mathematical representation of a static geometry in an arbitrary curvilinear coordinate system. Then, we turn to the calculus of variations, see Section I.2.4 "A Primer on the Calculus of Variations", as a means to describe changes in the geometry. We frequently present simple examples, mostly for cylindrical and spherical geometries. In particular, we apply the results for cylindrical geometries in Section IV.1 "Collective Cell Migration Affects Morphogenesis" and Section IV.2 "Between Morphogenesis and Hydrodynamic Flows".

I.3.1 EXTRINSIC AND INTRINSIC COORDINATE SYSTEMS

Laboratory frame.   From an abstract point of view, an actively moving organism is equivalent to a deforming geometry. To describe this geometry and all active agents (for example, cells or myosin motors) within, we make an important distinction between *three* coordinate systems, which we explain in this section. The *extrinsic* coordinate system refers to the laboratory frame, or *Eulerian frame*, in which the deforming geometry is embedded. Thus, we will also frequently refer to the laboratory frame as *embedding*. Based on this laboratory frame, as the

observers that we are, we can define and measure reference coordinates for all active agents and geometric landmarks in the deforming geometry. Specifically, we choose a three-dimensional Cartesian coordinate system, which is spanned by an orthonormal basis with basis vectors $\hat{\boldsymbol{e}}_i$. The position of any point in the laboratory frame in then specified by a three-component vector:

$$\boldsymbol{x} = \sum_i x_i \, \hat{\boldsymbol{e}}_i \equiv \left[\!\!\left[\begin{array}{c} x_1 \\ x_2 \\ x_3 \end{array}\right]\!\!\right], \tag{I.11}$$

where the double-struck braces indicate embedding coordinates. This embedding provides us not only with reference coordinates, but also with an intuition of length. Specifically, the distance between a particle "1" and a particle "2" is given by their Euclidean distance, $\Delta\boldsymbol{x}_{12} = \|\boldsymbol{x}_2 - \boldsymbol{x}_1\|$.

Co-moving frame. In contrast, an *intrinsic* coordinate system refers to the co-moving frame, or *Lagrangian frame*, of some tracer particle in the deforming geometry. This tracer particle can be an active agent, a material coordinate of some passive substance, or a geometric landmark. In the co-moving frame, we assign local coordinates to the tracer particle and all points that lie in its vicinity. We distinguish between two types of tracer particles, which (i) are either in the body of our geometry ("bulk"), or (ii) lie on the boundary of our geometry ("surface"). Therefore, in general, we need two sets of intrinsic coordinate systems:

$$\boldsymbol{\omega}_\bullet \equiv \left[\begin{array}{c} \omega_\bullet^1 \\ \omega_\bullet^2 \\ \omega_\bullet^3 \end{array}\right], \quad \text{and} \quad \boldsymbol{\omega}_\circ \equiv \left[\begin{array}{c} \omega_\circ^1 \\ \omega_\circ^2 \end{array}\right], \tag{I.12}$$

where $\boldsymbol{\omega}_\bullet \in \mathbb{R}^3$ refers to the bulk coordinates and $\boldsymbol{\omega}_\circ \in \mathbb{R}^2$ refers to the boundary coordinates. Having two intrinsic coordinate systems can lead to a double

EXAMPLE 1: INTRINSIC COORDINATES

Cylindrical Coordinates	Spherical Coordinates
One describes cylindrical coordinates via the radial distance r to the centerline, the axial coordinate z, and the azimuthal angle ϕ:	One describes spherical coordinates via the radial distance r to the center point, the azimuthal angle θ and the polar angle ϕ:
$$\boldsymbol{\omega}_\bullet \equiv \left[\begin{array}{c} r \\ z \\ \phi \end{array}\right], \quad \text{and} \quad \boldsymbol{\omega}_\circ \equiv \left[\begin{array}{c} z \\ \phi \end{array}\right].$$	$$\boldsymbol{\omega}_\bullet \equiv \left[\begin{array}{c} r \\ \theta \\ \phi \end{array}\right], \quad \text{and} \quad \boldsymbol{\omega}_\circ \equiv \left[\begin{array}{c} \theta \\ \phi \end{array}\right].$$

allocation of mathematical symbols, since any physical quantity can be defined either in the bulk or on the boundary. To avoid ambiguity, we use "●" as an indicator for quantities in the bulk of the geometry. Analogously, we use "○" as an indicator for quantities on the surface of the geometry. We drop these indicators in cases where there is no ambiguity in interpretation, or in contexts that apply identically to both coordinate systems.

Both the bulk and the boundary of our geometry are embedded in the laboratory frame. Therefore, any point coordinate ω in the co-moving frame of a tracer particle must have a corresponding position x in the extrinsic coordinate system. In return, any position in the extrinsic coordinate system also has at least one point coordinate assigned to it in the co-moving frame. We refer to this relation as a local chart, with a local surjective mapping (see Fig. I.3):

$$\Gamma : \omega \mapsto x . \tag{I.13}$$

With *local* we mean that the co-moving frames of different tracer particles can have different charts. As an example, one can imagine two nearby active agents that explore and draw their own charts of their surroundings, but use different landmarks and different length measures. Then, the local coordinate system of one active agent does not naturally match the coordinate system of the other active agent. Instead, both coordinate systems have to be stitched together where they meet. For the two active agents to have matching charts, they have

EXAMPLE 2: MAPPING

Cylindrical Coordinates	Spherical Coordinates
The bulk mapping is given by:	The bulk mapping is given by:
$$\Gamma_\bullet(\omega_\bullet) = \left[\!\!\left[\begin{matrix} r \cos(\phi) \\ r \sin(\phi) \\ z \end{matrix}\right]\!\!\right].$$	$$\Gamma_\bullet(\omega_\bullet) = \left[\!\!\left[\begin{matrix} r \sin(\theta) \cos(\phi) \\ r \sin(\theta) \sin(\phi) \\ r \cos(\theta) \end{matrix}\right]\!\!\right].$$
For any coordinate (r, z, ϕ), the distance from the center must lie within the domain bounds, $r \leq R(z, \phi)$. The boundary mapping is then given by:	For any coordinate (r, θ, ϕ), the distance from the center must lie within the domain bounds, $r \leq R(\theta, \phi)$. The boundary mapping is then given by:
$$\Gamma_\circ(\omega_\circ) = \left[\!\!\left[\begin{matrix} R(z, \phi) \cos(\phi) \\ R(z, \phi) \sin(\phi) \\ z \end{matrix}\right]\!\!\right].$$	$$\Gamma_\circ(\omega_\circ) = \left[\!\!\left[\begin{matrix} R(\theta, \phi) \sin(\theta) \cos(\phi) \\ R(\theta, \phi) \sin(\theta) \sin(\phi) \\ R(\theta, \phi) \cos(\theta) \end{matrix}\right]\!\!\right].$$
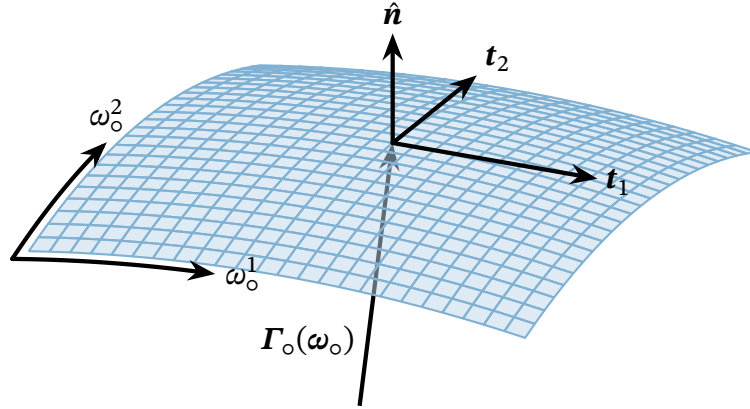
Figure I.3: Parameterization of a two-dimensional surface in a three-dimensional Cartesian embedding. This surface is defined by a local surjective mapping $\boldsymbol{\Gamma}_\circ(\boldsymbol{\omega}_\circ): \mathbb{R}^2 \mapsto \mathbb{R}^3$, and is locally spanned by two tangent vectors $\boldsymbol{t}_1$ and $\boldsymbol{t}_2$. In later sections, we extend the local non-orthonormal coordinate system on the surface with the local unit normal vector $\hat{\boldsymbol{n}}$. Then, we can not only describe the position of objects on the surface, but can also describe the position of objects near the surface.

to agree on common navigation points (for example, celestial objects). Alternatively, they could also rely on an external observer (like a satellite) to define an extrinsic coordinate system.

Now suppose that a geometry is defined by several charts, each having an intrinsic coordinate system $\boldsymbol{\omega}_i \in \Omega_i$ with domain Ω_i, and a corresponding mapping $\boldsymbol{\Gamma}_i$ to the embedding. Then, the *image* of this geometry is given by the union of all its extrinsic coordinates in the laboratory frame:

$$X = \bigcup_i \left\{ \boldsymbol{\Gamma}(\boldsymbol{\omega}_i) \,\middle|\, \boldsymbol{\omega}_i \in \Omega_i \right\}. \tag{I.14}$$

The boundary image is simply given by the boundary of the bulk image, $X_\circ = \partial X_\bullet$. Finally, note that one particular geometry can have many different mappings that share the same image and thus the same shape. This *freedom of choice* for the representation of the geometry allows us to make extensive use of transformations that alter some local chart, see Section I.3.4 "Physical Quantities in Curvilinear Coordinates".

The metric encodes the concept of length. So far, we have defined the bulk and the boundary of our geometry, setting the stage for the shape and mechanochemical dynamics of the organism. In doing so, we have distinguished between extrinsic coordinates in the embedding (laboratory frame)

and intrinsic coordinates in the co-moving frame of some tracer particle. Next, we explain how to measure lengths in this co-moving frame.

To that end, we place ourselves as observers into the co-moving frame of the tracer particle. From our perspective, we keep track of two nearby particles[9] labeled "1" and "2". Not knowing that the nearby particles can move, we choose them as landmarks with immutable intrinsic coordinates: particle "1" has coordinates $\boldsymbol{\omega}$ and particle "2" has coordinates $\boldsymbol{\omega} + d\boldsymbol{\omega}$. This argument can be extended to an arbitrary number of particles in the vicinity. Then, the motion of all particles is encoded in the surjective mapping $\boldsymbol{\Gamma}(\boldsymbol{\omega})$, which defines their (extrinsic) position in the laboratory frame. Meanwhile, the intrinsic position of all particles, and thus the domain of the mapping, remains invariant in the co-moving frame. Therefore, only the mapping $\boldsymbol{\Gamma}$, which describes the embedding into an extrinsic coordinate system, carries information about the physical position of particles relative to our reference frame.

Now, we extract the information that the mapping $\boldsymbol{\Gamma}$ holds about the geometric positions of particles and their distances in the embedding. As before, we consider two particles labeled "1" and "2", with intrinsic coordinates $\boldsymbol{\omega}$ and $\boldsymbol{\omega} + d\boldsymbol{\omega}$ in our co-moving reference frame. By performing a Taylor expansion of the mapping $\boldsymbol{\Gamma}$, we then find that the distance vector between the two particles is to linear order given by:

$$d\boldsymbol{x} = \boldsymbol{\Gamma}(\boldsymbol{\omega} + d\boldsymbol{\omega}) - \boldsymbol{\Gamma}(\boldsymbol{\omega}) = \sum_i \left(\frac{\partial \boldsymbol{\Gamma}}{\partial \omega_i} \right) d\omega_i \, . \tag{I.15}$$

Thus, our co-moving reference frame is spanned by the following basis vectors (see Fig. I.3):

$$\boldsymbol{b}_i = \frac{\partial \boldsymbol{\Gamma}_\bullet}{\partial \omega_\bullet^i} \, , \quad \text{or} \quad \boldsymbol{t}_i = \frac{\partial \boldsymbol{\Gamma}_\circ}{\partial \omega_\circ^i} \, , \tag{I.16}$$

depending on whether our tracer particle lies in the bulk "$\bullet$" or on the surface "$\circ$" of the geometry. For clarity, we use distinct representations for the basis vectors in the bulk of the geometry, $\boldsymbol{b}_i$, and for the tangent vectors on the surface of the geometry, $\boldsymbol{t}_i$, where possible. These basis vectors span the local vector space and are, in general, neither normalized nor orthogonal. In some cases that equally apply to both the bulk and the boundary, we use a placeholder for the basis vectors, $\boldsymbol{\lambda}_{\bullet,i} \equiv \boldsymbol{b}_i$ and $\boldsymbol{\lambda}_{\circ,i} \equiv \boldsymbol{t}_i$; this is the case in Section I.3.4 "Physical Quantities in Curvilinear Coordinates".

For an index-free representation, we define the two bases that parameterize the bulk and the surface of the geometry as follows:

$$\boldsymbol{V}_\bullet := \boldsymbol{B} = \begin{bmatrix} \boldsymbol{b}_1, \boldsymbol{b}_2, \boldsymbol{b}_3 \end{bmatrix}, \quad \text{and} \quad \boldsymbol{V}_\circ := \boldsymbol{T} = \begin{bmatrix} \boldsymbol{t}_1, \boldsymbol{t}_2 \end{bmatrix}. \tag{I.17}$$

---

[9] Our position could also coincide with one of these two particles. Then, the particle would lie at the origin of the co-moving frame.

EXAMPLE 3: BASIS VECTORS

Cylindrical Coordinates with Rotational Symmetry

The bulk basis vectors are given by:

$$\boldsymbol{b}_r = \left[\!\!\left[\begin{array}{c} \cos(\phi) \\ \sin(\phi) \\ 0 \end{array} \right]\!\!\right], \quad \boldsymbol{b}_z = \left[\!\!\left[\begin{array}{c} 0 \\ 0 \\ 1 \end{array} \right]\!\!\right], \quad \text{and} \quad \boldsymbol{b}_\phi = \left[\!\!\left[\begin{array}{c} -r\,\sin(\phi) \\ r\,\cos(\phi) \\ 0 \end{array} \right]\!\!\right].$$

The boundary tangent vectors are given by:

$$\boldsymbol{t}_z = \left[\!\!\left[\begin{array}{c} \partial_z R(z)\,\cos(\phi) \\ \partial_z R(z)\,\sin(\phi) \\ 1 \end{array} \right]\!\!\right], \quad \text{and} \quad \boldsymbol{t}_\phi = \left[\!\!\left[\begin{array}{c} -R(z)\,\sin(\phi) \\ R(z)\,\cos(\phi) \\ 0 \end{array} \right]\!\!\right].$$

Note that these bulk basis vectors and boundary tangent vectors are orthogonal, but not normalized.

Spherical Coordinates with Rotational Symmetry

We abstain from giving an example here because the corresponding vectors are quite long and do not give additional insight. As for the cylindrical geometry, the bulk basis vectors and the boundary tangent vectors are orthogonal, but not normalized.

As before, "●" refers to the bulk of the geometry while "○" refers to the surface of the geometry. Using these bases, the distance vector between the two particles "1" and "2" is given by $d\boldsymbol{x} = \boldsymbol{V} \cdot d\boldsymbol{\omega}$. The squared Euclidean distance between the two particles "1" and "2" is then given by (Kreyszig, 1959; Kamien, 2002; Lebedev and Cloud, 2003; Pressley, 2010; Frankel, 2011; Grinfeld, 2013; Deserno, 2015; Tu, 2017):

$$\|d\boldsymbol{x}\|^2 = d\boldsymbol{\omega}^T \cdot \boldsymbol{V}^T \cdot \boldsymbol{V} \cdot d\boldsymbol{\omega} = d\boldsymbol{\omega}^T \cdot \boldsymbol{g} \cdot d\boldsymbol{\omega}, \tag{I.18}$$

where we have defined the metric tensor as $\boldsymbol{g} := \boldsymbol{V}^T \cdot \boldsymbol{V}$. Equation (I.18) is valid both for the bulk and for the surface of our geometry.

Our discussion so far shows that intrinsic coordinates in the co-moving frame *a priori* share no information about physical distances and lengths. In particular, one can imagine these intrinsic coordinates as the indices of a space-filling mesh, which by themselves have no physical meaning. The concept of a physical length is then endowed by an embedding in an extrinsic coordinate system (laboratory frame). Such an embedding implies a mapping from the intrinsic coordinates in the co-moving frame to the extrinsic coordinates in the laboratory

EXAMPLE 4: METRIC

Cylindrical Coordinates with Rotational Symmetry

The bulk metric and the boundary metric are given by:

$$\mathbf{g}_\bullet = \begin{bmatrix} 1 & 0 & 0 \\ 0 & 1 & 0 \\ 0 & 0 & r^2 \end{bmatrix} \quad \text{and} \quad \mathbf{g}_\circ = \begin{bmatrix} 1 + (\partial_z R)^2 & 0 \\ 0 & R^2 \end{bmatrix}.$$

Note that this is an orthogonal coordinate system, but not orthonormal.

Spherical Coordinates with Rotational Symmetry

The bulk metric and the boundary metric are given by:

$$\mathbf{g}_\bullet = \begin{bmatrix} 1 & 0 & 0 \\ 0 & r^2 & 0 \\ 0 & 0 & r^2 \sin^2(\theta) \end{bmatrix} \quad \text{and} \quad \mathbf{g}_\circ = \begin{bmatrix} R^2 + (\partial_\theta R)^2 & 0 \\ 0 & R^2 \sin^2(\theta) \end{bmatrix}.$$

Note that this is an orthogonal coordinate system, but not orthonormal.

frame. This, however, does not preclude that an active agent could make length measurements along geodesics[10] and angle measurements, just like people do on the surface of Earth. To make such measurements, the active agent does not need to be aware of the embedding at all, yet the very existence of the embedding will affect the measurements. For example, the surface of the Earth looks approximately flat from the perspective of a person. Then, this person could define a local orthonormal frame on the surface, which would be a very good approximation if the person considers lengths that are much smaller than the size of the geometry (that is, Earth). In its local orthonormal frame, the person will expect Euclidean geometry to hold. Thus, the person will expect that the sum of all angles in a triangle adds to 180 degrees, that locally parallel straight lines never intersect, that two straight lines can only intersect once, and so on. However, if the person tries to expand its local orthonormal frame to describe the whole geometry, then it will be met with failure. In particular, on the curved surface of Earth, one can define three geodesic lines with pairwise intersections at right angles, locally parallel straight lines *will* intersect, straight lines intersect twice, and so on. Then, by doing such measurements on the surface of Earth, the person can extract information about its embedding, like the curvature of

---

[10] A geodesic is the shortest path between two points in a particular geometry, for example between two points on a surface.

Earth's surface (Frankel, 2011).

Here, however, we do not bother with extracting information about the embedding from an unwitting active agent's perspective. Instead, being observers aware of the embedding, we have the freedom to switch between the co-moving frame of the active agent and the laboratory frame of the embedding. Then, by constructing the local metric, we can define the Euclidean distance that the active agent travels between two points. In doing so, we also construct a local basis that spans the co-moving frame. For example, a co-moving frame in the bulk is spanned by three non-orthonormal basis vectors $\boldsymbol{b}_i$ forming a parallelepiped, while on the surface it is spanned by two non-orthogonal tangent vectors $\boldsymbol{t}_i$ forming a parallelogram. By using the metric, we can then compute local integration measures such as volume and surface elements (Capovilla et al., 2003; Frankel, 2011; Deserno, 2015):

$$dV = \sqrt{\det \boldsymbol{g}_\bullet}\, d\omega_\bullet^1\, d\omega_\bullet^2\, d\omega_\bullet^3, \quad \text{and} \quad dS = \sqrt{\det \boldsymbol{g}_\circ}\, d\omega_\circ^1\, d\omega_\circ^2. \tag{I.19}$$

As before, "$\bullet$" refers to the bulk of the geometry while "$\circ$" refers to the surface of the geometry. With the definition of the metric tensor Eq. (I.18), we can rewrite Eq. (I.19) as follows:

$$dV = \det(\boldsymbol{V}_\bullet)\, d\omega_\bullet^1\, d\omega_\bullet^2\, d\omega_\bullet^3, \quad \text{and} \quad dS = \det(\boldsymbol{V}_\circ)\, d\omega_\circ^1\, d\omega_\circ^2. \tag{I.20}$$

I.3.2   TRANSFORMATIONS IN CURVILINEAR COORDINATES

In our discussion so far, we have shown how one can describe a complex geometry through a set of charts. Furthermore, we have seen how one can compute length measures in the bulk and on the surface of this geometry. Now, we introduce two handy coordinate system transformations that will make our lives easier in the remainder of the thesis: *basis orthonormalization* and *basis rotation*. In particular, without giving explicit mathematical forms, we discuss important mathematical properties of these two transformations. All of our discussion is based on our freedom of choice when constructing a representation of some geometry, as discussed in Section I.3.1 "Extrinsic and Intrinsic Coordinate Systems". In particular, one can define different charts, which have corresponding mappings $\boldsymbol{\Gamma}$ to the embedding and thus different bases $\boldsymbol{V}$, but share the same geometric image, see Eq. (I.14). We exploit this property to switch between different representations of the same geometrical and physical objects, always on the lookout for routes to simplify our description.

Basis orthonormalization.   As before, we place ourselves as observers into the co-moving reference frame of some tracer particle. Suppose that we start with the most general case, where the co-moving frame is spanned by some

non-orthonormal basis $\boldsymbol{V}$. While this representation is a natural choice given an existing mapping $\boldsymbol{\Gamma}$ from the intrinsic coordinates in the co-moving frame to the embedding, it is hardly intuitive. In particular, to even get a sense of length, one has to first determine the metric tensor, see Eq. (I.18). In stark contrast, the Cartesian coordinate system of the embedding is easy to grasp: all position coordinates have intuitive units of length, and all coordinate axes are independent. Given our freedom for the representation of the geometry, however, what we can do is to simply define a different local coordinate system that spans the co-moving frame of our tracer particle. For our intuition from the Cartesian coordinate system to carry over, we choose a local coordinate system that has an orthonormal basis $\boldsymbol{V}_{\oplus}$. Thus, the metric of our new coordinate system takes the form of an identity mapping:

$$\boldsymbol{g}_{\oplus} = \boldsymbol{V}_{\oplus}^{T} \cdot \boldsymbol{V}_{\oplus} = \boldsymbol{I}\,. \tag{I.21}$$

This new coordinate system is not required to represent the whole geometry faithfully, as we can stitch together all the charts that represent the space around different particles, see Eq. (I.14).

Now, we have an additional coordinate system, which seems like a complication at first. However, based on our intuition for the orthonormal coordinate system with the basis $\boldsymbol{V}_{\oplus}$, we can derive important relations that must hold for the non-orthonormal coordinate system with a basis $\boldsymbol{V}$. To do so, we introduce the following basis transformation, which is an invertible linear map:

$$\boldsymbol{V}_{\oplus} = \boldsymbol{V} \cdot \boldsymbol{O}\,. \tag{I.22}$$

This *orthonormalization* $\boldsymbol{O}$ takes the following specific form in the bulk "$\bullet$" and on the surface "$\circ$" of our geometry:

$$\boldsymbol{b}_{\oplus,k} = \sum_{i} \boldsymbol{b}_{i}\, O_{\bullet,ik}\,, \quad \text{and} \quad \boldsymbol{t}_{\oplus,k} = \sum_{i} \boldsymbol{t}_{i}\, O_{\circ,ik}\,. \tag{I.23}$$

As before, $\boldsymbol{b}_{i} \in \boldsymbol{B} \equiv \boldsymbol{V}_{\bullet}$ refer to the basis vectors in the bulk and $\boldsymbol{t}_{i} \in \boldsymbol{T} \equiv \boldsymbol{V}_{\circ}$ refer to the tangent vectors on the surface. The components of the orthonormalization matrix are given by O_{ik}.

Such a local orthonormalization changes the coordinate system and thus the intrinsic coordinates of all particles in the co-moving frame. To illustrate this, we again consider two specific particles labeled "1" and "2". In the original non-orthonormal coordinate system, these two particles have intrinsic coordinates $\boldsymbol{\omega}$ and $\boldsymbol{\omega} + d\boldsymbol{\omega}$, respectively. In the new orthonormal coordinate system, they have intrinsic coordinates $\boldsymbol{\omega}_{\oplus}$ and $\boldsymbol{\omega}_{\oplus} + d\boldsymbol{\omega}_{\oplus}$, respectively. However, this is just a matter of representation, because an orthonormalization cannot change the physical positions in the embedding, $\boldsymbol{x}$ and $\boldsymbol{x} + d\boldsymbol{x}$, of the particles "1" and "2",

respectively. As a consequence, the distance vector between the two particles "1" and "2" must be the same both in the orthonormal and in the non-orthonormal co-moving coordinate system:

$$d\boldsymbol{x} = \boldsymbol{V}_{\oplus} \cdot d\boldsymbol{\omega}_{\oplus} = \boldsymbol{V} \cdot d\boldsymbol{\omega}\,. \tag{I.24}$$

This implies that the intrinsic coordinates in the co-moving frame transform as follows under orthonormalization:

$$d\boldsymbol{\omega}_{\oplus} = \boldsymbol{O}^{-1} \cdot d\boldsymbol{\omega}\,. \tag{I.25}$$

As the identity metric, Eq. (I.21), and our discussion indicate, the transformed intrinsic coordinates in the new orthonormal basis naturally represent physical lengths and distances, where $\|d\boldsymbol{\omega}_{\oplus}\|^2 = \|d\boldsymbol{x}\|^2$. Therefore, in the following we refer to $d\boldsymbol{\omega}_{\oplus}$ as the *arc distance vector*.

Finally, we note that there is a direct relationship between the orthonormalization matrix and the metric in the non-orthonormal coordinate system. Using the definitions of the metric tensor, Eq. (I.18), and of the basis transformation under orthonormalization, Eq. (I.22), we find:

$$\boldsymbol{g} = \boldsymbol{O}^{-T} \cdot \boldsymbol{O}^{-1}\,, \quad \text{and} \quad \boldsymbol{g}^{-1} = \boldsymbol{O} \cdot \boldsymbol{O}^{T}\,, \tag{I.26}$$

for the metric tensor $\boldsymbol{g}$ and its inverse $\boldsymbol{g}^{-1}$, respectively. The above equation and the definition of the metric tensor itself, Eq. (I.18), both show that the metric tensor and its inverse are symmetric.

Basis rotation. As before, we place ourselves as observers into the co-moving reference frame of some tracer particle. Now, we are interested in rotating the local coordinate system until, for example, its axes align with some local axes of symmetry. By exploiting such symmetries, we can drastically simplify our local description. To do so, we apply the *rotation* matrix $\boldsymbol{R}$ to the vector $\boldsymbol{v}$ in the embedding, as follows:

$$\boldsymbol{v}_{\circlearrowleft} = \boldsymbol{R} \cdot \boldsymbol{v}\,. \tag{I.27}$$

This operation results in a rotated vector $\boldsymbol{v}_{\circlearrowleft}$ with the same length as the original vector, $\|\boldsymbol{v}_{\circlearrowleft}\| = \|\boldsymbol{v}\|$. If we apply the same rotation to a second vector $\boldsymbol{u}$, then the angle between the two vectors $\boldsymbol{u}$ and $\boldsymbol{v}$ remains unaffected, $\boldsymbol{u} \cdot \boldsymbol{v} = \boldsymbol{u}_{\circlearrowleft} \cdot \boldsymbol{v}_{\circlearrowleft}$.

Therefore, a rotation of the whole basis that spans the co-moving frame,

$$\boldsymbol{V}_{\circlearrowleft} = \boldsymbol{R} \cdot \boldsymbol{V}\,, \tag{I.28}$$

will preserve the lengths of the basis vectors as well as their relative angles. As a consequence, the local metric is invariant with respect to rotations,

$$\boldsymbol{g}_{\circlearrowleft} = \boldsymbol{V}_{\circlearrowleft}^{T} \cdot \boldsymbol{V}_{\circlearrowleft} = \boldsymbol{V}^{T} \cdot \boldsymbol{V} = \boldsymbol{g}\,, \quad \text{which implies} \quad \boldsymbol{R}^{T} \cdot \boldsymbol{R} = \boldsymbol{I}\,. \tag{I.29}$$

This shows that the transpose of a rotation matrix is equal to its inverse.

Projection of a vector. Suppose that we are interested in extracting the part of a vector $\boldsymbol{v}$ that is parallel to some other (reference) vector $\boldsymbol{n}$. The reference vector points in the direction $\hat{\boldsymbol{n}} = \boldsymbol{n}/\|\boldsymbol{n}\|$. We obtain this component by projecting our vector,

$$\boldsymbol{P}_{\oplus} \cdot \boldsymbol{v} = \left(\hat{\boldsymbol{n}} \otimes \hat{\boldsymbol{n}}\right) \cdot \boldsymbol{v} = \hat{\boldsymbol{n}}\left(\hat{\boldsymbol{n}} \cdot \boldsymbol{v}\right), \tag{I.30}$$

where "$\otimes$" refers to an outer product (also called tensor product or dyadic product). Here, the outer product corresponds to a matrix product between a column vector $\boldsymbol{u}$ ($N \times 1$ matrix) and a row vector $\boldsymbol{v}^T$ ($1 \times N$ matrix), $\boldsymbol{u} \otimes \boldsymbol{v} \equiv \boldsymbol{u} \cdot \boldsymbol{v}^T$. When we express vectors via matrices, the symbol "$\cdot$" identifies a matrix multiplication. Because this trick can cause a clash with the notation of an inner vector product, we only use it in two places of the present thesis, and explicitly state where we do so.

Now suppose that we are interested in extracting the part of a vector $\boldsymbol{v}$ that is perpendicular to some other (reference) vector $\boldsymbol{n}$. For this purpose, we again project our vector,

$$\boldsymbol{P}_{\ominus} \cdot \boldsymbol{v} = \left(\boldsymbol{I} - \hat{\boldsymbol{n}} \otimes \hat{\boldsymbol{n}}\right) \cdot \boldsymbol{v}, \tag{I.31}$$

where $\boldsymbol{I}$ is the identity mapping. This is equivalent to projecting the vector $\boldsymbol{v}$ onto the surface defined by the normal vector $\hat{\boldsymbol{n}}$.

I.3.3 MEASURING THE SHAPE OF A SURFACE

So far, we have shown in Section I.3.1 "Extrinsic and Intrinsic Coordinate Systems" how one can describe a complex geometry through a set of charts and how to compute length measures in this geometry. We have also discussed how one can describe the same geometry through different parameterizations, see Eq. (I.14). But how do the geometry and, in particular, its surface look like? To answer this question, we put the two coordinate system transformations, *basis orthonormalization* and *basis rotation*, which we have introduced in Section I.3.2 "Transformations in Curvilinear Coordinates", to good use. For a more detailed treatise, we refer to (Kreyszig, 1959; Kamien, 2002; Lebedev and Cloud, 2003; Pressley, 2010; Frankel, 2011; Grinfeld, 2013; Deserno, 2015; Tu, 2017).

Unit normal vector on the surface. As our first step, we extend the non-orthonormal coordinate system on the surface of our geometry by introducing the unit normal vector (Fig. I.3):

$$\hat{\boldsymbol{n}} := \pm \frac{\boldsymbol{t}_1 \times \boldsymbol{t}_2}{\sqrt{\det \boldsymbol{g}_{\circ}}} \, . \tag{I.32}$$
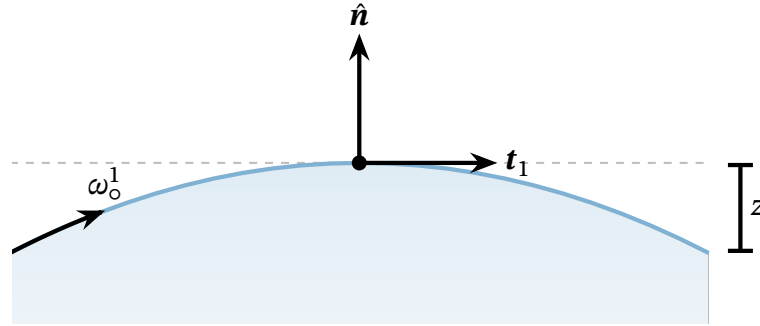
Figure I.4: Side view of a two-dimensional surface in a three-dimensional Cartesian embedding. We extend the local non-orthonormal coordinate system on the surface with the local unit normal vector $\hat{\boldsymbol{n}}$, which points away from the bulk of the geometry (blue gradient). By doing so, we can describe the position of objects near the surface. Furthermore, this allows us to parameterize the distance d that the surface curves away, at the surface coordinate $\boldsymbol{\omega}_{\mathrm{o}} + d\boldsymbol{\omega}_{\mathrm{o}}$, from the tangent plane at the surface coordinate $\boldsymbol{\omega}_{\mathrm{o}}$.

By definition, the unit normal vector is normalized and orthogonal to both tangent vectors. However, the direction of the unit normal vector is not uniquely defined. Here, we choose the convention that the unit normal vector points *outwards*, that is, away from the geometry (Fig. I.4). Using the unit normal vector, we can now not only describe points that lie strictly on the tangent plane of our geometry, but also points that are close but at a finite distance from the surface. The ability to do so is crucial for our next step.

The shape tensor of a surface. Finally, we determine the shape of the surface. To that end, just as we have done in Paragraph "The metric encodes the concept of length" (Section I.3.1), we again place ourselves as observers into the co-moving frame of some tracer particle. We keep track of two nearby particles labeled "1" and "2", which have intrinsic coordinates $\boldsymbol{\omega}_{\mathrm{o}}$ and $\boldsymbol{\omega}_{\mathrm{o}} + d\boldsymbol{\omega}_{\mathrm{o}}$. In Paragraph "The metric encodes the concept of length" (Section I.3.1), we have described the distance vector between the particles "1" and "2". To that end, we have used a Taylor series of the surjective mapping $\boldsymbol{\Gamma}(\boldsymbol{\omega}_{\mathrm{o}})$ from the intrinsic coordinates in the co-moving frame to the extrinsic coordinates in the embedding, see Eq. (I.15). By doing so, we have determined the basis $\boldsymbol{T}$ with tangent vectors $\boldsymbol{t}_i \in \boldsymbol{T}$ that span the tangent plane of the surface, see Eq. (I.16). Now, we ask: *How far is the particle "2" away from the tangent plane at the position of the particle "1"?* To answer this question, we again perform a Taylor expansion of the

surjective mapping, but this time keep all terms up to first nonlinear order:

$$dx = \Gamma_\circ(\omega_\circ + d\omega_\circ) - \Gamma_\circ(\omega_\circ) = \sum_i \left(\frac{\partial \Gamma_\circ}{\partial \omega_\circ^i} \right) d\omega_\circ^i$$
$$+ \frac{1}{2} \sum_{i,k} \left(\frac{\partial^2 \Gamma_\circ}{\partial \omega_\circ^i \partial \omega_\circ^k} \right) d\omega_\circ^i \, d\omega_\circ^k \,. \quad (I.33)$$

We obtain the distance z between particle "2" and the tangent plane, by projecting the distance vector between the two particles onto the (unit) normal vector of the tangent plane, $P_\oplus \cdot dx = z \, \hat{n}$. Thus, the distance between particle "2" and the tangent plane is given by (Kreyszig, 1959; Kamien, 2002; Lebedev and Cloud, 2003; Pressley, 2010; Frankel, 2011; Grinfeld, 2013; Deserno, 2015; Tu, 2017)

$$z = \hat{n} \cdot dx = \frac{1}{2} \sum_{i,k} \hat{n} \cdot \left(\frac{\partial^2 \Gamma_\circ}{\partial \omega_\circ^i \partial \omega_\circ^k} \right) d\omega_\circ^i \, d\omega_\circ^k = \frac{1}{2} d\omega_\circ^T \cdot h \cdot d\omega_\circ \,, \quad (I.34)$$

where we have defined the components of the shape tensor h as follows (Kreyszig, 1959; Kamien, 2002; Lebedev and Cloud, 2003; Pressley, 2010; Frankel, 2011; Grinfeld, 2013; Deserno, 2015; Tu, 2017):

$$h_{ik} := \hat{n} \cdot \left(\frac{\partial^2 \Gamma_\circ}{\partial \omega_\circ^i \partial \omega_\circ^k} \right) = \hat{n} \cdot \left(\frac{\partial t_i}{\partial \omega_\circ^k} \right) = -t_i \cdot \left(\frac{\partial \hat{n}}{\partial \omega_\circ^k} \right) \,. \quad (I.35)$$

Here, we have first inserted the definition of the tangent vectors, Eq. (I.16), and then used $\hat{n} \cdot t_i = 0$. Because the particle labeled "2" is a point on the surface, Eq. (I.34) gives a measure for the out-of-plane bending of the surface. Thus, Eq. (I.35) defines the shape of the surface.

The two principal curvatures of a surface. To gain some intuitive insight from Eq. (I.35), we make use of the orthonormalization matrix, which is discussed in Paragraph "Basis orthonormalization" (Section I.3.2). Specifically, in addition to the local non-orthonormal basis T in the co-moving frame, we also introduce the local orthonormal basis $T_\oplus = T \cdot O$, see Eq. (I.22). To preserve lengths and distances between particles in the embedding, the intrinsic coordinates must transform inversely under orthonormalization, $d\omega_\oplus = O^{-1} \cdot d\omega_\circ$, see Eq. (I.25). Thus, starting from Eq. (I.34), we arrive at the following expression for the out-of-plane bending of the surface:

$$z = \frac{1}{2} d\omega_\oplus^T \cdot O^T \cdot h \cdot O \cdot d\omega_\oplus = \frac{1}{2} d\omega_\oplus^T \cdot h_\oplus \cdot d\omega_\oplus \,, \quad (I.36)$$

where we have defined the shape tensor in the orthonormalized basis as $\boldsymbol{h}_\oplus :=$ $\boldsymbol{O}^T \cdot \boldsymbol{h} \cdot \boldsymbol{O}$. Here, $d\boldsymbol{\omega}_\oplus$ represents the arc distance vector between our two particles labeled "1" and "2" in the co-moving frame, $\|d\boldsymbol{\omega}_\oplus\|^2 = \|d\boldsymbol{x}\|^2$, because we have orthonormalized the corresponding basis.

Both the shape tensor $\boldsymbol{h}$ and its orthonormalized counterpart $\boldsymbol{h}_\oplus$ are real-valued symmetric matrices, as one can see from Eq. (I.35). Therefore, there must exist a rotation $\boldsymbol{R}$ that diagonalizes the orthonormalized shape tensor $\boldsymbol{h}_\oplus$, which then takes the following form:

$$\boldsymbol{h}_\circlearrowleft = \boldsymbol{R}^T \cdot \boldsymbol{h}_\oplus \cdot \boldsymbol{R} \equiv \begin{bmatrix} \kappa_1 & 0 \\ 0 & \kappa_2 \end{bmatrix} . \tag{I.37}$$

We refer to κ_1 and κ_2 as *principal curvatures*. Thus, by using appropriate basis transformations, one can find an orthonormal basis where the deviation from the tangent plane is given by $z = \frac{1}{2}\kappa_1 (d\omega_\circlearrowleft^1)^2 + \frac{1}{2}\kappa_2 (d\omega_\circlearrowleft^2)^2$. This can be seen by inserting Eq. (I.37) into Eq. (I.36) while taking into account the rotation.

While this may sound complicated at first, there is actually no need to search for specific basis transformations. In particular, one can cyclically permute the arguments in the trace of the rotated and orthonormalized shape tensor,

$$\kappa_1 + \kappa_2 = \mathrm{tr}\left(\boldsymbol{R}^T \cdot \boldsymbol{O}^T \cdot \boldsymbol{h} \cdot \boldsymbol{O} \cdot \boldsymbol{R}\right) = \mathrm{tr}\left(\boldsymbol{O}^T \cdot \boldsymbol{h} \cdot \boldsymbol{O}\right) = \mathrm{tr}\left(\boldsymbol{h} \cdot \boldsymbol{O} \cdot \boldsymbol{O}^T\right), \tag{I.38}$$

to get rid of the rotation matrices and rearrange the orthogonalization matrices. Similarly, because all involved terms are square matrices, one can also rearrange the arguments in the determinant of the rotated and orthonormalized shape tensor,

$$\kappa_1 \kappa_2 = \det\left(\boldsymbol{R}^T \cdot \boldsymbol{O}^T \cdot \boldsymbol{h} \cdot \boldsymbol{O} \cdot \boldsymbol{R}\right) = \det\left(\boldsymbol{O}^T \cdot \boldsymbol{h} \cdot \boldsymbol{O}\right) = \det\left(\boldsymbol{h} \cdot \boldsymbol{O} \cdot \boldsymbol{O}^T\right), \tag{I.39}$$

EXAMPLE 5: PRINCIPAL CURVATURES

Cylindrical Coordinates with Rotational Symmetry

The two principal curvatures are given by:

$$\kappa_z = \frac{\partial_z^2 R}{\sqrt{1 + (\partial_z R)^2}^3}, \quad \text{and} \quad \kappa_\phi = -\frac{1}{R}\frac{1}{\sqrt{1 + (\partial_z R)^2}}.$$

Spherical Coordinates with Rotational Symmetry

The two principal curvatures are given by:

$$\kappa_\theta = -\frac{1}{R}\frac{1 + 2(\partial_\theta R/R)^2 - \partial_\theta^2 R/R}{\sqrt{1 + (\partial_\theta R/R)^2}^3}, \quad \text{and} \quad \kappa_\phi = -\frac{1}{R}\frac{1 - (\partial_\theta R/R)\cot\theta}{\sqrt{1 + (\partial_\theta R/R)^2}}.$$

in an analogous way. By using Eq. (I.26) to relate the orthonormalization matrix to the inverse metric tensor, $\boldsymbol{O} \cdot \boldsymbol{O}^T = \boldsymbol{g}^{-1}$, we then find that the total curvature and the Gaussian curvature (Kreyszig, 1959; Kamien, 2002; Lebedev and Cloud, 2003; Pressley, 2010; Frankel, 2011; Grinfeld, 2013; Deserno, 2015; Tu, 2017),

$$H = \kappa_1 + \kappa_2 = \operatorname{tr}\left(\boldsymbol{h} \cdot \boldsymbol{g}^{-1}\right), \quad \text{and} \quad K = \kappa_1 \kappa_2 = \det\left(\boldsymbol{h} \cdot \boldsymbol{g}^{-1}\right), \tag{I.40}$$

are basis-invariant measures of the surface shape. Note that our sign convention for the curvatures suggests that a surface has positive curvature if it is bent towards its (outwards-pointing) unit normal vector; this means that a sphere has negative curvature.

I.3.4 PHYSICAL QUANTITIES IN CURVILINEAR COORDINATES

So far, we have shown in Section I.3.1 "Extrinsic and Intrinsic Coordinate Systems" how one can describe a complex geometry through a set of charts and how to compute length measures in this geometry. Furthermore, in Section I.3.2 "Transformations in Curvilinear Coordinates" we have introduced two coordinate system transformations: *basis orthonormalization* and *basis rotation*. In Section I.3.3 "Measuring the Shape of a Surface", we have then determined the shape of a two-dimensional surface that is embedded in a three-dimensional Cartesian space. In this section, we continue to put the above concepts to good use. We first introduce the physical quantities that we want to describe: scalar fields, vector fields and tensor fields. Then, we show how to compute derivatives of these physical quantities in curvilinear coordinates, which is essential for any physical theory. For a more detailed treatise, we refer to (Kreyszig, 1959; Lebedev and Cloud, 2003; Pressley, 2010; Frankel, 2011; Grinfeld, 2013; Tu, 2017).

Fields and Physical Quantities.   We place ourselves as observers into the comoving reference frame of some tracer particle. Our reference frame is spanned by the basis $\boldsymbol{V}$ with basis vectors $\boldsymbol{\lambda}_i \in \boldsymbol{V}$. In this reference frame, we now aim beyond our initial description of positions and distances, towards a description of interactions. To that end, we use *fields*. The most basic type of field that we consider is a *scalar field* $c(\boldsymbol{\omega})$, which assigns a scalar value to the coordinate $\boldsymbol{\omega}$. This scalar field must be independent of parameterization, to have any physical meaning. Examples of scalar fields include particle density fields, temperature fields, pressure fields, and many others. In particular, the density of particles is a coarse-grained description where we, instead of keeping track of each individual

particle and its position, rather tell how many particles are on average within a given infinitesimal volume.

Another type of field that we consider is a *vector field* $\boldsymbol{v}(\boldsymbol{\omega})$, which assigns a vector value to coordinate $\boldsymbol{\omega}$. We describe this field, in the bulk "•" and on the surface "○" of our geometry, as follows:

$$\boldsymbol{v}_\bullet = \sum_i v_\bullet^i \, \boldsymbol{b}_i \,, \quad \text{or} \quad \boldsymbol{v}_\circ = \sum_i v_\circ^i \, \boldsymbol{t}_i \,. \tag{I.41}$$

As before, $\boldsymbol{b}_i \in \boldsymbol{B} \equiv V_\bullet$ refer to the basis vectors in the bulk and $\boldsymbol{t}_i \in \boldsymbol{T} \equiv V_\circ$ refer to the tangent vectors on the surface. This particular notation for the field variables is called *contravariant notation*: for any basis transformation that we apply to the basis vectors (they co-vary), we have to apply the inverse transformation to the vector components. Only then will the vector field have a physical meaning, independent of parameterization. Examples of such fields include velocity fields, momentum density fields, electrical fields, and many others.

The last type of field that we consider is a *tensor field* of rank 2. We describe this field, in the bulk "•" and on the surface "○" of our geometry, as follows:

$$\boldsymbol{\sigma}_\bullet = \sum_{i,k} \sigma_\bullet^{ik} \, \boldsymbol{b}_i \otimes \boldsymbol{b}_k \,, \quad \text{or} \quad \boldsymbol{\sigma}_\circ = \sum_{i,k} \sigma_\circ^{ik} \, \boldsymbol{t}_i \otimes \boldsymbol{t}_k \,. \tag{I.42}$$

As mentioned earlier, "$\otimes$" refers to an outer product (also called tensor product). Just as we have discussed for the vector field, the tensor field must also be independent of parameterization, to have any physical meaning. Examples of such fields include stress and strain fields.

In the following, we illustrate how one can compute derivatives of these different fields. To simplify our notation, we use a placeholder $\lambda \in V$ for the basis vectors that span the bulk and for the tangent vectors that span the boundary:

$$\lambda_{\bullet,i} \equiv \boldsymbol{b}_i \,, \quad \text{and} \quad \lambda_{\circ,i} \equiv \boldsymbol{t}_i \,. \tag{I.43}$$

All results are equally applicable to the bulk and to the surface of the geometry.

Gradient of a scalar field in curvilinear coordinates. First, we determine the gradient of a scalar field c in a curvilinear co-moving frame, with a non-orthonormal basis V and basis vectors $\lambda_i \in V$. This is necessary, for example, to determine the net particle fluxes that arise due to diffusion. Analogously to Section I.3.2 "Transformations in Curvilinear Coordinates", we first construct a local orthonormal coordinate system, with the basis $V_\oplus$ and basis vectors $\lambda_{\oplus,i} \in V_\oplus$.

We consider two points that are near each other in space: (i) The first point has coordinates $\boldsymbol{\omega}$ in the local non-orthonormal basis and coordinates $\boldsymbol{\omega}_\oplus$ in the local

orthonormal basis. Its position in the embedding is given by $\boldsymbol{x}$. (ii) The second point has coordinates $\boldsymbol{\omega} + d\boldsymbol{\omega}$ in the local non-orthonormal basis and coordinates $\boldsymbol{\omega}_\oplus + d\boldsymbol{\omega}_\oplus$ in the local orthonormal basis. Its position in the embedding is given by $\boldsymbol{x} + d\boldsymbol{x}$. The intrinsic coordinates in the orthonormal coordinate system naturally represent lengths and distances, so that $\|d\boldsymbol{\omega}_\oplus\|^2 = \|d\boldsymbol{x}\|^2$. Therefore, the arc distance vector between our two points is given by $d\boldsymbol{\omega}_\oplus$.

In the local orthonormal coordinate system, the local gradient of a scalar field is then given by

$$\nabla c = \sum_i \frac{\partial c}{\partial \omega_\oplus^i} \boldsymbol{\lambda}_{\oplus,i} \equiv \frac{\partial c}{\partial \boldsymbol{\omega}_\oplus} \cdot \boldsymbol{V}_\oplus . \tag{I.44}$$

Next, we generalize the above expression to our non-orthonormal coordinate system with the basis $\boldsymbol{V}$. To that end, we consider the orthonormalization $\boldsymbol{O}$, which transforms our non-orthonormal basis to our orthonormal basis, $\boldsymbol{V}_\oplus = \boldsymbol{V} \cdot \boldsymbol{O}$, as defined in Eq. (I.22). Our basis transformation must preserve the physical distances between different points, so that $\boldsymbol{\lambda}_{\oplus,i} = \sum_l (\partial \omega^l / \partial \omega_\oplus^i) \boldsymbol{\lambda}_l$, see Eq. (I.24). Furthermore, we only have to deal with the change of the local basis and the local coordinates, while the scalar field c must remain invariant to have physical meaning. Then, by using the chain rule of differentiation, we obtain the following interim expression:

$$\nabla c = \sum_{i,k} \frac{\partial c}{\partial \omega^k} \frac{\partial \omega^k}{\partial \omega_\oplus^i} \boldsymbol{\lambda}_{\oplus,i} = \sum_{i,k,l} \frac{\partial c}{\partial \omega^k} \frac{\partial \omega^k}{\partial \omega_\oplus^i} \frac{\partial \omega^l}{\partial \omega_\oplus^i} \boldsymbol{\lambda}_l . \tag{I.45}$$

To preserve the physical distances between different points, our basis transformation must occur in tandem with a coordinate transformation, $d\boldsymbol{\omega}_\oplus = \boldsymbol{O}^{-1} \cdot d\boldsymbol{\omega}$, see Eq. (I.25). This leads to the following relation between the coordinates and the orthonormalization: $\partial \omega^k / \partial \omega_\oplus^i = O_{ki}$. Thus, we finally arrive at the following expression for the gradient of a scalar field in curvilinear coordinates (Kreyszig, 1959; Lebedev and Cloud, 2003; Frankel, 2011; Grinfeld, 2013):

$$\nabla c = \sum_{i,k,l} \frac{\partial c}{\partial \omega^k} O_{ki} O_{li} \boldsymbol{\lambda}_l = \sum_{k,l} \frac{\partial c}{\partial \omega^k} g_{kl}^{-1} \boldsymbol{\lambda}_l \equiv \frac{\partial c}{\partial \boldsymbol{\omega}} \cdot \boldsymbol{g}^{-1} \cdot \boldsymbol{V} , \tag{I.46}$$

where we have used Eq. (I.26) to relate the orthonormalization matrix to the inverse metric tensor, $\boldsymbol{O} \cdot \boldsymbol{O}^T = \boldsymbol{g}^{-1}$. The gradient of a scalar field is a vector field.

Gradient of a vector field in curvilinear coordinates. Now, we determine the gradient of a vector field $\boldsymbol{v}$ in a curvilinear co-moving frame with non-orthonormal basis $\boldsymbol{V}$ and basis vectors $\boldsymbol{\lambda}_i \in \boldsymbol{V}$. This is necessary, for example, to determine the strain tensor of some elastic material. Analogous to Section I.3.2 "Transformations in Curvilinear Coordinates", we first construct

a local orthonormal coordinate system with the basis $V_\oplus$ and basis vectors $\lambda_{\oplus,i} \in V_\oplus$. We then proceed in full analogy to Paragraph "Gradient of a scalar field in curvilinear coordinates".

First, we define the gradient of a vector field in our local orthonormal coordinate system as follows:

$$\boldsymbol{\nabla} \otimes \boldsymbol{v} = \sum_i \frac{\partial \boldsymbol{v}}{\partial \omega_\oplus^i} \otimes \lambda_{\oplus,i} = \sum_{i,k} \frac{\partial(v^k \lambda_k)}{\partial \omega_\oplus^i} \otimes \lambda_{\oplus,i}. \tag{I.47}$$

As mentioned earlier, "$\otimes$" refers to an outer product (also called tensor product). Then, analogous to Paragraph "Gradient of a scalar field in curvilinear coordinates", we transform back from our local orthonormal basis $V_\oplus$ to the local non-orthonormal basis V in the co-moving frame. By doing so, we obtain the following general expression for the gradient of a vector field in curvilinear coordinates (Lebedev and Cloud, 2003; Frankel, 2011; Grinfeld, 2013):

$$\boldsymbol{\nabla} \otimes \boldsymbol{v} = \sum_{k,l} g_{kl}^{-1} \frac{\partial \boldsymbol{v}}{\partial \omega^k} \otimes \lambda_l. \tag{I.48}$$

Note that the partial derivative of the vector field also contains the change of the local curvilinear basis as a function of intrinsic coordinates. The gradient of a vector field is a tensor field of rank 2.

Divergence of a vector field in curvilinear coordinates. Next, we determine the divergence of a vector field $\boldsymbol{v}$ in a curvilinear co-moving frame with non-orthonormal basis V and basis vectors $\lambda_i \in V$. This is necessary, for example, to determine the divergence of particle fluxes. For reference, the divergence of

EXAMPLE 6: GRADIENT OF A SCALAR FIELD

Cylindrical Coordinates

The gradient of a scalar field c in the bulk is given by:

$$\boldsymbol{\nabla} c = (\partial_r c)\, \lambda_r + (\partial_z c)\, \lambda_z + \frac{1}{r^2}\,(\partial_\phi c)\, \lambda_\phi.$$

Spherical Coordinates

The gradient of a scalar field c in the bulk is given by:

$$\boldsymbol{\nabla} c = (\partial_r c)\, \lambda_r + \frac{1}{r^2}\,(\partial_\theta c)\, \lambda_\theta + \frac{1}{r^2 \sin^2 \theta}\,(\partial_\phi c)\, \lambda_\phi.$$

a vector field in a local orthonormal coordinate system, with basis $\boldsymbol{V}_\oplus$ and basis vectors $\boldsymbol{\lambda}_{\oplus,i} \in \boldsymbol{V}_\oplus$, is given by

$$\boldsymbol{\nabla} \cdot \boldsymbol{v} = \sum_i \frac{\partial(\boldsymbol{v} \cdot \boldsymbol{\lambda}_{\oplus,i})}{\partial \omega_\oplus^i} \,. \tag{I.49}$$

In principle, we could proceed in a similar way as we have done in Paragraph "Gradient of a scalar field in curvilinear coordinates" and Paragraph "Gradient of a vector field in curvilinear coordinates". However, as the mapping between intrinsic and extrinsic coordinates depends on the location, so does the orthonormalization matrix. Alternatively, we could also take the trace of the vector gradient, Eq. (I.48), to determine the divergence (Kreyszig, 1959; Lebedev and Cloud, 2003; Frankel, 2011; Grinfeld, 2013). Both of these approaches would, however, require us to explicitly account for the derivatives of the basis vectors with respect to the coordinates.

Instead, here we choose to take a shortcut and define the divergence operator through Gauss's theorem. Gauss's theorem states that the divergence of a vector field in a volume element is given by the flux across its boundary:

$$\int dV \, \boldsymbol{\nabla} \cdot \boldsymbol{v} = \sum_i \oint d\boldsymbol{S} \cdot \boldsymbol{\lambda}_i \, v^i \,. \tag{I.50}$$

If we consider the bulk of the geometry, then the three basis vectors span a parallelepiped. Analogously, if we consider the surface of the geometry, then the two tangent vectors span a parallelogram. In both cases, the volume element is given by $dV = \sqrt{\det \boldsymbol{g}} \, d^n\boldsymbol{\omega}$, where n is the number of dimensions, see Eq. (I.19). For the boundary integral, we integrate along the boundary of a parallelepiped (if we are in the bulk) or a parallelogram (if we are on the surface).

EXAMPLE 7: DIVERGENCE OF A VECTOR FIELD

Cylindrical Coordinates

The divergence of a vector field $\boldsymbol{v}$ in the bulk is given by:

$$\boldsymbol{\nabla} \cdot \boldsymbol{v} = \frac{1}{r} \partial_r(r \, v^r) + \partial_z v^z + \partial_\phi v^\phi \,.$$

Spherical Coordinates

The divergence of a vector field $\boldsymbol{v}$ in the bulk is given by:

$$\boldsymbol{\nabla} \cdot \boldsymbol{v} = \frac{1}{r^2} \partial_r(r^2 \, v^r) + \frac{1}{\sin\theta} \partial_\theta(\sin\theta \, v^\theta) + \partial_\phi v^\phi \,.$$

The boundary is spanned by a subspace of the basis V, which has co-dimension 1. For example, if we consider the bulk of the geometry with a basis of three vectors, then the boundary is always spanned by two of these three vectors. The scalar product between the directed boundary element dS and another basis vector λ_i is then given by $dS \cdot \lambda_i = \varepsilon_{ikl}\sqrt{\det g}\, d\omega^k d\omega^l$ (if we are in the bulk) or $dS \cdot \lambda_i = \varepsilon_{ik}\sqrt{\det g}\, d\omega^k$ (if we are on the surface); ε is the Levi-Civita symbol. With these considerations, we arrive at the following expression for the divergence of a vector field in curvilinear coordinates (Kreyszig, 1959; Lebedev and Cloud, 2003; Frankel, 2011; Grinfeld, 2013):

$$\nabla \cdot v = \sum_i \frac{1}{\sqrt{\det g}} \frac{\partial}{\partial \omega^i} \left(\sqrt{\det g}\, v^i \right) . \tag{I.51}$$

Equation (I.51) is also called the Voss-Weyl formula (Grinfeld, 2013). The divergence of a vector field is a scalar field.

Divergence of a rank 2 tensor field in curvilinear coordinates. Finally, we determine the divergence of a rank 2 tensor field σ in a curvilinear co-moving frame with non-orthonormal basis V and basis vectors $\lambda_i \in V$. This is necessary, for example, to determine the divergence of the stress tensor in linear elasticity theory or fluid mechanics. For reference, the divergence of a rank 2 tensor field in a local orthonormal coordinate system, with basis $V_\oplus$ and basis vectors $\lambda_{\oplus,i} \in V_\oplus$, is given by

$$\nabla \cdot \sigma = \sum_{i,k} \frac{\partial(\sigma \cdot \lambda_{\oplus,i})}{\partial \omega_\oplus^i} . \tag{I.52}$$

We use the same shortcut as in Paragraph "Divergence of a vector field in curvilinear coordinates", and find the following expression for the divergence of a rank 2 tensor field in curvilinear coordinates (Lebedev and Cloud, 2003; Frankel, 2011; Grinfeld, 2013):

$$\nabla \cdot \sigma = \sum_{i,k} \frac{1}{\sqrt{\det g}} \frac{\partial}{\partial \omega^i} \left(\sqrt{\det g}\, \sigma^{ik} \lambda_k \right) . \tag{I.53}$$

The divergence of a rank 2 tensor field is a vector field.

I.3.5 DESCRIBING A DYNAMIC GEOMETRY

In Section I.3.1 "Extrinsic and Intrinsic Coordinate Systems" and Section I.3.3 "Measuring the Shape of a Surface", we have introduced the mathematical tools that are necessary to describe a static geometry. Then, we have discussed in Section I.3.4 "Physical Quantities in Curvilinear Coordinates" how to describe

EXAMPLE 8: DIVERGENCE OF A RANK 2 TENSOR FIELD

Cylindrical Coordinates with Rotational Symmetry

The divergence of a rank 2 tensor field, $\boldsymbol{f} = \boldsymbol{\nabla} \cdot \boldsymbol{\sigma}$, is given by (Amenzade, 1979):

$$f^r = \frac{1}{r} \partial_r \left(r \, \sigma^{rr} \right) + \partial_z \sigma^{rz} - r \, \sigma^{\phi\phi} \,,$$

$$f^z = \frac{1}{r} \partial_r \left(r \, \sigma^{rz} \right) + \partial_z \sigma^{zz} \,,$$

$$f^\phi = \frac{1}{r} \partial_r \left(r \, \sigma^{r\phi} \right) + \partial_z \sigma^{z\phi} + \frac{2}{r} \, \sigma^{r\phi} \,.$$

Note that we have here assumed that the tensor is symmetric.

Spherical Coordinates with Rotational Symmetry

The divergence of a rank 2 tensor field, $\boldsymbol{f} = \boldsymbol{\nabla} \cdot \boldsymbol{\sigma}$, is given by (Amenzade, 1979):

$$f^r = \frac{1}{r^2} \partial_r \left(r^2 \, \sigma^{rr} \right) + \frac{1}{\sin\theta} \partial_\theta \left(\sin\theta \, \sigma^{\theta r} \right) - r \, \sigma^{\theta\theta} - r \sin^2\theta \, \sigma^{\phi\phi} \,,$$

$$f^\theta = \frac{1}{r^2} \partial_r \left(r^2 \, \sigma^{r\theta} \right) + \frac{1}{\sin\theta} \partial_\theta \left(\sin\theta \, \sigma^{\theta\theta} \right) + \frac{2}{r} \, \sigma^{r\theta} - \sin\theta \, \cos\theta \, \sigma^{\phi\phi} \,,$$

$$f^\phi = \frac{1}{r^2} \partial_r \left(r^2 \, \sigma^{r\phi} \right) + \frac{1}{\sin\theta} \partial_\theta \left(\sin\theta \, \sigma^{\theta\phi} \right) + \frac{2}{r} \, \sigma^{r\phi} + 2\cot\phi \, \sigma^{\theta\theta} \,.$$

Note that we have here assumed that the tensor is symmetric.

physical quantities in our geometry, and derivatives thereof. In this section, we discuss how one can describe a *dynamic* geometry. Specifically, we treat gradual deformations of the geometry by using the calculus of variations. These necessary concepts pave the way towards describing complex interactions between mechanics, chemistry, and geometry.

Deformation field in the embedding. We describe our (moving) geometry by three distinct types of coordinate systems, as discussed in Section I.3.1 "Extrinsic and Intrinsic Coordinate Systems". In particular, we place ourselves as observers into the co-moving frame of some tracer particle. In this co-moving frame, we parameterize all material points in the bulk and on the surface of the geometry via intrinsic coordinates $\boldsymbol{\omega}$. Because our tracer particle can lie either in the bulk or on the surface of our geometry, we need two intrinsic coordinate systems. Each intrinsic coordinate $\boldsymbol{\omega}$ maps to an extrinsic position in the three-

dimensional Cartesian embedding, $\boldsymbol{\Gamma}(\boldsymbol{\omega})$.

To gain additional intuition, one can imagine the intrinsic coordinates $\boldsymbol{\omega}$ as the *indices* of an (infinitesimal) mesh that spans the geometry. Now, we consider some position-dependent deformation field $\boldsymbol{u}(\boldsymbol{\omega})$ that displaces the mesh nodes. Because moving the mesh nodes does not affect their indices, the intrinsic coordinates remain completely unaffected by deformations. Instead, deformations move the extrinsic position of each material point from an initial position $\boldsymbol{x}$ to a different position $\tilde{\boldsymbol{x}}$ in the deformed configuration:

$$\tilde{\boldsymbol{x}} = \tilde{\boldsymbol{\Gamma}}(\boldsymbol{\omega}) = \boldsymbol{\Gamma}(\boldsymbol{\omega}) + \boldsymbol{u}(\boldsymbol{\omega}) = \boldsymbol{x} + \boldsymbol{u}\,, \tag{I.54}$$

which we interpret as a change of the surjective mapping $\boldsymbol{\Gamma}$.

The strain as a variation of the metric. The co-moving reference frame of our tracer particle is spanned by the basis $\boldsymbol{V}$ with the basis vectors $\lambda_i \in \boldsymbol{V}$. In our reference frame, we observe and keep track of two nearby particles labeled "1" and "2", which have intrinsic coordinates $\boldsymbol{\omega}$ and $\boldsymbol{\omega} + d\boldsymbol{\omega}$. Now, as discussed in Paragraph "Deformation field in the embedding", we apply a deformation field $\boldsymbol{u}$ that does not change the intrinsic coordinates of our particles. However, the deformation field changes the extrinsic (that is, physical) coordinates of the particles by displacing them in the three-dimensional Cartesian embedding. Therefore, the distance vector between the particles labeled "1" and "2" will change as well:

$$d\tilde{\boldsymbol{x}} = \sum_i \left(\lambda_i + \frac{\partial \boldsymbol{u}}{\partial \omega^i} \right) d\omega^i = \sum_i \left(\lambda_i + \sum_{k,l} \frac{\partial \boldsymbol{u}}{\partial \omega^k} g_{kl}^{-1} g_{li} \right) d\omega^i$$

$$= \sum_i \left(\lambda_i + \sum_{k,l} \frac{\partial \boldsymbol{u}}{\partial \omega^k} g_{kl}^{-1} \lambda_l \cdot \lambda_i \right) d\omega^i = \left(\boldsymbol{I} + \sum_{k,l} g_{kl}^{-1} \frac{\partial \boldsymbol{u}}{\partial \omega^k} \otimes \lambda_l \right) \cdot \sum_i \lambda_i \, d\omega^i\,. \tag{I.55}$$

Here, we have proceeded in successive steps by (i) performing a Taylor expansion of the distance vector up to linear order, (ii) squeezing in a Kronecker delta, $\sum_l g_{kl}^{-1} g_{li} = \delta_{ki}$, (iii) inserting the definition of the metric tensor, $g_{li} = \lambda_l \cdot \lambda_i$, see Eq. (I.18), and finally (iv) rearranging the different terms. By comparing Eq. (I.55) with the expression for the gradient of a vector field in curvilinear coordinates, Eq. (I.48), we find the following expression for the physical distance vector between the particles labeled "1" and "2", after we have applied a deformation:

$$d\tilde{\boldsymbol{x}} = (\boldsymbol{I} + \boldsymbol{\nabla} \otimes \boldsymbol{u}) \cdot \boldsymbol{V} \cdot d\boldsymbol{\omega} = (\boldsymbol{I} + \boldsymbol{\nabla} \otimes \boldsymbol{u}) \cdot d\boldsymbol{x}\,. \tag{I.56}$$

As it should be, the change of the physical distance vector between any two particles, which occurs due to a deformation, is basis-independent and thus the same

for any parameterization that we may choose. Then, the squared Euclidean distance between our particles "1" and "2" is given by:

$$\|d\tilde{\boldsymbol{x}}\|^2 = d\boldsymbol{\omega}^T \cdot \boldsymbol{V}^T \cdot \left[\boldsymbol{I} + (\boldsymbol{\nabla} \otimes \boldsymbol{u})^T\right] \cdot \left[\boldsymbol{I} + \boldsymbol{\nabla} \otimes \boldsymbol{u}\right] \cdot \boldsymbol{V} \cdot d\boldsymbol{\omega} = d\boldsymbol{\omega}^T \cdot \tilde{\boldsymbol{g}} \cdot d\boldsymbol{\omega}, \quad (I.57)$$

where we have introduced the metric $\tilde{\boldsymbol{g}}$ in the deformed configuration.

By defining the (nonlinear) Green-Lagrange strain tensor $\boldsymbol{E}$ and its linearized counterpart $\boldsymbol{\varepsilon}$ (Amenzade, 1979; Landau, Pitaevskii, et al., 1986; Lai et al., 2010; Murea, 2018),

$$\boldsymbol{E} := \boldsymbol{\varepsilon} + \frac{1}{2}(\boldsymbol{\nabla} \otimes \boldsymbol{u})^T \cdot (\boldsymbol{\nabla} \otimes \boldsymbol{u}), \quad \text{and} \quad \boldsymbol{\varepsilon} := \frac{1}{2}\left[(\boldsymbol{\nabla} \otimes \boldsymbol{u})^T + \boldsymbol{\nabla} \otimes \boldsymbol{u}\right], \quad (I.58)$$

we find that the metric tensor in the deformed configuration is given by $\tilde{\boldsymbol{g}} = \boldsymbol{g} + 2\boldsymbol{V}^T \cdot \boldsymbol{E} \cdot \boldsymbol{V}$. To proceed, we make use of the definition of the metric, $\boldsymbol{g} = \boldsymbol{V}^T \cdot \boldsymbol{V}$, Eq. (I.18), and introduce the dual basis[11] $\boldsymbol{V}^{-1}$. Then, we find that the relative variations of the metric are related to the Green-Lagrange strain tensor by a similarity transformation:

$$\delta\boldsymbol{g} \cdot \boldsymbol{g}^{-1} = (\tilde{\boldsymbol{g}} - \boldsymbol{g}) \cdot \boldsymbol{g}^{-1} = 2\boldsymbol{V}^T \cdot \boldsymbol{E} \cdot \boldsymbol{V}^{-T}. \quad (I.59)$$

This shows that the trace and the determinant of the strain tensor faithfully give scalar basis-invariant measures for the deformation of a material:

$$\text{tr}\left[(\delta\boldsymbol{g} \cdot \boldsymbol{g}^{-1})^n\right] = \text{tr}\left[2^n \boldsymbol{E}^n\right], \quad \text{and} \quad \det\left[(\delta\boldsymbol{g} \cdot \boldsymbol{g}^{-1})^n\right] = \det\left[2^n \boldsymbol{E}^n\right], \quad (I.60)$$

for all integer values of n. This property allows constructing a basis-invariant free energy functional, which describes the energy stored in elastic deformations.

The strain rate as gradual changes of the metric. In Paragraph "The strain as a variation of the metric", we have explained how a deformation field $\boldsymbol{u}$ will change the metric tensor, and defined the strain tensor as a measure of this change. Unless we are dealing with discontinuities such as cracks in the material, a deformation does not appear instantaneously but rather through some finite flow velocity, $\delta\boldsymbol{u} = \boldsymbol{v}\,\delta t$. Based on Eq. (I.58), this leads to the following expression for the strain rate tensor (Landau and Lifshitz, 1987; Lai et al., 2010; Murea, 2018):

$$\dot{\boldsymbol{\varepsilon}} = \frac{1}{2}\left[(\boldsymbol{\nabla} \otimes \boldsymbol{v})^T + \boldsymbol{\nabla} \otimes \boldsymbol{v}\right]. \quad (I.61)$$

---

[11] The dual basis is an example of an orthonormalization matrix. One can confirm this by replacing all occurrences of the orthonormalization matrix with the dual basis in Paragraph "Basis orthonormalization" (Section I.3.2).

EXAMPLE 9: LINEARIZED STRAIN TENSOR

Cylindrical Coordinates with Rotational Symmetry

The linearized strain tensor is given by (Amenzade, 1979):

$$\begin{bmatrix} \varepsilon^{rr} & \varepsilon^{rz} & \varepsilon^{r\phi} \\ \varepsilon^{zr} & \varepsilon^{zz} & \varepsilon^{z\phi} \\ \varepsilon^{\phi r} & \varepsilon^{\phi z} & \varepsilon^{\phi\phi} \end{bmatrix} = \begin{bmatrix} \partial_r u^r & (\partial_z u^r + \partial_r u^z)/2 & \partial_r u^\phi/2 \\ (\partial_z u^r + \partial_r u^z)/2 & \partial_z u^z & \partial_z u^\phi/2 \\ \partial_r u^\phi/2 & \partial_z u^\phi/2 & u^r/r^3 \end{bmatrix}.$$

Note that the strain rate tensor has the same mathematical form.

Spherical Coordinates with Rotational Symmetry

We abstain from giving an example here because the corresponding components of the tensor are quite long and do not give additional insight.

Equation (I.61) does not have a nonlinear equivalent, because higher orders of the infinitesimal time step δt naturally vanish. Using the strain rate tensor, one can define the viscous stress tensor that arises in fluids and solids in response to gradual flows and deformations (Landau and Lifshitz, 1987; Lai et al., 2010; Murea, 2018).

Gradual compression and dilation. If the metric tensor changes due to a gradual deformation, then so does the infinitesimal volume element that is spanned by the non-orthonormal basis $\boldsymbol{V}$ with basis vectors $\lambda_i \in \boldsymbol{V}$. In particular, the volume element is given by $dV = \sqrt{\det \boldsymbol{g}} \, d^n \omega$, where n is the number of dimensions, see Eq. (I.19). By using the expansion $\sqrt{\det(\boldsymbol{I} + 2\dot{\boldsymbol{\varepsilon}}\,\delta t)} = 1 + \mathrm{tr}(\dot{\boldsymbol{\varepsilon}})\,\delta t + \mathcal{O}(\delta t^2)$, we then find that the infinitesimal volume element changes as follows (Timoshenko and Gere, 1961; Amenzade, 1979; Landau, Pitaevskii, et al., 1986; Landau and Lifshitz, 1987; Lai et al., 2010; Murea, 2018):

$$\delta(dV) = \mathrm{tr}(\dot{\boldsymbol{\varepsilon}})\,\delta t\, dV = (\boldsymbol{\nabla} \cdot \boldsymbol{v})\,\delta t\, dV. \qquad (I.62)$$

This result is used to describe incompressibility in fluid mechanics (Landau and Lifshitz, 1987; Lai et al., 2010; Murea, 2018) and to separate bulk strain from shear strain in infinitesimal elasticity theory (Timoshenko and Gere, 1961; Amenzade, 1979; Landau, Pitaevskii, et al., 1986; Lai et al., 2010; Murea, 2018).

Equation (I.62) has another important consequence. If there is a conserved quantity such as particle number dN in a given volume element, then the change of the corresponding particle density $c = dN/dV$, due to compression or dila-

tion, is given by:

$$\delta c = \delta\left(\frac{dN}{dV}\right) = -(\boldsymbol{\nabla}\cdot\boldsymbol{v})\,c\,\delta t\,. \tag{I.63}$$

This leads to the continuity equation for conserved quantities, and is also valid for vector fields or tensor fields that obey some conservation law. The momentum density field $\boldsymbol{p}$ is one example of such a conserved quantity.

Advection in the embedding.   So far, we have discussed how gradual deformations affect the metric tensor, the size of infinitesimal volume elements, and how these changes translate to physical quantities in the co-moving frame of some tracer particle. Now, we place ourselves back into the laboratory frame and ask: *How will the motion of our tracer particles, which we describe with the velocity field $\boldsymbol{v}(\boldsymbol{x})$, change the spatial distribution of our physical quantities in the laboratory frame?* Such *advection* can also show itself in the co-moving frame of a tracer particle if there are fields that remain stationary in the laboratory frame. Advection over some small time interval δt maps all material positions $\boldsymbol{x}$ to new material positions, $\boldsymbol{x} \to \boldsymbol{x} + \boldsymbol{v}\,\delta t$. Then, the value of an advected scalar density field at position $\boldsymbol{x}$ is given by:

$$c(\boldsymbol{x} - \boldsymbol{v}\,\delta t) = c(\boldsymbol{x}) - \boldsymbol{\nabla}c\cdot\boldsymbol{v}\,\delta t\,, \tag{I.64}$$

where we have performed a Taylor expansion up to linear order in physical position $\boldsymbol{x}$. By then using Eq. (I.46) for the gradient of a scalar field in curvilinear coordinates, one finds:

$$\delta c = -\boldsymbol{\nabla}c\cdot\boldsymbol{v}\,\delta t = -\sum_i \frac{\partial c}{\partial\omega^i}\,v^i\,\delta t\,, \tag{I.65}$$

where $\boldsymbol{\omega}$ refers to the intrinsic coordinates in the co-moving frame. One can proceed analogously for an advected vector field $\boldsymbol{p}$ and use Eq. (I.48) for the gradient of a vector field in curvilinear coordinates, to find:

$$\delta\boldsymbol{p} = -(\boldsymbol{\nabla}\otimes\boldsymbol{p})\cdot\boldsymbol{v}\,\delta t = -\sum_i \frac{\partial\boldsymbol{p}}{\partial\omega^i}\,v^i\,\delta t\,, \tag{I.66}$$

where $\boldsymbol{\omega}$ refers to the intrinsic coordinates in the co-moving frame. Advection is an essential part of fluid mechanics (Landau and Lifshitz, 1987; Lai et al., 2010; Murea, 2018).

Variation of the surface.   In our discussion so far, we have only considered motion that occurs entirely *within* a given domain, for example in the bulk or on the surface of our geometry. We refer to the corresponding displacements on
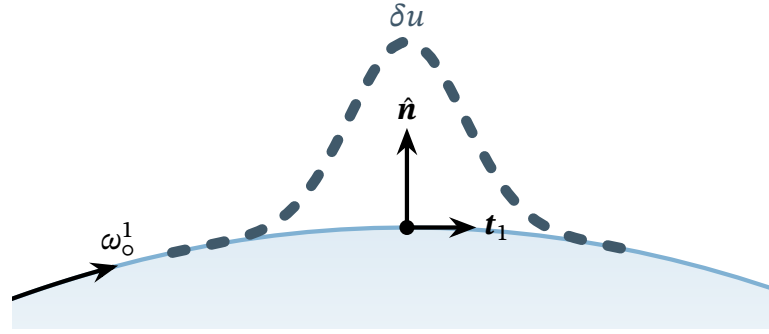
Figure I.5: Side view of a two-dimensional surface in a three-dimensional Cartesian embedding. We move the surface by some distance δu along its unit normal vector. This is called a *normal variation*.

the surface, which move a given surface point to a different nearby point in the tangent plane, as *tangential variations*. Because the tangent plane locally spans the surface, see Eq. (I.15), tangential variations do not change the surface shape. They do, however, affect the surface metric as described by the surface strain tensor, Eq. (I.58), and the surface strain rate tensor, Eq. (I.61). Consequently, one observes changes in surface area, Eq. (I.62), as well as the surface density of all conserved quantities, Eq. (I.63), in the co-moving frame of some tracer particle. Looking at the surface from the laboratory frame, one then finds advection of scalar fields, Eq. (I.65), vector fields, Eq. (I.66), as well as tensor fields of higher order.

But advection is not restricted to motion parallel to the surface only. In the following, we discuss what happens if the surface moves by some small distance along its unit normal vector, thereby advecting all surface quantities *out of plane*. To that end, as observers we again place ourselves into the co-moving frame of some tracer particle on the surface. In this co-moving frame, all nearby points are parameterized by intrinsic coordinates $\omega_\circ$ and map to extrinsic (that is, physical) coordinates in the Cartesian embedding $x \equiv \Gamma(\omega_\circ)$, as discussed in Section I.3.1 "Extrinsic and Intrinsic Coordinate Systems". Now, we introduce a *normal variation* by some small distance $\delta u(\omega_\circ)$, which moves all surface points:

$$\tilde{x}_\circ = \tilde{\Gamma}(\omega_\circ) = \Gamma(\omega_\circ) + \delta u(\omega_\circ)\,\hat{n}(\omega_\circ) \equiv x + \delta u\,\hat{n}\,, \tag{I.67}$$

along the unit normal vector $\hat{n}$ of the surface (Fig. I.5). Based on the new surjective mapping $\tilde{\Gamma}(\omega_\circ)$ from the intrinsic coordinates in the co-moving frame to the extrinsic coordinates in the embedding, we now have to determine the new metric tensor and the new shape tensor of the surface. To do so, we in principle proceed analogously to Section I.3.1 "Extrinsic and Intrinsic Coordinate Systems" and Section I.3.3 "Measuring the Shape of a Surface". However, we

have to keep in mind the little subtlety that both the normal vector $\hat{\boldsymbol{n}}$ and the variation δu depend on their intrinsic coordinates $\boldsymbol{\omega}_\circ$.

Variation of the boundary metric. To find out how the metric tensor on the boundary changes after applying our variation δu, we first determine the new tangent vectors on the surface, see Eq. (I.16):

$$\tilde{\boldsymbol{t}}_i = \frac{\partial \tilde{\boldsymbol{\Gamma}}}{\partial \omega_\circ^i} = \boldsymbol{t}_i + \left(\frac{\partial \hat{\boldsymbol{n}}}{\partial \omega_\circ^i} \right) \delta u + \hat{\boldsymbol{n}} \left(\frac{\partial (\delta u)}{\partial \omega_\circ^i} \right). \tag{I.68}$$

As we have discussed in Section I.2.4 "A Primer on the Calculus of Variations", the variation is maximal at the intrinsic coordinates $\boldsymbol{\omega}_\circ$ where it is applied, and decays to zero within some small physical distance away from this position. Therefore, the last term in Eq. (I.68) must vanish[12]. The components of the metric tensor, Eq. (I.18), *after* applying the variation, are then given by:

$$\tilde{g}_{ik} = \tilde{\boldsymbol{t}}_i \cdot \tilde{\boldsymbol{t}}_k = \boldsymbol{t}_i \cdot \boldsymbol{t}_k + \boldsymbol{t}_i \cdot \left(\frac{\partial \hat{\boldsymbol{n}}}{\partial \omega_\circ^k} \right) \delta u + \boldsymbol{t}_k \cdot \left(\frac{\partial \hat{\boldsymbol{n}}}{\partial \omega_\circ^i} \right) \delta u. \tag{I.69}$$

By then using the definition of the shape tensor, $h_{ik} = -\boldsymbol{t}_i \cdot \left(\partial \hat{\boldsymbol{n}} / \partial \omega_\circ^k \right)$, see Eq. (I.35), and its symmetry, we find that a normal variation directly affects the surface metric as follows (Kreyszig, 1959; Zhong-can and Helfrich, 1989; Capovilla et al., 2003; Deserno, 2015):

$$\delta \boldsymbol{g} \cdot \boldsymbol{g}^{-1} = (\tilde{\boldsymbol{g}} - \boldsymbol{g}) \cdot \boldsymbol{g}^{-1} = -2\,\boldsymbol{h} \cdot \boldsymbol{g}^{-1}\,\delta u. \tag{I.70}$$

Comparing the above expression to Eq. (I.59), we then find that a normal variation directly induces strain when it changes the length measure on the surface:

$$\delta \boldsymbol{E} = -\boldsymbol{T}^{-T} \cdot \boldsymbol{h} \cdot \boldsymbol{g}^{-1} \cdot \boldsymbol{T}^T\,\delta u, \tag{I.71}$$

where $\boldsymbol{T}$ refers to the basis that spans the tangent plane with tangent vectors $\boldsymbol{t}_i \in \boldsymbol{T}$. By virtue of Eq. (I.62), this surface strain affects the surface area of our geometry, $\delta(dS) = \text{tr}(\delta \boldsymbol{E})\,dS$, and the surface density of conserved quantities, Eq. (I.63). To summarize, any movement by some distance δu along the unit normal vector of the surface will induce the following change in surface area dS and (particle) density c (Kreyszig, 1959; Pressley, 2010; Frankel, 2011; Grinfeld, 2013; Deserno, 2015):

$$\delta(dS) = -\,\text{tr}(\boldsymbol{h} \cdot \boldsymbol{g}^{-1})\,dS\,\delta u = -H\,dS\,\delta u, \quad \text{and} \quad \delta c = H\,c\,\delta u. \tag{I.72}$$

---

[12] Note that Eq. (I.69) actually follows from Eq. (I.68) in a more generic context, without a need to invoke any specific properties of the variation δu. The reason is that the unit normal vector is perpendicular to the tangent vectors, $\hat{\boldsymbol{n}} \cdot \boldsymbol{t}_i = 0$.

One can intuitively understand these results by considering a balloon, which has total curvature $H = \kappa_1 + \kappa_2 < 0$. If one inflates the balloon, then its surface area increases while the density of conserved material decreases due to stretching. For surfaces under isotropic tension, such a variation in surface area leads to a Laplace pressure (S. Safran, 2003; D. Nelson et al., 2004). In Section IV.1 "Collective Cell Migration Affects Morphogenesis" and Section IV.2 "Between Morphogenesis and Hydrodynamic Flows", we generalize the Laplace pressure to anisotropic surface tension, which arises from cell orientation.

Variation of the boundary shape.   Finally, we investigate how the shape tensor of the boundary changes in response to our variation δu. We proceed by breaking up our calculation into several small steps, to help us keep track of subtleties that may arise. Taking the derivative of the post-variation tangent vector, Eq. (I.68), and inserting our result into the definition of the shape tensor, Eq. (I.35), we arrive at the following expression:

$$\tilde{h}_{ik} = \hat{\boldsymbol{n}} \cdot \left(\frac{\partial \tilde{\boldsymbol{t}}_i}{\partial \omega_\circ^k} \right) = \hat{\boldsymbol{n}} \cdot \left[\frac{\partial \boldsymbol{t}_i}{\partial \omega_\circ^k} + \frac{\partial^2 \hat{\boldsymbol{n}}}{\partial \omega_\circ^i \partial \omega_\circ^k} \delta u + \hat{\boldsymbol{n}} \frac{\partial^2 (\delta u)}{\partial \omega_\circ^i \partial \omega_\circ^k} \right]. \qquad \text{(I.73)}$$

Here, we have used $\hat{\boldsymbol{n}} \cdot (\partial \hat{\boldsymbol{n}} / \partial \omega_\circ^i) = 0$ to cancel several contributions in the square brackets[13]. In the following, we take a closer look and rewrite the remaining terms in the square brackets.

To proceed, we again make extensive use of orthonormalization, as introduced in Paragraph "Basis orthonormalization" (Section I.3.2) and applied in various contexts so far. Specifically, we consider a transformation $\boldsymbol{O}$ that maps our non-orthonormal tangent basis to an orthonormal tangent basis, $\boldsymbol{T}_\oplus = \boldsymbol{T} \cdot \boldsymbol{O}$, with orthonormal tangent vectors $\boldsymbol{t}_{\oplus,i} \in \boldsymbol{T}_\oplus$. Then, we express the identity mapping in terms of the orthonormal tangent vectors, $\boldsymbol{I} = \sum_l \boldsymbol{t}_{\oplus,l} \otimes \boldsymbol{t}_{\oplus,l}$. Furthermore, we express the scalar product (inner product) through a formal matrix multiplication between a row vector $\boldsymbol{s}^T$ ($1 \times N$ matrix) and a column vector $\boldsymbol{r}$ ($N \times 1$ matrix), $\boldsymbol{s} \cdot \boldsymbol{r} \equiv \boldsymbol{s}^T \cdot \boldsymbol{r}$. Analogously, we also rewrite the tensor product (outer product) as the formal matrix multiplication between a column vector $\boldsymbol{s}$ ($N \times 1$ matrix) and a row vector $\boldsymbol{r}^T$ ($1 \times N$ matrix), $\boldsymbol{s} \otimes \boldsymbol{r} \equiv \boldsymbol{s} \cdot \boldsymbol{r}^T$. When we express vectors via matrices, the symbol "·" identifies a matrix multiplication. Because this trick can cause a clash with the notation of an inner vector product, we only use it in two places of the present thesis, and explicitly state where we do so. Taking all of these considerations together, we rewrite the second term in the square

---

[13] Alternatively, one can also simply drop all linear derivatives of the variation δu, which is maximal at the intrinsic coordinates $\omega_\circ$ where it is applied.

brackets of Eq. (I.73) as follows:

$$\hat{\boldsymbol{n}} \cdot \frac{\partial^2 \hat{\boldsymbol{n}}}{\partial \omega_\circ^i \partial \omega_\circ^k} = -\left(\frac{\partial \hat{\boldsymbol{n}}}{\partial \omega_\circ^i}\right) \cdot \left(\frac{\partial \hat{\boldsymbol{n}}}{\partial \omega_\circ^k}\right) = -\left(\frac{\partial \hat{\boldsymbol{n}}}{\partial \omega_\circ^i}\right) \cdot \left(\sum_l \boldsymbol{t}_{\oplus,l} \otimes \boldsymbol{t}_{\oplus,l}\right) \cdot \left(\frac{\partial \hat{\boldsymbol{n}}}{\partial \omega_\circ^k}\right)$$

$$\equiv -\left(\frac{\partial \hat{\boldsymbol{n}}^T}{\partial \omega_\circ^i}\right) \cdot \left(\sum_{l,m,n} \boldsymbol{t}_m \, O_{ml} \, O_{ln}^T \, \boldsymbol{t}_n^T\right) \cdot \left(\frac{\partial \hat{\boldsymbol{n}}}{\partial \omega_\circ^k}\right) = -\sum_{m,n} h_{im} \, g_{mn}^{-1} \, h_{nk}, \quad \text{(I.74)}$$

where we have used $\boldsymbol{O} \cdot \boldsymbol{O}^T = \boldsymbol{g}^{-1}$ in the last step, see Eq. (I.26).

Now, we take a closer look at the third term in the square brackets of Eq. (I.73). We start with the (as we will see *a posteriori*) closely related expression of the Hessian of our variation in curvilinear coordinates, projected onto the basis $\boldsymbol{T}$ of our non-orthonormal co-moving frame:

$$\boldsymbol{t}_m^T \cdot \left[\boldsymbol{\nabla} \otimes \boldsymbol{\nabla}(\delta u)\right] \cdot \boldsymbol{t}_n = \sum_{k,l} g_{kl}^{-1} \boldsymbol{t}_m \cdot \frac{\partial[\boldsymbol{\nabla}(\delta u)]}{\partial \omega_\circ^k} \boldsymbol{t}_l \cdot \boldsymbol{t}_n = \boldsymbol{t}_m \cdot \frac{\partial[\boldsymbol{\nabla}(\delta u)]}{\partial \omega_\circ^n}$$

$$= \boldsymbol{t}_m \cdot \frac{\partial}{\partial \omega_\circ^n} \left[\sum_{k,l} g_{kl}^{-1} \frac{\partial(\delta u)}{\partial \omega_\circ^k} \boldsymbol{t}_l\right]. \quad \text{(I.75)}$$

Here, we have proceeded by (i) inserting the definition of the gradient of a vector field, Eq. (I.48), (ii) using the definition of the metric tensor, $\boldsymbol{t}_l \cdot \boldsymbol{t}_n = g_{ln}$, see Eq. (I.18), to get rid of several indices, and then (iii) inserting the definition of the gradient of a scalar field, Eq. (I.46). Because the variation δu is maximal at the intrinsic coordinates $\boldsymbol{\omega}_\circ$ where it is applied, its first-order partial derivatives must vanish there, $\partial(\delta u)/\partial \omega_\circ^k = 0$. Only for such a scalar field that is maximal at the point of expansion, does the following relation then hold:

$$\boldsymbol{t}_m^T \cdot \left[\boldsymbol{\nabla} \otimes \boldsymbol{\nabla}(\delta u)\right] \cdot \boldsymbol{t}_n = \sum_{k,l} \frac{\partial^2(\delta u)}{\partial \omega_\circ^n \partial \omega_\circ^k} g_{kl}^{-1} \boldsymbol{t}_m \cdot \boldsymbol{t}_l = \frac{\partial^2(\delta u)}{\partial \omega_\circ^n \partial \omega_\circ^m}. \quad \text{(I.76)}$$

We strongly emphasize that this is *only* valid because the variation δu is maximal at the point of expansion. In all other cases, one must account for the derivatives of the tangent vectors, which constitutes the curvilinear property of our basis.

Finally, we insert our intermediate results, Eq. (I.74) and Eq. (I.76) back into Eq. (I.73):

$$\tilde{\boldsymbol{h}} = \boldsymbol{h} - \boldsymbol{h} \cdot \boldsymbol{g}^{-1} \cdot \boldsymbol{h} \, \delta u + \boldsymbol{T}^T \cdot \left[\boldsymbol{\nabla} \otimes \boldsymbol{\nabla}(\delta u)\right] \cdot \boldsymbol{T}. \quad \text{(I.77)}$$

Then, we arrive at the following expression for the variation of the shape tensor (Zhong-can and Helfrich, 1989; Capovilla et al., 2003; Deserno, 2015):

$$\tilde{\boldsymbol{h}} \cdot \tilde{\boldsymbol{g}}^{-1} - \boldsymbol{h} \cdot \boldsymbol{g}^{-1} = \tilde{\boldsymbol{h}} \cdot \boldsymbol{g}^{-1} \cdot (\boldsymbol{I} + 2\boldsymbol{h} \cdot \boldsymbol{g}^{-1} \delta u) - \boldsymbol{h} \cdot \boldsymbol{g}^{-1}$$

$$= (\boldsymbol{h} \cdot \boldsymbol{g}^{-1})^2 \, \delta u + \boldsymbol{T}^T \cdot \left[\boldsymbol{\nabla} \otimes \boldsymbol{\nabla}(\delta u)\right] \cdot \boldsymbol{T}^{-T}, \quad \text{(I.78)}$$

where we have used Eq. (I.70) to approximate the metric after applying our variation δu. Thus, the first variation of the total curvature is given by (Zhong-can and Helfrich, 1989; Capovilla et al., 2003; Deserno, 2015):

$$\delta H = \text{tr}\big[(\boldsymbol{h} \cdot \boldsymbol{g}^{-1})^2\big]\,\delta u + \boldsymbol{\nabla}^2(\delta u) = \big(H^2 - 2K\big)\,\delta u + \boldsymbol{\nabla}^2(\delta u)\,. \qquad (I.79)$$

This result is particularly important for calculating the bending stresses of a lipid membrane, or of thin shells in general. In Section II.1 "Mechanochemical Coupling between Proteins and Membranes", we apply these concepts to study the binding kinetics of membrane-deforming proteins.

II BETWEEN PROTEIN PATTERNS AND MECHANICS

II.1 MECHANOCHEMICAL COUPLING BETWEEN PROTEINS AND MEMBRANES

In this project, we draw a connection between two central themes of intracellular dynamics: (i) mechanochemical interactions and (ii) protein pattern formation via reactions and diffusion. Our main results are published in "Protein Recruitment through Indirect Mechanochemical Interactions", Physical Review Letters **123**, 178101 (2019). We refer to pages 61–66 for a reprint of the main text and to pages 67–73 for a reprint of the Supplementary Material. The following serves as an introduction into the project and a summary of its main results, for the convenience of the reader. Furthermore, we also discuss the theory in light of the introduction to differential geometry in Section I.3 "A Foundation for Patterns in Adapting Organisms".

A note about the notation. To be consistent with the rest of the thesis, we choose the notation $c_\circ$ to indicate the surface density of proteins, instead of m which was used in the original article (A. Goychuk and Frey, 2019). Furthermore, we denote the mechanical rigidity coefficients with k instead of κ, because the latter is reserved for curvatures in this thesis. Then, for the reaction rates, we choose the notation r instead of k, which was used in the original article (A. Goychuk and Frey, 2019). Finally, we also denote the placeholder variable, which can represent either total curvature or lipid density, with ψ instead of u, because the latter is reserved for deflections in this thesis.

II.1.1 STARTING POINT OF THE PROJECT

General Scope and Relevance. In biological systems, coupling between mechanical and chemical degrees of freedom is a frequent motif. For example, different polymers and proteins can bind to and deform lipid membranes (Ford et al., 2002; Tsafrir et al., 2003; Lee et al., 2005; Gov and Gopinathan, 2006; Zimmerberg and Kozlov, 2006; Prinz and Hinshaw, 2009; Stachowiak et al., 2012;

McMahon and Boucrot, 2015; Jarsch et al., 2016; Gov, 2018; Yuan et al., 2021). This includes proteins with Bin/Amphiphysin/Rvs (BAR) domains, which bend the membrane to their curved shape through molecular interactions (Zimmerberg and McLaughlin, 2004; Peter et al., 2004; Bhatia et al., 2009; Mim and Unger, 2012; Zhu et al., 2012; Prévost et al., 2015; Simunovic et al., 2015). Remarkably, recent experiments show that the Min family of proteins can also deform giant unilamellar vesicles (Litschel et al., 2018; Fu et al., 2021). Given that mechanochemical interactions between proteins and elastic membranes are so abundant, inducing membrane deformations might not be an exclusive ability of specialized proteins. Instead, because the forces that enable binding are reciprocal, any protein that binds to phospholipid bilayer membranes could deform these membranes as a side effect. Then, what are the implications of such mechanochemical interactions for intracellular dynamics?

It is known that by inducing deformations of elastic membranes via reciprocal forces, proteins can interact with other membrane-binding proteins (Phillips, Ursell, et al., 2009; Weikl, 2018; Idema and Kraft, 2019). This coupling between membrane-bound particles manifests in an effective pairwise attraction or repulsion (Haselwandter and Phillips, 2013; Schweitzer and Kozlov, 2015; van der Wel et al., 2016; Vahid and Idema, 2016), and can for example lead to sorting according to particle size (Idema, Semrau, et al., 2010). Furthermore, as a consequence of membrane-mediated pairwise interactions, the proteins can form different aggregates (Idema and Kraft, 2019). For example, membrane-bound particles can accumulate into clusters (Schmidt et al., 2008), align into bundles and linear aggregates (Shlomovitz and Gov, 2009; Vahid and Idema, 2016; Vahid, Šarić, et al., 2017; Vahid, Dadunashvili, et al., 2019), generate tubular membrane protrusions (H. Zhao et al., 2011; Mesarec et al., 2016), or form lattice-like structures (Haselwandter and Wingreen, 2014; Olinger et al., 2016). Here, however, we focus on an entirely different and independent type of dynamics. Instead of considering particles that are permanently bound to a lipid membrane, we investigate the binding and unbinding kinetics between a protein and a membrane. Such particle exchange between the cytosol and the membrane is a crucial mechanism for several protein pattern forming systems (Halatek, Brauns, et al., 2018), which directly leads to our main question.

Research Question and Hypothesis. In pattern-forming systems, some membrane-bound proteins favor the attachment of additional proteins to the membrane, resulting in a phenomenon termed *recruitment* (Halatek, Brauns, et al., 2018). For example, in the *Escherichia Coli* Min system, MinD recruits both itself and MinE to the membrane. In three-dimensional solutions that are not coupled to a two-dimensional surface, one would invoke classical theories of binding cooperativity, where proteins can present multiple binding sites for

ligands, to explain such nonlinear reaction rates (Hill, 1913; M. I. Stefan and Le Novère, 2013). In a system such as ours, however, we have additional degrees of freedom that describe the mechanical conformation of the membrane. Therefore, we hypothesize that through mechanochemical interactions with the proteins, the membrane can mediate their cooperative binding.

II.1.2   SUMMARY OF THE MAIN RESULTS

Membrane-binding proteins change the mechanical conformation of the membrane, by attaching via reciprocal interactions. This signifies a competition: binding proteins yields an energy benefit, while membrane deformations incur an energy cost. If the surface density of membrane-bound proteins is small, then binding is unfavorable. But as more proteins bind to and deform the membrane, the membrane's surface becomes more favorable for binding. Thus, one has a positive feedback loop, where the binding rate of proteins to the membrane increases nonlinearly with the surface density of already bound proteins.

These results constitute a novel and purely physical mechanism of protein cooperativity, which does not rely on protein conformation changes and chemical affinity between proteins. Our mechanism applies equally well to all proteins that induce mechanical deformations of the membrane, and is therefore general. We expect that the *nonlinearity* of protein recruitment can be tuned by applying external stresses to the membrane, and thereby shifting its reference configuration. This effect should drastically change the dynamics of pattern-forming systems that rely on membrane-mediated recruitment via mechanical interactions. Such pattern-forming systems would then be able to detect mechanical signals in the environment.

II.1.3   TECHNICAL SUMMARY AND ADDITIONAL DISCUSSION

Here, we discuss some of the more technical aspects of this project, which involve differential geometry, variational calculus, and the calculation of first-passage times.

The cost and benefit of protein binding.   First, we investigate the binding and unbinding dynamics between proteins and membranes by considering pairwise interactions among lipids and proteins. Molecular interactions among lipids endow the membrane with mechanical rigidity against stretching and bending. Analogously, binding of proteins to the membrane requires molecular interactions between lipids and proteins. To model crowding effects, we also consider molecular interactions among proteins, which become relevant at high protein surface density, c_o. We treat the binding process itself as

reversible, so that the heat generation is entirely determined by the entropy production. Therefore, we can construct a Helmholtz free energy functional, which describes the mechanochemical configuration of the membrane and the membrane-bound proteins:

$$F = \oint dS \left[f_{mech}(\boldsymbol{u}) + c_\circ E_{bind}(\boldsymbol{u}) + f_{pp}(c_\circ) \right], \tag{II.1}$$

where $\oint dS$ indicates a surface integral. Next, we take a closer look at the different contributions to Eq. (II.1).

The first term in the square brackets of Eq. (II.1), $f_{mech}(\boldsymbol{u})$, refers to the free energy density of a deformed membrane with mechanical configuration $\boldsymbol{u}$. We treat lipid membranes as thin elastic sheets, with a bulk modulus k_s that penalizes stretching and a bending modulus k_b that penalizes bending (Helfrich, 1973; Seifert, 1997; S. Safran, 2003). To lowest order, the energy costs of pure bending and pure stretching are then given by

$$f_{stretch}(\rho) = \frac{1}{2} k_s (\rho - \rho_0)^2, \quad \text{and} \quad f_{bend}(H) = \frac{1}{2} k_b (H - H_0)^2, \tag{II.2}$$

where ρ is the surface density of lipids and H is the total curvature of the surface. The equilibrium configuration of the membrane is determined by a reference lipid density ρ_0 and a spontaneous curvature H_0 (Helfrich, 1973; Seifert, 1997; S. Safran, 2003). To make our theory as simple as possible, we neglect any coupling between bending and stretching modes that may occur. This approximation is valid if: (i) stretching has a far greater cost than bending, so that the surface area of a bent membrane remains approximately constant (Seifert, 1997), or (ii) we treat stretching as an isolated process in an approximately planar membrane with negligible bending, or (iii) we consider a symmetric membrane where bending and stretching must decouple because of the symmetry. Note that in a more general setting, which we do not study here, one would have to consider such a coupling (Seifert, 1997; S. Safran, 2003).

The second term in the square brackets of Eq. (II.1), $E_{bind}(\boldsymbol{u})$, refers to the binding energy of each protein, which depends on the mechanical configuration of the membrane, $\boldsymbol{u}$. We perform a Taylor expansion of the binding energy $E_{bind}(\boldsymbol{u})$, to lowest order around the optimal membrane conformation $\boldsymbol{u}_{opt}$ where protein binding is strongest. The binding energy of each protein is then weighted with the surface density of membrane-bound proteins $c_\circ$ to account for the whole population of proteins. Finally, the last term in the square brackets, $f_{pp}(c_\circ)$, models interactions among proteins.

Eliminating the mechanical degrees of freedom. Based on Eq. (II.1), one can then distinguish the following different degrees of freedom: (i) deformations of the membrane are mechanical degrees of freedom, while (ii) particle

exchange due to the binding and unbinding dynamics of proteins corresponds to chemical degrees of freedom. We are mainly interested in the chemical degrees of freedom, where cytosolic proteins diffuse a finite distance to the membrane and bind there. Such binding events alter the number of proteins on the membrane, and thereby the Helmholtz free energy, Eq. (II.1). Then, each protein that binds to the membrane has to either pay an energy cost or will reap an energy benefit, which is given by its chemical potential (Landau and Lifshitz, 1980):

$$\mu_c = \frac{\delta F}{\delta c_\circ} . \tag{II.3}$$

If the mechanical and the chemical degrees of freedom are completely independent, then the chemical potential coincides with the binding energy, $\mu_c = E_{bind}(\boldsymbol{u})$. However, this is not the case here: when proteins bind to the membrane, they change its mechanical configuration $\boldsymbol{u}$ and thus the binding energy of all other nearby proteins. This relaxation of the mechanical degrees of freedom occurs via infinitesimal membrane motion, which is much faster than the chemical dynamics. Therefore, we adiabatically eliminate the mechanical degrees of freedom as discussed next. To that end, we determine the mechanical stresses that act on the membrane, by studying variations of the surface and its free energy, Eq. (II.1). Note that the surface density of particles and the curvature of the surface transform differently under variations, see Eq. (I.72) and Eq. (I.79). Therefore, for a detailed description we have to distinguish between membrane-stretching and membrane-bending proteins, as we discuss next.

Coupling between proteins and the membrane via stretching. Suppose that the membrane-binding proteins insert an "anchor" into the lipid membrane, which then locally interacts with the lipids and affects their local density. As discussed in Paragraph "The cost and benefit of protein binding" and in (A. Goychuk and Frey, 2019), in this case the free energy of the membrane and the membrane-bound proteins is given by:

$$F = \oint dS \left[\frac{1}{2} k_s (\rho - \rho_0)^2 + c_\circ \left(E_{opt} + \frac{1}{2} \epsilon_s (\rho - \rho_{opt})^2 \right) + f_{pp}(c_\circ) \right], \tag{II.4}$$

where E_{opt} is the binding energy of a protein under optimal conditions, and ϵ_s characterizes the sensitivity of the protein to the mechanical conformation of the membrane. The binding of proteins to the membrane is strongest at the "optimal" lipid density ρ_{opt}. First, we ask: *How will the insertion or removal of a protein affect the mechanical conformation of the membrane?* From Eq. (II.4), it follows that insertion of a protein into the membrane will affect the chemical potential profile of lipids, $\mu_\rho = \delta F/\delta\rho$. In turn, gradients in this chemical

potential correspond to the following thermodynamic forces:

$$-\boldsymbol{\nabla}\mu_\rho \equiv -\boldsymbol{\nabla}\left[\frac{\delta F}{\delta\rho}\right] = -\boldsymbol{\nabla}\left[k_s\left(\rho-\rho_0\right) + \epsilon_s\,c_\circ\left(\rho-\rho_{opt}\right)\right]. \qquad \text{(II.5)}$$

These thermodynamic forces, $-\boldsymbol{\nabla}\mu_\rho$, according to Onsager's theory of non-equilibrium thermodynamics (Balian, 2007), drive lateral lipid fluxes along the membrane. Thus, insertion of a protein into the membrane will induce lateral redistribution of lipids until the lipid membrane reaches mechanical equilibrium. In mechanical equilibrium, the chemical potential of lipids μ_ρ should adopt a constant value, which in principle is determined by external constraints (for example, a fixed total area of the membrane). Here, we consider a large (for all practical purposes infinite) membrane with equilibrated lipid density, $\rho|_{\partial S} = \rho_0$, and vanishing protein density, $c_\circ|_{\partial S} = 0$ in the far field. Then, the membrane adopts the following mechanical conformation (A. Goychuk and Frey, 2019):

$$\rho = \rho_0 + (\rho_{opt} - \rho_0)\frac{\epsilon_s\,c_\circ}{k_s + \epsilon_s\,c_\circ}. \qquad \text{(II.6)}$$

If no proteins bind to the membrane, then the lipid density takes its reference value, ρ_0. Once more proteins bind to the membrane, the configuration of the membrane will shift towards the lipid density that is preferred by the proteins, ρ_{opt}.

Note that in this context, the chemical potential of the lipids acts as an effective surface tension, $-\mu_\rho$, which becomes even more apparent if one considers normal variations of the membrane. Then, we find that a displacement of the surface by some small distance δu along its unit normal vector can only be counteracted by the following externally applied stress[1]:

$$\frac{\delta F}{\delta u} = \left[\frac{1}{2}\,k_s\left(\rho^2-\rho_0^2\right) + \epsilon_s\,c_\circ\,\rho\left(\rho-\rho_{opt}\right) + c_\circ\,\frac{\partial f_{pp}}{\partial c_\circ} - f_{pp}\right]H, \qquad \text{(II.7)}$$

where we have used Eq. (I.72) to account for the changes in surface area and surface density of particles. By making the approximation that the surface density of lipids remains close to its reference value, $\rho \approx \rho_0$, we find the following expression:

$$\frac{\delta F}{\delta u} \approx \left[k_s\left(\rho-\rho_0\right) + \epsilon_s\,c_\circ\left(\rho-\rho_{opt}\right)\right]\rho_0\,H = \mu_\rho\,\rho_0\,H. \qquad \text{(II.8)}$$

Here, we have also neglected protein-protein interactions under the condition that they only become relevant at high surface density of proteins (that is, protein-protein interactions are nonlinear). We find that Eq. (II.8) exactly corresponds to a Laplace pressure with effective surface tension $\tau \equiv -\mu_\rho\,\rho_0$.

---

[1] The surface itself exerts a stress $-\delta F/\delta u$ onto its surroundings.

Coupling between proteins and the membrane via bending. Now, suppose that the interactions between the membrane-binding proteins and the membrane induce bending of the latter, as is the case for proteins that contain BAR domains (Zimmerberg and McLaughlin, 2004; Peter et al., 2004; Bhatia et al., 2009; Mim and Unger, 2012; Zhu et al., 2012; Prévost et al., 2015; Simunovic et al., 2015). As discussed in Paragraph "The cost and benefit of protein binding" and in (A. Goychuk and Frey, 2019), in this case the free energy of the membrane and the membrane-bound proteins is given by:

$$F = \oint dS \left[\frac{1}{2} k_b \left(H - H_0 \right)^2 + c_\circ \left(\frac{1}{2} \epsilon_b \left(H - H_{opt} \right)^2 \right) + f_{pp}(c_\circ) \right], \qquad \text{(II.9)}$$

where E_{opt} is the binding energy of a protein under optimal conditions, and ϵ_b characterizes the sensitivity of the protein to the shape of the membrane. The binding of proteins to the membrane is strongest at the "optimal" curvature H_{opt}. As before, we ask: *How will the insertion or removal of a protein affect the shape of the membrane?* To answer this question, we again have to consider normal variations of the membrane, because tangential variations do not affect the shape of a surface. Then, we find that a displacement of the surface by some small distance δu along its unit normal vector can only be counteracted by the following externally applied stress (A. Goychuk and Frey, 2019):

$$\frac{\delta F}{\delta u} = \frac{1}{2} k_b \left(H - H_0 \right) \left(H^2 - 4K + H H_0 \right) + \epsilon_b c_\circ \left(H - H_{opt} \right) \left(H^2 - 2K \right)$$
$$+ \boldsymbol{\nabla}^2 \left[k_b (H - H_0) + \epsilon_b c_\circ \left(H - H_{opt} \right) \right] + \left[c_\circ \frac{\partial f_{pp}}{\partial c_\circ} - f_{pp} \right] H. \quad \text{(II.10)}$$

To arrive at above expression, we have used Eq. (I.72) to account for the changes in surface area and surface density of particles, as well as Eq. (I.79) to account for the changes in curvature. Note that accounting for the variation of the curvature, Eq. (I.79), gives a term that is proportional to the Laplacian of the variation, $\boldsymbol{\nabla}^2(\delta u)$. To get rid of this term, one has to integrate the variation of the free energy, δF, twice by parts, using the short introduction to the calculus of variations in Section I.2.4 "A Primer on the Calculus of Variations".

We assume that deflections of the membrane are small, so that the membrane remains near its intrinsic curvature, $H \approx H_0$. Furthermore, we assume that the surface density of protein is sufficiently small, so that interactions among proteins do not induce appreciable deformations of the membrane. Then, we may linearize Eq. (II.10) to the following simplified expression:

$$\frac{\delta F}{\delta u} \approx \boldsymbol{\nabla}^2 \left[k_b (H - H_0) + \epsilon_b c_\circ \left(H - H_{opt} \right) \right]. \qquad \text{(II.11)}$$

In mechanical equilibrium, the mechanical stresses should vanish, $\delta F/\delta u = 0$, leading to a shape equation that we can solve by integration. As before in Paragraph "Coupling between proteins and the membrane via stretching", we here consider a large (for all practical purposes infinite) membrane. In the far field, the curvature should be equilibrated, $H|_{\partial S} = H_0$, and the protein density should vanish, $c_{\rm o}|_{\partial S} = 0$. Then, the shape equation, $\delta F/\delta u = 0$, see Eq. (II.11), is solved by (A. Goychuk and Frey, 2019):

$$H = H_0 + (H_{opt} - H_0) \frac{\epsilon_b \, c_{\rm o}}{k_b + \epsilon_b \, c_{\rm o}} \, . \tag{II.12}$$

First-passage time of protein binding.   In Paragraph "Coupling between proteins and the membrane via stretching" and Paragraph "Coupling between proteins and the membrane via bending", we have used the condition that mechanical stresses must vanish in mechanical equilibrium. By doing so, we have found the equilibrium configuration $\boldsymbol{u}(c_{\rm o})$ of a membrane with $c_{\rm o}$ bound proteins per unit surface area. In agreement with (A. Goychuk and Frey, 2019), but in slightly more detail, we have shown that the membrane adopts the following mechanical configuration:

$$\psi = \psi_0 + (\psi_{opt} - \psi_0) \frac{\epsilon \, c_{\rm o}}{k + \epsilon \, c_{\rm o}} \, , \tag{II.13}$$

where $\psi \in \{\rho, H\}$ is a placeholder variable. Analogously, we have introduced placeholder parameters for the rigidity of the membrane, $k \in \{k_s, k_b\}$, and for the sensitivity of the proteins to the mechanical conformation of the membrane, $\epsilon \in \{\epsilon_s, \epsilon_b\}$. We then adiabatically eliminate the mechanical degrees of freedom, so that the mechanical conformation of the membrane changes instantly upon protein binding. Having eliminated the mechanical degrees of freedom, the chemical potential $\mu_c = \delta F/\delta c_{\rm o}$ then becomes an *effective* binding energy that takes into account both mechanical and chemical interactions (A. Goychuk and Frey, 2019):

$$\mu_c = E_{opt} + \left[c_{\rm o} \frac{\partial f_{pp}}{\partial c_{\rm o}} + f_{pp} \right] + \frac{1}{2} \frac{\epsilon \, (u_{opt} - u_0)^2}{(1 + c_{\rm o} \, \epsilon/k)^2} \, . \tag{II.14}$$

Now, all that is left is to determine the mean first passage time of a protein that diffuses from the cytosol to the membrane, where it is absorbed by binding. To that end, we have to make some assumptions about the chemical potential landscape of a protein that diffuses in the cytosol and then approaches the membrane. In (A. Goychuk and Frey, 2019), a piecewise linear approximation of the chemical potential landscape was considered, provided that there is no energy barrier that the protein has to cross before binding to the membrane. As we discuss next, one can make very similar conclusions by instead considering a
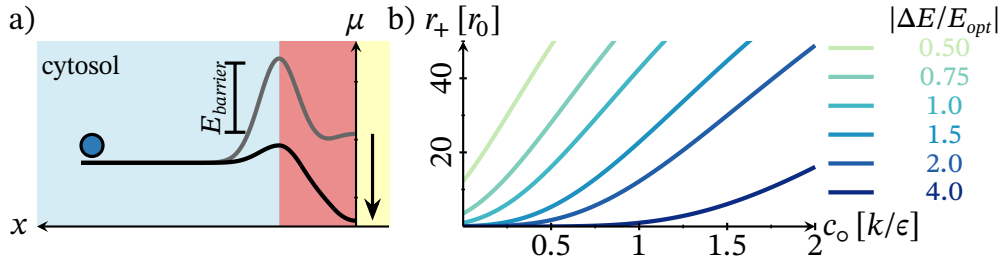
Figure II.1: a) A chemical potential profile with a barrier. A protein (filled blue circle) starts in the cytosol (blue), and has to cross a chemical potential barrier to enter the region (red) where attractive interactions with the membrane (yellow) become relevant. By attaching to the membrane, proteins deform the membrane into a more binding-favorable mechanical conformation, as in (A. Goychuk and Frey, 2019). Therefore, the chemical potential at the membrane shifts towards lower values (black arrow), and reduces the height of the chemical potential barrier that the proteins have to overcome before binding to the membrane. b) These changes in the chemical potential barrier lead to a nonlinear increase of the binding rate as a function of the protein surface density. This recruitment is especially pronounced if the proteins are more sensitive to the mechanical conformation of the membrane. Here, we have defined the binding energy difference between the reference configuration of the membrane and the most binding-favorable configuration of the membrane, $\Delta E = \frac{1}{2} \epsilon (u_{opt} - u_0)^2$. This figure is adapted from (A. Goychuk and Frey, 2019) under the terms of the ©① Creative Commons Attribution 4.0 International License, and modified to add a chemical potential barrier.

finite chemical potential barrier of magnitude $\mu_c + E_{barrier}$, which the protein has to overcome before it can bind to the membrane (Fig. II.1a). To that end, we assume that the chemical potential difference $E_{barrier}$ between the maximum of the barrier and the chemical potential at the membrane is constant. Such a chemical potential barrier ("activation barrier") could arise, for example, if the protein experiences some mechanical resistance when inserting an anchor into the membrane.

Addendum: An activation barrier in the chemical potential profile. If there is a large chemical potential barrier, with $E_{barrier} \gg \mu_c$, then the problem of finding the first-passage time maps exactly to Kramers' theory of reaction kinetics (Kramers, 1940; Hänggi et al., 1990). Then, one obtains an Arrhenius equation for the protein attachment rate (Arrhenius, 1889):

$$r_+ = r_0 \, \exp\left(-\frac{\mu_c}{k_B T}\right) , \tag{II.15}$$

where r_0 is some reference rate that depends on the height of the chemical potential barrier. Binding of proteins to the membrane leads to deformations of the latter, and to a more binding-favorable environment. This reduces the chemical potential barrier by shifting the chemical potential at the membrane downwards (Fig. II.1a), leading to a positive feedback loop and recruitment of proteins. Therefore, we find a nonlinear increase of the protein binding rate, as a function of the surface density of membrane-bound proteins (Fig. II.1b). In (A. Goychuk and Frey, 2019), the same result was obtained without explicitly adding a potential barrier that a protein has to overcome before it can bind to the membrane. Instead, the chemical potential directly at the membrane can act like such a barrier if $\mu_c > 0$, for small density of membrane-bound proteins. On a final note, if the height of the chemical potential barrier is defined by a constant offset relative to the chemical potential at the membrane, $\mu_c + E_{barrier}$, then the detachment rate will be constant: $r_- = r_0$. This is different than in (A. Goychuk and Frey, 2019), where the detachment rate was also affected by the mechanical conformation of the membrane. Which of these models reflects reality better, depends on the microscopic details of the molecular interactions. However, the main result of a nonlinear surface density dependent attachment rate (recruitment) is robust against these microscopic details.

II.1.4 Manuscript M1

Title:

Protein Recruitment through Indirect Mechanochemical Interactions

Authors:

Andriy Goychuk and Erwin Frey

Protein Recruitment through Indirect Mechanochemical Interactions

Andriy Goychuk and Erwin Frey[*]

Arnold Sommerfeld Center for Theoretical Physics and Center for NanoScience, Department of Physics,
Ludwig-Maximilians-Universität München, Theresienstraße 37, D-80333 Munich, Germany

Some of the key proteins essential for important cellular processes are capable of recruiting other proteins from the cytosol to phospholipid membranes. The physical basis for this cooperativity of binding is, surprisingly, still unclear. Here, we suggest a general feedback mechanism that explains cooperativity through mechanochemical coupling mediated by the mechanical properties of phospholipid membranes. Our theory predicts that protein recruitment, and therefore also protein pattern formation, involves membrane deformation and is strongly affected by membrane composition.

Protein pattern formation is essential for the spatial organization of intracellular processes [1]. Examples of biological significance include Min oscillations that guide the positioning of the *Z* ring to midcell in *E. coli* [2], the roles of cell polarization in determining the position of a new growth zone or bud site in *S. cerevisiae* [3] and the anteroposterior axis of the embryo in *C. elegans* [4], and spatiotemporal patterns formed by members of the Rho family of GTPases in eukaryotic cells [5]. Such self-organized patterns are the product of a dynamic interplay between diffusion (both in the cytosol and on the membrane) and biochemical reactions among proteins and between proteins and the membrane. A crucial motif in all of the biochemical reaction networks that drive these processes is a nonlinear feedback mechanism, which is generally termed *recruitment*. Here, membrane-bound proteins facilitate the binding of other soluble proteins from the cytosol to the membrane [1]. For example, in *E. coli*, membrane-bound MinD is said to recruit both cytosolic MinD and MinE to the membrane. What, then, is the physical basis for such cooperative binding between proteins and the membrane? One could adopt a purely chemical perspective and suggest an explanation based on classical concepts of binding cooperativity [6,7]. However, an indiscriminately high chemical affinity between recruiting proteins would also promote protein aggregation in the cytosol as an unwanted side effect. Then, to still facilitate specific recruitment to the membrane, a possible strategy is for individual proteins to change their conformation upon binding to the membrane so as to become chemically affine

scaffolds for other proteins [8,9]. In addition to these chemical interactions, binding of proteins to membranes inevitably invokes forces that can lead to membrane deformation.

Here, we show how such mechanochemical coupling can lead to a mechanism for the cooperative recruitment of proteins to phospholipid membranes and thereby provide an alternative strategy for cooperative membrane binding. The basic idea is very simple: Attractive forces between proteins and phospholipids facilitate protein attachment to the membrane. As equal and opposite forces must act on the membrane as well, protein binding will induce mechanical deformation of the membrane. Indeed, it is well known that membrane shape changes can be caused by curvature-inducing polymers and proteins [10–19] containing Bin-Amphiphysin-Rvs (BAR) domains [20–26] and—as recently shown [27]—also by the Min family of proteins. Equilibrium theories of the coupling between proteins and the membrane generally lead to membrane-mediated interactions between membrane-bound proteins, as reviewed in Refs. [28–30]. The physical origin of such interactions may be a hydrophobic mismatch for integral proteins [31–35], surface interactions that depend on curvature [24,25,32,36–41], or membrane shape fluctuations [42,43]. Furthermore, these interactions may also depend on the packing density [44] and composition [45,46] of the membrane. Then, proteins that are bound to the membrane effectively attract or repel each other [47–50] and form different aggregates [30,38,40,51–54]. Here, however, we do not focus on such self-organization effects. Instead, we ask a different and independent question, namely, how membrane deformations affect the *affinity and kinetic (un)binding rates* of proteins. We propose a general protein recruitment mechanism caused by indirect interactions facilitated through mechanical deformations of the membrane.

As we are interested in quantifying the effect of membrane-mediated interactions on the *kinetic rates of*

protein membrane binding and unbinding, we need to analyze the *dynamics of proteins* that are subject to both cytosolic diffusion (with diffusion constant D) and a chemical potential gradient $\mu(\mathbf{x})$ caused by the mechanochemical interaction of proteins with the membrane. This is described by a Smoluchowski equation [55,56] for the cytosolic protein density $c(\mathbf{x}, t)$:

$$\partial_t c(\mathbf{x}, t) = D\nabla^2 c(\mathbf{x}, t) + \frac{D}{k_B T}\nabla(c(\mathbf{x}, t)\nabla\mu(\mathbf{x})). \quad (1)$$

As proteins diffuse freely in the cytosol and interact with the membrane only within some narrow range d, a typical spatial profile of the chemical potential is initially flat in the cytosol ($\mu = 0$) and then monotonically approaches that of the proteins at the membrane, $\mu_m(m, \mathbf{u}) = \delta F[m(\boldsymbol{\sigma}), \mathbf{u}(\boldsymbol{\sigma})]/\delta m(\boldsymbol{\sigma})$, where F denotes the free energy functional describing the mechanochemical interaction between proteins and the membrane [57]. In general, F will depend on both the membrane's protein density $m(\boldsymbol{\sigma})$ and its mechanical state $\mathbf{u}(\boldsymbol{\sigma})$ at position $\boldsymbol{\sigma}$ on the membrane surface; see Fig. 1 for an illustration.

The local free energy density describing the mechanochemical coupling between proteins and the membrane is determined by lipid-lipid and protein-lipid interactions. We assume that a fluid phospholipid membrane can, on a coarse-grained level, be considered as an elastically deformable thin sheet, with bulk modulus κ_s, vanishing shear modulus, and a bending modulus κ_b that is equal for both principal curvatures [58]. For low levels of strain, we separate the mechanical degrees of freedom (d.o.f.) of the membrane into lateral stretching and out-of-plane bending [59] and write each mechanical contribution to the free energy as

$$f_{\text{mech}}(u) = \frac{1}{2}\kappa(u - u_0)^2. \quad (2)$$

Here, $u \in \{\rho, H\}$ is a placeholder variable for the mechanical state (conformation) of the membrane, $\kappa \in \{\kappa_s, \kappa_b\}$ denotes the respective membrane bulk and bending modulus, and u_0 denotes the equilibrium conformation (equilibrium density or intrinsic spontaneous curvature [60]).

As outlined above, there are several factors that determine the interaction between proteins and the membrane. Conceptually, one may distinguish between two limiting cases [Fig. 1(b)]: (A) protein anchorage through a membrane targeting domain that penetrates into the inner leaflet of the phospholipid bilayer and induces lateral membrane strain, or (B) protein attachment to the membrane by surface interactions and membrane bending. In both cases, the binding energy, $E_B \geq E_{\text{opt}}$, of a protein to the membrane will depend on the mechanical state (conformation) of the membrane, u. In particular, the binding will be strongest, $E_B = E_{\text{opt}}$, for some optimal mechanical state u_{opt}, where it attains an optimal value
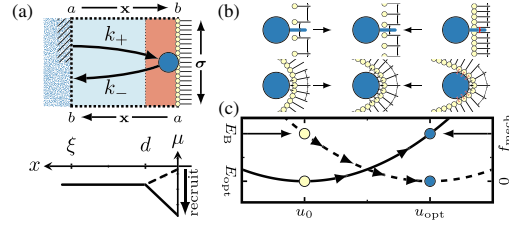

FIG. 1. (a) We divide intracellular space into reaction compartments (top), each containing one protein on average (blue dot), and identify the distance from the membrane x as the reaction coordinate. The proteins diffuse freely far away from the membrane ($x > d$, blue area) and sense a chemical potential μ close to the membrane ($x < d$, red area), which facilitates protein binding. Membrane-bound proteins modulate the chemical potential μ (arrow) and therefore induce a positive feedback in the attachment rate k_+. (b) Exaggerated membrane deformation illustrates protein interactions. Attachment occurs by (top) insertion of an anchor into the inner leaflet or by (bottom) deposition through attractive surface interactions. (c) In both cases, the mechanical state change (arrows, $u \in \{\rho, H\}$) influences both the energy density f_{mech} (solid line) stored in the deformation of the membrane and the binding energy of a protein E_B (dashed line).

$E_{\text{opt}} < 0$ [Fig. 1(c)]. This optimal conformation can be understood as a compromise between maximal attractive interactions between proteins and lipids, and minimal steric repulsion [Fig. 1(b)]. As the membrane becomes crowded with proteins, the binding energy will be reduced due to protein-protein interactions [61]. Given that the repulsive part of the Lennard-Jones potential scales as $\propto r^{-12}$ at small distances r, this may be accounted for by a factor $1 + \gamma m^6$, with $\gamma < 0$; note that the membrane protein density scales as $m \propto r^{-2}$. Then, a Taylor expansion of the chemical free energy density to lowest order in the membrane conformation, u, yields

$$f_{\text{chem}}(u, m) = m\left[E_{\text{opt}}(1 + \gamma m^6) + \frac{1}{2}\epsilon(u - u_{\text{opt}})^2\right], \quad (3)$$

where the parameter ϵ characterizes how strongly the membrane conformation affects protein binding. As noted above, there is a broad range of cytosolic proteins that bind to lipid membranes in a curvature-dependent manner [17,20–23,26,62]; cf. Fig. 1(b), lower panel. For example, protein-curvature coupling can arise from bending proteins to the local membrane curvature [25,37,39,40,63–65] or by bending the membrane to the shape of the proteins in order to maximize attractive interactions [Fig. 1(b)]. In the following, we specifically consider proteins that couple to the membrane curvature (sum of the two principal curvatures), $u \equiv H$, and discuss lipid-density-coupling proteins in the Supplemental Material (SM) [66].

As mechanical d.o.f. relax much faster than protein densities, we adiabatically eliminate the mechanical d.o.f. by assuming $\partial_u f = 0$, where $f = f_{\mathrm{mech}} + f_{\mathrm{chem}}$ [73]. This yields a relation between the membrane conformation u and the protein density m on the membrane: $u(m) = u_0 + (u_{\mathrm{opt}} - u_0)m/(m_\times + m)$. Here, the ratio between the mechanical modulus κ and the mechanochemical coupling parameter ϵ defines a characteristic membrane protein density: $m_\times = \kappa/\epsilon$. For low membrane protein density, $m < m_\times$, the interaction between the lipids dominates, and the mechanical state of the membrane is given by the equilibrium value u_0; cf. yellow symbols in Fig. 1(c). With an increasing number of attached proteins, the membrane gradually deforms and adopts the mechanical state that is preferred by the proteins; cf. blue symbols in Fig. 1(c). There is an interplay between a mechanical energy cost that is lowest at the relaxed state of the membrane, u_0, and a binding energy gain that is highest in the deformed state of the membrane, which is optimal for protein binding, u_{opt}. The difference of mechanical free energy density and binding energy between the membrane conformations preferred by the proteins and the lipids reads $\Delta f \equiv \Delta f_{\mathrm{mech}} = \frac{1}{2}\kappa(u_{\mathrm{opt}} - u_0)^2$ and $\Delta E \equiv \Delta E_{\mathrm{B}} = \frac{1}{2}\epsilon(u_{\mathrm{opt}} - u_0)^2$, respectively.

Upon eliminating the mechanical d.o.f. using $u(m)$, the interplay between chemical and mechanical terms becomes obvious in the dependence of the free energy density on membrane protein density [Fig. 2(a)],

$$\frac{f}{\Delta f} = \frac{\tilde{m}}{1 + \tilde{m}} + \tilde{m}(1 + \tilde{\gamma}\tilde{m}^6)\frac{E_{\mathrm{opt}}}{\Delta E}, \qquad (4)$$

where $\tilde{m} := m/m_\times$ and $\tilde{\gamma} := \gamma/m_\times^6$. The first term encodes free energy costs for membrane deformation through protein binding. With increasing protein density m, this contribution saturates, as the membrane deforms towards a binding-favorable conformation, implying that the corresponding mechanical free energy costs for binding of additional proteins diminish. For intermediate membrane protein densities, the benefit from protein binding [second term in Eq. (4)] dominates. Finally, for very high protein densities, protein binding becomes unfavorable due to crowding ($\tilde{\gamma} < 0$).

The chemical potential at the membrane, $\mu_{\mathrm{m}} = \partial_m f$, i.e., the energy needed to bind one additional protein to the membrane, reads

$$\frac{\mu_{\mathrm{m}}(\tilde{m})}{E_{\mathrm{opt}}} = 1 + 7\tilde{\gamma}\tilde{m}^6 + \frac{\Delta E}{E_{\mathrm{opt}}}\frac{1}{(1 + \tilde{m})^2}. \qquad (5)$$

In the absence of crowding effects, the chemical potential approaches the optimal value $E_{\mathrm{opt}} < 0$ for large protein densities on the membrane, $m \gg m_\times$, meaning that there is an energy gain upon binding [Fig. 2(b), dashed lines]. Crowding counteracts this gain, such that protein binding at
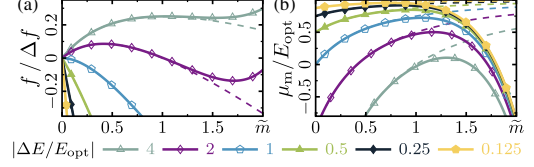

FIG. 2. (a) Free energy density $f/\Delta f$ and (b) membrane chemical potential $\mu_{\mathrm{m}}/E_{\mathrm{opt}}$ plotted as a function of the density of membrane-bound proteins, $m/m_\times$, for a series of different protein binding specificities, $|\Delta E/E_{\mathrm{opt}}|$, indicated in the graph. Solid lines represent $\tilde{\gamma} = -0.004$; dashed lines represent a system without crowding effects, $\tilde{\gamma} = 0$.

high densities becomes unfavorable [Fig. 2(b), solid lines]. For low densities ($m < m_\times$), protein binding is also disfavored, as there is a free energy cost for mechanically deforming the membrane that is largest for low membrane protein densities m; cf. the last term in Eq. (5). The amplitude of this reduction is given by $|\Delta E/E_{\mathrm{opt}}|$, which we term the protein *binding specificity*, as proteins with a higher specificity have a greater preference for mechanical states other than the relaxed state of the membrane [Fig. 2(b)]. The less specific the binding of a protein, the smaller the changes in the chemical potential as a function of the protein density on the membrane.

What, then, are the implications of these thermodynamic considerations for the kinetics of protein binding and detachment? To answer this question, one has to solve a first-passage-time problem for a particle diffusing in a chemical potential as described by the Smoluchowski equation (1). This is a well-studied problem, which dates back to Kramers' theory of reaction kinetics [74]. For a one-dimensional reaction coordinate x, with a reflective boundary at $x = a$ and an absorbing boundary at $x = b$, the first-passage time is given by [55,56]

$$\tau = \frac{1}{D}\int_a^b dx\, e^{+\mu(x)/k_{\mathrm{B}}T}\int_a^x dy\, e^{-\mu(y)/k_{\mathrm{B}}T}, \qquad (6)$$

where $\mu(x)$ is the spatial profile of the chemical potential. In Kramers' classical escape problem, the reaction rate depends on the height of the barrier that the particle has to cross by diffusion to reach its target [74]. In our case, however, there is no such barrier. Instead, as discussed above, we expect the landscape to exhibit a monotonically increasing or decreasing profile, depending on whether the chemical potential at the membrane, μ_{m}, is larger or smaller than the value in the bulk of the cytosol ($\mu_{\mathrm{cyt}} = 0$); for an illustration, see Fig. 1.

To estimate the kinetic rates, we simplify the geometry of the cell as follows. We divide the space near the membrane into small reaction compartments with respective sizes given by the average distance ξ between proteins, such that each compartment contains a single protein on average.

Then, one may approximate a binding process as a one-dimensional diffusion process: An initially unbound protein diffusing in the cytosol enters one of these compartments at a distance ξ from the membrane and, after some time, encounters the membrane located at $x = 0$. To calculate the corresponding first-passage time, the membrane is considered as an absorbing boundary. The cytosolic boundary of each compartment can effectively be approximated as a reflective boundary since (on average) there is always one protein within each compartment; i.e., a protein leaving the compartment at $x = \xi$ is replaced by one entering the compartment. Similarly, an unbinding process may be idealized as a stochastic process, where an initially bound protein detaches at $x = 0$ (reflective boundary) and leaves the compartment at $x = \xi$ (absorbing boundary).

Given our limited knowledge of the profile of the chemical potential, we chose to approximate it by a piecewise linear function [Fig. 1(a)]. The protein diffuses freely ($\mu = 0$) at large distances from the membrane ($x > d$). In the vicinity of the membrane ($x < d$), we assume a linear profile $\mu = \mu_m(1 - x/d)$. In the following, we discuss—for simplicity—the case where $\xi = d$. The more general (and more realistic) case, where the protein also crosses a preceding flat potential of length $\xi - d > 0$, yields qualitatively similar results and is discussed in the SM [66]. With these approximations, we can use Eq. (6) to obtain an explicit analytic expression for the mean first-passage times $\tau_\pm$ of attachment and detachment [75]. The corresponding kinetic rates, $k_\pm = \tau_\pm^{-1}$, expressed in units of the basic diffusion time $\tau := 2D/\xi^2$, are found to be

$$k_\pm \tau = \frac{1}{2}\left(\frac{\mu_m}{k_B T}\right)^2 \left(e^{\pm\mu_m/k_B T} \mp \frac{\mu_m}{k_B T} - 1\right)^{-1}. \quad (7)$$

These rates exhibit a pronounced nonlinear dependence on the membrane protein density (Fig. 3). Hence, protein attachment and detachment are both cooperative processes, owing to the mechanochemical coupling mediated by membrane elasticity. By fitting the attachment rate, Eq. (7), at low densities with $k_+ \approx a + b\tilde{m}^n$, we infer a relationship between the protein specificity $|\Delta E/E_{opt}|$ and the (Hill) cooperativity coefficient n [Figs. 3(c) and 3(d)]; for an analysis in terms of Hill curves, refer to the SM [66]. Strong cooperativity ($n > 1$) occurs only for high protein specificities, $|\Delta E/E_{opt}| > 1$. This implies that induction of a membrane conformation that favors protein binding requires the binding of a disproportionally large number of proteins to the membrane. Therefore, in the deterministic limit, proteins would not attach to the membrane at all [Fig. 2(a), empty triangles and diamonds]. However, stochastic binding events, while unlikely at low protein densities, reduce the free energy cost of subsequent binding events and thereby increase their likelihood. This positive feedback leading to recruitment is a purely stochastic effect
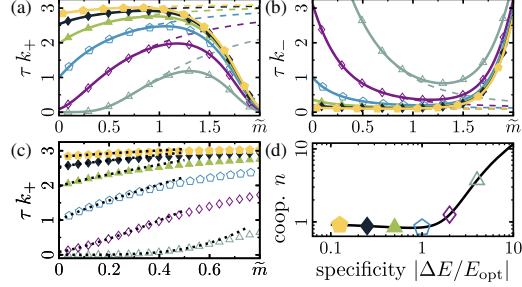

FIG. 3. Kinetic rates for membrane attachment $k_+\tau$ (a) and detachment $k_-\tau$ (b) as a function of $\tilde{m}$ for $E_{opt} = -5k_B T$ and a set of protein specificities $|\Delta E/E_{opt}|$ as in Fig. 2. Solid and dashed lines represent $\tilde{\gamma} = -0.004$ and $\tilde{\gamma} = 0$, respectively. (c) For low membrane protein concentrations $\tilde{m}$, the attachment rate can be approximated by $a + b\tilde{m}^n$; corresponding fits are indicated by the dotted lines. (d) The cooperativity coefficient n increases with protein specificity $|\Delta E/E_{opt}|$.

and is related to nucleation during discontinuous phase transitions.

To assess whether the proposed indirect cooperativity mechanism could actually come into play at physiological protein concentrations, we estimate its various parameters from known literature values. For proteins with a membrane curvature sensing domain, typical values for the optimal curvature and binding energy are $H_{opt} = 0.1$ nm^{-1} [21,76] and $E_{opt} \approx -5k_B T$ [77]; we assume vanishing spontaneous curvature ($H_0 = 0$). Across different studies, the bending modulus of a phospholipid bilayer was measured to be in the range of $\kappa \approx 10\ldots50k_B T$, suggesting a typical value $\kappa \approx 30k_B T$ [28,78,79]. Taking a value $|\Delta E/E_{opt}| = 2$ for protein specificity where nonlinear binding kinetics is significant (recruitment) [Fig. 3(d)], the corresponding range of concentrations, $m < m_\times \approx 3 \times 10^4\ \mu m^{-2}$, easily encompasses any physiological value; the maximum packing density of proteins with size 10 nm is $1 \times 10^4\ \mu m^{-2}$.

In summary, we have shown that mechanochemical coupling between proteins provides a possible mechanism for the nonlinear binding kinetics (recruitment) of proteins to the membrane. The effect originates from the interplay between protein-lipid and lipid-lipid interactions, which induce mechanical deformations of the membrane and thereby alter the protein binding environment. As protein-lipid interactions become dominant with increasing concentrations of membrane-bound proteins, the membrane's mechanical state becomes more favorable for binding. This shows how cooperativity and the recruitment of proteins can naturally emerge without any reliance on direct chemical interactions and conformational changes. The results should certainly be applicable to proteins that are known to bend membranes, e.g., proteins containing

BAR domains [20–23,26]. As recent experiments have unexpectedly shown that Min protein oscillations can lead to oscillations in vesicle shape [27], we would argue that our theory should also apply to the broad class of NTPases that are essential for cellular protein pattern formation. Thus, strain sensing and generation might not only be a property of a few specialized proteins but might actually be a prominent and perhaps general feature of membrane-binding proteins. Further exploration of curvature sensing during macroscopic pattern formation might be highly rewarding [80–82]. Our theory predicts that one can alter the recruitment exponent n of membrane-binding proteins by tuning the protein specificity (possibly by changing the membrane composition or introducing permanently bound membrane-bending proteins). Such a change in cooperativity should have a much stronger effect on emerging protein patterns than the tuning of reaction rates because it changes the nature of the nonlinear coupling. We would expect profound changes in the protein dynamics that could be explored using appropriately modified reaction-diffusion models for various cellular systems [83–88], as well as by experimentally tinkering with the composition of the membrane. Finally, it would be highly interesting and rewarding to quantify the mechanochemical effect for specific membrane-binding proteins experimentally. This would provide an interesting basis for theoretical models of pattern-forming protein systems and contribute towards revealing the universal role of membrane elasticity in cellular functions.

[*]Corresponding author.
frey@lmu.de

[1] J. Halatek, F. Brauns, and E. Frey, Phil. Trans. R. Soc. B **373**, 20170107 (2018).
[2] J. Lutkenhaus, Annu. Rev. Biochem. **76**, 539 (2007).
[3] D. I. Johnson, Microbiol. Mol. Biol. Rev. **63**, 54 (1999).
[4] B. Goldstein and I. G. Macara, Dev. Cell **13**, 609 (2007).
[5] C. D. Lawson and A. J. Ridley, J. Cell Biol. **217**, 447 (2018).
[6] A. V. Hill, Biochem. J. **7**, 471 (1913).
[7] M. I. Stefan and N. Le Novère, PLoS Comput. Biol. **9**, e1003106 (2013).
[8] E. Fischer-Friedrich and N. Gov, Phys. Biol. **8**, 026007 (2011).
[9] M. Encinar, A. V. Kralicek, A. Martos, M. Krupka, S. Cid, A. Alonso, A. I. Rico, M. Jiménez, and M. Vélez, Langmuir **29**, 9436 (2013).
[10] M. G. J. Ford, I. G. Mills, B. J. Peter, Y. Vallis, G. J. K. Praefcke, P. R. Evans, and H. T. McMahon, Nature (London) **419**, 361 (2002).
[11] I. Tsafrir, Y. Caspi, M.-A. Guedeau-Boudeville, T. Arzi, and J. Stavans, Phys. Rev. Lett. **91**, 138102 (2003).
[12] M. C. Lee, L. Orci, S. Hamamoto, E. Futai, M. Ravazzola, and R. Schekman, Cell **122**, 605 (2005).
[13] N. S. Gov and A. Gopinathan, Biophys. J. **90**, 454 (2006).
[14] J. Zimmerberg and M. M. Kozlov, Nat. Rev. Mol. Cell Biol. **7**, 9 (2006).
[15] W. A. Prinz and J. E. Hinshaw, Crit. Rev. Biochem. Mol. Biol. **44**, 278 (2009).
[16] J. C. Stachowiak, E. M. Schmid, C. J. Ryan, H. S. Ann, D. Y. Sasaki, M. B. Sherman, P. L. Geissler, D. A. Fletcher, and C. C. Hayden, Nat. Cell Biol. **14**, 944 (2012).
[17] H. T. McMahon and E. Boucrot, J. Cell Sci. **128**, 1065 (2015).
[18] I. K. Jarsch, F. Daste, and J. L. Gallop, J. Cell Biol. **214**, 375 (2016).
[19] N. S. Gov, Phil. Trans. R. Soc. B **373**, 20170115 (2018).
[20] J. Zimmerberg and S. McLaughlin, Curr. Biol. **14**, R250 (2004).
[21] B. J. Peter, H. M. Kent, I. G. Mills, Y. Vallis, P. J. G. Butler, P. R. Evans, and H. T. McMahon, Science **303**, 495 (2004).
[22] V. K. Bhatia, K. L. Madsen, P.-Y. Bolinger, A. Kunding, P. Hedegård, U. Gether, and D. Stamou, EMBO J. **28**, 3303 (2009).
[23] C. Mim and V. M. Unger, Trends Biochem. Sci. **37**, 526 (2012).
[24] C. Zhu, S. L. Das, and T. Baumgart, Biophys. J. **102**, 1837 (2012).
[25] C. Prévost, H. Zhao, J. Manzi, E. Lemichez, P. Lappalainen, A. Callan-Jones, and P. Bassereau, Nat. Commun. **6**, 8529 (2015).
[26] M. Simunovic, G. A. Voth, A. Callan-Jones, and P. Bassereau, Trends Cell Biol. **25**, 780 (2015).
[27] T. Litschel, B. Ramm, R. Maas, M. Heymann, and P. Schwille, Angew. Chem. Int. Ed. **57**, 16286 (2018).
[28] R. Phillips, T. Ursell, P. Wiggins, and P. Sens, Nature (London) **459**, 379 (2009).
[29] T. R. Weikl, Annu. Rev. Phys. Chem. **69**, 521 (2018).
[30] T. Idema and D. J. Kraft, Curr. Opin. Colloid Interface Sci. **40**, 58 (2019).
[31] H. Huang, Biophys. J. **50**, 1061 (1986).
[32] P. Wiggins and R. Phillips, Biophys. J. **88**, 880 (2005).
[33] O. S. Andersen and R. E. Koeppe, Annu. Rev. Biophys. Biomol. Struct. **36**, 107 (2007).
[34] D. Milovanovic, A. Honigmann, S. Koike, F. Göttfert, G. Pähler, M. Junius, S. Müllar, U. Diederichsen, A. Janshoff, H. Grubmüller, H. J. Risselada, C. Eggeling, S. W. Hell, G. van den Bogaart, and R. Jahn, Nat. Commun. **6**, 5984 (2015).
[35] A. Grau-Campistany, E. Strandberg, P. Wadhwani, J. Reichert, J. Bürck, F. Rabanal, and A. S. Ulrich, Sci. Rep. **5**, 9388 (2015).
[36] M. S. Turner and P. Sens, Phys. Rev. Lett. **93**, 118103 (2004).

[37] A. Iglič, T. Slivnik, and V. Kralj-Iglič, J. Biomech. **40**, 2492 (2007).

[38] R. Shlomovitz and N. S. Gov, Phys. Biol. **6**, 046017 (2009).

[39] Ś. Perutková, V. Kralj-Iglič, M. Frank, and A. Iglič, J. Biomech. **43**, 1612 (2010).

[40] L. Mesarec, W. Góźdź, V. K. Iglič, S. Kralj, and A. Iglič, Colloids Surf. B **141**, 132 (2016).

[41] J. Agudo-Canalejo and R. Lipowsky, Soft Matter **13**, 2155 (2017).

[42] M. Goulian, R. Bruinsma, and P. Pincus, Europhys. Lett. **22**, 145 (1993).

[43] R. Golestanian, M. Goulian, and M. Kardar, Europhys. Lett. **33**, 241 (1996).

[44] L. V. Schäfer, D. H. de Jong, A. Holt, A. J. Rzepiela, A. H. de Vries, B. Poolman, J. A. Killian, and S. J. Marrink, Proc. Natl. Acad. Sci. U.S.A. **108**, 1343 (2011).

[45] L. D. Renner and D. B. Weibel, J. Biol. Chem. **287**, 38835 (2012).

[46] V. Corradi, E. Mendez-Villuendas, H. I. Ingólfsson, R.-X. Gu, I. Siuda, M. N. Melo, A. Moussatova, L. J. DeGagné, B. I. Sejdiu, G. Singh, T. A. Wassenaar, K. D. Magnero, S. J. Marrink, and D. P. Tieleman, ACS Cent. Sci. **4**, 709 (2018).

[47] C. A. Haselwandter and R. Phillips, Europhys. Lett. **101**, 68002 (2013).

[48] Y. Schweitzer and M. M. Kozlov, PLoS Comput. Biol. **11**, e1004054 (2015).

[49] C. van der Wel, A. Vahid, A. Šarić, T. Idema, D. Heinrich, and D. J. Kraft, Sci. Rep. **6**, 32825 (2016).

[50] A. Vahid and T. Idema, Phys. Rev. Lett. **117**, 138102 (2016).

[51] U. Schmidt, G. Guigas, and M. Weiss, Phys. Rev. Lett. **101**, 128104 (2008).

[52] C. A. Haselwandter and N. S. Wingreen, PLoS Comput. Biol. **10**, e1003932 (2014).

[53] A. Vahid, A. Šarić, and T. Idema, Soft Matter **13**, 4924 (2017).

[54] A. Vahid and T. Idema, bioRxiv https://doi.org/10.1101/336545 (2018).

[55] C. Gardiner, *Stochastic Methods* (Springer, Berlin, 2009).

[56] R. Zwanzig, *Nonequilibrium Statistical Mechanics* (Oxford University Press, Oxford, 2001).

[57] In general, note that this implies that the chemical potential is a function of cytosolic position $\mathbf{x}$ and a functional of membrane protein density, $m(\boldsymbol{\sigma})$.

[58] W. Helfrich, Z. Naturforsch. C **28C**, 693 (1973).

[59] U. Seifert, Adv. Phys. **46**, 13 (1997).

[60] We further relate our approach to Helfrich's formulation of the bending energy cost [58] in the SM [66].

[61] Note that the entropic effects of a large protein density can also reduce the protein binding energy, as discussed in the SM [66]. There, we show that the general result of nonlinear protein recruitment to the membrane remains valid.

[62] W. F. Zeno, U. Baul, W. T. Snead, A. C. M. DeGroot, L. Wang, E. M. Lafer, D. Thirumalai, and J. C. Stachowiak, Nat. Commun. **9**, 4152 (2018).

[63] V. Kralj-Iglič, V. Heinrich, S. Svetina, and B. Žekš, Eur. Phys. J. B **10**, 5 (1999).

[64] R. Shlomovitz, N. S. Gov, and A. Roux, New J. Phys. **13**, 065008 (2011).

[65] B. Božič, S. L. Das, and S. Svetina, Soft Matter **11**, 2479 (2015).

[66] See Supplemental Material at http://link.aps.org/supplemental/10.1103/PhysRevLett.123.178101 for further details and an additional analysis of the model, which includes Refs. [67–72].

[67] O.-Y. Zhong-can and W. Helfrich, Phys. Rev. A **39**, 5280 (1989).

[68] B. Božič, V. Kralj-Iglič, and S. Svetina, Phys. Rev. E **73**, 041915 (2006).

[69] M. Doi, *Soft Matter Physics* (Oxford University Press, Oxford, 2013).

[70] M. Deserno, Chem. Phys. Lipids **185**, 11 (2015).

[71] A. Guckenberger and S. Gekle, J. Phys. Condens. Matter **29**, 203001 (2017).

[72] A. Goychuk, L. Würthner, M. Wigbers, and E. Frey (to be published).

[73] A further generalization yielding normal and tangential stresses involves variational surface calculus and is briefly outlined in the SM [66]. There, we show that the analysis presented here is valid in the limit of small deformations.

[74] H. A. Kramers, Physica **7**, 284 (1940).

[75] S. Bell and E. M. Terentjev, Biophys. J. **112**, 2439 (2017).

[76] W. Wu, K.-T. Park, T. Holyoak, and J. Lutkenhaus, Mol. Microbiol. **79**, 1515 (2011).

[77] L. Ma, Y. Cai, Y. Li, J. Jiao, Z. Wu, B. O'Shaughnessy, P. De Camilli, E. Karatekin, and Y. Zhang, eLife **6**, e30493 (2017).

[78] R. Dimova, Adv. Colloid Interface Sci. **208**, 225 (2014).

[79] J. F. Nagle, M. S. Jablin, S. Tristram-Nagle, and K. Akabori, Chem. Phys. Lipids **185**, 3 (2015).

[80] B. Peleg, A. Disanza, G. Scita, and N. Gov, PLoS One **6**, e18635 (2011).

[81] D. Thalmeier, J. Halatek, and E. Frey, Proc. Natl. Acad. Sci. U.S.A. **113**, 548 (2016).

[82] Z. Wu, M. Su, C. Tong, M. Wu, and J. Liu, Nat. Commun. **9**, 136 (2018).

[83] K. C. Huang, Y. Meir, and N. S. Wingreen, Proc. Natl. Acad. Sci. U.S.A. **100**, 12724 (2003).

[84] J. Halatek and E. Frey, Cell Rep. **1**, 741 (2012).

[85] B. Klünder, T. Freisinger, R. Wedlich-Söldner, and E. Frey, PLoS Comput. Biol. **9**, e1003396 (2013).

[86] J. Denk, S. Kretschmer, J. Halatek, C. Hartl, P. Schwille, and E. Frey, Proc. Natl. Acad. Sci. U.S.A. **115**, 4553 (2018).

[87] A. B. Goryachev and M. Leda, Mol. Biol. Cell **28**, 370 (2017).

[88] J. Halatek and E. Frey, Nat. Phys. **14**, 507 (2018).

178101-6

Protein recruitment through indirect mechanochemical interactions – Supplementary Material

Andriy Goychuk[1] and Erwin Frey[1]

[1]*Arnold Sommerfeld Center for Theoretical Physics and Center for NanoScience, Department of Physics, Ludwig-Maximilians-Universität München, Theresienstraße 37, D-80333 Munich, Germany*

S.I. EQUIVALENT FORMS OF THE FREE ENERGY DENSITY

In the literature one finds various equivalent representations of the free energy density describing the thermodynamics of membrane-bound proteins that are coupled to membrane curvature. This section serves to show how these can be related to our model. As described in the main text, the free energy density is given by

$$f(u, m) = \tfrac{1}{2}\kappa\,(u - u_0)^2$$
$$+ m\left[E_{\text{opt}}\,(1 + \gamma\,m^6) + \tfrac{1}{2}\,\epsilon\,(u - u_{\text{opt}})^2\right]. \quad (\text{S1})$$

Upon collecting all terms that depend on the membrane deformation u, an equivalent form of the free energy is:

$$f(u, \widetilde{m}) = \tfrac{1}{2}\kappa\,(1 + \widetilde{m})\,(u - u_\times)^2$$
$$+ \left[\frac{\widetilde{m}}{1 + \widetilde{m}} + \widetilde{m}\big(1 + \widetilde{\gamma}\,\widetilde{m}^6\big)\frac{E_{\text{opt}}}{\Delta E}\right]\Delta f\,. \quad (\text{S2})$$

Here, we have defined a characteristic membrane protein density, $m_\times = \kappa/\epsilon$, and rescaled our variables accordingly, $\widetilde{m} := m/m_\times$ and $\widetilde{\gamma} := \gamma/m_\times^6$. In this form of the free energy, the characteristic membrane conformation, $u_\times = u_0 + (u_{\text{opt}} - u_0)\,\widetilde{m}/(1 + \widetilde{m})$, directly gives the membrane deformation minimizing the free energy. Moreover, one can directly read off that protein attachment enhances the stiffness parameter: $\kappa_{\text{eff}} = \kappa\,(1 + \widetilde{m})$. The second line of Eq. (S2) represents a free energy density contribution that only depends on the protein density but not on the membrane conformation. This corresponds to Eq. (4) in the main text, as $u = u_\times$ minimizes Eq. (S2).

Next we show how one can use Eq. (S2) to obtain a Helfrich bending energy containing a spontaneous curvature that linearly depends on the membrane protein density [1, 2]. We set $u \equiv H$ and $u_{\text{opt}} \equiv H_{\text{opt}}$, and assume that the membrane is symmetric in the absence of membrane-bound proteins. Then, the intrinsic spontaneous curvature of the membrane vanishes, $u_0 \equiv H_0 = 0$. If the density of membrane-bound proteins is sufficiently small, $\widetilde{m} \ll 1$, then the first line of Eq. (S2) simplifies to:

$$\tfrac{1}{2}\kappa\,(H - \widetilde{m}\,H_{\text{opt}})^2\,. \quad (\text{S3})$$

This term can be rewritten in terms of protein surface coverage, $\theta = m/m_{\text{s}} = \widetilde{m}/\widetilde{m}_{\text{s}}$, where m_{s} is the surface saturation density of proteins. We also rescale the optimal curvature, $H_{\text{opt}/\theta} = \widetilde{m}_{\text{s}}\,H_{\text{opt}}$, to arrive at:

$$\tfrac{1}{2}\kappa\,(H - \theta\,H_{\text{opt}/\theta})^2\,. \quad (\text{S4})$$

The above expression is sometimes used when coupling proteins to membrane curvature [1, 2].

S.II. ADDITIONAL FREE ENERGY CONTRIBUTIONS

In the main text, we have restricted ourselves to repulsive interactions between the proteins, $f_{\text{rep}} = \gamma m^6$, mainly in order to bound the surface density of surface proteins and to introduce a saturation coverage. Here, we study the additional effects of entropic mixing of proteins and attractive interactions between proteins. The main conclusion drawn from the following analysis is: 1. Importantly, in the high protein specificity and low protein density regime, where we find protein recruitment in the main text, both of these contributions have only minor effects on the binding kinetics. 2. In the low protein specificity and high protein density regime, both of these contributions play major roles, as we will discuss below.

A. Mixing entropy of membrane-bound proteins

The free energy density including the mixing entropy but neglecting repulsive interactions is given by

$$f(u, m) = \tfrac{1}{2}\kappa\,(u - u_0)^2 + m\left[E_{\text{opt}} + \tfrac{1}{2}\,\epsilon\,(u - u_{\text{opt}})^2\right]$$
$$+ k_{\text{B}}T\left[m\ln\left(\frac{m}{m_{\text{s}}}\right) + (m_{\text{s}} - m)\ln\left(\frac{m_{\text{s}} - m}{m_{\text{s}}}\right)\right], \quad (\text{S5})$$

where the second line denotes the mixing entropy contribution, with m_{s} as the saturation density of the membrane. We proceed similar as described in the main text by adiabatically eliminating the mechanical degrees of freedom. Then, we find the following expression for the chemical potential at the membrane:

$$\frac{\mu_{\text{m}}(\widetilde{m})}{E_{\text{opt}}} = 1 + \frac{\Delta E}{E_{\text{opt}}}\frac{1}{(1 + \widetilde{m})^2} + \frac{k_{\text{B}}T}{E_{\text{opt}}}\ln\left[\frac{\widetilde{m}}{\widetilde{m}_{\text{s}} - \widetilde{m}}\right], \quad (\text{S6})$$

where $\widetilde{m}_{\text{s}} := m_0/m_\times$ is the non-dimensionalized saturation density. Comparing the chemical potentials, which include contributions from (A) mixing entropy, Eq. (S6), *or* (B) repulsion between proteins, Eq. (5) in the main text, we find that both variants show strong repulsion at high protein densities [Fig. S1a]. At low protein densities, we find that both chemical potential variants become more similar as we increase protein specificity, thereby reducing the relative weight of the entropic/repulsive terms
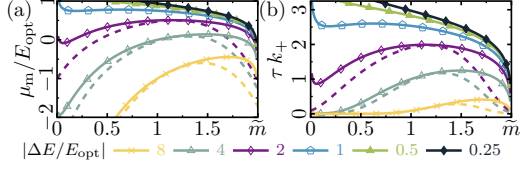
FIG. S1.   Comparison between the influence of mixing entropy (solid lines), and explicit repulsive interactions between proteins (dashed lines) on binding kinetics. Membrane chemical potential (a), $\mu_\mathrm{m}/E_\mathrm{opt}$, and kinetic attachment rate (b), $k_+\,\tau$, plotted as a function of the density of membrane-bound proteins, $m/m_\times$, for a series of different protein binding specificities, $|\Delta E/E_\mathrm{opt}|$, indicated in the graph. The optimal binding energy is given by $E_\mathrm{opt} = -5k_\mathrm{B}T$, and the membrane saturation concentration by $\widetilde{m}_\mathrm{s} = 2.0$.
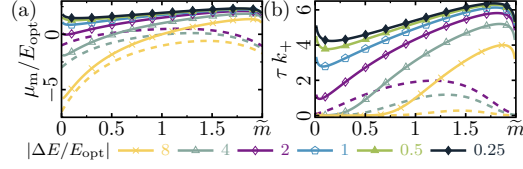
FIG. S2.   Comparison between the influence of mixing entropy with explicit attractive interactions between proteins (solid lines), and explicit repulsive interactions between proteins (dashed lines) on binding kinetics. Membrane chemical potential (a), $\mu_\mathrm{m}/E_\mathrm{opt}$, and kinetic attachment rate (b), $k_+\,\tau$, plotted as a function of the density of membrane-bound proteins, $m/m_\times$, for a series of different protein binding specificities, $|\Delta E/E_\mathrm{opt}|$, indicated in the graph. The optimal binding energy is given by $E_\mathrm{opt} = -5k_\mathrm{B}T$, the membrane saturation concentration by $\widetilde{m}_\mathrm{s} = 2.0$, and the attractive interaction strength between proteins is given by $\widetilde{\chi} = 2.5k_\mathrm{B}T$.

in Eqs. (S6) and (5), respectively [Fig. S1, compare solid with dashed lines].

We proceed as described in the main text and use the chemical potential at the membrane to determine the protein binding rates. Analogously to the main text, the protein attachment rates increase nonlinearly as a function of membrane-bound protein density, for high protein specificities and low protein densities [Fig. S1b, crosses and empty triangles]. As discussed above, in this regime, where recruitment can be observed, the mixing entropy does not play a major role for the binding kinetics. However, for low protein specificities, the binding rates monotonically decrease (for all densities) with increasing membrane-bound protein density [Fig. S1b, filled markers], because the proteins always compete for the available space. Note that, in contrast, in the main text, the attachment rates only decrease when repulsive interactions between proteins become dominant at high protein densities [Fig. 2b].

B.   Attractive interactions between proteins

Motivated by Ref. [2], we additionally study the effect of attractive interactions between membrane-bound proteins, which could for example arise from a conformational change upon attachment to the membrane. Then, the free energy density is captured by a (modified) Flory-Huggins theory, including interactions between proteins and the membrane:

$$f(u,m) = \tfrac{1}{2}\kappa\,(u-u_0)^2 + m\left[E_\mathrm{opt} + \tfrac{1}{2}\,\epsilon\,(u-u_\mathrm{opt})^2\right]$$
$$+ k_\mathrm{B}T\left[m\,\ln\left(\tfrac{m}{m_\mathrm{s}}\right) + (m_\mathrm{s}-m)\,\ln\left(\tfrac{m_\mathrm{s}-m}{m_\mathrm{s}}\right)\right] - \chi m^2\,, \tag{S7}$$

where m_s is the saturation density of the membrane and χ encodes the strength of the attractive interactions between proteins. We proceed similar as described in the main text by adiabatically eliminating the mechanical degrees of freedom. Then, we find the following expression

for the chemical potential at the membrane:

$$\frac{\mu_\mathrm{m}(m)}{E_\mathrm{opt}} = 1 + \frac{\Delta E}{E_\mathrm{opt}}\,\frac{1}{(1+\widetilde{m})^2}$$
$$+ \frac{k_\mathrm{B}T}{E_\mathrm{opt}}\ln\left[\frac{\widetilde{m}}{\widetilde{m}_\mathrm{s}-\widetilde{m}}\right] - \frac{2\,\widetilde{\chi}}{E_\mathrm{opt}}\widetilde{m}\,. \tag{S8}$$

where $\widetilde{m}_\mathrm{s} := m_0/m_\times$ is the non-dimensionalized saturation density and $\widetilde{\chi} := \chi\,m_\times$ is the rescaled protein-protein interaction strength. For small membrane-bound protein densities, the contribution of attractive interactions between proteins to the chemical potential vanishes, as the last term in Eq. (S8) becomes negligible. Then, one obtains a similar behavior as in Sec. S.II A [Fig. S2a, compare solid with dashed lines]: with increasing protein specificity, the chemical potential, Eq. (S8), approaches the values from the main text, given by Eq. (5).

We proceed as described in the main text and use the chemical potential at the membrane to determine the protein binding rates. Analogously to the main text, for high protein specificities, we find a nonlinear recruitment of proteins from the cytosol to the membrane [Fig. S2b, crosses and empty triangles]. At low protein densities, the contribution from the attractive interactions between proteins becomes negligible. Then, recruitment originates from the mechanochemical interactions between proteins and membrane, as described in detail in the main text. At high protein densities, where mechanochemical contributions to the binding rates saturate regardless of protein specificity, attractive interactions becomes dominant and lead to recruitment. Therefore, we conclude that cooperative protein recruitment from the cytosol to the membrane is obtained for the following cases (i) at low protein densities by a highly specific mechanochemical coupling between proteins and membrane (tunable nonlinear recruitment), *or* (ii) at high protein densities by attractive chemical interactions between proteins. Here, however,
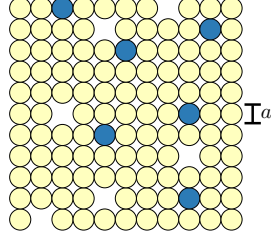
FIG. S3. Lattice gas model of a membrane with N lattice sites of size a^2. Most of the available sites are occupied by N_l phospholipids (yellow), which exhibit strong attractive interactions with other phospholipids. The remaining sites are either occupied by N_p protein anchors (blue), which bind to the membrane through attractive interactions with phospholipids, or remain empty.

we observe only a linear/sublinear increase of the attachment rates with the membrane-bound protein density [Fig. S2b, empty diamonds and pentagons, filled triangles and diamonds].

S.III.   PROTEIN BINDING THROUGH ANCHOR INSERTION

In the main text, we have constructed a description of protein-membrane interactions via symmetry arguments. Then, we have argued that it applies to different types of membrane deformations, like lateral strain by lipid density changes. However, one might ask how single proteins can affect the local lipid density, given that any changes of the lipid density *in between* membrane-targeting protein anchors should relax quickly. While this is certainly correct, at a finite density of membrane-bound proteins, the free energy density is affected by three factors: (i) lipid-lipid interactions, (ii) protein-lipid interactions, and (iii) the corresponding mixing entropy. In the following, we derive such free energy, and thereby provide a more detailed rationalization for the description of protein-lipid coupling.

We assume that the membrane can be described as a ternary lattice gas consisting of N_l lipids, N_p protein anchors, and $N - N_l - N_p$ unoccupied lattice sites [Fig. S3]. In a lipid membrane, there should be much more lipids than protein anchors or unoccupied lattice sites: $N_l \gg N_p$ and $N_l \gg N - N_l - N_p$. To make our calculations as simple as possible, we assume that each lattice site (size of a^2) can be occupied by one of these three key players. Then, the mixing entropy contribution to the free energy density of such a ternary mixture is given by [3]:

$$f_{\mathrm{mix}} = k_{\mathrm{B}}T\Big[\rho\ln\Big(\tfrac{\rho}{\rho_{\mathrm{s}}}\Big) + m\ln\Big(\tfrac{m}{\rho_{\mathrm{s}}}\Big) + (\rho_{\mathrm{s}} - \rho - m)\ln\Big(\tfrac{\rho_{\mathrm{s}} - \rho - m}{\rho_{\mathrm{s}}}\Big)\Big], \quad (S9)$$

where we have introduced the saturation density $\rho_{\mathrm{s}} = 1/a^2$, the lipid density $\rho = N_l/(Na^2)$ and the protein density $m = N_p/(Na^2)$. In addition to mixing entropy, we assume that lipids strongly attract each other with an interaction energy $E_{\mathrm{ll}} \gg k_{\mathrm{B}}T$. Furthermore, protein anchors and lipids also mutually attract each other $E_{\mathrm{lp}} > k_{\mathrm{B}}T$; this attraction should exceed thermal energy to make protein binding favorable. In summary, we then obtain the following Flory-Huggins free energy:

$$f = -\tfrac{E_{\mathrm{ll}}}{\rho_{\mathrm{s}}}\rho^2 - \tfrac{E_{\mathrm{lp}}}{\rho_{\mathrm{s}}}\rho\, m + f_{\mathrm{mix}}. \quad (S10)$$

We collect the terms in the mixing free energy, Eq. (S9), into a protein mixing free energy density (this contribution does not depend on the lipid density),

$$f_{\mathrm{mix/m}} = k_{\mathrm{B}}T\Big[m\ln\Big(\tfrac{m}{\rho_{\mathrm{s}}}\Big) + (\rho_{\mathrm{s}} - m)\ln\Big(\tfrac{\rho_{\mathrm{s}} - m}{\rho_{\mathrm{s}}}\Big)\Big], \quad (S11a)$$

and the remainder, $f_{\mathrm{mix/r}} = f_{\mathrm{mix}} - f_{\mathrm{mix/m}}$,

$$f_{\mathrm{mix/r}} = k_{\mathrm{B}}T\Big[\rho\ln\Big(\tfrac{\rho}{\rho_{\mathrm{s}} - \rho - m}\Big) + (\rho_{\mathrm{s}} - m)\ln\Big(\tfrac{\rho_{\mathrm{s}} - \rho - m}{\rho_{\mathrm{s}} - m}\Big)\Big]. \quad (S11b)$$

Then, given that membrane-bound protein densities should be small, we expand the remainder $f_{\mathrm{mix/r}}$ into a Taylor series, to first order in m in the vicinity of $m = 0$:

$$f_{\mathrm{mix/r}} = f_{\mathrm{mix/\rho}} - m\, k_{\mathrm{B}}T\ln\Big(\tfrac{\rho_{\mathrm{s}} - \rho}{\rho_{\mathrm{s}}}\Big), \quad (S11c)$$

where we have introduced the lipid mixing free energy density

$$f_{\mathrm{mix/\rho}} = k_{\mathrm{B}}T\Big[\rho\ln\Big(\tfrac{\rho}{\rho_{\mathrm{s}}}\Big) + (\rho_s - \rho)\ln\Big(\tfrac{\rho_s - \rho}{\rho_{\mathrm{s}}}\Big)\Big]. \quad (S11d)$$

In summary, for small membrane-bound protein densities, the free energy density is given by:

$$f = -\tfrac{E_{\mathrm{ll}}}{\rho_{\mathrm{s}}}\rho^2 + f_{\mathrm{mix/\rho}} + f_{\mathrm{mix/m}} - m\Big[\tfrac{E_{\mathrm{lp}}}{\rho_{\mathrm{s}}}\rho + k_{\mathrm{B}}T\ln\Big(\tfrac{\rho_s - \rho}{\rho_{\mathrm{s}}}\Big)\Big]. \quad (S12)$$

For large attractive interaction energies between lipids, the first line of Eq. (S12) will have a minimum at an intrinsically preferred lipid density ρ_0, which is close to the saturation density. Then, we can expand the first line of Eq. (S12) to second order in the vicinity of its minimum:

$$-\tfrac{E_{\mathrm{ll}}}{\rho_{\mathrm{s}}}\rho^2 + f_{\mathrm{mix/\rho}} \approx \tfrac{1}{2}\kappa(\rho - \rho_0)^2 + \mathrm{const}. \quad (S13)$$

In addition, we also expand the last term of Eq. (S12) to second order in ρ in the vicinity of its minimum

$$\rho_{\mathrm{opt}} = \rho_{\mathrm{s}}\Big(1 - \tfrac{k_{\mathrm{B}}T}{E_{\mathrm{lp}}}\Big), \quad (S14)$$

where $E_{\mathrm{lp}} > k_{\mathrm{B}}T$. Having done all that, we finally arrive at an expression which is analogous to the one used in the

main text (plus an expression that contains the mixing entropy of proteins),

$$f = \tfrac{1}{2}\kappa(\rho - \rho_0)^2 + m\left[E_{\mathrm{opt}} + \tfrac{1}{2}\epsilon(\rho - \rho_{\mathrm{opt}})^2\right] + f_{\mathrm{mix}/m}, \tag{S15}$$

where the optimal binding energy is given by

$$E_{\mathrm{opt}} = k_{\mathrm{B}}T\left(1 + \ln\frac{E_{\mathrm{lp}}}{k_{\mathrm{B}}T} - \frac{E_{\mathrm{lp}}}{k_{\mathrm{B}}T}\right), \tag{S16}$$

and the coupling between proteins and membrane is given by

$$\epsilon = \frac{2E_{\mathrm{lp}}^2}{\rho_s^2 \, k_{\mathrm{B}}T}. \tag{S17}$$

Therefore, an explicit thermodynamic calculation yields the same results that were obtained in the main text through symmetry arguments. Effectively, this models a situation where high lipid densities prevent anchor insertion by steric repulsion, while low lipid densities lack the attractive interaction between the lipids and the anchor that is necessary for binding. Then, protein anchors, which are inserted into the inner membrane leaflet, induce bulk strain in the inner leaflet by increasing the density of lipids, while leaving the outer leaflet unperturbed.

S.IV.   REALISTIC CHEMICAL POTENTIAL PROFILE

In the main text, we have considered the special case where a protein interacts with the membrane across the whole reaction compartment ($\xi = d$). Here we also discuss the general case $\xi > d$, where a protein diffuses freely (flat chemical potential) in the region $x \in [d\dots\xi]$, and interacts (ramp potential) with the membrane within the range $x \in [0\dots d]$. Then, the kinetic rates for biding and unbinding are given by:

$$k_{\pm}\tau = \xi^2\left((\xi - d)^2 + 2\,d^2\Gamma_2 \mp 2d(\xi - d)\Gamma_1\right)^{-1} \tag{S18}$$

$$\Gamma_2 = \left(\frac{k_{\mathrm{B}}T}{\mu_{\mathrm{m}}}\right)^2\left(e^{\pm\mu_{\mathrm{m}}/k_{\mathrm{B}}T} \mp \frac{\mu_{\mathrm{m}}}{k_{\mathrm{B}}T} - 1\right), \tag{S19}$$

$$\Gamma_1 = \left(\frac{k_{\mathrm{B}}T}{\mu_{\mathrm{m}}}\right)\left(e^{\pm\mu_{\mathrm{m}}/k_{\mathrm{B}}T} - 1\right), \tag{S20}$$

where μ_{m} is the chemical potential of membrane-bound proteins and $\tau = \xi^2/2D$ is the basic timescale of diffusion across the compartment. For $\xi \to d$ we recover the case discussed in the main text [Eq. (7)], while for $d \to 0$ there is no spatial variation in the chemical potential and the resulting kinetic rates reduce to $k_{\pm} = \tau^{-1}$.

We will discuss a situation where the protein does not interact with the membrane throughout most of the reaction compartment ($\xi - d \gg d$); for specificity, we consider $\xi - d = 100\,d$. Then, we observe a much smaller variation of the detachment rates compared to the main text, where $\xi - d = 0$ [compare Fig. S4b with Fig. 3b].

This reduction can be explained as follows. After detachment the protein starts diffusing in the chemical potential landscape at the membrane. Therefore, to leave the reaction compartment, the protein first has to traverse the interaction range d, across which it interacts with the membrane and senses a steep chemical potential [Fig. 1a, bottom panel]. The shorter the interaction range d, the faster the protein leaves the steep chemical potential and enters the region of free diffusion, which is why for $\xi - d \gg d$ the rate-limiting timescale given by time τ that it takes to diffuse across the reaction compartment.

In contrast, as in the main text, the attachment rate is a highly nonlinear function of the membrane-bound protein concentration $\widetilde{m}$ [Fig. S4a]. This is surprising since one might expect that, similar as for the detachment process, diffusion in the extended flat region of the chemical potential is the dominant rate-limiting factor. However, this is not the case. To understand the origin for this difference, note that the boundary conditions of these two processes are different. During unbinding, the protein detaches from the membrane, whose reflective boundary condition quickly drives the protein across the interaction range d. The situation is genuinely different for the attachment process, where the protein originates from the bulk and first has to diffuse across the distance $\xi - d$ to reach the membrane. Then, near the membrane, the protein enters the interaction range d with its steep chemical potential, which is repulsive for small membrane-bound protein concentrations and only becomes attractive for high protein concentrations. As there is no nearby reflective boundary (effectively driving the protein away from it), the rate limiting factor of the attachment process becomes the time needed to diffuse against the steep chemical potential and to reach the absorbing boundary at the membrane.

As discussed above, the detachment rate only varies slightly depending on the membrane-bound protein concentration $\tau\,k_- \in [0.7\dots1]$. The nonlinear dependence of the binding rate k_+ on the membrane protein density $\widetilde{m}$ is well approximated by a Hill-like curve:
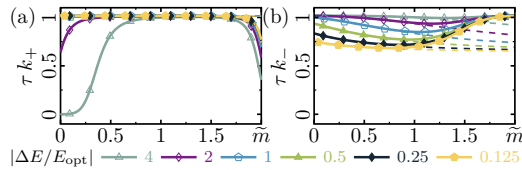
FIG. S4.   Membrane attachment and detachment rates of proteins for $E_{\mathrm{opt}} = -5k_{\mathrm{B}}T$ and $\xi - d = 100\,d$. Solid lines represent $\widetilde{\gamma} = -0.004$; dashed lines represent $\widetilde{\gamma} = 0$. (a) The attachment rate increases as a function of the concentration $\widetilde{m}$ of membrane-bound proteins until the membrane saturates. (b) The detachment rate remains more or less constant as a function of the concentration $\widetilde{m}$ of membrane-bound proteins.
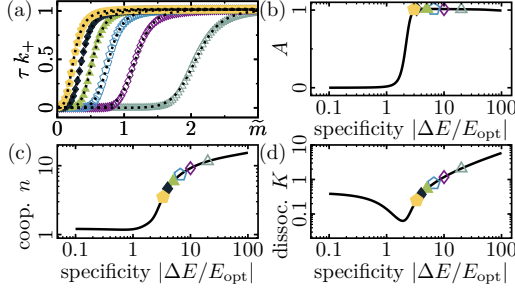
FIG. S5. Effective representation of binding cooperativity for the parameter values in Fig. S4. (a) The fit $\tau\left(k_+ - k_+|_{\widetilde{m}=0}\right) \approx A\,\widetilde{m}^n/(K^n + \widetilde{m}^n)$ (indicated by the dotted lines) is in good agreement with the attachment rate. (b) The scale factor A, which indicates whether the attachment rate is constant or follows a Hill-like curve, indicates a transition from a diffusion-limited to a highly nonlinear attachment process at a protein specificity $|\Delta E/E_{\mathrm{opt}}| \approx 2$. Both the cooperativity coefficient (c) and the apparent dissociation constant (d) increase with the specificity of the protein $|\Delta E/E_{\mathrm{opt}}|$. Note that both measures only capture the prominent properties of the attachment process when $A \approx 1$.

$\tau\left(k_+ - k_+|_{\widetilde{m}=0}\right) \approx A\,\widetilde{m}^n/(K^n + \widetilde{m}^n)$ [Fig. S5a], with $A \approx 1$ [Fig. S5b]. Similar as in the main text [cf. Fig. 3d], this shows that proteins with a higher specificity $|\Delta E / E_{\mathrm{opt}}|$ show higher cooperativity n [Fig. S5c]. Here, the scale factor A indicates whether the attachment rate is constant or nonlinear: $k_+ \approx k_+|_{\widetilde{m}=0}$ if $A = 0$, while $k_+ \approx \tau^{-1}\,\widetilde{m}^n/(K^n + \widetilde{m}^n)$ if $A \approx 1$; note that $\max(k_+) \approx \tau^{-1}$ [cf. Figs. S4a, S5a]. We find that the attachment process becomes highly non-linear above a protein specificity $|\Delta E/E_{\mathrm{opt}}| \approx 2$. Then, both the cooperativity coefficient [Fig. S5c] and the apparent dissociation constant [Fig. S5d] increase with the specificity of the protein.

Taken together, as in the main text, increasing protein density deforms the membrane towards a binding-favorable conformation, and ultimately increases the attachment rate in a pronounced nonlinear fashion.

S.V. VARIATIONAL TREATMENT OF THE MEMBRANE

In this section, we sketch how one can extend the model presented in the main text to describe membranes of arbitrary shape. Furthermore, we show how gradients in membrane conformation drive in-plane flows of membrane-bound proteins.

A. Shape equation for arbitrary deformations

In the main text, we have adiabatically eliminated the mechanical degrees of freedom in the free energy by finding the membrane conformation that *locally* minimizes the free energy density. However, it is a priori not clear why this should also correspond to the minimum of the *global* free energy functional. In this section, we show that the results obtained from the main text are valid as long as membrane deformations are sufficiently small.

We assume that proteins couple to the membrane curvature. Then, analogously to the main text, the free energy density is given by:

$$f(u, m) = \tfrac{1}{2}\kappa\,(H - H_0)^2 \\ + m\left[E_{\mathrm{opt}} + \tfrac{1}{2}\,\epsilon\,(H - H_{\mathrm{opt}})^2\right] + f_{\mathrm{PP}}(m), \quad \text{(S21)}$$

where $f_{\mathrm{PP}}(m)$ models direct interactions between proteins (which can be attractive, repulsive, or entropic). Note that, in principle, one could also consider proteins that couple to the lipid density in the membrane. Such a coupling could be achieved by insertion of lipid-targeting anchors into the inner leaflet of the membrane, while leaving the outer leaflet unperturbed. To account for such a coupling, one would separately consider the lipid densities in both membrane leaflets, which leads to a description of membrane deformations within the area-difference-elasticity model [4]. Below, we will determine an equation for the membrane shape that minimizes the free energy functional associated with Eq. (S21).

In-plane motion arising from tangential stresses always keeps the membrane shape fixed, while out-of-plane motion due to normal stresses changes the membrane shape. Therefore, to find the equilibrium shape of the membrane, one has to first determine the normal stresses acting on its surface. This is achieved by considering a virtual displacement of all surface points by an infinitesimal distance φ orthogonal to the basis vectors that span the membrane; this is called a *variation*. Such a variation affects the free energy functional, $F \to F + \delta F$, by changing membrane curvature, $H + \delta H$, surface area, $S + \delta S$, and surface protein density $m + \delta m$. Then, one can determine the normal stress, $\sigma_z = \delta F/\delta \varphi$, by a straight-forward calculation involving variational calculus [5]:

$$\sigma_z = \tfrac{1}{2}\kappa\left(H - H_0\right)(H^2 - 4K + HH_0) + \Delta_S\left[\kappa\left(H - H_0\right)\right] \\ + \epsilon\,m\left(H - H_{\mathrm{opt}}\right)\left(H^2 - 2K\right) + \Delta_S\left[\epsilon\,m\left(H - H_{\mathrm{opt}}\right)\right] \\ + H\left[m\,\partial_m f_{\mathrm{PP}}(m) - f_{\mathrm{PP}}(m)\right], \quad \text{(S22)}$$

where K denotes the Gaussian curvature and Δ_S the surface Laplacian operator. The above equation has three main contributions, which we list below sorted by lines:

1. stress from bending the membrane away from its intrinsic curvature [6–8],

2. stress from mechanochemical coupling between proteins and membrane, and

3. stress from protein-protein interactions.

Note that the last line suggests that interactions between proteins can lead to membrane deformations, for example by protein crowding [9]. In mechanical equilibrium, normal stresses on the membrane must vanish, $\sigma_z = 0$. This yields the shape equation that minimizes the free energy functional associated with Eq. (S21).

B. Shape equation for small deformations

Here, we use the results from Sec. S.V A to derive a shape equation that is valid for sufficiently small curvatures. We assume that intrinsic membrane curvature, H_0, and membrane curvature, H, are both sufficiently small, and therefore neglect the corresponding nonlinear terms in Eq. (S22). Furthermore, we assume that direct interactions between proteins do not significantly contribute to membrane deformations, and therefore neglect the third line of Eq. (S22). Then, the shape equation dramatically reduces to a Laplace equation:

$$\Delta_S\bigl[\kappa\,(H - H_0) + \epsilon\,m\,(H - H_{\mathrm{opt}})\bigr] = 0\,, \qquad \text{(S23)}$$

which can be easily solved by integrating twice. To that end, we consider a large membrane with fixed curvature, $H|_{\partial S} = H_0$, and vanishing surface protein density, $m|_{\partial S} = 0$, at the boundaries of integration. The only solution to Eq. (S23) that always satisfies these boundary conditions is given by

$$H = H_0 + (H_{\mathrm{opt}} - H_0)\frac{\epsilon\,m}{\kappa + \epsilon\,m}\,, \qquad \text{(S24)}$$

which is identical to the expression derived in the main text. Therefore, we conclude that, as long as the curvature induced by the proteins remains sufficiently small, the results obtained in the main text can be applied to a general spatially extended setting.

C. Tangential forces on the proteins

In the main text, we have neglected the effects of gradients in membrane conformation and protein density on the distribution of proteins. When one considers such gradients, one finds that proteins can self-organize on the membrane [10–18]. Specifically, for proteins that *locally force* the membrane to a given shape, one finds that proteins with a symmetric curvature profile repel each other on the membrane, while crescent-shaped proteins can also attract each other [19]. Here, we consider proteins that do not strictly enforce a density-independent local curvature, but *gradually* deform the membrane with increasing protein density. In that case, one finds attractive interactions between proteins that lead to the accumulation of proteins in regions of preferred curvature, which we will briefly outline in this section.

Tangential displacements of surface points keep the shape of the membrane (principal curvatures and surface area) fixed, while translating the protein density along the surface. Analogously to out-of-plane motion, see Sec. S.V A, in-plane translations can also have an effect on the free energy, which then resulting in effective tangential forces. We proceed by determining the chemical potential, $\mu_m(m) = \delta F/\delta m$, which is encodes how a protein density variation affects the free energy functional:

$$\mu_{\mathrm{m}}(m) = \tfrac{1}{2}\,\epsilon\,(H - H_{\mathrm{opt}})^2 \\ + \epsilon\,(H - H_{\mathrm{opt}})\,m\,\partial_m H + \partial_m f_{\mathrm{PP}}(m)\,. \quad \text{(S25)}$$

Here, the membrane curvature depends on the protein density, as the mechanical degrees of freedom are assumed to relax instantaneously. Each protein that moves in the chemical potential, Eq. (S25), experiences an in-plane force given by $\mathbf{f} = -\boldsymbol{\nabla}_S \mu_{\mathrm{m}}(m)$. This becomes relevant when one considers protein self-organization on the surface (agglomeration towards regions of preferred curvature) in addition to protein recruitment, but has no effect on the binding kinetics itself.

[1] R. Shlomovitz and N. S. Gov, Phys. Biol. **6**, 046017 (2009).

[2] C. Zhu, S. L. Das, and T. Baumgart, Biophys. J. **102**, 1837 (2012).

[3] M. Doi, *Soft Matter Physics* (Oxford University Press, Oxford, 2013).

[4] U. Seifert, Adv. Phys. **46**, 13 (1997).

[5] A. Goychuk, L. Würthner, M. Wigbers, and E. Frey, (to be published).

[6] A. Guckenberger and S. Gekle, J. Phys. Condens. Matter **29**, 203001 (2017).

[7] M. Deserno, Chem. Phys. Lipids **185**, 11 (2015).

[8] O.-Y. Zhong-can and W. Helfrich, Phys. Rev. A **39**, 5280 (1989).

[9] J. C. Stachowiak, E. M. Schmid, C. J. Ryan, H. S. Ann, D. Y. Sasaki, M. B. Sherman, P. L. Geissler, D. A. Fletcher, and C. C. Hayden, Nat. Cell Biol. **14**, 944– (2012).

[10] B. Božič, V. Kralj-Iglič, and S. Svetina, Phys. Rev. E **73**, 041915 (2006).

[11] C. A. Haselwandter and R. Phillips, Europhys. Lett. **101**, 68002 (2013).

[12] C. A. Haselwandter and N. S. Wingreen, PLoS Comput. Biol. **10**, e1003932 (2014).

[13] A. Vahid and T. Idema, Phys. Rev. Lett. **117**, 138102 (2016).

[14] C. van der Wel, A. Vahid, A. Šarić, T. Idema, D. Heinrich, and D. J. Kraft, Sci. Rep. **6**, 32825 (2016).

7

[15] J. Agudo-Canalejo and R. Lipowsky, Soft Matter **13**, 2155 (2017).

[16] A. Vahid, A. Šarić, and T. Idema, Soft Matter **13**, 4924 (2017).

[17] A. Vahid and T. Idema, bioRxiv https://doi.org/10.1101/336545 (2018).

[18] T. Idema and D. J. Kraft, Curr. Opin. Colloid Interface Sci. **40**, 58 (2019).

[19] Y. Schweitzer and M. M. Kozlov, PLoS Comput. Biol. **11**, e1004054 (2015).

II.2 PROTEIN FLUXES INDUCE GENERIC TRANSPORT OF CARGO

In Section II.1 "Mechanochemical Coupling between Proteins and Membranes", we have focused on the binding dynamics of proteins that attach to a membrane. Such a particle exchange between the cytosol and the membrane corresponds to reactive fluxes *perpendicular* to the surface of the membrane. Now, we put the spotlight on particle fluxes *parallel* to the surface of the membrane, which are a crucial aspect of intracellular pattern formation. We find that net diffusive fluxes of particles, driven by the generation of surface density gradients through out-of-equilibrium reactions, can transport entirely unrelated molecules. Our main results are published in "A diffusiophoretic mechanism for ATP-driven transport without motor proteins", Nature Physics **17**, 850 (2021). We refer to pages 83–108 for a reprint of the main text and to pages 109–168 for a reprint of the Supplementary Material. All data are deposited in a publicly accessible repository maintained by the Max Planck Society, see pages 171–197. The following serves as an introduction into the project and a summary of its main results, for the convenience of the reader.

Research Contribution. This project is also a part of the dissertation of Beatrice Ramm, who performed the experiments (Ramm, 2020). For this project, I developed the entire theory and performed simulations using the finite element method.

II.2.1 STARTING POINT OF THE PROJECT

General Scope and Relevance. Cells organize and control their internal dynamics through protein patterns (Halatek, Brauns, et al., 2018). These protein patterns can result from a dynamic interplay between reactive fluxes that build up density gradients and diffusive fluxes that degrade density gradients (Halatek, Brauns, et al., 2018). The *Escherichia coli* Min system is a prime example of such a pattern-forming reaction-diffusion system, which is based on the ATPase MinD and the ATPase activating protein MinE (Raskin and de Boer, 1999; Loose, Fischer-Friedrich, Ries, et al., 2008). The two proteins MinD and MinE form a relatively simple reaction scheme based on reversible membrane binding, which one can summarize as *cycling between an active membrane-bound state and an inactive cytosolic state* (Huang et al., 2003; Halatek and Frey, 2012). In the cytosol, MinD proteins first switch into an active conformation by exchanging ADP with ATP, and then cooperatively bind to the bacterial membrane (Huang et al., 2003; Halatek and Frey, 2012). In turn, membrane-bound MinD recruits

more MinD proteins as well as MinE proteins from the cytosol to the membrane. The former constitutes a positive feedback loop, while the latter leads to the formation of MinDE complexes that ultimately detach from the membrane (Huang et al., 2003; Halatek and Frey, 2012). These nonlinear reactions lead to a preferential attachment of MinD in regions of high MinD surface density, and to a preferential detachment of MinD in regions of low MinD (and high MinE) surface density. Thus, the *reactive fluxes* perpendicular to the membrane surface, and the resulting continuous exchange of particles between the membrane and the cytosol, build up surface density gradients of proteins on the membrane as well as cytosolic density gradients. This build-up of protein density gradients drives diffusive fluxes, from regions of high protein density towards regions of low protein density.

In *Escherichia Coli*, these reaction-diffusion dynamics result in pole to pole oscillations (Hu and Lutkenhaus, 1999; Raskin and de Boer, 1999; Hale et al., 2001; F. Wu et al., 2015), involved in regulating the placement of the bacterial division axis (de Boer et al., 1989; Hu and Lutkenhaus, 1999; Raskin and de Boer, 1999; Lutkenhaus, 2007; Ramm, Heermann, et al., 2019). To further analyze how these patterns form, the *Escherichia Coli* Min system was also reconstituted on planar membranes *in vitro*, where one observes traveling waves or stationary patterns (Loose, Fischer-Friedrich, Ries, et al., 2008; Vecchiarelli et al., 2016; Glock et al., 2019). Placing the reconstituted *in vitro* Min system in geometric confinement, similar in shape to the bacterium *Escherichia Coli*, one can recover oscillations (Zieske and Schwille, 2014; Caspi and Dekker, 2016). But the interior of a cell is not as "clean" as a reconstituted *in vitro* system. The former contains many different densely packed protein species (van den Berg et al., 2017), while the latter is a comparatively dilute solution in the bulk; only on the membrane do the proteins occupy a high fraction of the available area (Loose, Fischer-Friedrich, Herold, et al., 2011; Ramm, Glock, et al., 2018). Interestingly, when taking the reconstituted *in vitro* system closer to its *in vivo* counterpart by placing additional unrelated particles on the membrane, one observed that the MinDE patterns could regulate the localization of these particles (Ramm, Glock, et al., 2018; Shih et al., 2019). However, the physical mechanism that underlies these observations remained to be uncovered.

Research Question and Hypothesis. In our joint experimental and theoretical project, we aim to answer the following question: *What is the physical mechanism that allows MinDE protein patterns to induce cargo transport of unrelated molecules?* To that end, we devise four different hypotheses, which we test by placing artificial cargo on the membrane and measuring its redistribution by MinDE patterns. We choose experimental conditions where the MinDE patterns form a quasi-steady state, which means that the mesoscopic appearance

of the patterns remains constant over time although proteins continuously undergo reactions on a microscopic scale.

Our first three hypotheses rely on thermodynamic mechanisms to describe the distribution of the passive cargo in response to the protein patterns, but these ultimately prove insufficient to explain the experimental observations of our collaborators. First, depletion attraction is a classical thermodynamic effect that can lead to the aggregation of larger particles in a field of smaller particles (Asakura and Oosawa, 1954). This effect can be relevant for biological phenomena such as filament bundling (Marenduzzo et al., 2006). However, we observe no such aggregation of cargo in a homogeneous field of membrane-bound MinD, thus ruling out our first hypothesis.

Second, the surface coverage of membrane-bound MinD is rather high, reaching values of roughly 20%, while diffusion of the MinD proteins on the membrane is very slow under the given conditions (Loose, Fischer-Friedrich, Herold, et al., 2011). Therefore, in a drastic approximation, the MinD proteins could act as roughly immobile obstacles for the cargo molecules, thus biasing their diffusion by restricting the accessible areas. However, in this approximation one would expect that the distribution of the cargo molecules in response to the MinDE protein patterns should not depend on any intrinsic properties of the cargo molecules themselves. Because this contradicts the experimental observations of our collaborators, we must also exclude our second hypothesis.

As our third and final thermodynamic hypothesis, we relax the approximation that the MinD proteins are immobile. Instead, only the spatial distribution of MinD proteins is maintained by reactions, in the form of a continuous particle exchange between cytosol and the membrane. Then, we ask: *Since protein patterns imply a well-defined inhomogeneous surface density of MinDE proteins, can the resulting constraints on the mixing entropy lead to an effective repulsion of our artificial cargo?* To test this hypothesis, we proceed analogously as in Paragraph "From Osmotic Pressure Differences to Diffusion" (Section I.2.3), by tessellating the membrane surface into many infinitesimal compartments. In each compartment, we consider the membrane-bound particles as a well-mixed lattice gas with local particle densities c_i, where each artificial cargo molecule effectively behaves like a polymer. This allows us to construct a free energy functional F based on the Flory-Huggins theory of mixing (Huggins, 1941; Flory, 1942; de Gennes, 1979). From this free energy functional, we then derive the local chemical potential of each molecular species on the membrane, $\mu_i = \delta F / \delta c_i$. The non-equilibrium reaction dynamics of the MinDE proteins build up and maintain a fixed density distribution, c_p, and thus fixed chemical potential gradients $\nabla \mu_p \neq 0$ for these active proteins. In contrast, the distribution of passive cargo, c_g, relaxes towards a thermal equilibrium configuration with vanishing chemical potential gradients, $\nabla \mu_g = 0$. This condition allows us to determine

the distribution of the passive cargo molecules in response to the active MinDE protein patterns. We find that entropic mixing effects can, in principle, lead to an effective repulsion of cargo molecules from regions with high MinD protein density. However, the resulting redistribution of the cargo molecules is much weaker than in the experiments done by our collaborators, which indicates that our theory must still be missing something. In particular, as we discuss next, the net diffusive fluxes of different membrane-bound particles couple via an effective mesoscopic friction.

II.2.2 SUMMARY OF THE MAIN RESULTS

All thermodynamic hypotheses fail to explain the experimental observations of our collaborators, which suggests that a genuinely non-equilibrium mechanism could be at play. Therefore, we now explicitly consider the fluxes $\boldsymbol{j}_i$ of each species. According to Onsager's theory (Balian, 2007), such fluxes arise in response to chemical potential gradients (thermodynamic forces), $\boldsymbol{\nabla}\mu_i$. Then, as we have discussed in Paragraph "From Osmotic Pressure Differences to Diffusion" (Section I.2.3), one can view the diffusion of a species c_i as an effective balance between thermodynamic forces, $\boldsymbol{\nabla}\mu_i$, and a friction ξ_i with the embedding fluid. In addition, the surface density of particles on the membrane is so large that the mean-free path between any to membrane-bound particles is only about 50 Å. Then, the fluxes of different species can couple via an effective "mesoscopic friction" ζ_{ik}, which is mediated by hydrodynamic interactions or direct interactions. Taken together, we then formulate a Maxwell-Stefan-like effective force-balance equation for each molecular species (Maxwell, 1866; J. Stefan, 1871; Krishna and Wesselingh, 1997):

$$-\boldsymbol{\nabla}\mu_i = \xi_i \frac{\boldsymbol{j}_i}{c_i} + \sum_{i,k} c_k \zeta_{ik} \left(\frac{\boldsymbol{j}_i}{c_i} - \frac{\boldsymbol{j}_k}{c_k} \right). \tag{II.16}$$

Note that for vanishing coupling between the diffusive fluxes of different species, $\zeta_{ik} \to 0$, Eq. (II.16) reduces to the equilibrium Flory-Huggins model where the chemical potential gradients of passive species must vanish, $\boldsymbol{\nabla}\mu_g = 0$. This already leads to a redistribution of the passive cargo, in response to the actively maintained spatial profile of the MinD proteins, albeit too weak to explain the experimental results of our collaborators. In the case of a finite coupling, $\zeta_{ik} \neq 0$, this redistribution is further superimposed by advective transport, because protein fluxes establish an additional effective frictional force on the cargo molecules. As it turns out, this mesoscopic frictional force is the missing link of our previous equilibrium thermodynamic approach. Using our non-equilibrium model, Eq. (II.16), we not only quantitatively explain the

experimental observation of strong cargo redistribution by MinDE patterns, but also predict sorting of different cargo species according to their interaction strength with the protein fluxes. Furthermore, given that we formulated our theory in terms of particle fluxes, it also applies to the more general situation of *dynamic* protein patterns. In that case, we observe that traveling MinDE waves elicit long-ranged cargo transport in the direction of the wave vector.

In a non-biological context, it is well known that density gradients of small solute molecules can induce directed transport of large colloid particles (Anderson et al., 1982; Prieve, Anderson, et al., 1984; Abécassis et al., 2008; Palacci et al., 2010; Paustian et al., 2015; Shin et al., 2016; Shi et al., 2016; Illien et al., 2017; Prieve, Malone, et al., 2019; Marbach and Bocquet, 2019; Golestanian, 2019). Our study presents an example that diffusiophoretic transport mechanisms can actually occur in a biological setting. This agrees with other theoretical studies, which have suggested that diffusiophoresis might play a role in a biological context (Banigan et al., 2011; Agudo-Canalejo et al., 2018; Adeleke-Larodo et al., 2019; Sear, 2019). Finally, we expect that similar effects could, in general, also occur in any crowded environment such as the cell interior. However, many other processes can occur in cells, so it is not clear what role diffusiophoresis could play there: *Can cells harness diffusiophoretic transport, or do they have to work against it?* The truth probably lies somewhere in between. Finally, we hypothesize that unspecific mechanical coupling between proteins can lead to alignment or synchronization of biochemically distinct pattern-forming systems when placed in the same geometry. It would be interesting to test this hypothesis experimentally by combining two biochemically distinct reconstituted pattern-forming systems, once available.

II.2.3 MANUSCRIPT M2

TITLE:

A DIFFUSIOPHORETIC MECHANISM FOR ATP-DRIVEN TRANSPORT WITHOUT MOTOR PROTEINS

AUTHORS:

Beatrice Ramm*, **Andriy Goychuk***, Alena Khmelinskaia, Philipp Blumhardt, Hiromune Eto, Kristina A. Ganzinger, Erwin Frey and Petra Schwille

The asterisk symbol (*) indicates shared first authorship.

AUTHOR CONTRIBUTIONS:

B.R., A.G., E.F. and P.S. conceived the study. A.G. and E.F. designed the theoretical analysis. A.G. conducted the theoretical analysis. B.R., A.K. and P.B. designed experiments. B.R. performed all experiments. A.K. designed DNA origami. A.K. and B.R. prepared origami. H.E. and B.R. fabricated chromium-patterned slides. K.A.G. developed single-particle tracking code. B.R., A.G., P.B. and K.A.G. analysed data. B.R., A.G., E.F. and P.S. wrote the manuscript. All authors discussed and interpreted the results and revised the manuscript.

Check for updates

OPEN

A diffusiophoretic mechanism for ATP-driven transport without motor proteins

Beatrice Ramm [1,4,6], Andriy Goychuk [2,6], Alena Khmelinskaia [1,5], Philipp Blumhardt[1], Hiromune Eto [1], Kristina A. Ganzinger [3], Erwin Frey [2 ✉] and Petra Schwille [1 ✉]

The healthy growth and maintenance of a biological system depends on the precise spatial organization of molecules within the cell through the dissipation of energy. Reaction–diffusion mechanisms can facilitate this organization, as can directional cargo transport orchestrated by motor proteins, by relying on specific protein interactions. However, transport of material through the cell can also be achieved by active processes based on non-specific, purely physical mechanisms, a phenomenon that remains poorly explored. Here, using a combined experimental and theoretical approach, we discover and describe a hidden function of the *Escherichia coli* MinDE protein system: in addition to forming dynamic patterns, this system accomplishes the directional active transport of functionally unrelated cargo on membranes. Remarkably, this mechanism enables the sorting of diffusive objects according to their effective size, as evidenced using modular DNA origami–streptavidin nanostructures. We show that the diffusive fluxes of MinDE and non-specific cargo couple via density-dependent friction. This non-specific process constitutes a diffusiophoretic mechanism, as yet unknown in a cell biology setting. This nonlinear coupling between diffusive fluxes could represent a generic physical mechanism for establishing intracellular organization.

Spatiotemporal organization of cells generally emerges through redistribution and transport of molecules via motor proteins[1], self-assembling cytoskeletal elements[2] or self-organizing reaction–diffusion systems[3]. Coupling of cargo to energy-dissipating NTPases that drive the transport is usually mediated by specific protein–protein interactions. Non-specific coupling of biomolecules, by contrast, is poorly explored in biology and, so far, only a few examples of molecular transport based on purely physical mechanisms have been reported. For example, a study in mouse oocytes showed that actin-coated vesicles generated a pressure gradient that positioned large objects like the nucleoid in the cell centre[4,5]. In the *Caenorhabditis elegans* zygote, cortical flows were shown to couple to the PAR reaction–diffusion system via advective transport[6]. Another recent example comes from in vitro studies of the *Escherichia coli* Min system[7,8].

The Min system, a paradigmatic model for pattern formation in biology, regulates the site of cell division in *E. coli*[9–12]. The core of this reaction–diffusion system consists of only two proteins, the ATPase MinD and the ATPase activating protein MinE, which interact and reversibly bind to the membrane[11,13]. Despite this simple reaction scheme, the Min system exhibits rich dynamics that have been explored in vivo[9–11,14], reconstituted in vitro[13,15,16] and described by physical theories[17–21]. In the rod-shaped *E. coli*, MinDE oscillate from pole to pole[10,11,14]. In vitro, MinDE proteins form travelling surface waves or quasi-stationary patterns on planar artificial membranes[13,15,16] and exhibit oscillations when geometrically confined[22,23]. These dynamics can provide spatial cues for particular proteins. MinC specifically binds to MinD and thus follows its movements[10,22,24–26]. In turn, MinC constrains the localization of the main divisome protein FtsZ by inhibiting its polymerization[27,28].

Besides this well-described patterning by specific interactions with clear physiological evidence, MinDE self-organization has

recently shown an intriguing hidden function in vitro: MinDE regulated the localization of unrelated membrane-bound molecules in space and time in the absence of MinC/FtsZ[7,8]. These results suggested that MinDE oscillations could further enhance cell division by prepositioning membrane proteins to the cell middle[7]. However, the underlying physics and the broader biological implications have remained unknown.

Here, through a joint experimental and theoretical investigation, we have deciphered the physical mechanism underlying this non-specific transport phenomenon. We quantitatively probed MinDE-dependent transport using a synthetic membrane-bound cargo based on composite DNA nanostructures. We discerned how the effective size (that is, membrane footprint) and diffusion coefficient of the cargo, as well as the type of MinDE patterns, determine the transport that takes place. Exploiting these effects, we revealed that MinDE can even spatially sort different cargo species. Theoretical analysis of these data demonstrated a diffusiophoretic effect: an effective density-dependent inter-particle friction creates cargo transport along the diffusive fluxes of MinD proteins. This type of NTPase-driven diffusiophoresis might represent a generic active transport mechanism in cells that neither requires motor proteins nor specific protein interactions. As such, it might be particularly important for prokaryotes and could have been prevalent in early stages of life on Earth.

Probing MinDE-induced transport with a synthetic cargo
We set out to understand how MinDE dynamics can spatiotemporally regulate other membrane-bound, yet unrelated molecules (henceforth referred to as non-specific 'cargo') into patterns and gradients[7,8]. Specifically, we asked whether cargo transport can arise from MinDE patterns per se via thermodynamic forces, or whether it requires active processes and non-equilibrium particle fluxes.

[1]Max Planck Institute of Biochemistry, Martinsried, Germany. [2]Arnold-Sommerfeld-Center for Theoretical Physics and Center for NanoScience, Ludwig-Maximilians-Universität München, Munich, Germany. [3]Living Matter Program, AMOLF, Amsterdam, Netherlands. [4]Present address: Department of Physics, Princeton University, Princeton, NJ, USA. [5]Present address: University of Washington, Institute for Protein Design, Seattle, WA, USA. [6]These authors contributed equally: Beatrice Ramm, Andriy Goychuk. ✉e-mail: frey@lmu.de; schwille@biochem.mpg.de

To experimentally address this question and test possible mechanisms, we set up a highly controllable minimal in vitro platform. To this end, we reconstituted MinDE pattern formation on supported lipid bilayers (SLBs)[13]. For simplicity, we first chose conditions under which initially chaotic, laterally moving MinDE waves transition into quasi-stationary labyrinth patterns[16]. To quantitatively assess the interaction between MinDE and cargo molecules on the membrane, we employed a synthetic cargo: a composite object consisting of a DNA origami nanostructure as scaffold and streptavidin molecules that serve as modular building blocks and connectors to the membrane (Fig. 1a). In particular, the origami[29] featured 7 dyes on the upper facet for visualization and 42 sites at the bottom facet that could be specifically addressed for the incorporation of biotinylated oligonucleotide handles. These handles in turn bound to streptavidin coupled to biotinylated lipids in the SLB.

When we initiated MinDE self-organization with ATP in the presence of this synthetic cargo, the cargo components—that is, the origami structures and streptavidin—reorganized into patterns from an initially homogeneous state (Fig. 1b,c, Supplementary Fig. 1 and Supplementary Video 1). As expected, the origami and streptavidin co-localized. Accordingly, in the following, origami fluorescence serves as a proxy for cargo localization. For the entire duration of the experiment, cargo always gathered in MinD-depleted regions, forming patterns that were anti-correlated to the MinDE patterns (Fig. 1b,c). Similarly, when we altered the established MinDE/cargo patterns by adding more MinE, the cargo channel reflected the changes in MinDE patterns, moving in an anti-correlated fashion (Supplementary Fig. 2 and Supplementary Video 2). By contrast, when MinE (which stimulates MinD ATP hydrolysis) was omitted, MinD and the cargo molecules remained uniformly distributed (Extended Data Fig. 1). These findings indicate that the spatial heterogeneity of the cargo is not caused by depletion attraction, such as in filament bundling[30]. For one, depletion attraction should lead to aggregation of large particles (cargo), even in a homogeneous field of smaller particles (MinD)[31]. Furthermore, depletion attraction would imply a preferred agglomeration of cargo in regions of high MinD density, which we also did not observe (Supplementary Information). Hence, our data demonstrate that cargo transport is active, because it requires the presence of MinDE and ATP, and thus active MinDE self-organization.

Effective cargo size determines the extent of cargo demixing

Having shown that MinDE redistribute our synthetic cargo, we next exploited the modular nature of our cargo to systematically vary its interaction with MinDE. MinD and lipid-anchored streptavidin both form a monomolecular layer of height ~5 nm on membranes[32,33], whereas the lower facet of the origami scaffold lies at ~5–11 nm above the membrane (Supplementary Note 1). MinDE thus move on the membrane below the altitude of the origami

scaffold and should mainly interact with the membrane-bound streptavidin. Hence, varying the number of streptavidin ($n \in \{1, 2, 5, 15, 28, 42\}$) bound to the origami scaffold enables fine control over a large dynamic range of the membrane footprint or effective size of the cargo (henceforth cargo-n, Fig. 1). In this way, we modulated the interaction of the cargo-n with MinDE, as well as its diffusion on the membrane.

To quantitatively assess the interaction between MinDE and the respective cargo, we analysed the resulting, final quasi-stationary patterns (Fig. 1d and Extended Data Fig. 2). As a measure for molecule enrichment, we determined the Michelson contrast, $(I_{max} - I_{min})/(I_{max} + I_{min})$, of the fluorescence images on a scale from zero for a homogeneous distribution to one for a binary distribution. Cargo patterns became much sharper with increasing cargo size (Fig. 1e and Extended Data Fig. 2). This increase in the contrast of cargo patterns was accompanied by sharper and also narrower MinDE patterns, as indicated by an increased region of pixels classified as MinD minima (Fig. 1f,g). Thus, MinDE dynamics dictate the localization of cargo on the membrane in a size-dependent manner, and are in turn also impacted by their presence. At first glance, these results could be interpreted as simply being a consequence of steric repulsion between cargo and MinDE. However, although a static gradient of accessible space would indeed induce a gradient of cargo molecules, this effect should be equal for all cargo species, irrespective of their effective size (Supplementary Information). Therefore, even though the diffusion of MinD on the membrane under the given conditions is very slow ($D = 0.013\,\mu m^2\,s^{-1}$)[25], we conclude that MinD proteins do not simply act as immobile obstacles on the membrane that would bias cargo diffusion via static volume exclusion, a second option for a thermodynamic force.

Thermodynamic forces cannot explain cargo transport by MinDE

As our experimental data disqualified both depletion attraction and static volume exclusion as possible explanations for cargo redistribution, we wondered whether mobile MinD proteins could effectively repel cargo in a size-dependent manner by imposing local constraints on the entropy of mixing. To test this third (thermodynamic) hypothesis, we formulated a fully quantitative Flory–Huggins theory (FH) without fitting parameters. Specifically, each origami scaffold crosslinks n streptavidin into a passive polymer-like cargo (Fig. 2a), while the remaining free streptavidin (for $n < 15$; Extended Data Fig. 2) behave independently (Supplementary Information). Given these constraints, we characterized the membrane in terms of local surface densities of c_g cargo, c_s free streptavidin and c_p MinD (Supplementary Table 1), assuming a well-mixed lattice gas on the microscopic scale. On the mesoscopic scale, we then asked 'what is the equilibrium distribution of passive particles (cargo and free streptavidin) in the presence of a heterogeneous distribution of active MinD proteins?' To answer this question, we used our FH model to calculate the corresponding chemical


Fig. 1 | MinDE-driven cargo demixing depends on the effective size (membrane footprint) of the cargo. a, Schematic of the synthetic membrane-anchored cargo consisting of a DNA origami scaffold (20-helix bundle; 110 × 16 × 8 nm) and streptavidin building blocks. The DNA origami nanostructure illustrates the position of 7 dyes at the upper facet and 42 addressable sites for incorporation of biotinylated oligonucleotides at the lower facet. Biotinylated oligonucleotides bind to lipid-anchored streptavidin on the SLB. MinDE self-organize by concerted attachment and detachment to and from the membrane powered by ATP hydrolysis into ADP and P$_i$ (inorganic phosphate). The self-organization assay is performed in an open chamber. **b,c**, Representative time series (**b**) and kymograph (along the line selection in **b**) (**c**) of MinDE self-organization inducing patterns of cargo-2 (1 μM MinD (30% EGFP-MinD), 1.5 μM MinE-His, 0.1 nM origami-Cy5 with two biotinylated oligonucleotides, Alexa568-streptavidin). **d**, Representative images and fluorescence intensity line plots (smoothed) of established MinDE labyrinth patterns and anti-correlated DNA origami and streptavidin patterns when no origami, cargo-2, cargo-15 or cargo-42 is present. The contrast of the resulting patterns and size of the MinD minima increase with increasing number of incorporated streptavidin per cargo. **e–g**, Box plots of the contrast of cargo (**e**), MinD patterns (**f**) and the fraction of pixels classified as MinD minima (**g**) when no origami, cargo-1, cargo-2, ..., or cargo-42 is present. Lines in box plots are medians, box limits are quartiles 1 and 3, whiskers are 1.5× interquartile range (IQR) and points are outliers. Data are from at least two independent experiments with total numbers of analysed images per condition N(No origami) = 32, N(Cargo-1) = 96, N(Cargo-2) = 41, N(Cargo-5) = 32, N(Cargo-15) = 94, N(Cargo-28) = 32, N(Cargo-42) = 87. Scale bars, 50 μm (**b,c,d**).

ARTICLES

potentials μ_i for each species (Supplementary Information). Furthermore, we assumed that the passive particles adopt a thermal equilibrium state with vanishing chemical potential gradients ($\nabla\mu_g = \nabla\mu_s = 0$) in an adiabatic response to the imposed steady-state distribution of active particles ($\nabla\mu_p \neq 0$). Our theoretical analysis shows that entropic mixing effects can, in principle, create a
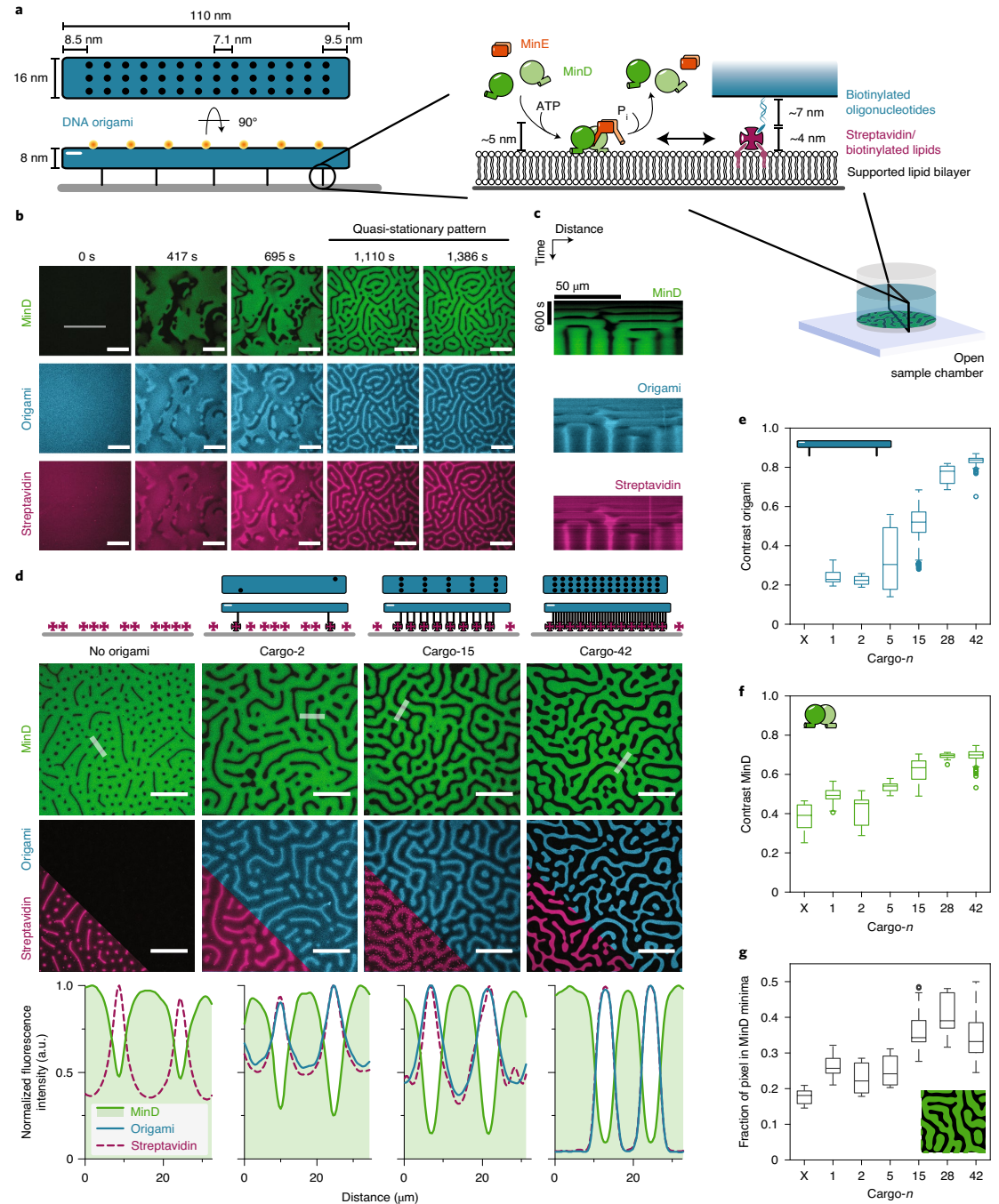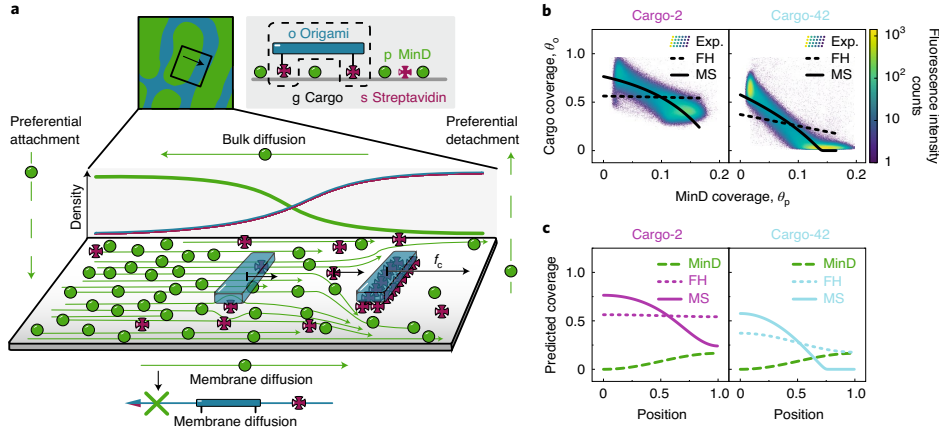
Fig. 2 | MinDE-dependent cargo transport is explained by mesoscopic friction between particle fluxes, not by mixing or volume exclusion. a, Schematic of the phenomenological MS-type model. MinD protein density gradients are determined by a closed cycle of reactive fluxes (MinD membrane attachment/detachment, dashed green arrows) and diffusive fluxes (green arrows). Mediated by hydrodynamic or direct interactions, the diffusive MinD membrane fluxes exert a frictional force $\mathbf{f}_c$ (black arrow) on the cargo molecules. Then, cargo density gradients are determined by a balance between these frictional forces and thermodynamic forces (entropic repulsion and mixing). **b**, Cross-correlation between MinD coverage ($\theta_p = a_p c_p$) and DNA origami coverage ($\theta_o = a_o c_g$), for two different cargo species, cargo-2 and cargo-42. Respective membrane footprints: MinD dimer $a_p = 25\,\mathrm{nm^2}$, DNA origami $a_o = 1{,}760\,\mathrm{nm^2} \approx 70 a_p$. The colour-coded two-dimensional histogram represents the experimental data of selected days (Exp.), where the raw images were smoothed by a one-pixel-wide Gaussian kernel. Solid and dashed lines correspond to two candidate models. The FH-type model (dashed lines), whose parameters are fully determined by our experiments, fails to account for cargo transport: weak entropic sorting of streptavidin in an external gradient of MinD is not sufficient to overcome the strong repulsion of the bulky DNA origami scaffolds. Instead, we find that the MS model (solid lines), with an estimated interaction parameter, explains cargo transport. The MS model allows stronger reorganization of cargo than the FH model, because, in addition to thermodynamic forces, cargo transport is further driven by frictional coupling to MinD protein fluxes. **c**, Spatial distribution of cargo molecules in response to the (imposed) MinD profile, corresponding to the cross-correlation functions in **b**. Model parameters: (cargo-2) average coverages $\overline{\theta_p} = 0.0825$, $\overline{\theta_s} = 0.149$ and $\overline{\theta_o} = 0.55$; interaction parameter in terms of MinD coverage $\theta_\times^{-1} = a_p^{-1} c_\times^{-1} = 220$; (cargo-42) average coverages $\overline{\theta_p} = 0.0825$, $\overline{\theta_s} = 0$ and $\overline{\theta_o} = 0.28$; interaction parameter $\theta_\times^{-1} = a_p^{-1} c_\times^{-1} = 620$.

gradient of passive cargo in response to a gradient of active MinD, where the cargoes' crosslinked streptavidin experience a weak entropic bias towards MinD-depleted regions (due to volume exclusion effects). However, this effect will be partly compensated by the analogous entropic repulsion between origami scaffolds, which prevents high cargo densities, in stark contrast to our experimental observations (Fig. 2b,c and Extended Data Fig. 3). Consequently, we also rejected entropic mixing in fixed external (chemical potential) gradients as the mechanism underlying MinDE-dependent cargo transport.

**Coupling between particle fluxes explains cargo transport**

Taken together, thermodynamic mechanisms alone cannot explain MinDE-induced cargo transport in our experiments, suggesting that the underlying mechanism is genuinely non-equilibrium in nature. Therefore, we generalized our equilibrium FH model to consider the non-equilibrium dynamics of particles. Specifically, MinDE gradients build up due to particle exchange between the bulk solution and membrane (reactive fluxes)[16,18,19,21,25], leading to chemical potential gradients $\nabla\mu_i$ on the membrane (thermodynamic forces). According to Onsager's theory[34], thermodynamic forces imply particle fluxes $\mathbf{j}_i$. Conceptually, diffusive fluxes on the membrane then arise from an effective force balance of thermodynamic and friction forces between the different macromolecules and lipids (with friction coefficients ξ_i). Furthermore, in a crowded environment such as the membrane surface in our experiments (mean free path of ~50 Å; Supplementary Information), hydrodynamic or also direct interactions between particles can mediate a 'mesoscopic friction'

that couples their respective fluxes (with coupling constants ζ_{ik}). Using these arguments, we formulated a phenomenological theory where each membrane-bound species obeys a Maxwell–Stefan (MS)-like effective force-balance equation[35,36]:

$$\nabla\mu_i + \xi_i \frac{\mathbf{j}_i}{c_i} + \sum_k c_k \zeta_{ik}\left(\frac{\mathbf{j}_i}{c_i} - \frac{\mathbf{j}_k}{c_k}\right) = 0. \qquad (1)$$

As before, the index $i \in \{p, g, s\}$ refers to MinD proteins, cargo with bound streptavidin and free streptavidin, respectively. Although our theory is intrinsically dynamic (Methods), we first analysed the non-equilibrium steady state, $\partial_t c_i = 0$, reflecting the quasi-stationary MinDE patterns. Then, cargo and streptavidin exhibit Brownian motion and relax to a thermal equilibrium state with vanishing fluxes $\mathbf{j}_g = \mathbf{j}_s = 0$. The MinD protein patterns maintain a non-equilibrium steady state and finite protein fluxes $\mathbf{j}_p \neq 0$ via off-equilibrium chemical reactions (ATPase activity). In the absence of mutual friction between the macromolecules ($\zeta_{ik} = 0$), equation (1) reduces to the FH model ($\nabla\mu_g = \nabla\mu_s = 0$), which readily implies weak cargo redistribution in a static gradient of active proteins. As a decisive factor in addition to these entropic demixing effects, the presence of frictional coupling ($\zeta_{ik} \neq 0$) between cargo and MinD leads to advective cargo transport by the non-equilibrium protein fluxes ($\mathbf{j}_p \neq 0$) of MinD (Fig. 2a). The additional bias conferred by these protein fluxes leads to cargo redistribution, which is much stronger than by equilibrium thermodynamic forces alone and thus quantitatively explains our experimental data (Fig. 2b,c and Extended Data Fig. 3).
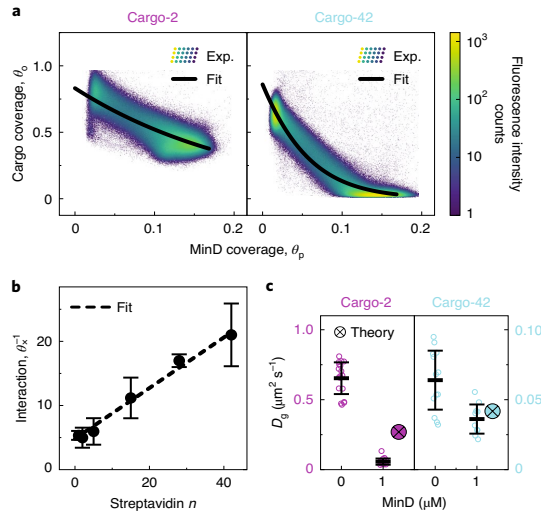
Fig. 3 | Reduced model predicts that large MinD densities slow down cargo diffusion. a, Cross-correlation between MinD coverage ($\theta_{\mathrm{p}} = a_{\mathrm{p}}c_{\mathrm{p}}$) and DNA origami coverage ($\theta_{\mathrm{o}} = a_{\mathrm{o}}c_{\mathrm{g}}$) for cargo-2 and cargo-42. Respective membrane footprints: MinD dimer $a_{\mathrm{p}} = 25\,\mathrm{nm}^2$, DNA origami $a_{\mathrm{o}} = 1{,}760\,\mathrm{nm}^2$. The colour-coded two-dimensional histogram represents experimental data for selected days (Exp.), identical to Fig. 2b, while the solid line (Fit) is a fit curve of our reduced model. **b**, Interaction parameter in terms of MinD coverage, $\theta_{\times}^{-1} = a_{\mathrm{p}}^{-1}c_{\times}^{-1}$, obtained by the fitting procedure in **a**. The interaction linearly increases when more streptavidin is incorporated per cargo, starting from the base interaction of the origami scaffold. The dashed line indicates a linear fit of the interaction parameter $\theta_{\times}^{-1} = (\zeta_{\mathrm{po}} + n\zeta_{\mathrm{ps}})/(a_{\mathrm{p}}\xi_{\mathrm{p}})$ as a function of n. In contrast to our initial estimate (Fig. 2c), entropic repulsion between cargo molecules was neglected for simplicity, thus probably underestimating the interaction parameter. **c**, Cargo molecule diffusion coefficient in the absence or presence of 1 μM MinD (1 μM MinD (30% EGFP-MinD), 0.1–1 pM origami-Cy3b with 2 or 42 biotinylated oligonucleotides, non-labelled streptavidin, SLB: DOPC/DOPG/biotinyl-CAP-PE 70/30/0.01 mol%), measured via single-particle tracking and predicted with the fitted interaction parameters from **b**. Cargo-42 typically diffuses slower than cargo-2 (indicated by a smaller diffusion coefficient D_{g} at 0 μM MinD). Increasing MinD density has a much stronger effect on cargo-2 than on cargo-42, both in theory and experiment. Points are mean values of individual measurements (*M*), line and error bars represent the mean value and standard deviation. Data were obtained from the number of sample chambers S(Cargo-2) = 7, S(Cargo-42) = 5, S(Cargo-2, MinD) = 4, S(Cargo-42, MinD) = 3; number of measurements M(Cargo-2) = 18, M(Cargo-42) = 13, M(Cargo-2,MinD) = 19, M(Cargo-42, MinD) = 10; number of analysed single-particle tracks N(Cargo-2) = 15,755, N(Cargo-42) = 19,481, N(Cargo-2, MinD) = 7,924, N(Cargo-42, MinD) = 4,542; average track length TL(Cargo-2) = 339, TL(Cargo-42) = 546, TL(Cargo-2, MinD) = 772, TL(Cargo-42, MinD) = 647; fraction of mobile DNA origami MF(Cargo-2) = 0.81, MF(Cargo-42) = 0.67, MF(Cargo-2, MinD) = 0.70, MF(Cargo-42, MinD) = 0.63.

MinDE impair cargo diffusion via mesoscopic friction

Next, we simplified our theoretical model by neglecting membrane saturation effects (Supplementary Information), reducing the chemical potential of particles with size a_i to $\mu_i \approx k_{\mathrm{B}}T\ln(a_i c_i)$. The force-balance equation, equation (1), then becomes a generalized Fick's law:

$$\mathbf{j}_{\mathrm{p}} \approx -\frac{k_{\mathrm{B}}T}{\xi_{\mathrm{p}} + c_{\mathrm{g}}\zeta_{\mathrm{pg}} + c_{\mathrm{s}}\zeta_{\mathrm{ps}}}\boldsymbol{\nabla}c_{\mathrm{p}} \equiv -D_{\mathrm{p}}\left(c_{\mathrm{g}}, c_{\mathrm{s}}\right)\boldsymbol{\nabla}c_{\mathrm{p}} \qquad (2)$$

where the density-dependent diffusion coefficient of MinD, $D_{\mathrm{p}}(c_{\mathrm{g}}, c_{\mathrm{s}})$, decreases through friction (that is, interactions) with cargo and streptavidin. For cargo with strong coupling ζ_{pg}, maintaining the diffusive fluxes that balance reactive protein turnover requires sharper protein gradients, which explains the progressively sharper and narrower MinDE patterns (Fig. 1f,g).

Assuming that the typically small number of free streptavidin (Supplementary Information) does not notably contribute to the dynamics, $c_{\mathrm{s}}\zeta_{\mathrm{ps}} \ll c_{\mathrm{g}}\zeta_{\mathrm{pg}}$, one obtains a closed expression for the cargo distribution:

$$c_{\mathrm{g}}\left(c_{\mathrm{p}}\right) = c_{\times}W_0\left[\frac{c_{\mathrm{g}}(0)}{c_{\times}}\exp\left(\frac{c_{\mathrm{g}}(0) - c_{\mathrm{p}}}{c_{\times}}\right)\right], \qquad (3)$$

with typical interaction density $c_{\times} = \xi_{\mathrm{p}}/\zeta_{\mathrm{pg}}$. Fitting equation (3) to our experimental data (Fig. 3a,b and Extended Data Fig. 3), we demonstrate that the coupling constant ζ_{pg} between MinD and cargo-*n* has a contribution from the origami scaffold and from the *n* incorporated streptavidin, $\zeta_{\mathrm{pg}} = \zeta_{\mathrm{po}} + n\zeta_{\mathrm{ps}}$, explaining why cargo transport increases with the number of streptavidin per cargo (Fig. 1d–g).

To test our theoretical model experimentally, we performed single-particle tracking of cargo-2 and cargo-42, both in the presence and absence of MinD. In the former case, we emulated high MinD membrane densities in the maxima of MinDE patterns by adding 1 μM MinD and ATP, but no MinE. We found that the diffusion coefficient of cargo-2 decreased from $0.65 \pm 0.12\,\mu\mathrm{m}^2\,\mathrm{s}^{-1}$ in the absence of MinD to $0.06 \pm 0.02\,\mu\mathrm{m}^2\,\mathrm{s}^{-1}$ at high MinD density (Fig. 3c). By contrast, the diffusion coefficient of cargo-42, which was already low in the absence of MinD ($0.06 \pm 0.02\,\mu\mathrm{m}^2\,\mathrm{s}^{-1}$), hardly changed at high MinD density ($0.036 \pm 0.011\,\mu\mathrm{m}^2\,\mathrm{s}^{-1}$) (Fig. 3c). Subsequently, we used our fitted interaction parameters to predict the diffusion coefficient of cargo at high protein densities, based on the experimental values in the absence of proteins (Supplementary Information). Our predictions were in good quantitative agreement with our experimental findings, validating our model. At first, it might seem counterintuitive that MinD affects cargo-42 diffusion less than that of cargo-2, despite stronger frictional coupling. However, even in the absence of MinD, cargo-42 diffuses much slower than cargo-2 due to the friction between its many streptavidin and the membrane, which dominates over the additional friction with MinD. This observation highlighted the parameter interdependence that arises due to streptavidin serving both as building block and connector to the membrane and raised the question whether cargo transport is affected more by its effective size or its diffusion coefficient. To answer this, we employed an alternative membrane attachment strategy for the DNA origami scaffolds via cholesteryl moieties (Extended Data Figs. 4 and 5 and Supplementary Note 2). We found that cargoes with a larger membrane footprint (that is, effective size) and at the same time similar diffusion as cargo-2 were strongly redistributed (Extended Data Fig. 5 and Supplementary Note 2), corroborating that it is indeed the effective cargo size that determines the interaction with MinD. In conclusion, the dependence of the cargo diffusion coefficient on the ambient protein density is a direct experimental proof of friction between MinD and cargo and that the effective cargo size governs the corresponding friction coefficient.

MinDE spatially sort different cargo species

Can we use our obtained knowledge to selectively position cargo molecules, that is, to sort them according to their properties, along protein gradients? To answer this question, we placed two differently labelled cargo species, cargo-2 and cargo-42, in the same assay (Fig. 4a). We found, as predicted by our model (Fig. 4d), that cargo-
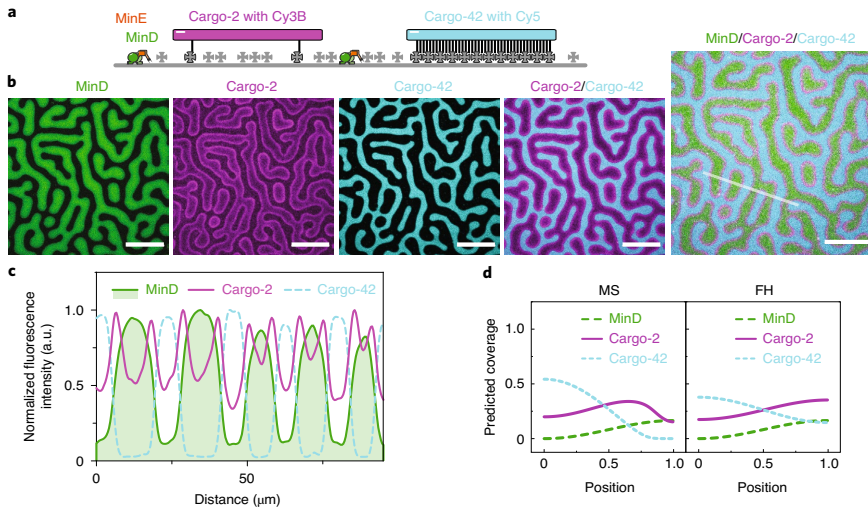
Fig. 4 | MinDE spatially sort cargo according to effective size. a, Schematic of the experimental set-up. MinDE self-organization was performed in the presence of two different cargo species with distinct fluorescent labels, cargo-2 with Cy3B and cargo-42 with Cy5 (1 μM MinD (30% EGFP-MinD), 1.5 μM MinE-His, 50 pM origami-Cy3b with two biotinylated oligonucleotides, and 50 pM origami-Cy5 with 42 biotinylated oligonucleotides, non-labelled streptavidin). **b,c**, Representative images of individual and overlaid channels (**b**) and line plot (**c**) (smoothed) of the indicated selection of MinDE-induced sorting of cargo species. Scale bars, 50 μm. The experiment was performed three times under identical conditions. **d**, Spatial distribution of two cargo species in response to the (imposed) MinD profile. The phenomenological MS-type model allows for stronger reorganization of cargo molecules than the FH-type model. In particular, the phenomenological MS-type model predicts that cargo-2 accumulates between cargo-42 and MinD. Model parameters: average coverage of MinD proteins $\overline{\theta_p} = 0.0825$, streptavidin $\overline{\theta_s} = 0$, cargo-2 $\overline{\theta_{o-2}} = 0.26$ and cargo-42 $\overline{\theta_{o-42}} = 0.26$; interaction parameter (in terms of MinD coverage: $\theta_\times^{-1} = a_p^{-1} c_\times^{-1}$) of cargo-2 $\theta_{\times-2}^{-1} = 220$ and cargo-42 $\theta_{\times-42}^{-1} = 620$. Respective membrane footprints: MinD dimer $a_p = 25 \text{ nm}^2$, streptavidin $a_s = 25 \text{ nm}^2$, DNA origami $a_o = 1{,}760 \text{ nm}^2 \approx 70 a_p$.

42 gathered in MinD-free regions and was framed by cargo-2 (Fig. 4b,c, Supplementary Fig. 3 and Supplementary Video 3). Thus, cargo-2 exhibited a similar behaviour as when present in the assay alone. By contrast, the localization of cargo-2 relative to MinD changed when cargo-42 was also present (Figs. 1d and 4c). The observed spatial separation of cargo species was not an artefact due to fluorescent channel crosstalk, dye selection or quenching (Extended Data Fig. 6). Hence, the clear MinDE-induced spatial sorting of cargo species according to their effective size further refutes thermodynamic models (Fig. 4d), corroborating that MinDE indeed transport molecules via friction.
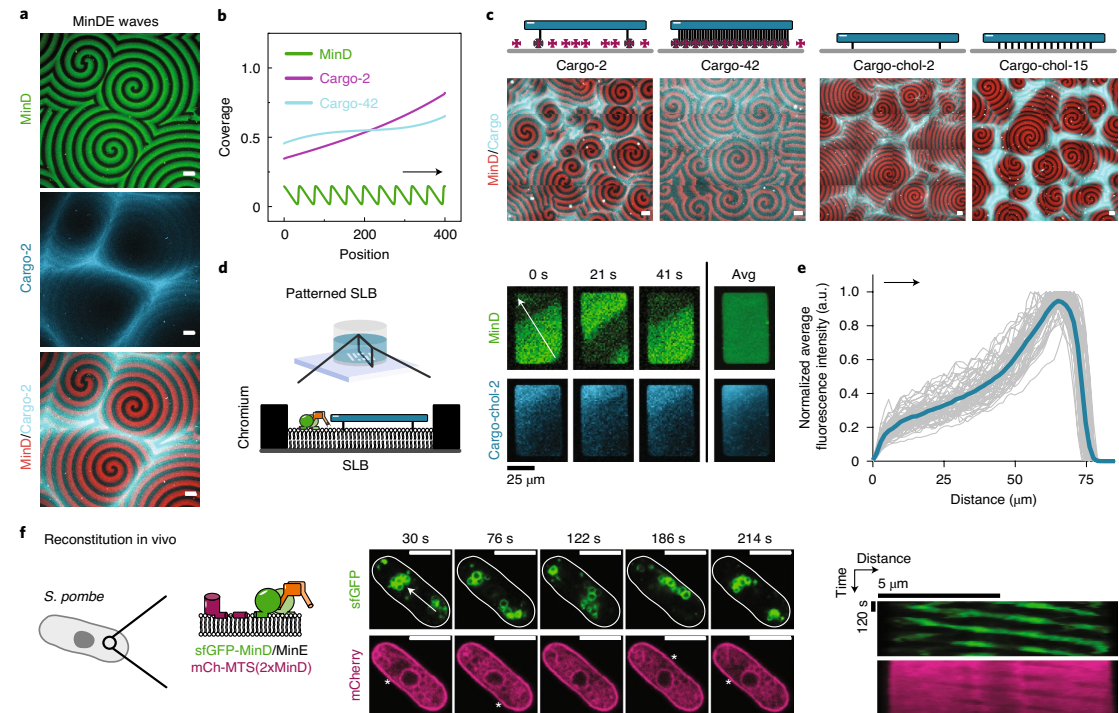
MinDE waves direct net cargo transport via diffusiophoresis

Having confirmed diffusiophoretic transport in the context of quasi-stationary MinDE patterns, we turned to conditions where MinDE form travelling surface waves[7,8]. As in previous experiments with lipid-anchored streptavidin alone[7,8], MinDE waves induced anti-correlated patterns of our synthetic cargo-2 that were superimposed with macroscopic gradients across multiple MinDE wavelengths, indicating net transport (Fig. 5a). Consequently, cargo accumulated between opposing wavefronts (Fig. 5a and Supplementary Video 4). Despite their distinct appearance, stationary as well as moving MinDE patterns are maintained by the same kind of non-equilibrium reaction and diffusion fluxes[16,18,19,21,25]. Thus, we could directly apply our theory to this dynamic setting, without further assumptions (Methods). We found that, in addition to the interaction between MinDE and cargo, macroscopic transport also requires matching timescales between MinDE

wave propagation and cargo diffusion: cargo with small mobility cannot keep up with the MinDE wave. In agreement with our simulations (Fig. 5b), the slowly diffusing cargo-42 hardly formed long-ranged gradients (Fig. 5c and Supplementary Fig. 4), despite its strong frictional coupling to MinDE, supporting our prediction that low cargo mobility can limit macroscopic transport. This was further corroborated by the emergence of macroscopic gradients for cholesterol-anchored cargo-chol-2 and cargo-chol-15 (Fig. 5c and Supplementary Fig. 4), which display similarly high coupling to MinDE, but diffuse faster than cargo-42 (Extended Data Fig. 5).

Next, we exploited the geometry-sensitivity of MinDE waves that travel along the longest axis on geometrically patterned planar membranes with chromium barriers[37]. On these membranes, MinDE waves indeed transported cargo directionally along their wavevector, resulting in reproducible gradients (Fig. 5d,e, Extended Data Fig. 7 and Supplementary Videos 5 and 6). These density gradients are clearly visible on the macroscopic scale, while directed movement of single cargo molecules cannot be discerned from diffusion (Extended Data Fig. 8 and Supplementary Note 3). This observation highlights the difference between ATP-driven diffusiophoresis and translational motor proteins.

Our findings raised the question of whether MinDE-dependent transport via diffusiophoresis could occur in vivo. To our knowledge, no direct observation of this mechanism in *E. coli* has been reported, which may be attributed to bacterial sizes close to the optical resolution limit or specific interactions concealing such occurrence. Thus, we reconstituted MinDE oscillations together with inert model peripheral membrane proteins (mCh-MTS)[7] in the evolutionary distant fission yeast *Schizosaccharomyces pombe*[38]

Fig. 5 | Directed net transport of cargo by MinDE waves via diffusiophoresis. a, Representative images of MinDE travelling surface waves that transport cargo-2 establishing long-range gradients (1 μM MinD, 5 μM His-MinE, 0.1 nM origami-Cy3b with two biotinylated oligonucleotides, non-labelled streptavidin). **b**, Simulation of cargo transport by a protein wave with skewed sinusoidal waveform (green, skewness $\gamma = -0.9$), which emulates MinD travelling waves (40 μm wavelength, 1.4 μm s^{-1} velocity) in one-dimensional geometry (the black arrow indicates the wavevector). After a very long simulation time of 28 h, we find only weak redistribution of cargo-42 compared with the strong redistribution of cargo-2. Interaction parameters are as in Fig. 3b, (bare) cargo diffusion coefficients $D_g(0)$ as in Fig. 3c and the (bare) MinD diffusion coefficient is set to $D_p = 0.425$ μm^2 s^{-1} (ref. [25]). Both cargo coverages are set to $\overline{\theta_o} = 0.55$ (thus neglecting the reduced surface coverage of cargo-42) to improve comparability. Cargo coverages are averaged over the last 17 min. **c**, Representative images of MinDE inducing large-scale gradients of cargo-2, cargo-chol-2 and cargo-chol-15, but not of cargo-42 (1 μM MinD, 5 μM His-MinE, 0.1 nM origami-Cy5 with 2 or 42 biotinylated oligonucleotides, non-labelled streptavidin or 0.1 nM origami-Cy3b with 2 or 15 hybridizing oligonucleotides, 10 nM TEG-cholesteryl oligonucleotide). **d**, Representative time series and average of MinDE travelling surface waves transporting cargo-chol-2 along the wavevector when oriented along the longest axis on chromium-patterned SLBs **e**, Normalized average fluorescence intensity profiles of cargo along the wavevector in **d**. The bold coloured line represents the mean profile, generated from $N = 56$ membrane patches from three independent experiments. **f**, MinDE dynamics spatiotemporally regulates the model peripheral membrane proteins mCh-MTS(2xMinD) when reconstituted in the fission yeast *S. pombe*. Decreased fluorescence in the mCherry channel is highlighted by white asterisks. Arrows indicate wave direction. Scale bars, 50 μm (**a**,**c**), 25 μm (**d**) and 5 μm (**f**).

(Fig. 5f, Extended Data Figs. 9 and 10 and Supplementary Videos 7 and 8). We found that in this in vivo model system MinDE formed dynamic patterns with similar wavelength and velocity as in its native host *E. coli*[11,12] (Supplementary Note 4) and, indeed, spatiotemporally regulated mCh-MTS proteins on intracellular membranes (Extended Data Fig. 10).

Diffusiophoresis drives molecular transport in biology
In conclusion, combining in vitro and in vivo reconstitution experiments with theoretical modelling and analysis, we showed that the prokaryotic MinDE proteins can non-specifically transport and even sort membrane-bound cargo molecules by a diffusiophoretic effect: the diffusive fluxes of MinD and cargo couple via friction in a mechanical rather than thermodynamic fashion (Fig. 6). This process is driven by ATP-consuming MinDE self-organization, which

generates a net diffusive flux of MinD towards low densities. This flux establishes an effective frictional force on cargo, driving diffusiophoretic cargo transport towards areas of low MinD density. Hence, the friction between cargo and MinD increases with the effective size of the cargo (for example, with the number of streptavidin building blocks). The bare diffusion coefficient of cargo only becomes relevant in the case of dynamic MinDE waves where cargo diffusion has to 'keep up' with the MinDE waves to induce macroscopic gradients.

Similar transport effects have been reported previously in a non-biological context: diffusiophoresis generally refers to particle transport in fluids, induced by concentration gradients of small solutes[39–49]. Interestingly, diffusiophoresis was also treated in terms of particle fluxes[48], suggesting that a flux-centred viewpoint may be appropriate for multicomponent mixtures out of equilibrium.
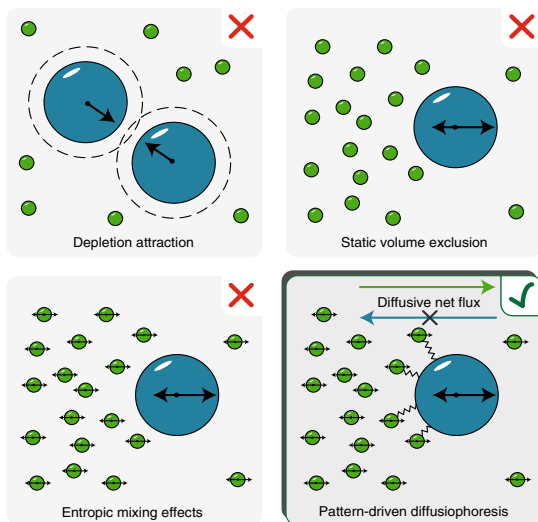
Fig. 6 | Diffusiophoresis explains cargo transport by protein self-organization. Thermodynamic forces, such as depletion attraction, static volume exclusion or entropic mixing effects, cannot explain MinDE-dependent cargo transport in our experiments. However, it can be explained by diffusiophoresis: active protein self-organization generates gradients and hence net diffusive fluxes. As the proteins interact non-specifically with the cargo, the diffusive fluxes establish an effective frictional force, driving the accumulation of cargo in areas of low protein density.

A phenomenologically similar effect has been demonstrated in gases with the MS theory of diffusion[35,36,50,51]. In a biologically relevant context, theoretical studies have suggested that diffusiophoresis might occur in enzyme chemotaxis[52] and alignment[53], during ParABS-mediated chromosome segregation in bacteria[54] and that metabolism-dependent gradients of small molecules (for example, ATP) could induce transport of large particles[55]. The here described diffusiophoresis driven by protein patterns that are maintained by NTPase cycles might constitute a novel mechanism of coupling energy dissipation to active spatiotemporal positioning in cell biology. Diffusiophoretic transport is presumably not a special feature of the *E. coli* MinDE system or reaction–diffusion systems in general, but can potentially be exerted by any active system producing concentration gradients. For example, such a mechanism could be underlying the secretion-induced protein patterning that has been observed in fission yeast[56] or be at play for the plethora of intracellular (actin) waves in eukaryotes whose purpose and mode of action has remained elusive[57]. The mechanism might not even be limited to the membrane as a reaction surface, but potentially extends to other cellular surfaces and even cytosolic gradients. For example, the strong concentration gradients that are built up during liquid–liquid phase-separation processes could potentially similarly impact other molecules[58]. We also propose that distinct pattern-forming systems sharing the same reaction space should align to minimize friction, even if their constituents are chemically independent. This could potentially link and synchronize pathways to increase their efficacy or provide a rescue mechanism against mutations affecting the chemical coupling via specific interactions (for example, between MinC and FtsZ). That this non-specific means of transport was discovered and described in an in vitro reconstitution assay is

not a coincidence, but highlights that the complexity of cells with more sophisticated and stronger specific interactions presumably masks such occurrence. Finally, simple as it is in comparison to eukaryotic, translational motor proteins, this mechanism could be interpreted as an alternative, more rudimentary mode of mechano-chemical coupling and as such might be prevalent in prokaryotes and might have been present in early forms of life.

Online content

Any methods, additional references, Nature Research reporting summaries, source data, extended data, supplementary information, acknowledgements, peer review information; details of author contributions and competing interests; and statements of data and code availability are available at https://doi.org/10.1038/s41567-021-01213-3.

References

1. Vale, R. D. The molecular motor toolbox for intracellular transport. *Cell* **112**, 467–480 (2003).
2. Theriot, J. A. The polymerization motor. *Traffic* **1**, 19–28 (2000).
3. Halatek, J., Brauns, F. & Frey, E. Self-organization principles of intracellular pattern formation. *Phil. Trans. R. Soc. B* **373**, 20170107 (2018).
4. Almonacid, M. et al. Active diffusion positions the nucleus in mouse oocytes. *Nat. Cell Biol.* **17**, 470–479 (2015).
5. Colin, A. et al. Active diffusion in oocytes nonspecifically centers large objects during prophase I and meiosis I. *J. Cell Biol.* **219**, e201908195 (2020).
6. Goehring, N. W. et al. Polarization of PAR proteins by advective triggering of a pattern-forming system. *Science* **334**, 1137–1141 (2011).
7. Ramm, B. et al. The MinDE system is a generic spatial cue for membrane protein distribution in vitro. *Nat. Commun.* **9**, 3942 (2018).
8. Shih, Y.-L. et al. Active transport of membrane components by self-organization of the Min proteins. *Biophys. J.* **116**, 1469–1482 (2019).
9. de Boer, P. A. J., Crossley, R. E. & Rothfield, L. I. A division inhibitor and a topological specificity factor coded for by the minicell locus determine proper placement of the division septum in *E. coli*. *Cell* **56**, 641–649 (1989).
10. Hu, Z. & Lutkenhaus, J. Topological regulation of cell division in *Escherichia coli* involves rapid pole to pole oscillation of the division inhibitor MinC under the control of MinD and MinE. *Mol. Microbiol.* **34**, 82–90 (1999).
11. Raskin, D. M. & de Boer, P. A. J. Rapid pole-to-pole oscillation of a protein required for directing division to the middle of *Escherichia coli*. *Proc. Natl Acad. Sci. USA* **96**, 4971–4976 (1999).
12. Ramm, B., Heermann, T. & Schwille, P. The *E. coli* MinCDE system in the regulation of protein patterns and gradients. *Cell. Mol. Life Sci.* **76**, 4245–4273 (2019).
13. Loose, M., Fischer-Friedrich, E., Ries, J., Kruse, K. & Schwille, P. Spatial regulators for bacterial cell division self-organize into surface waves in vitro. *Science* **320**, 789–792 (2008).
14. Wu, F., van Schie, B. G. C., Keymer, J. E. & Dekker, C. Symmetry and scale orient Min protein patterns in shaped bacterial sculptures. *Nat. Nanotechnol.* **10**, 719–726 (2015).
15. Vecchiarelli, A. G. et al. Membrane-bound MinDE complex acts as a toggle switch that drives Min oscillation coupled to cytoplasmic depletion of MinD. *Proc. Natl Acad. Sci. USA* **113**, E1479–E1488 (2016).
16. Glock, P. et al. Stationary patterns in a two-protein reaction-diffusion system. *ACS Synth. Biol.* **8**, 148–157 (2019).
17. Huang, K. C., Meir, Y. & Wingreen, N. S. Dynamic structures in *Escherichia coli*: spontaneous formation of MinE rings and MinD polar zones. *Proc. Natl Acad. Sci. USA* **100**, 12724–12728 (2003).
18. Halatek, J. & Frey, E. Highly canalized MinD transfer and MinE sequestration explain the origin of robust MinCDE-protein dynamics. *Cell Rep.* **1**, 741–752 (2012).
19. Denk, J. et al. MinE conformational switching confers robustness on self-organized Min protein patterns. *Proc. Natl Acad. Sci. USA* **115**, 4553–4558 (2018).
20. Glock, P., Brauns, F., Halatek, J., Frey, E. & Schwille, P. Design of biochemical pattern forming systems from minimal motifs. *eLife* **8**, e48646 (2019).
21. Halatek, J. & Frey, E. Rethinking pattern formation in reaction–diffusion systems. *Nat. Phys.* **14**, 507–514 (2018).
22. Zieske, K. & Schwille, P. Reconstitution of self-organizing protein gradients as spatial cues in cell-free systems. *eLife* **3**, e03949 (2014).
23. Caspi, Y. & Dekker, C. Mapping out Min protein patterns in fully confined fluidic chambers. *eLife* **5**, e19271 (2016).

ARTICLES

24. Raskin, D. M. & De Boer, P. A. J. MinDE-dependent pole-to-pole oscillation of division inhibitor MinC in *Escherichia coli*. *J. Bacteriol.* **181**, 6419–6424 (1999).

25. Loose, M., Fischer-Friedrich, E., Herold, C., Kruse, K. & Schwille, P. Min protein patterns emerge from rapid rebinding and membrane interaction of MinE. *Nat. Struct. Mol. Biol.* **18**, 577–583 (2011).

26. Hale, C., Meinhardt, H. & de Boer, P. Dynamic localisation cycle of the cell division regulator MinE in *Escherichia coli*. *EMBO J.* **20**, 1563–1572 (2001).

27. Hu, Z., Mukherjee, A., Pichoff, S. & Lutkenhaus, J. The MinC component of the division site selection system in *Escherichia coli* interacts with FtsZ to prevent polymerization. *Proc. Natl Acad. Sci. USA* **96**, 14819–14824 (1999).

28. Mcquillen, R. & Xiao, J. Insights into the structure, function and dynamics of the bacterial cytokinetic FtsZ-ring. *Annu. Rev. Biophys.* **49**, 311–343 (2020).

29. Khmelinskaia, A., Franquelim, H. G., Petrov, E. P. & Schwille, P. Effect of anchor positioning on binding and diffusion of elongated 3D DNA nanostructures on lipid membranes. *J. Phys. D* **49**, 194001 (2016).

30. Marenduzzo, D., Finan, K. & Cook, P. R. The depletion attraction: an underappreciated force driving cellular organization. *J. Cell Biol.* **175**, 681–686 (2006).

31. Asakura, S. & Oosawa, F. On interaction between two bodies immersed in a solution of macromolecules. *J. Chem. Phys.* **22**, 1255–1256 (1954).

32. Miyagi, A., Ramm, B., Schwille, P. & Scheuring, S. High-speed AFM reveals the inner workings of the MinDE protein oscillator. *Nano Lett.* **18**, 288–296 (2018).

33. Scheuring, S., Müller, D. J., Ringler, P., Heymann, J. B. & Engel, A. Imaging streptavidin 2D crystals on biotinylated lipid monolayers at high resolution with the atomic force microscope. *J. Microsc.* **193**, 28–35 (1999).

34. Balian, R. *From Microphysics to Macrophysics* (Springer, 2007).

35. Maxwell, J. C. IV On the dynamical theory of gases. *Phil. Trans. R. Soc. Lond.* **157**, 49–88 (1866).

36. Stefan, J. Über das Gleichgewicht und die Bewegung, insbesondere die Diffusion von Gasgemengen. *Sitzber. Akad. Wiss. Wien.* **63**, 63–124 (1871).

37. Schweizer, J. et al. Geometry sensing by self-organized protein patterns. *Proc. Natl Acad. Sci. USA* **109**, 15283–15288 (2012).

38. Terbush, A. D., Porzondek, C. A. & Osteryoung, K. W. Functional analysis of the chloroplast division complex using *Schizosaccharomyces pombe* as a heterologous expression system. *Microsc. Microanal.* **22**, 275–289 (2016).

39. Anderson, J. L., Lowell, M. E. & Prieve, D. C. Motion of a particle generated by chemical gradients. Part 1. Non-electrolytes. *J. Fluid Mech.* **117**, 107–121 (1982).

40. Prieve, D. C., Anderson, J. L. & Lowell, M. E. Motion of a particle generated by chemical gradients. Part 2. Electrolytes. *J. Fluid Mech.* **148**, 247–269 (1984).

41. Prieve, D. C., Malone, S. M., Khair, A. S., Stout, R. F. & Kanj, M. Y. Diffusiophoresis of charged colloidal particles in the limit of very high salinity. *Proc. Natl Acad. Sci. USA* **116**, 18257–18262 (2019).

42. Shin, S. et al. Size-dependent control of colloid transport via solute gradients in dead-end channels. *Proc. Natl Acad. Sci. USA* **113**, 257–261 (2016).

43. Paustian, J. S. et al. Direct measurements of colloidal solvophoresis under imposed solvent and solute gradients. *Langmuir* **31**, 4402–4410 (2015).

44. Illien, P., Golestanian, R. & Sen, A. 'Fuelled' motion: phoretic motility and collective behaviour of active colloids. *Chem. Soc. Rev.* **46**, 5508–5518 (2017).

45. Abécassis, B., Cottin-Bizonne, C., Ybert, C., Ajdari, A. & Bocquet, L. Boosting migration of large particles by solute contrasts. *Nat. Mater.* **7**, 785–789 (2008).

46. Palacci, J., Abécassis, B., Cottin-Bizonne, C., Ybert, C. & Bocquet, L. Colloidal motility and pattern formation under rectified diffusiophoresis. *Phys. Rev. Lett.* **104**, 138302 (2010).

47. Marbach, S. & Bocquet, L. Osmosis, from molecular insights to large-scale applications. *Chem. Soc. Rev.* **48**, 3102–3144 (2019).

48. Shi, N., Nery-Azevedo, R., Abdel-Fattah, A. I. & Squires, T. M. Diffusiophoretic focusing of suspended colloids. *Phys. Rev. Lett.* **117**, 258001 (2016).

49. Golestanian, R. Phoretic active matter. Preprint at https://arxiv.org/pdf/1909.03747v3.pdf (2019).

50. Duncan, J. B. & Toor, H. L. An experimental study of three component gas diffusion. *AIChE J.* **8**, 38–41 (1962).

51. Krishna, R. & Wesselingh, J. A. The Maxwell–Stefan approach to mass transfer. *Chem. Eng. Sci.* **52**, 861–911 (1997).

52. Agudo-Canalejo, J., Illien, P. & Golestanian, R. Phoresis and enhanced diffusion compete in enzyme chemotaxis. *Nano Lett.* **18**, 2711–2717 (2018).

53. Adeleke-Larodo, T., Agudo-Canalejo, J. & Golestanian, R. Chemical and hydrodynamic alignment of an enzyme. *J. Chem. Phys.* **150**, 115102 (2019).

54. Banigan, E. J., Gelbart, M. A., Gitai, Z., Wingreen, N. S. & Liu, A. J. Filament depolymerization can explain chromosome pulling during bacterial mitosis. *PLoS Comput. Biol.* **7**, e1002145 (2011).

55. Sear, R. P. Diffusiophoresis in cells: a general nonequilibrium, nonmotor mechanism for the metabolism-dependent transport of particles in cells. *Phys. Rev. Lett.* **122**, 128101 (2019).

56. Gerganova, V. et al. Cell patterning by secretion-induced plasma membrane flows. Preprint at *bioRxiv* https://doi.org/10.1101/2020.12.18.423457 (2020).

57. Yang, Y. & Wu, M. Rhythmicity and waves in the cortex of single cells. *Phil. Trans. R. Soc. B* **373**, 20170116 (2018).

58. Hyman, A. A., Weber, C. A. & Jülicher, F. Liquid–liquid phase separation in biology. *Annu. Rev. Cell Dev. Biol.* **30**, 39–58 (2014).

Methods

Theoretical description in the presence of travelling waves. We have formulated our theory, equation (1), in terms of particle fluxes. Given these fluxes **j**$_i$, the spatiotemporal dynamics of each molecular species is determined by the balance equation

$$\partial_t c_i + \nabla \cdot \mathbf{j}_i = r_i\,(\ldots)\,, \qquad (4)$$

where r_i signify reaction terms. We considered two species, passive cargo molecules c_g that do not engage in reactions, $r_g = 0$, and active MinD proteins c_p. Instead of considering specific reaction terms, we assumed that the interplay between diffusive and reactive fluxes of MinDE leads to travelling waves. Then, we took these travelling MinD protein waves with wavelength λ and speed v:

$$c_p\,(x, t) = c_p\left(2\pi \frac{x - vt}{\lambda}\right) \equiv c_p\,(z) \qquad (5)$$

as a given. As specific waveform, we assumed a skewed sinusoidal curve (Fig. 5b):

$$c_p\,(z) = \frac{2}{\pi\gamma}\arctan\left[\frac{\gamma\cos z}{1 - \gamma\sin z}\right], \qquad (6)$$

where the parameter $\gamma \in [-1\ldots1]$ determines the 'skewness' of the waveform. In principle, we could also choose a different waveform (for example, a sinusoidal curve that is skewed in the opposite direction). Choosing a different waveform does not change the general result of a macroscopic net transport along the wavevector, but it can change the magnitude of the transport because the local gradient magnitude is affected.

Furthermore, for simplicity, we neglected membrane saturation effects (Supplementary Information), so that the chemical potential of a particle with size a_i reduces to $\mu_i \approx k_B T \ln(a_i c_i)$. This is the same assumption as in the derivation of the fitting function for the stationary patterns, equation (3), and hence has the same limitations at high particle densities. Taken together, the spatiotemporal dynamics of the passive cargo species is determined by the following transport equation:

$$\partial_t c_g = -\nabla \cdot \mathbf{j}_g = \nabla \cdot \left[D_g \frac{(1 + c_g/c_\times)\nabla c_g + (c_g/c_\times)\nabla c_p}{1 + c_g/c_\times + (D_g/D_p)(c_p/c_\times)}\right], \qquad (7)$$

where the interaction density is given by $c_\times = \xi_p/\zeta_{pg}$ and the two diffusion coefficients are given by $D_g = k_B T/\xi_g$ and $D_p = k_B T/\xi_p$. We used FEniCS[59] to numerically solve equation (7) in a one-dimensional geometry with no-flux boundary conditions for the cargo.

Plasmids, strains and proteins. A list of all plasmids and primers is provided in Supplementary Tables 2 and 3. The plasmids pET28a-His-MinD_MinE[13], pET28a-His-EGFP-MinD[60], pET28a-His-MinE[13] and pET28a-MinE-His[16] were used for purification of His-MinD, His-EGFP-MinD, His-MinE and MinE-His, respectively, as described in detail previously[61]. In brief, proteins were expressed in *E. coli* BL21 (DE3) and then purified via Ni-NTA affinity and size-exclusion chromatography in storage buffer (50 mM HEPES/KOH pH 7.2, 150 mM KCl, 10% glycerol, 0.1 mM EDTA, 0.4 mM tris(2-carboxyethyl)phosphine (TCEP)). Proteins were snap-frozen in liquid nitrogen and stored in small aliquots until further use at −80 °C.

Plasmids for heterologous co-expression of MinD, MinE and model peripheral membrane proteins pREP41X-sfGFP-MinD, pREP42X-MinE, pREP41X_coex_ sfGFP-MinD_MinE, pREP42X-mCherry-BsMTS, pREP42X-mCherry and pREP42X-mCherry-BsMTS were constructed analogously to plasmids devised by Terbush and colleagues[38]. pREP41X and pREP42X, and the leucine and uracil auxotroph *S. pombe* strain FY61 (h- ura4-D18 leu1-32), were a kind gift from S. Forsburg, University of Southern California[62]. All constructs based on pREP41X and pREP42X express the respective proteins under the control of the inducible nmt1* promoter. For details see Supplementary Methods.

Reconstitution in *S. pombe*. Details of *S. pombe* culture and transformation are provided in the Supplementary Methods. For image acquisition, 5-ml cultures with selective medium were inoculated with the respective strains from glycerol stocks or plates and grown for 48–72 h at 30 °C. Cover slides were rinsed with ethanol and ddH$_2$O, and further cleaned in a plasma cleaner with oxygen as the process gas. Subsequently, Grace Bio-LABs reusable culture well gaskets (diameter of 9 mm, GBL103240, Sigma-Aldrich) or sticky slides (#81818, ibidi) were attached to the clean cover slides. Poly-L-lysine solution (0.01%, P4707, Sigma-Aldrich) was added to the wells and incubated for more than 30 min. Wells were washed with the respective media once before 10–50 μl of cell suspension was added for microscopy at a constant room temperature of 23 °C.

DNA origami nanostructures. The elongated DNA origami nanostructure used here was previously designed and described in ref. [29]. The 20-helix bundle with hexagonal lattice is based on the M13mp18 7,429-nucleotide-long scaffold plasmid (p7429; Bayou Biolabs) and was modified using CaDNAno[63]. Staple oligonucleotides, 5′-Cy3B/Cy5-functionalized oligonucleotides, the

5′-cholesteryl-TEG functionalized oligonucleotides (high-purity, salt-free, Eurofins MWG Operon) and 5′-biotin-TEG functionalized oligonucleotides (Sigma-Aldrich) were purchased or diluted in Milli-Q ultrapure water at a concentration of 100 μM. Origami structures with 1–15 anchors were based on the previous design[29], which was further modified for functionalization with 42 anchors (Supplementary Fig. 5). The assembly of the origami structure was performed in a one-pot reaction mix as described previously[29]. In brief, the components were mixed at a final concentration of 20 nM p7429 scaffold plasmid and 200 nM staple oligonucleotides in folding buffer (5 mM Tris-HCl, 1 mM EDTA, 20 mM MgCl$_2$, pH 8.0) and annealed in a thermocycler (Mastercycler) over a 41-h cooling scheme from 65 to 40 °C. Folded nanostructures were purified to remove excess staple strands by centrifugation (14,000g, three cycles for 3 min, one cycle for 5 min) in Amicon Ultra 100 kDa molecular weight cutoff filters (Merck Millipore) using reaction buffer (25 mM Tris-HCl pH 7.5, 150 mM KCl, 5 mM MgCl$_2$). The concentration of folded Cy5-labelled origami structures was estimated by fluorescence intensity measurements using a one-drop measurement unit of a Jasco FP-8500 spectrofluorometer and subsequent comparison with an intensity calibration curve obtained for free Cy5 dye corrected for the multiple labelling of the origami. Cy3B-labelled DNA origami concentration was measured by absorption at 260 nm on a NanoDrop spectrophotometer (ThermoFisher Scientific) and related to Cy5-labelled structures of known concentrations. Cy3B/Cy5-labelled DNA origami structures contained seven Cy3B/Cy5-labelled oligonucleotides attached to extended staples on the upper facet. At the lower facet, the biotin-functionalized origami contained multiple 18-nucleotide (nt) extensions that were hybridized with complementary 5′ biotin-TEG-functionalized oligonucleotides (5′ biotin-TEG-AACCAGACCACCCATAGC) at defined positions. DNA origami that were bound to the membrane via cholesteryl oligonucleotides contained single or multiple 18-nt extensions on the lower facet that can hybridize with the complementary 5′ TEG-cholesteryl-functionalized oligonucleotides (5′ chol-TEG-AACCAGACCACCCATAGC) supplied in the self-organization assay.

Preparation of SLBs. SLBs were prepared as described in detail in refs. [13,61]. In brief, cover slides were rinsed with ddH$_2$O and ethanol, and a plastic chamber was glued on top. Slides were further cleaned by plasma cleaning with oxygen as the process gas (model Zepto, Diener Electronic). Chloroform-dissolved lipids (Avanti Polar Lipids) were dried by a nitrogen stream and subsequently in a desiccator before slow rehydration at a concentration of 4 mg ml^{-1} in reaction buffer (25 mM Tris-HCl pH 7.5, 150 mM KCl, 5 mM MgCl$_2$). Small unilamellar vesicles were generated by sonication in a bath sonicator and subsequently added to the cleaned reaction chambers at a concentration of 0.5 mg ml^{-1}. After 4 min of incubation on a 37 °C warm heating block, the SLB was washed 10 times with a total of 2 ml of wash buffer (25 mM Tris-HCl pH 7.5, 150 mM KCl) to remove excess vesicles. All mentioned concentrations refer to the final volume of the reaction chamber of 200 μl. To prepare chambers for self-organization experiments with biotin-functionalized origami, the SLB was generated with a lipid composition of 69/30/1 mol% DOPC/DOPG/biotinyl-CAP-PE or with 70/30/0.01 mol% DOPC/DOPG/biotinyl-CAP-PE for single-particle tracking experiments and subsequently incubated with non-labelled or Alexa568-labelled streptavidin (ThermoFisher Scientific) at a final concentration of 1 μg ml^{-1}. After incubation for 5–10 min, unbound streptavidin was removed by washing five times with a total volume of 1 ml of reaction buffer. The buffer was adjusted to a volume of 100 μl and the origami was incubated at a final concentration of 0.1 nM for 10 min, before the buffer was adjusted to the final volume of 200 μl. To prepare chambers for self-organization experiments with cholesteryl-bound origami, the SLB was generated with a lipid composition of 70/30 mol% DOPC/DOPG. The buffer was adjusted to a volume of 100 μl and the 5′ TEG-cholesteryl-functionalized oligonucleotides for binding were added at a final concentration of 10 nM. Subsequently, the origami was added at a final concentration of 0.1 nM and incubated for 10 min, before buffer adjustment to 200 μl. For experiments involving more than one type of DNA origami, DNA origami species were premixed in DNA LoBind tubes (Eppendorf) before addition to the sample chamber at a final concentration of 50 pM for each DNA origami, keeping the overall DNA origami concentration at 0.1 nM. Note that at these experimental conditions, DNA origami does not bind non-specifically to the lipid membrane in the absence of biotin-TEG-anchors/streptavidin or cholesteryl-TEG-anchors, due to the high net negative charge of both the SLB and DNA origami[64,65].

Chromium-patterned cover slides. Chromium-patterned cover slides for patterned SLBs[66,67] were generated by photolithography and metal evaporation. Cover slides were first cleaned by rinsing with pure ethanol and ddH$_2$O and subsequently by plasma cleaning with oxygen as the process gas (model Zepto, 20–60 s, 40–50% power and 0.3 mbar). The vapour of bis(trimethylsilyl)amine (HDMS) was deposited on the cover slide for 2 min as adhesion promoter. Subsequently, positive photoresist (AZ ECI 3027, MicroChemicals) was spin-coated onto the cover slide (40 s, 4,000 r.p.m., start/stop acceleration 2,000 r.p.m. s^{-1}) resulting in an ~3-μm-thick layer of photoresist. After pre-baking (90 s, 90 °C) the photoresist was patterned using ultraviolet lithography (μPG101, Heidelberg Instruments) with a 10-mm write head, nominal output power

ARTICLES

of 35 mW at a wavelength of 375 nm, before passing a 45% attenuation filter. Afterwards, the slides were post baked (60 s, 110 °C) before applying developer (AZ 351B, NaOH-based, diluted 1:4 (vol/vol), MicroChemicals) for 4 min. Finally, slides were rinsed with ddH$_2$O and dried with a nitrogen stream. Chromium was deposited onto these slides by evaporation at 22–33 mA at a rate of ~1 Å s^{-1} to a final thickness of ~30 nm. After chromium deposition, the photoresist was lifted off in acetone with sonication for 5 min in a sonicator bath. Afterwards, slides were rinsed with isopropanol and dried with a nitrogen stream. SLBs were formed on the chromium-patterned slides as described above.

Self-organization assay. Self-organization assays were performed essentially as described in detail in ref. [61]. In short, they were performed on preformed SLBs in 200 μl of reaction buffer (25 mM Tris-HCl pH 7.5, 150 mM KCl, 5 mM MgCl$_2$) supplemented with 2.5 mM Mg-ATP (stock: 100 mM ATP, in 100 mM MgCl$_2$, adjusted to pH 7.5) and at a constant room temperature of 23 °C. MinD was typically used at 1 μM (0.3 μM EGFP-MinD, 0.7 μM MinD) with either 1.5 μM MinE-His[16] to generate quasi-stationary labyrinth patterns or 5 μM His-MinE[7,13] to generate regular travelling surface waves. Time series showing the initial development of patterns were acquired by starting the self-organization with Mg-ATP directly before image acquisition. Tile scans used for quantification of quasi-stationary patterns or gradients induced by regular travelling waves on unconstrained and patterned SLBs were acquired 30–60 min after the start of self-organization, in areas of the chamber that had not been imaged previously.

Single-particle tracking. Single-particle tracking of DNA origami was conducted at a concentration of DNA origami and anchors that can be described as diluted, so that interaction between individual DNA origami was minimized[68]. DNA origami was diluted in DNA LoBind tubes (Eppendorf) and added to a chamber at a final concentration of 0.1–1 pM (biotin-functionalized origami, SLB with 70/30/0.01 mol% DOPC/DOPG/biotinyl-CAP-PE; cholesteryl functionalized origami, SLB with 70/30 mol% DOPC/DOPG, 0.1 nM 5′ TEG-cholesteryl-functionalized oligonucleotides). Owing to the superior brightness and photostability, single-particle tracking was exclusively performed using Cy3B-labelled DNA origami. To further reduce photobleaching and blinking as well as photopolymerization of MinD, single-particle tracking was performed in the presence of an oxygen scavenger system (3.7 U ml^{-1} pyranose oxidase, 90 U ml^{-1} catalase, 0.8% glucose)[69] and trolox. Experiments were performed in the absence of any protein or in the presence of 1 μM MinD (30% EGFP-MinD) and 2.5 mM ATP to emulate conditions in the MinD maxima in a simplified fashion. For single-particle tracking of cargo in the presence of MinDE travelling waves, 1 μM MinD (30% EGFP-MinD) and 5 μM His-MinE were used and tracking was performed more than 30 min after starting the reaction with 2.5 mM ATP to obtain regular waves.

Microscopy. All images, except for single-particle tracking, were taken on a Zeiss LSM780 confocal laser scanning microscope using a Zeiss C-Apochromat ×40/1.20 water-immersion objective, ×20 air objective for chromium-patterned SLBs or ×60/1.4 differential interference contrast (DIC) oil-immersion objective for *S. pombe* cells (all Carl Zeiss). Longer time series were acquired using the built-in autofocus system. All two- or three-colour images were acquired with alternating illumination for the 488/633 nm and 561 nm laser lines to avoid crosstalk. EGFP-MinD or sfGFP-MinD was excited using a 488 nm argon laser; Cy3B-labelled origami, Alexa568-streptavidin or mCherry in *S. pombe* were excited using a 561 nm diode-pumped solid-state (DPSS) laser and Cy5-labelled origami using a 633 nm He–Ne laser. Images were typically recorded with a pinhole size of 2.6–4 Airy units for the EGFP and origami channels, 1 Airy unit for the streptavidin channel, 512 × 512-pixel resolution and a pixel dwell time of 1.27 μs. Time series were typically acquired with ~14-s intervals for unconstrained SLBs or 4-s intervals for chromium-patterned SLBs and *S. pombe* cells. For single-particle tracking of DNA, origami images were acquired on a custom-built total internal reflection fluorescence microscope (TIRFM)[70] using a NIKON SR Apo TIRF ×100/1.49 oil-immersion objective, constructed around a Nikon Ti-S microscope body (both Nikon). Two laser lines (490 nm (Cobolt Calypso, 50 mW nominal) and 561 nm (Cobolt Jive, 50 mW nominal), Cobolt AB)) were controlled in power and timing (AOTF, Gooch & Housego TF-525-250) and spatially filtered (kineFLEX-P-3-S-405.640-0.7-FCS-P0, Qioptiq). The beam was further collimated, expanded (10×) and focused on the objective's back aperture by standard achromatic doublet lenses. The TIRF angle was controlled by precise parallel offset of the excitation beam (Q545, PI). The emission light was notch-filtered to remove residual excitation light, spectrally separated by a dichroic beamsplitter (T555lpxr-UF1, Chroma Technology Cooperation), bandpass-filtered 525/50 and 593/46 (both Chroma), respectively, and repositioned on two halves of the electron-multiplying charge-coupled device (EMCCD) camera (Andor iXon Ultra 897, Andor Technologies). Images were recorded with Andor Solis software (version 4.28, Andor Technologies).

Image analysis. All images were processed using Fiji (version v1.52p), MATLAB (R2018a, The Math-Works) or Python (Python Software Foundation). Brightness or contrast adjustments of all displayed images were applied homogeneously.

For line plots, the images were smoothed with a Gaussian filter with pixel width of 2 in Fiji.

For the cross-correlation plots, the images were smoothed with a Gaussian kernel of pixel width 1. The theoretical models were formulated as boundary-value problems and solved in a one-dimensional geometry using a finite-difference scheme using SciPy[71]. Curve fitting was performed with lmfit[72].

Single-particle tracking analysis. Analysis of single-particle tracking was conducted as described previously using previously established code[73]. In brief, a custom-written MATLAB code was used to detect DNA origami fluorescence in each frame and extract its position. Origami trajectories on the membrane were analysed using jump-distance analysis[74,75]. The distances between particle locations between subsequent frames were analysed and diffusion coefficients of particle ensembles were obtained by fitting the cumulative histograms. As, usually, some of the origami in the field of view were immobile and did not diffuse, cumulative histograms of obtained jump distances were fitted with two components, where for the second component the upper boundary was set to 0.1 μm^2 s^{-1}, and usually resulted in diffusion coefficients of less than 0.01 μm^2 s^{-1}.

Analysis of MinDE-dependent transport. Analysis of fluorescence intensities and contrast was essentially performed as described earlier[7]. In brief, tile scans were imported into Fiji, where the EGFP-MinD channel was used for segmentation to generate a binary mask of the patterns. The original non-modified images from the two or three spectral channels were analysed based on the binary mask using a custom-written MATLAB code. The average fluorescence intensity in the Alexa568-streptavidin or origami-Cy5 and EGFP-MinD spectral channel was obtained by pooling the means of individual images from one independent experiment. All means from one independent experiment and condition were pooled together. All fluorescence intensity values from one experimental set were normalized to the fluorescence intensity values obtained for the respective origami with one anchor. The Michelson contrast of the resulting cargo patterns was calculated for every individual image as the difference between the average intensity in the MinD minima and MinD maxima divided by the sum of the average intensities in the MinD maxima and minima. The contrast of the MinD patterns was calculated for every individual image as the difference between the average intensity in the MinD maxima and MinD minima divided by the sum of the average intensities in the MinDE minima and maxima.

Analysis of fluorescence profiles on chromium-patterned SLBs. Time-series from chromium-patterned SLB patches with regular travelling MinDE waves that aligned along the longest axis of the patch were selected and averaged in Fiji. The resulting average intensity of the cargo was plotted along the wavevector of the MinDE waves (that is, the longest axis of the patch) and exported as csv files. Subsequently, using MATLAB, the fluorescence intensity profiles were aligned at the beginning based on the increase of the signal, and the average profile was generated.

Reporting Summary. Further information on research design is available in the Nature Research Reporting Summary linked to this Article.

Data availability
The raw images that support the findings of this study are available at Edmond with the identifier https://dx.doi.org/10.17617/3.5n or from the corresponding authors upon request. Source data are provided with this paper.

Code availability
The code for the analysis is available at Edmond with the identifier https://dx.doi.org/10.17617/3.5n or from the corresponding authors upon request.

References
59. Logg, A., Mardal, K. A. & Wells, G. N. *Automated Solution of Differential Equations by the Finite Element Method* (Springer, 2012).
60. Zieske, K., Schweizer, J. & Schwille, P. Surface topology assisted alignment of Min protein waves. *FEBS Lett.* **588**, 2545–2549 (2014).
61. Ramm, B., Glock, P. & Schwille, P. In vitro reconstitution of self-organizing protein patterns on supported lipid bilayers. *J. Vis. Exp.* **137**, 58139 (2018).
62. Forsburg, S. L. Comparison of *Schizosaccharomyces pombe* expression systems. *Nucleic Acids Res.* **21**, 2955–2956 (1993).
63. Douglas, S. M. et al. Rapid prototyping of 3D DNA-origami shapes with caDNAno. *Nucleic Acids Res.* **37**, 5001–5006 (2009).
64. Czogalla, A. et al. Switchable domain partitioning and diffusion of DNA origami rods on membranes. *Faraday Discuss.* **161**, 31–43 (2013).
65. Khmelinskaia, A., Mücksch, J., Petrov, E. P., Franquelim, H. G. & Schwille, P. Control of membrane binding and diffusion of cholesteryl-modified DNA origami nanostructures by DNA spacers. *Langmuir* **34**, 14921–14931 (2018).
66. Groves, J. T., Ulman, N. & Boxer, S. G. Micropatterning fluid lipid bilayers on solid supports. *Science* **275**, 651–653 (1997).
67. Groves, J. T., Ulman, N., Cremer, P. S. & Boxer, S. G. Substrate–membrane interactions: mechanisms for imposing patterns on a fluid bilayer membrane. *Langmuir* **14**, 3347–3350 (1998).

NATURE PHYSICS

68. Czogalla, A., Kauert, D. J., Seidel, R., Schwille, P. & Petrov, E. P. DNA origami nanoneedles on freestanding lipid membranes as a tool to observe isotropic–nematic transition in two dimensions. *Nano Lett.* **15**, 649–655 (2015).
69. Swoboda, M. et al. Enzymatic oxygen scavenging for photostability without pH drop in single-molecule experiments. *ACS Nano* **6**, 6364–6369 (2012).
70. Mücksch, J. et al. Quantifying reversible surface binding via surface-integrated fluorescence correlation spectroscopy. *Nano Lett.* **18**, 3185–3192 (2018).
71. Virtanen, P. et al. SciPy 1.0: fundamental algorithms for scientific computing in Python. *Nat. Methods* **17**, 261–272 (2020).
72. Newville, M. et al. lmfit/lmfit-py 1.0.0 (2019); https://doi.org/10.5281/ZENODO.3588521
73. Weimann, L. et al. A quantitative comparison of single-dye tracking analysis tools using Monte Carlo simulations. *PLoS ONE* **8**, e64287 (2013).
74. Schütz, G. J., Schindler, H. & Schmidt, T. Single-molecule microscopy on model membranes reveals anomalous diffusion. *Biophys. J.* **73**, 1073–1080 (1997).
75. Kues, T., Peters, R. & Kubitscheck, U. Visualization and tracking of single protein molecules in the cell nucleus. *Biophys. J.* **80**, 2954–2967 (2001).

Author contributions

B.R., A.G., E.F. and P.S. conceived the study. A.G. and E.F. designed the theoretical analysis. A.G. conducted the theoretical analysis. B.R., A.K. and P.B. designed experiments. B.R. performed all experiments. A.K. designed DNA origami. A.K. and B.R. prepared origami. H.E. and B.R. fabricated chromium-patterned slides. K.A.G. developed single-particle tracking code. B.R., A.G., P.B. and K.A.G. analysed data. B.R., A.G., E.F. and P.S. wrote the manuscript. All authors discussed and interpreted the results and revised the manuscript.

Competing interests

The authors declare no competing interests.

Additional information

Extended data is available for this paper at https://doi.org/10.1038/s41567-021-01213-3.

Supplementary information The online version contains supplementary material available at https://doi.org/10.1038/s41567-021-01213-3.
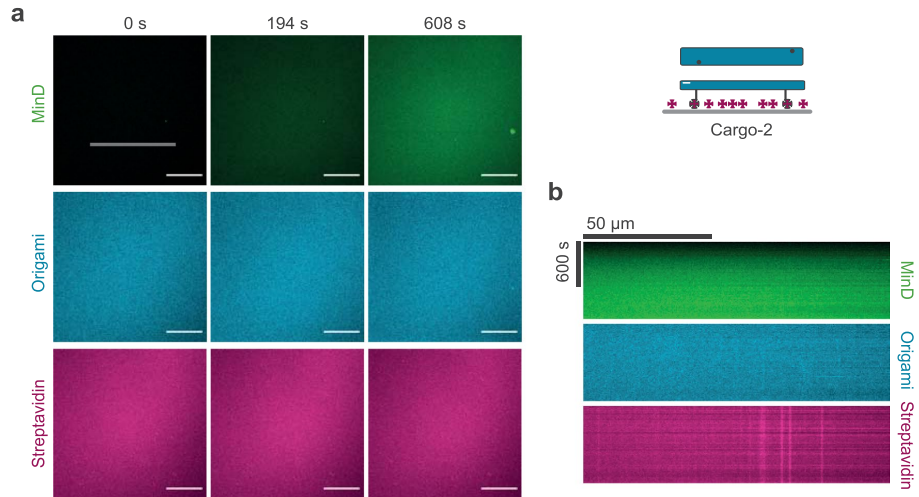
Correspondence and requests for materials should be addressed to E.F. or P.S.

Peer review information *Nature Physics* thanks Jodi Camberg and the other, anonymous, reviewer(s) for their contribution to the peer review of this work.

Reprints and permissions information is available at www.nature.com/reprints.

Extended Data Fig. 1 | Pattern formation of cargo depends on active self-organization by MinDE. a, Representative time series of MinD membrane binding on SLBs in the presence of cargo-2 and ATP, but in the absence of MinE (1 µM MinD (30% EGFP-MinD), 0.1 nM origami-Cy5 with 2 biotinylated oligonucleotides, Alexa568-streptavidin, ATP). Scale bars, 50 µm. **b**, Kymographs of the line selection indicated in a.
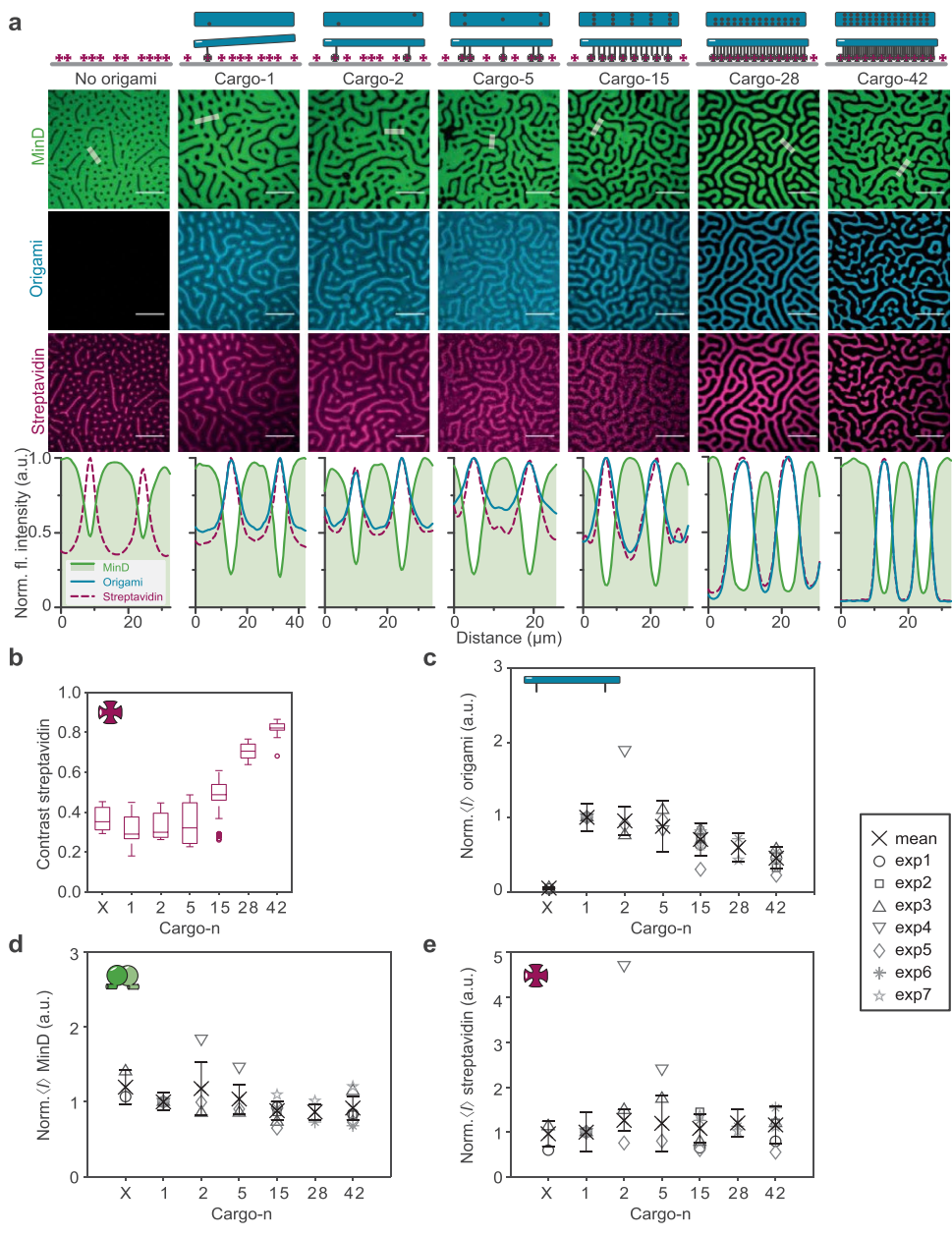
ARTICLES

Extended Data Fig. 2 | See next page for caption.

ARTICLES

Extended Data Fig. 2 | Extent of the MinDE-driven cargo demixing depends on the effective size (that is, membrane footprint) of the cargo. a, Representative images and fluorescence intensity line plots (smoothed) of established MinDE labyrinth patterns and anti-correlated DNA origami and streptavidin patterns when no origami or cargo-1, cargo-2, …, cargo-42 is present (1 μM MinD (30% EGFP-MinD), 1.5 μM MinE-His, with or without 0.1 nM origami-Cy5 with n biotinylated oligonucleotides, Alexa568-streptavidin). Panels "no origami, cargo-2, cargo-15 and cargo-42" are identical to Fig. 1d. Scale bars, 50 μm. **b**, Contrast of the resulting streptavidin patterns increases with increasing number of streptavidin incorporated into the cargo. Box plot lines are median, box limits are quartiles 1 and 3, whiskers are 1.5× interquartile range (IQR) and points are outliers. Mean fluorescence intensity of **c**, DNA origami, **d**, EGFP-MinD and **e**, Alexa568-streptavidin of patterns formed when no origami or cargo-1, cargo-2, …, cargo-42 is present; data is taken from the full image and normalised to the intensity of experiments containing cargo-1. Cross and error bars represent the mean value and standard deviation of two or more independent experiments with total number of analysed images per condition N(No origami)=32, N(Cargo-1)=96, N(Cargo-2)=41, N(Cargo-5)=32, N(Cargo-15)=94, N(Cargo-28)=32, N(Cargo-42)=87.
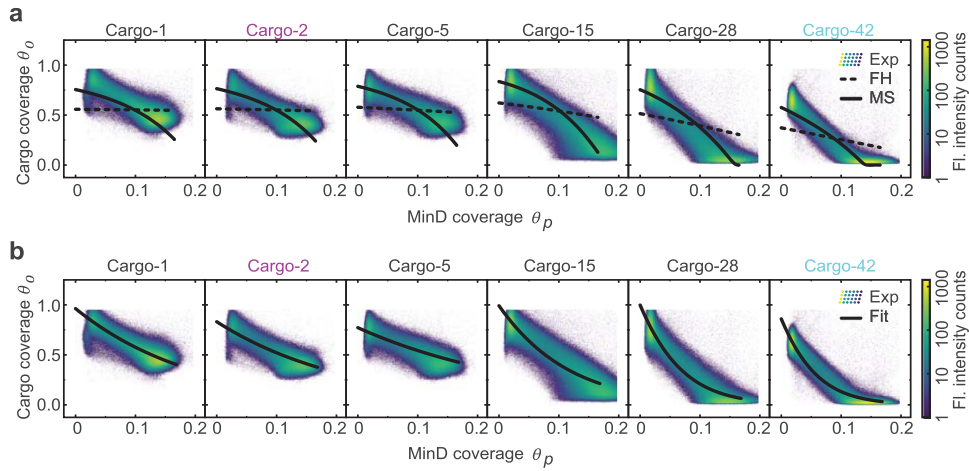
Extended Data Fig. 3 | Comparison between theory and experiment for different cargo molecules. a, Cross-correlation function between MinD coverage (θ_p) and DNA origami coverage (θ_o), for different cargo species. The color-coded 2D-histogram represents our experimental data of selected days (Exp), where the images were smoothed by a one-pixel-wide gaussian kernel. Solid and dashed lines correspond to two candidate models. The Flory-Huggins type model (FH), whose parameters are fully determined by our experiments, fails to account for cargo transport: the weak entropic sorting of streptavidin in an external gradient of proteins is not sufficient to overcome the strong repulsion of the bulky DNA origami scaffolds. Instead, we find that the phenomenological MS-type model, with an estimated interaction parameter, explains cargo transport. Model parameters: (cargo-n) average coverages $\overline{\theta_p} = 0.0825$, $\overline{\theta_s} = \max(0.165 - 0.55n/70, 0)$ and $\overline{\theta_o} = \min(11.55/n, 0.55)$; interaction parameter (in terms of MinD coverage) $\theta_\times^{-1} = 200 + 10n$. Surface coverages $\boldsymbol{\theta} = ac$ and surface densities c are related via the particle size a. **b**, The color-coded 2D-Histogram represents our experimental data of selected days (Exp), while the solid line (Fit) is a fit curve of our reduced model (Supplementary Information section I.5 "Analytic solution and fitting of reduced model").
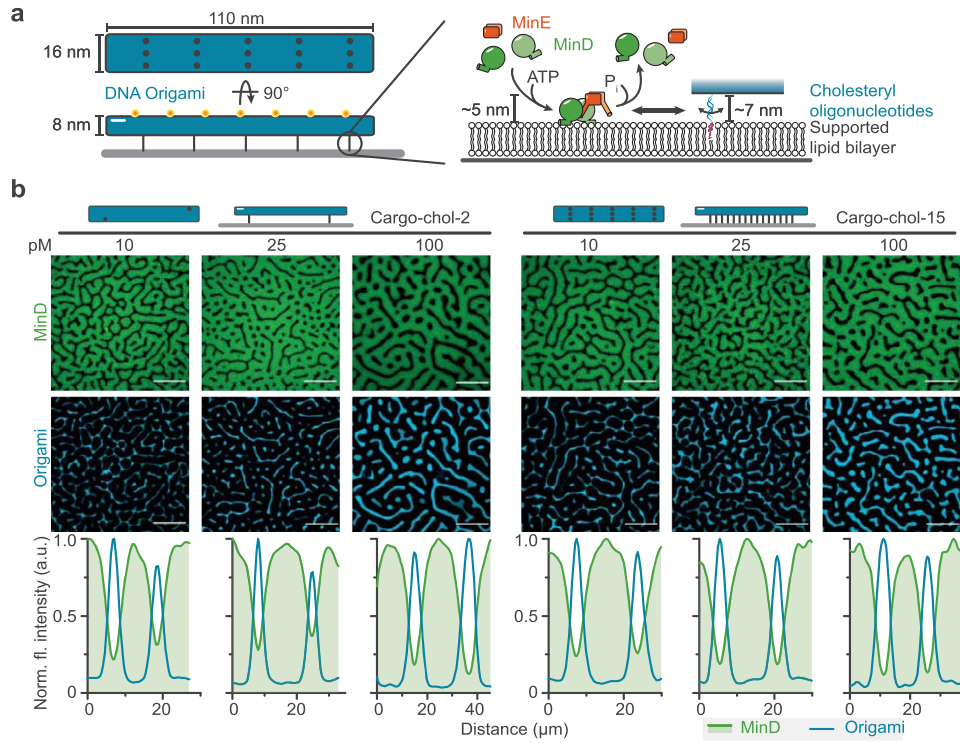
Extended Data Fig. 4 | MinDE induces pattern formation of cargo that is bound to the membrane via cholesteryl oligonucleotides. a, Schematic of the synthetic cargo consisting of a DNA origami scaffold that is bound to the membrane via cholesteryl moieties. DNA origami are bound via hybridization of DNA oligonucleotides at the indicated positions with the complementary TEG-cholesteryl oligonucleotides in the lipid membrane. **b**, Representative images and fluorescence intensity line plots (smoothed) of established MinDE labyrinth patterns and anti-correlated DNA origami patterns when 10, 25 or 100 pM of cargo-chol2 or cargo-chol-15 are present (1 μM MinD (30% EGFP-MinD), 1.5 μM MinE-His with 10, 25 or 100 pM origami-Cy3b with 2 or 15 hybridizing oligonucleotides, 10 nM TEG-cholesteryl oligonucleotide). Scale bars, 50 μm.
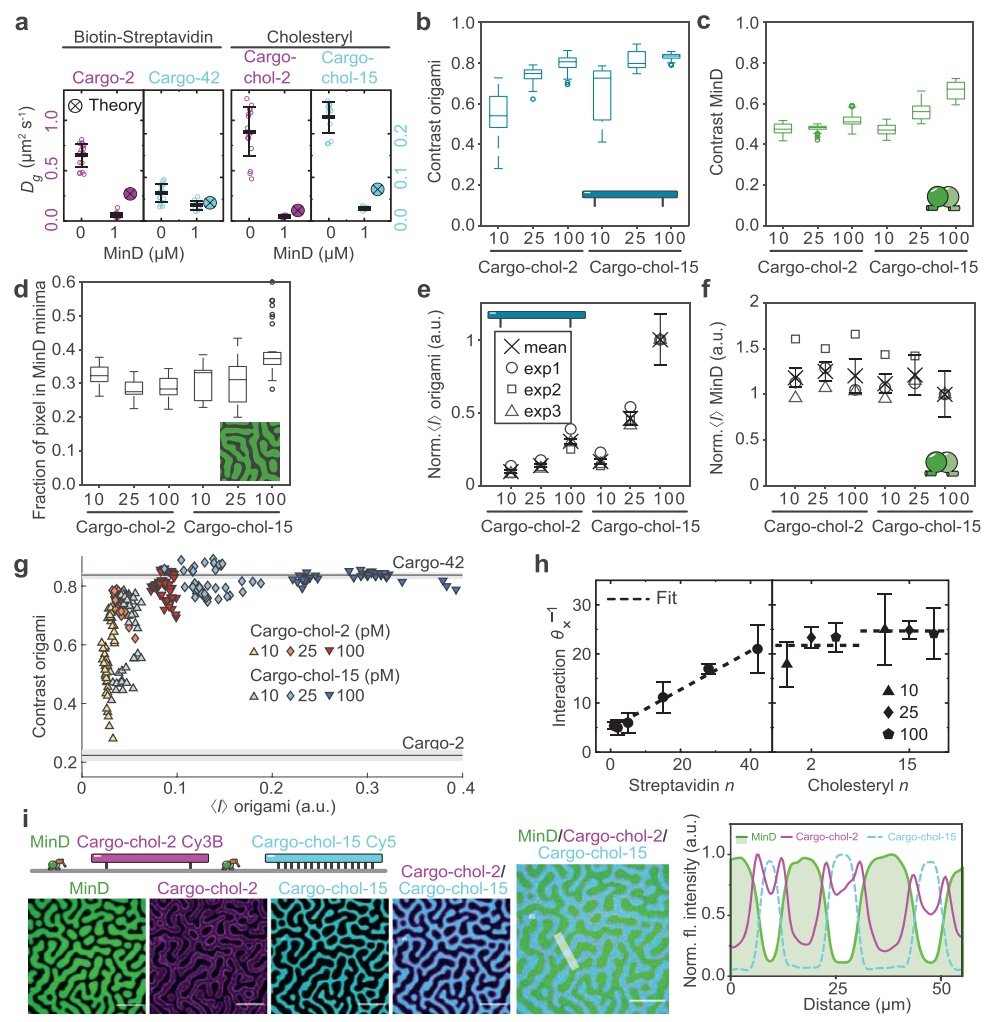
Extended Data Fig. 5 | See next page for caption.

ARTICLES

Extended Data Fig. 5 | MinDE-driven cargo demixing indeed depends on the effective size (membrane footprint) of the cargo and not on the diffusion coefficient. a, Cargo molecule diffusion coefficient in absence or presence of 1 μM MinD (with or without 1 μM MinD (30% EGFP-MinD), 0.1-1 pM origami-Cy3b with 2 or 15 hybridizing oligonucleotides, 0.1 nM TEG-cholesteryl oligonucleotide), as obtained from single particle tracking and predicted with the fitted interaction parameters obtained in h. Points are mean values of individual measurements (M), line and error bars represent the mean value and standard deviation. Left part identical to Fig. 3c. Data obtained from number of sample chambers S(Cargo-chol-2)=7, S(Cargo-chol-15)=5, S(Cargo-chol-2, MinD)=3, S(Cargo-chol-15, MinD)=2; number of measurements M(Cargo-chol-2)=16, M(Cargo-chol-15)=12, M(Cargo-chol-2, MinD)=14, M(Cargo-chol-15, MinD)=6; number of analysed single particle tracks N(Cargo-chol-2)=19,647, N(Cargo-chol-15)=23,365, N(Cargo-chol-2, MinD)=1,879, N(Cargo-chol-15, MinD)=8,338; average track-length TL(Cargo-chol-2)=303, TL(Cargo-chol-15)=353, TL(Cargo-chol-2, MinD)=964, TL(Cargo-chol-15, MinD)=749; fraction of mobile DNA origami MF(Cargo-chol-2)=0.85, MF(Cargo-chol-15)=0.87, MF(Cargo-chol-2, MinD)=0.73, MF(Cargo-chol-15, MinD)=0.67. Box plot of the contrast of **b**, cargo, **c**, MinD patterns, and **d**, of the fraction of pixels classified as MinD minima, when 10, 25 or 100 pM of cargo-chol2 or cargo-chol-15 are present (1 μM MinD (30% EGFP-MinD), 1.5 μM MinE-His with 10, 25 or 100 pM origami-Cy3b with 2 or 15 hybridizing oligonucleotides, 10 nM TEG-cholesteryl oligonucleotide). Box plot lines are median, box limits are quartiles 1 and 3, whiskers are 1.5× interquartile range (IQR) and points are outliers. Mean fluorescence intensity of **e**, DNA origami and **f**, EGFP-MinD of the full image, normalised to the intensity of experiments with 100 pM cargo-chol-15. Cross and error bars represent the mean value and standard deviation. **g**, Increased membrane density leads to an apparent increase in contrast. Data from three independent experiments with total number of analysed images per condition N(Cargo-chol-2, 10 pM)=48, N(Cargo-chol-2, 25 pM)=48, N(Cargo-chol-2, 100 pM)=64, N(Cargo-chol-15, 10 pM)=45, N(Cargo-chol-15, 25 pM)=48, N(Cargo-chol-15, 100 pM)=41. Lines represent median and quartiles 1 and 3 of cargo-2 and cargo-42 contrast for comparison. **h**, Interaction parameter (in terms of MinD coverage; surface coverages $\theta = ac$ and surface densities c are related via the particle size a) as obtained from our fitting procedure. The interaction for cargo-chol-2 and cargo-chol-15 is larger than for cargo with streptavidin building blocks. Left part is identical to Fig. 3b. The dashed line indicates a linear fit of the interaction parameter $\theta_\times^{-1}$ as a function of n. **i**, Representative images of individual and overlaid channels, and line plot of indicated selection of MinDE-induced sorting of cargo-chol-2 and cargo-chol-15 (1 μM MinD (30% EGFP-MinD), 1.5 μM MinE-His with 50 pM origami-Cy3b with 2 and 50 pM origami-Cy5 with 15 hybridizing oligonucleotides, 10 nM TEG-cholesteryl oligonucleotide). Scale bars, 50 μm.
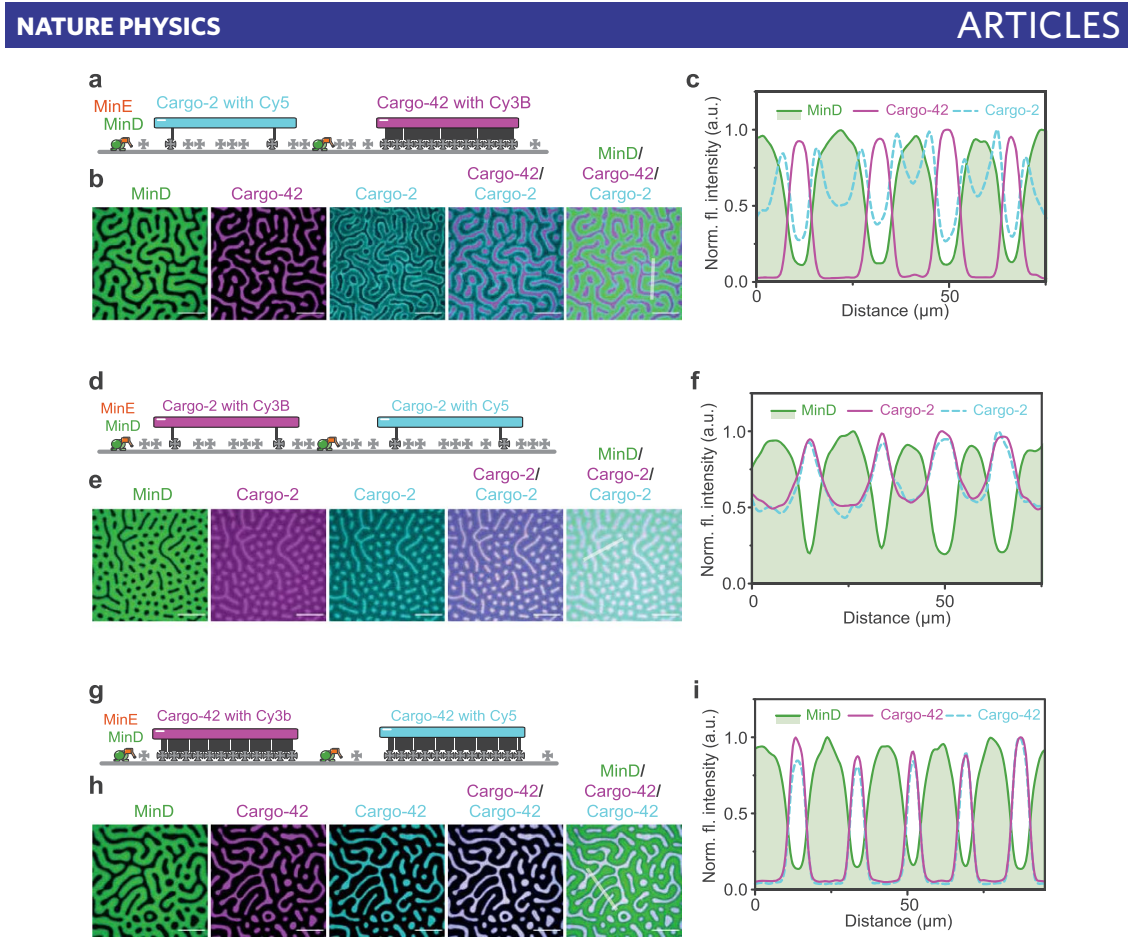
Extended Data Fig. 6 | The spatial sorting of cargo by MinDE according to the effective cargo size is not an artefact. a-c, Spatial sorting of cargo-2 and cargo-42 by MinDE also occurs when dyes are swapped. **a**, Schematic of the experimental setup. MinDE self-organization was performed in presence of two different cargo species with distinct fluorescent labels, cargo-2 with Cy5 and cargo-42 with Cy3B. **b**, Representative images and **c**, line plots of MinDE-induced sorting of cargo-2 and cargo-42 (1 μM MinD, 1.5 μM MinE-His, 50 pM origami-Cy5 with 2 biotinylated oligonucleotides, 50 pM origami-Cy3B with 42 biotinylated oligonucleotides, non-labelled streptavidin). Experiment was performed three times under identical conditions. **d-i**, MinDE-induced distributions of differentially labelled, but otherwise identical cargo are superimposable. **d**, and **g**, Schematic of the experimental setup: two identical cargoes are labelled with distinct dyes. Pattern formation is induced by addition of MinDE (1 μM MinD, 1.5 μM MinE-His, 50 pM origami-Cy5 and 50 pM origami-Cy3B with either both 2 or both 42 biotinylated oligonucleotides, non-labelled streptavidin). Representative images and line plot of pattern formation in presence of **e**, **f**, two differently labelled cargo-2 and **h**, **i**, two differently labelled cargo-42. Experiments were performed two times under identical conditions. Scale bars, 50 μm.
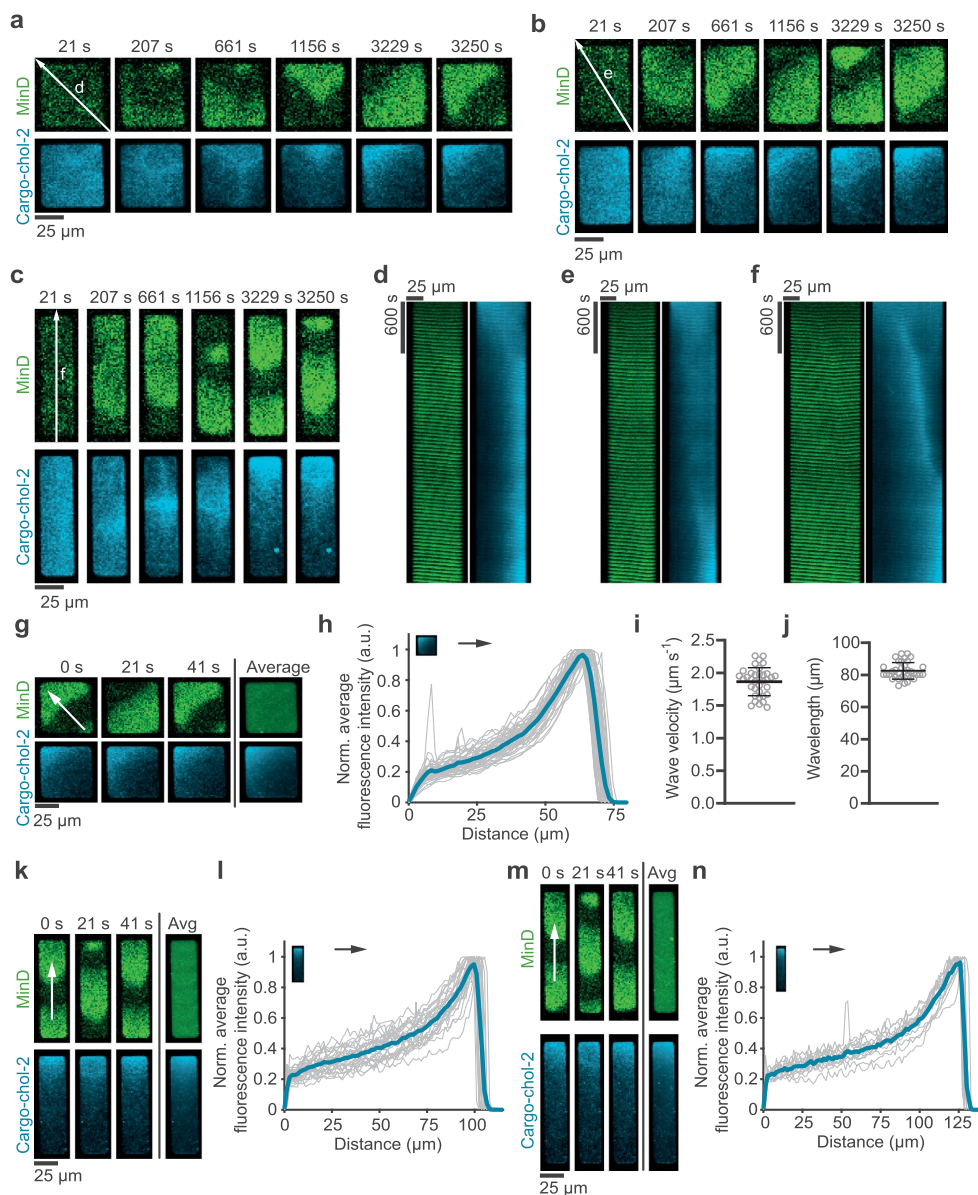
Extended Data Fig. 7 | Directed cargo transport by MinDE on chromium patterned bilayers. a,b,c, Representative time series and **d,e,f**, corresponding kymograph of MinDE traveling surface waves establishing cargo-chol-2 gradients from an initially homogeneous distribution on chromium patterned SLBs (1 μM MinD, 5 μM His-MinE, 0.1 nM origami-Cy3b with 2 hybridizing oligonucleotides, 10 nM TEG-cholesteryl oligonucleotide). **g,k,m**, Representative time-series and average of MinDE traveling surface waves and cargo-chol-2 gradient along the wave vector after regular waves have formed (>30 minutes of incubation), along the longest axis on chromium-patterned bilayers for three geometries and **h,l,n**, the respective normalised average fluorescence intensity profiles of cargo along the wave vector in g,k,m. Bold, colored line represents the mean profile, generated from N = 44, N = 27 and N = 13 membrane patches, respectively. **i**, Wave velocity and **j**, wavelength of MinDE waves on chromium patterned bilayers in presence of cargo-chol-2 or cargo-chol-15 with N = 52 analysed membrane patches. Arrows indicate wave direction. Scale bars, 25 μm.

a

Cargo-2

MinD   Cargo

50 µm

60 s

b

Cargo-chol-2

MinD   Cargo

50 µm

60 s
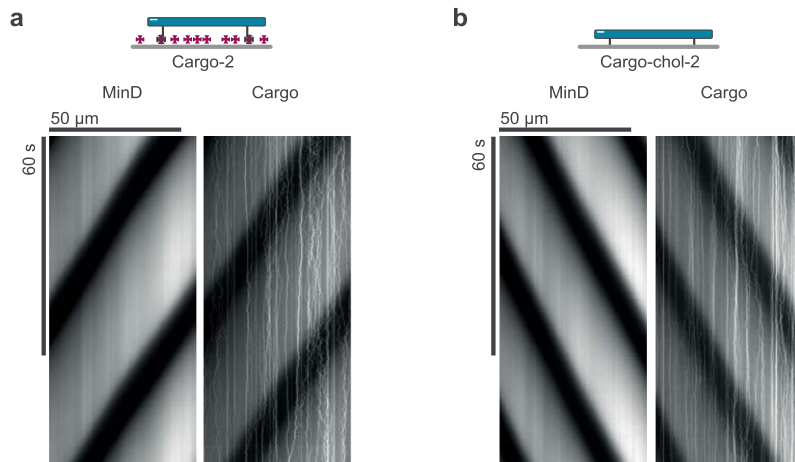
Extended Data Fig. 8 | No directed cargo movement can be observed on the single particle level. Representative kymographs of MinD waves and **a**, single cargo-2 and **b**, single cargo-chol-2 molecules in presence of regular directional MinDE travelling waves (1 µM MinD (30% EGFP-MinD), 5 µM His-MinE, 0.1-1 pM origami-Cy3b with 2 hybridizing oligonucleotides and 0.1 nM TEG-cholesteryl oligonucleotide or with 2 biotinylated oligonucleotides, non-labelled streptavidin, SLB: DOPC/DOPG/Biotinyl-CAP-PE 70/30/0.01 mol%.).
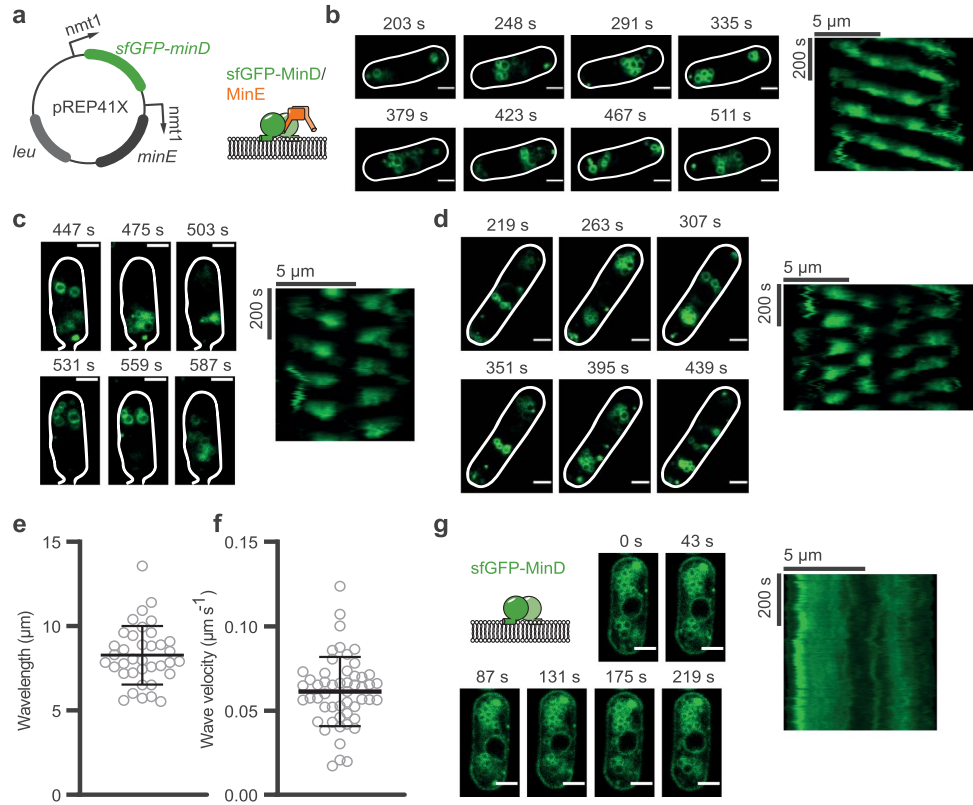
Extended Data Fig. 9 | MinDE self-organize in the fission yeast *S. pombe* at a similar spatiotemporal scale as in *E. coli*. a, Schematic of the plasmid employed for co-expression of sfGFP-MinD and MinE. **b-d**, Representative time-series and kymograph of *S. pombe* cells harbouring the co-expression plasmid for sfGFP-MinD and MinE, displaying MinD dynamics: **b**, travelling waves, **c**, pole-to-pole like oscillations and **d**, more complex dynamics. Analysis of **e**, the wavelength and **f**, wave velocity obtained from manually fitting the kymographs of cells displaying MinDE travelling waves. Lines represent the median and standard deviation. Data from three experiments with in total analysed cells e, N = 37 and f, N = 52. White boundaries represent cell outline obtained from average fluorescence images. **g**, No MinD dynamics can be observed when sfGFP-MinD is expressed in *S. pombe* in the absence of MinE. Scale bars, 2 μm.
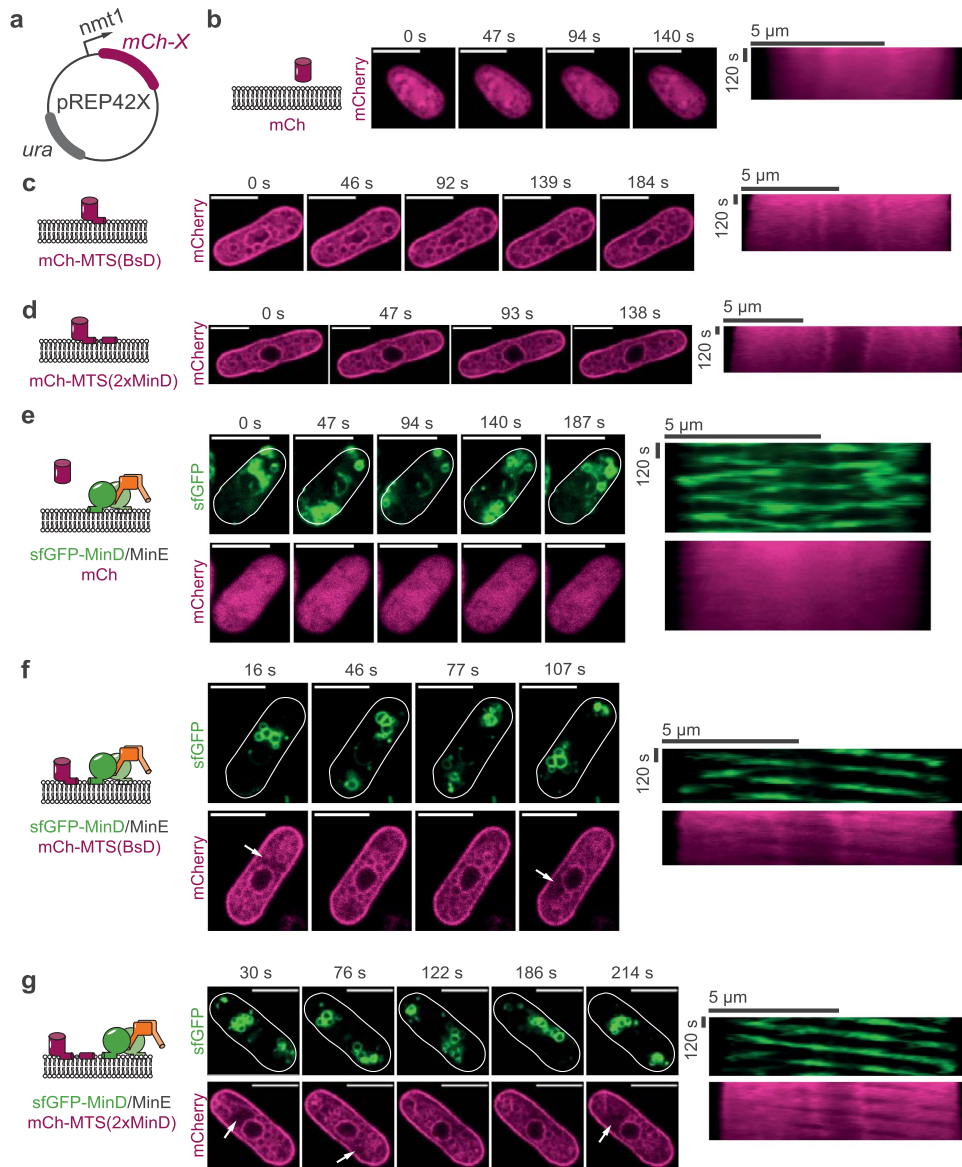
Extended Data Fig. 10 | MinDE spatiotemporally regulate model peripheral membrane proteins when reconstituted in *S. pombe*. a, Schematic of the plasmid used for expression of mCherry versions in *S. pombe*. Representative time-lapse and kymographs (over the entire cell length) of *S. pombe* cells expressing **b**, soluble mCherry, mCh which remains cytoplasmic, or a model peripheral membrane protein **c**, mCh-MTS(BsD) and **d**, mCh-MTS(2xMinD) which bind to membranes. Representative time-lapse and kymographs of *S. pombe* cells heterologously expressing sfGFP-MinD, MinE and **e**, mCh or **f**, mCh-MTS(BsD) or **g**, mCh-MTS(2xMinD). MinDE self-organization spatiotemporally regulates the model peripheral membrane proteins mCh-MTS(BsD) and mCh-MTS(2xMinD) highlighted by white arrows, but not mCh. Panel g is identical to Fig. 5f. White boundaries represent cell outline obtained from average fluorescence images. Scale bars, 5 μm.

nature research

Corresponding author(s): Erwin Frey, Petra Schwille

Last updated by author(s): Feb 10, 2021

Reporting Summary

Nature Research wishes to improve the reproducibility of the work that we publish. This form provides structure for consistency and transparency in reporting. For further information on Nature Research policies, see our Editorial Policies and the Editorial Policy Checklist.

Statistics

For all statistical analyses, confirm that the following items are present in the figure legend, table legend, main text, or Methods section.

n/a	Confirmed	
☐	☒	The exact sample size (n) for each experimental group/condition, given as a discrete number and unit of measurement
☐	☒	A statement on whether measurements were taken from distinct samples or whether the same sample was measured repeatedly
☒	☐	The statistical test(s) used AND whether they are one- or two-sided *Only common tests should be described solely by name; describe more complex techniques in the Methods section.*
☒	☐	A description of all covariates tested
☒	☐	A description of any assumptions or corrections, such as tests of normality and adjustment for multiple comparisons
☒	☐	A full description of the statistical parameters including central tendency (e.g. means) or other basic estimates (e.g. regression coefficient) AND variation (e.g. standard deviation) or associated estimates of uncertainty (e.g. confidence intervals)
☒	☐	For null hypothesis testing, the test statistic (e.g. F, t, r) with confidence intervals, effect sizes, degrees of freedom and P value noted *Give P values as exact values whenever suitable.*
☒	☐	For Bayesian analysis, information on the choice of priors and Markov chain Monte Carlo settings
☒	☐	For hierarchical and complex designs, identification of the appropriate level for tests and full reporting of outcomes
☒	☐	Estimates of effect sizes (e.g. Cohen's d, Pearson's r), indicating how they were calculated

Our web collection on statistics for biologists contains articles on many of the points above.

Software and code

Policy information about availability of computer code

Data collection	Zen Black (Zeiss), Andor Solis (Ver. 4.28, Andor 542 Technologies)
Data analysis	Fiji (version v1.52p); Matlab (R2018a, The Math-Works, 546 Natick, USA); Origin 2018; GraphPadPrism8; Python (Python Software Foundation) with the following packages: numpy, scipy, pandas, sympy, lmfit, pims, matplotlib and bokeh

For manuscripts utilizing custom algorithms or software that are central to the research but not yet described in published literature, software must be made available to editors and reviewers. We strongly encourage code deposition in a community repository (e.g. GitHub). See the Nature Research guidelines for submitting code & software for further information.

Data

Policy information about availability of data

All manuscripts must include a data availability statement. This statement should provide the following information, where applicable:
- Accession codes, unique identifiers, or web links for publicly available datasets
- A list of figures that have associated raw data
- A description of any restrictions on data availability

The raw images that support the findings of this study are available at Edmond with the identifier https://dx.doi.org/10.17617/3.5n or from the corresponding author upon request.

1

Field-specific reporting

Please select the one below that is the best fit for your research. If you are not sure, read the appropriate sections before making your selection.

☒ Life sciences ☐ Behavioural & social sciences ☐ Ecological, evolutionary & environmental sciences

For a reference copy of the document with all sections, see nature.com/documents/nr-reporting-summary-flat.pdf

Life sciences study design

All studies must disclose on these points even when the disclosure is negative.

Sample size	No sample size was calculated. Due to the large magnitude of the observed effects, we assume that our sample size is adequate.
Data exclusions	Images were only excluded from analysis when supported lipid bilayers were defective or when the MinDE patterns were dynamic and not in the quasi-stationary state. For directed transport on chromium patterned membranes, membrane patches that did not show alignment of MinDE waves along the longest axis were excluded.
Replication	The numbers of experimental repeats are indicated in the respective figure legends. All experiments were performed at least in two or more independent experiments with at least one sample chamber each under the same conditions, so that the total sample number was always ≥2.
Randomization	This study does not include work with participants or living organisms.
Blinding	This study does not include work with participants or living organisms.

Reporting for specific materials, systems and methods

We require information from authors about some types of materials, experimental systems and methods used in many studies. Here, indicate whether each material, system or method listed is relevant to your study. If you are not sure if a list item applies to your research, read the appropriate section before selecting a response.

Materials & experimental systems

n/a	Involved in the study
☒	Antibodies
☒	Eukaryotic cell lines
☒	Palaeontology and archaeology
☒	Animals and other organisms
☒	Human research participants
☒	Clinical data
☒	Dual use research of concern

Methods

n/a	Involved in the study
☒	ChIP-seq
☒	Flow cytometry
☒	MRI-based neuroimaging

2

Supplementary information

A diffusiophoretic mechanism for ATP-driven transport without motor proteins

In the format provided by the authors and unedited

Supplementary Information

A diffusiophoretic mechanism for ATP-driven transport without motor proteins

Beatrice Ramm[1,2,#], Andriy Goychuk[3,#], Alena Khmelinskaia[1,4], Philipp Blumhardt[1], Hiromune Eto[1], Kristina A. Ganzinger[5], Erwin Frey[3,*] & Petra Schwille[1,*]

[1]Max Planck Institute of Biochemistry, Am Klopferspitz 18, 82152 Martinsried, Germany.
[2]Present affiliation: Department of Physics, Princeton University, 08544 Princeton, NJ, USA
[3]Arnold-Sommerfeld-Center for Theoretical Physics and Center for NanoScience, Ludwig-Maximilians-Universität München, D-80333 München, Germany
[4]Present affiliation: University of Washington, Institute for Protein Design, 98195 Seattle, WA, USA
[5]Living Matter Program, AMOLF, 1098 XG Amsterdam, The Netherlands
#These authors contributed equally: Beatrice Ramm and Andriy Goychuk
*Correspondence to: frey@lmu.de, schwille@biochem.mpg.de

Contents

2

Supplementary Theoretical Description

I. Chemical potential gradients induce flows, which couple by an out-of-equilibrium diffusiophoretic mechanism

Elaborating the brief description in the main text, we here explain our theory in full detail. First, we estimate the abundance of membrane-bound molecules, which provides important information for the correct formulation of our theory (sections I.1 "Large particle density in MinD-rich regions and large mean particle density" and I.2 "Cargo density is limited by abundance of streptavidin and origami"). Then, to formulate a theoretical model, we treat the population of membrane-bound molecules as a lattice gas. Specifically, we use the Flory-Huggins theory of mixing to calculate the local chemical potential of each molecular species (section I.3 "Flory-Huggins theory of mixing: an equilibrium picture"). Finally, we consider chemical-potential-induced particle flows, and their coupling via an effective inter-particle friction (referred to as Maxwell-Stefan-like phenomenological approach, cf. section I.4 "Phenomenological coupling between diffusive fluxes: an out-of-equilibrium picture"). In section I.5 "Analytic solution and fitting of reduced model", we then reduce our model to find an analytic solution and to fit it to our experimental data. Based on our fitting parameters, we predict the diffusion coefficient of cargo in the presence of MinD from its measured value in the dilute limit (section I.6 "Diffusion coefficient of cargo molecules"). Section I.7 "Determining the spatial distribution of multiple cargo species" then serves as a brief outline on how our theory can be extended by additional cargo species.

1. Large particle density in MinD-rich regions and large mean particle density

The MinD monomer density in the MinD maxima reaches a value of about $13\,200\ \mu m^{-2}$ [1,2], which corresponds to a MinD dimer density of $6\,600\ \mu m^{-2}$. Since a single MinD dimer occupies approximately $25\ nm^2$ on the membrane, this gives an estimated maximal surface coverage of 16.5%. Assuming a circular packing of the free areas around different MinD dimers (cf. illustration "Estimation of the mean free path between MinD dimers"), the mean free path between two MinD dimers is then estimated to be 2.7 MinD dimer radii, which corresponds to 67 Å.

3
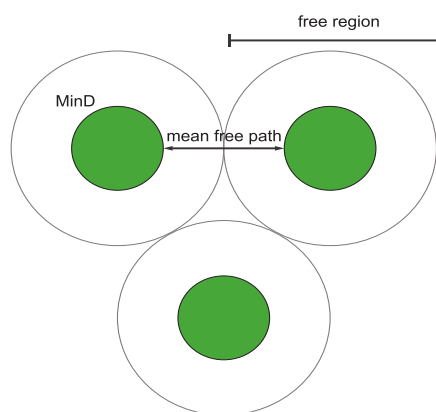
Estimation of the mean free path between MinD dimers. We represent MinD dimers (or streptavidin molecules) by disks with radii $R_p \approx 2.5$ nm, and assume that around these disks there are circular "free regions" with radii R_{free} which are devoid of other membrane-bound particles. These "free regions" can cover at most $\pi/(2\sqrt{3}) \sim 91\%$ of the membrane. This estimate yields an average mean free path between membrane-bound particles of 46 Å (67 Å for the average distance between MinD dimers in the MinD maxima). Treating the MinD dimers (or streptavidin molecules) as square plates of size 5×5 nm^2 instead of circular disks yields a very similar estimate for the average mean free path between membrane-bound particles of 51 Å (73 Å for the average distance between MinD dimers in the MinD maxima).

For an assumed sinusoidal MinD profile, we estimate that on average 8.25% of the membrane is covered by MinD[a]. Furthermore, on average another 16.5% of the membrane is covered by streptavidin molecules, as measured by Fluorescence Correlation Spectroscopy-based image calibration[2]. A single streptavidin molecule occupies 25 nm^2 on the membrane, like a MinD dimer. Thus, the mean free path between two arbitrary membrane-bound particles (MinD dimer or streptavidin) is 46 Å. To conclude, the above estimates show that the mean free path between any two membrane-bound particles is comparable to the particle size itself, which suggests that there are significant interactions between particles.

2. Cargo density is limited by abundance of streptavidin and origami

Each cargo molecule is a composite object consisting of a DNA origami scaffold and multiple streptavidin building blocks, which also serve as membrane tethers for the DNA origami

---

[a] We base this estimate on the known value for the maximum MinD surface coverage and assume that the spatial distribution of MinD is a perfect sinusoidal curve. Computing the mean MinD coverage from the mean intensity can yield a slightly higher value of approximately 10% but does not significantly affect our results.

4

scaffolds (cf. Fig. 1a in the main text). A DNA origami scaffold can only bind to the membrane by binding to streptavidin molecules via their biotinylated oligonucleotide handles. The streptavidin molecules in turn are coupled to biotinylated lipids in the SLB. Hence, the total number of membrane-bound cargo (N_g) should be limited by the abundance of both the number of DNA origami (N_{o+}) in the assay and the available membrane-bound streptavidin (N_s). In the following, we will estimate how many DNA origami are bound to the membrane via streptavidin (i.e. the abundance of cargo) as well as the abundance of free streptavidin molecules (i.e. those that are not linked to DNA origami).

The amount of biotinylated lipids in the membrane determines the number of membrane-bound streptavidin. The tetrameric streptavidin binds two to three biotinylated lipids simultaneously and as the streptavidin-biotin interaction is very strong the streptavidin off-rate is negligible on the time-scales of our experiments[3]. Since we incubate the membrane with surplus streptavidin before we wash away any unbound streptavidin, we assume that all biotinylated lipids are bound to streptavidin. Hence, one can estimate the (average) streptavidin density from the molar fraction of biotinylated lipids (here 1%), their density and the streptavidin/biotinylated lipid binding valency (here 2.5)[3] to be about $\overline{c_s} \approx 6.6 \times 10^3 \ \mu m^{-2}$. We previously also confirmed this density estimate using Fluorescence Correlation Spectroscopy-based image calibration[2]. For a membrane of size A, this yields a total of $N_s = A \ \overline{c_s}$ streptavidin molecules that are bound to the membrane.

The number of membrane-bound streptavidin molecules (N_s) and the number of available DNA origami scaffolds (N_{o+}) are constant for all experiments. Each DNA origami scaffold has n biotinylated oligonucleotide handles that can attach to membrane-bound streptavidin. Because of the strong binding between biotin and streptavidin we expect that all biotin-streptavidin bonds are saturated (if there are sufficient DNA origami, each with n biotinylated oligonucleotide handles, in the system) and that a membrane-bound streptavidin only binds to one biotinylated oligonucleotide at a time[b]. If all DNA origami were to bind to the membrane, then this would correspond to an average density of $\overline{c_{o+}} = N_{o+}/A$. This would

---

[b] Under the conditions used in our experiments, each membrane-bound streptavidin has a residual biotin binding valency of 1.5[3]. This low residual valency, and also the spacing of individual biotinylated oligonucleotide handles, should prevent binding of multiple handles to one streptavidin. However, binding of multiple biotinylated oligonucleotide handles to one streptavidin cannot be entirely excluded for cargo with many handles and consequently smaller handle spacing, i.e. cargo-15, cargo-28 and cargo-42.

5

leave $N_s - n\,N_{o+}$ freely diffusing (i.e. not linked to DNA origami scaffolds) streptavidin molecules on the membrane. In contrast, for large numbers of biotinylated oligonucleotide handles per origami ($n > N_s/N_{o+}$), all streptavidin molecules would bind to DNA origami scaffolds. Then, the DNA origami scaffolds would compete for the available membrane-bound streptavidin molecules, due to volume exclusion effects between different DNA origami[c] and a strong entropic penalty for binding DNA origami to the membrane. This competition would effectively result in only $N_g = N_s/n$ membrane-bound DNA origami (corresponding to an average membrane-bound cargo density of $\overline{c_g} = N_g/A$), while leaving $N_{o+} - N_g$ DNA origami scaffolds unbound. Thus, we expect that the number of biotinylated oligonucleotide handles on the DNA origami (n) determines the number (n) of cross-linked streptavidin building blocks per DNA origami (cf. Figs. 1d and 2a in the main text), as this corresponds to the minimal amount of membrane-bound DNA origami that at the same time maximizes the number of biotin-streptavidin bonds. To summarize, the abundance (average concentration) of membrane-bound cargo is given by $\overline{c_g} = \min(\overline{c_{o+}}, \overline{c_s}/n)$.

With the given amount of streptavidin on the membrane and origami in the assay (Supplementary Table 1), we expect that all streptavidin molecules are bound to the biotinylated oligonucleotide handles on the DNA origami scaffolds for a number of handles $n \geq \overline{c_s}/\overline{c_{o+}} \approx 21$. Consequently, for origami with a larger number of biotinylated oligonucleotide handles such as $n = 28$ or $n = 42$ in our experiments (which is equivalent to a larger number of cross-linked streptavidin molecules), not all origami can bind to membrane-bound streptavidin. Thus, we would expect a decrease of the surface density of DNA origami for $n > 21$, and that in this case there are no free streptavidin molecules left on the membrane. In good agreement with these arguments, the average fluorescence intensity of DNA origami scaffolds in our experiments indicates that the average density of membrane-bound streptavidin molecules is the limiting factor for the binding of DNA origami to the membrane for $n \geq 15$ (Extended Data Fig. 2c). Conversely, this means that for $n < 15$ the limiting factor for the binding of DNA origami to the membrane is the abundance of DNA origami themselves. Then, all of the available DNA origami will bind to the membrane via

---

[c] In our experiments, we observe that membrane-bound DNA origami scaffolds cover up to 55% of the membrane (based on the total amount of DNA origami scaffolds in the experimental assay).

6

streptavidin, resulting in an average coverage of 55%. As discussed above, at these densities one should expect significant volume exclusion effects.

3. Flory-Huggins theory of mixing: an equilibrium picture

In order to describe the thermodynamics of the free streptavidin molecules and the artificial cargo (i.e. streptavidin molecules that are crosslinked into an effective polymer) on the membrane, we formulated a Flory-Huggins theory[4–6]. To that end, we assumed that any (infinitesimally small) region on the membrane can (on the molecular scale) be described as a well-mixed lattice gas. On the mesoscopic scale, we then considered particle density gradients on the membrane surface. Then, we specifically asked: given a (externally imposed) heterogeneous distribution of active particles (i.e., we assume that there are stationary MinD protein density gradients on the membrane), what is the ensuing thermal equilibrium distribution of passive particles (cargo and free streptavidin molecules)? To answer this question, we determined the corresponding chemical potentials μ_i for each species as discussed next.

In order to formulate a theoretical model, it is instructive to consider the architecture of the cargo molecules used in the experiments (see illustration "Conceptualized model geometry"). Each cargo molecule is a composite object, which consists of a DNA origami scaffold and multiple streptavidin building blocks. The lower facet of the rod-shaped DNA origami is located between 5 and 11 nm above the membrane (see Supplementary Note 1). The streptavidin building blocks also serve as membrane tethers with a height of roughly 5 nm. Furthermore, MinD proteins bind to the membrane and form a monomolecular layer about 5 nm high[7]. These geometric properties of the system imply that cargo transport is dominated by interactions between MinD and streptavidin. As a consequence of the architecture of our cargo molecules, there are two distinct interaction layers (see illustration "Conceptualized model geometry"): (σ) the *proximal plane* refers to the thin layer near the membrane, which has a height of 11 nm, and (τ) the *distal plane* refers to the thin layer above the proximal plane, which has a height of 8 nm. In our theoretical analysis, we considered these two layers, the proximal plane and the distal plane, as two distinct lattice gases that are strictly coupled

7
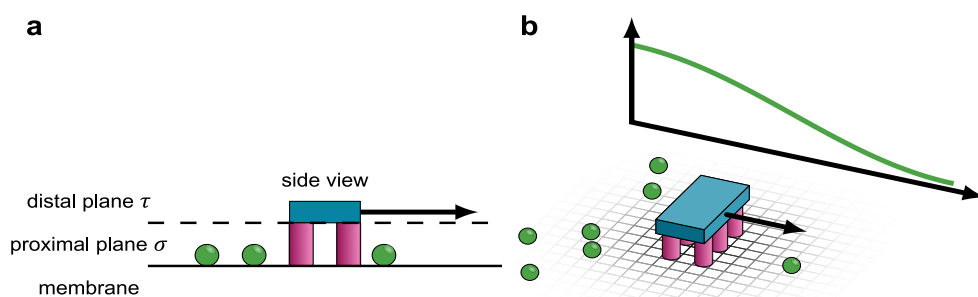
Conceptualized model geometry (cf. Fig. 2a in the main text). a, Side view of the artificial cargo and MinD on the membrane. **b,** Isometric view of the artificial cargo and MinD on the membrane. Cargo molecules are composite objects which consist of a DNA origami scaffold (blue) and multiple streptavidin building blocks (magenta). The lower facet of the rod-shaped DNA origami is located between 5 and 11 nm above the membrane, from where the DNA origami body extends a further 8 nm (see Supplementary Note 1). The streptavidin building blocks also serve as membrane tethers. Furthermore, MinD proteins (green spheres) bind to the membrane in a monomolecular layer of about 5 nm height[7]. Therefore, we expect that cargo transport is dominated by interactions between MinD and streptavidin. This setup signifies two distinct interaction layers of the cargo with the proteins, which we indicate with the following labels: (σ) In the *proximal plane*, each DNA origami crosslinks multiple streptavidin blocks into a polymer-like object g, which intersperses with MinD proteins p, free streptavidin molecules s, and solvent. (τ) In the *distal plane*, we assume that only solvent surrounds the bulky DNA origami body o. We describe both interaction layers as lattice gases (indicated by the black grid), but with different lattice constants in the proximal and in the distal plane. MinDE protein density gradients introduce a bias to the diffusion of the cargo molecule (black arrow).

through the cargo molecules (which are present in *both* layers with a common local density c_g but distinct effective sizes a_g and a_o). Here and in the following, we use the term "size" to refer to the 2D projected area of the different particles on the membrane (i.e. membrane footprint). We choose the lattice constants of the proximal plane ($\ell_\sigma = 5$ nm, corresponds to the diameter of a typical MinD dimer or streptavidin molecule) and the distal plane ($\ell_\tau = 16$ nm, corresponds to the short side of the DNA origami) to match the typical length of the associated particles, respectively.

Directly above the membrane (*proximal plane σ*), each DNA origami scaffold crosslinks multiple streptavidin blocks into a polymer-like object g, which intersperses with MinD proteins[d] p, free streptavidin molecules s, and solvent. Because streptavidin molecules and MinD dimers have a diameter of roughly 5 nm, we choose the lattice constant of the proximal

---

[d] In the following, we neglect the distribution of MinE proteins. MinE proteins are recruited to the membrane by MinD proteins and therefore typically localize to the edge of MinD patterns. Therefore, we assume that MinD is a good proxy for the total distribution of MinDE proteins.

8

plane accordingly: $\ell_\sigma = 5$ nm. Then, each individual MinD dimer, free streptavidin molecule, and patch of solute occupies one lattice site of size (area) $a_\sigma = \ell_\sigma^2$. Cargo molecules with n streptavidin building blocks occupy n lattice sites and therefore have an effective size of $a_g = n\, a_\sigma$ on the membrane. We assume that these four species of molecules form a lattice gas with a free energy density f^σ, which is described by the Flory-Huggins theory of mixing[4–6]

$$\frac{f^\sigma}{k_B T} = \sum_i c_i \ln \theta_i + \sum_{i,j} c_i \theta_j \, \chi_{ij} \ .\tag{S1}$$

Here, c_i and θ_i refer to the surface density and surface coverage of each species (cargo g, free streptavidin s, MinD proteins p and solvent ϱ), respectively, while the Flory-Huggins parameters χ_{ij} are a measure for the interaction energy between different molecular species. At this point, we assume that there is no direct attraction or repulsion between the different species (e.g. due to electrostatic interactions); thus, all of the interaction parameters between the different species must vanish: $\chi_{ij} = 0$. On the membrane, each lattice site is either occupied by cargo g, free streptavidin s, MinD proteins p, or solvent ϱ. Specifically, cargo molecules occupy a local surface fraction $\theta_g(\boldsymbol{x}) = n\, a_\sigma\, c_g(\boldsymbol{x})$ at a surface density of $c_g(\boldsymbol{x})$, free streptavidin molecules occupy a local surface fraction $\theta_s(\boldsymbol{x}) = a_\sigma\, c_s(\boldsymbol{x})$ at a surface density of $c_s(\boldsymbol{x})$, and MinD proteins occupy a local surface fraction $\theta_p(\boldsymbol{x}) = a_\sigma\, c_p(\boldsymbol{x})$ at a surface density of $c_p(\boldsymbol{x})$. Then, the solvent occupies the remainder of the surface at a local surface fraction $\theta_\varrho(\boldsymbol{x}) = 1 - \theta_g(\boldsymbol{x}) - \theta_s(\boldsymbol{x}) - \theta_p(\boldsymbol{x})$, which corresponds to a local surface density of $c_\varrho(\boldsymbol{x}) = \theta_\varrho(\boldsymbol{x})/a_\sigma$. By taking the derivative of the free energy density, Eq. (S1), with respect to the surface density of cargo molecules, one obtains the contribution of the *proximal plane* σ (near the membrane) to the total chemical potential of a cargo molecule:

$$\frac{\mu_g^\sigma(\boldsymbol{x})}{k_B T} = \frac{\partial}{\partial c_g} \frac{f^\sigma}{k_B T} = \ln[\theta_g(\boldsymbol{x})] - n \ln[1 - \theta_g(\boldsymbol{x}) - \theta_s(\boldsymbol{x}) - \theta_p(\boldsymbol{x})] + (1 - n)\ .\tag{S2a}$$

Here, $\theta_g(\boldsymbol{x}) = n\, a_\sigma\, c_g(\boldsymbol{x})$ indicates the local surface fraction occupied by cargo molecules, $\theta_s(\boldsymbol{x}) = a_\sigma\, c_s(\boldsymbol{x})$ indicates the local surface fraction occupied by free streptavidin molecules, and $\theta_p(\boldsymbol{x}) = a_\sigma\, c_p(\boldsymbol{x})$ indicates the local surface fraction occupied by MinD proteins. The second term of Eq. (S2a) corresponds to a *volume exclusion* effect, where a local increase of cargo density will lead to a local depletion of solvent. The size ratio between cargo and the solvent patches is given by $(n\, a_\sigma)/(a_\sigma)$, and contributes to this volume exclusion effect. The third term of Eq. (S2a) is a constant and thus drops out when one calculates the gradients of the chemical potential. Analogously, the chemical potential of a free streptavidin molecule is

9

given by

$$\frac{\mu_s^\sigma(\boldsymbol{x})}{k_B T} = \frac{\partial}{\partial c_s} \frac{f^\sigma}{k_B T} = \ln[\theta_s(\boldsymbol{x})] - \ln[1 - \theta_g(\boldsymbol{x}) - \theta_s(\boldsymbol{x}) - \theta_p(\boldsymbol{x})]. \tag{S2b}$$

The second term of Eq. (S2b) corresponds to a *volume exclusion* effect, where a local increase of streptavidin density will lead to a local depletion of solvent. The streptavidin molecules have the same size as the solute patches (a_σ), and thus there is no pre-factor before the volume exclusion term. Finally, the chemical potential of a membrane-bound MinD protein is given by

$$\frac{\mu_p^\sigma(\boldsymbol{x})}{k_B T} = \frac{\partial}{\partial c_p} \frac{f^\sigma}{k_B T} = \ln[\theta_p(\boldsymbol{x})] - \ln[1 - \theta_g(\boldsymbol{x}) - \theta_s(\boldsymbol{x}) - \theta_p(\boldsymbol{x})]. \tag{S2c}$$

The second term of Eq. (S2c) corresponds to a *volume exclusion* effect, where a local increase of MinD dimer density will lead to a local depletion of solvent. The MinD dimers have the same size as the solute patches (a_σ), and thus there is no pre-factor before the volume exclusion term.

At an altitude of 11 nm above the membrane, the *distal plane τ* contains only DNA origami scaffolds and solvent. Because each DNA origami scaffold is 16 nm wide and 110 nm long, we choose the lattice constant of the proximal plane accordingly: $\ell_\tau = 16$ nm. Then, each DNA origami scaffold occupies roughly seven lattice sites with a total size of $a_o = 7\,a_\tau$ (yielding a width of 16 nm and a length of 112 nm), while each patch of solute has an effective size of $a_\tau = \ell_\tau^2$. Specifically, the DNA origami scaffolds occupy a local surface fraction $\theta_o(\boldsymbol{x}) = 7\,a_\tau\,c_g(\boldsymbol{x})$, at a local surface density of $c_o(\boldsymbol{x}) = c_g(\boldsymbol{x})$. Then, the solvent occupies the remainder of the distal plane at a local surface fraction $\theta_\varrho(\boldsymbol{x}) = 1 - \theta_o(\boldsymbol{x})$, which corresponds to a local surface density of $c_\varrho(\boldsymbol{x}) = \theta_\varrho(\boldsymbol{x})/a_\tau$. Analogously to Eq. (S1), we assume that these two species of molecules form a lattice gas with a free energy density f^τ, which is described by the Flory-Huggins theory of mixing[4–6]:

$$\frac{f^\tau}{k_B T} = \sum_i c_i \ln \theta_i + \sum_{i,j} c_i \theta_j\, \chi_{ij}. \tag{S3}$$

Here, c_i and θ_i refer to the surface density and surface coverage of each species (DNA origami o and solvent ϱ), respectively, while $\chi_{o\varrho}$ is a measure for the interaction energy between the two species. As before, we assume that there is no direct interaction between the different species in the distal layer (e.g. due to electrostatic interactions); thus, the corresponding interaction parameter vanishes: $\chi_{o\varrho} = 0$. Then, by taking the derivative of the free energy

10

density, Eq. (S3), with respect to the surface density of cargo molecules, we find the contribution of the *distal plane* τ (11 nm above the membrane) to the total chemical potential of a cargo molecule[e]:

$$\frac{\mu_g^\tau(\boldsymbol{x})}{k_B T} = \frac{\partial}{\partial c_g} \frac{f^\tau}{k_B T} = \ln[\theta_o(\boldsymbol{x})] - 7\ln[1 - \theta_o(\boldsymbol{x})] - 6. \qquad (S4)$$

Here, $\theta_o(\boldsymbol{x}) = 7\, a_\tau\, c_g(\boldsymbol{x})$ refers to the surface fraction occupied by the bulky DNA origami scaffolds.

The total chemical potential of a cargo molecule has a contribution from the proximal plane σ, Eq. (S2a), and a contribution from the distal plane τ, Eq. (S4). To find an expression for this chemical potential, we integrated out the two interaction layers near the membrane. Specifically, we again started from the Flory-Huggins theory of mixing[4–6], but now expressed the free energy density *per volume* in terms of the surface particle densities (in comparison, Eqs. (S1) and (S3) describe the free energy density *per area*). The proximal interaction layer has a thickness of $d^\sigma = 11$ nm and the distal layer has a thickness of $d^\tau = 8$ nm. We neglected variations in the cross-sectional area of the different molecular species within the proximal and distal layers, respectively. We assumed that the local volumetric density of cargo is given by $c_g/(d^\sigma + d^\tau)$ in both layers, while the volume fraction that is locally occupied by cargo is given by the surface coverage in the corresponding interaction layer (θ_g in the proximal layer, θ_o in the distal layer). We also applied these arguments for the MinD proteins (only present in the proximal layer at a volumetric density c_p/d^σ and volume fraction θ_p), free streptavidin molecules (only present in the proximal layer at a volumetric density c_s/d^σ and volume fraction θ_s) and the solvent patches in both interaction layers. Then, we integrated the free energy density per volume across both interaction layers to arrive at the free energy density per area. By taking the derivative of the resulting free energy density per area with respect to the surface density of cargo molecules, we found the following expression for the total chemical potential of a cargo molecule:

---

[e] Here, we have approximated the DNA origami as a polymer with 7 segments. Alternatively, one could also treat the distal layer as an ideal solution (i.e. set the "polymer factor" to 1). This alternative choice does not affect our general results which will be discussed in more detail at the end of this section. Specifically, due to the resulting entropic repulsion between different DNA origami, entropic volume exclusion effects are not sufficient to explain the strong cargo gradients that we observed in our experiments (reaching near-saturation values in DNA origami coverage $\theta_o \to 1$ where the second term in Eq. (S4) and the equivalent third term in Eq. (S5) diverge logarithmically).

11

$$\frac{\mu_g(\boldsymbol{x})}{k_B T} = \ln\big[\theta_g(\boldsymbol{x})\big] - n \ln\big[1 - \theta_g(\boldsymbol{x}) - \theta_s(\boldsymbol{x}) - \theta_p(\boldsymbol{x})\big] - 7 \ln[1 - \theta_o(\boldsymbol{x})], \qquad \text{(S5)}$$

where we have used $d^\sigma/(d^\sigma + d^\tau) \ln\big[\theta_g(\boldsymbol{x})\big] + d^\tau/(d^\sigma + d^\tau) \ln[\theta_o(\boldsymbol{x})] = \ln\big[\theta_g(\boldsymbol{x})\big] + cst$, and omitted all constant terms. Note that Eq. (S5) contains *both* a saturation term in the proximal layer (second term) as well as in the distal layer (third term). The chemical potentials of the streptavidin molecules, Eq. (S2b), and of the MinD proteins, Eq. (S2c), remain the same as calculated earlier, i.e. $\mu_s(\boldsymbol{x}) \equiv \mu_s^\sigma(\boldsymbol{x})$ and $\mu_p(\boldsymbol{x}) \equiv \mu_p^\sigma(\boldsymbol{x})$.

In our experimental assay, ATP-consuming reactions continuously drive the MinDE protein distribution out of equilibrium and maintain a non-equilibrium, spatially non-uniform steady state that exhibits protein gradients (and fluxes)[8–11]. In stark contrast to the Min proteins, the cargo molecules and the free streptavidin molecules show only thermal Brownian diffusion while being bound to the membrane; they can be considered permanently bound to the membrane as they have a negligible detachment rate due to their strong membrane anchoring[3]. As a consequence, both the cargo molecules and free streptavidin molecules adopt a thermal equilibrium state, which is lacking any gradients in the chemical potentials ($\boldsymbol{\nabla}\mu_g = \boldsymbol{\nabla}\mu_s = 0$). In other words, the (passive) Brownian particles in different regions of the membrane have identical chemical potentials in an adiabatic response to the externally imposed distribution of active particles, the MinD proteins: $\boldsymbol{\nabla}\mu_p \equiv \boldsymbol{\nabla}\mu_p^\sigma \neq 0$. Given these constraints regarding the spatial profile of the chemical potential, we then determined the distribution of all passive particles as follows.

The constraint that the cargo molecules are in local thermal equilibrium, $\boldsymbol{\nabla}\mu_g = 0$, yields the following partial differential equation by taking the gradient of Eq. (S5) and using the chain rule for multivariable functions,

$$\left[\frac{\partial\mu_g}{\partial\theta_g}\frac{\partial\theta_g}{\partial\theta_o} + \frac{\partial\mu_g}{\partial\theta_o}\right]\boldsymbol{\nabla}\theta_o + \frac{\partial\mu_g}{\partial\theta_s}\boldsymbol{\nabla}\theta_s + \frac{\partial\mu_g}{\partial\theta_p}\boldsymbol{\nabla}\theta_p = 0\,, \qquad \text{(S6a)}$$

while the constraint $\boldsymbol{\nabla}\mu_s \equiv \boldsymbol{\nabla}\mu_s^\sigma = 0$ directly implies, by using the chain rule for multivariable functions,

$$\frac{\partial\mu_s^\sigma}{\partial\theta_g}\frac{\partial\theta_g}{\partial\theta_o}\boldsymbol{\nabla}\theta_o + \frac{\partial\mu_s^\sigma}{\partial\theta_s}\boldsymbol{\nabla}\theta_s + \frac{\partial\mu_s^\sigma}{\partial\theta_p}\boldsymbol{\nabla}\theta_p = 0\,. \qquad \text{(S6b)}$$

The ratio $\partial\theta_g/\partial\theta_o = a_g/a_o = (n\, a_\sigma)/(7\, a_\tau) \approx n/70$ is fully determined by the number n of streptavidin blocks per cargo. Since a heterogeneous spatial distribution of proteins (Min pattern), i.e. $\boldsymbol{\nabla}\theta_p$, is externally maintained, Eqs. (S6a) and (S6b) form a closed set of partial

12

differential equations[f] in the variables θ_o and θ_s (together with the additional constraint that the average density of the different molecular species is conserved).

Finally, we will now impose a (externally maintained) spatial distribution of MinDE proteins and solve Eqs. (S6a) and (S6b) with the constraint that the average density of the different molecular species is conserved (mass conservation). Note that neither the precise functional form of the MinDE protein coverage distribution θ_p nor the dimension of the geometry are important: In general, the equilibrium distribution of the cargo coverage will be determined by the distribution of MinD proteins and the abundance of all molecules in the assay, and therefore have the form $\theta_o(\theta_p, \overline{\theta_p}, \overline{\theta_o}, \overline{\theta_s}, n)$. Similarly, the equilibrium distribution of the streptavidin coverage has the form $\theta_s(\theta_p, \overline{\theta_p}, \overline{\theta_o}, \overline{\theta_s}, n)$. Thus, by using the (multivariable) chain rule of differentiation, one could fully eliminate all gradients from Eqs. (S6a) and (S6b):

$$\left[\frac{n\, a_\sigma}{7\, a_\tau} \frac{\partial \mu_g}{\partial \theta_g} + \frac{\partial \mu_g}{\partial \theta_o} \right] \frac{\partial \theta_o}{\partial \theta_p} + \frac{\partial \mu_g}{\partial \theta_s} \frac{\partial \theta_s}{\partial \theta_p} + \frac{\partial \mu_g}{\partial \theta_p} = 0, \tag{S6a*}$$

$$\frac{n\, a_\sigma}{7\, a_\tau} \frac{\partial \mu_s^\sigma}{\partial \theta_g} \frac{\partial \theta_o}{\partial \theta_p} + \frac{\partial \mu_s^\sigma}{\partial \theta_s} \frac{\partial \theta_s}{\partial \theta_p} + \frac{\partial \mu_s^\sigma}{\partial \theta_p} = 0, \tag{S6b*}$$

and directly solve for the coverage of passive particles as a function of the protein coverage. Note that Eqs. (S6a*) and (S6b*) can also be obtained by directly setting $\mu_g = cst$ and $\mu_s = cst$, and expanding the resulting equations to first order in the protein coverage θ_p. Alternatively, one can also obtain Eqs. (S6a*) and (S6b*) by integrating Eqs. (S6a) and (S6b) over an arbitrary infinitesimal line segment $d\boldsymbol{s}$, and perform a change of variables $d\boldsymbol{s} \cdot \boldsymbol{\nabla}\theta = d\theta$. Since we were also interested in the spatial distribution of passive molecules, however, we translated Eqs. (S6a) and (S6b) into a boundary value problem, in a 1D geometry of length $L \equiv 1$. Specifically, this boundary value problem enforces the constraint that the average density of the different molecular species is conserved. We introduced two fields for the *cumulative coverage* (this corresponds to the *cumulative mass* for density fields) of DNA origami $\Theta_o = \frac{1}{L} \int_0^x dy\, \theta_o(y)$ and streptavidin molecules $\Theta_s = \frac{1}{L} \int_0^x dy\, \theta_s(y)$, resulting in the additional two differential equations

$$\theta_o = L\, \boldsymbol{\nabla}\Theta_o, \tag{S6c}$$
$$\theta_s = L\, \boldsymbol{\nabla}\Theta_s. \tag{S6d}$$

---

[f] To keep the equations concise, we have chosen not to insert the partial derivatives of the chemical potentials with respect to particle coverage, $\partial \mu_i / \partial \theta_j$. These partial derivatives are easily obtained from Eqs. (S2b) and (S5).

13

Thus, in summary, we have four partial differential equations (S6a), (S6b), (S6c) and (S6d) with the four boundary conditions $\Theta_s(0) = 0$, $\Theta_s(L) = \overline{\theta_s}(n)$, $\Theta_o(0) = 0$, and $\Theta_o(L) = \overline{\theta_o}(n)$. As we have discussed in section I.2 "Cargo density is limited by abundance of streptavidin and origami", the average coverage of free streptavidin molecules and cargo (equivalent to their density or abundance) depend on the number of streptavidin blocks per cargo molecule. Then, we imposed the following coverage distribution of proteins[g]:

$$\theta_p = \overline{\theta_p}\, 2 \cos\left(\frac{\pi\, x}{2\, L}\right)^2 , \qquad (S7)$$

and numerically solved the closed set of partial differential equations (S6a), (S6b), (S6c) and (S6d), as shown in Fig. 2b,c in the main text and Extended Data Fig. 3a. These results show that entropic mixing effects can in principle lead to transport of passive particles in a gradient of active particles (Fig. 2b,c in the main text and Extended Data Fig. 3a). However, this disagrees with our experiments where we observed a far stronger redistribution of the passive cargo molecules than entropic mixing would predict (Fig. 2b in the main text and Extended Data Fig. 3a). This observation can be explained as follows. The weak entropic sorting of the cargo's small streptavidin blocks in a fixed gradient of MinD proteins originates from the second term in the proximal chemical potential of cargo, Eq. (S2a), and the equivalent second term in the total chemical potential of cargo, Eq. (S5), which corresponds to a volume exclusion term (free streptavidin molecules experience analogous entropic sorting according to Eq. (S2b)). Specifically, the fixed distribution of active MinD proteins constrains the local mixture of cargo, streptavidin molecules and MinD proteins. In response, the passive cargo and streptavidin molecules will distribute in such a way that maximizes the local area fraction that is occupied by solvent (mixing). However, just as there is volume exclusion between particles in the proximal layer σ, there is also volume exclusion between particles in the distal layer τ which accommodates the DNA origami scaffolds (cf. illustration "Conceptualized model geometry"). Furthermore, the particles in the distal layer are much larger than the particles in the proximal layer. Thus, agglomeration of cargo is prevented by the second term in the distal chemical potential of cargo, Eq. (S4), and the equivalent third term in the total chemical

---

[g] This specific choice serves to (roughly) approximate the spatial profile of MinD in the assay that contains cargo-15, cargo-28 or cargo-42 (cf. Fig. 1d in the main text). There, roughly 30-50% of the raw image pixels can be classified as MinD-minima (Fig. 1g in the main text), which suggests an almost symmetric MinD profile. The spatial profile of MinD becomes increasingly asymmetric for cargo with decreasing number of streptavidin n. However, the precise form of the MinD profile should not be relevant, as the spatial dimension x can be fully eliminated from Eqs. (S6a) and (S6b), cf. resulting Eqs. (S6a*) and (S6b*).

14

potential of cargo, Eq. (S5), which diverges logarithmically as the area fraction θ_o that is covered by DNA origami scaffolds approaches saturation, $\theta_o \to 1$. As the volume exclusion term in the distal chemical potential of cargo, Eq. (S4), that prevents cargo agglomeration (cf. the equivalent third term in the total chemical potential of cargo, Eq. (S5)) has a greater weight than the volume exclusion term in the proximal chemical potential of cargo, Eq. (S2a), which creates cargo gradients in response to the imposed distribution of MinD proteins (cf. the equivalent second term in the total chemical potential of cargo, Eq. (S5)), we conclude that mixing effects alone may *never* be sufficient to reach near-saturation densities (cf. section I.2 "Cargo density is limited by abundance of streptavidin and origami") like in our experiments.

4. Phenomenological coupling between diffusive fluxes: an out-of-equilibrium picture

As described in the main text, we next relaxed our previous assumption of fixed external chemical potential gradients and considered their dynamics. According to Onsager's theory of nonequilibrium thermodynamics[12], gradients in a chemical potential $\boldsymbol{\nabla}\mu_i$ imply particle fluxes $\boldsymbol{j}_i$. In the present context, a possible candidate for a non-equilibrium process in a crowded environment is the coupling of particle fluxes through (mesoscopic) friction caused by non-specific interactions between proteins and cargo molecules on the membrane. This phenomenological friction may originate from hydrodynamic interactions, or also from collisions given that the mean free path between membrane-bound particles is only about 50 Å (see section I.1 "Large particle density in MinD-rich regions and large mean particle density"). In fluids, a frictional coupling between the diffusive fluxes of dilute solutes is mediated by hydrodynamic interactions (and a two-particle interaction potential) and has been predicted by Derjaguin[13] (cf. section "Discussion of related non-equilibrium transport mechanisms"). In gases, a phenomenologically similar (but mechanistically distinct) coupling between diffusive fluxes originates from a direct momentum transfer due to binary collisions and has been predicted by the Maxwell-Stefan theory of diffusion[14,15], as well as experimentally observed for three-component gas mixtures[16,17]. Since there are different microscopic mechanisms that can lead to a coupling between diffusive fluxes, we formulated a phenomenological theory where each species on the membrane obeys a Maxwell-Stefan-

15

like effective force-balance equation[14,15,h,i]:

$$\boldsymbol{\nabla}\mu_i + \xi_i \frac{\boldsymbol{j}_i}{c_i} + \sum_k c_k\, \zeta_{ik}\left(\frac{\boldsymbol{j}_i}{c_i} - \frac{\boldsymbol{j}_k}{c_k}\right) = 0 \,. \qquad \left(\begin{array}{c} \text{S8,} \\ \text{1 in main text} \end{array}\right)$$

Here, the index $i \in \{p, g, s\}$ refers to MinD proteins, cargo molecules with bound streptavidin, and free streptavidin molecules, respectively. Conceptually, the thermodynamic driving forces, caused by chemical potential gradients, are balanced by friction forces between the different macromolecules and lipid molecules (with friction coefficients ξ_i) as well as among the different macromolecules themselves (with coupling constants ζ_{ik}). Note that, according to Onsager's reciprocal relations[12], the matrix of coupling constants must be symmetric: $\zeta_{ik} = \zeta_{ki}$. Then, by summing the effective force balance equations for each particle species weighted with the respective particle concentration, one can verify that all friction forces due to particle-particle interactions cancel out. The underlying physical reason for these cancellations is the conservation law for the global momentum (i.e. global force balance). The last term in Eq. (S8) corresponds to a momentum transfer between any two particle species. On average, these momentum transfers must cancel out to satisfy momentum conservation. The second term in Eq. (S8) dissipates momentum into the membrane, and the first term in Eq. (S8) is a potential force which in our case originates from the free energy of mixing[j].

Since our experiments showed a nonequilibrium steady state, $\partial_t c_i = 0$, we continued to analyse the steady state of the model. While cargo and streptavidin molecules exhibit Brownian motion and relax to a thermal equilibrium state with vanishing fluxes $\boldsymbol{j}_g = \boldsymbol{j}_s = 0$, the MinD protein patterns are kept in a non-equilibrium steady state maintained by off-equilibrium chemical reactions (ATPase activity). Because the fluxes of passive cargo and streptavidin molecules vanish, there is no need to consider a coupling ζ_{sg} between them. Furthermore, Eq. (S8) shows that the self-coupling coefficients ζ_{ii} are irrelevant for the mean field dynamics. For single molecules, however, such a self-coupling should lead to a density-dependent self-diffusion coefficient, as has been observed for MinD by Loose et al.[1] using

---

[h] The last term in Eq. (S8) corresponds to an effective friction (i.e. momentum transfer) that is proportional to the velocity difference between the fluxes of different particle species. Note that one would use analogous terms to couple different fluids in dense multi-component liquids.

[i] The validity of the phenomenological theory that is presented here is independent of the detailed microscopic mechanism, because it relies on very general Onsager-like arguments. Calculating the coupling coefficients from a microscopic picture is an interesting problem on its own, which is hinted at in section III.1 "Illustrative derivation of the diffusiophoretic drift velocity in 3D solutions".

[j] In general, the potential force can also contain contributions from electrostatic or other interactions between particles.

16

single-particle tracking and for membrane-bound DNA origami using Fluorescence Correlation Spectroscopy[18].

Since the fluxes of the passive particles, cargo and streptavidin molecules, vanish ($\boldsymbol{j}_g = \boldsymbol{j}_s = 0$), the fluxes of the MinD proteins are given by

$$\boldsymbol{j}_p = -\frac{c_p\,\boldsymbol{\nabla}\mu_p}{\xi_p + c_g\,\zeta_{pg} + c_s\,\zeta_{ps}}\ , \tag{S9}$$

where the chemical potential gradient of the MinD proteins is given by Eq. (S2c). After inserting Eq. (S9) back into the force balance equation, Eq. (S8), one obtains the following relations between the externally maintained chemical potential gradients of the active particles (MinD proteins) and the induced chemical potential gradients of the passive particles (streptavidin and cargo molecules), respectively:

$$\boldsymbol{\nabla}\mu_g = \zeta_{pg}\,\boldsymbol{j}_p = -\frac{c_p\,\zeta_{pg}}{\xi_p + c_g\,\zeta_{pg} + c_s\,\zeta_{ps}}\,\boldsymbol{\nabla}\mu_p, \tag{S10a}$$

$$\boldsymbol{\nabla}\mu_s = \zeta_{ps}\,\boldsymbol{j}_p = -\frac{c_p\,\zeta_{ps}}{\xi_p + c_g\,\zeta_{pg} + c_s\,\zeta_{ps}}\,\boldsymbol{\nabla}\mu_p. \tag{S10b}$$

Here, the chemical potential gradient of the cargo molecules is given by Eq. (S5), the chemical potential gradient of streptavidin molecules is given by Eq. (S2b), and the chemical potential gradient of the MinD proteins is given by Eq. (S2c). Analogous to our numerical solution of the Flory-Huggins model (see section I.3 "Flory-Huggins theory of mixing: an equilibrium picture"), we formulated Eqs. (S10a) and (S10b) as a 1D boundary-value problem in a domain of size $L \equiv 1$, by introducing the two additional fields $\Theta_o = \frac{1}{L}\int_0^x dy\,\theta_o(y)$ and $\Theta_s = \frac{1}{L}\int_0^x dy\,\theta_s(y)$ and their respective boundary conditions $\Theta_s(0) = 0$, $\Theta_s(L) = \overline{\theta}_s(n)$, $\Theta_o(0) = 0$, and $\Theta_o(L) = \overline{\theta}_o(n)$. As before, we imposed the distribution of MinD proteins (externally maintained by a reaction-diffusion system) as given by Eq. (S7).

In the absence of mutual friction between the macromolecules ($\zeta_{ik} = 0$), Eq. (S8) reduces to the Flory-Huggins model ($\boldsymbol{\nabla}\mu_g = \boldsymbol{\nabla}\mu_s = 0$) which implies weak cargo redistribution in a stationary gradient of active proteins. In contrast, in the presence of (frictional) coupling ($\zeta_{ik} \neq 0$) between cargo molecules and MinD protein fluxes ($\boldsymbol{j}_p \neq 0$), the cargo molecules are not only redistributed due to entropic demixing effects, but in addition they are transported along protein gradients by these nonequilibrium protein fluxes. As consequence of this additional bias, cargo redistribution is significantly stronger than by equilibrium thermodynamic forces alone, which quantitatively explains our experimental data (Fig. 2b,c in

17

the main text and Extended Data Fig. 3a). We expect that individual streptavidin molecules experience a coupling ζ_{ps} to MinD fluxes, which arises from a mesoscopic friction. Consequently, we also expect that the coupling constant ζ_{pg} between MinD and a specific cargo has a contribution from the origami scaffold as well as from each of its n streptavidin molecules:

$$\zeta_{pg} = \zeta_{po} + n\,\zeta_{ps}\,.\tag{S11}$$

This implies that the extent of cargo redistribution should increase with the number of streptavidin integrated into the cargo, as indeed observed in our experiments (Fig. 1e in the main text). This suggests that diffusiophoresis is not limited to the transport of large cargo, but can also explain the transport of small molecules (with similar size as MinD proteins), such as individual membrane-bound streptavidin molecules as reported in this study (Fig. 1d in the main text) and previous ones[2,19].

5. Analytic solution and fitting of reduced model

To further elucidate the mechanism underlying MinDE-induced transport, we simplified our theoretical model. Specifically, we neglected membrane saturation effects (i.e. the second terms in Eqs. (S2a), (S2b), (S2c), (S4) and thus both the second and third terms in Eq. (S5)), so that the chemical potential of a particle with size a_i reduces to $\mu_i \approx k_B T \ln(a_i c_i)$. Then, the effective force-balance equation, Eq. (S8), takes the form of a generalized Fick's law for the MinD protein fluxes in the non-equilibrium steady state with a density-dependent diffusion coefficient $D_p(c_g, c_s)$:

$$\boldsymbol{j}_p \approx -\frac{k_B T}{\xi_p + c_g\,\zeta_{pg} + c_s\,\zeta_{ps}}\,\boldsymbol{\nabla}c_p \equiv -D_p(c_g, c_s)\,\boldsymbol{\nabla}c_p\,.\qquad \left(\begin{array}{c}\text{S12,}\\ \text{2 in main text}\end{array}\right)$$

Because the number of free streptavidin is typically small (see section I.2 "Cargo density is limited by abundance of streptavidin and origami"), we assumed that free streptavidin molecules do not significantly contribute to the dynamics, $c_s\,\zeta_{ps} \ll c_g\,\zeta_{pg}$. After inserting Eq. (S12) back into the force balance equation, Eq. (S8), one obtains the following relation between cargo molecule and MinD protein gradients:

$$\boldsymbol{\nabla}c_g = -\frac{c_g}{c_\times + c_g}\boldsymbol{\nabla}c_p\,,\tag{S13}$$

with typical *interaction density* $c_\times = \xi_p/\zeta_{pg}$. In the equilibrium state, where the fluxes of cargo molecules vanish $\boldsymbol{j}_g = 0$, the distribution of the cargo molecules will be determined by the distribution of MinD proteins, the abundance of molecules in the assay, and the

18
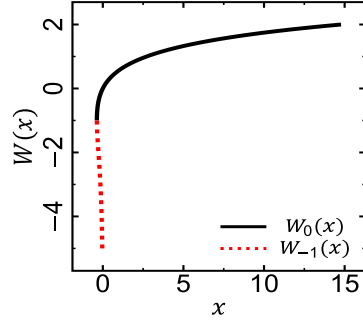
Lambert W-function. The Lambert W-function is defined as the inverse function of $f(x) = x\,e^x$ and has two real branches, W_0 and W_{-1}.

interaction density $c_\times$. Therefore, the local cargo density will have the form $c_g(c_p, c_\times, \overline{c_g}, \overline{c_p})$. Thus, by using the chain rule of differentiation, one can fully eliminate all gradients from Eq. (S13) to obtain the following ordinary differential equation:

$$\frac{\partial c_g}{\partial c_p} = -\frac{c_g}{c_\times + c_g}. \tag{S14}$$

Alternatively, one can also obtain the ordinary differential equation (S14) by integrating Eq. (S13) over an arbitrary infinitesimal line segment $d\boldsymbol{s}$, and performing a change of variables $d\boldsymbol{s} \cdot \boldsymbol{\nabla} c = dc$. Eq. (S14) can be solved by integration, and yields the following relationship between the cargo molecule density and the MinD protein density:

$$c_g(c_p) = c_\times\, W_0\left[\frac{c_g(0)}{c_\times} \exp\left(\frac{c_g(0) - c_p}{c_\times}\right)\right]. \qquad \left(\begin{array}{c} \text{S15,} \\ \text{3 in main text} \end{array}\right)$$

Here, W_0 refers to the principal branch of the Lambert W-function, which is defined as the inverse function of $f(x) = x\,e^x$ (cf. illustration "Lambert W-function"). In terms of fluorescence intensities, $I_g = \alpha_g c_g$ and $I_p = \alpha_p c_p$, Eq. (S15) can be rewritten as

$$I_g(I_p) = r\, I_\times\, W_0\left[\frac{I_g(0)}{r\, I_\times} \exp\left(\frac{I_g(0)}{r\, I_\times} - \frac{I_p}{I_\times}\right)\right], \tag{S16}$$

where we have defined the fluorescence ratio $r = \alpha_g/\alpha_p$ and the typical MinD intensity corresponding to the interaction density $I_\times = \alpha_p c_\times$. In our experiments, we controlled the abundance of all fluorescent molecules.

Our experimental data were collected over a set of experiments performed on different days. Each set of samples (that were measured on a particular day) contains at least one

19

measurement that was performed with cargo-1. Thus, as reference values for each day, we used the mean fluorescence intensities of the different channels in the cargo-1 samples. Then, we normalised all fluorescence channels to their respective reference values. Since the normalised average fluorescence intensity of the DNA origami is 1.0 for the cargo-1 samples and their average density is $313\ \mu m^{-2}$ (assuming that all DNA origami bind to the membrane), we estimated the (normalised) fluorescence yield of a DNA origami/cargo molecule as $\alpha_g \approx 3.2 \times 10^{-3}\ \mu m^2$. The MinD monomer density in the MinD maxima reaches a value of about $13\ 200\ \mu m^{-2}$ [1,2]. Thus, by measuring the normalised fluorescence intensity in the MinD maxima (1.47, normalised to the average MinD fluorescence), we estimated the fluorescence yield of a MinD dimer as $\alpha_p \approx 2.2 \times 10^{-4}\ \mu m^2$. This results in the following fluorescence ratio: $r \approx 14.5$. Having estimated the fluorescence ratio r from our experiments, we then fitted Eq. (S16) to the experimental data, with $I_\times$ as fit parameter (Fig. 3a in the main text and Extended Data Fig. 3b). Then, we determined the interaction parameter, $\theta_\times^{-1} = \left(a_p c_\times\right)^{-1} = I_\times^{-1}\left(\alpha_p/a_p\right) \propto \zeta_{pg}$; here, α_p refers to the MinD fluorescence yield and a_p refers to the size of a MinD dimer. Our fitting procedure confirmed our initial expectation $\zeta_{pg} = \zeta_{po} + n\,\zeta_{ps}$, as can be seen from Fig. 3b in the main text and Extended Data Fig. 5h[k].

6. Diffusion coefficient of cargo molecules

Our theory suggests that increasing the surface density of membrane-bound molecules (MinD, streptavidin, or cargo) will also increase the friction that each molecule experiences; specifically, Eq. (S8) states that each molecule not only transfers momentum to the membrane, but also to surrounding molecules. Thus, we expect that the diffusion coefficient of all molecules depends on the local density of membrane-bound molecules, as we have demonstrated with Eq. (S12) for the expected diffusion coefficient of MinD. To further validate our model, we determined the (mesoscopic) diffusion coefficient of the cargo molecules from our theory, and then compared these predictions with experimental data on the (microscopic) diffusion coefficient of cargo molecules that we obtained from single particle tracking.

---

[k] The absolute value of the fitted interaction parameter is smaller than the value that we have estimated for our full model (cf. Supplementary Table 1), because we have neglected saturation effects in deriving our fit curve, Eq. (S16). As discussed in section I.5 "Flory-Huggins theory of mixing: an equilibrium picture", saturation effects strongly counteract the buildup of cargo gradients and thus require a stronger coupling parameter ζ_{pg} to generate significant cargo gradients.

20

To obtain theoretical predictions, we neglected membrane saturation effects analogously to section I.5 "Analytic solution and fitting of reduced model", so that the chemical potential of a particle with size a_i reduces to $\mu_i \approx k_B T \ln(a_i c_i)$. Furthermore, because the number of free streptavidin molecules is typically small (see section I.2 "Cargo density is limited by abundance of streptavidin and origami")[I], we neglected the density of free streptavidin molecules ($c_s \approx$ 0). Then, the effective force-balance equation, Eq. (S8), takes the form of a generalized Fick's law for the cargo fluxes, where gradients in the cargo molecule density ($\boldsymbol{\nabla} c_g$) relax with a density-dependent diffusion coefficient $D_g(c_p)$:

$$\boldsymbol{j}_g \approx -\frac{k_B T}{\xi_g + c_p \, \zeta_{pg}} \, \boldsymbol{\nabla} c_g \equiv -D_g(c_p) \, \boldsymbol{\nabla} c_g \, . \tag{S17}$$

By substituting the typical interaction density $c_\times = \xi_p/\zeta_{pg}$, the diffusion coefficient of cargo molecules in the dilute limit $D_g^0 = k_B T/\xi_g$, and the diffusion coefficient of MinD proteins in the dilute limit $D_p^0 = k_B T/\xi_p$, one obtains:

$$D_g(c_p) \approx \frac{D_g^0}{1 + (D_g^0/D_p^0)(c_p/c_\times)} \, . \tag{S18}$$

We measured the diffusion coefficient of cargo-2 and of cargo-42, D_g^0, in the dilute limit (Fig. 3c in the main text). The diffusion coefficient of membrane-bound MinD proteins in the dilute limit was assumed to be $D_p^0 \approx 0.425 \; \mu m^2 s^{-1}$, based on single particle tracking data from Loose et al[1]. Using these data and the interaction parameters that we obtained by fitting the reduced model, Eq. (S16), to the experimental data (cf. Fig. 3a in the main text and Extended Data Fig. 3b for examples of the fits as well as Fig. 3b in the main text and Extended Data Fig. 5h for the fitted interaction parameters), we then predicted how the diffusion coefficient of a cargo molecule should change in the presence of MinD, in reference to its diffusion coefficient in the dilute limit. Comparing our prediction of the diffusion coefficient with experimental measurements, we found good agreement (Fig. 3c in the main text and Extended Data Fig. 5a). Specifically, we also found that cargo with more streptavidin blocks is affected *less* by the

---

[I] The assumptions made in section I.2 "Cargo density is limited by abundance of streptavidin and origami" should remain valid for the single particle tracking experiments even though the overall densities are about 100 times lower, as the ratio between membrane-bound streptavidin (biotinylated lipids) and DNA origami is kept similar: We use 100 times less biotinylated lipids (0.01%) and 100-1000 times less DNA origami than in the other experiments.

21

presence of MinD, because the base value of its diffusion coefficient (in the dilute limit) is much smaller (Fig. 3c in the main text and Extended Data Fig. 5a).

7. Determining the spatial distribution of multiple cargo species

The numerical computation of the cargo distributions in response to an imposed spatial profile of MinD, when multiple cargo species are present in the assay, were performed analogously to the numerical computations for only one cargo species by determining the corresponding boundary value problem. Specifically, note that in deriving our Flory-Huggins and phenomenological Maxwell-Stefan type models, we have *already* considered two passive species (cargo and streptavidin molecules). Adding one more cargo species does not introduce new physical concepts. Thus, it is straightforward to extend these equations by one additional chemical potential for the second cargo species (cf. Eqs. (S2a), (S2b), (S2c), (S4) and (S5)) and one additional equation for the flux of the second cargo species (i.e. so that there are three passive species), just by following the calculations that we have already presented for two passive species[m]. These calculations then yield an additional partial differential equation that determines the distribution of the third passive species in response to the spatial profile of MinD proteins (cf. Eqs. (S6a) and (S6b) for the Flory-Huggins type model and Eqs. (S10a) and (S10b) for the phenomenological Maxwell-Stefan type model). Similarly, this procedure also yields an additional partial differential equation for the cumulative coverage of the third species, cf. Eqs. (S6c) and (S6d), which enforces the mass conservation of the additional density field. Furthermore, for the sake of simplicity, we assumed equal abundance of all different cargo species on the membrane[n]; analogously, in our experimental assays we also provided an equal abundance of different DNA origami (i.e. with different numbers of biotinylated oligonucleotide handles).

---

[m] As the number of species increases, these equations become increasingly complicated. Thus, we used a symbolic math package (SymPy for Python)[69] to determine the constitutive equations and translate them into matrix form.

[n] In principle, it is possible that different cargo molecules (i.e. cargo molecules with different numbers of biotinylated oligonucleotide handles on the DNA origami) are present at different surface densities even though they have the same abundance in the assay. Specifically, DNA origami with more biotinylated oligonucleotide handles have a stronger binding to the membrane, while all DNA origami experience an entropic penalty for binding due to volume exclusion effects. Here, however, we have not considered a detailed theory of such a competitive binding as it mostly affects the time frame before the beginning of the actual experiments.

22

II.   Discussion of alternative thermodynamic transport mechanisms

In the following, we will first elaborate that neither depletion attraction (section II.1 "Depletion attraction cannot explain cargo transport") nor a volume exclusion by immobile MinD proteins (section II.2 "Static volume exclusion cannot explain cargo transport") can explain the cargo transport phenomenon that we observed in our experiments. Then, we revisit our previous Flory-Huggins and phenomenological Maxwell-Stefan type theories, and ask how they behave in the limit of small densities (section II.3 "Flory-Huggins mixing in the limit of small densities"), i.e. when steric repulsion between different cargo molecules can be neglected on a mesoscopic scale. Finally, we discuss that we do not expect a significant impact of cargo on the MinDE reaction kinetics (section II.4 "Significant impact of cargo on MinDE reaction kinetics is unlikely").

1.   Depletion attraction cannot explain cargo transport

Depletion attraction arises from a classical entropic effect, where finite-sized molecules (like MinD) can access a larger spatial region if larger molecules (like DNA-Origami) "clump" together[20]; see Fig. 6 in the main text for an illustration. This results in effective (Asakura-Oosawa) depletion forces[20] that act on the larger molecules and which are proportional to the concentration of the smaller molecules, c_p. Phenomenologically, one can represent this depletion attraction as a *negative pressure*, $p \propto -c_p$. If the concentration of the smaller molecule, c_p, is spatially heterogeneous, then this will result in effective pressure gradients, $-\boldsymbol{\nabla} p \propto \boldsymbol{\nabla} c_p$. Consequently, one would expect depletion attraction to lead to an accumulation of cargo molecules in MinD-rich regions. Because this expectation contradicted our experiments, we concluded that depletion attraction plays no significant role for cargo transport. Furthermore, we did not observe depletion-force-induced aggregation of cargo molecules when MinD was homogenously distributed (Extended Data Fig. 1).

2.   Static volume exclusion cannot explain cargo transport

To simplify our experimental setup as much as possible, suppose that membrane-bound MinD proteins act as static obstacles of size a_p and surface density c_p. Then, such obstacles locally occupy a fraction $\theta_p = a_p c_p$ of the surface, thereby reducing the space accessible by the cargo molecules. In thermal equilibrium, cargo molecules spread uniformly across the accessible space, which implies $c_g \propto \theta_{\text{free}} = \left(1 - \theta_p\right)$ for the cargo molecule density. Formally, one way

23

that this expectation can be seen° is by solving for the steady-state solution of cargo diffusing in a porous medium:

$$\partial_t c_g = \boldsymbol{\nabla}\left[D_g\,\theta_{\text{free}}\,\boldsymbol{\nabla}(c_g/\theta_{\text{free}})\right]. \tag{S19}$$

A porous medium is best explained by comparing it to a sponge. Let us suppose that the pores in this sponge contain a solution. A concentration difference across nearby pores corresponds to an osmotic pressure and leads to solute fluxes between these pores. In the end, all pores will contain the same concentration of solute (c_g/θ_{free}). Here, an onlooker that doesn't know about the existence of these pores (e.g. if one were to only image radioactively labelled solute particles) will observe a local concentration of c_g, which will in general not be homogeneous. Eq. (S19) corresponds to the continuum limit of such a porous medium. In our case, MinD takes up space on the membrane, and thus the MinD-free areas can be interpreted as "pores". Eq. (S19) then corresponds to Darcy's law[21], with a local osmotic pressure that is proportional to the local particle density c_g/θ_{free} in each "pore". This relation shows that protein gradients may induce cargo gradients solely by locally reducing the accessible space. However, it also implies that the resulting distribution of cargo molecules does not depend on any intrinsic features of the cargo molecules, contradicting our experimental observations (Fig. 1d-g in the main text). We conclude that MinD proteins do not act as static obstacles for the cargo molecules.

3. Flory-Huggins mixing in the limit of small densities

We have seen in section I.3 "Flory-Huggins theory of mixing: an equilibrium picture" that, in principle, entropic mixing effects may lead to a gradient of passive particles (cargo or streptavidin molecules) in response to a gradient of active particles (MinD proteins). This phenomenon originates from volume exclusion effects (cf. second term in the proximal chemical potential of cargo, Eq. (S2a), and the equivalent second term in the total chemical potential of cargo, Eq. (S5)) and the corresponding steric repulsion between diffusing cargo and diffusing MinD proteins. However, there must also be a steric repulsion between the bulky DNA-origami scaffolds of the cargo molecules (cf. second term in the distal chemical potential

---

° Another way to see this expectation is by writing down the Flory-Huggins mixing entropy (cf. section I.3 "Flory-Huggins theory of mixing: an equilibrium picture") and the resulting equilibrium condition, but with the distinct difference that the MinD proteins *may not move at all* and thus reduce the accessible volume: $f/(k_B T) = \theta_{\text{free}}\sum_i(c_i/\theta_{free})\ln(\theta_i/\theta_{free})$. This constrains the possible distribution of particles more strongly than only an imposed spatial profile of MinD, as we have done in section I.3 "Flory-Huggins theory of mixing: an equilibrium picture".

24

of cargo, Eq. (S4), and the equivalent third term in the total chemical potential of cargo, Eq. (S5), which diverges logarithmically as the local cargo density approaches saturating values by covering the whole locally available membrane area), which counteracts the buildup of cargo gradients. Thus, as we have seen, at the particle densities in our experiments, mixing effects alone cannot account for the strong density gradients of passive particles.

Yet, one may ask: what if the cargo density is much smaller than in our setup, so that mesoscopic volume exclusion effects between different DNA-origami scaffolds may be neglected? Then, we can drop the second term of Eq. (S4), which would diverge logarithmically at high densities and which is equivalent to the third term of Eq. (S5), so that the total chemical potential of membrane-bound cargo in our Flory-Huggins model is given by:

$$\frac{\mu_g(\boldsymbol{x})}{k_B T} = \ln[\theta_g(\boldsymbol{x})] - n \ln[1 - \theta_g(\boldsymbol{x}) - \theta_s(\boldsymbol{x}) - \theta_p(\boldsymbol{x})], \tag{S20a}$$

where we have neglected constant contributions. The fraction of the area covered by the DNA origami scaffolds, $\theta_o(\boldsymbol{x})$, is related to the area fraction covered by the cargo's streptavidin blocks, $\theta_g(\boldsymbol{x})$, as follows: $\theta_o(\boldsymbol{x}) = \theta_g(\boldsymbol{x}) (7\, a_\tau)/(n\, a_\sigma)$. Furthermore, the chemical potential of free streptavidin molecules is given by (cf. Eq. (S2b)):

$$\frac{\mu_s(\boldsymbol{x})}{k_B T} = \ln[\theta_s(\boldsymbol{x})] - \ln[1 - \theta_g(\boldsymbol{x}) - \theta_s(\boldsymbol{x}) - \theta_p(\boldsymbol{x})]. \tag{S20b}$$

We assume that the passive cargo molecules and the free streptavidin molecules reach an equilibrium state in an adiabatic response to the distribution of active MinD proteins, so that gradients in the chemical potential vanish, $\boldsymbol{\nabla}\mu_g(\boldsymbol{x}) = 0$ and $\boldsymbol{\nabla}\mu_s(\boldsymbol{x}) = 0$. Note that this equilibrium condition is equivalent to $\mu_g(\boldsymbol{x}) = cst$ and $\mu_s(\boldsymbol{x}) = cst$. Then, we solve the equation $\mu_s(\boldsymbol{x}) = cst$ for θ_s and set the (general) boundary values $\theta_s(0)$ and $\theta_g(0)$ to obtain the following equation for the local amount of free streptavidin molecules:

$$\theta_s = \frac{\theta_s(0)}{1 - \theta_g(0)}\left[1 - \theta_g - \theta_p\right]. \tag{S21a}$$

By inserting Eq. (S21a) into Eq. (S20a), solving the equation $\mu_g(\boldsymbol{x}) = cst$ for θ_p and setting the (general) boundary value $\theta_g(0)$, this yields the following implicit equation for the local amount of cargo molecules:

$$\theta_p = 1 - \theta_g(\theta_p) - \left[1 - \theta_g(0)\right]\left[\frac{\theta_g(\theta_p)}{\theta_g(0)}\right]^{\frac{1}{n}}. \tag{S21b}$$

25
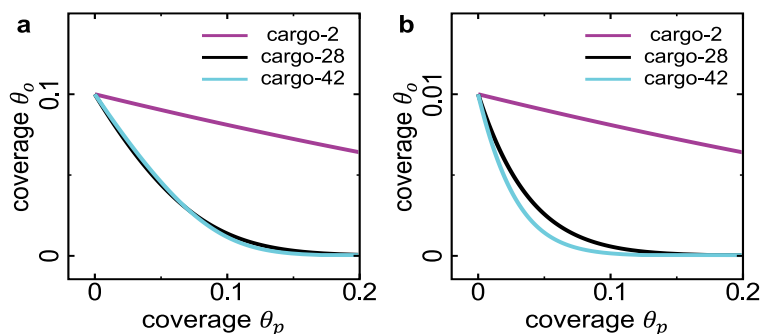
Cross-correlation between cargo coverage and MinD coverage at very low cargo densities. To obtain this graph, we have used Eq. (S21b) and the relation $\theta_o(x) = \theta_g(x)\,(7\,a_\tau)/(n\,a_\sigma) \approx \theta_g(x)\,(70/n)$. Furthermore, we have assumed that the cargo molecules do not exceed (**a**) a coverage of 0.1, which is 1 order of magnitude smaller than the typical values in our experiments, or (**b**) a coverage of 0.01, which is 2 orders of magnitude smaller than the typical values in our experiments.

As the illustration "Cross-correlation between cargo coverage and MinD coverage at very low cargo densities" shows, at large densities of MinD proteins (similar to our experiments) it would be possible to generate a gradient in the cargo molecules even without a diffusiophoretic mechanism if the density of cargo molecules is sufficiently small (one or two orders of magnitude smaller than in our experiments).

In a cell, the density of MinD proteins is expected to be smaller than in our experimental setup. Thus, we have also tested in our model whether one would still expect a pattern in the passive cargo if the density of MinD was one order of magnitude smaller, and if the density of passive molecules was one or two orders of magnitude smaller than in our experiments. As the illustration "Low MinD and low cargo density" shows, a diffusiophoretic mechanism leads to much stronger gradients in the cargo molecules than entropic sorting effects.

Our theoretical analysis in this section thus shows: if the cargo density is much smaller than in our experimental assay, then mixing effects can readily build up cargo gradients as long as the MinD density remains high (cf. illustration "Cross-correlation between cargo coverage and MinD coverage at very low cargo densities"). If the MinD density is also reduced compared to our experiments, then a diffusiophoretic mechanism is mandatory to create significant cargo gradients (cf. illustration "Low MinD and low cargo density").

26
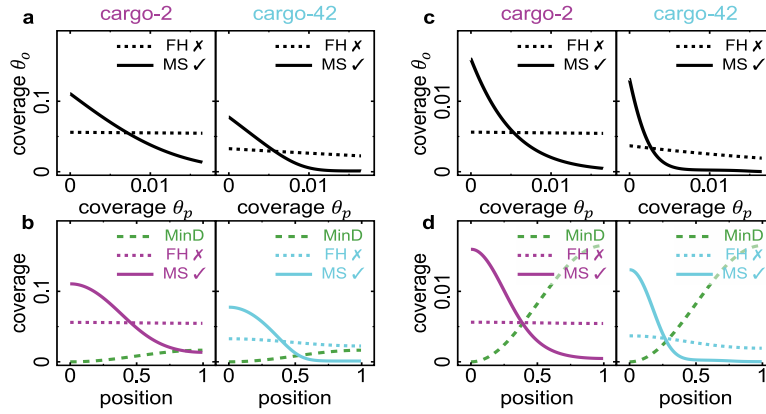
Low MinD and low cargo density. We tested our model in a regime where the MinD density is one order of magnitude smaller than in our experiments. **a,b** Cargo coverage one order of magnitude smaller than in our experiments. Model parameters: (cargo-2) average coverages $\overline{\theta_p} = 0.00825$, $\overline{\theta_s} = 0.0149$ and $\overline{\theta_o} = 0.055$; interaction parameter (in terms of MinD coverage) $\theta_\times^{-1} = 220$; (cargo-42) average coverages $\overline{\theta_p} = 0.00825$, $\overline{\theta_s} = 0$ and $\overline{\theta_o} = 0.028$; interaction parameter (in terms of MinD coverage) $\theta_\times^{-1} = 620$. Surface coverages $\theta = a\,c$ and surface densities c are related via the particle size a. **c,d** Cargo coverage two orders of magnitude smaller than in our experiments. Model parameters: (cargo-2) average coverages $\overline{\theta_p} = 0.00825$, $\overline{\theta_s} = 0.00149$ and $\overline{\theta_o} = 0.0055$; interaction parameter (in terms of MinD coverage) $\theta_\times^{-1} = 220$; (cargo-42) average coverages $\overline{\theta_p} = 0.00825$, $\overline{\theta_s} = 0$ and $\overline{\theta_o} = 0.0028$; interaction parameter (in terms of MinD coverage) $\theta_\times^{-1} = 620$. Surface coverages $\theta = a\,c$ and surface densities c are related via the particle size a.

4. Significant impact of cargo on MinDE reaction kinetics is unlikely

As the MinDE distribution was influenced by the presence of cargo, we wondered whether cargo may change the kinetic (un)binding rates of MinDE. To answer this question, we analysed the average fluorescence intensity of the patterns, i.e. the membrane density of the molecules. While we found that the density of streptavidin and MinD were relatively similar for all conditions, the density of membrane-bound DNA origami decreased by roughly 44% when we increased the number of streptavidin building blocks from 1 to 42 (Extended Data Fig. 2c-e). The latter suggested that the average density of membrane-bound streptavidin, which remained unaffected, is the limiting factor for binding of DNA origami to the membrane (see section I.2 "Cargo density is limited by abundance of streptavidin and origami" for details). As the presence of cargo did not change the average membrane density of MinD (Extended Data Fig. 2d), it is unlikely to significantly affect their (un)binding rates. Furthermore, cargo always accumulated in regions where both the MinD density and thus

27

protein recruitment to the membrane are already low, and is thus unlikely to significantly hinder protein (un)binding.

Cargo and streptavidin molecules have a strong membrane affinity and negligible detachment rates[3]. Therefore, MinD-induced detachment of cargo or streptavidin from the membrane is highly unlikely.

28

III. Discussion of related non-equilibrium transport mechanisms

In the following, we will relate our Maxwell-Stefan-like phenomenological approach to diffusiophoresis to a commonly employed hydrodynamic theory for 3D solutions[22–35] which was pioneered by Derjaguin[13]. In particular, we will follow the reasoning and calculations by Marbach & Bocquet[31], as well as by Golestanian[32] to derive a phoretic drift velocity for uncharged particles. We will place special emphasis on the assumptions underlying these calculations and discuss their validity for our experimental system. Taken together, the analysis below will show that diffusive fluxes are essential to obtain a finite diffusiophoretic drift velocity.

1. Illustrative derivation of the diffusiophoretic drift velocity in 3D solutions

We assume that the passive cargo molecules are much larger than the MinD proteins. This approximation should be appropriate for the DNA origami scaffold of the cargo molecules since we use DNA-Origami with a size of 110×16 nm and a MinD dimer has a size of 5×5 nm (although this size difference creates only a weak length scale separation along the DNA-Origami's long axis). However, this assumption may not be strictly valid for streptavidin molecules[p], which have roughly the same size as a membrane-bound MinD dimer (5×5 nm). Although the following calculations have limited applicability to our experimental setup with only weak length scale separation between cargo and solute (while being perfectly valid for colloidal systems), they will conceptually illustrate how diffusiophoretic transport may emerge from microscopic interactions.

The approximation that the length scales of cargo and of the MinD dimer separate allows one to consider the MinD proteins as a solute field with density c_p, whose temporal evolution is given by the Smoluchowski equation,

$$\partial_t c_p = \boldsymbol{\nabla} \cdot \left[D_p \boldsymbol{\nabla} c_p + c_p \frac{D_p}{k_B T} \boldsymbol{\nabla} \Psi - c_p \boldsymbol{v} \right] \equiv -\boldsymbol{\nabla} \cdot \boldsymbol{j}_p \,. \tag{S22}$$

Here, Ψ denotes the interaction potential between the MinD proteins and the cargo, and $\boldsymbol{v}$ refers to the local advection velocity due to flow in the surrounding fluid. As we will show below, the interactions Ψ between MinD proteins and the cargo will induce a slip flow $\boldsymbol{v}$ in

---

[p] A more general treatment would require describing the hydrodynamic interactions between solute molecules with the Rotne-Prager tensor. Here, we will not carry out such a calculation, especially since additional caveats (discussed below in more detail) like the coupling between 2D fluid membrane and 3D aqueous solution apply.

29

the surrounding fluid. Furthermore, we put ourselves in the (moving) reference frame of a cargo molecule, and consider the cargo molecule as a rigid one-dimensional wall placed at position $z = 0$. Since all particles involved in the process are small, we assume that the fluid dynamics is described by a stationary Stokes flow at low Reynolds number,

$$\eta \Delta \boldsymbol{v} - \boldsymbol{\nabla} P - c_p \boldsymbol{\nabla} \Psi = 0 \,, \tag{S23a}$$
$$\boldsymbol{\nabla} \cdot \boldsymbol{v} = 0 \,. \tag{S23b}$$

Here, the field P denotes the local pressure in the fluid. The velocity field $\boldsymbol{v}$ also advects the MinD proteins, cf. Eq. (S22). In the third term of Eq. (S23a), the body force acting on each MinD protein due to its interaction with the cargo molecule is transferred to the fluid, which drives the fluid flow $\boldsymbol{v}$.

There are several important reservations one might have with regard to the above approach: (i) First, the typical mean free path between two membrane-bound particles in our experimental system is only 46 Å, which amounts to roughly 15 water molecules. Continuum hydrodynamic approaches are typically valid down to a molecular scale of 10 Å, below which the microscopic properties of water (i.e. viscosity) begin to significantly deviate from its bulk properties[36]. Thus, if any two MinD dimers or streptavidin molecules come closer than 10 Å (which may happen fairly regularly given that their average distance is only 46 Å), then a continuum hydrodynamic theory loses its validity at such small scales and one needs a particle-based kinetic analysis. (ii) Second, the above theoretical approach (more specifically, Eq. (S23a)) is based on the assumption that the Reynolds number is small ($Re \ll 1$). With the Reynolds number given by $Re = \frac{vL}{\eta}$, where L is the typical length scale of the fluid flow, this requires a relatively small fluid flow velocity. To estimate whether this assumption is valid for our experimental setup, we have to investigate the typical velocity of the particles at the molecular scale. The typical length scale of the corresponding hydrodynamic problem is $L = 46$ Å and the kinematic viscosity of water at 20°C is given by[37] $\eta = 1 \times 10^{-6} \mathrm{m}^2 \mathrm{s}^{-1}$. The typical velocity of the fluid between two membrane-bound particles should be in the range between the thermal velocity of these particles and the thermal velocity of water molecules. In the following, we will estimate the typical thermal velocity of a particle as the root mean square velocity:

30

$$\sqrt{\langle v^2 \rangle} = \sqrt{\frac{f\,k_B T}{m}}, \tag{S24}$$

where f refers to the number of translational degrees of freedom ($f = 2$ for 2D motion and $f = 3$ for 3D motion). MinD dimers have a molecular weight of 66 kDa, while streptavidin molecules (tetramers) have a molecular weight of 53 kDa. These membrane-bound molecules are confined to planar 2D motion and thus (at 20°C) move with a thermal velocity of $8.6~\text{ms}^{-1}$ and $9.6~\text{ms}^{-1}$ for MinD dimers and streptavidin, respectively. Water has a molecular weight of 18 Da and may move in the whole 3D solution, thus with a thermal velocity of $637~\text{ms}^{-1}$. Consequently, the Reynolds number will typically be in a range between $Re \sim 0.04$ (if the fluid moves at the thermal velocity of a MinD protein) and $Re \sim 2.9$ (if the fluid moves at the thermal velocity of a water molecule)[q]. These estimates suggest that at the given length scales one might have to take into account the momentum terms of the Navier-Stokes equations, thus possibly invalidating Eq. (S23a). (iii) Third, the Knudsen number for the membrane-bound particles, which relates the molecular free path to the molecular scale (5 nm for a MinD dimer or a streptavidin molecule), is only $Kn \sim 0.92$. At such small length scales, any gas (which can also mean a gas of solutes) will begin to show hydrodynamic properties like viscosity. In the case of MinD proteins, this is suggested by the density-dependence of their diffusion constant, which decreases as the surface density of MinD increases[1]. For a gas, it is possible to derive these hydrodynamic properties from the Boltzmann equation with the Chapman-Enskog theory[38,r]. (iv) Fourth and finally, in the above approach one considers a single fluid only, while actually in our experimental setup there are two fluids with different viscosities: a 3D half-space of water and a 2D lipid bilayer that contains membrane-bound molecules.

With these reservations in mind, we will in the following explore the consequences of the above approach to our experimental system. Despite the possible limitations in applicability, it will provide important conceptual insights into the mechanisms underlying diffusiophoresis. Thus, we will now turn to analyse the continuum approach for a cargo particle that is much

---

[q] The lipid bilayer membrane is a fluid whose kinematic viscosity should be significantly larger than that of water. Specific values are 0.06 Pa s for the dynamic viscosity of a 5 nm thick membrane of DOPC[70]. Assuming a close packing of the phospholipids where each phospholipid takes up 10Å^2, and taking the typical mass of a DOPC molecule[71] as 786 Da, this results in a kinematic viscosity of $23 \times 10^{-6} \text{m}^2\text{s}^{-1}$. Thus, any flow in the liquid upper leaflet of the supported lipid bilayer will be associated with smaller Reynolds numbers.

[r] Here, a careful theoretical treatment would be needed. The Chapman-Enskog theory is typically applied to gases, where particles only interact via collisions. In our case, particles may also interact via hydrodynamic interactions.

31
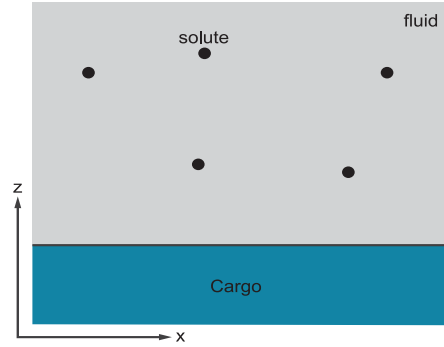
Simplified geometry of a cargo which is surrounded by solute molecules and fluid. We approximate the cargo molecule as a rigid wall by assuming that there is a length scale separation between cargo and solute.

larger than the MinD proteins. Due to the separation of length scales, we consider the surface of the cargo molecule as a solid wall (cf. illustration "Simplified geometry of a cargo which is surrounded by solute molecules and fluid"). The interaction potential, $\Psi(z)$, should only depend on the relative distance between a MinD protein and the wall. We assume that the cargo is rigid and thus that the wall is impermeable, so that the flow velocity and the particle fluxes along the normal axis (z-axis) vanish: $v_z = 0$ and $j_{p,z} = 0$. Then, in the stationary case, Eq. (S22) reduces to a balance between a diffusive flux and an advective flux due to the interaction potential $\Psi(z)$:

$$D_p \partial_z c_p + \frac{c_p D_p}{k_B T} \partial_z \Psi(z) = 0 \,. \tag{S25}$$

By integrating this expression over z, one obtains a Boltzmann-like protein profile,

$$c_p(z) = c_\infty \exp\left[-\frac{\Psi(z)}{k_B T}\right], \tag{S26}$$

where c_∞ corresponds to the far-field concentration of the MinD proteins. Similarly, by using $v_z = 0$, the z-component (perpendicular to the interface defined by the cargo molecule) of the Stokes equations, Eq. (S23a), yields the following force balance equation between the pressure gradient and the potential force $\partial_z \Psi$:

$$\partial_z P = -c_p \partial_z \Psi \,. \tag{S27}$$

Again, integrating once over z yields an expression for the hydrodynamic pressure field:

32

$$P_\infty - P(z) = -c_\infty \int_\infty^z dz'\, \partial_z \Psi(z') \exp\left[-\frac{\Psi(z')}{k_B T}\right] = -c_\infty \int_{\Psi_\infty}^\Psi d\Psi \exp\left[-\frac{\Psi}{k_B T}\right]. \qquad (S28)$$

Next, we require that the interaction potential vanishes in the far field, $\lim_{z\to\infty} \Psi(z) = \Psi_\infty = 0$, and thus obtain the following expression for the hydrodynamic pressure field

$$P(z) = P_\infty + k_B T c_\infty \left[\exp\left(-\frac{\Psi(z)}{k_B T}\right) - 1\right] = P_\infty + k_B T (c_p - c_\infty). \qquad (S29)$$

Here, P_∞ refers to the hydrostatic pressure in the far field, where the ambient fluid is at rest. In Eq. (S29), the term $c_p k_B T$ can be identified as a local osmotic pressure that is induced by interactions between MinD proteins and the cargo wall. As there is a density gradient of solutes in the far field, $\partial_x c_\infty$, the resulting pressure gradient drives fluid flow parallel to the cargo surface, i.e. along the x-axis. Furthermore, since our simplified geometry consists of an infinite wall as the cargo surface, we assume that the fluid flow is translation invariant along the x-axis, $\partial_x v_x \equiv 0$ and therefore $\partial_x^2 v_x \equiv 0$ (i.e. we assume that variations along the x-axis are significantly smaller than variations along the z-axis because of the separation of length scales). Then, we obtain the following equation for the x-compotent of the velocity field:

$$\eta \partial_z^2 v_x = \partial_x P = k_B T \left[\exp\left(-\frac{\Psi(z)}{k_B T}\right) - 1\right] \partial_x c_\infty. \qquad (S30)$$

This relation can be integrated using no shear stress boundary conditions in the far field, $\partial_z v_x|_{z\to\infty} = 0$. One obtains:

$$\int_0^\infty dz\, z\, \partial_z^2 v_x = [z\, \partial_z v_x]_0^\infty - \int_0^\infty dz\, \partial_z v_x = -v_x|_{z\to\infty} + v_x(0). \qquad (S31)$$

Finally, we use no-slip boundary conditions at the cargo surface, $v_x(0) = 0$, to obtain the far-field fluid slip velocity:

$$v_x|_{z\to\infty} = -\frac{k_B T}{\eta} \int_0^\infty dz\, z \left[\exp\left(-\frac{\Psi(z)}{k_B T}\right) - 1\right] \partial_x c_\infty. \qquad (S32)$$

Returning to the lab frame, the cargo slip velocity is given by[s]:

$$v_g = +\frac{k_B T}{\eta} \int_0^\infty dz\, z \left[\exp\left(-\frac{\Psi(z)}{k_B T}\right) - 1\right] \partial_x c_\infty. \qquad (S33)$$

---

[s] This is equivalent to assuming that the fluid is at rest in the far field, $v_x|_{z\to\infty} = 0$, and computing the corresponding boundary velocity $v_x(0)$.

For purely steric hard-sphere interactions between MinD and the cargo molecules,

$$\Psi(z) = \begin{cases} \infty, & z \leq R_p \\ 0, & z > R_p \end{cases} \tag{S34}$$

we can explicitly perform the integral in Eq. (S33). Then, the diffusiophoretic slip is given by

$$\boldsymbol{v}_g = -\frac{k_B T}{\eta} \frac{R_p^2}{2} \boldsymbol{\nabla} c_p . \tag{S35}$$

Thus, we have recapitulated the conceptual calculations by Marbach & Bocquet[31], as well as by Golestanian[32] to show how a density gradient of proteins can induce a diffusiophoretic drift (advection) via hydrodynamic interactions and an interaction potential. In the next section, we will discuss these results in depth.

2. Diffusiophoretic drift requires solute fluxes

At first glance, Eq. (S35) could be interpreted as a diffusiophoretic drift which is driven by a density gradient of solute molecules (in our case the MinD proteins). However, such an interpretation overlooks the fact that according to Fick's laws, particle density gradients and fluxes are closely related. Using the Stokes-Einstein relation for the diffusion coefficient of the solute molecules (MinD, assuming spherical particles in 3D solution), $D_p = k_B T / (6 \pi \eta R_p)$, and Fick's first law, $\boldsymbol{j}_p = -D_p \boldsymbol{\nabla} c_p$, Eq. (S35) can be rewritten as

$$\boldsymbol{v}_g = -3 \pi R_p^3 \, D_p \boldsymbol{\nabla} c_p = 3 \pi R_p^3 \, \boldsymbol{j}_p . \tag{S36}$$

In this form, the equation for the diffusiophoretic slip velocity reveals that the diffusiophoretic drift of a cargo molecule (in 3D and at low densities) is directly related to the diffusive flux $\boldsymbol{j}_p$ of the solute molecules (MinD). Consequently, while from Eq. (S35) one could conclude that a finite gradient $\boldsymbol{\nabla} c_p$ of solute molecules (MinD) is sufficient to observe a diffusiophoretic effect, Eq. (S36) shows that actually finite solute fluxes $\boldsymbol{j}_p$ are required. To further elucidate this point, let us suppose that there are no fluxes of solute molecules in the laboratory frame, and that instead their spatial distribution is fully determined by some stationary trapping potential V^t. Then the total flux of solute molecules in the laboratory frame becomes:

$$D_p \partial_x c_p + \frac{c_p D_p}{k_B T} \partial_x V \equiv 0 . \tag{S37}$$

---

[t] Such a trapping potential could be realized via an electrostatic field that selectively acts on charged solutes but does not affect the electrically neutral cargo. Typically, such an electrostatic field will lead to an electrophoretic current of the charged solutes. In a closed container, this electrophoretic current will eventually be balanced by a diffusive flux, yielding a steady state with a vanishing net flux of the charged solutes.

34

Inserting Eq. (S37) (flux-free steady state condition of the Smoluchowski equation in the laboratory frame) into Eq. (S22) (Smoluchowski equation in the co-moving frame of the cargo, in steady state and in addition also considering the trapping potential V), and using translation invariance of the interaction potential Ψ along the x-axis, this yields the following balance equation for the x-component of the flux of solute molecules in the co-moving frame of the cargo molecule:

$$-j_{p,x} = D_p \partial_x c_p + \frac{c_p D_p}{k_B T} \partial_x V - c_p v_x = -c_p v_x \,. \tag{S38}$$

Thus, if the advective fluxes that arise from some potential V and the diffusive fluxes balance in the laboratory frame, then the net flux in the co-moving frame will be determined solely by the velocity v_x of the co-moving frame and the local density c_p. In addition, as before, we assume that the cargo is rigid and thus that the cargo wall is impermeable, so that the fluid flow velocity and the particle fluxes along the normal axis (z-axis) vanish, $v_z = 0$ and $j_{p,z} = 0$. Together with the steady-state condition, $\partial_t c_p = -\boldsymbol{\nabla} \cdot \boldsymbol{j}_p = 0$, and the incompressibility of the fluid, $\boldsymbol{\nabla} \cdot \boldsymbol{v} = \partial_x v_x + \partial_z v_z = \partial_x v_x = 0$ (equivalent to the translation invariance that we have assumed before), this gives:

$$\boldsymbol{\nabla} \cdot \boldsymbol{j}_p = v_x \, \partial_x c_p = 0 \,. \tag{S39}$$

Thus, there is no diffusiophoretic slip velocity ($v_x = 0$) and the diffusiophoretic cross-mobility vanishes if there are no solute particle fluxes[u]. In that case, the distribution of cargo particles in response to the solute particles reduces to an equilibrium problem, which has been discussed in sections I.3 "Flory-Huggins theory of mixing: an equilibrium picture" and II.2 "Static volume exclusion cannot explain cargo transport". In summary, the main insight gained in this paragraph is that a diffusiophoretic slip of the cargo molecule can only occur if there are solute (MinD) fluxes. In contrast, in the absence of particle fluxes, the spatial distribution of all particles is determined solely by a free energy functional, i.e. by the laws of equilibrium thermodynamics.

---

[u] Another way to see this is by starting with the hydrodynamic pressure field, Eq. (S29), but with a position-dependent hydrostatic pressure in the far field: $P(x,z) = P_\infty(x) + k_B T (c_p - c_\infty)$. Assuming that the fluid is at rest in the far field, where the interaction potential vanishes, the x-component of the Stokes equations, cf. Eq. (S23a), in the far field is then given by $\partial_x P_\infty + c_\infty \partial_x V = 0$. If the distribution of solutes in the far field is determined by the potential V, cf. Eq. (S37), then the total driving force of the fluid vanishes, $\partial_x P(x,z) + c_p \partial_x V = 0$, which implies a vanishing diffusiophoretic slip velocity (i.e. the boundary velocity $v_x(0)$ vanishes).

35

3. Relation to our phenomenological approach to diffusiophoresis

The hydrodynamic approach discussed in sections III.1 "Illustrative derivation of the diffusiophoretic drift velocity in 3D solutions" and III.2 "Diffusiophoretic drift requires solute fluxes" relies on the assumption that particle densities are small. In the following, we will compare these results to the corresponding results of our Maxwell-Stefan-like phenomenological theory in the limit of small densities. We will indicate analogous terms in square brackets. The hydrodynamic approach, Eq. (S35), yields the following relation for the net flux of cargo molecules:

$$\boldsymbol{j}_g = -D_g \boldsymbol{\nabla} c_g - c_g \left[3\pi R_p^3\right]\left[D_p \boldsymbol{\nabla} c_p\right]. \tag{S40}$$

The corresponding current for the cargo molecules obtained from the Maxwell-Stefan-like phenomenological theory, Eq. (S8), in the limit of small densities (where self-diffusion is density-independent) and for two interacting particle species reads:

$$\boldsymbol{j}_g = -\frac{k_B T}{\xi_g} \boldsymbol{\nabla} c_g - c_g \left[\frac{\zeta_{pg}}{\xi_g}\right]\left[\frac{k_B T}{\xi_p} \boldsymbol{\nabla} c_p\right]. \tag{S41}$$

In our experiments, the resulting patterns are in a steady state (cf. Fig. 1b in the main text). The solute (MinD) molecules are in a nonequilibrium steady state with a finite flux $\boldsymbol{j}_p \neq 0$, due to their ATP-driven membrane (un)binding dynamics. In contrast, the *passive* cargo molecules (which are permanently bound to the planar membrane) can only relax towards a thermal equilibrium state with vanishing fluxes $\boldsymbol{j}_g = 0$.

Solving Eq. (S40) in the flux-free steady state, one finds that the distribution of cargo molecules in response to a gradient of proteins in a 3D solution is given by:

$$c_g(c_p) = c_g(0) \exp\left[-3\pi R_p^2 R_g \, c_p\right]. \tag{S42}$$

We can rewrite this equation, Eq. (S42), in terms of the volume fraction that is occupied by solute, $\theta_p = \frac{4}{3}\pi R_p^3 c_p$, and obtain:

$$c_g(\theta_p) = c_g(0) \exp\left[-\frac{9}{4}\frac{R_g}{R_p} \, \theta_p\right]. \tag{S43}$$

Analogously, Eq. (S41) yields

36

$$c_g(c_p) = c_g(0) \exp\left[-\frac{\zeta_{pg}}{\xi_p}c_p\right] = c_g(0) \exp\left[-\frac{c_p}{c_\times}\right], \tag{S44}$$

where we have defined the typical interaction parameter in the same way as in the main text $c_\times^{-1} = \zeta_{pg}/\xi_p$. In the main text, we have then expressed the interaction parameter in terms of the solute size (2D projected area), $\theta_\times^{-1} = 1/(a_p c_\times)$, where the surface fraction occupied by solute is given by $\theta_p = a_p c_p$.

We note that the stationary distributions that result from the 3D hydrodynamic theory, Eq. (S43), and from our Maxwell-Stefan-like phenomenological approach to particle diffusion on a 2D membrane, Eq. (S44), have identical mathematical form in the low-density limit. Furthermore, the corresponding transport equations that describe the dynamics before the onset of the steady state, Eqs. (S40) and (S41), are also formally equivalent. Keeping in mind all of our reservations concerning the applicability of the 3D hydrodynamic theory to our experimental setup (cf. section III.1 "Illustrative derivation of the diffusiophoretic drift velocity in 3D solutions"), we make a leap of faith and assume that Eqs. (S43) and (S44) are identical. Then, the interaction parameter $\theta_\times^{-1}$ would be given by

$$\theta_\times^{-1} = \frac{9}{4}\frac{R_g}{R_p}, \tag{S45}$$

where R_g is the radius of a cargo particle and R_p is the radius of a solute molecule (MinD dimer). For cargo molecules that are 22 times larger in diameter than the solute molecules (naively approximating the rod-like cargo as a sphere of radius $110\ nm$ and the MinD dimer as a sphere of radius 5 nm), this yields a value of $\theta_\times^{-1} \sim 50$. In comparison, our fitting procedure of the reduced model (cf. Fig. 3b in the main text and Extended Data Fig. 5h) yielded typical values around $\theta_\times^{-1} \sim 10^v$, while in our full model we used typical values around $\theta_\times^{-1} \sim 300^w$. While this comparison between the interaction parameters that one would expect from a 3D hydrodynamic theory and our 2D interaction parameters neglects many important details like the geometry of the problem, it illustrates conceptually that hydrodynamic interactions between different particles might actually be sufficient to drive a diffusiophoretic drift in our experiments. Given the relevance of 2D surfaces (membranes) and membrane-bound proteins

---

[v] To obtain our fit curves, we neglected entropic repulsion between different cargo molecules that arises due to volume exclusion. In doing so, our fitted parameters are likely smaller than the "true" interaction parameters.

[w] As discussed in section I.3 "Flory-Huggins theory of mixing: an equilibrium picture", for our full model we used a strong entropic repulsion term for the DNA origamis that originates from Flory-Huggins theory. Assuming an ideal solution instead yields a weaker repulsion and thus requires weaker interaction parameters.

37

for all forms of life, we believe that it might be interesting to generalize the current framework of diffusiophoresis[31,32] to a 2D+3D hydrodynamic setting.

In closing we would like to note that there may also be a second mechanism for the coupling of different particle fluxes, namely kinetic interactions. Specifically, our simple estimates of the Reynolds number suggest that inertial effects may be significant. This is further underlined by the small mean free path between the involved membrane-bound particles of only 46 Å. For example, in the case of an ideally elastic frontal collision, the momentum transfer during a single collision event is given by

$$\Delta p = -2\Delta v \frac{m_1 m_2}{m_1 + m_2}. \tag{S46}$$

Such a momentum transfer via particle collisions directly yields the coupling term in Eq. (S8).

To summarize, in this section we have discussed that the phenomenological coupling between particle fluxes in the Maxwell-Stefan-like phenomenological theory may originate from hydrodynamic interactions or from momentum transfer via direct interactions, yielding two microscopic mechanisms that can lead to a mesoscopic friction between different molecular species.

38

Supplementary Figures
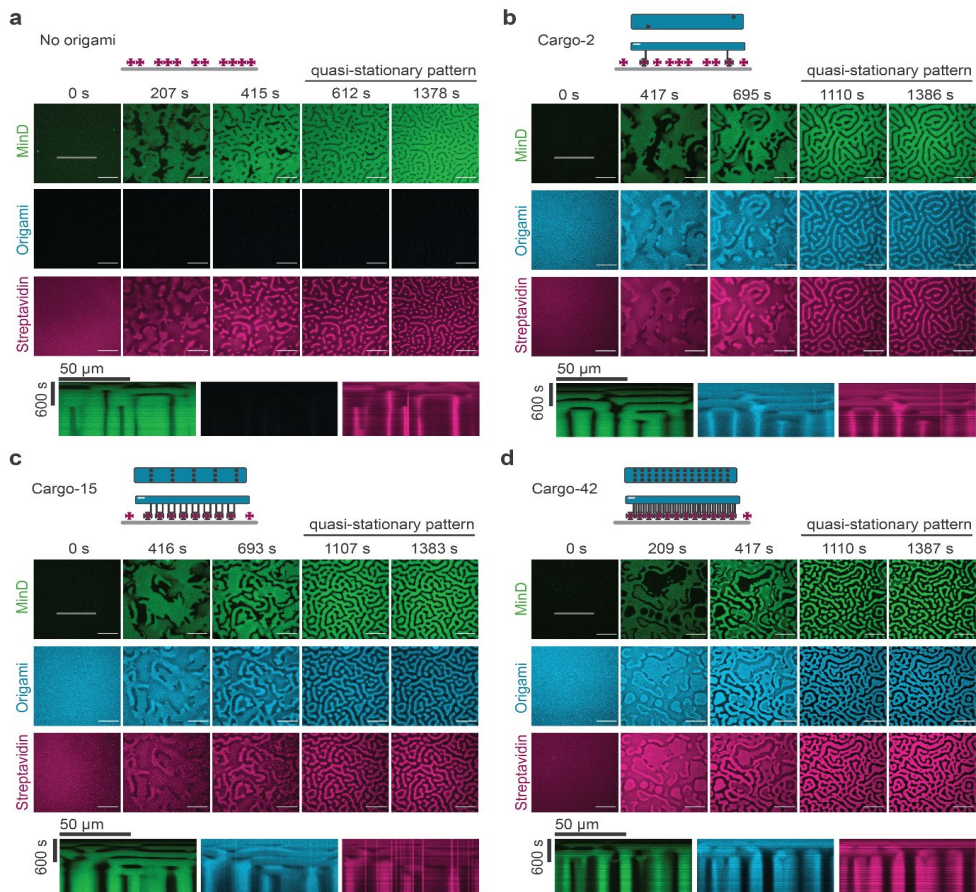
Supplementary Figure S1: MinDE induces pattern formation of cargo from an initially homogenous state. Representative time-series and kymograph (along line selection) of MinDE self-organization, which induces patterns of DNA origami and streptavidin when **a**, no origami, **b**, cargo-2, **c**, cargo-15 and **d**, cargo-42 is present (1 µM MinD (30% EGFP-MinD), 1.5 µM MinE-His, in absence or presence of 0.1 nM origami-Cy5 with 2, 15 or 42 biotinylated oligonucleotides, Alexa568-streptavidin). Panel b is identical to Figure 1b,c. Scale bars: 50 µm

39
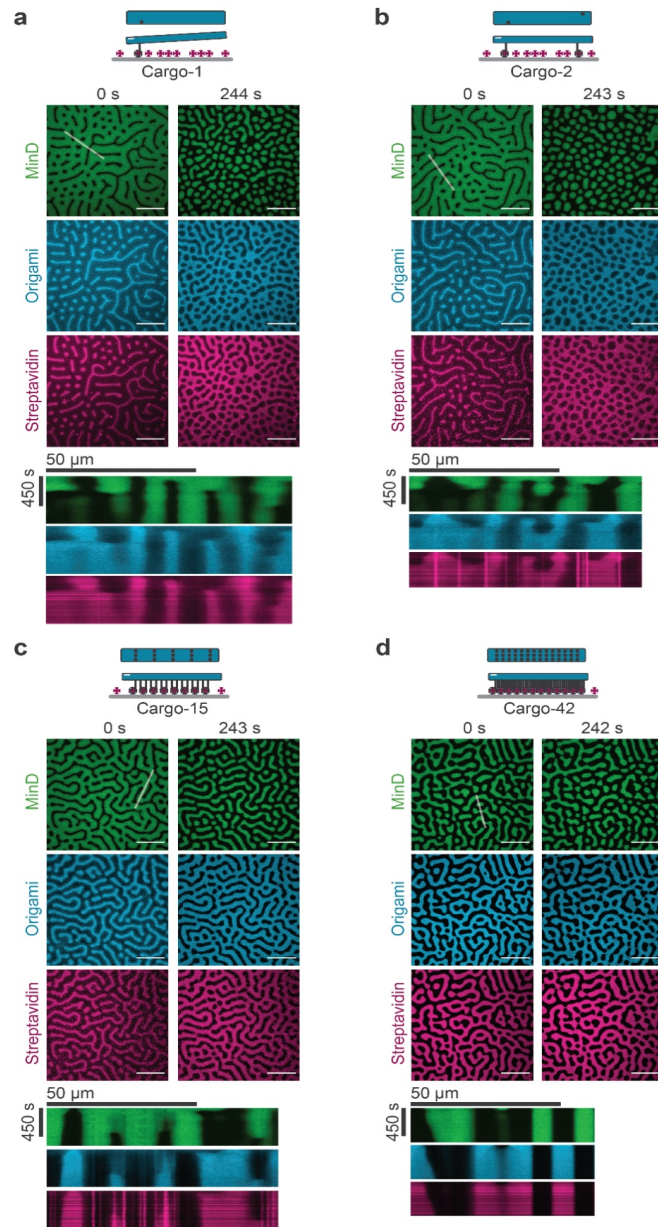
Supplementary Figure S2: Changes in the MinDE patterns are mimicked by cargo. Representative time-series and kymograph showing changes in MinD and cargo molecule patterns in presence of **a**, cargo-1, **b**, cargo-2, **c**, cargo-15 and **d**, cargo-42 (1 µM MinD (30% EGFP-MinD), 1.5 µM MinE-His, origami-Cy5 with 1, 2, 15 or 42 biotinylated oligonucleotides, Alexa568-streptavidin) upon addition of more MinE (addition of 1.5 µM MinE-His). MinE addition directly before t = 0 s. Scale bars: 50 µm

40
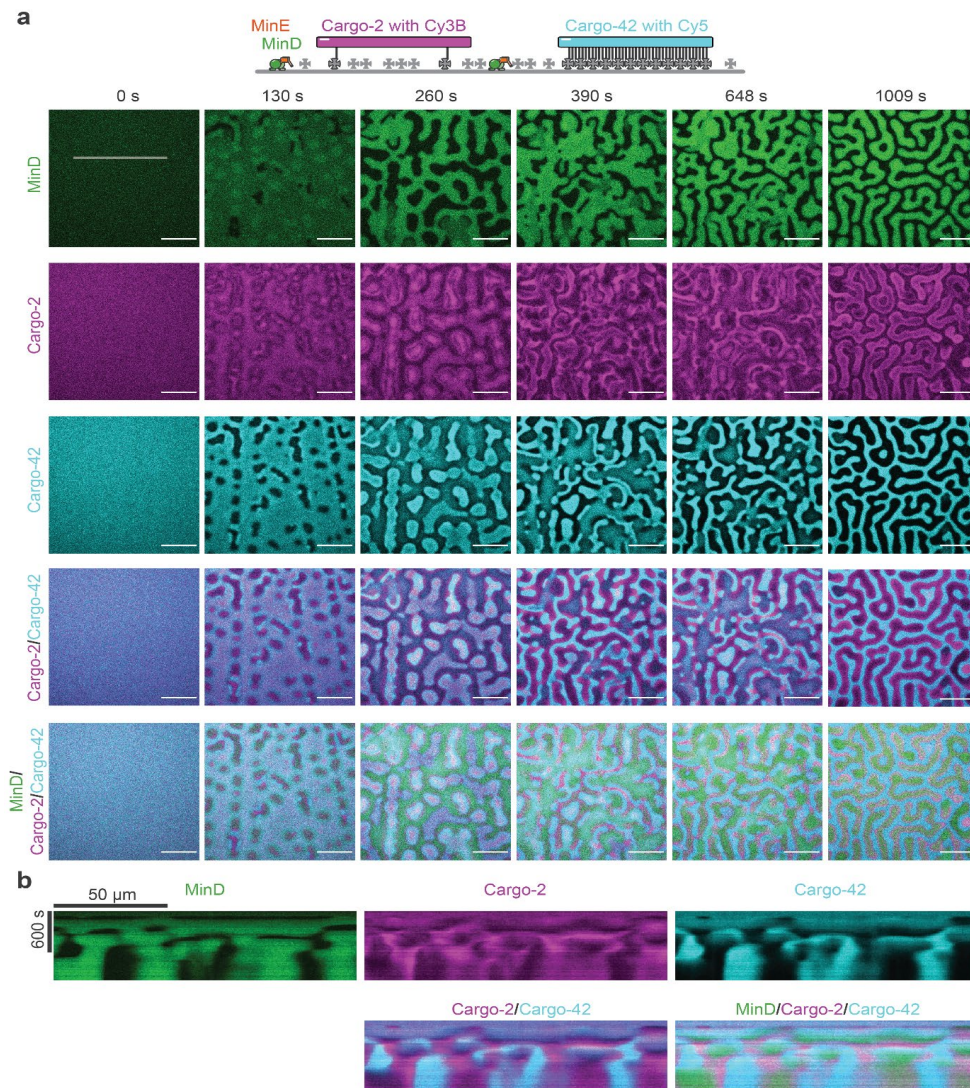
Supplementary Figure S3: MinDE induces pattern formation of two distinct cargoes, cargo-2 and cargo-42, from an initially homogenous state. a, Representative time-series of MinD, cargo-2 and cargo-42 pattern formation. ATP is added to start self-organization directly before t=0 s (1 µM MinD (30% EGFP-MinD), 1.5 µM MinE-His, 50 pM origami-Cy3B with 2 biotinylated oligonucleotides, 50 pM origami-Cy5 with 42 biotinylated oligonucleotides, non-labelled streptavidin). Scale bars: 50 µm **b**, Kymographs of the line selection shown in a.

41
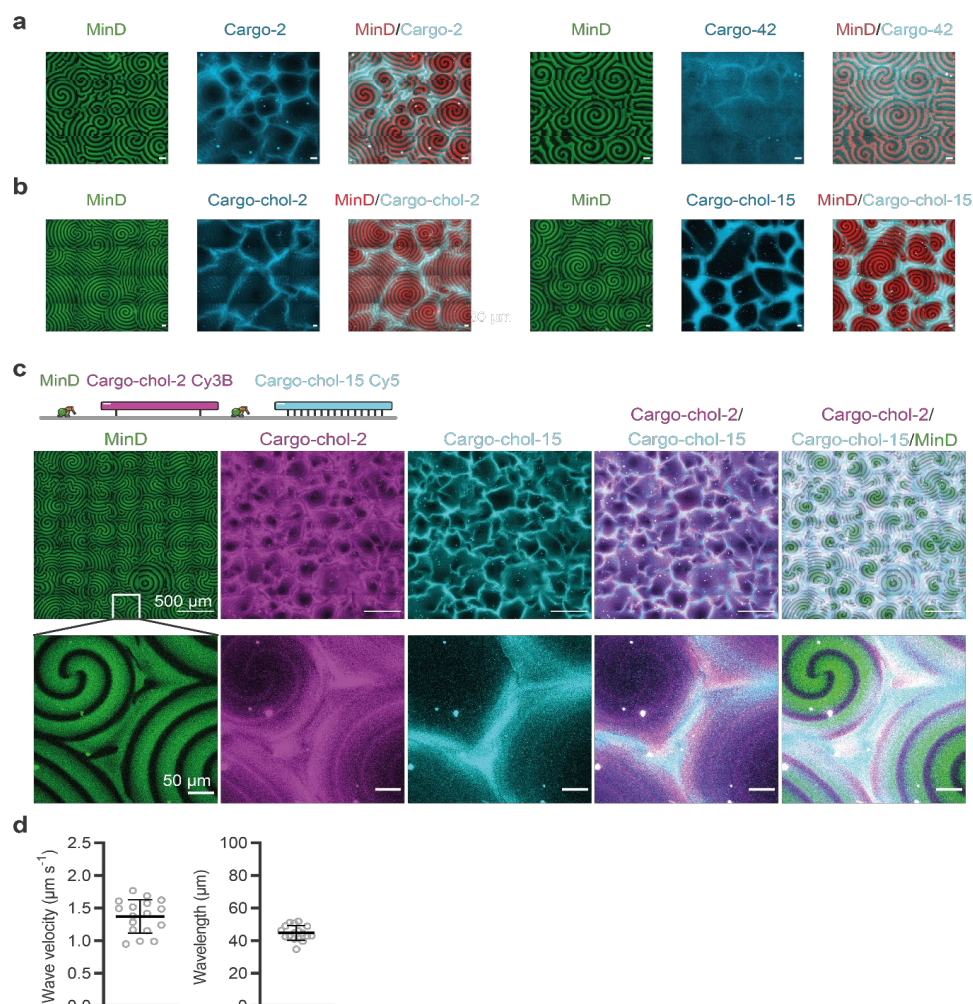
Supplementary Figure S4: Dynamic MinDE waves transport and sort cargo, establishing large-scale gradients. Representative images of large scale gradients originating from transport of **a**, cargo-2 and cargo-42 and **b,** cargo-Chol-2 and cargo-chol-15 (1 µM MinD, 5 µM His-MinE, with a, 0.1 nM origami-Cy5 with 2 or 42 biotinylated oligonucleotides, non-labeled streptavidin or b, 0.1 nM origami-Cy3b with 2 or 15 hybridizing oligonucleotides, 10 nM TEG-cholesteryl oligonucleotide) Scale bars: 50 µm. Overlaid images are identical to Figure 5c. **c,** Representative images of individual and overlaid channels of sorting of cargo-chol-2 and cargo-chol-15 by MinDE waves (1 µM MinD (30% EGFP-MinD), 5 µM His-MinE with 50 pM origami-Cy3b with 2 and 50 pM origami-Cy5 with 15 hybridizing oligonucleotides, 10 nM TEG-cholesteryl oligonucleotide). Scale bars: top, 500 µm; bottom, 50 µm. **d,** Wave velocity and wavelength of MinDE waves on unconstrained bilayers in presence of cargo-2, cargo-chol-2 or cargo-chol-15 with N=17 analysed time-series.
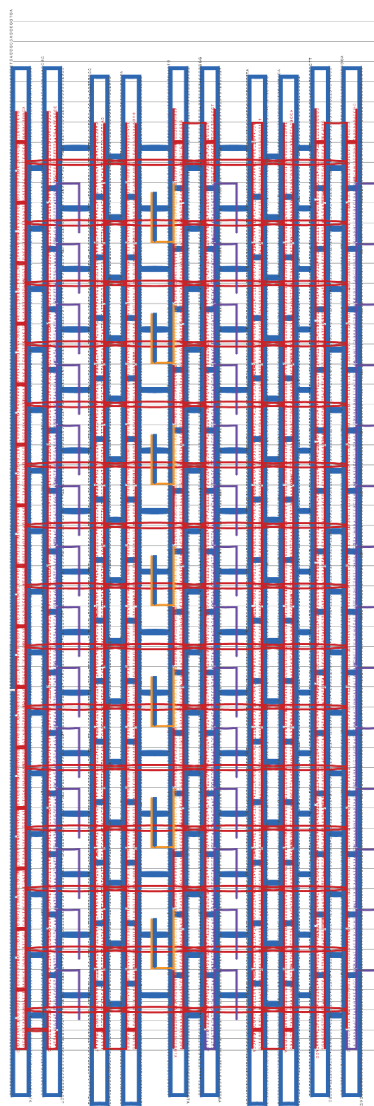
Supplementary Figure S5. Design of the elongated 20-helix bundle DNA origami with 42 handle positions. The dye-modified and connector oligonucleotides required for fluorescence detection are highlighted in orange, the 42 possible positions for incorporation of biotinylated oligonucleotide handles for binding to streptavidin in purple, core staples in black and the M13 p7249 scaffold is coloured in blue.

43

Supplementary Tables

Supplementary Table 1: Model Parameters and variables. Overview of the parameters and all dependent variables used in the Flory-Huggins type and phenomenological Maxwell-Stefan type theories.

Parameter	Value	Explanation
$\theta_\times^o$	200	Interaction parameter between origami scaffold and MinD, in terms of MinD coverage
$\theta_\times^s$	10	Interaction parameter between streptavidin and MinD, in terms of MinD coverage
n	1—42	Number of streptavidin attached to origami

Estimated from experiments:

$\overline{\theta_p}$	0.0825	Average MinD surface coverage. Derived from measured densities[1,2].
$\overline{\theta_{o+}}$	0.55	Average origami surface coverage (distal), if all available DNA origami in the assay (0.1 nM) were to bind to the available streptavidin molecules.
$\overline{\theta_{s+}}$	0.165	Average surface coverage of available streptavidin molecules (free + bound). Derived from measured densities[2].

Dependent variables:

$\overline{\theta_o}$	$\min(\overline{\theta_{o+}}, \overline{\theta_{s+}}\, a_o/a_c)$	Average origami surface coverage (distal), which is limited by the density of available streptavidin molecules.
$\overline{\theta_s}$	$\overline{\theta_{s+}} - \overline{\theta_o}\, a_c/a_o$	Average surface coverage of free streptavidin molecules.

44

Supplementary Table 2. List of plasmids used in this study.

Plasmid name	Source
pET28a-His-MinD_MinE	[39] (Addgene # 133621)
pET28a-His-EGFP-MinD	[40] (Addgene # 133622)
pET28a-His-MinE	[39]
pET28a-MinE-His	[41] (Addgene # 133623)
pREP41X	Susan Forsburg[42]
pREP42X	Susan Forsburg[42]
pMBL-sfGFP-MinDMinE	[41]
pET28a-mCherry-2xEcMTS	[2] (Addgene # 133624)
pET28a-mCherry-GGBSMTS	[2]
pREP41X-sfGFP-MinD	This study
pREP42X-MinE	This study
pREP41X_coex_sfGFP-MinD_MinE	This study
pREP42X-mCherry-BsMTS	This study
pREP42X-mCherry	This study
pREP42X-mCherry-BsMTS	This study

Supplementary Table 3. List of primers used in this study.

Name	Sequence 5' to 3'
BR64	CTTGTACAGCTCGTCCATGCC
BR223	GTTAAATCATACCTCGAGGGATCCACCATGAGCAAAGGAGAAGAACTTTTCAC
BR224	GACATTCCTTTTACCCGGGGATCCTTATCCTCCGAACAAGCGTTTGAG
BR225	GTTAAATCATACCTCGAGGGATCCACCATGGCATTACTCGATTTCTTTCTCTCG
BR226	GACATTCCTTTTACCCGGGGATCCTTATTTCAGCTCTTCTGCTTCCGGTAAG
BR227	GTTAAATCATACCTCGAGGGATCCACCATGGTGAGCAAGGGCGAG
BR228	GACATTCCTTTTACCCGGGGATCCTTAAGAACGAACACCGAAGAAAGATTTG
BR229	GATAATAATGGTTTCTTAGACGTGTCGATCGACTCTAGAGGATCAGAAAATTATC
BR230	GAAAAGTGCCACCTGACGTGCATTACTAATAGAAAGGATTATTTCACTTCTAATTACACAAATTCCG
KN_294	CAGAAACGCTGGTGAAAGTAAAA
KN_312	TTTTACTTTCACCAGCGTTTCTG
KN_644	GCATGGACGAGCTGTACAAGTAAGGATCCCCGGGTAAAAGGAATGTC
KN_645	TTCCTTTTACCCGGGGATCCCCGCAAGCTTTTATCCTCCGAACA
KN_646	GGATCCCCGGGTAAAAGGAATGTC
KN_647	GATCCCTCGAGGTATGATTTAAC

45

Supplementary Methods

Generation of plasmids

DNA fragments and vector backbones were amplified by PCR or obtained by restriction enzyme digestion so that they contained 15-20 bp overlaps between adjacent fragments that were combined using the GeneArt Seamless Cloning and Assembly Enzyme Mix (Thermo Fisher Scientific, Waltham, USA). pREP41X-sfGFP-MinD encodes the *E. coli* MinD with an N-terminal fusion of sfGFP, where the sfGFP-MinD coding region was amplified from pMBL-sfGFP-MinDMinE[41] (primer BR223/BR224) and the backbone was obtained by digesting pREP41X with BamHI. pREP42X-MinE encodes the *E. coli* MinE, where the MinE coding region was amplified from pMBL-sfGFP-MinDMinE[41] (primer BR225/BR226) and the backbone was obtained by digesting pREP42X with BamHI. pREP41X_coex_sfGFP-MinD_MinE encodes sfGFP-MinD and MinE under the same promoter that is duplicated on the plasmid. It was generated by amplifying the backbone from pREP41X-sfGFP-MinD (primer KN_646/KN_647) and the MinE fragment from pREP42X-MinE (primer R229/BR230). pREP42X-mCherry-BsMTS encodes the C-terminal fusion of the *B. subtilis* MinD membrane targeting sequence (MTS) (GSGKGMMAKIKSFFGVRS; AA 254-268) to mCherry, where the mCherry- BsMTS coding region was amplified from plasmid pET28a-mCherry-GGBSMTS[2] (primer BR227/BR228) and the backbone was obtained by digesting pREP42X with BamHI. pREP42X-mCherry encodes mCherry and was obtained by amplifying two regions from pREP42X-mCherry-BsMTS (primer KN_294/BR64, KN_312/KN_644). pREP42X-mCherry-2xEcMTS encodes the C-terminal fusion of two copies of the *E. coli* MinD MTS (GSGIEEEKKGFLKRLFGGGGSIEEEKKGFLKRLFGG; AA 256–270) to mCherry and was obtained by amplifying two regions from pREP42X-mCherry-BsMTS (primer KN_294/KN_647, KN_312/KN_646) and the insert was amplified from pET28a-mCherry-2xEcMTS[2] (primer KN_645/BR227).

S. pombe culture and transformation

YES media was prepared from yeast extract (5 g/l), glucose (30 g/l) and adenine, histidine, leucine, uracil and lysine (each 225 mg/l). Selective medium was prepared from EMM broth (Formedium, Norfolk, Great Britain) supplemented with adenine, histidine, leucine, uracil and lysine (each 225 mg/l) from which either leucine, uracil or both were omitted for selection of *S. pombe* carrying pREP41X, pREP42X or both plasmids, respectively. Solid medium was prepared with 2% Difco Bacto Agar.

46

For transformation a 5 ml YES media pre-culture was inoculated with FY61 and grown at 30 °C, 220 rpm for 16 h. A 50 ml YES culture was inoculated 1:200 from the pre-culture and grown at 30 °C, 220 rpm for 30-48 h until an OD600 of 0.5. Cells were pelleted by centrifugation (4 °C, 4000 g, 10 min) and washed once with 25 ml 1x TE buffer (10 mM Tris-HCl pH 7.5, 1 mM EDTA). After another centrifugation step, cells were resuspended in 1 ml LiAC/1xTE buffer (10 mM Tris-HCl pH 7.5, 1 mM EDTA, 100 mM Lithium Acetate pH 7.5) and incubated for 30 min at 30 °C. 200 µl of the suspension was transferred into a new tube and mixed with 20 µl of sonicated salmon sperm DNA (10 mg/ml, Agilent Technologies, Santa Clara, USA) as carrier and 1 µg plasmid, and subsequently incubated at room temperature for 10 min. Afterwards 1.2 ml of PEG/LiAc/TE buffer was added (40% PEG4000, 10 mM Tris-HCl pH 7.5, 1 mM EDTA, 100 mM Lithium Acetate pH 7.5) and the mixture was incubated for 3 min at 30 °C, 250 rpm. DMSO was added to a final concentration of 5%, before heatshock for 15 min at 42 °C. Cells were pelleted at 7000 g for 30 s, resuspended with 300 µl 1xTE buffer and spread on plates with the respective selective medium. After 3-5 days of incubation at 30 °C colonies were picked and restriked. Individual clones were picked and grown in selective medium to generate glycerol stocks (50% glycerol).

47

Supplementary Notes

Supplementary Note 1:

The lower facet of the 8 nm high DNA origami rod is located about 5-11 nm above the membrane, as it is bound to the membrane via several spacers: the dsDNA oligonucleotide linker, a TEG-biotin moiety and the streptavidin molecule. The length of the dsDNA linker can be estimated to about 6.1 nm taking into account the rise per basepair (bp) of 0.34 nm of B-DNA[43]. The oligonucleotide is connected to the anchoring biotin moiety via TEG with a length of about 1.4 nm[18]. Thus, the total linker length can be estimated to be about 7 nm. As the persistence length of dsDNA is about 50 nm[43–45], the dsDNA linker is rigid. However, the connection to the DNA origami is only single stranded giving the dsDNA linkers freedom for bending[46]. The height of membrane-bound streptavidin was measured to be ~4 nm[47] in good agreement with measurements from EM/crystal structures[48,49].

Supplementary Note 2:

To verify that it is indeed the effective cargo size (membrane footprint) rather than the number of membrane attachment sites (streptavidin building blocks), i.e. the membrane diffusion (Fig. 3c in the main text), that determines the extent of the cargo transport, we employed an alternative anchoring strategy for the DNA origami structures. The resulting cargo (cargo-chol) only consists of the DNA origami scaffold, in which we incorporated oligonucleotides at the bottom positions that could hybridize with oligonucleotides modified with a TEG-cholesteryl moiety that directly inserts into the lipid bilayer (Extended Data Fig. 4). As in the case for the composite cargo (consisting of a DNA origami scaffold and streptavidin building blocks) the total length of the linker is about 7 nm (6.1 nm dsDNA, 1.4 nm TEG moiety) and the connection of the linker to the DNA origami is single-stranded giving it freedom for bending. Hence, in this case the lower facet of the origami scaffold is located at an altitude of at most 7 nm above the membrane and thus the origami body can presumably directly interact with MinDE on the membrane. Increasing the number of attachment sites on cargo-chol from 2 to 15 (cargo-chol-2 and cargo-chol-15) slowed diffusion in absence of MinDE similar to our observations for the composite cargo (Extended Data Fig. 5a) and in line with previous studies on membrane diffusion of DNA origami nanostructures[18,46,50,51]. Cargo-chol-2 and cargo-chol-15 diffused slightly faster than the respective composite cargoes cargo-2 and cargo-42, which can presumably be explained by streptavidin binding 2-3 biotinylated lipids[3]. In the presence

48

of 1 μM MinD, both cargo-chol-2 and cargo-chol-15 are slowed similar to the composite cargoes, which indicates that they experience an additional friction due to the presence of MinD (Extended Data Fig. 5a). In contrast to the composite cargo, increasing the number of attachment sites on cargo-chol also strongly increased their ability to bind to the membrane (Extended Data Fig. 5e) as previously observed for cholesteryl-bound DNA origami nanostructures[46,50]. To account for these different membrane densities, we analysed the redistribution of cargo-chol-2 and cargo-chol-15 by MinDE at three different concentrations, determining the contrast of the resulting images and the interaction parameter (Extended Data Figs. 4b, 5b-d,h). While increasing membrane densities of cargo-chol-2 and cargo-chol-15 were accompanied by increasing contrast, it is clear that even at the lowest densities of cargo-chol-2 the contrast is higher than that of cargo-2 which diffuses similarly fast as cargo-chol2 (Extended Data Fig. 5g). At the highest membrane densities, the contrast of cargo-chol-2 and cargo-chol-15 rather resembles that of cargo-42. By fitting the 2D histograms of the images, we determined the interaction parameters of cargo-chol-2 and cargo-chol-15 (Extended Data Fig. 5h). The interaction parameter of cargo-chol-15 is slightly larger than that of cargo-chol-2, but both are on the same order of magnitude as that of cargo-42. When we let MinDE self-organize in the presence of differently labelled cargo-chol-2 and cargo-chol-15, we found that MinDE also induced sorting of these two cargo molecules. Similar to the composite cargoes, we found that the cargo with the higher interaction parameter, cargo-chol-15 was localized to MinD-free regions and was framed by cargo-chol-2 (Extended Data Fig. 5i). Importantly, that cargo-chol-2, which diffuses similar or even slightly faster than cargo-2 and one order of magnitude faster than cargo-42, interacts with MinD to a similar extent as cargo-42 shows that indeed the effective size of the cargo molecules determines the extent of the transport: the membrane footprint and thus the effective size of cargo-chol-2 is larger because presumably the entire origami scaffold with a membrane footprint of 1760 nm^2 (110 nm x 16 nm) interacts with MinD, whereas in the case of cargo-2 and cargo-42 mostly the streptavidin building blocks (membrane footprint of a single streptavidin: 25 nm^2) interact with MinD (total membrane footprint of cargo-2: 50 nm^2, cargo-42: 1050 nm^2).

Supplementary Note 3:

Since we have demonstrated MinDE-induced cargo transport with experiment and theory, we wondered whether it is possible to directly observe biased cargo motion on a single cargo level

49

using single particle tracking. To this end we tracked single cargo molecules under conditions where regular unidirectional MinDE waves had formed (Extended Data Fig. 8). As in our simplified single-particle tracking setup (i.e. with a homogeneous density of MinD, Fig. 3c in the main text, Extended Data Fig. 5a), we found that particles seemed to diffuse faster when located inside the MinD minima, i.e. in regions with low MinD density, and slower in the MinD maxima. However, we could not detect any directed motion. To confirm these experimental results, we made a simple theoretical estimate whether it would be possible to discern diffusion from advection in a system such as ours.

In the following, we specifically refer to our experimental realization where MinDE form traveling waves, because a stationary state with vanishing fluxes (while having the advantage of simplifying our analysis) only allows to reliably measure the stationary distribution of particles. In our experiments we have a true single particle tracking situation, i.e. a very low density of DNA origami molecules that do not interact with each other. In a situation with traveling waves, the MinDE gradients have a typical length scale of $40\ \mu m$ (Supplementary Fig. S4). The waves themselves travel at a velocity of $1.4\ \mu m\ s^{-1}$ and consist of both a forward-pointing and a backward-pointing gradient. Therefore, each cargo molecule is subjected to a forward-pointing MinD gradient over a typical time scale of $\Delta t = 30\ s$ per wave period, alternated with a backward-pointing gradient.

For single particles, the mean squared displacement due to diffusion in 2D is given by $2D_g\Delta t$, and due to advection is given by $\left(v_g\Delta t\right)^2$. The typical diffusion constant of cargo-42 in our experiments is $D_{g-42} = 0.06\ \mu m^2 s^{-1}$, while the typical diffusion constant of cargo-2 is $D_{g-2} = 0.65\ \mu m^2 s^{-1}$. Next, we will estimate the advection velocity v_g. Starting from Eq. (7) in the main text,

$$\partial_t c_g = -\boldsymbol{\nabla} \cdot \boldsymbol{j}_g = \boldsymbol{\nabla} \cdot \left[D_g \frac{(1 + c_g/c_\times)\,\boldsymbol{\nabla}c_g + (c_g/c_\times)\,\boldsymbol{\nabla}c_p}{1 + c_g/c_\times + (D_g/D_p)(c_p/c_\times)} \right], \qquad \left(\begin{matrix} \text{S47} \\ \text{7 in main text} \end{matrix} \right)$$

we invoke the low-density limit (true single particle tracking situation). With this simplification, we obtain the following equation for the cargo flux:

$$\boldsymbol{j}_g = -D_g\boldsymbol{\nabla}c_g - c_g D_g c_\times^{-1}\,\boldsymbol{\nabla}c_p \equiv -D_g\boldsymbol{\nabla}c_g + c_g v_g, \qquad \text{(S48)}$$

where the *interaction density* is given by $c_\times = \xi_p/\zeta_{pg}$. The first term of Eq. (S48) corresponds to diffusion and the second term corresponds to advection with an advection velocity of $v_g =$

50

$-D_g c_\times^{-1} \boldsymbol{\nabla} c_p$. By expressing surface densities in terms of coverage, $\theta_p = a_p c_p$ and $\theta_\times = a_p c_\times$, we may thus write the advection velocity as:

$$v_g = -D_g \theta_\times^{-1} \boldsymbol{\nabla} \theta_g .$$
$$(S49)$$

The typical effective interaction parameter is $\theta_{\times-2}^{-1} \sim 5.6$ for cargo-2 and $\theta_{\times-42}^{-1} \sim 21.4$ for cargo-42, as obtained from our fits (Fig. 3b in the main text). Overall, the MinD coverage is between 16.5% in the MinD maxima and 0% in the MinD minima. Thus, we may estimate the typical gradient of MinD coverage as $\left\| \boldsymbol{\nabla} \theta_p \right\| \approx 0.165/(20 \mu m) = 0.00825 \, \mu m^{-1}$. Taken together, these estimates yield a typical advection velocity of $v_{g-2} \approx 0.030 \, \mu m \, s^{-1}$ for cargo-2 and $v_{g-42} \approx 0.011 \, \mu m \, s^{-1}$ for cargo-42. Then, the dimensionless number

$$\frac{v_g \Delta t}{\left(2 D_g \Delta t \right)^{1/2}} \approx 0.14 \text{ for cargo-2, } 0.17 \text{ for cargo-42}$$

informs us that diffusive transport is stronger than advective transport on the scale of a single molecule. We can also make analogous estimates for cargo-chol-2 ($D_{g-c2} = 0.89 \, \mu m^2 s^{-1}$, $\theta_{\times-c2}^{-1} = 21.7$) and cargo-chol-15 ($D_{g-c15} = 0.24 \, \mu m^2 s^{-1}$, $\theta_{\times-c15}^{-1} = 24.7$), yielding dimensionless numbers of 0.65 and 0.39, respectively.

Consequently, it is difficult to discern advection from diffusion on the single molecule level. Even if we assume that the true interaction parameter is one order of magnitude larger (because we typically underfit the interaction parameters due to neglecting large particle densities), this still only yields a dimensionless factor of order unity. Combined with the back-and-forth motion of cargo due to the periodic nature of the MinDE waves, this would still make a distinction between advection and diffusion difficult.

Supplementary Note 4:

MinDE self-organization *in vitro* generally reproduces all features of their behaviour *in vivo*[52], except that the patterns *in vitro* occur on an about 10 times larger length scale than those *in vivo*[1,39,52–55]. This difference is thought to arise from differences in the physico-chemical properties of the reaction environment. For example, crowding in solution has been shown to reduce the wavelength *in vitro*[39,56,57]. Similarly, we have shown here (Fig. 1g in the main text) and previously[2] that crowding on the membrane reduces the length scale of the patterns *in vitro*. In order to test whether the difference in wavelength between *in vitro* and *in vivo* is

51

indeed caused by differences in the reaction environment, and whether MinDE patterns with a short wavelength would be able to regulate other proteins by diffusiophoresis under these more physiologically relevant conditions, we expressed MinDE as well as model peripheral membrane proteins[2] heterologously in the fission yeast *S. pombe*. In the, from *E. coli* evolutionary distant, fission yeast, other proteins can be seen as close to inert in regard to *E. coli* MinDE and the larger size and higher protein levels in *S. pombe* facilitate detection of protein dynamics by fluorescence microscopy.

Adapting a co-expression from Terbush *et al*.[58] we first designed a plasmid for co-expression of *E. coli* sfGFP-MinD and MinE under the same, duplicated promoter (Extended Data Fig. 9a). *S. pombe* cells harbouring this plasmid displayed bright foci that were dynamic. Closer inspection revealed that MinD seemed to preferentially bind to intracellular membranes over the plasma membrane. The round vesicular structures stained by MinD most likely represent vacuoles[59]. Most cells displayed traveling wave dynamics (Extended Data Fig. 9b), but also more complex dynamics and pole-to-pole oscillations could be observed (Extended Data Fig. 9c,d). In contrast, in regular sized *E. coli* MinDE usually perform pole-to-pole oscillations[54,60], in elongated *E. coli* they exhibit multi-node standing waves[54] and only in very rare cases traveling waves can be observed[61]. This deviation can be explained with the well-described geometry sensitivity of MinDE[56,62–65] and the larger dimensions of an *S. pombe* cell compared to *E. coli* (*S. pombe:* 3.5 µm x 8-14 µm[66]; *E. coli:* 0.7-1 µm x 2.6-4.0 µm[67]): in *E. coli* cells whose shape was greatly altered by mutations or custom shaping in microstructures, traveling waves and complex dynamics can also be observed[63–65]. Analysis of cells exhibiting traveling wave dynamics, allowed us to obtain an estimate of the wavelength and velocity of the MinDE dynamics in *S. pombe*. Intriguingly, the wavelength of MinDE dynamics in *S. pombe* of (8.3±1.7) µm (Extended Data Fig. 9e) was similar to the wavelength that has been reported for MinDE dynamics in *E. coli* of about 8-11 µm[52,54,55] and thus much smaller than the wavelength of MinDE self-organization *in vitro*[1,2,39]. The obtained velocity of (0.06±0.02) µm s^{-1} (Extended Data Fig. 9f) is lower than the values that have been reported for wave propagation on SLBs *in vitro* of about 0.1-0.6 µm s^{-1} [1,2,39,53]. The estimated oscillation period obtained from these values is about 140 s and thus slightly larger than the one reported for the dynamics in *E. coli* of about 40-120 s [52,54,63,68] which could be caused by differences in temperature, protein levels, density of anionic lipids, which are all factors reported to influence the velocity of wave propagation *in vivo* or *in vitro*[52].

52

As a control that the observed dynamics were indeed ascribable to MinDE self-organization, we expressed sfGFP-MinD in the absence of MinE in *S. pombe* (Extended Data Fig. 9g). As expected, sfGFP-MinD seemed to localize to the same intracellular membranes, but the overall distribution was far more homogenous and showed no obvious dynamics. Thus, MinDE self-organization can be reconstituted in the fission yeast *S. pombe*. Having shown that MinDE self-organize in *S. pombe* at a similar length scale as in their native host *E. coli*, we set out to show that MinDE can also regulate other proteins via diffusiophoresis under these physiologically more relevant conditions. To this end we constructed a second expression plasmid, that could be maintained in *S. pombe* next to the co-expression plasmid for sfGFP-MinD/MinE. For simplicity, we employed model peripheral proteins as cargo. We have previously shown that these proteins are also regulated by MinDE *in vitro*[2]: whenever MinD density was high, the density of the model peripheral membrane proteins was low. While these proteins have a much shorter membrane dwell time than the DNA origami nanostructures and thus are not subject to a net transport by MinDE[2], we believe that they also experience diffusiophoretic transport resulting in their redistribution. For expression in *S. pombe*, we generated plasmids encoding one of three different mCherry versions analogous to the ones used for the *in vitro* study[2]: soluble mCherry (mCh), mCherry fused to the membrane targeting sequence (MTS) of the *B. subtilis* MinD (mCh-MTS(BsD)) and mCherry fused to a tandem repeat of the MTS of the *E. coli* MinD itself (mCh-MTS(2xMinD)) (Extended Data Fig. 10a). When expressed in *S. pombe* in the absence of MinDE, mCh-MTS(BsD) and mCh-MTS(2xMinD) homogenously bound to cellular membranes (Extended Data Fig. 10c,d) and the soluble mCh exhibited a homogenous cytoplasmic localization (Extended Data Fig. 10b). When co-expressed with sfGFP-MinDE, the overall localization of all constructs was similar. Intriguingly, however, we found that wherever fluorescence intensity of MinDE was high, the intensity of mCh-MTS(BsD) and mCh-MTS(2xMinD) was reduced and vice versa (Extended Data Fig. 10f,g). In contrast, when MinDE was co-expressed with the soluble control protein mCh, no such changes in fluorescence intensity were observed (Extended Data Fig. 10e). Hence, MinDE-dependent transport of proteins by diffusiophoresis also occurs, when MinDE dynamics are reconstituted in *S. pombe*.

53

Supplementary References

1. Loose, M., Fischer-Friedrich, E., Herold, C., Kruse, K. & Schwille, P. Min protein patterns emerge from rapid rebinding and membrane interaction of MinE. *Nat. Struct. Mol. Biol.* **18**, 577–583 (2011).

2. Ramm, B. *et al.* The MinDE system is a generic spatial cue for membrane protein distribution in vitro. *Nat. Commun.* **9**, 3942 (2018).

3. Dubacheva, G. V. *et al.* Controlling Multivalent Binding through Surface Chemistry: Model Study on Streptavidin. *J. Am. Chem. Soc.* **139**, 4157–4167 (2017).

4. Flory, P. J. Thermodynamics of High Polymer Solutions. *J. Chem. Phys.* **10**, 51–61 (1942).

5. Huggins, M. L. Solutions of Long Chain Compounds. *J. Chem. Phys.* **9**, 440 (1941).

6. de Gennes, P.-G. *Scaling concepts in polymer physics*. (Cornell University Press, 1979).

7. Miyagi, A., Ramm, B., Schwille, P. & Scheuring, S. High-speed AFM reveals the inner workings of the MinDE protein oscillator. *Nano Lett.* **18**, 288–296 (2018).

8. Halatek, J. & Frey, E. Highly Canalized MinD Transfer and MinE Sequestration Explain the Origin of Robust MinCDE-Protein Dynamics. *Cell Rep.* **1**, 741–752 (2012).

9. Halatek, J. & Frey, E. Rethinking pattern formation in reaction-diffusion systems. *Nat. Phys.* **14**, 507–514 (2018).

10. Halatek, J., Brauns, F. & Frey, E. Self-organization principles of intracellular pattern formation. *Philos. Trans. R. Soc. B Biol. Sci.* **373**, 20170107 (2018).

11. Brauns, F., Halatek, J. & Frey, E. Phase-space geometry of reaction-diffusion dynamics. *arXiv* 1812.08684v1 http://arxiv.org/abs/1812.08684 (2018).

12. Balian, R. *From Microphysics to Macrophysics*. (Springer, Berlin, Heidelberg, 2007). doi:10.1007/978-3-540-45480-9.

13. Derjaguin, B. V., Sidorenkov, G. P., Zubashchenko, E. A. & Kiseleva, E. V. Kinetic phenomena in boundary films of liquids. *Kolloidn. Zh* **9**, 335–347 (1947).

14. Maxwell, J. C. IV. On the dynamical theory of gases. *Philos. Trans. R. Soc. London* **157**, 49–88 (1866).

54

15. Stefan, J. Über das Gleichgewicht und die Bewegung, insbesondere die Diffusion von Gasgemengen. *Sitzber. Akad. Wiss. Wien* **63**, 63–124 (1871).

16. Duncan, J. B. & Toor, H. L. An experimental study of three component gas diffusion. *AIChE J.* **8**, 38–41 (1962).

17. Krishna, R. & Wesselingh, J. A. The Maxwell-Stefan approach to mass transfer. *Chem. Eng. Sci.* **52**, 861–911 (1997).

18. Czogalla, A., Kauert, D. J., Seidel, R., Schwille, P. & Petrov, E. P. DNA origami nanoneedles on freestanding lipid membranes as a tool to observe isotropic-nematic transition in two dimensions. *Nano Lett.* **15**, 649–655 (2015).

19. Shih, Y.-L. *et al.* Active Transport of Membrane Components by Self-Organization of the Min Proteins. *Biophys. J.* **116**, 1469–1482 (2019).

20. Asakura, S. & Oosawa, F. On interaction between two bodies immersed in a solution of macromolecules. *J. Chem. Phys.* **22**, 1255–1256 (1954).

21. Sahimi, M. *Applications of percolation theory*. (Taylor & Francis, London, 1995).

22. Anderson, J. L., Lowell, M. E. & Prieve, D. C. Motion of a particle generated by chemical gradients Part 1. Non-electrolytes. *J. Fluid Mech.* **117**, 107–121 (1982).

23. Prieve, D. C., Anderson, J. L. & Lowell, M. E. Motion of a particle generated by chemical gradients Part 2. Electrolytes. *J. Fluid Mech.* **148**, 247–269 (1984).

24. Sear, R. P. Diffusiophoresis in Cells: A General Nonequilibrium, Nonmotor Mechanism for the Metabolism-Dependent Transport of Particles in Cells. *Phys. Rev. Lett.* **122**, 128101 (2019).

25. Shi, N., Nery-Azevedo, R., Abdel-Fattah, A. I. & Squires, T. M. Diffusiophoretic Focusing of Suspended Colloids. *Phys. Rev. Lett.* **117**, 258001 (2016).

26. Shin, S. *et al.* Size-dependent control of colloid transport via solute gradients in dead-end channels. *Proc. Natl. Acad. Sci. U. S. A.* **113**, 257–261 (2016).

27. Nasouri, B. & Golestanian, R. Exact Phoretic Interaction of Two Chemically Active Particles. *Phys. Rev. Lett.* **124**, 168003 (2020).

55

28. Illien, P., Golestanian, R. & Sen, A. 'Fuelled' motion: Phoretic motility and collective behaviour of active colloids. *Chem. Soc. Rev.* **46**, 5508–5518 (2017).

29. Abécassis, B., Cottin-Bizonne, C., Ybert, C., Ajdari, A. & Bocquet, L. Boosting migration of large particles by solute contrasts. *Nat. Mater.* **7**, 785–789 (2008).

30. Palacci, J., Abécassis, B., Cottin-Bizonne, C., Ybert, C. & Bocquet, L. Colloidal motility and pattern formation under rectified diffusiophoresis. *Phys. Rev. Lett.* **104**, 138302 (2010).

31. Marbach, S. & Bocquet, L. Osmosis, from molecular insights to large-scale applications. *Chem. Soc. Rev.* **48**, 3102–3144 (2019).

32. Golestanian, R. Phoretic Active Matter. *arXiv* 1909.03747v3 http://arxiv.org/abs/1909.03747 (2019).

33. Agudo-Canalejo, J., Illien, P. & Golestanian, R. Phoresis and Enhanced Diffusion Compete in Enzyme Chemotaxis. *Nano Lett.* **18**, 2711–2717 (2018).

34. Paustian, J. S. *et al.* Direct measurements of colloidal solvophoresis under imposed solvent and solute gradients. *Langmuir* **31**, 4402–4410 (2015).

35. Prieve, D. C., Malone, S. M., Khair, A. S., Stout, R. F. & Kanj, M. Y. Diffusiophoresis of charged colloidal particles in the limit of very high salinity. *Proc. Natl. Acad. Sci. U. S. A.* **116**, 18257–18262 (2019).

36. Bocquet, L. & Charlaix, E. Nanofluidics, from bulk to interfaces. *Chem. Soc. Rev.* **39**, 1073–1095 (2010).

37. Kestin, J., Sokolov, M. & Wakeham, W. A. Viscosity of Liquid Water in the Range -8 °C to 150 °C. *J. Phys. Chem. Ref. Data* **7**, 941–948 (1978).

38. Brilliantov, N. V. & Poeschel, T. *Kinetic Theory of Granular Gases*. (Oxford University Press, 2004).

39. Loose, M., Fischer-Friedrich, E., Ries, J., Kruse, K. & Schwille, P. Spatial regulators for bacterial cell division self-organize into surface waves in vitro. *Science* **320**, 789–792 (2008).

40. Zieske, K., Schweizer, J. & Schwille, P. Surface topology assisted alignment of Min protein waves. *FEBS Lett.* **588**, 2545–2549 (2014).

56

41. Glock, P. *et al.* Stationary patterns in a two-protein reaction-diffusion system. *ACS Synth. Biol.* **8**, 148–157 (2019).

42. Forsburg, S. L. Comparison of Schizosaccharomyces pombe expression systems. *Nucleic Acids Res.* **21**, 2955–2956 (1993).

43. Bloomfield, V. A., Crothers, D. M. & Tinoco, J. I. *Nucleic Acids: Structures, Properties, and Functions. University Science Books* (2000). doi:10.1007/s00897000456a.

44. Rivetti, C., Guthold, M. & Bustamante, C. Scanning force microscopy of DNA deposited onto mica: Equilibration versus kinetic trapping studied by statistical polymer chain analysis. *J. Mol. Biol.* **264**, 919–932 (1996).

45. Smith, S. B., Cui, Y. & Bustamante, C. Overstretching B-DNA: The elastic response of individual double-stranded and single-stranded DNA molecules. *Science* **271**, 795–799 (1996).

46. Khmelinskaia, A., Mücksch, J., Petrov, E. P., Franquelim, H. G. & Schwille, P. Control of Membrane Binding and Diffusion of Cholesteryl-Modified DNA Origami Nanostructures by DNA Spacers. *Langmuir* **34**, 14921–14931 (2018).

47. Scheuring, S., Müller, D. J., Ringler, P., Heymann, J. B. & Engel, A. Imaging streptavidin 2D crystals on biotinylated lipid monolayers at high resolution with the atomic force microscope. *J. Microsc.* **193**, 28–35 (1999).

48. Weber, P. C., Ohlendorf, D. H., Wendoloski, J. J. & Salemme, F. R. Structural Origins of High-Affinity Biotin Binding. *Science* **243**, 85–88 (1989).

49. Fan, X. *et al.* Single particle cryo-EM reconstruction of 52 kDa streptavidin at 3.2 Angstrom resolution. *Nat. Commun.* **10**, 2386 (2019).

50. Khmelinskaia, A., Franquelim, H. G., Petrov, E. P. & Schwille, P. Effect of anchor positioning on binding and diffusion of elongated 3D DNA nanostructures on lipid membranes. *J. Phys. D. Appl. Phys.* **49**, 194001 (2016).

51. Kocabey, S. *et al.* Membrane-Assisted Growth of DNA Origami Nanostructure Arrays. *ACS Nano* **9**, 3530–3539 (2015).

52. Ramm, B., Heermann, T. & Schwille, P. The E . coli MinCDE system in the regulation of

57

protein patterns and gradients. *Cell. Mol. Life Sci.* **76**, 4245–4273 (2019).

53. Vecchiarelli, A. G., Li, M., Mizuuchi, M. & Mizuuchi, K. Differential affinities of MinD and MinE to anionic phospholipid influence Min patterning dynamics in vitro. *Mol. Microbiol.* **93**, 453–463 (2014).

54. Raskin, D. M. & de Boer, P. A. J. Rapid pole-to-pole oscillation of a protein required for directing division to the middle of Escherichia coli. *Proc. Natl. Acad. Sci. U. S. A.* **96**, 4971–4976 (1999).

55. Touhami, A., Jericho, M. & Rutenberg, A. D. Temperature dependence of minD oscillation in Escherichia coli: Running hot and fast. *J. Bacteriol.* **188**, 7661–7667 (2006).

56. Schweizer, J. *et al.* Geometry sensing by self-organized protein patterns. *Proc. Natl. Acad. Sci. U. S. A.* **109**, 15283–15288 (2012).

57. Martos, A. *et al.* FtsZ Polymers Tethered to the Membrane by ZipA Are Susceptible to Spatial Regulation by Min Waves. *Biophys. J.* **108**, 2371–2383 (2015).

58. Terbush, A. D., Porzondek, C. A. & Osteryoung, K. W. Functional analysis of the chloroplast division complex using schizosaccharomyces pombe as a heterologous expression system. *Microsc. Microanal.* **22**, 275–289 (2016).

59. Takegawa, K. *et al.* Vesicle-mediated protein transport pathways to the vacuole in Schizosaccharomyces pombe. *Cell Struct. Funct.* **28**, 399–417 (2003).

60. Hu, Z. & Lutkenhaus, J. Topological regulation of cell division in Escherichia coli involves rapid pole to pole oscillation of the division inhibitor MinC under the control of MinD and MinE. *Mol. Microbiol.* **34**, 82–90 (1999).

61. Bonny, M., Fischer-Friedrich, E., Loose, M., Schwille, P. & Kruse, K. Membrane Binding of MinE Allows for a Comprehensive Description of Min-Protein Pattern Formation. *PLoS Comput. Biol.* **9**, e1003347 (2013).

62. Zieske, K. & Schwille, P. Reconstitution of pole-to-pole oscillations of min proteins in microengineered polydimethylsiloxane compartments. *Angew. Chemie Int. Ed.* **52**, 459–462 (2013).

63. Wu, F., van Schie, B. G. C., Keymer, J. E. & Dekker, C. Symmetry and scale orient Min

58

protein patterns in shaped bacterial sculptures. *Nat. Nanotechnol.* **10**, 719–726 (2015).

64.   Corbin, B. D., Yu, X. & Margolin, W. Exploring intracellular space: function of the Min system in round-shaped Escherichia coli. *Embo J.* **21**, 1198–2008 (2008).

65.   Männik, J. *et al.* Robustness and accuracy of cell division in Escherichia coli in diverse cell shapes. *Proc. Natl. Acad. Sci.* **109**, 6957–6962 (2012).

66.   Fantes, P. A. Control of cell size and cycle time in Schizosaccharomyces pombe. *J. Cell Sci.* **24**, 51–67 (1977).

67.   Zaritsky, A. & Woldringh, C. L. Chromosome replication rate and cell shape in Escherichia coli: Lack of coupling. *J. Bacteriol.* **135**, 581–587 (1978).

68.   Raskin, D. M. & De Boer, P. A. J. MinDE-Dependent Pole-to-Pole Oscillation of Division Inhibitor MinC in Escherichia coli. *J. Bacteriol.* **181**, 6419–6424 (1999).

69.   Meurer, A. *et al.* SymPy: symbolic computing in Python. *PeerJ Comput. Sci.* **3**, e103 (2017).

70.   Block, S. Brownian Motion at Lipid Membranes: A Comparison of Hydrodynamic Models Describing and Experiments Quantifying Diffusion within Lipid Bilayers. *Biomolecules* **8**, 30 (2018).

71.   National Center for Biotechnology Information. PubChem Database. CID=10350317, https://pubchem.ncbi.nlm.nih.gov/compound/1_2-Dioleoyl-sn-Glycero-3-Phosphocholine (accessed on July 22, 2020).

Reprint of published manuscript

59

DATA — A DIFFUSIOPHORETIC MECHANISM FOR ATP-DRIVEN TRANSPORT WITHOUT MOTOR PROTEINS

AUTHORS:

Beatrice Ramm*, **Andriy Goychuk***, Alena Khmelinskaia, Philipp Blumhardt, Hiromune Eto, Kristina A. Ganzinger, Erwin Frey and Petra Schwille

The asterisk symbol (*) indicates shared first authorship.

`00` MinDE protein patterns spatially organize artificial cargo

The following notebooks serve the purpose of an interactive playground to explore our experimental data, as well as different proposed models. We consider all models to be in quasi-steady state, since the experimental system is also in a quasi-steady state.

1. **Spatial organization of a single cargo species by MinDE:** First, we investigate how a single species of membrane-bound cargo is influenced by an externally maintained gradient of MinD proteins.

   A. **01_Experiment_1:** In a first set of experiments, we explore the spatial patterning of a single species of membrane-bound cargo. Each cargo binds permanently to the membrane via a fixed number of biotin/streptavidin anchors.

   B. **02_Theory_FH_a:** As a first theoretical approach, we investigate with a Flory-Huggins theory whether entropic effects can recapitulate the experimental observations. The idea here is that the imposed gradient of MinD proteins constrains the combinatorial entropy of mixing. We test this approach in two levels of detail:

      a. **03_Theory_FH_b:** A simplified implementation of the Flory-Huggins model that neglects saturation effects when surface coverage becomes large.

      b. **04_Theory_FH_c:** A more detailed implementation of the Flory-Huggins model that considers saturation effects.

   C. **05_Theory_MS_a:** As a second theoretical approach, we investigate whether a Maxwell-Stefan-like phenomenological model can recapitulate the experimental observations. We test this approach in two levels of detail:

      a. **06_Theory_MS_b:** An implementation of the Maxwell-Stefan-like phenomenological model that builds on 04_Theory_FH_c and thus considers membrane saturation effects.

      b. **07_Theory_MS_Fit:** Again neglecting saturation effects, we derive a fit curve from our Maxwell-Stefan-like phenomenological model and fit it to our experimental data (cf. 01_Experiment_1). As expected from our Maxwell-Stefan-like phenomenological model, we find that the interaction strength increases linearly with the number of Streptavidin anchors.

2. Second, we investigate how two species of membrane-bound cargo are influenced by

an externally maintained gradient of MinD proteins.

A. **08_Experiment_2:** We find that cargo with different effective sizes sort in a gradient of MinD proteins. These MinD proteins are maintained by biochemical reactions.

B. **09_Theory_MS_Sorting:** The Maxwell-Stefan-like phenomenological model recapitulates cargo sorting.

Spatial organization of a single cargo species by MinDE

We observe the buildup of cargo gradients in the presence of MinDE patterns. These MinDE patterns are driven out of equilibrium by biochemical reactions (Min cycling). Each cargo binds permanently to the membrane via a fixed number of biotin/streptavidin anchors.

01 What can we observe in the experiments?

This notebook serves the purpose of an interactive playground to explore our experimental data without comparing it yet to any proposed model. Therefore, we do not perform any fitting procedures in this notebook, and instead rely on numerical techniques like the generation of LOESS (locally estimated scatterplot smoothing) curves. Note that LOESS curves should be used with care and only provide a visual guide, because they can be easily skewed by outlier data.

To explore our experimental data, execute the code below. The "Images" tab contains images of all three channels. The "Correlations" tab contains cross-correlation plots. The "Quality" tab indicates whether we consider the system in quasi-steady state or not, and whether the membrane had a good quality. The "Keyfile" tab contains contains a spreadsheet with details of the experiments (e.g. the day of the experiments).

The cell below is *non-editable*. If you need to modify its contents, either make it *editable* or copy its contents to a new cell.

```
In [ ]:    # Add directory above current directory to path
           import sys; sys.path.insert(0, '..')

           # Import necessary packages
           from Source.Experiment import Data
           from Source.Visual import Experiment_1S

           path = '../Data/Experiments/1_Cargo-n/'
           data = Data.Series(
               path = path,
               extended = True,
           )

           explore = Experiment_1S.Explore(
               data,
               # Use this line to indicate the url of the jupyter notebook.
               # Typically either "127.0.0.1:8888" or "localhost:8888".
               notebook_url = "127.0.0.1:8888", port = 5006
           )
           explore.run()
```

Select the number of anchors:

| 0 | 1 | 2 | 5 | 15 | 28 | 42 |

Select frame to display:

| 0 | 1 | 2 | 3 | 4 | 5 | 6 | 7 | 8 | 9 | 10 | 11 | 12 | 13 | 14 | 15 |

File:

file_10 ▼

Gaussian smoothing range: 0

Show Coverage   Good Quality

Images   Correlations   Mean Values   Keyfile

MinD   Streptavidin   DNA_Origami

Spatial organization of a single cargo species by MinDE

We observe the buildup of cargo gradients in the presence of MinDE patterns. These MinDE patterns are driven out of equilibrium by biochemical reactions (Min cycling). Each cargo binds permanently to the membrane via a fixed number of biotin/streptavidin anchors.

02 Can we reproduce the experiments with a Flory-Huggins model that is based on the entropy of mixing?

The following notebooks serve the purpose of an interactive playground to test whether a mixing-entropy based model can reproduce our experiments. In the present notebook, we first explain the rationale that underlies this type of model.

The Flory-Huggins theory of solutions is a thermodynamic model that considers a polymer solution as a lattice gas. Each lattice site has size a_0, and each particle/polymer takes up an area of a_i, thus occupying a_i/a_0 lattice sites. In our experiments, each DNA origami scaffold crosslinks several streptavidin molecules into an effective polymer-like object.

We assume that there is no direct attraction or repulsion between different species (e.g. due to electrostatic interaction), so that we can neglect the corresponding Flory Huggins coupling parameters. Then, the Flory-Huggins free energy of mixing is determined solely by entropic terms:

$$\frac{f}{k_B T} = \sum_i c_i \log\left[a_i c_i\right] + \left[\frac{1}{a_0} \sum_i a_i c_i\right] \log\left[1 - \sum_i a_i c_i\right].\tag{1}$$

Here, a_0 is the typical size of a solvent patch (i.e. a lattice site), while a_i and c_i are the sizes and surface densities of all other particle species. The particle densitiy profile of one of the species (MinD, active) is externally maintained by reactions (Min cycling), thus placing constraints on the combinatorial entropy of mixing and the corresponding Flory-Huggins free energy of mixing. With these constraints, we then determine the distribution of all other (passive) species that minimizes the Flory-Huggins free energy of mixing. To do so, we calculate the local chemical potential $\mu_i = \partial f/\partial c_i$ that affects each particle:

$$\frac{\mu_i}{k_B T} = \log\left[a_i c_i\right] + \frac{a_i}{a_0}\log\left[1 - \sum_i a_i c_i\right] + \text{cst}.\tag{2}$$

Note that the second term of the above equation confers an effective volume exclusion between different species. Gradients in a chemical potential, $\nabla \mu_i$, correspond to effective entropic forces, which act on all particle species and drive the system towards an equilibrium steady state. The distribution of MinD proteins is maintained in a nonequilibrium steady state by off-equilibrium biochemical reactions (Min cycling). If we neglect coupling between the fluxes of different particles (we will lift this assumption in our Maxwell-Stefan-like phenomenological approach, cf. 05_Theory_MS_a), then the steady state is reached once gradients in the chemical potential of the passive particles vanish, $\mu_i = \mathrm{cst.}$ or $\nabla \mu_i = 0$, while the chemical potential gradient of the Min proteins remains finite $\nabla \mu_p \neq 0$. This corresponds to the assumption that the passive particles (cargo, streptavidin) reach an equilibrium steady state in an adiabatic response to the imposed distribution of active particles (MinD proteins). The code that is executed in the following notebooks determines numerically the corresponding surface densities of all passive particles in the equilibrium steady state.

All parameters are based on values that we have approximated from the experiments. The solvent in the proximal layer directly above the membrane is represented by patches with a size of 25nm^2 (equivalent to 0.01 in dimensionless quantities). Similarly, the solvent in the distal plane directly above the proximal plane is represented by patches with a size of roughly 250nm^2 (equivalent to 0.1 in dimensionless quantities). MinD proteins occupy up to 16.5% of the membrane and have a size of 25nm^2. Streptavidin molecules have an average surface coverage of 16.5% of the membrane and a size of roughly 25nm^2. DNA-Origami scaffolds have a surface coverage of up to 55% (cytosolic side) and a cytosolic size of 1760nm^2; the corresponding surface coverage and effective size in the proximal plane depend on the number of anchors. The added mass (integrated density) of all DNA-Origami should be constant; a model value of 0.79 corresponds to the surface coverages in the experiments.

Considered models:

1. **03_Theory_FH_b:** A simplified implementation of the Flory-Huggins model that neglects saturation effects when surface coverage becomes large. Thus, we consider only entropic effects in the proximal plane directly above the membrane, which correspond to an effective volume exclusion between MinD proteins, free streptavidin molecules, and streptavidin molecules that are crosslinked into effective polymers via the DNA origami scaffolds.

2. **04_Theory_FH_c:** A more detailed implementation of the Flory-Huggins model that considers saturation effects. Thus, in addition to entropic effects in the proximal plane directly above the membrane (due to volume exclusion), we also consider entropic effects relating to the DNA-Origami scaffolds in the distal plane directly above the

proximal plane (due to volume exclusion). Furthermore, we also consider that the density of membrane-bound cargo (DNA origami scaffolds with bound streptavidin) is limited by the density of available membrane-bound streptavidin molecules.

Spatial organization of a single cargo species by MinDE

We observe the buildup of cargo gradients in the presence of MinDE patterns. These MinDE patterns are driven out of equilibrium by biochemical reactions (Min cycling). Each cargo binds permanently to the membrane via a fixed number of biotin/streptavidin anchors.

03 Simplified description of our Flory-Huggins model, which only includes entropic effects near the membrane

Based on the arguments in 02_Theory_FH_a, in this notebook we consider a simplified version of our Flory-Huggins model. Specifically, we make two big assumptions:

1. We consider only entropic effects in the proximal plane directly above the membrane, which correspond to an effective volume exclusion between MinD proteins, free streptavidin molecules, and streptavidin molecules that are crosslinked into effective polymers via the DNA origami scaffolds. We neglect entropic effects in the distal plance directly above the proximal plane, which correspond to an effective volume exclusion between the bulky DNA origami scaffolds. Note that the limitation of this assumption is that the DNA origami scaffold in the distal plane is actually larger than the region taken up by the (crosslinked) streptavidin anchors in the proximal plane. This assumption can in principle lead to an oversaturation of the membrane surface (i.e. the DNA origami scaffolds may cover more space than is actually available since we have neglected the corresponding volume exclusion terms).

2. The density of free streptavidin molecules is constant and independent of the number of streptavidin molecules that can bind to a single DNA origami scaffold.

> **❗ Important**
>
> The sorting efficiency (i.e. the absolute density difference between enriched and depleted regions on the membrane) in this model is best for cargo with small numbers of streptavidin molecules bound to each DNA origami scaffold. **This spectacularly contradicts our experiments. Therefore, this model cannot explain our experimental observations.**
>
> Note that the density of membrane bound cargo (DNA origami scaffolds with bound streptavidin) can *in principle* exceed the saturation density in this model. **To correct**

Snapshot of supplementary data

this, we will lift the above-mentioned assumptions in the next notebook, 04_Theory_FH_c.

> **ⓘ Info**
> Note that here the "Streptavidin"-channel corresponds to free (i.e. not bound to DNA origami scaffolds) streptavidin!

> **</> Code**
> ▶ Click to show code for running the numerical optimization (not necessary since pre-computed data is already provided).

To explore our numerical data, execute the code below. The cell below is *non-editable*. If you need to modify its contents, either make it *editable* or copy its contents to a new cell.

In [ ]:
```python
# Add directory above current directory to path
import sys; sys.path.insert(0, '..')

# Import necessary packages
import numpy as np
from Source.Visual import Model_1S
from Source.Model import Particles

particles = Particles.particles

# Visualize
with np.load('../Data/Numeric/FloryHuggins_1_inf.npz') as data:
    r, x, y_all = data.values()
    explore = Model_1S.Explore(
        particles, r, x, y_all,
        # Use this line to indicate the url of the jupyter notebook.
        # Typically either "127.0.0.1:8888" or "localhost:8888".
        notebook_url = "127.0.0.1:8888", port = 5006
    )
    explore.run()
```

Select number of Streptavidin Anchors bound to DNA-Origami:

| Anchors DNA-Origami: 1.00 | Show Coverage |

Profiles   Correlations   Sorting Efficiency   Parameters

Spatial Profile (Density)

Spatial Profile (Density)
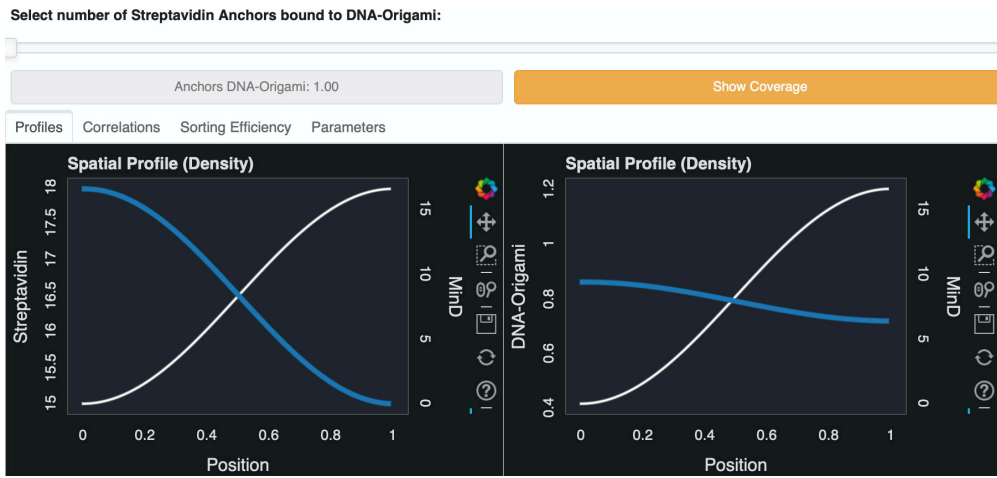
Spatial organization of a single cargo species by MinDE

We observe the buildup of cargo gradients in the presence of MinDE patterns. These MinDE patterns are driven out of equilibrium by biochemical reactions (Min cycling). Each cargo binds permanently to the membrane via a fixed number of biotin/streptavidin anchors.

04 Detailed description of our Flory-Huggins model, which includes entropic effects both near and further away from the membrane

Based on the arguments in 02_Theory_FH_a, in this notebook we consider a more detailed version of our Flory-Huggins model. Specifically, we now lift the two big assumptions that we have made in 03_Theory_FH_b:

1. As before, we consider entropic effects in the proximal plane directly above the membrane, which correspond to an effective volume exclusion between MinD proteins, free streptavidin molecules, and streptavidin molecules that are crosslinked into effective polymers via the DNA origami scaffolds. In addition, we now also consider entropic effects in the distal plance directly above the proximal plane, which correspond to an effective volume exclusion between the bulky DNA origami scaffolds. This will strictly prevent oversaturation of the membrane surface (i.e. the DNA origami scaffolds may **never** cover more space than is actually available).

2. The DNA origami scaffolds attach to the membrane by binding to streptavidin molecules. Therefore, the density of free streptavidin molecules shrinks with increasing number of biotinylated sites on the DNA origami scaffolds that can crosslink with streptavidin. We assume that each site on a DNA origami scaffold that can bind to a streptavidin molecule **will** actually do so to maximize the attractive interactions with the membrane. Then, the density of membrane-bound cargo (DNA origami scaffolds with bound streptavidin) has an upper bound, which is given by the streptavidin density divided by the number of biotinylated sites on each DNA origami scaffold.

> **❶ Important**
> **This model does NOT allow the strong redistribution of cargo (specifically, cargo with small numbers of streptavidin molecules bound to each DNA origami scaffold) that is observed in our experiments, cf. 01_Experiment_1. Similarly, it also does NOT allow a strong redistribution of free streptavidin molecules.**

Furthermore, we observe that the DNA-Origami densities *never* become depleted, in stark contradiction to our experiments. Taken together, neither the simplified Flory Huggins theory presented in 03_Theory_FH_b nor the generalized Flory Huggins theory presented in this notebook can explain our experiments. Therefore, this type of theory must be missing something!

In fact, so far we have neglected dynamic effects like a coupling between the fluxes of different particles due to mesoscopic friction. **We will lift this assumption in the next notebook, 05_Theory_MS_a.**

> ⓘ **Info**
>
> Note that here the "Streptavidin"-channel corresponds to free (i.e. not bound to DNA origami scaffolds) streptavidin!

</> Code

▶ Click to show code for running the numerical optimization (not necessary since pre-computed data is already provided).

To explore our numerical data, execute the code below. The cell below is *non-editable*. If you need to modify its contents, either make it *editable* or copy its contents to a new cell.

```python
In [ ]:
# Add directory above current directory to path
import sys; sys.path.insert(0, '..')

# Import necessary packages
import numpy as np
from Source.Visual import Model_1S
from Source.Model import Particles

particles = Particles.particles

# Visualize
with np.load('../Data/Numeric/FloryHuggins_1_010.npz') as data:
    r, x, y_all = data.values()
    explore = Model_1S.Explore(
        particles, r, x, y_all,
        # Use this line to indicate the url of the jupyter notebook.
        # Typically either "127.0.0.1:8888" or "localhost:8888".
        notebook_url = "127.0.0.1:8888", port = 5006
    )
    explore.run()
```

Snapshot of supplementary data

Snapshot of supplementary data

Select number of Streptavidin Anchors bound to DNA-Origami:

| Anchors DNA-Origami: 1.00 | Show Coverage |

Profiles Correlations Sorting Efficiency Parameters
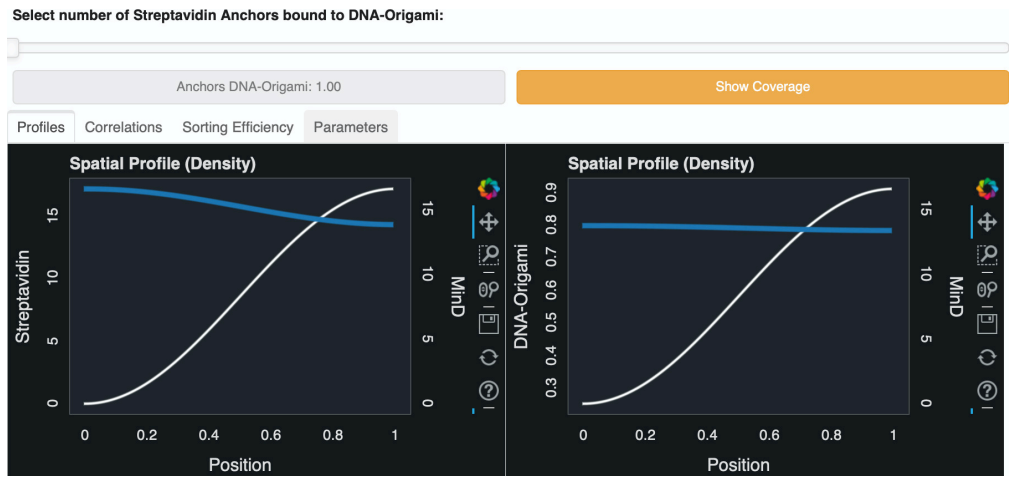
Spatial organization of a single cargo species by MinDE

We observe the buildup of cargo gradients in the presence of MinDE patterns. These MinDE patterns are driven out of equilibrium by biochemical reactions (Min cycling). Each cargo binds permanently to the membrane via a fixed number of biotin/streptavidin anchors.

05 Can we reproduce the experiments with a phenomenological flux-based model?

The following notebooks serve the purpose of an interactive playground to test whether a Maxwell-Stefan-like phenomenological model that is based on particle fluxes can reproduce our experiments. In the present notebook, we first explain the rationale that underlies this type of model.

In a previous notebook, 02_Theory_FH_a, we have sketched how one can derive the chemical potential of a membrane-bound particle from the Flory-Huggins free energy of mixing, f. Then, each particle is affected by the following local chemical potential $\mu_i = \partial f / \partial c_i$:

$$\frac{\mu_i}{k_B T} = \log(a_i c_i) + \frac{a_i}{a_0} \log \left[1 - \sum_i a_i c_i \right] + \mathrm{cst} \,, \tag{1}$$

where a_0 is the typical size of a solvent patch, while a_i and c_i are the sizes and surface densities of all other particle species. As discussed before, the particle densitiy profile of one of the species (MinD, active) is externally maintained by reactions (Min cycling), thus placing constraints on the combinatorial entropy of mixing, the corresponding Flory-Huggins free energy of mixing and the resulting chemical potentials. The second term of the above equation confers an effective volume exclusion between different species (in the proximal plane directly above the membrane: MinD proteins, free streptavidin molecules, streptavidin molecules that are crosslinked into effective polymers via the DNA origami scaffolds, and solvent; in the distal plane directly above the proximal plane: only DNA origami scaffolds and solvent). As we have done in the previous notebook, 04_Theory_FH_c, we here consider entropic effects in both the proximal plane directly above the membrane and in the distal plane directly above the proximal plane.

Gradients in a chemical potential, $\nabla \mu_i$, correspond to effective entropic forces, which act on all particle species and drive the system towards an equilbrium steady state. In the previous notebooks (02_Theory_FH_a, 03_Theory_FH_b and 04_Theory_FH_c), we have assumed that the passive particles (cargo, streptavidin) reach an equilibrium steady state in

an adiabatic response to the imposed distribution of active particles (MinD proteins). Now, we will relax this assumption. Specifically, according to Onsager's theory of nonequilibrium thermodynamics, chemical potentials $\nabla\mu_i$ always imply particle fluxes $\boldsymbol{j}_i$. Since we are now dealing with an intrinsically dynamic theory, we account for the friction between membrane-bound particles and the membrane, and in addition also a mesoscopic friction between different particle species. Such an effective inter-particle friction can arise, for example, from direct particle-particle interactions (i.e. collisions) or hydrodynamic interactions. Then, the effective Maxwell-Stefan-like force balance equation for each particle species reads:

$$-\nabla\mu_i - \xi_i \frac{\boldsymbol{j}_i}{c_i} - \sum_k \zeta_{ik} c_k \left[\frac{\boldsymbol{j}_i}{c_i} - \frac{\boldsymbol{j}_k}{c_k} \right] = 0\,, \qquad (2)$$

where the first term covers thermodynamic forces, the second term covers friction between particles and the membrane, and the last term couples the fluxes of different particle species. Note that the *interaction parameter* ζ_{ik} correponds to an effective friction between particle species i and k. Furthermore, note that the term in square brackets corresponds to a velocity difference (slip) between the fluxes of any two species. We assume that the imposed distribution of MinD proteins is in a nonequilibrium steady state that is maintained by off-equilibrium biochemical reactions (i.e. reactive fluxes due to Min cycling between membrane and bulk solution) and diffusive fluxes on the membrane surface $\boldsymbol{j}_p \neq 0$. In contrast, the passive particles (streptavidin and cargo) do not partake in reactions and remain permanently bound to the membrane. Therefore, the passive particles will approach a thermal equilibrium state with vanishing fluxes $\boldsymbol{j}_i = 0$, $\forall i \neq p$. The code that is executed in the following notebooks exploits this property to numerically determine the corresponding surface densities of all passive particles. Note that for vanishing coupling parameters, $\zeta_{ik} \to 0$, this model reduces to our Maxwell Stefan theory, cf. 04_Theory_FH_c.

All parameters are based on values that we have approximated from the experiments. The solvent in the proximal layer directly above the membrane is represented by patches with a size of 25nm^2 (equivalent to 0.01 in dimensionless quantities). Similarly, the solvent in the distal plane directly above the proximal plane is represented by patches with a size of roughly 250nm^2 (equivalent to 0.1 in dimensionless quantities). MinD proteins occupy up to 16.5% of the membrane and have a size of 25nm^2. Streptavidin molecules have an average surface coverage of 16.5% of the membrane and a size of roughly 25nm^2. DNA-Origami scaffolds have a surface coverage of up to 55% (cytosolic side) and a cytosolic size of 1760nm^2; the corresponding surface coverage and effective size in the proximal plane depend on the number of anchors. The added mass (integrated density) of all DNA-Origami should be constant; a model value of 0.79 corresponds to the surface coverages in the experiments.

Considered models:

1. **06_Theory_MS_b:** Full implementation of our phenomenological Maxwell-Stefan-like model based on the chemical potentials in 04_Theory_FH_c.

2. **07_Theory_MS_Fit:** Again neglecting saturation effects, we derive a fit curve from our Maxwell-Stefan-like phenomenological model and fit it to our experimental data (cf. 01_Experiment_1). As expected from our Maxwell-Stefan-like phenomenological model, we find that the interaction strength increases linearly with the number of Streptavidin anchors.

Snapshot of supplementary data

Spatial organization of a single cargo species by MinDE

We observe the buildup of cargo gradients in the presence of MinDE patterns. These MinDE patterns are driven out of equilibrium by biochemical reactions (Min cycling). Each cargo binds permanently to the membrane via a fixed number of biotin/streptavidin anchors.

06 Detailed implementation of our Maxwell-Stefan-like phenomenological model

> 💡 **Agreement with experiments**
> **This model ALLOWS reaching the range of DNA-Origami densities (coverages) that we have observed in our experiments, cf. 01_Experiment_1.** Specific examples of experimental data sets that one can use for comparison:
>
> - **"file_5"**, which corresponds to 42 Anchors and to a mean coverage of 0.15, reaching coverages up to 0.5.
> - **"file_23"**, which corresponds to 42 Anchors and to a mean coverage of 0.35, reaching coverages up to 1 (full coverage).
>
> **Furthermore, we observe that the DNA-Origami densities CAN become depleted, in full agreement with the experiments. In addition, we also observe that the redistribution if free streptavidin molecules is also significantly stronger than in the Flory-Huggins model, 04_Theory_FH_c, thus providing better agreement with our experiments.**

> **</> Code**
> ▶ Click to show code for running the numerical optimization (not necessary since pre-computed data is already provided).

To explore our numerical data, execute the code below. The cell below is *non-editable*. If you need to modify its contents, either make it *editable* or copy its contents to a new cell.

```python
# Add directory above current directory to path
import sys; sys.path.insert(0, '..')

# Import necessary packages
import numpy as np
from Source.Visual import Model_1S
from Source.Model import Particles

particles = Particles.particles

# Visualize
with np.load('../Data/Numeric/MaxwellStefan_1_010.npz') as data:
    r, x, y_all = data.values()
    explore = Model_1S.Explore(
        particles, r, x, y_all,
        # Use this line to indicate the url of the jupyter notebook.
        # Typically either "127.0.0.1:8888" or "localhost:8888".
        notebook_url = "127.0.0.1:8888", port = 5006
    )
    explore.run()
```
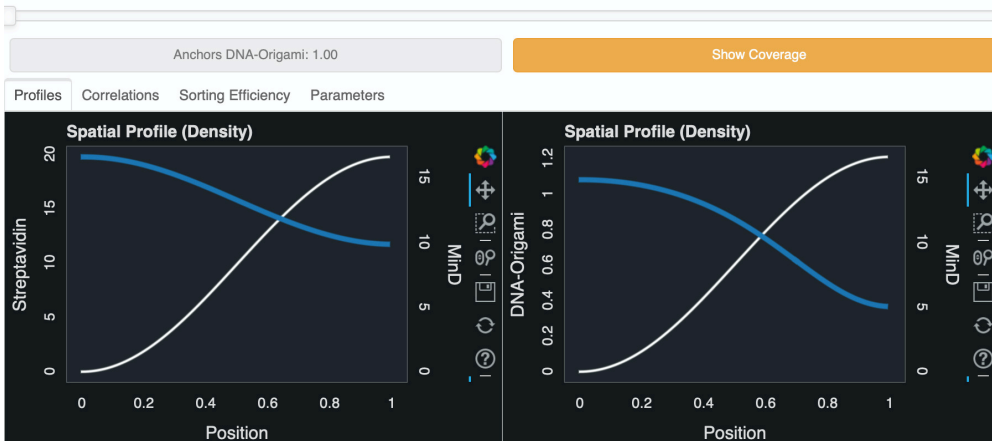
Spatial organization of a single cargo species by MinDE

We observe the buildup of cargo gradients in the presence of MinDE patterns. These MinDE patterns are driven out of equilibrium by biochemical reactions (Min cycling). Each cargo binds permanently to the membrane via a fixed number of biotin/streptavidin anchors.

07 Fitting the experimental data with a simplified flux-based model

We have seen that our experimental data is best explained by a phenomenological model that accounts for interactions between the diffusive fluxes of particles, in the form of a mesoscopic friction (cf. 05_Theory_MS_a). In the present notebook, we will fit our experimental data (cf. 01_Experiment_1) with a drastically simplified model that neglects volume exclusion effects both in the proximal and in the distal layer. Furthermore, we only account for a single cargo species (DNA origami), and therefore neglect coupling between MinD proteins and free streptavidin molecules. While these are indeed drastic simplifications, they allow us to find an analytic solution for the cross-correlation function between the distributions of MinD proteins and DNA origami.

First, we will determine how interactions with DNA origami affect the diffusive flux of MinD proteins. With the simplifications outlined above, the chemical potential of a particle with a size of a_i and a surface density of c_i is given by $k_\mathrm{B}T \log(a_i c_i)$. Therefore, we consider the following effective force balance equation for MinD proteins (cf. 05_Theory_MS_a):

$$-k_\mathrm{B}T \frac{\boldsymbol{\nabla} c_p}{c_p} - \xi_p \frac{\boldsymbol{j}_p}{c_p} - \zeta_{pg}\, c_g \left[\frac{\boldsymbol{j}_p}{c_p} - \frac{\boldsymbol{j}_g}{c_g} \right] = 0\,, \tag{1}$$

where p and g denote MinD proteins and cargo molecules (DNA origami scaffolds with bound streptavidin), respectively. Here, the first term corresponds to thermodynamic forces that gradually equilibrate gradients in chemical potential (cf. 02_Theory_FH_a and 05_Theory_MS_a), which in this case is equivalent to an equilibration of particle density gradients. Cargo molecules are chemically inert and permanently bound to the membrane, so that any net flux $\boldsymbol{j}_g$ can only occur *parallel to the surface* of the membrane. Therefore, as mentioned in 05_Theory_MS_a, all net fluxes of cargo molecules must vanish in steady state. However, for MinD proteins, the story is different. MinD proteins can detach from the membrane and form a reaction cycle. Therefore, diffusive fluxes of MinD on the membrane can be counteracted by reactive fluxes.

With these conditions in mind ($\boldsymbol{j}_g = 0$ and $\boldsymbol{\nabla} c_p \neq 0$), we find the following equation for the diffusive fluxes of the Min proteins:

$$\boldsymbol{j}_p = -\frac{k_\mathrm{B} T}{\xi_p + \zeta_{pg}\, c_g}\, \boldsymbol{\nabla} c_p\,. \tag{2}$$

Therefore, we find that the diffusion of MinD proteins becomes slower with increasing concentration of cargo molecules, which explains why we observe narrower MinD patterns on supported lipid bilayers with membrane-bound DNA-Origami. There is also a converse effect: the higher the concentration of MinD proteins on the supported lipid bilayer, the slower the diffusion of DNA-Origami; we have directly observed this phenomenon in experiments.

From our full phenomenological Maxwell-Stefan-like model, cf. 06_Theory_MS_b, we have found that an imposed distribution of MinD proteins easily induces density gradients of cargo molecules. These density gradients then in turn correspond to a space-dependent diffusion coefficient of MinD, which we can determine from our full phenomenological Maxwell-Stefan-like model, cf. 06_Theory_MS_b:

ℹ️ **We see that a large density of cargo drastically reduces the diffusive flux of MinD proteins.**
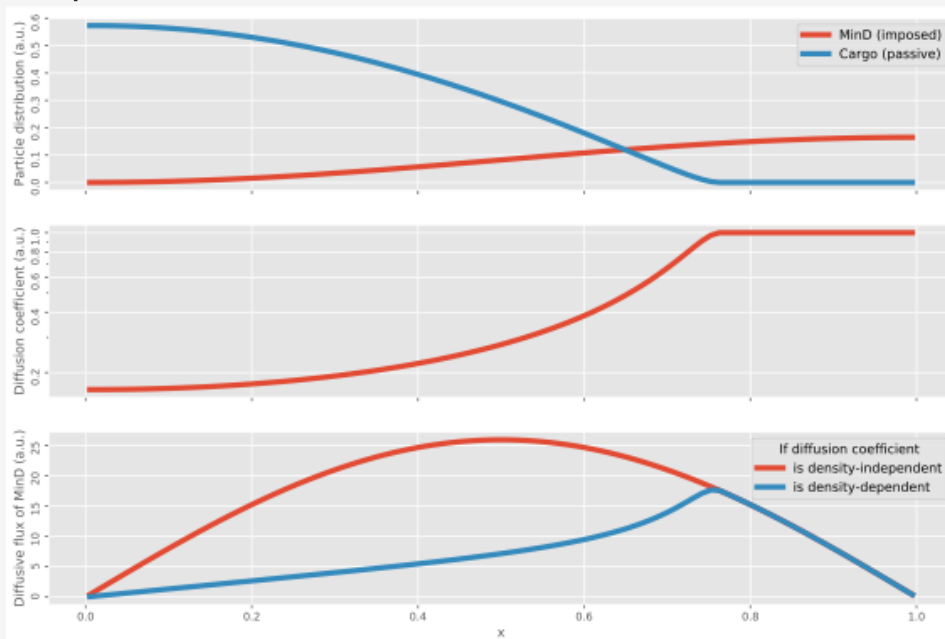
</> Code

▶ Click to show code for generating this figure.

Analogously to MinD proteins, the effective force balance equation for cargo molecules is given by:

$$-k_{\mathrm{B}}T\frac{\boldsymbol{\nabla} c_g}{c_g} - \xi_g\frac{\boldsymbol{j}_g}{c_g} - \zeta_{pg}\, c_p\left[\frac{\boldsymbol{j}_g}{c_g} - \frac{\boldsymbol{j}_p}{c_p}\right] = 0\,, \tag{3}$$

where, as before, the first term corresponds to thermodynamic forces that drive the system towards equilibrium. As discussed above, the diffusive fluxes of the cargo molecules must vanish in steady state, $\boldsymbol{j}_g = 0$. Then, the effective forces that are exerted on cargo molecules through mesoscopic friction with the net diffusive fluxes of MinD proteins, $\boldsymbol{j}_p \neq 0$ (cf. last term of the above equation), are balanced by a build-up of cargo molecule gradients and the corresponding thermodynamic forces (first term of the above equation). Finally, we obtain the following relation between gradients in cargo density and gradients in MinD density:

$$\boldsymbol{\nabla} c_g = -\boldsymbol{\nabla} c_p\,\frac{\zeta_{pg}\, c_g}{\xi_p + \zeta_{pg}\, c_g}\,. \tag{4}$$

As discussed above, the distribution of cargo molecules is stationary (steady state) and is only influenced by MinD proteins. Therefore, the concentration of cargo molecules must be a function of the local concentration of MinD proteins alone, $c_g \equiv c_g(c_p)$, and some additional global parameters like the total amount of the different species. Therefore, we rewrite the above equation as

$$\frac{\partial c_g}{\partial c_p} = -\frac{\zeta_{pg}\, c_g}{\xi_p + \zeta_{pg}\, c_g}\,. \tag{5}$$

The solution to the above ODE is given by the principal branch of the Lambert W-Function:

$$c_g(c_p) = c_\times W\left[\frac{c_g(0)}{c_\times}\exp\left(\frac{c_g(0) - c_p}{c_\times}\right)\right]\,, \tag{6}$$

where we have introduced the typical *interaction density* $c_\times = \xi_p/\zeta_{pg}$. In the experiments, we do not have direct access to the actual surface densities. Instead, we measure fluorescence intensity values, which are proportional to the surface densities, $I_g = \alpha_g c_g$ and $I_p = \alpha_p c_p$. Therefore, we will fit the following equation:

$$I_g(I_p) = r\, I_\times\, W\left[\frac{I_g(0)}{r\, I_\times}\exp\left(\frac{I_g(0)}{r\, I_\times} - \frac{I_p}{I_\times}\right)\right] \tag{7}$$

to the intensity cross-correlations obtained in our experiments, cf. 01_Experiment_1. Here, we have defined: $I_\times = \alpha_p c_\times$. Having normalized the fluorescence intensities, we estimate the ratio of fluoresence intensities, $r = \alpha_g/\alpha_p$, to be $r \approx 14.5$.

</> Code

▶ Click to show code for getting the fluorescence ratio.
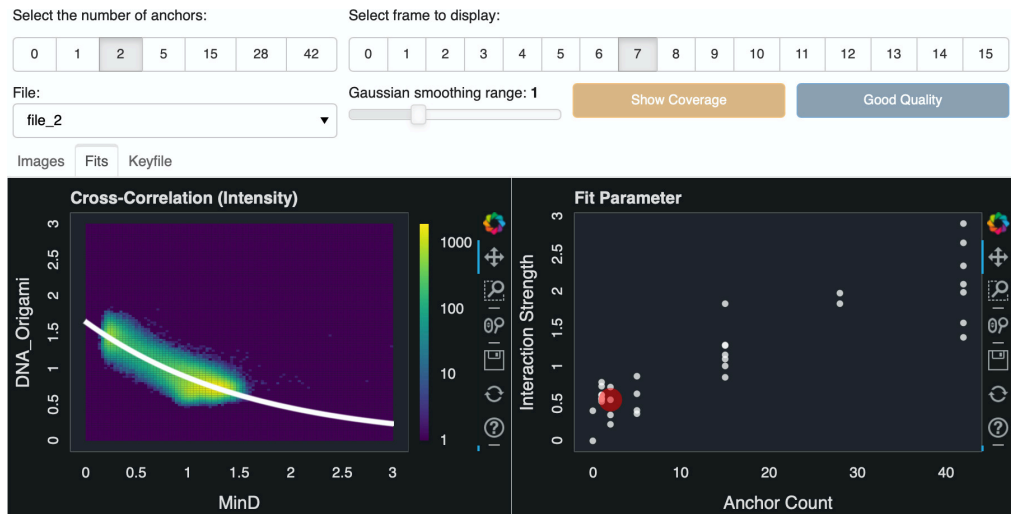
</> Code

▶ We have also performed experiments with a different anchoring strategy via cholesteryl moieties. Since these measurements do not have a streptavidin channel, they cannot be explored with the code below. For this alternative anchoring strategy, we have also performed a fitting procedure, but with a slightly different fluorescence ration of $r \approx 13.9$. Click to show code for getting the fluorescence ratio.

In [ ]:

```python
# Add directory above current directory to path
import sys; sys.path.insert(0, '..')

# Import necessary packages
from Source.Experiment import Data
from Source.Experiment import Fit
from Source.Visual import Experiment_1F

path = '../Data/Experiments/1_Cargo-n/'
data = Data.Series(
    path = path,
)
fits = Fit.Series(
    path = path,
    series = data,
    ratio = 14.5,
    smooth = 1)
explore = Experiment_1F.Explore(
    data, fits,
    # Use this line to indicate the url of the jupyter notebook.
    # Typically either "127.0.0.1:8888" or "localhost:8888".
    notebook_url = "127.0.0.1:8888", port = 5006
)
explore.run()
```

Snapshot of supplementary data

Snapshot of supplementary data

In [ ]:

Spatial organization of multiple species by MinDE

We observe the buildup of cargo gradients in the presence of MinDE patterns. These MinDE patterns are driven out of equilibrium by biochemical reactions (Min cycling). Each cargo binds permanently to the membrane via a fixed number of biotin/streptavidin anchors.

We find that MinDE protein patterns allow the sorting of different cargo species.

08 What can we observe in the experiments?

This notebook serves the purpose of an interactive playground to explore our experimental data without comparing it yet to any proposed model. Therefore, we do not perform any fitting procedures in this notebook.

To explore our experimental data, execute the code below. The "Images" tab contains images of all three channels. The "Correlations" tab contains cross-correlation plots. The "Keyfile" tab contains contains a spreadsheet with details of the experiments (e.g. the day of the experiments).

The cell below is *non-editable*. If you need to modify its contents, either make it *editable* or copy its contents to a new cell.

```python
# Add directory above current directory to path
import sys; sys.path.insert(0, '..')

# Import necessary packages
from Source.Experiment import DataFolder
from Source.Visual import Experiment_2S

path = '../Data/Experiments/5_Two-species_Cargo-n/'
data = DataFolder.Series(
    path = path,
)

explore = Experiment_2S.Explore(
    data,
    # Use this line to indicate the url of the jupyter notebook.
    # Typically either "127.0.0.1:8888" or "localhost:8888".
    notebook_url = "127.0.0.1:8888", port = 5006
)
explore.run()
```

Snapshot of supplementary data

Snapshot of supplementary data

Select the type of anchors:

Biotin_2/Biotin_42 ▾

File:

Cargo-2-Cy5_Cargo-42-Cy3b/Ch1_1D_15EH▾

Select frame to display:

| 0 | 1 | 2 | 3 | 4 | 5 | 6 | 7 | 8 | 9 | 10 | 11 | 12 | 13 | 14 | 15 |

Gaussian smoothing range: 1

Images Correlations Keyfile

MinD Biot_42 Biot_2

Spatial organization of multiple species by MinDE

We observe the buildup of cargo gradients in the presence of MinDE patterns. These MinDE patterns are driven out of equilibrium by biochemical reactions (Min cycling). Each cargo binds permanently to the membrane via a fixed number of biotin/streptavidin anchors.

We find that MinDE protein patterns allow the sorting of different cargo species.

09 Maxwell–Stefan-like phenomenological model recapitulates spatial sorting of different cargo species by MinDE patterns

> 💡 **Agreement with experiments**
> **This model ALLOWS sorting of different cargo species as observed in the experiments!** Therefore, we find that the Maxwell-Stefan-like phenomenological can explain our experimental findings. In contrast, the Flory Huggins model alone cannot do so.

> **</> Code**
> ▶ Click to show code for running the numerical optimization (not necessary since pre-computed data is already provided).

To explore our numerical data, execute the code below. The cell below is *non-editable*. If you need to modify its contents, either make it *editable* or copy its contents to a new cell.

Snapshot of supplementary data

```
In [ ]:   # Add directory above current directory to path
          import sys; sys.path.insert(0, '..')

          # Import necessary packages
          import numpy as np
          from Source.Visual import Model_2S
          from Source.Model import Particles

          particles = Particles.particles
          particles = particles.append({**Particles._cargo_origami, 'key':'2'}, ignore_
          particles.loc[particles.description=='DNA-Origami', 'total_mass'] = 0.4

          with np.load('../Data/Numeric/MaxwellStefan_2_010.npz') as data:
              r, x, y_all = data.values()
              explore = Model_2S.Explore(
                  particles, r, x, y_all,
                  # Use this line to indicate the url of the jupyter notebook.
                  # Typically either "127.0.0.1:8888" or "localhost:8888".
                  notebook_url = "127.0.0.1:8888", port = 5006
              )
              explore.run()
```
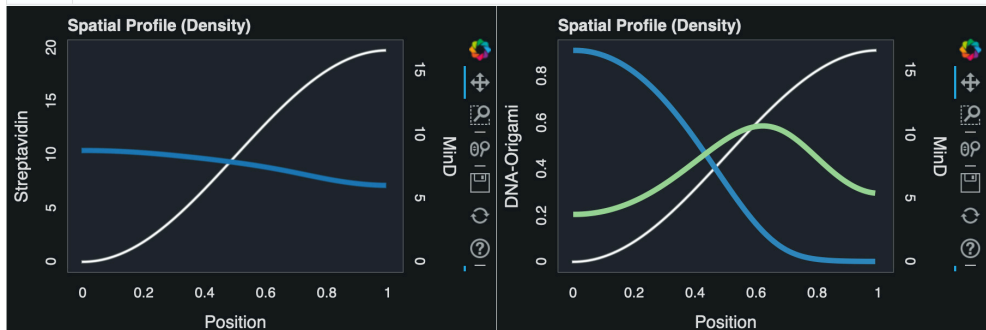
Select number of Streptavidin Anchors bound to DNA-Origami:

| Anchors DNA-Origami: 17.98 | Anchors DNA-Origami: 1.00 | Show Coverage |
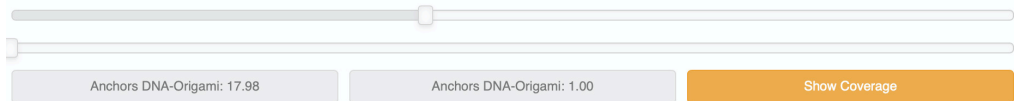
Profiles   Parameters

III FROM CELLULAR DYNAMICS TO SELF-ORGANIZATION

III.1 COLLECTIVE CELL DYNAMICS IN RIGID ENVIRONMENTS

So far, in Chapter II "Between Protein Patterns and Mechanics" we have focused mainly on processes related to intracellular organization and pattern formation. Now, we will switch gears and instead put the spotlight on one possible consequence of intracellular organization: cell migration. To that end, we develop a generalization of the discrete *Cellular Potts* model (Graner and Glazier, 1992) that aims at describing the migration of polar cells, both as single entities and in collectives, on two-dimensional surfaces. Our main results are published in "Bridging the gap between single-cell migration and collective dynamics", eLife **8**, e46842 (2019). We refer to pages 209–228 for a reprint of the main text and to pages 229–248 for a reprint of the Supplementary Material. The following serves as an introduction into the project and a summary of its main results, for the convenience of the reader.

Research Contribution.   This project is also a part of the dissertation of Florian Thüroff, who developed the original implementation of the model (F. P. Thüroff, 2014). During my studies, I continued the development and reimplemented the model. In particular, I devised the cell division algorithm that is discussed in (F. Thüroff et al., 2019), reinterpreted the model as the active surface wetting process of a droplet, and motivated the model by mapping it to a first-passage-time problem. Then, I used these results, as discussed in Section III.2 "Cell Migration and Shape in Soft Environments", to determine the traction stresses that the simulated cells exert on the surface, thus leading to substrate deformations.

A note about the notation.   To be consistent with the rest of the thesis, we denote the mechanical rigidity coefficients with k instead of κ, because the latter is reserved for curvatures in this thesis. We denote the cytoskeletal update rate

with r_ϵ instead of μ, because the latter is reserved for chemical potentials in this thesis. We discuss our model in terms of the Helmholtz free energy of a spatially extended cell.

III.1.1 STARTING POINT OF THE PROJECT

Cell migration plays a crucial role during the development and homeostasis of an organism. If the organism receives a wound, then at the re-epithelialization stage the cells in the epidermis will proliferate and collectively migrate into the cleft, thus closing the wound and restoring the integrity of the organism's skin (Rodrigues et al., 2019). *In vitro*, one can recreate these processes in so-called *wound-healing assays*, where two fronts of confluent tissue are separated by a cell-free area (Friedl, Hegerfeldt, et al., 2004; Friedl and Gilmour, 2009; Poujade et al., 2007). Furthermore, cell migration not only plays a role for wound closure, but is also relevant for inflammatory processes where immune cells clean the wound of pathogens (Rodrigues et al., 2019). To do so, individual immune cells have to first reach the wound by migrating through the tissue, which is a crucial step for any inflammatory response (Friedl and Weigelin, 2008). Cell migration also occurs during development, where stem cells have to first reach their correct position before differentiating for example into neurons (Reece et al., 2014), or as a driver of morphogenesis (Lecaudey and Gilmour, 2006). The unpleasant side of cell migration is that it also plays a role in disease-related processes such as cancer metastasis (Yamaguchi et al., 2005; Spatarelu et al., 2019). Because cell migration occurs in so many life-related processes, there is a general interest in studying its physical underpinnings. To that end, a large number of successful theoretical models were developed over the years, some aimed at understanding single-cell dynamics (Marée, Jilkine, et al., 2006; Mogilner, 2009; Shao, Rappel, et al., 2010; Marée, Grieneisen, et al., 2012; Ziebert, Swaminathan, et al., 2012; Ziebert and Aranson, 2013; Camley, Y. Zhao, et al., 2013; Albert and Schwarz, 2014; Dietrich et al., 2018; Brückner et al., 2019) and some aimed at understanding the dynamics of tissues (B. Szabó et al., 2006; A. Szabó, Ünnep, et al., 2010; Kabla, 2012; Sepúlveda et al., 2013; Basan et al., 2013; Banerjee et al., 2015; Alt et al., 2017; Tarle et al., 2017). Models that can resolve both single and collective cell migration can be largely categorized into two groups, namely phase-field models that describe each cell as a continuous field variable (Shao, Rappel, et al., 2010; Ziebert, Swaminathan, et al., 2012; Shao, Levine, et al., 2012; Camley, Y. Zhao, et al., 2013; Camley, Zhang, et al., 2014; Löber et al., 2015) and *Cellular Potts* models that discretize cells into different tiles (Graner and Glazier, 1992; A. Szabó, Ünnep, et al., 2010; Kabla, 2012; A. Szabó and R. M. Merks, 2013; van Oers et al., 2014; Segerer et al., 2015; Niculescu et al., 2015; Albert and Schwarz, 2016; Rens and R. M. H. Merks, 2017).

III.1.2 GOAL OF THE PROJECT

Our aim is to develop a versatile and extensible model, which can efficiently describe the dynamics of both single cells and cell collectives. We then apply our model to several exemplary cases to test its validity. Studying single cell motility, we find that individual cells break symmetry by polarizing. Then, each cell performs a persistent random walk with ballistic motion on short timescales and diffusive motion on long timescales. Placing multiple cells into a circular confinement, we find that the polar cells minimize viscous shear by migrating in cohesive groups. Therefore, we observe collective rotations on circular micropatterns, starting from small groups of cells (Segerer et al., 2015) all the way to large cell collectives. Finally, studying large extended tissues in the context of wound healing, we find that the polarizing cells actively invade the cell-free region and pull on the trailing cells. Because the leading cells pull on the trailing cells, we find that stress typically propagates from the front towards the back of the tissue, leading to X-shaped kymographs of the traction stress as a function of position and time. This mode of invasion is markedly different compared to dynamics that are dominated by cell proliferation.

III.1.3 TECHNICAL SUMMARY

Elasticity and homogeneous contractility of a cell. We consider the dynamics of a contractile three-dimensional cell, which remains round in suspension and whose deformations are subject to elastic constraints. This three-dimensional cell can make contact with a two-dimensional surface that is spanned by the two tangent vectors $\hat{\boldsymbol{e}}_x$ and $\hat{\boldsymbol{e}}_y$, forming a Cartesian basis. We only consider a single substrate contact of topological genus 0, that is, a simply connected contact area with zero holes that has an area $A(t)$ and is bounded by a perimeter $P(t)$. Driven by the contractility of the cell's actin cortex (Salbreux et al., 2012; Chugh and Paluch, 2018) and the elastic properties of its membrane and cytoskeleton, the contact area will collapse to a point when the cell becomes spherical. During these processes, the cell performs work, which it draws from a Helmholtz free energy that we assume to be a quadratic function of the contact area and perimeter:

$$F_{el} = k_A\, A^2(t) + k_P\, P^2(t)\,. \tag{III.1}$$

Here, the parameters k_A and k_P both model the elastic properties and the *homogeneous* contractility of the cell.

Adhesion and force generation. When the cell makes contact with a surface, it can form adhesions via integrin molecules (Charras and Sahai, 2014; De Pas-

calis and Etienne-Manneville, 2017). This leads to an effective temporary glue-ing of the cell to the surface, which we henceforth also refer to as "substrate". As we will see, our model is completely equivalent to the wetting dynamics of an active fluid droplet on a surface. For this reason, we also refer to "adhesion" as "wetting". We describe this wetting through the chemical potential difference between a substrate-bound integrin molecule and a free integrin molecule, the substrate adhesion energy $\Delta\mu_{ad} < 0$. The total adhesion energy of the cell is then given by:

$$F_{ad} = \int d^2\boldsymbol{x}\; \Delta\mu_{ad}\, c_{ad}(\boldsymbol{x}),\qquad\qquad\text{(III.2)}$$

where $c_{ad}(\boldsymbol{x})$ is the density of substrate-bound integrin molecules. Note that if adhesions can undergo maturation, growing and strengthening over time (Ber-shadsky et al., 2006), then the chemical potential of an adhesion can also be a function of time and space, $\Delta\mu_{ad}(\boldsymbol{x}, t)$. Given our discussion in Paragraph "Cou-pling between proteins and the membrane via stretching" (Section II.1.3), we can also interpret the substrate adhesion energy of each integrin molecule as a (negative) tension[1]. This analogy will become important in the next two para-graphs. But first, we turn the spotlight to the cell cytoskeleton, which enables the cell to generate active forces and propel itself forward after forming adhe-sions with the substrate (Lauffenburger and Horwitz, 1996; Pollard and Borisy, 2003; Mogilner, 2009; Mogilner and Keren, 2009). The cell cytoskeleton gener-ates two active stress contributions on the substrate, which we discuss next.

Inhomogeneous contractility of the cell cytoskeleton.   The actin cortex is a network of polar actin filaments that slide relative to each other due to the activity of myosin motors (Salbreux et al., 2012; Gross et al., 2017; Chugh and Paluch, 2018). On a coarse-grained level, we therefore consider the actin cortex as a meshwork of contractile (or extensile) rods, each having one end pointing in the direction

$$\hat{\boldsymbol{e}}_\theta = \cos(\theta)\,\hat{\boldsymbol{e}}_x + \sin(\theta)\,\hat{\boldsymbol{e}}_y,\qquad\qquad\text{(III.3)}$$

and the other end pointing in the opposite direction. We assume that each rod obeys local force balance between its two ends, leading to the following popula-

---

[1] In our model, we account for intercellular adhesions in an analogous way, by invoking a neg-ative line tension between neighboring cells. We then implement intercellular shear friction by making the cost for breaking cell-cell contacts higher than the energy benefit for making new contacts, thus dissipating energy.

tion averaged tension tensor[2]:

$$\boldsymbol{\tau}_{crt}(\boldsymbol{x}) = \int_{-\pi}^{\pi} d\theta \; P(\boldsymbol{x}, \theta) \, \tau(\boldsymbol{x}) \, \hat{\boldsymbol{e}}_\theta \otimes \hat{\boldsymbol{e}}_\theta \,, \qquad \text{(III.4)}$$

where $P(\theta)$ is the angular distribution of the rods and $\tau(\boldsymbol{x})$ encodes their contractile (or extensile) properties. This means that each individual rod only performs work when it contracts along the direction $\hat{\boldsymbol{e}}_\theta$, and does nothing in the perpendicular direction. In general, the contractility $\tau(\boldsymbol{x})$ will depend on the local density of cytoskeletal material and myosin motors.

If we make the drastic approximation of an isotropic distribution of contractile rods, $P(\boldsymbol{x}, \theta) = 1/(2\pi)$, then the tension tensor simplifies to

$$\boldsymbol{\tau}_{crt}(\boldsymbol{x}) = \tau(\boldsymbol{x}) \, \boldsymbol{I} \,. \qquad \text{(III.5)}$$

Since the contractility $\tau(\boldsymbol{x})$ depends on the local density of cytoskeletal material, a lowest order approximation yields $\tau(\boldsymbol{x}) \propto c_{ad}(\boldsymbol{x})$. Now, we remind on the equivalence between the substrate adhesion energy of each integrin molecule and an effective negative tension. On these grounds, we can absorb the (isotropic) active tension, Eq. (III.5), into a modified form of Eq. (III.2) with remapped chemical potential, $\Delta\mu_{ad} \to \Delta\mu_{ad} + \tau/c_{ad}$.

The cell cytoskeleton generates pushing forces. The actin network can generate directed pushing forces on the membrane via assembly and disassembly of cytoskeletal structures (Pollard and Borisy, 2003; Mogilner, 2009). For a spatially extended body such as a cell, we can model these pushing forces as the gradient of some pseudo-(chemical)-potential, which we do not specify further. Taking all of our arguments together, we treat cell migration on a substrate as an effective *active wetting* process[3]. To that end, we redefine the substrate adhesion energy, Eq. (III.2), to take into account the generation of active stresses by the cell cytoskeleton:

$$F_{ad} := - \int d^2\boldsymbol{x} \; \epsilon(\boldsymbol{x}, t) \, \rho(\boldsymbol{x}) \,. \qquad \text{(III.6)}$$

Here, $\epsilon(\boldsymbol{x}, t) > 0$ is the effective "strength" of each adhesion. In the following, we also refer to $\epsilon(\boldsymbol{x}, t)$ as the "polarization field", because it determines cell polarity. We represent the corresponding effective surface density of substrate

---

[2] We will encounter a very similar tension tensor in Section IV.1 "Collective Cell Migration Affects Morphogenesis".

[3] Active wetting was recently used to describe the transformation of extended epithelial tissues from two-dimensional monolayers to a three-dimensional spherical shape (Pérez-González et al., 2019). Furthermore, substrate wetting was also recently studied in the context of cell migration, by modeling the dynamics of the vertical cross-section of a cell (Cao et al., 2019).

adhesions (and cytoskeletal structures) with the variable $\rho(\boldsymbol{x}) \equiv 1/a(\boldsymbol{x})$, where $a(\boldsymbol{x})$ is the effective area of a substrate adhesion at position $\boldsymbol{x}$. This will become crucial when we study cell migration on soft deformable substrates in Section III.2 "Cell Migration and Shape in Soft Environments". For now, we consider rigid substrates with a constant and homogeneous size of substrate adhesions, $a(\boldsymbol{x}) = const$. Finally, the effective local substrate adhesion energy, $\epsilon(\boldsymbol{x}, t)$, is regulated in space and time by intracellular signaling cascades. Through these intracellular signaling cascades, the cell is continuously driven out of equilibrium.

Protrusion and retraction as a first-passage-time problem. The non-equilibrium activity of a cell shows itself via protrusions and retractions, where the cell changes its contact area with the substrate, by some small variation δA and δP. To simulate these dynamics, we tessellate the substrate into hexagonal tiles of area $\delta A \equiv a(\boldsymbol{x})$, but their specific shape is of no significance. What *is* important is that the cell can reap (or has to pay) an effective free energy benefit (or loss) for changing its configuration[4]:

$$\delta F = \delta F_{el} + \delta F_{ad} = \left[2\, k_A\, A + 2\, k_P\, P\, \frac{\delta P}{\delta A} - \epsilon(\boldsymbol{x}, t)\, \rho(\boldsymbol{x}) \right] \delta A\,, \qquad \text{(III.7)}$$

via creating or relinquishing substrate contacts. For the purpose of our simulations, we treat each hexagonal tile as one adhesion. Then, making or breaking contact with a hexagonal tile (equivalent to particle exchange) is associated with the following chemical potential difference:

$$\Delta\mu_\epsilon(\boldsymbol{x}) = \left[2\, k_A\, A + 2\, k_P\, P\, \frac{\delta P}{\delta A} \right] a(\boldsymbol{x}) - \epsilon(\boldsymbol{x}, t)\,, \qquad \text{(III.8)}$$

between having an engaged substrate contact, "+" and a disengaged substrate contact, "−".

Now, we consider the dynamics of making and losing adhesions as a first-passage-time problem, where the cell has to first overcome a large potential barrier. Such a potential barrier could arise, for example, if the cell has to first deform the membrane at no benefit before it can make a protrusion. Analogous to the discussion in Section II.1 "Mechanochemical Coupling between Proteins and Membranes", our problem then maps exactly to Kramers' theory of reaction kinetics (Kramers, 1940; Hänggi et al., 1990). Then, one obtains an Arrhenius equation for the protrusion or retraction rate (Arrhenius, 1889):

$$\frac{r_\pm}{r_0} = \exp\left(\mp \frac{\Delta\mu_\epsilon}{k_B T} \right)\,, \qquad \text{(III.9)}$$

---

[4] Note that $\delta P/\delta A = -\kappa$, where κ is the curvature of the boundary (projected onto the substrate).

where r_0 is some reference rate that depends on the height of the chemical potential barrier. Because we can freely choose the time stepping of our simulations, we make it sufficiently large so that many forward and backward reactions can occur during each time step. Then, each adhesion is in local thermal equilibrium and we can interpret the rate of forward and backward reactions, $r_\pm/r_0$, as the Boltzmann weight of finding an engaged substrate contact, "+", or a disengaged substrate contact, "−". In our simulations, we choose the Metropolis algorithm, which also fulfills the condition of local detailed balance. These protrusion and retraction dynamics continuously take the cell closer to equilibrium in our model. To then drive the cell out of equilibrium, we need to inject energy through a different process that cannot be mapped to gradient dynamics. In our simulations, we realize this by continuously updating the effective adhesion energy, $\epsilon(\boldsymbol{x})$, via out-of-equilibrium reactions. This process mimics the active remodeling of the cell cytoskeleton, as discussed next.

Intracellular signaling regulates effective substrate wetting. To drive its motion, the cell continuously builds up and degrades cytoskeletal structures in a complex sequence of different feedback mechanisms (Lauffenburger and Horwitz, 1996). For example, the cell can detect extracellular mechanical stimuli through integrin (and other) molecules, which subsequently regulate the Rho family of GTPases (Schwartz and Shattil, 2000; Parsons et al., 2010; Hodge and Ridley, 2016). In turn, the Rho family of GTPases regulates the cytoskeleton (Lauffenburger and Horwitz, 1996; Ridley, 2001; Ridley et al., 2003; Ridley, 2015; Lawson and Ridley, 2018). Here, we do not describe the complex reaction networks of all these different protein species in full detail. Instead, we only focus on the generic property of such reaction networks to have multiple feedback mechanisms, positive or negative alike, which allow the cell to detect mechanical stimuli (Marée, Jilkine, et al., 2006; Marée, Grieneisen, et al., 2012). Using this rationale, we simplify the complex feedback processes that take place during cell migration (Lauffenburger and Horwitz, 1996; Schwartz and Shattil, 2000; Parsons et al., 2010). To that end, we introduce a bookkeeping field in each cell, $m(\boldsymbol{x})$, which integrates all signals within a given time window (the discrete time step of our simulations). This bookkeeping field measures whether the cell has performed more protrusions, $m(\boldsymbol{x}) > 0$, or more retractions, $m(\boldsymbol{x}) < 0$, within the signaling distance R. Using the bookkeeping field $m(\boldsymbol{x})$, we then construct two prototypic feedback loops, where protrusive activity reinforces the effective adhesion of the cell to the substrate, while retractive activity does the opposite. Assuming that the cell cytoskeleton is remodeled with a typical rate r_ϵ, we then update the "polarization field" as follows:

$$\partial_t \epsilon(\boldsymbol{x}, t) = r_\epsilon \left[\left(\epsilon_0 + \frac{\Delta\epsilon}{2} \operatorname{sgn} m(\boldsymbol{x}) \right) - \epsilon(\boldsymbol{x}, t) \right], \qquad \text{(III.10)}$$

where ϵ_0 is the reference value for the polarization (average polarization field) and $\Delta\epsilon$ is the polarizability (maximum cell polarity). It is this non-equilibrium reaction which drives the out-of-equilibrium dynamics of our *in silico* cell.

Model limitations. In our model, we have merged the dynamics of cell-substrate adhesion and force generation by the actomyosin cytoskeleton into a single field, $\epsilon(\boldsymbol{x}, t)$. Furthermore, we have drastically simplified all intracellular signaling processes into only two feedback loops. In further research, it would be interesting to investigate these processes in greater detail. Furthermore, here we have assumed a rigid substrate that does not permit deformations. In Section III.2 "Cell Migration and Shape in Soft Environments", we lift this assumption.

III.1.4 Manuscript M3

Title:

Bridging the gap between single-cell migration and collective dynamics

Authors:

Florian Thüroff*, **Andriy Goychuk***, Matthias Reiter and Erwin Frey

The asterisk symbol (*) indicates shared first authorship.

Author contributions:

Florian Thüroff, Conceptualization, Software, Formal analysis, Validation, Investigation, Visualization, Methodology; Andriy Goychuk, Conceptualization, Data curation, Software, Formal analysis, Validation, Investigation, Visualization, Methodology; Matthias Reiter, Software, Formal analysis, Validation, Investigation, Visualization, Methodology; Erwin Frey, Conceptualization, Resources, Formal analysis, Supervision, Funding acquisition, Validation, Investigation, Methodology, Project administration

RESEARCH ARTICLE

Bridging the gap between single-cell migration and collective dynamics

Florian Thüroff[†], Andriy Goychuk[†], Matthias Reiter, Erwin Frey*

Arnold Sommerfeld Center for Theoretical Physics and Center for NanoScience, Department of Physics, Ludwig-Maximilians-Universität München, Munich, Germany

Abstract Motivated by the wealth of experimental data recently available, we present a cellular-automaton-based modeling framework focussing on high-level cell functions and their concerted effect on cellular migration patterns. Specifically, we formulate a coarse-grained description of cell polarity through self-regulated actin organization and its response to mechanical cues. Furthermore, we address the impact of cell adhesion on collective migration in cell cohorts. The model faithfully reproduces typical cell shapes and movements down to the level of single cells, yet allows for the efficient simulation of confluent tissues. In confined circular geometries, we find that specific properties of individual cells (polarizability; contractility) influence the emerging collective motion of small cell cohorts. Finally, we study the properties of expanding cellular monolayers (front morphology; stress and velocity distributions) at the level of extended tissues.

Introduction

Cell movements range from uncoordinated ruffling of cell boundaries to the migration of single cells (*Ridley et al., 2003*) to the collective motions of cohesive cell groups (*Friedl and Gilmour, 2009*). Single-cell migration enables cells to move towards and between tissue compartments – a process that plays an important role in the inflammation-induced migration of leukocytes (*Friedl and Weigelin, 2008*). One can distinguish between amoeboid and mesenchymal migration, which are characterized by widely different cell morphologies and adhesive interactions with their respective environments (*Friedl, 2004*; *Lämmermann and Sixt, 2009*). Cells may also form cohesive clusters and mobilize as a collective (*Trepat et al., 2009*; *Angelini et al., 2011*; *Doxzen et al., 2013*; *Deforet et al., 2014*; *Vedula et al., 2012*; *Marel et al., 2014*). This last mode of cell migration is known to drive tissue remodelling during embryonic morphogenesis (*Lecaudey and Gilmour, 2006*) and wound repair (*Poujade et al., 2007*).

Despite this broad diversity of migration modes, there appears to be a general consensus that all require (to varying degrees) the following factors: (i) Cell polarization, cytoskeletal (re)organization, and force generation driven by the interplay between actin polymerization and contraction of acto-myosin networks. (ii) Cell-cell cohesion and coupling mediated by adherens-junction proteins which are coupled to the cytoskeleton. (iii) Guidance by chemical and physical signals. The basic functionalities implemented by these different factors confer on cells the ability to generate forces, adhere (differentially) to each other and to a substrate, and respond to mechanical and chemical signals. However, a fully mechanistic understanding of how these basic functionalities are integrated into single-cell migration and coordinated multicellular movement is still lacking.

Here, we present a computational model which enables us to study cell migration at various scales, and thus provides an integrative perspective on the basic cell functions that enable the emergence of collective cell migration. While a variety of very successful modeling approaches has been used to describe single-cell dynamics (*Mogilner, 2009*; *Marée et al., 2006*; *Marée et al., 2012*; *Shao et al., 2010*; *Ziebert et al., 2012*; *Ziebert and Aranson, 2013*; *Camley et al., 2013*; *Albert and Schwarz, 2014*; *Dietrich et al., 2018*; *Goychuk et al., 2018*) or the movements of

extended tissues (*Szabó et al., 2006*; *Szabó et al., 2010*; *Kabla, 2012*; *Sepúlveda et al., 2013*; *Basan et al., 2013*; *Banerjee et al., 2015*; *Alt et al., 2017*; *Tarle et al., 2017*), these models are hard to reconcile with each other. Models that focus on single cells are typically difficult to extend to larger cell numbers, largely due to their computational complexity. On the other hand, approaches which are designed to capture the dynamics at the scale of entire tissues generally adopt a rather coarse-grained point of view, and are therefore difficult to transfer to single cells or small cell cohorts. At present there are two partly competing and partly complementary approaches to bridge the gap between single-cell migration and collective dynamics, namely phase-field models (*Shao et al., 2010*; *Ziebert et al., 2012*; *Shao et al., 2012*; *Camley et al., 2014*; *Camley and Rappel, 2014*; *Löber et al., 2015*), and cellular Potts models (CPMs) (*Szabó et al., 2010*; *Kabla, 2012*; *Szabó and Merks, 2013*; *van Oers et al., 2014*; *Segerer et al., 2015*; *Niculescu et al., 2015*; *Albert and Schwarz, 2016*; *Rens and Merks, 2017*) first introduced by *Graner and Glazier (1992)*.

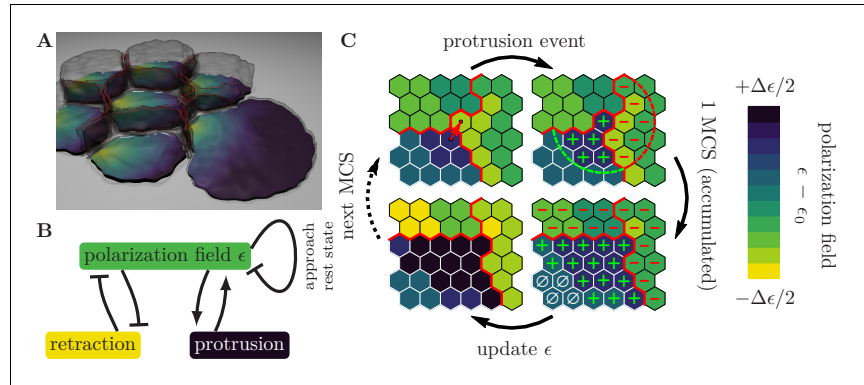## Box 1. A simple description of complex cells?

Mammalian cells are made up of around 10^9 interacting proteins (*Milo and Phillips, 2015*) in an aqueous compartment enclosed by a lipid bilayer membrane. A substantial fraction of these proteins is devoted to the structural support of the cell. The cytoskeletal systems that perform this function also mediate elastic deformations of the cell through stresses induced by motor proteins. Cell migration is enabled by transient, transmembrane attachment of the cytoskeleton to external structures (extracellular matrix or a substrate) via integrins, and regulated by various signaling pathways. To gain insights into such a complex system, we simplify these networks, each comprised of many interacting components, into coarse building blocks, which might seem arbitrary at first, but serve to qualitatively capture generic features of the underlying machinery. These generic and qualitative building blocks allow us to finally arrive at a quantitative description of cell dynamics.

Building on and generalizing the CPM (*Graner and Glazier, 1992*), we present a cellular automaton model that is designed to capture essential cellular features even in the context of the migration of single cells and of small sets of cells. At the same time, it is computationally efficient for simulations with very large cell numbers (currently up to $\mathcal{O}(10^4)$ cells), thus permitting investigations of collective dynamics at the scale of tissues. Our model reproduces the most pertinent features of cell migration even in the limiting case of solitary cells, and is compatible with a wealth of experimental evidence derived from both small cell groups and larger collectives made up of several thousand cells. Specifically, by studying the characteristics of single-cell trajectories and of small cell groups confined to circular territories, we demonstrate that persistency of movements is significantly affected by cell stiffness and cell polarizability. Moreover, we investigate the dynamics of tissues in the context of a typical wound-healing assay (*Poujade et al., 2007*; *Trepat et al., 2009*; *Serra-Picamal et al., 2012*), and show that the model exhibits the recurring mechanical waves observed experimentally (*Serra-Picamal et al., 2012*), a feature which we attribute to the coupling between cell-sheet expansion and cell-density-induced growth inhibition.

Computational model
Model geometry
We consider cells that adhere to a two-dimensional surface, spanned by the coordinates (x, y), through some contact area (*Figure 1A*). Membrane protrusions and retractions, which determine cell motion and shape (*Pollard and Borisy, 2003*; *Lauffenburger and Horwitz, 1996*), correspond to size and shape changes of the surface contact area. We assume that processes that take place at the cell boundary drive cell motion, and therefore disregard the cell body, which extends into the z-direction. In our computational model, we tesselate the available surface into a honeycomb lattice, where each hexagon corresponds to a discrete adhesion between the cell and the substrate. Then, protrusion and retraction events correspond to the gain and loss of hexagons at the boundary of the substrate contact area, respectively. The occurrence of these events is determined by a Monte Carlo scheme gradually minimizing an effective energy, $\mathcal{H}$, which is associated with the cell configuration.

Figure 1. Illustration of the computational model with the pertinent simulation steps. (A) Illustration of a small cell cohort that adheres to a surface ((x, y)-plane). The polarization field, ϵ, is defined on the contact surface with the adhesion plane. The magnitude of the polarization field, which is indicated by the colorbar in Figure (C), encodes the local strength of cell-substrate adhesions and emulates the local mass of force-generating (pushing) cytoskeletal structures. Cell-cell adhesions are indicated in red. (B) Cytoskeletal structures respond to external mechanical stimuli through reaction networks involving different feedback loops. We greatly simplify these complex processes into two prototypic feedback loops, which break detailed balance and drive cell migration, as follows. The polarization field induces membrane protrusions and inhibits retractions. In turn, protrusions increase the polarization field (positive feedback) and therefore the likelihood of further protrusive activity, while retractions decrease the polarization field (negative feedback). In the absence of mechanochemical signals, the polarization field approaches its rest state. (C) Zoom-in to a common boundary shared between the substrate contact areas of three cells (bounded by the red lines), each represented by a contiguous set of occupied grid sites (hexagons). *Top left:* The upper right corner of the lower left cell (source cell) initiates a protrusion event against a neighboring element in the cell to its right (target cell), as indicated by the arrow, in an attempt to displace it. The success of each such attempted elementary event depends on the balance between contractile forces, cytoskeletal forces, and cell adhesion. *Top right:* If the protrusion event is successful, then the levels of regulatory factors are increased (decreased) in integer steps, at all lattice sites inside the source (target) cell that lie within a radius R of the accepted protrusion event (as indicated by the plus and minus signs). *Bottom right:* During the course of one MCS, different levels of regulatory factors accumulate locally within each cell, with positive levels of regulatory factors (green plus signs) promoting a build-up of cytoskeletal structures, negative levels of regulatory factors (red minus signs) causing degradation of cytoskeletal structures, and neutral levels of regulatory factors (white zero signs) causing relaxation towards a resting state, as indicated in the *lower left image*. The color code indicates local levels of cytoskeletal structures, ϵ.

The cell is perpetually driven out of equilibrium by active reorganization of its actomyosin network and focal adhesions.

Coarse-grained cellular mechanics

As discussed above, the configuration of a cell at any given time t is associated with a substrate contact area $A(t)$ and perimeter $P(t)$. We assume that the membrane and cortex deformations of each cell are constrained by the elastic energy

$$\mathcal{H}_{\text{cont}}(t) = \kappa_A A^2(t) + \kappa_P P^2(t), \tag{1}$$

where κ_A and κ_P are cell-type-specific stiffness parameters, similar to the original implementation of the CPM (*Graner and Glazier, 1992*). If the cell does not form adhesions to the substrate, then membrane and cortex contractility will round up the cell body, thereby collapsing the substrate contact area into a contact point.

Gripping the surface through the cell cytoskeleton

Detachment of the cell from the substrate is counteracted by focal adhesions, where the cell cytoskeleton is connected to the underlying substrate by integrins. Cellular protrusions are driven by outward pushing forces generated by the assembly and disassembly of cytoskeletal structures (*Pollard and Borisy, 2003*; *Mogilner, 2009*). As a first approximation, we subsume all of these complex dynamic processes, like the formation/degradation of focal adhesions and the assembly/disassembly of cytoskeletal structures, into a single time-dependent and spatially resolved internal field for each cell, $\epsilon(\mathbf{x}, t)$. This *polarization field* emulates the mass of force-generating cytoskeletal structures in the associated hexagon, at position $\mathbf{x}$, which results in an effective, locally regulated, adhesion energy between cell and substrate. Consequently, the total energy associated with this polarization field is given by

$$\mathcal{H}_{\mathrm{cyto}}(t) = -\sum_{\mathbf{x}} \epsilon(\mathbf{x}, t). \tag{2}$$

The polarization field must vanish at positions that are not occupied by a cell. Therefore, a retraction is associated with an energy penalty due to the loss of a substrate adhesion. Consequently, a protrusion, where one source hexagon 'conquers' a nearby target hexagon, is associated with an energy gain due to an increase of the substrate contact area. Here, we assume that the newly incorporated hexagon has the same polarization field as its conqueror.

There are several biological factors that constrain the local density of actin filaments, myosin and focal adhesions, whose limited availability corresponds to an upper bound on the polarization field. Furthermore, we assume that there is some minimal attachment energy associated with adhesions that prevents the cells from detaching from the substrate, which implies a lower bound on the polarization field. This motivates to introduce cell-type-specific bounds for the polarization field: $\epsilon(\mathbf{x}, t) \in [\epsilon_0 - \Delta\epsilon/2,\ \epsilon_0 + \Delta\epsilon/2]$, where ϵ_0 is the average polarization field and $\Delta\epsilon$ is the maximum cell polarity.

Active self-regulation of the cytoskeleton

Assembly and disassembly of cytoskeletal structures are controlled by a myriad of accessory proteins (*Lauffenburger and Horwitz, 1996*; *Ridley et al., 2003*). These regulatory proteins form a reaction network involving different feedback mechanisms, which allow cytoskeletal structures to respond to external mechanical stimuli (*Marée et al., 2006*; *Marée et al., 2012*). Furthermore, cytoskeletal structures like integrins play a role in the spatiotemporal control of these regulatory proteins (*Schwartz and Shattil, 2000*). Here, we refrain from formulating a detailed reaction-diffusion model that accounts for the interactions between all of these contributing players. Instead, we assume that the internal chemistry of the cell will generically produce protein patterns, with a typical length scale R, which locally up- or down-regulate cellular cytoskeleton and focal adhesion (dis)assembly. Then, we greatly simplify these complex processes (*Lauffenburger and Horwitz, 1996*; *Schwartz and Shattil, 2000*; *Ridley et al., 2003*) into two prototypic feedback loops (*Figure 1B,C*):

A. The polarization field locally promotes outward motion of the membrane, because it contains a contribution from the local amount of actin filaments. Membrane protrusions facilitate the formation of substrate adhesions and further polymerization of actin filaments, leading to a positive feedback on the polarization field within a range R.

B. The polarization field also locally inhibits inward motion of the membrane, by emulating the local adhesion strength of the cell to the substrate. If a membrane retraction is successful, then the loss of substrate adhesions locally further increases cell contractility, leading to a negative feedback on the polarization field within a range R.

In the absence of regulatory signals, we assume that the polarization field decays to a fixed value, $\epsilon \to \epsilon_0$, which corresponds to a *resting state* of the cell cytoskeleton and focal adhesions. For the sake of keeping our model as simple as possible, we assume that all protein patterns have the same range R, and that the regulation of the cell cytoskeleton and focal adhesions follows a single timescale that corresponds to an *update rate* μ. Because at heart, our model is only based on generic feedback loops with a certain signaling range R, we would argue that *any* model with similar feedback should, in general, lead to similar cell behavior. Indeed, mutually repressing feedback loops (*Marée et al., 2006*) and mutually activating feedback loops (*Shao et al., 2010*; *Ziebert et al.,*

2012; *Albert and Schwarz, 2016*) are crucial recurring motifs among multiple cell migration studies. Notably, these theoretical approaches all recover comparable cell behavior even when the model setup seems quite different at first glance:

1. Cell migration couples mechanochemically to a scalar field (*Shao et al., 2010*), if stresses in the cell are isotropic; this is analogous to the present study.
2. Cell migration couples mechanochemically to a vector field (*Marée et al., 2006*; *Ziebert et al., 2012*), if stresses in the cell are anisotropic.
3. Cell migration couples to a single polarity vector (*Albert and Schwarz, 2016*), if propulsive forces are distributed homogeneously throughout the cell. However, this simplification of the former two cases cannot account for the formation of multiple competing lamellopodia/pseudopods.

These different modeling approaches (of varying complexity) surprisingly yield a universal phenomenology. The puzzling similarity between these models suggests generic common features that determine cell shape and motility: mechanical constraints like cell elasticity and mechanochemical feedback mechanisms that break detailed balance, maintain cell polarity and drive cell motion.

Intercellular adhesion and friction

In addition to internal remodeling of the cytoskeleton, adhesion of cells to neighboring cells and to the substrate plays a key role in explaining migratory phenotypes (*Mogilner, 2009*; *Friedl and Gilmour, 2009*). From a mechanical point of view, the implications of cell adhesion are two-fold:

1. Cell adhesion supports growth of cell-cell and cell-matrix contacts and may thus be described in terms of effective surface energies. In our computational model, cell-matrix contacts are readily accounted for by the polarization field, ϵ. In addition, we associate the formation of cell-cell adhesions with an energy benefit B, which we call *cell-cell adhesion parameter*.
2. Once formed, adhesive bonds anchor the cell to the substrate and to neighboring cells. During cell migration, these anchoring points must continuously be broken up and reassembled (*Webb et al., 2002*; *Gumbiner, 2005*) and, hence, provide a constant source of energy dissipation. Therefore, we assume that the cost for rupturing an existing cell-cell adhesion, $B + \Delta B > B$, exceeds the gain from forming a new cell-cell adhesion. Then, the dissipative nature of cell-cell adhesions is accounted for by the *cell-cell friction parameter ΔB*. Similarly, cell-matrix contacts can also provide a source of dissipation, which is further discussed in Appendix 2.

Environmental cues

The polarization field, ϵ, readily includes contributions from cell-substrate adhesions, which are locally up- or down-regulated by the cell. These cell-substrate adhesions require the abundance of surface ligands, which serve as substrate tethers that the cell can attach to, and which are not necessarily distributed homogeneously. By substrate micropatterning, one can arrange areas where the cell is likely to adhere to the surface, and *no-go-areas*, where the cell adheres less (or cannot adhere at all). To replicate such environmental cues, we introduce a second scalar field $\varphi(\mathbf{x})$, whose value is taken to reflect the relative availability of substrate sites at which focal adhesions between cell and substrate can be formed. Here, we have chosen to model micropatterns as impenetrable walls; we locally add a large energy penalty, $\varphi \ll 0$, to the polarization field ($\epsilon \rightarrow \epsilon + \varphi$), that a cell has to pay for trespassing onto a *no-go-area*. However, it is equally valid to treat φ as a multiplicative constant modulating the polarization field ($\epsilon \rightarrow \varphi \epsilon$), where $\varphi = 0$ models a local inability of the cell to attach to the substrate. Analogously to cell-cell contacts, we account for the dissipative nature of cell-substrate adhesions by associating the breaking of such contacts with an additional energy cost D.

Tissue growth by cell division

In the description so far, the cells are arrested in the cell cycle (mitostatic). To investigate the effect of cell proliferation on tissue dynamics, we introduce a simplified three-state model of cell division. Cells start off in a quiescent state, in which their properties remain constant over time. The cell sizes fluctuate around an average value determined by the cell properties and the local tissue pressure. Cell growth typically arrests at large cell densities, in a phenomenon coined *contact inhibition of proliferation* (*Stoker and Rubin, 1967*; *Puliafito et al., 2012*; *Pavel et al., 2018*). Since large cell

densities correspond to a small spread area for each individual cell, this implies that cell growth is arrested below a critical threshold size (A_T). Upon exceeding this threshold size due to size fluctuations, cells leave the quiescent state and enter a growth state. The duration of the quiescent state is thus a random variable, whose average value depends on the tissue pressure, and lower pressure (due to a lower cell density) leads to a shorter quiescent state. During the subsequent deterministic growth state of duration T_g, cells double all of their cellular material and thus double in size. We model this growth as a gradual decrease in the effective cell contractility (κ_A and κ_P). As there is no a priori reason to assume that a cell's migratory behavior should depend on its size, we constrain the parameters accordingly; this is described in detail in Appendix 2. After having grown for a duration T_g, cells switch to a deterministic division state of duration T_d. During division, cells strongly contract, which leads to mitotic rounding and a drastic decrease of their contact area with the substrate (*Jones et al., 2018*; *Lock et al., 2018*). In principle, a decrease of cell contact area could also lead to perturbations of the stress field in the monolayer. Here, however, we neglect the decrease of the cell spreading area, as the division phase is short compared to the growth phase. We expect that a drastic increase of cell contractility also leads to a loss of polarity in the cell's migratory machinery. Therefore, each cell reduces its polarizability to zero ($\Delta\epsilon \rightarrow 0$) in order to utilize its cytoskeleton for the separation of the cellular material, leading to mitotic rounding. At the end of the division state, each dividing cell splits into two identical daughter cells, whose properties and parameters are identical to the mother cell's initial values in the quiescent state. Finally, the daughter cells re-initialize migration from an unpolarized state. For a detailed and more technical description we refer the interested reader to Appendix 1.

Results

Persistent migration of single cells

The macroscopic properties of cell clusters and tissues emerge from an interplay between many individual cells. Then, what determines the mechanical and migratory features of these individual cells? In our computational model, we have studied this question by screening its multidimensional parameter space. For such a brute force approach to be numerically feasible, one must first distinguish relevant parameters (these determine the resulting dynamics) from irrelevant parameters. Specifically, in our extended cellular Potts model, there are *reference parameters* whose sole purpose is to control the spatial and temporal discretization of the numerical model:

1. The cytoskeletal update rate endows the cellular Potts model with a reference timescale and determines the temporal discretization. In this study, we have set $\mu = 0.1$.
2. The average polarization field ϵ_0 encodes the energy gain for creating new cell-substrate adhesions, while the area stiffness κ_A represents the energy cost for increasing the substrate contact area. Then, the number of hexagons occupied by the cell is proportional to the ratio ϵ_0/κ_A. If we use a desired cell area as reference value, then the ratio ϵ_0/κ_A controls the spatial discretization of the cell. To study the migration of single cells and small cell cohorts, we have set the average polarization field to $\epsilon_0 = 225$ and the area stiffness to $\kappa_A = 0.18$.
3. In cellular Potts models, which are Monte-Carlo simulations, the reference energy of fluctuations is determined by an effective temperature. In this study, we have set $k_\mathrm{B}T \equiv 1$.

Furthermore, we used a large computational grid with $9 \cdot 10^4$ sites and periodic boundary conditions to study the migration of single cells. This leaves three parameters that control cell motility in the absence of cell-substrate dissipation: cell polarizability $\Delta\epsilon$, cell contractility κ_P and signalling radius R. However, it is not clear yet whether all of these are independent relevant parameters. In fact, in the following sections it will become clear that cell polarizability and contractility are *degenerate parameters* (in the sense that the phenomenology only depends strongly on their ratio, which is the corresponding relevant parameter).
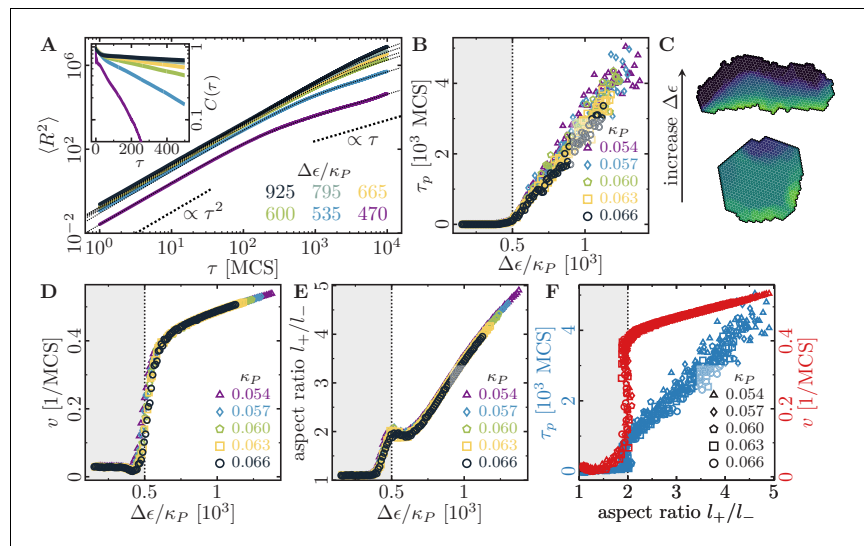
Cell persistence increases with polarizability

First, we investigated the impact of varying levels of cell perimeter stiffness κ_P and maximum cell polarity $\Delta\epsilon$ on the cell's migratory patterns (*Figure 2—video 1*), at a fixed signaling radius $R = 5$. To assess the statistics of the cell trajectories, we recorded the cell's orientation $\hat{\mathbf{v}}(t) \equiv \mathbf{v}(t)/\|\mathbf{v}(t)\|$ ($\mathbf{v}$: cell velocity) and (geometrical) center of mass position $\mathbf{R}(t)$ during a total simulation time of

$T_{sim} = 10^4$ Monte-Carlo steps (MCS). For each set of parameters, we performed 100 statistically independent simulations, from which we computed the mean squared displacement, $\mathrm{MSD}(\tau) \equiv \langle [\mathbf{R}(t+\tau) - \mathbf{R}(t)]^2 \rangle$, and the normalized velocity auto-correlation function, $C(\tau) \equiv \langle \hat{\mathbf{v}}(t+\tau) \cdot \hat{\mathbf{v}}(t) \rangle$. Here, $\langle \ldots \rangle$ denotes an average with respect to simulation time t as well as over all 100 independent simulations.

These computer simulations show that the statistics of the migratory patterns is well described by a *persistent random walk model* (*Stokes et al., 1991*; *Wu et al., 2014*) with its two hallmarks: a mean square displacement that exhibits a crossover from ballistic to diffusive motion (*Figure 2A*), and on sufficiently long time scales an exponential decay of the velocity autocorrelation function $C(\tau) \propto e^{-\tau/\tau_p}$ (inset of *Figure 2A*). We determined the persistence time of directed migration, τ_p, by fitting the mean squared displacement with a persistent random walk model. In addition, we also measured cell speed, v, and cell aspect ratio, l_+/l_-, to further characterize cell motility and shape.

Figure 2. Cell shape and persistence of migration as a function of cell polarizability. (**A**) Mean-squared displacement (MSD) for single-cell movements at different maximum cell polarity $\Delta\epsilon$ (stiffness parameters $\kappa_P = 0.060$, $\kappa_A = 0.18$; average polarization field $\epsilon_0 = 225$; signaling radius $R = 5$; cell-substrate dissipation $D = 0$; cell-substrate adhesion penalty $\varphi = 0$; cytoskeletal update rate $\mu = 0.1$; 100 independent simulations for each set of parameters). Single cells perform a persistent random walk, i.e. they move ballistically (MSD $\propto \tau^2$) for $\tau \ll \tau_p$, and diffusively (MSD $\propto \tau$) for $\tau \gg \tau_p$. *Inset:* Normalized velocity auto-correlation function for the same parameters as in the main figure. (**B**) Persistence time of directed cell migration plotted as a function of maximum cell polarity $\Delta\epsilon$, and perimeter stiffness κ_P (area stiffness $\kappa_A = 0.18$; average polarization field $\epsilon_0 = 225$; signaling radius $R = 5$; cell-substrate dissipation $D = 0$; cell-substrate adhesion penalty $\varphi = 0$; cytoskeletal update rate $\mu = 0.1$; 100 independent simulations for each set of parameters). The persistence time of the random walk increases with increasing cytoskeletal polarity and decreasing perimeter elasticity. (**C**) Cytoskeletal polarity also controls cell shapes, with crescent cell shapes (long persistence times) being observed at large cytoskeletal polarities, and round cell shapes (short persistence times) at small cytoskeletal polarities. Color code: cell polarization; cf. color bar in *Figure 1C*. (**D**) Single cell speed plotted as a function of maximum cell polarity $\Delta\epsilon$, and perimeter stiffness κ_P. (**E**) Single cell aspect ratio plotted as a function of maximum cell polarity $\Delta\epsilon$, and perimeter stiffness κ_P. (**F**) Speed and persistence time of single cells are correlated with the cell aspect ratio.

The online version of this article includes the following video and figure supplement(s) for figure 2:

Figure supplement 1. Role of substrate dissipation for cell shape and motility.

Figure 2—video 1. Single cell motility and shape for different maximum cell polarities ($\kappa_P = 0.060$, $R = 5$).
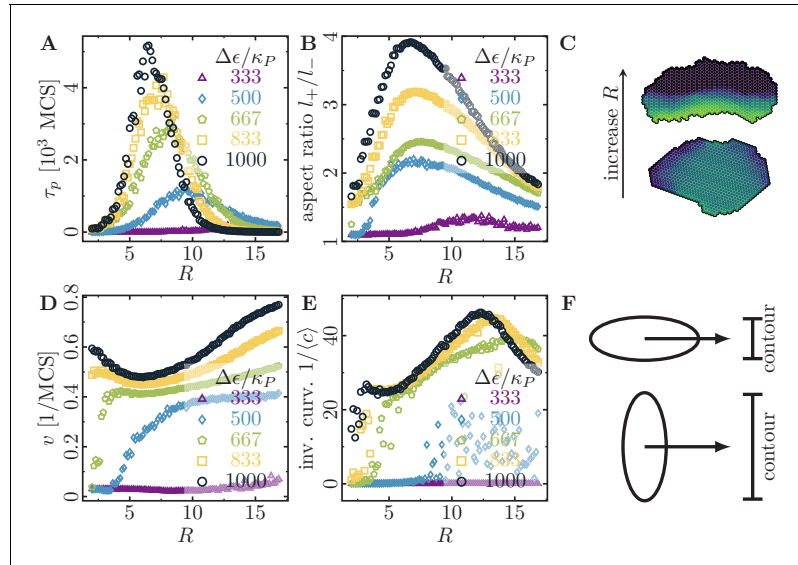https://elifesciences.org/articles/46842#fig2video1

Surprisingly, for each of these variables we found a master curve that only depends on the ratio between cell polarizability and cell contractility, $\Delta\epsilon/\kappa_P$ (*Figure 2B,D,E*). This data collapse suggests $\Delta\epsilon/\kappa_P$ as a relevant parameter (while cell polarizability and contractility are degenerate parameters), which we will henceforth refer to as *specific polarizability*.

The cells' persistence times of directed migration, speeds and aspect ratios all show a characteristic dependence on the specific cell polarizability. There is a threshold value for the specific polarizability, $\Delta\epsilon/\kappa_P \approx 500$, below which cells remain immobile (*Figure 2B,D,E*; grey regions). Above this threshold, the persistence time of directed migration, speed and aspect ratio increase markedly with the specific polarizability (*Figure 2B,D,E*). In our model, the area and perimeter stiffnesses refer to global and homogeneous cell contractility, while the cell polarization field drives cell migration. As discussed in 'Gripping the surface through the cell cytoskeleton', the cell polarization field does not explicitly distinguish between a local extensibility (e.g. due to actin polymerization), a local contractility (due to myosin-induced contraction) of the cytoskeleton or spatially regulated cell-substrate adhesions. For example, if cell migration is driven by actin polymerization, then blebbistatin treatment will decrease the global cell contractility, which we predict to lead to more elongated cells that move faster and exhibit extended episodes of ballistic motion. Indeed, an increase of cell migration speed after blebbistatin treatment was observed for mouse hepatic stellate cells (*Liu et al., 2010*). Alternatively, cell migration could also be driven by myosin contractility, for example by pulling the cell forward or by locally detaching adhesions. Then, polarizability and contractility concomitantly depend on the ability of the cell to exert forces, which can be inhibited by blebbistatin treatment. If polarizability, $\Delta\epsilon$, and contractility, κ_P, are equally reduced by a blebbistatin-dependent prefactor, then the *specific polarizability*, $\Delta\epsilon/\kappa_P$, and the resulting cell phenomenology should remain unchanged. Indeed, blebbistatin treatment of keratocytes and keratocyte fragments was reported not to affect cell shape and speed to any significant degree (*Wilson et al., 2010*; *Ofer et al., 2011*). Therefore, blebbistatin treatment can either increase or decrease cell motility, depending on the cell type and possibly on the specific mechanism that drives cell migration.

Interestingly, because of this universal dependence of all the mentioned quantities on the specific polarizability, our simulations also show that there is a strong correlation between cell shape (aspect ratio) and cell motility (speed and persistence time of directed migration); see *Figure 2F*. While highly persistent trajectories are observed for cells with 'crescent' shapes, more erratic cell motion is typically found for cells with more rounded outlines (*Figure 2C*). In other words, our computational model predicts that cells which are able to polarize their cytoskeletal structures more strongly will adopt crescent shapes and show a higher degree of persistent cell motion. It would be interesting to further test these predictions by using phenotypic variations in cell shapes like those reported in experiments with keratocytes (*Keren et al., 2008*); there, the authors also found a correlation between cell shape and speed.

Feedback range determines whether individual cells move persistently or rotate

Moreover, we investigated the influence of different signaling radii R (typical range in which signalling molecules diffuse and mediate feedback mechanisms during a single Monte-Carlo step) on the persistence of single-cell trajectories. Since R is the relevant parameter that controls the spatial organization of lamellipodium formation, its value should strongly affect the statistics of a cell's trajectory (*Figure 3A*). Indeed, at small values of R, we observe that the spatial coherence of cytoskeletal rearrangements is low, which frequently results in the disruption of ballistic motion due to the formation of independent lamellipodia in spatially separate sectors of the cell boundary (*Figure 3C*, lower snapshot). In contrast, at larger values of R, we find that spatial coherence is restored, and the formation of one extended lamellipodium across the cell's leading edge maintains a distinct front-rear axis of cell polarity (*Figure 3C*, upper snapshot). However, when the signaling radius is too large compared to the cell size, we find an inhibition of ballistic motion and rounding of the cells as signals originating from one cell edge begin to reach the opposing edge. This effect may also occur when cells in tissue become smaller due to an increase of cell density through proliferation or compression; in other words, this means that the cells become smaller than the typical length scale of the chemical patterns that control cell migration. Then, one would not expect these chemical patterns to form (*Hubatsch et al., 2019*). Therefore, depending on the cell polarizability ($\Delta\epsilon$), there is an

Figure 3. Migratory behavior of single cells as a function of the cell's signaling radius R at different values for the maximal cytoskeletal polarity $\Delta\epsilon$. (Stiffness parameters $\kappa_P = 0.060$, $\kappa_A = 0.18$; average polarization field $\epsilon_0 = 225$; cell-substrate dissipation $D = 0$; cell-substrate adhesion penalty $\varphi = 0$; cytoskeletal update rate $\mu = 0.1$; 100 independent simulations for each set of parameters). (**A**) The persistence times of directed migration of single cells exhibit a pronounced maximum at an optimal signaling radius, which depends on cell polarizability. (**B**) The shapes of single cells exhibit a pronounced maximal elongation at an optimal signaling radius, which depends on cell polarizability. (**C**) The signaling radius critically determines the synchronicity of internal cytoskeletal remodeling processes. Small signaling radii frequently lead to transient formation of mutually independent lamellipodia at different positions around the cell perimeter, thereby interrupting persistent motion (reducing persistence times of directed migration). Large signaling radii lead to structurally stable front-rear polarization profiles across the entire cell body (long persistence times of directed migration). Color code: cell polarization; cf. color bar in **Figure 1C**. (**D**) The speed of single cells does not drop to zero even when their persistence time of directed migration vanishes. This indicates single cell rotations. (**E**) The inverse curvature of the cell trajectories as a function of the signaling radius. (**F**) Depending on whether a cell migrates along its long axis (top) or short axis (bottom), it has to move a different projected contour length. If each protrusion takes roughly the same amount of time, then migration along the long axis (top; cell has to move a smaller projected contour length) allows for greater cell speeds than migration along the short axis (bottom; cell has to move a larger projected contour length).

The online version of this article includes the following video for figure 3:

Figure 3—video 1. Single cell motility and shape for different signaling radii ($\Delta\epsilon = 60$, $\kappa_P = 0.060$).
https://elifesciences.org/articles/46842#fig3video1

optimal signaling radius that shows both maximal cell elongation and maximal cell persistence (**Figure 3A,B**).

Cells with low polarizability need a large signaling radius to feed the positive feedback mechanism and to form a single large cell front. In contrast, highly polarizable cells can already sustain the positive feedback mechanism with a short signaling radius and easily form at least one (or even multiple competing) short cell front(s). With increasing signaling radius, these cell fronts become increasingly correlated and finally merge. Surprisingly, at small signaling radii, we observed that highly polarizable cells slow down with increasing signaling radius (**Figure 3D**; yellow squares and black circles), in contrast to the behavior of cells with low polarizability. Furthermore, at large signaling radii, highly polarizable cells *speed up*, although their persistence time of directed migration has dropped to small values (cf. **Figure 3A,D**; blue diamonds, green pentagons, yellow squares and

black circles). To find an intuitive explanation for these observations, we inspected time-lapse videos of a cell at high polarizability ($\Delta\epsilon/\kappa_P = 1000$; cf. *Figure 3—video 1*, top row), which show a qualitative shift in cell behavior:

- For small signaling radii, $R = 2$, short polarization fronts 'pull' the cell behind them, allowing for transient polarization and quick but erratic movement along the long axis of the cell.
- For intermediate signaling radii, $R = 6$, broad and correlated polarization fronts emerge, and both the cell polarization and movement always orient themselves along the short axis of the cell.
- For large signaling radii $R = 15$, we observed circular motion of the cell; because of the large signaling radius, signals originating from the trailing edge affect the leading edge of the cell and vice versa. Due to this circular motion, the cell exhibits a non-zero speed and a vanishing persistence time of directed migration.

Therefore, we find that the cell can transiently polarize and migrate along its long axis for small signaling radii and for high polarizability. Furthermore, in a broad parameter regime, we find keratocyte-like motion and polarization along the short axis of the cell. Note that we do not consider the formation of stress fibers, which could lead to cell migration along the long axis in a broad parameter regime (*Kassianidou et al., 2019*). Such stress fibers could be modeled via a nematic field that represents the anisotropic part of the intracellular stress. Our counter-intuitive observation that cell migration along the long axis is faster than cell migration along the short axis can be explained as follows: If the cell migrates along its short axis, then it has to move a greater projected contour length than if it migrates along its long axis (*Figure 3F*). Considering that each protrusion takes roughly the same amount of time, migration along the long axis allows for greater cell speeds than migration along the short axis, because the cell has to spend less time to move a smaller projected contour length (*Figure 3F*).

To further characterize the single cell rotations that occur at large signaling radii, we determined the average curvature of the trajectories $\langle c \rangle = \langle \|\partial_s \hat{\mathbf{v}}(s) \cdot \hat{\mathbf{v}}(s)\| \rangle$, where s is the contour length along the corresponding trajectory. Here, we averaged the tangent vector $\hat{\mathbf{v}}(s)$ over 10 Monte-Carlo steps to integrate out fluctuations that occur on short timescales (the internal dynamics of the cell has an intrinsic time scale of 10 Monte-Carlo steps due to our choice of the cytoskeletal update rate, $\mu = 0.1$). We find that the curvature of the trajectories has a pronounced minimum at large signaling radii (where the persistence time of directed migration vanishes), which indicates a transition from straight to circular trajectories (*Figure 3E*). Such a transition from persistent migration to single cell rotations was previously observed in experiments (*Lou et al., 2015*; *Raynaud et al., 2016*) and in theory (*Reeves et al., 2018*; *Allen et al., 2018*).
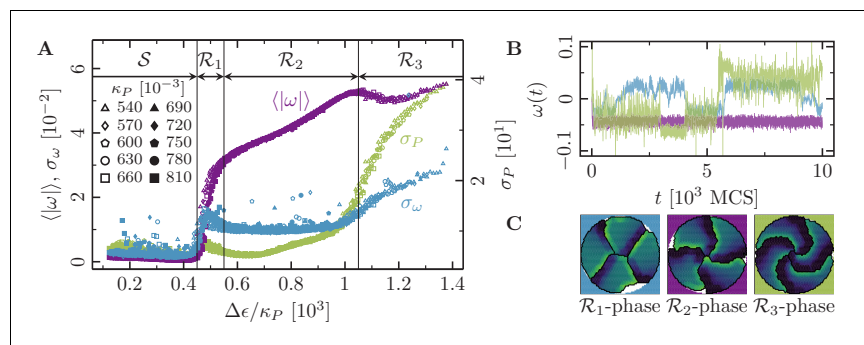
Cell clusters on circular micropatterns

To assess the transition to collective cell motion, we next studied the dynamics of small cell groups confined to circular micropatterns (*Huang et al., 2005*; *Doxzen et al., 2013*; *Deforet et al., 2014*; *Segerer et al., 2015*). We implemented these structures in silico by setting $\varphi(\mathbf{x}) = 0$ inside a radius r_0 and $\varphi(\mathbf{x}) \to -\infty$ outside. During each simulation run, the number of cells was also kept constant by deactivating cell division. We previously employed this setup to compare our numerical results with actual experimental measurements, and found very good agreement (*Segerer et al., 2015*). Here, we generalize these studies and present a detailed analysis of the statistical properties of the collective dynamics of cell groups in terms of the key parameters of the computational model.

When adhesive groups of two or more motile cells are confined on a circular island, they arrange themselves in a state of spontaneous collective migration, which manifests itself in the form of coordinated and highly persistent cell rotations about the island's midpoint $\mathbf{x}_0$ (*Huang et al., 2005*; *Doxzen et al., 2013*; *Deforet et al., 2014*; *Segerer et al., 2015*). The statistics of these states of rotational motion provide insight into the influence of cellular properties on the group's ability to coordinate cell movements. To quantify collective rotations, we recorded the average signed angular velocity of the cell cluster $\omega(t) = \hat{\mathbf{e}}_z \cdot \langle \tilde{\mathbf{v}}(t) \times \tilde{\mathbf{R}}(t)/\|\tilde{\mathbf{R}}(t)\|^2 \rangle_{\mathcal{C}}$. Here, $\hat{\mathbf{e}}_z$ is the out-of-plane unit vector, $\langle \ldots \rangle_{\mathcal{C}}$ denotes an average with respect to the cell population, and $\tilde{\mathbf{v}}(t) = \mathbf{v}(t) - \langle \mathbf{v}(t) \rangle_{\mathcal{C}}$ as well as $\tilde{\mathbf{R}} = \mathbf{R}(t) - \langle \mathbf{R}(t) \rangle_{\mathcal{C}}$ measure the velocity and position of each cell relative to the cell cluster (we have omitted the indices that identify individual cells for the sake of convenience and clarity). The resulting random variables for the magnitude of the angular velocity of the cell assembly, $|\omega(t)|$, and the

average cell perimeter $P(t) \equiv \langle P_\alpha(t) \rangle_{\mathcal{C}}$ were then used to characterize the statistics of collective cell rotation. For each specific choice of simulation parameters, we monitored $|\omega(t)|$ and $P(t)$ for a set of 100 statistically independent systems, each of which was observed over $T_{sim} = 10^4$ MCS. From these data, we then computed the mean overall rotation speed $\langle |\omega| \rangle$, its standard deviation σ_ω, and the standard deviation of the cell perimeter, σ_P.

Figure 4 illustrates the characteristic properties of collective cell rotations in systems containing $|\mathcal{C}| = 4$ cells endowed with varying maximum cell polarity $\Delta\epsilon$ and varying cell contractility κ_P. Analogously to our observations for single cells, the statistical measures shown in *Figure 4A* do not separately depend on cell contractility and maximum cell polarity, but depend only on the *specific polarizability* $\Delta\epsilon/\kappa_P$. Overall, we find that upon increasing the specific polarizability there is a marked transition from a quiescent state to a state where the cells are collectively moving. Below a threshold value for the specific polarizability ($\Delta\epsilon/\kappa_P \approx 450$ in *Figure 4A*), the rotation speed $\langle |\omega| \rangle$ (purple curves in *Figure 4A*) vanishes and the cells are immobile. In this regime, which we term the *stagnation phase*, or $\mathcal{S}$-phase, cytoskeletal forces are too weak to initiate coherent cell rotation, and the system's dynamics is dominated by relatively strong contractile forces, which tend to arrest the system in a 'low energy' configuration. Beyond this threshold, we identify three distinct phases of collective cell rotation. In the $\mathcal{R}_1$-phase, we find a steep increase in the average rotation speed and a local maximum in the fluctuations of both cell shape and rotation speed; cf. green (σ_P) and blue (σ_ω) curves in *Figure 4A*. Now, cytoskeletal forces are sufficiently large to establish actual membrane

Figure 4. Phases of collective motion. (4-cell systems; confinement radius $r_0 = 30.6$; area stiffness $\kappa_A = 0.18$; average polarization field $\epsilon_0 = 225$; signaling radius $R = 5$; cytoskeletal update rate $\mu = 0.1$; cell-cell adhesion $B = 0$; cell-cell dissipation $\Delta B = 12$; cell-substrate dissipation $D = 0$; cell-substrate adhesion penalty $\varphi = 0$ ($r < r_0$), $\varphi \rightarrow -\infty$ ($r > r_0$); 100 independent simulations for each set of parameters). (A) Characteristic observables of collective cell rotation at different values of the cell perimeter stiffness parameter κ_P: mean ($\langle |\omega| \rangle$) and standard deviation (σ_ω) of the magnitude of the cell cluster's angular velocity, and the standard deviation of the cell perimeter (σ_P). The statistics of collective cell motion depends only on the ratio of maximum cell polarity, $\Delta\epsilon$, to cell contractility, κ_P (specific polarizability). (B) Representative angular trajectories and (C) cell shapes (color code represents cell polarization; cf. *Figure 1C*) for the different parameter regimes as described in the main text. The cellular dynamics in the different parameter regimes are shown in *Figure 4—video 1*, *Figure 4—video 2* and *Figure 4—video 3*.

The online version of this article includes the following video and figure supplement(s) for figure 4:

Figure supplement 1. Collective motion for varying number of cells at low polarizability.

Figure supplement 2. Collective motion for varying number of cells at intermediate polarizability.

Figure supplement 3. Collective motion for varying number of cells at high polarizability.

Figure 4—video 1. Collective rotations of 4 cells in the $\mathcal{R}_1$-phase ($\Delta\epsilon = 28$; $\Delta\epsilon/\kappa_P = 467$).
https://elifesciences.org/articles/46842#fig4video1

Figure 4—video 2. Collective rotations of 4 cells in the $\mathcal{R}_2$-phase ($\Delta\epsilon = 50$; $\Delta\epsilon/\kappa_P = 833$).
https://elifesciences.org/articles/46842#fig4video2

Figure 4—video 3. Collective rotations of 4 cells in the $\mathcal{R}_3$-phase ($\Delta\epsilon = 70$; $\Delta\epsilon/\kappa_P = 1167$).
https://elifesciences.org/articles/46842#fig4video3

protrusions against the contractile forces, and cells begin to rotate (*Figure 4B,C*). However, the contractile forces still dominate, such that cellular interfaces tend to straighten out and lamellipodium formation is sustained only over finite lifetimes. Thus, due to the dominance of contractile forces, the systems frequently experience transient episodes of stagnation and repeatedly change their direction of rotation (cf. blue trajectory in *Figure 4B*).
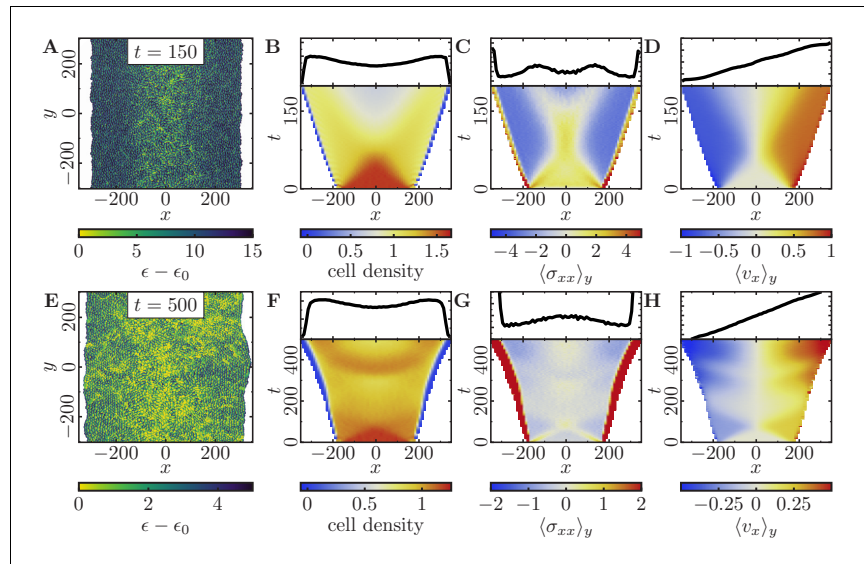
At intermediate values of specific polarizability ($\mathcal{R}_2$-phase), the cellular systems reach a regime of enduring rotational motion, where $\langle|\omega|\rangle$ varies linearly with the local specific polarizability, and where σ_P and σ_ω exhibit a rather broad minimum (*Figure 4A*). In this regime, a range of 'optimal ratios' of cytoskeletal to contractile forces sustains stable cell shapes, and sets the stage for the formation of extended lamellipodia and the establishment of permanent front-rear polarizations of cells. As a result, the cells' persistence times of directed migration become very large, rendering cellular rotations strictly unidirectional within the observed time window (*Figure 4B*). Finally, at large values of the specific polarizability ($\mathcal{R}_3$-phase), the system's dynamics is dominated by cytoskeletal forces and the rotational speed $\langle|\omega|\rangle$ saturates at some maximal value. Due to the relatively small contractile forces, cell shapes tend to become unstable, as reflected in the growing variance of the cell perimeter σ_P (green curve in *Figure 4A*). These instabilities in cell shape frequently lead to a loss of persistence in the rotational motion of the cells (growing σ_ω; blue curve in *Figure 4A*).

Tissue-level dynamics

As an application of our computational model at the tissue level, we considered a setup in which an epithelial cell sheet expands into free space. As in recent experimental studies (*Serra-Picamal et al., 2012*; *Sepúlveda et al., 2013*; *Trepat et al., 2009*; *Poujade et al., 2007*), we confined cells laterally between two fixed boundaries, within which they proliferated until they reached confluence; in the y-direction we imposed periodic boundary conditions. Then we removed the boundaries and studied how the cell sheet expands. In order to quantify tissue expansion, we monitored cell density and velocity, as well as the mechanical stresses driving the expansion process. *Figure 5* shows our results for two representative parameter regimes that highlight the difference between a dynamics dominated by cell motility in the absence of cell proliferation, and a contrasting regime where cells with low motility grow and divide depending on the local cell density. To simulate large numbers of cells, we decreased the amount of hexagons that are typically occupied by each cell (the simulation cost scales linearly with the summed area of all cells) by setting the average polarization field to $\epsilon_0 = 35$. For each set of parameters, we performed and averaged 100 independent simulations.

We first investigated how a densely packed pre-grown tissue of mitostatic cells with high polarizability (large $\Delta\epsilon$) expands into cell-free space upon removal of the confining boundaries at the tissue's lateral edges (*Figure 5A*). As the cells migrate into the cell-free space, we observe a strongly (spatially) heterogeneous decrease in the initially high and uniform cell density and mechanical pressure in the expanding monolayer (*Figure 5B,C*). This is quite distinct from the behavior of a homogeneous and ideally elastic thin sheet, which would simply show a homogeneous relaxation in density as it relaxes towards its rest state. Moreover, cell polarization and the ensuing active cell migration lead to inhomogeneously distributed traction stresses in the monolayer. After initial expansion of the monolayer, facilitated by high mechanical pressure, the cells at the monolayer edge begin to polarize outwards, which enhances outward front migration. These actively propagating cells exert traction on the trailing cells, and thereby yield a trailing region with negative stress (*Figure 5C*). Taken together, this gives rise to a characteristic X-shaped pattern in the kymograph of the total mechanical stresses $\langle\sigma_{xx}\rangle_y$ (*Figure 5C*). This profile closely resembles the first period of mechanical waves observed experimentally (*Serra-Picamal et al., 2012*). It illustrates how stress is transferred towards the center of the monolayer when cells are highly motile and collectively contribute to tissue expansion. At the end of the simulated time window, the cell density exhibited a minimum in the center of the sheet (*Figure 5B*). This is due to stretching of the central group of cells caused by the equally strong traction forces exerted by their migrating neighbors on both sides. Finally, the simulations also show that outward cell velocities increase approximately linearly with the distance from the center, confirming that in this configuration the entire cell sheet contributes to the monolayer expansion (*Figure 5D*).

To explore the possible range of tissue dynamics and expansion, we also investigated a qualitatively different parameter regime where cells are less densely packed and can also polarize less due

eLIFE Research article

Figure 5. Expansion of a confluent epithelial cell sheet after removal of boundaries positioned at $x = \pm 175$ for two different parameter settings. (Stiffness parameters $\kappa_P = 0.12$, $\kappa_A = 0.18$; average polarization field $\epsilon_0 = 35$; signaling radius $R = 2$; cytoskeletal update rate $\mu = 0.1$; cell-cell adhesion $B = 12$; cell-cell dissipation $\Delta B = 0$; cell-substrate dissipation $D = 0$; cell-substrate adhesion penalty $\varphi = 0$; 100 independent simulations for each set of parameters). (A–D) Tissue expansion for a migration-dominated setup without explicit cell growth and mitosis. (3300-cell system; maximum cell polarity $\Delta\epsilon = 30$). (E–H) Tissue expansion at low density and cell polarizability for a cell sheet comprised of dividing cells. (Initially a 2500-cell system; maximum cell polarity $\Delta\epsilon = 10$; growth time $T_g = 180$; division time $T_d = 20$; size threshold for cell growth $A_T = 1\,A_{\text{ref}}$, where A_{ref} is the size of a solitary cell in equilibrium). (A, E) Snapshots of the polarization field ϵ; cf. *Figure 5—video 1* and *Figure 5—video 2*. (B, F) Kymographs showing the cell density averaged over the y-direction and (top) final snapshots of the cell density profiles. (C, G) Kymographs showing the component σ_{xx} of the stress tensor averaged over the y-direction and (top) final snapshots of the stress profiles. (D, H) Kymographs showing the component v_x of the cell velocities averaged over the y-direction and (top) final snapshot of the velocity profiles. The online version of this article includes the following video and figure supplement(s) for figure 5:

Figure supplement 1. Monolayer expansion depends on dissipation and cell polarizability.

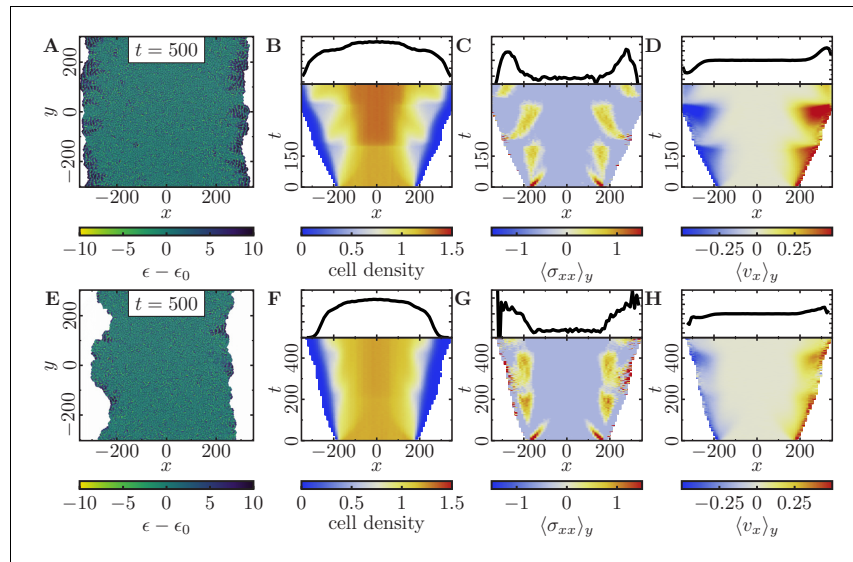**Figure 5—video 1.** Motility-dominated tissue dynamics.

https://elifesciences.org/articles/46842#fig5video1

Figure 5—video 2. Proliferation-dominated tissue dynamics.

https://elifesciences.org/articles/46842#fig5video2

to a narrower range of polarizability (*Figure 5E*). Here, the expansion of the monolayer is mainly driven by cell division, and cells keep dividing until they reach a homeostatic cell density (*Figure 5F*). Even though cells should typically exceed the threshold size and hence enter the growth phase at different times, we observe that the cell sheet exhibits periodic 'bursts' of growth (*Figure 5F*) coinciding with the total duration of a complete cell cycle (200 MCS) and alternating with cell migration (*Figure 5H*). These periodic 'bursts' can be explained as follows. Initially, the slightly compressed monolayer expands to relieve mechanical pressure. Due to this initial motion, the cells at the monolayer edge begin to polarize outwards. As in the previous case, where cell proliferation is absent (*Figure 5A–D*), the polarized cells enhance outward front migration and stretch the cells in the bulk of the cell sheet. For the same reasons as before, we observe a typical X-shaped stress pattern in the kymograph (*Figure 5G*), albeit less pronounced due to the lower polarizability of the cells (cf. *Figure 5C*). Because a broad region in the monolayer bulk is stretched by the actively migrating cell

Figure 6. Expansion of a confluent epithelial cell sheet after removal of boundaries positioned at $x = \pm 175$ for two different parameter settings that produce rough tissue fronts. (Initially a 2500-cell system; stiffness parameters $\kappa_P = 0.10$, $\kappa_A = 0.18$; average polarization field $\epsilon_0 = 35$; maximum cell polarity $\Delta\epsilon = 20$; signaling radius $R = 5$; cytoskeletal update rate $\mu = 0.1$; cell-cell adhesion $B = 5$; cell-cell dissipation $\Delta B = 10$; cell-substrate dissipation $D = 0$; cell-substrate adhesion penalty $\varphi = 0$; growth time $T_g = 180$; division time $T_d = 20$; 100 independent simulations for each set of parameters). (A–D) Tissue expansion at low density and cell polarizability for a cell sheet comprised of quickly dividing cells. (Size threshold for cell growth $A_T = 1.05 A_{\text{ref}}$, where A_{ref} is the size of a solitary cell in equilibrium). (E–H) Tissue expansion at low density and cell polarizability for a cell sheet comprised of slowly dividing cells. (Size threshold for cell growth $A_T = 1.10 A_{\text{ref}}$, where A_{ref} is the size of a solitary cell in equilibrium). (A, E) Snapshots of the polarization field ϵ; cf. *Figure 6—video 1* and *Figure 6—video 2*. (B, F) Kymographs showing the cell density averaged over the y-direction and (*top*) final snapshots of the cell density profiles. (C, G) Kymographs showing the component σ_{xx} of the stress tensor averaged over the y-direction and (*top*) final snapshots of the stress profiles. (D, H) Kymographs showing the component v_x of the cell velocities averaged over the y-direction and (*top*) final snapshot of the velocity profiles.

The online version of this article includes the following video(s) for figure 6:

Figure 6—video 1. Weak monolayer roughening (fingering) in motility-dominated tissue with quick proliferation.
https://elifesciences.org/articles/46842#fig6video1

Figure 6—video 2. Strong monolayer roughening in motility-dominated tissue with slow proliferation.
https://elifesciences.org/articles/46842#fig6video2

fronts, these cells exceed the threshold size and begin growing approximately in phase. Once the mechanical pressure of the cell sheet is relieved, it will stop expanding (*Figure 5H*). However, cell growth and division once more lead to an increase in mechanical pressure (and cell density) in the monolayer (*Figure 5F,G*). This cycle of migration-dominated monolayer expansion and cell-density-dependent cell growth and division results in a periodic recurrence of the X-shaped stress pattern (*Figure 5G*), closely resembling the pattern observed in experiments (*Serra-Picamal et al., 2012*). On a sidenote, the synchronization of the cell division and cell migration phases by the deterministic portion of the cell cycle can be counteracted by introducing additional stochastic terms in the transition between the different phases of the cell cycle (cf. 'Cell proliferation and mitosis' in Appendix 1).

Note that the inhomogeneously distributed traction stresses in the monolayer, and its wave-like behavior, ultimately emerge from cell polarization and the ensuing active cell migration. Therefore,

these traction patterns would look much less prominent if one were to inhibit cell motility (compare *Figure 5C* with *Figure 5G*).

Finally, we investigated which parameters control the roughness of the tissue fronts. We found that increasing cell motility, or increasing cell-cell dissipation leads to rougher front morphologies (*Figure 5—figure supplement 1* and 'Velocity and roughness of spreading tissue' in Appendix 2). Therefore, we hypothesized that one could observe *fingering* of cell monolayers by adjusting the parameters accordingly:

- Increase of cell motility by decreasing the membrane stiffness and at the same time increasing polarizability and signaling radius of the cells.
- Increase of cell-cell dissipation and slight decrease of cell-cell adhesion.
- Slower and less homogeneously distributed cell division by increasing the cell threshold size.

Indeed, we then observe a drastic roughening of the cell fronts and small cohorts of cells that coherently move into cell-free space (*Figure 6*). This roughening is more pronounced if we further increase the threshold size that a cell has to exceed to initiate growth (cf. *Figure 6A,E*). Analogously to our previous discussion, we observe that an increasing mechanical pressure in the monolayer due to the division of cells initiates outward cell migration (*Figure 6B,F*). Then, cells in the tissue begin to polarize outwards and coordinate their motion with their neighboring cells, leading to small coordinated cell cohorts. As before, we also find distinct traction force patterns, as recurring waves of high stress travel backwards relative to the leading edges (*Figure 6C,G*), and distinct recurring velocity patterns (*Figure 6D,H*).

Discussion

In this work, we have proposed a generalization of the cellular Potts model (*Graner and Glazier, 1992*). The model implements a coarse-grained routine that captures the salient features of cytoskeletal remodeling processes on subcellular scales, while being computationally tractable enough to allow for the simulation of entire tissues containing up to $\mathcal{O}(10^4)$ cells. We have used the model to study the transition from single-cell to cohort cell migration in terms of the interplay between the pertinent cellular functions. Specifically, we have demonstrated that our model consistently reproduces the dynamics and morphology of motile cells down to the level of solitary cells. Our studies also

Table 1. Source and parameter files used for each figure.
All source and parameter files are found in *Source data 1*.

Figure	Simulation code	Processing code	Parameters
Figure 2	CPM_NoDivision	TrajectoryAnalysisSingle	single_Q
Figure 2—figure supplement 1 (A-D)	CPM_NoDivision	TrajectoryAnalysisSingle	single_DQ
Figure 2—figure supplement 1 (E-H)	CPM_NoDivision	TrajectoryAnalysisSingle	single_DM
Figure 3	CPM_NoDivision	TrajectoryAnalysisSingle	single_R
Figure 4	CPM_NoDivision	TrajectoryAnalysisCircularPattern	rotation_Q
Figure 4—figure supplement 1	CPM_NoDivision	TrajectoryAnalysisCircularPattern	rotation_N_R1
Figure 4—figure supplement 2	CPM_NoDivision	TrajectoryAnalysisCircularPattern	rotation_N_R2
Figure 4—figure supplement 3	CPM_NoDivision	TrajectoryAnalysisCircularPattern	rotation_N_R3
Figure 5 (A-D)	CPM_Division		wound_nodiv
Figure 5 (E-H)	CPM_Division		wound_div
Figure 5—figure supplement 1 (A-B)	CPM_Division_Supplement	FrontAnalysis	wound_div_A
Figure 5—figure supplement 1 (C-D)	CPM_Division_Supplement	FrontAnalysis	wound_div_D
Figure 5—figure supplement 1 (E, F)	CPM_Division_Supplement	FrontAnalysis	wound_div_Q
Figure 6 (A-D)	CPM_Division		wound_div_fing_1.0
Figure 6 (E-H)	CPM_Division		wound_div_fing_1.1
Appendix 2—figure 1	CPM_NoDivision	TrajectoryAnalysisSingle	single_A

reveal that cytoskeletal forces (relative to cell contractility), as well as the spatial organization of the cells' lamellipodia, significantly affect the statistics of cellular trajectories, both in the context of single-cell motion and in cohesive cell groups restricted to circular micropatterns. On larger scales, our simulation results suggest that the dynamics of expanding tissues strongly depends on the specific properties of the constituent cells. If monolayer expansion is driven by active cell migration throughout the tissue, then the cell sheet exhibits typical traction-force patterns and an X-shape in the corresponding kymograph. Additionally, a cell-density-dependent cell growth leads to a periodic recurrence of these traction-force patterns in a cycle of migration-dominated expansion and 'burst'-like cell proliferation.

Taken together, our results further highlight the intricacies of collective cell migration, which involves a multitude of intra- and inter-cellular signaling mechanisms operating at different scales in length and time. Establishing a comprehensive picture that incorporates and elucidates the mechanistic basis of these phenomena remains a pressing and challenging task. The multiscale modeling approach proposed here provides a direct link between subcellular processes and macroscopic dynamic observables, and might thus offer a viable route towards this goal.

Materials and methods

The computational model is described in section 'Computational model'. The numerical implementation of the model is discussed in detail in Appendix 1. The parameter files and source files associated with the figures are given in *Table 1*.

Acknowledgements

Additional information

Author contributions

Florian Thüroff, Conceptualization, Software, Formal analysis, Validation, Investigation, Visualization, Methodology; Andriy Goychuk, Conceptualization, Data curation, Software, Formal analysis, Validation, Investigation, Visualization, Methodology; Matthias Reiter, Software, Formal analysis, Validation, Investigation, Visualization, Methodology; Erwin Frey, Conceptualization, Resources, Formal analysis, Supervision, Funding acquisition, Validation, Investigation, Methodology, Project administration

Author ORCIDs
Andriy Goychuk https://orcid.org/0000-0001-6776-9437
Erwin Frey https://orcid.org/0000-0001-8792-3358

Decision letter and Author response
Decision letter https://doi.org/10.7554/eLife.46842.sa1
Author response https://doi.org/10.7554/eLife.46842.sa2

Additional files

Supplementary files
- Source code 1. Simulation code, processing code and parameter files.

- Transparent reporting form

Data availability
We have uploaded the source code used in the main part of our study as well as the one used in the appendix. Furthermore, we have provided the full list of parameters in the figure captions, as well as exemplary parameter files for all applicable figures.

References

Albert PJ, Schwarz US. 2014. Dynamics of cell shape and forces on micropatterned substrates predicted by a cellular potts model. *Biophysical Journal* **106**:2340–2352. DOI: https://doi.org/10.1016/j.bpj.2014.04.036, PMID: 24896113

Albert PJ, Schwarz US. 2016. Dynamics of cell ensembles on adhesive micropatterns: bridging the gap between single cell spreading and collective cell migration. *PLOS Computational Biology* **12**:e1004863. DOI: https://doi.org/10.1371/journal.pcbi.1004863, PMID: 27054883

Alberts B, Johnson A, Lewis J, Raff M. 2015. *Molecular Biology of the Cell*. Sixth Edition . Garland Science.

Allen GM, Lee KC, Barnhart EL, Tsuchida MA, Wilson CA, Gutierrez E, Groisman A. 2018. Cell mechanics at the rear act to steer the direction of cell migration. *bioRxiv*. DOI: https://doi.org/10.1101/443408

Alt S, Ganguly P, Salbreux G. 2017. Vertex models: from cell mechanics to tissue morphogenesis. *Philosophical Transactions of the Royal Society B: Biological Sciences* **372**:20150520. DOI: https://doi.org/10.1098/rstb.2015.0520

Angelini TE, Hannezo E, Trepat X, Marquez M, Fredberg JJ, Weitz DA. 2011. Glass-like dynamics of collective cell migration. *PNAS* **108**:4714–4719. DOI: https://doi.org/10.1073/pnas.1010059108, PMID: 21321233

Banerjee S, Utuje KJ, Marchetti MC. 2015. Propagating stress waves during epithelial expansion. *Physical Review Letters* **114**:228101. DOI: https://doi.org/10.1103/PhysRevLett.114.228101, PMID: 26196647

Barber F, Ho PY, Murray AW, Amir A. 2017. Details matter: noise and model structure set the relationship between cell size and cell cycle timing. *Frontiers in Cell and Developmental Biology* **5**:92. DOI: https://doi.org/10.3389/fcell.2017.00092, PMID: 29164112

Basan M, Elgeti J, Hannezo E, Rappel WJ, Levine H. 2013. Alignment of cellular motility forces with tissue flow as a mechanism for efficient wound healing. *PNAS* **110**:2452–2459. DOI: https://doi.org/10.1073/pnas.1219937110, PMID: 23345440

Camley BA, Zhao Y, Li B, Levine H, Rappel WJ. 2013. Periodic migration in a physical model of cells on micropatterns. *Physical Review Letters* **111**:158102. DOI: https://doi.org/10.1103/PhysRevLett.111.158102, PMID: 24160631

Camley BA, Zhang Y, Zhao Y, Li B, Ben-Jacob E, Levine H, Rappel WJ. 2014. Polarity mechanisms such as contact inhibition of locomotion regulate persistent rotational motion of mammalian cells on micropatterns. *PNAS* **111**: 14770–14775. DOI: https://doi.org/10.1073/pnas.1414498111, PMID: 25258412

Camley BA, Rappel W-J. 2014. Velocity alignment leads to high persistence in confined cells. *Physical Review E* **89**:062705. DOI: https://doi.org/10.1103/PhysRevE.89.062705

Deforet M, Hakim V, Yevick HG, Duclos G, Silberzan P. 2014. Emergence of collective modes and tri-dimensional structures from epithelial confinement. *Nature Communications* **5**:3747. DOI: https://doi.org/10.1038/ncomms4747, PMID: 24796352

Dietrich M, Le Roy H, Brückner DB, Engelke H, Zantl R, Rädler JO, Broedersz CP. 2018. Guiding 3D cell migration in deformed synthetic hydrogel microstructures. *Soft Matter* **14**:2816–2826. DOI: https://doi.org/10.1039/C8SM00018B, PMID: 29595213

Doxzen K, Vedula SR, Leong MC, Hirata H, Gov NS, Kabla AJ, Ladoux B, Lim CT. 2013. Guidance of collective cell migration by substrate geometry. *Integrative Biology* **5**:1026–1035. DOI: https://doi.org/10.1039/c3ib40054a, PMID: 23784144

Friedl P. 2004. Prespecification and plasticity: shifting mechanisms of cell migration. *Current Opinion in Cell Biology* **16**:14–23. DOI: https://doi.org/10.1016/j.ceb.2003.11.001, PMID: 15037300

Friedl P, Gilmour D. 2009. Collective cell migration in Morphogenesis, regeneration and Cancer. *Nature Reviews Molecular Cell Biology* **10**:445–457. DOI: https://doi.org/10.1038/nrm2720, PMID: 19546857

Friedl P, Weigelin B. 2008. Interstitial leukocyte migration and immune function. *Nature Immunology* **9**:960–969. DOI: https://doi.org/10.1038/ni.f.212, PMID: 18711433

Gibson WT, Gibson MC. 2009. Cell topology, geometry, and morphogenesis in proliferating epithelia. *Current Topics in Developmental Biology* **89**:87–114. DOI: https://doi.org/10.1016/S0070-2153(09)89004-2, PMID: 19737643

Glazier JA, Graner F. 1993. Simulation of the differential adhesion driven rearrangement of biological cells. *Physical Review E* **47**:2128–2154. DOI: https://doi.org/10.1103/PhysRevE.47.2128

Goychuk A, Brückner DB, Holle AW, Spatz CPB, Frey E. 2018. Morphology and motility of cells on soft substrates. *arXiv*. https://arxiv.org/abs/1808.00314.

Graner F, Glazier JA. 1992. Simulation of biological cell sorting using a two-dimensional extended potts model. *Physical Review Letters* **69**:2013–2016. DOI: https://doi.org/10.1103/PhysRevLett.69.2013, PMID: 10046374

Gumbiner BM. 2005. Regulation of cadherin-mediated adhesion in morphogenesis. *Nature Reviews Molecular Cell Biology* **6**:622–634. DOI: https://doi.org/10.1038/nrm1699, PMID: 16025097

Huang S, Brangwynne CP, Parker KK, Ingber DE. 2005. Symmetry-breaking in mammalian cell cohort migration during tissue pattern formation: role of random-walk persistence. *Cell Motility and the Cytoskeleton* **61**:201–213. DOI: https://doi.org/10.1002/cm.20077, PMID: 15986404

Hubatsch L, Peglion F, Reich JD, Rodrigues NTL, Hirani N, Illukkumbura R, Goehring NW. 2019. A cell-size threshold limits cell polarity and asymmetric division potential. *Nature Physics* **15**:1078–1085. DOI: https://doi.org/10.1038/s41567-019-0601-x

Jones MC, Askari JA, Humphries JD, Humphries MJ. 2018. Cell adhesion is regulated by CDK1 during the cell cycle. *The Journal of Cell Biology* **217**:3203–3218. DOI: https://doi.org/10.1083/jcb.201802088, PMID: 29930204

Kabla AJ. 2012. Collective cell migration: leadership, invasion and segregation. *Journal of the Royal Society Interface* **9**:3268–3278. DOI: https://doi.org/10.1098/rsif.2012.0448

Kassianidou E, Probst D, Jäger J, Lee S, Roguet AL, Schwarz US, Kumar S. 2019. Extracellular matrix geometry and initial adhesive position determine stress fiber network organization during cell spreading. *Cell Reports* **27**:1897–1909. DOI: https://doi.org/10.1016/j.celrep.2019.04.035, PMID: 31067472

Keren K, Pincus Z, Allen GM, Barnhart EL, Marriott G, Mogilner A, Theriot JA. 2008. Mechanism of shape determination in motile cells. *Nature* **453**:475–480. DOI: https://doi.org/10.1038/nature06952, PMID: 18497816

Kovacs EM, Goodwin M, Ali RG, Paterson AD, Yap AS. 2002. Cadherin-directed actin assembly: e-cadherin physically associates with the Arp2/3 complex to direct actin assembly in nascent adhesive contacts. *Current Biology : CB* **12**:379–382. DOI: https://doi.org/10.1016/s0960-9822(02)00661-9, PMID: 11882288

Lämmermann T, Sixt M. 2009. Mechanical modes of 'amoeboid' cell migration. *Current Opinion in Cell Biology* **21**:636–644. DOI: https://doi.org/10.1016/j.ceb.2009.05.003, PMID: 19523798

Landau LD, Pitaevskii LP, Kosevich AM, Lifshitz EM. 1986. *Theory of Elasticity*. Third Edition. Butterworth-Heinemann.

Lauffenburger DA, Horwitz AF. 1996. Cell migration: a physically integrated molecular process. *Cell* **84**:359–369. DOI: https://doi.org/10.1016/S0092-8674(00)81280-5, PMID: 8608589

Lecaudey V, Gilmour D. 2006. Organizing moving groups during morphogenesis. *Current Opinion in Cell Biology* **18**:102–107. DOI: https://doi.org/10.1016/j.ceb.2005.12.001, PMID: 16352429

Leckband DE, le Duc Q, Wang N, de Rooij J. 2011. Mechanotransduction at cadherin-mediated adhesions. *Current Opinion in Cell Biology* **23**:523–530. DOI: https://doi.org/10.1016/j.ceb.2011.08.003, PMID: 21890337

Li JF, Lowengrub J. 2014. The effects of cell compressibility, motility and contact inhibition on the growth of tumor cell clusters using the cellular potts model. *Journal of Theoretical Biology* **343**:79–91. DOI: https://doi.org/10.1016/j.jtbi.2013.10.008, PMID: 24211749

Liu Z, van Grunsven LA, Van Rossen E, Schroyen B, Timmermans JP, Geerts A, Reynaert H. 2010. Blebbistatin inhibits contraction and accelerates migration in mouse hepatic stellate cells. *British Journal of Pharmacology* **159**:304–315. DOI: https://doi.org/10.1111/j.1476-5381.2009.00477.x, PMID: 20039876

Löber J, Ziebert F, Aranson IS. 2015. Collisions of deformable cells lead to collective migration. *Scientific Reports* **5**:9172. DOI: https://doi.org/10.1038/srep09172, PMID: 25779619

Lock JG, Jones MC, Askari JA, Gong X, Oddone A, Olofsson H, Göransson S, Lakadamyali M, Humphries MJ, Strömblad S. 2018. Reticular adhesions are a distinct class of cell-matrix adhesions that mediate attachment during mitosis. *Nature Cell Biology* **20**:1290–1302. DOI: https://doi.org/10.1038/s41556-018-0220-2, PMID: 30361699

Lou SS, Diz-Muñoz A, Weiner OD, Fletcher DA, Theriot JA. 2015. Myosin light chain kinase regulates cell polarization independently of membrane tension or rho kinase. *The Journal of Cell Biology* **209**:275–288. DOI: https://doi.org/10.1083/jcb.201409001, PMID: 25918227

Marée AF, Jilkine A, Dawes A, Grieneisen VA, Edelstein-Keshet L. 2006. Polarization and movement of keratocytes: a multiscale modelling approach. *Bulletin of Mathematical Biology* **68**:1169–1211. DOI: https://doi.org/10.1007/s11538-006-9131-7, PMID: 16794915

Marée AF, Grieneisen VA, Edelstein-Keshet L. 2012. How cells integrate complex stimuli: the effect of feedback from phosphoinositides and cell shape on cell polarization and motility. *PLOS Computational Biology* **8**:e1002402. DOI: https://doi.org/10.1371/journal.pcbi.1002402, PMID: 22396633

Reprint of published manuscript

Marel AK, Zorn M, Klingner C, Wedlich-Söldner R, Frey E, Rädler JO. 2014. Flow and diffusion in channel-guided cell migration. *Biophysical Journal* **107**:1054–1064. DOI: https://doi.org/10.1016/j.bpj.2014.07.017, PMID: 251 85541

Milo R, Phillips R. 2015. *Cell Biology by the Numbers.* First Edition. Garland Science.

Minc N, Piel M. 2012. Predicting division plane position and orientation. *Trends in Cell Biology* **22**:193–200. DOI: https://doi.org/10.1016/j.tcb.2012.01.003, PMID: 22321291

Mogilner A. 2009. Mathematics of cell motility: have we got its number? *Journal of Mathematical Biology* **58**: 105–134. DOI: https://doi.org/10.1007/s00285-008-0182-2, PMID: 18461331

Niculescu I, Textor J, de Boer RJ. 2015. Crawling and gliding: a computational model for Shape-Driven cell migration. *PLOS Computational Biology* **11**:e1004280. DOI: https://doi.org/10.1371/journal.pcbi.1004280, PMID: 26488304

Ofer N, Mogilner A, Keren K. 2011. Actin disassembly clock determines shape and speed of lamellipodial fragments. *PNAS* **108**:20394–20399. DOI: https://doi.org/10.1073/pnas.1105333108, PMID: 22159033

Ouchi NB, Glazier JA, Rieu J-P, Upadhyaya A, Sawada Y. 2003. Improving the realism of the cellular potts model in simulations of biological cells. *Physica A: Statistical Mechanics and Its Applications* **329**:451–458. DOI: https://doi.org/10.1016/S0378-4371(03)00574-0

Pavel M, Renna M, Park SJ, Menzies FM, Ricketts T, Füllgrabe J, Ashkenazi A, Frake RA, Lombarte AC, Bento CF, Franze K, Rubinsztein DC. 2018. Contact inhibition controls cell survival and proliferation via YAP/TAZ-autophagy Axis. *Nature Communications* **9**:2961. DOI: https://doi.org/10.1038/s41467-018-05388-x, PMID: 30054475

Pollard TD, Borisy GG. 2003. Cellular motility driven by assembly and disassembly of actin filaments. *Cell* **112**: 453–465. DOI: https://doi.org/10.1016/S0092-8674(03)00120-X, PMID: 12600310

Poujade M, Grasland-Mongrain E, Hertzog A, Jouanneau J, Chavrier P, Ladoux B, Buguin A, Silberzan P. 2007. Collective migration of an epithelial monolayer in response to a model wound. *PNAS* **104**:15988–15993. DOI: https://doi.org/10.1073/pnas.0705062104, PMID: 17905871

Puliafito A, Hufnagel L, Neveu P, Streichan S, Sigal A, Fygenson DK, Shraiman BI. 2012. Collective and single cell behavior in epithelial contact inhibition. *PNAS* **109**:739–744. DOI: https://doi.org/10.1073/pnas.1007809109, PMID: 22228306

Ranft J, Basan M, Elgeti J, Joanny JF, Prost J, Jülicher F. 2010. Fluidization of tissues by cell division and apoptosis. *PNAS* **107**:20863–20868. DOI: https://doi.org/10.1073/pnas.1011086107, PMID: 21078958

Raucher D, Sheetz MP. 2000. Cell spreading and lamellipodial extension rate is regulated by membrane tension. *The Journal of Cell Biology* **148**:127–136. DOI: https://doi.org/10.1083/jcb.148.1.127, PMID: 10629223

Raynaud F, Ambühl ME, Gabella C, Bornert A, Sbalzarini IF, Meister J-J, Verkhovsky AB. 2016. Minimal model for spontaneous cell polarization and edge activity in oscillating, rotating and migrating cells. *Nature Physics* **12**:367–373. DOI: https://doi.org/10.1038/nphys3615

Reeves C, Winkler B, Ziebert F, Aranson IS. 2018. Rotating lamellipodium waves in polarizing cells. *Communications Physics* **1**:73. DOI: https://doi.org/10.1038/s42005-018-0075-7

Rens EG, Merks RMH. 2017. Cell contractility facilitates alignment of cells and tissues to static uniaxial stretch. *Biophysical Journal* **112**:755–766. DOI: https://doi.org/10.1016/j.bpj.2016.12.012, PMID: 28256235

Ridley AJ, Schwartz MA, Burridge K, Firtel RA, Ginsberg MH, Borisy G, Parsons JT, Horwitz AR. 2003. Cell migration: integrating signals from front to back. *Science* **302**:1704–1709. DOI: https://doi.org/10.1126/science.1092053, PMID: 14657486

Schwartz MA, Shattil SJ. 2000. Signaling networks linking integrins and rho family GTPases. *Trends in Biochemical Sciences* **25**:388–391. DOI: https://doi.org/10.1016/S0968-0004(00)01605-4, PMID: 10916159

Segerer FJ, Thüroff F, Piera Alberola A, Frey E, Rädler JO. 2015. Emergence and persistence of collective cell migration on small circular micropatterns. *Physical Review Letters* **114**:228102. DOI: https://doi.org/10.1103/PhysRevLett.114.228102, PMID: 26196648

Sepúlveda N, Petitjean L, Cochet O, Grasland-Mongrain E, Silberzan P, Hakim V. 2013. Collective cell motion in an epithelial sheet can be quantitatively described by a stochastic interacting particle model. *PLOS Computational Biology* **9**:e1002944. DOI: https://doi.org/10.1371/journal.pcbi.1002944, PMID: 23505356

Serra-Picamal X, Conte V, Vincent R, Anon E, Tambe DT, Bazellieres E, Butler JP, Fredberg JJ, Trepat X. 2012. Mechanical waves during tissue expansion. *Nature Physics* **8**:628–634. DOI: https://doi.org/10.1038/nphys2355

Shao D, Rappel WJ, Levine H. 2010. Computational model for cell morphodynamics. *Physical Review Letters* **105**: 108104. DOI: https://doi.org/10.1103/PhysRevLett.105.108104, PMID: 20867552

Shao D, Levine H, Rappel WJ. 2012. Coupling actin flow, adhesion, and morphology in a computational cell motility model. *PNAS* **109**:6851–6856. DOI: https://doi.org/10.1073/pnas.1203252109, PMID: 22493219

Shraiman BI. 2005. Mechanical feedback as a possible regulator of tissue growth. *PNAS* **102**:3318–3323. DOI: https://doi.org/10.1073/pnas.0404782102, PMID: 15728365

Stoker MG, Rubin H. 1967. Density dependent inhibition of cell growth in culture. *Nature* **215**:171–172. DOI: https://doi.org/10.1038/215171a0, PMID: 6049107

Stokes CL, Lauffenburger DA, Williams SK. 1991. Migration of individual microvessel Endothelial-Cells - Stochastic-Model and parameter measurement. *Journal of Cell Science* **99 Pt 2**:419–430. PMID: 1885678

Szabó B, Szöllösi GJ, Gönci B, Jurányi Z, Selmeczi D, Vicsek T. 2006. Phase transition in the collective migration of tissue cells: experiment and model. *Physical Review E* **74**:061908. DOI: https://doi.org/10.1103/PhysRevE.74.061908

Szabó A, Ünnep R, Méhes E, Twal WO, Argraves WS, Cao Y, Czirók A. 2010. Collective cell motion in endothelial monolayers. *Physical Biology* **7**:046007. DOI: https://doi.org/10.1088/1478-3975/7/4/046007, PMID: 21076204

Szabó A, Merks RM. 2013. Cellular potts modeling of tumor growth, tumor invasion, and tumor evolution. *Frontiers in Oncology* **3**:87. DOI: https://doi.org/10.3389/fonc.2013.00087, PMID: 23596570

Tarle V, Gauquelin E, Vedula SRK, D'Alessandro J, Lim CT, Ladoux B, Gov NS. 2017. Modeling collective cell migration in geometric confinement. *Physical Biology* **14**:035001. DOI: https://doi.org/10.1088/1478-3975/aa6591, PMID: 28467320

Trepat X, Wasserman MR, Angelini TE, Millet E, Weitz DA, Butler JP, Fredberg JJ. 2009. Physical forces during collective cell migration. *Nature Physics* **5**:426–430. DOI: https://doi.org/10.1038/nphys1269

van Oers RF, Rens EG, LaValley DJ, Reinhart-King CA, Merks RM. 2014. Mechanical cell-matrix feedback explains pairwise and collective endothelial cell behavior in vitro. *PLOS Computational Biology* **10**:e1003774. DOI: https://doi.org/10.1371/journal.pcbi.1003774, PMID: 25121971

Vedula SR, Leong MC, Lai TL, Hersen P, Kabla AJ, Lim CT, Ladoux B. 2012. Emerging modes of collective cell migration induced by geometrical constraints. *PNAS* **109**:12974–12979. DOI: https://doi.org/10.1073/pnas.1119313109, PMID: 22814373

Webb DJ, Parsons JT, Horwitz AF. 2002. Adhesion assembly, disassembly and turnover in migrating cells – over and over and over again. *Nature Cell Biology* **4**:E97–E100. DOI: https://doi.org/10.1038/ncb0402-e97, PMID: 11944043

Wilson CA, Tsuchida MA, Allen GM, Barnhart EL, Applegate KT, Yam PT, Ji L, Keren K, Danuser G, Theriot JA. 2010. Myosin II contributes to cell-scale actin network treadmilling through network disassembly. *Nature* **465**:373–377. DOI: https://doi.org/10.1038/nature08994, PMID: 20485438

Wu PH, Giri A, Sun SX, Wirtz D. 2014. Three-dimensional cell migration does not follow a random walk. *PNAS* **111**:3949–3954. DOI: https://doi.org/10.1073/pnas.1318967111, PMID: 24594603

Ziebert F, Swaminathan S, Aranson IS. 2012. Model for self-polarization and motility of keratocyte fragments. *Journal of the Royal Society Interface* **9**:1084–1092. DOI: https://doi.org/10.1098/rsif.2011.0433

Ziebert F, Aranson IS. 2013. Effects of adhesion dynamics and substrate compliance on the shape and motility of crawling cells. *PLOS ONE* **8**:e64511. DOI: https://doi.org/10.1371/journal.pone.0064511

Appendix 1

Computational model

In this section, we describe in detail the implementation of our computational model, which has been outlined briefly in the main text. While the biological rationale behind our modeling approach has been discussed in the main text, our focus here is on the technical aspects and the details of the numerical implementation. To facilitate subsequent discussions on implementation details, we start by introducing some model-specific terminology which will be used throughout this section to illustrate the mechanics of our model.
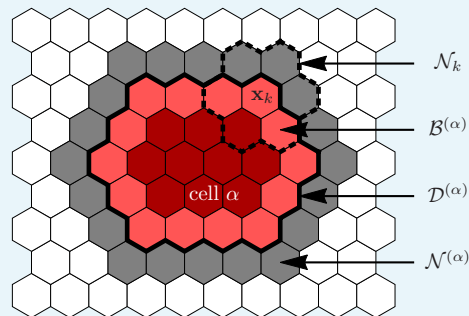
Computational grid

The basic data structure that underlies our computational model is referred to as the *grid*; see *Appendix 1—figure 1*. The grid itself is implemented as a regular, space-filling lattice with lattice vectors $\{\mathbf{x}_i\}_{i=1,\dots,N}$. Each lattice vector $\mathbf{x}_i$ is understood to represent its associated Voronoi cell which will be referred to as *grid site*. To be specific, we consider triangular tilings $\{\mathbf{x}_i\}_{i=1,\dots,N}$, such that each grid site is a hexagon, which is surrounded by 6 nearest-neighbor sites that define the neighborhood $\mathcal{N}_k$ of $\mathbf{x}_k$:

$$\mathcal{N}_k = \left\{ \mathbf{x}_j \mid \mathbf{x}_j \text{ is nearest neighbor of } \mathbf{x}_k \right\} \tag{S1}$$

Overall, the grid represents our general notion of (discretized) space, and each grid site holds information specific to cells as well as to environmental factors. In what follows, distances on this spatial grid will be measured in units of the distance between the midpoints of neighboring lattice sites, i.e.

$$\|\mathbf{x}_k - \mathbf{x}_j\| = 1 \iff j \in \mathcal{N}_k. \tag{S2}$$

This then implies for the side length ℓ and the two-dimensional volume (area) a of each hexagonal grid site: $\ell = 1/\sqrt{3}$ and $a = 3\sqrt{3}\,\ell^2/2$.

Appendix 1—figure 1. Illustration of the various sets defining a cell and its environment. Grid sites occupied by cell α, i.e. its domain $\mathcal{D}^{(\alpha)}$, are indicated in red colors. The cell's membrane sites, $\mathcal{B}^{(\alpha)}$, are indicated by the lighter red color, the cell's immediate neighborhood, $\mathcal{N}^{(\alpha)}$, is indicated in gray. Elementary events involving cell α always involve one grid site in $\mathcal{B}^{(\alpha)}$ and one grid site in $\mathcal{N}^{(\alpha)}$. For the hexagonal lattices used in this work, each grid site $\mathbf{x}_k$ is surrounded by 6 nearest neighbors which we collectively denote by $\mathcal{N}_k$.

Representation of biological cells

In the spirit of the cellular Potts model (**Graner and Glazier, 1992**; **Glazier and Graner, 1993**), each cell is represented by a simply connected set of lattice sites

$$\mathcal{D}^{(\alpha)} = \left\{ \mathbf{x}_k \mid c(\mathbf{x}_k) = \alpha \right\}, \tag{S3}$$

where the indicator function $c(\mathbf{x}_k)$ gives the index of the cell occupying $\mathbf{x}_k$. Here and in the following, we use latin indices to reference lattice sites, and greek indices to reference cells. The set $\mathcal{D}^{(\alpha)}$ used to represent the spatial extension of cell α, will be referred to as the *domain* of cell α. In our model, each grid site $\mathbf{x}_k$ can be occupied by at most one cell (i.e. we do not allow for overlapping cell domains). The absence of cells at $\mathbf{x}_k$ is numerically implemented by negative values of the indicator function, $c(\mathbf{x}_k) < 0$. Following this terminology, the area and the perimeter of cell α are given by:

$$A_\alpha = a \sum_{k=1}^{N} \delta_{\alpha, c(\mathbf{x}_k)} = \frac{3\sqrt{3}}{2} \ell^2 \sum_{k=1}^{N} \delta_{\alpha, c(\mathbf{x}_k)}, \tag{S4a}$$

$$P_\alpha = \ell \sum_{k=1}^{N} \sum_{\mathbf{x}_l \in \mathcal{N}_k} \delta_{\alpha, c(\mathbf{x}_k)} \left(1 - \delta_{\alpha, c(\mathbf{x}_l)}\right). \tag{S4b}$$

Model dynamics

Protrusion and retraction of cells

Biological cells are highly dynamic entities which constantly change shape and move around in space. To reflect this dynamic behavior computationally, the domain $\mathcal{D}^{(\alpha)}$ of cell α changes over time. The evolution of cell shape and position, as represented by $\mathcal{D}^{(\alpha)}$, proceeds via a succession of *elementary events*. In our numerical model, elementary events come in one of two basic flavors: *protrusion events* and *retraction events*. During a protrusion event, cell α (referred to as *source cell*) incorporates one grid site $\mathbf{x}_t$ (referred to as *target grid site*) from its neighborhood $\mathcal{N}^{(\alpha)}$,

$$\mathcal{D}_{\text{old}}^{(\alpha)} \to \mathcal{D}_{\text{new}}^{(\alpha)} = \mathcal{D}_{\text{old}}^{(\alpha)} \cup \{\mathbf{x}_t\}, \quad \mathbf{x}_t \in \mathcal{N}^{(\alpha)}, \tag{S5}$$

thereby increasing its cellular domain by one grid site. Here, the neighborhood of cell α, $\mathcal{N}^{(\alpha)}$, is defined as

$$\mathcal{N}^{(\alpha)} = \left\{ \mathbf{x}_l \mid \min_{\mathbf{x}_k \in \mathcal{D}^{(\alpha)}} \|\mathbf{x}_l - \mathbf{x}_k\| = 1 \right\}. \tag{S6}$$

During a retraction event, source cell α expels one of its membrane grid sites $\mathbf{x}_s \in \mathcal{B}^{(\alpha)}$,

$$\mathcal{D}_{\text{old}}^{(\alpha)} \to \mathcal{D}_{\text{new}}^{(\alpha)} = \mathcal{D}_{\text{old}}^{(\alpha)} \setminus \{\mathbf{x}_s\}, \quad \mathbf{x}_s \in \mathcal{B}_{\text{old}}^{(\alpha)}, \tag{S7}$$

where the set of membrane grid sites $\mathcal{B}^{(\alpha)}$ is defined as

$$\mathcal{B}^{(\alpha)} = \left\{ \mathbf{x}_k \in \mathcal{D}^{(\alpha)} \mid \min_{\mathbf{x}_l \in \mathcal{N}^{(\alpha)}} \|\mathbf{x}_k - \mathbf{x}_l\| = 1 \right\}. \tag{S8}$$

Protrusion and retraction events are the numerical analogs of cell protrusions and cell retractions.

In implementing the reassignment rules, **Equation S5** and **Equation S7**, we have to take into account that cellular domains must not overlap. For solitary cells moving in free space this does not imply any restrictions, and **Equation S5** and **Equation S7** apply directly. In the bulk of a confluent monolayer of adhesive cells, however, any protrusion of source cell α into the domain of cell β (referred to as *target cell*) must be accompanied by a corresponding

retraction event $\mathcal{D}_{\text{old}}^{(\beta)} \to \mathcal{D}_{\text{new}}^{(\beta)} = \mathcal{D}_{\text{old}}^{(\beta)} \setminus \{\mathbf{x}_t\}$, where $\mathbf{x}_t$ denotes the target grid site annexed by cell α. We emphasize, however, that the reverse is not generally true. If source cell α retracts, i.e. loses one of its boundary grid sites $\mathbf{x}_s \in \mathcal{B}^{(\alpha)}$, the lost grid site $\mathbf{x}_s$ faces either one of two conceivable fates: If, on the one hand, cohesion among cells is sufficiently strong (cf. section 'Rupture of cell contacts' for a definition of the notion 'sufficiently strong'), then the retraction of cell α exerts a pulling force on one of its neighboring cells β (the *target cell*) and forces the target cell to fill the emerging void at $\mathbf{x}_s$, i.e. $\mathcal{D}_{\text{old}}^{(\beta)} \to \mathcal{D}_{\text{new}}^{(\beta)} = \mathcal{D}_{\text{old}}^{(\beta)} \cup \{\mathbf{x}_s\}$, where $\mathbf{x}_s$ denotes the grid site lost by cell α. On the other hand, if adhesion between cells is weak, then retraction of the source cell α can lead to a rupture of pre-existing cell contacts between α and other cells at $\mathbf{x}_s$, such that the lost grid site $\mathbf{x}_s$ becomes free space $[c(\mathbf{x}_s) = \alpha \geq 0 \to c(\mathbf{x}_s) < 0]$. Details on the actual implementation of cell rupture are discussed in section 'Rupture of cell contacts'.

Monte-Carlo scheme

In the spirit of a standard Monte-Carlo scheme, the actual simulation proceeds via a succession of *Monte-Carlo steps*, where each Monte-Carlo step (MCS) propagates the state of the simulated cell population from time t to time $t + \Delta t$, where we set the time step to $\Delta t \equiv 1$. One MCS consists in a series of attempts to perform elementary events, originating from randomly chosen membrane grid sites of randomly chosen cells. The duration of one MCS, i.e. the actual number of attempted elementary events, is chosen such that each of the cells' membrane segments is given the opportunity to attempt, on average, one elementary event per MCS. During each MCS, cell domains $\mathcal{D}^{(\alpha)}$ as well as the numerical values of cell areas A_α and perimeters P_α are updated 'on the fly', while the cells' polarization fields are updated only once at the end of each MCS; cf. section 'Cytoskeletal structures and focal adhesion' for the details of this update rule. The simulation then proceeds along the following Monte-Carlo scheme:

1. Initialize the cell population and define the duration of the simulation, i.e. the number of MCS, T_{sim}, to be performed.
2. Set the simulation time $t = 0$.
3. Perform the next MCS; this step is further detailed below.
4. Update polarization fields (cf. section 'Cytoskeletal structures and focal adhesion').
5. Set $t = t + \Delta t$, where $\Delta t \equiv 1$.
6. Repeat steps 3–5 while $t < T_{\text{sim}}$.

The implementation of a MCS, i.e. the sequence of elementary events, is based on the following general considerations:

i. *Choice of source and target grid sites.* Each elementary event $\mathcal{T}$ originates from a membrane grid site $\mathbf{x}_s \in \mathcal{B}^{(\alpha)}$ of some cell α, referred to as *source cell*. This membrane grid site will be referred to as *source grid site*. In addition, each elementary event involves a second grid site which lies in the neighborhood of the source grid site $\mathbf{x}_s$ and which is not currently occupied by cell α: $\mathbf{x}_t \in \mathcal{N}_s \setminus \mathcal{D}^{(\alpha)}$. In what follows, this additional grid site $\mathbf{x}_t$ will be referred to as *target grid site*. This grid site may either be an empty substrate site or a membrane site of another cell β, in which case the respective cell will be referred to as *target cell*. While the source grid site determines the location of the attempted elementary event, the target grid site determines the direction along which the elementary event is bound to proceed.

ii. *Monte-Carlo method to generate the system's dynamics.* As mentioned above, the actual dynamics of cells in our computational model is driven by a succession of elementary events, whose cumulative effects over time allow cells to change shapes and to move relative to the substrate as well as relative to each other. Following a standard Monte-Carlo procedure, the probability of occurrence of elementary events $\mathcal{T}$ is determined by a goal function $p(\mathcal{T})$ [cf. point (iii) below]. However, since elementary events come in two basic flavors, protrusions $\mathcal{T}_{\text{pro}}$ and retractions $\mathcal{T}_{\text{ret}}$, their actual occurrence is controlled by a two-step process, once source and target grid sites have been determined: In a first step, two alternative scenarios are proposed where either the source cell protrudes toward $\mathbf{x}_t$, or retracts from $\mathbf{x}_s$. Then, a decision is made with equal probabilities as to whether one attempts $\mathcal{T}_{\text{pro}}$ or $\mathcal{T}_{\text{ret}}$. In a second step, the goal function p is used to compute the

occurrence probability of the attempted event $\mathcal{T}$. Finally, this elementary event $\mathcal{T}$ is being accepted with probability $p(\mathcal{T})$.

iii. *Choice of the goal function $p(\mathcal{T})$.* As has been detailed above, we use a goal function $p(\mathcal{T})$ to control the occurrence and acceptance of elementary events $\mathcal{T}$. Following the standard cellular Potts model (**Graner and Glazier, 1992**; **Glazier and Graner, 1993**), this goal function takes into account the effects of cell contractility and cell-cell adhesion, using, however, a slightly different implementation; cf. sections 'Cell contractility' and 'Cell adhesion'. In addition, we generalized the definition of the goal function $p(\mathcal{T})$ to explicitly take into account a simplified model of cytoskeletal structures and the ensuing polarization of cells. The actual definition of the goal function will be developed in section 'Implementation of cellular traits', where, moreover, details concerning the implementation of the cell polarization model will be discussed.

The implementation of a single MCS loop is then given by the following simulation scheme:

1. Determine the current number of trials per Monte-Carlo step (MCS), $K = \sum_\alpha P_\alpha / \ell$, and set the trial counter $n = 0$.
2. With equal probability, choose a cell membrane segment (cf. solid black line in **Appendix 1—figure 1**) from a random cell α of the cell population. Because the cell membrane represents the border between lattice sites occupied by cell α and unoccupied by cell α, the chosen membrane segment automatically defines the source grid site $\mathbf{x}_s \in \mathcal{B}^{(\alpha)}$ and the corresponding target grid site $\mathbf{x}_t \in \mathcal{N}^{(\alpha)} \cap \mathcal{N}_s$.
3. With equal probability, choose whether to attempt a protrusion event ($\mathcal{T}_{\text{pro}}$) or a retraction event ($\mathcal{T}_{\text{ret}}$).
4. Compute the prospective acceptance probability $p(\mathcal{T}_{\text{pro/ret}})$ corresponding to the attempted event, and decide whether to accept the attempted event on the basis of this probability.
5. If the attempted elementary event has been accepted, then update the cellular domains of source cell α and opponent cell β; for details see section 'Cell domain update routine'.
6. If $n < K$, set $n \to n + 1$ and then repeat steps 2 through 5.

Implementation of cellular traits

In this section, we discuss the various contributions of cellular traits to the overall acceptance probability $p(\mathcal{T})$ of an elementary event $\mathcal{T}$. Specifically, our model takes into account cell contractility, the assembly and disassembly of cytoskeletal structures, cell-cell adhesion, and focal adhesions. We will assume that each of these cellular properties contributes independently to the acceptance probability p, such that

$$p = \min\{1, p_{\text{cont}} \cdot p_{\text{cyto}} \cdot p_{\text{adh}}\}. \tag{S9}$$

Anticipating our discussions in section 'Cytoskeletal structures and focal adhesion', the effects due to focal adhesions have been combined with the effects due to assembly and disassembly of cytoskeletal structures in $p_{\text{cyto}}(\mathcal{T})$. In the following sections, we give detailed discussions for each of these contributions, separately.

Cell contractility

In biological cells, membrane fluctuations are constrained by elastic forces and contractile cytoskeletal structures, which play a vital role in cell migration (**Alberts et al., 2015**; **Raucher and Sheetz, 2000**; **Friedl, 2004**). In our computational approach, we take cell contractility into account by assigning a contractile 'energy'

$$\mathcal{H}_{\text{cont}} = \sum_\alpha \left[\kappa_P^{(\alpha)} P_\alpha^2 + \kappa_A^{(\alpha)} A_\alpha^2 \right], \tag{S10}$$

with positive coupling constants $\kappa_P^{(\alpha)}$ and $\kappa_A^{(\alpha)}$ characterizing the contractility of cell α; for empty substrate sites ($\alpha < 0$) we set $\kappa_P^{(\alpha)} = \kappa_A^{(\alpha)} = 0$. According to **Equation S10**, the cell's 'contractile energy' increases with increasing cell perimeter and increasing cell area. The model Hamiltonian $\mathcal{H}_{\text{cont}}$ can then be used to specify the contractile contribution to the goal function $p(\mathcal{T})$. To this end, let $\Delta\mathcal{H}_{\text{cont}}(\mathcal{T})$ denote the contractile contribution to the energy

Cell Biology | Physics of Living Systems

difference entailed by accepting an elementary event $\mathcal{T}$. Following a standard Metropolis algorithm, we then define

$$p_{\mathrm{cont}}(\mathcal{T}) := \exp[-\Delta\mathcal{H}_{\mathrm{cont}}(\mathcal{T})/k_{\mathrm{B}}T], \tag{S11}$$

where we set the effective thermal energy to $k_{\mathrm{B}}T \equiv 1$. The contractile 'energy', *Equation S10*, is similar to the corresponding energy model commonly used in cellular Potts models (*Ouchi et al., 2003*). Unlike the standard cellular Potts model, however, where a target area and target perimeter are used to keep the simulated cells from collapsing, the energetic contribution in *Equation S10* strictly contracts the cell's body. As will be detailed in the next section, to counteract these contractile forces, we explicitly model cytoskeletal structures within each cell, which provide outward pushing forces to balance cell contraction.

Cytoskeletal structures and focal adhesion

The cytoskeleton plays key roles both in maintaining the mechanical integrity of the cell and in the process of active cell migration (*Alberts et al., 2015*; *Friedl, 2004*; *Mogilner, 2009*). Our model design aims at achieving high computational efficiency to allow for the simulation of very large cell numbers (currently, cell numbers up to $\mathcal{O}(10^4)$ can be achieved at acceptable computation times) and, at the same time, to capture the essential effects of cytoskeletal dynamics to attain meaningful results down to the level of single cells. Thus, instead of accounting for a detailed biochemical description by means of reaction-diffusion networks (*Marée et al., 2006*; *Marée et al., 2012*), we resort to a simplified implementation of the most pertinent features of cytoskeletal dynamics. Specifically, we propose a rule-based algorithm to model cytoskeletal structures and to assess the integrated effects of cell polarity, cell contractility and adhesion on the collective dynamics of cells as parts of larger groups.

To this end, we define a scalar field $\epsilon(\mathbf{x}_n)$, $\mathbf{x}_n \in \mathcal{D}^{(\alpha)}$, on the domain of each cell α. The local quantity $\epsilon(\mathbf{x}_n)$ will be referred to as *polarization field* and is taken to be a measure for the density of cytoskeletal structures at position $\mathbf{x}_n$ within the cell's body. The field variable $\epsilon(\mathbf{x}_n)$ is dynamically updated as the simulation progresses, reflecting cytoskeletal remodeling. To set up a system of rules underlying the actual implementation of these cytoskeletal remodeling processes, we resort to the following biologically motivated premises:

1. *The scalar polarization field ϵ is bounded*: The dynamics of cytoskeletal remodeling not only depends on the local number (density) of actin monomers and polymers, but also on a multitude of accessory proteins controlling cytoskeleton assembly and disassembly. Several biological factors—including the action of sequestering proteins like thymosin-β4, which act to suppress actin polymerization, limited amounts of nucleating proteins like the activated Arp2/3 complex, and the action of capping proteins—keep the local density of actin filaments bounded. We, therefore, introduce bounds for the *polarization field*: $\epsilon(\mathbf{x}_n, t) \in [\epsilon_0 - \Delta\epsilon/2, \ \epsilon_0 + \Delta\epsilon/2]$. These bounds are cell-type specific. While the upper bound $\epsilon_0 + \Delta\epsilon/2$ mainly reflects the limited availability of protein resources, the lower bound $\epsilon_0 - \Delta\epsilon/2$ serves to prevent cells from collapsing.

2. *Regulatory proteins affect assembly and disassembly of cytoskeletal structures*: The assembly and disassembly of cytoskeletal structures, numerically encoded by $\epsilon(\mathbf{x}_n)$, is regulated by a myriad of accessory proteins. In our computational model we simplify these complex processes by resorting to a single 'bookkeeping variable' which we will refer to as 'regulatory factors'. Its local level is stored as an integer variable $F(\mathbf{x}_n)$ for each grid site $\mathbf{x}_n \in \mathcal{D}^{(\alpha)}$. We use $F(\mathbf{x}_n)$ to implement the overall action of regulatory cytoskeletal proteins in an effective and collective manner. Specifically, since the formation of lamellipodial structures depends on active nucleation promoting factors (*Pollard and Borisy, 2003*), we assume that positive levels, $F(\mathbf{x}_n) > 0$, reflect local conditions in support of network-assembly, whereas negative levels, $F(\mathbf{x}_n) < 0$, represent predominantly degrading (or disassembly) conditions. For neutral levels, $F(\mathbf{x}_n) = 0$, the network gradually restores its rest state.

3. *Feedback between cytoskeletal structures and regulatory factors*: The activities of accessory cytoskeletal proteins which regulate the local levels of cytoskeletal structures are themselves controlled by a number of mechanical and chemical signals received by the cell. Here and in the following, our focus will be on mechanical signals. For example, important regulatory proteins like the Arp2/3 complex are activated locally at the cell membrane, from where they

Reprint of published manuscript

diffuse into the bulk of the cell until they are bound by actin (*Kovacs et al., 2002*; *Pollard and Borisy, 2003*; *Leckband et al., 2011*). Adopting a coarse level of description, this diffusion-degradation dynamics entails a finite range of regulatory proteins, which are activated at the cell's membrane. In our model, we use the integer variable $F(\mathbf{x}_n)$ to implement this propagation of mechanical information, perceived by cell α at its periphery $\mathcal{B}^{(\alpha)}$, across a certain spatial distance R. The local levels of $F(\mathbf{x}_n)$ are continuously updated as the MCS loop progresses. The actual update procedure is given by the following set of rules; cf. *Appendix 1—figure 2*:

- if a *protrusion event* has been accepted at the source site $\mathbf{x}_s \in \mathcal{B}^{(\alpha)}$ (source cell: α; target cell: β), then for all sites $\mathbf{x}_n$ within a range R (i.e. $\|\mathbf{x}_n - \mathbf{x}_s\| < R$) the integer variable signifying regulatory factors is incremented up and down for the protruding and the retracting cell, respectively:

$$F(\mathbf{x}_n) \rightarrow \begin{cases} F(\mathbf{x}_n) + 1, & \mathbf{x}_n \in \mathcal{D}^{(\alpha)}, \\ F(\mathbf{x}_n) - 1, & \mathbf{x}_n \in \mathcal{D}^{(\beta)}. \end{cases} \tag{S12a}$$

- Similarly, if a *retraction event* has been accepted at the source site $\mathbf{x}_s \in \mathcal{B}^{(\alpha)}$, and the (local) cell contact between source cell α and target cell β has remained intact, then within a range R one applies the inverse update rule:

$$F(\mathbf{x}_n) \rightarrow \begin{cases} F(\mathbf{x}_n) - 1, & \mathbf{x}_n \in \mathcal{D}^{(\alpha)}, \\ F(\mathbf{x}_n) + 1, & \mathbf{x}_n \in \mathcal{D}^{(\beta)}. \end{cases} \tag{S12b}$$

- If a *retraction event* has been accepted at the source site $\mathbf{x}_s \in \mathcal{B}^{(\alpha)}$, and in addition the (local) cell contact between source cell α and target cell β has *ruptured*, then the regulatory factors are reduced only within a range R in the retracting cell:

$$F(\mathbf{x}_n) \rightarrow \begin{cases} F(\mathbf{x}_n) - 1, & \mathbf{x}_n \in \mathcal{D}^{(\alpha)}, \\ \text{no update}, & \text{else}. \end{cases} \tag{S12c}$$

Finally, if the target grid site $\mathbf{x}_t$ is not occupied by any cell (substrate is indicated by $\beta < 0$) prior to the elementary event, then only the first two lines in the above update scheme apply.

By virtue of the above update scheme, *Equation S12*, 'regulatory factors' are continuously distributed across each cell's domain $\mathcal{D}^{(\alpha)}$ as the current MCS progresses. At the end of each MCS, the accumulated (local) values of $F(\mathbf{x}_n)$ are used to update the local values of the polarization field $\epsilon(\mathbf{x}_n)$ inside each cell $\alpha \geq 0$ ($\mathbf{x}_n \in \mathcal{D}^{(\alpha)}$): We assume that for positive values, $F(\mathbf{x}_n) > 0$, there is assembly of cytoskeletal structures and ϵ is increased by an amount proportional to the distance of ϵ from its upper bound $\epsilon_0 + \Delta\epsilon/2$:

$$\epsilon(\mathbf{x}_n, t + \Delta t) = \epsilon(\mathbf{x}_n, t) + \Delta t \, \mu \, [\epsilon_0 + \Delta\epsilon/2 - \epsilon(\mathbf{x}_n, t)], \tag{S13a}$$
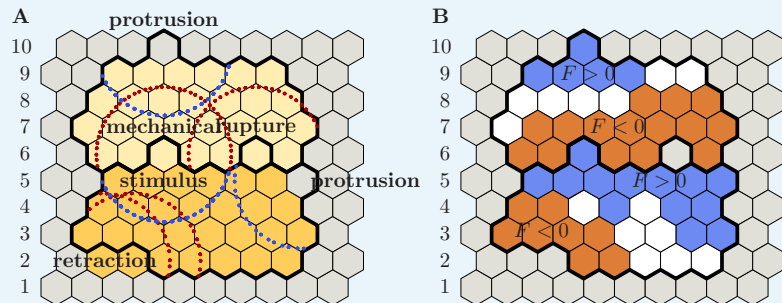
where the time step is defined as $\Delta t \equiv 1$. Thereby $\epsilon_0 + \Delta\epsilon/2$ is a fixed point of this map and limits the build-up of cytoskeletal structures. In contrast, for negative values, $F(\mathbf{x}_n) < 0$, disassembly prevails, and we assume that ϵ then tends towards its lower bound $\epsilon_0 - \Delta\epsilon/2$:

$$\epsilon(\mathbf{x}_n, t + \Delta t) = \epsilon(\mathbf{x}_n, t) + \Delta t \, \mu \, [\epsilon_0 - \Delta\epsilon/2 - \epsilon(\mathbf{x}_n, t)], \tag{S13b}$$

where the time step is defined as $\Delta t \equiv 1$. Neutral values, $F(\mathbf{x}_n, t) = 0$, lead to relaxation of ϵ towards a resting state

$$\epsilon(\mathbf{x}_n, t + \Delta t) = \epsilon(\mathbf{x}_n, t) + \Delta t \, \mu \, [\epsilon_0 - \epsilon(\mathbf{x}_n, t)], \tag{S13c}$$

where the time step is defined as $\Delta t \equiv 1$. The parameter μ signifies the rate at which cytoskeletal structures respond to the regulatory factors F. For the parameters and cell sizes used in this work ($\epsilon_0 = \mathcal{O}(100)$ and $\Delta\epsilon = \mathcal{O}(10)$, and each cell occupying approximately 1000 grid sites) we set $\mu = 0.1$.

Appendix 1—figure 2. Distribution of regulatory factors on the basis of accepted elementary events. For ease of reference, grid rows have been numbered from 1 to 10. *Left* (**A**): Solid black lines indicate cells' membrane positions *after* acceptance of the respective elementary event; colors indicate cellular domains *before* the respective elementary event has been accepted (gray: substrate; shades of yellow: cells). Blue and red circular arcs (of radius R) delineate areas of local increase or decrease in the level of regulatory factors, respectively. The following elementary events are depicted: (i) lower cell retracts (two grid sites in row 2); (ii) lower cell protrudes (row 5); (iii) upper cell protrudes (row 10). In addition, the following elementary events occur across the cell-cell boundary: (iv) retraction of upper cell leads to rupture of cell-cell contacts (row 6, right event); (v) either the lower cell protrudes and pushes the upper cell or the upper cell retracts and pulls on the lower cell (row 6, left event). Specifically, event (v) entails mechanical signaling between the upper and lower cell and, therefore, affects the distribution of regulatory factors in both cells. *Right* (**B**): Identical copy of the left image (**A**). Colors indicate local levels of regulatory factors F (blue: F is positive; white: F is zero; red: F is negative; gray: substrate site). Note, in particular, that a substrate grid site has been inserted where cell rupture occurred (row 6, right grid site). The following cases can be distinguished: (i) Grid site $\mathbf{x}_k$ lies in the zone of influence of only positive (blue circles) or negative (red circles) chemical feedback, in which case the level of regulatory factors is positive or negative, respectively (e.g. red grid sites in row 2, or blue grid sites in row 5). (ii) Grid site $\mathbf{x}_k$ lies outside of any zone of influence, in which case the level regulatory factors is zero (e.g. white grid sites in row 2). (iii) Grid site $\mathbf{x}_k$ lies in the zone of influence of equally many positive and negative feedbacks, in which case the level of regulatory factors remains zero (e.g. fourth grid site in row 4). (iv) Grid site $\mathbf{x}_k$ lies in a zone of predominantly positive or negative feedback, in which case the level of regulatory factors is positive or negative, respectively (e.g. third grid site in row 4). Recall that only the sign of F is of significance to update the cells' polarization field; cf. *Equation S13*.

After this update procedure for $\epsilon(\mathbf{x}_n, t)$ is completed, all regulatory factors are reset, $F(\mathbf{x}_n) \to 0, \ \forall n$. This prevents 'spurious memory effects' which may arise once the cell's rear reaches its initial leading edge position as time goes on. In essence, resetting regulatory factors upon completion of one MCS implies that the diffusion-degradation dynamics, underlying the distribution of regulatory factors, is fast on the scale of one MCS.

We emphasize that the polarization field $\epsilon(\mathbf{x}_n)$ is defined only for grid sites $\mathbf{x}_n \in \mathcal{D}^{(\alpha)}$ occupied by an actual cell ($\alpha \geq 0$). To allow for spatial variations of substrate properties, we therefore introduce a second scalar field variable $\varphi(\mathbf{x}_n)$, which is defined on the entire computational grid. The scalar field $\varphi(\mathbf{x}_n)$ is taken to measure the local density of anchoring points that a cell might use to form focal adhesions. Although one might consider to treat φ as a time-dependent field variable, in this work φ is used to implement static substrate patterns, only. The field $\varphi(\mathbf{x}_n)$ is thus initialized once at the beginning of the simulation and kept fixed throughout the entire simulation.

Having introduced the fields $\epsilon(\mathbf{x}_n)$ and $\varphi(\mathbf{x}_n)$, we now discuss their impact on the system's dynamics by giving their contribution to the goal function $p(\mathcal{T})$. Suppose that the elementary event $\mathcal{T}$ is attempted by a source cell α at source grid site $\mathbf{x}_s \in \mathcal{B}^{(\alpha)}$. Further, let $\mathbf{x}_t$ denote the

target grid site and β denote the index of the target cell (where as usual $\beta \geq 0$ indicates that $\mathbf{x}_t$ is occupied by an actual cell, $\beta < 0$ means that $\mathbf{x}_t$ exposes substrate). We then define the *'polarization energy'* $\Delta\mathcal{H}_{\mathrm{cyto}}(\mathcal{T})$ as follows:

$$\Delta\mathcal{H}_{\mathrm{cyto}}(\mathcal{T}) \equiv \begin{cases} \epsilon(\mathbf{x}_t) - \epsilon(\mathbf{x}_s), & \mathcal{T} \,\widehat{=}\, \mathcal{T}_{\mathrm{pro}} \,\wedge\, \beta \geq 0, \\ \epsilon(\mathbf{x}_s) - \epsilon(\mathbf{x}_t), & \mathcal{T} \,\widehat{=}\, \mathcal{T}_{\mathrm{ret}} \,\wedge\, \beta \geq 0, \\ -[\epsilon(\mathbf{x}_s) + \varphi(\mathbf{x}_t)], & \mathcal{T} \,\widehat{=}\, \mathcal{T}_{\mathrm{pro}} \,\wedge\, \beta < 0, \\ \epsilon(\mathbf{x}_s) + \varphi(\mathbf{x}_t), & \mathcal{T} \,\widehat{=}\, \mathcal{T}_{\mathrm{ret}} \,\wedge\, \beta < 0, \end{cases} \tag{S14a}$$

Here, the definition of $\Delta\mathcal{H}_{\mathrm{cyto}}$ is such that the likelihood of cell protrusions is enhanced if the concentration of cytoskeletal structures at the source grid site, $\epsilon(\mathbf{x}_s)$, is larger than the concentration at the target grid site, $\epsilon(\mathbf{x}_t)$ (first row of *Equation S14a*), and vice versa for cell retractions (second row of *Equation S14a*). The strength of focal adhesions is taken to be measured by the sum $\epsilon + \varphi$. Their associated 'anchoring effects' (which increase with growing strength of focal adhesions) promote the formation of cell protrusions against unoccupied substrate sites (third row of *Equation S14a*), and, correspondingly, impede cell retractions (fourth row of *Equation S14a*). Note, in particular, that the first two rows of *Equation S14a* can be obtained from a combined evaluation of the lower two rows. For example, if source cell α annexes $\mathbf{x}_t$ starting from $\mathbf{x}_s$, two things need to happen: First, focal adhesions formed by the target cell β must be broken, implying a contribution $\Delta\mathcal{H}_{\mathrm{cyto}} = \epsilon(\mathbf{x}_t) + \varphi(\mathbf{x}_t)$ (fourth row of *Equation S14a*). Secondly, new focal adhesions are formed by the source cell α, implying a contribution $\Delta\mathcal{H}_{\mathrm{cyto}} = -[\epsilon(\mathbf{x}_s) + \varphi(\mathbf{x}_t)]$ (third row of *Equation S14a*). Taking the sum of both contributions gives the expression in the first row of *Equation S14a*. An analogous line of arguments leads to the expression in the second row of *Equation S14a*.

The contribution to the goal function $p(\mathcal{T})$ due to the *polarization energy* $\Delta\mathcal{H}_{\mathrm{cyto}}(\mathcal{T})$ is then defined by

$$p_{\mathrm{cyto}}(\mathcal{T}) := \exp[-\Delta\mathcal{H}_{\mathrm{cyto}}(\mathcal{T})/k_{\mathrm{B}}T], \tag{S14b}$$

where we set the effective thermal energy to $k_{\mathrm{B}}T \equiv 1$. The characteristic 'energy scale' for $\Delta\mathcal{H}_{\mathrm{cyto}}$ is set by the polarization bounds $\epsilon_0 - \Delta\epsilon/2$ and $\epsilon_0 + \Delta\epsilon/2$, which turns out to have important implications for collective cell dynamics, as discussed in the main text.

Cell adhesion

To implement the ability of cells to establish cell adhesions across cell-cell interfaces, we use a special form for the respective contribution to the goal function p, which is designed to distinguish between the formation of new and the breakage of existing cell-cell adhesion sites.

To this end, we define *adhesion matrices* $B_{\alpha,\beta}$ and $B'_{\alpha,\beta}$ quantifying the system's change in 'energy' upon forming a new contact between cells α and β [$B_{\alpha,\beta}$] and upon breaking a pre-existing contact between those cells by an 'intruder cell' $\gamma \neq \alpha, \beta$ [$B'_{\alpha,\beta}$]. In our computational model, we assume that formation of new cell-cell contacts is energetically favored, and that breaking of pre-existing contacts by intruder cells is energetically penalized. The matrix entries of $B_{\alpha,\beta}$ and $B'_{\alpha,\beta}$, therefore, have a definite sign, which we take to be positive. The ordering of the cell index pair of $B_{\alpha,\beta}$ and $B'_{\alpha,\beta}$ is of no physical significance, i.e. the adhesion matrices are symmetric. We also assume that a given cell α does not interact with itself, such that the diagonal elements of the adhesion matrices vanish. Finally, there is no adhesion between cells and empty substrate sites, such that all matrix elements containing a negative cell index vanish. In summary, the adhesion matrices $B_{\alpha,\beta}$ and $B'_{\alpha,\beta}$ exhibit the following properties:

$$B_{\alpha,\beta} = B_{\beta,\alpha} \geq 0, \tag{S15a}$$

$$B'_{\alpha,\beta} = B'_{\beta,\alpha} \geq 0, \tag{S15b}$$

$$B_{\alpha,\alpha} = B'_{\alpha,\alpha} = 0, \tag{S15c}$$

$$B_{\alpha,\beta} = B'_{\alpha,\beta} = 0, \quad \text{if } \alpha < 0 \ \vee \ \beta < 0. \tag{S15d}$$

In addition, we assume that the energy cost associated with the breakage of a given cell-cell contact exceeds the energetic benefit of its initial formation, i.e.

$$B'_{\alpha,\beta} \geq B_{\alpha,\beta}, \tag{S15e}$$

where equality of both quantities would reproduce the assumption underlying the standard cellular Potts model (**Graner and Glazier, 1992**; **Glazier and Graner, 1993**). We shall refer to this property as the 'dissipative nature of cell-cell adhesion'.

To implement the effects of cell-cell adhesion, we compute the 'energy difference' $\Delta\mathcal{H}_{\mathrm{adh}}(\mathcal{T})$ for any given elementary event $\mathcal{T}$ according to the scheme illustrated in **Appendix 1—figure 3**. One has to distinguish between *protrusion* and *retraction* events. First, say that a cell α attempts a protrusion event $\mathcal{T}_{\mathrm{pro}}$, involving the source grid site $\mathbf{x}_s \in \mathcal{B}^{(\alpha)}$ and the target grid site $\mathbf{x}_t \in \mathcal{B}^{(\beta)}$, as illustrated in **Appendix 1—figure 3A**. In this case, cell α acts as intruder cell, since the depicted protrusion event affects three pre-existing contacts between the target cells β and a 'third party' cell γ. Acceptance of the depicted protrusion event would have the following energetically relevant effects: (i) All pre-existing contacts between the target cell β and third party cell $\gamma \neq \alpha, \beta$ at the target grid site $\mathbf{x}_t$ are torn apart. (ii) New contacts between the source cell α and third party cell $\gamma \neq \alpha, \beta$ are established. (iii) The length of the cell contact line between source cell α and target cell β is changed. Altogether, these three effects lead to the following cell adhesion energy difference,

$$\begin{aligned}
\Delta\mathcal{H}_{\mathrm{adh}}(\mathcal{T}_{\mathrm{pro}}) \equiv \ & -\ell \sum_{\mathbf{x}_j \in \mathcal{N}_t} \left[B_{\alpha,c(\mathbf{x}_j)} - \delta_{\alpha,c(\mathbf{x}_j)} B_{\beta,c(\mathbf{x}_j)} \right] \\
& +\ell \sum_{\mathbf{x}_j \in \mathcal{N}_t} B'_{\beta,c(\mathbf{x}_j)} (1 - \delta_{\alpha,c(\mathbf{x}_j)}),
\end{aligned} \tag{S16a}$$

where ℓ is the length of a hexagon edge. The first term in this expression accounts for the (energetically favored) formation of new cellular contacts, as well as for the remodeling of the interface between source cell α and target cell β [points (ii) and (iii)]. The second term measures the (energetically penalized) breaking of pre-existing cell contacts [point (i)] and, therefore, impedes cell α's ability to intrude. Conversely, if source cell α attempts a retraction event $\mathcal{T}_{\mathrm{ret}}$, then the same reasoning as the one leading to **Equation S16a** applies, only this time the elementary event proceeds in reverse, i.e. from the target site $\mathbf{x}_t$ to the source site $\mathbf{x}_s$; cf. **Appendix 1—figure 3A**:

$$\begin{aligned}
\Delta\mathcal{H}_{\mathrm{adh}}(\mathcal{T}_{\mathrm{ret}}) \equiv \ & -\ell \sum_{\mathbf{x}_j \in \mathcal{N}_s} \left[B_{\beta,c(\mathbf{x}_j)} - \delta_{\beta,c(\mathbf{x}_j)} B_{\alpha,c(\mathbf{x}_j)} \right] \\
& +\ell \sum_{\mathbf{x}_j \in \mathcal{N}_s} B'_{\alpha,c(\mathbf{x}_j)} (1 - \delta_{\beta,c(\mathbf{x}_j)}),
\end{aligned} \tag{S16b}$$

where ℓ is the length of a hexagon edge.

Appendix 1—figure 3. Cell-cell adhesion. (**A**) Adhesive energy contribution in a cyclic process, where a protrusion of source cell α against target cell β is followed by the inverse retraction event. Both events involve a third party cell γ, leading to net energy dissipation after the cyclic process has been completed. *Protrusion*: (i) Three pre-existing cell-cell contacts between β and γ are torn apart (red dashed contacts); (ii) three new contacts between α and γ are formed; (iii) the contact length between source cell α and target cell β increases by one unit of length. This implies $\Delta\mathcal{H}_{\mathrm{adh}}(\mathcal{T}_{\mathrm{pro}}) = \ell\,(3B'_{\beta,\gamma} - 3B_{\alpha,\gamma} - B_{\alpha,\beta})$. *Retraction*: (i) Three pre-existing cell-cell contacts between α and γ are torn apart (red dashed contacts); (ii) three new contacts between β and γ are formed; (iii) the contact length between source cell α and target cell β decreases by one unit of length. This implies $\Delta\mathcal{H}_{\mathrm{adh}}(\mathcal{T}_{\mathrm{ret}}) = \ell\,(3B'_{\alpha,\gamma} - 3B_{\beta,\gamma} + B_{\alpha,\beta})$. Altogether, this leads to $\Delta\mathcal{H}_{\mathrm{adh}}^{(\mathrm{cycl})} = \Delta\mathcal{H}_{\mathrm{adh}}(\mathcal{T}_{\mathrm{pro}}) + \Delta\mathcal{H}_{\mathrm{adh}}(\mathcal{T}_{\mathrm{ret}}) = \ell\,(3(\Delta B)_{\alpha,\gamma} + 3(\Delta B)_{\beta,\gamma}) \geq 0$, i.e. a (non-negative) dissipative contribution, whose magnitude depends on the dissipation matrix $(\Delta B)_{\alpha,\beta} = B'_{\alpha,\beta} - B_{\alpha,\beta} \geq 0$. (**B**) Shear viscosity due to cell-cell adhesion. Consider two rows of adhesive cells sliding past each other as indicated in the figure (left row of cells moves up by one grid site; colors indicate different cells). The associated adhesion energy change (per cell) reads $\Delta\mathcal{H}_{\mathrm{adh}}/n_c = 2\,(B' - B) \geq 0$, where n_c denotes the number of cells sliding past each other, and where we assumed cells of like type, i.e. $B_{\alpha,\beta} \equiv B$ and $B'_{\alpha,\beta} \equiv B'$ ($\alpha \neq \beta$). The condition $B'>B$, *Equation S15e*, thus implies positive friction associated with cellular shear flows, whose magnitude is proportional to the number of cells sliding past each other. Note that this shear viscosity vanishes for $B' = B$, i.e. for zero dissipation matrix.

We may now use *Equation S16a* and *Equation S16b* to illustrate the 'dissipative nature' of adhesive interactions by means of two archetypical examples. First, consider the adhesive energy contribution to any cyclic process. By a cyclic process we mean a sequence of two mutually inverse elementary events, e.g. a protrusion event $\mathcal{T}_{\mathrm{pro}}$, which is immediately followed by its inverse retraction event $\mathcal{T}_{\mathrm{ret}}$, such that the system's final configuration is identical to its initial configuration. Using *Equation S16* we find for the total adhesive energy contribution to a cyclic process:

$$\Delta\mathcal{H}_{\mathrm{adh}}^{(\mathrm{cycl})} = \ell \sum_{\mathbf{x}_j \in \mathcal{N}_t \backslash (\mathcal{D}^{(\alpha)} \cup \mathcal{D}^{(\beta)})} \left[(\Delta B)_{\alpha, c(\mathbf{x}_j)} + (\Delta B)_{\beta, c(\mathbf{x}_j)} \right], \tag{S17}$$

$$(\Delta B)_{\alpha,\beta} := B'_{\alpha,\beta} - B_{\alpha,\beta} \geq 0, \tag{S18}$$

and can therefore conclude that

$$\Delta\mathcal{H}_{\mathrm{adh}}^{(\mathrm{cycl})} \geq 0,$$

where $\mathcal{N}_t$ denotes the neighborhood of the grid site which temporarily changes its cell index, and where α and β are the indices of the source and target cells involved in the cyclic process; cf. *Appendix 1—figure 3A*. Since $(\Delta B)_{\alpha,\beta} \geq 0$, the above adhesive energy contribution is non-negative, thus leading to an amount of energy equal to $\Delta\mathcal{H}_{\mathrm{adh}}^{(\mathrm{cycl})}$ being dissipated as the cyclic process completes. This leads us to refer to the parameter matrix $(\Delta B)_{\alpha,\beta}$ as *dissipation matrix*. Second, consider two (infinitely extended) columns of cells in

adhesive contact, sliding past each other. This situation is depicted in *Appendix 1—figure 3B*, where the left column of cells moves (as a whole) upwards by one grid site, while the right column of cells remains stationary. To assess the adhesive energy contribution along the contact line connecting both cell columns, note that the depicted transformation can be implemented by letting each cell in the left column protrude its leading (i.e. upper) edge by one grid site. For each protruding (source) cell α, this transformation entails to the following energetic effects (cf. discussion above): (i) Two of the pre-existing cell-cell contacts between the source cell's upper neighbor in the left column (target cell β) and the corresponding cell in the right column (third party cell γ) get torn apart, leading to an energetic contribution $2B'_{\beta,\gamma}$. (ii) In return, two new contacts between the protruding (source) cell α and cell γ are being established, leading to a contribution $-2B_{\alpha,\gamma}$. (iii) Since the length of the contact line between cells in the left column (i.e. between protruding source cell α and retracting target cell β) remains unchanged, there's no further energetic contribution due to adhesive contacts between cells in the left column. Assuming that all cells in the system are of equal types, we write $B_{\alpha,\beta} \equiv B$ and $B'_{\alpha,\beta} \equiv B'$ ($\alpha \neq \beta$), and therefore, find

$$\Delta\mathcal{H}_{\mathrm{adh}}^{(\mathrm{visc})} = 2\ell\,(B' - B) \equiv 2\ell\,\Delta B \geq 0, \tag{S19}$$

i.e. a non-negative dissipative contribution per cell. The size of the dissipation parameter ΔB thus introduces a natural means to tune the system's *shear viscosity*.

With the above definitions of the adhesive energy changes, *Equation S16*, we define the contribution of cell adhesion to the goal function $p(\mathcal{T})$ as follows:

$$p_{\mathrm{adh}}(\mathcal{T}) := \exp\!\left[-\Delta\mathcal{H}_{\mathrm{adh}}(\mathcal{T})/k_{\mathrm{B}}T\right], \tag{S20}$$

where we set the effective thermal energy to $k_{\mathrm{B}}T \equiv 1$.

Rupture of cell contacts

By now, we have introduced all components making up the total acceptance probability $p(\mathcal{T})$, *Equation S9*. To conclude our discussions concerning the implementation of cellular traits, we highlight one additional aspect of elementary events. So far, the notion of an elementary event can be summarized as follows: Once source and target grid sites, $\mathbf{x}_s$ and $\mathbf{x}_t$, have been selected, acceptance of a protrusion [retraction] event causes (among other things like the distribution of regulatory factors) the cell index to be copied from $\mathbf{x}_s$ to $\mathbf{x}_t$ [from $\mathbf{x}_t$ to $\mathbf{x}_s$]. In other words, the domain $\mathcal{D}^{(\alpha)}$ of source cell α annexes $\mathbf{x}_t$ [loses $\mathbf{x}_s$], while the domain $\mathcal{D}^{(\beta)}$ of target cell β is forced to let go $\mathbf{x}_t$ [accommodate $\mathbf{x}_s$]. However, if both source and target cells are actual cells, i.e. $\alpha, \beta \geq 0$, and if the source cell attempts a retraction event, there is one additional possible outcome: If cell cohesion is weak, then the pulling force exerted by the retracting source cell α on its neighboring cells might also result in rupture of all pre-existing contacts between the retracting source cell and its neighboring cells at $\mathbf{x}_s$, rather than forcing one of its neighboring cells (the target cell) to fill the void created at $\mathbf{x}_s$ once α retracts; cf. rupture event depicted in *Appendix 1—figure 2*. To test for the occurrence of cell rupture, the total energetic cost of each attempted retraction event between two actual cells is evaluated under two different assumptions: First, we assume that the pulling force exerted by the retracting source cell α on target cell β is strong enough to force β to fill the void created at $\mathbf{x}_s$ (i.e. to accommodate $\mathbf{x}_s$), and call this a regular retraction event $\mathcal{T}_{\mathrm{ret}}$. Secondly, we assume that the retraction of source cell α causes all pre-existing cell-cell contacts of cell α at $\mathbf{x}_s$ to rupture, leaving a free substrate site at $\mathbf{x}_s$ after the retraction event has been accepted. This latter event will be referred to as rupture event $\mathcal{T}_{\mathrm{rup}}$. We then compute the total energy differences

$$\Delta\mathcal{H}(\mathcal{T}_{\mathrm{ret}}) = \Delta\mathcal{H}_{\mathrm{cont}}(\mathcal{T}_{\mathrm{ret}}) + \Delta\mathcal{H}_{\mathrm{cyto}}(\mathcal{T}_{\mathrm{ret}}) + \Delta\mathcal{H}_{\mathrm{adh}}(\mathcal{T}_{\mathrm{ret}})$$

and

$$\Delta\mathcal{H}(\mathcal{T}_{\mathrm{rup}}) = \Delta\mathcal{H}_{\mathrm{cont}}(\mathcal{T}_{\mathrm{rup}}) + \Delta\mathcal{H}_{\mathrm{cyto}}(\mathcal{T}_{\mathrm{rup}}) + \Delta\mathcal{H}_{\mathrm{adh}}(\mathcal{T}_{\mathrm{rup}})$$

under both assumptions (the energy difference associated with accepting $\mathcal{T}_{\mathrm{rup}}$ can be computed with **Equation S16b** by using the substrate $\beta = -1$ as new target cell) and compare the respective outcomes. If the rupture event is energetically favored over the regular retraction event, i.e. $\Delta\mathcal{H}(\mathcal{T}_{\mathrm{rup}}) < \Delta\mathcal{H}(\mathcal{T}_{\mathrm{ret}})$, then cohesion between cells is weak. In this case, the rupture event $\mathcal{T}_{\mathrm{rup}}$, rather than the regular retraction event $\mathcal{T}_{\mathrm{ret}}$ will be attempted. Otherwise, cohesion is strong and a regular retraction event $\mathcal{T}_{\mathrm{ret}}$ will be attempted.

Rupture of substrate contacts

In our discussion so far, a cyclic process that follows up a protrusion event $\mathcal{T}_{\mathrm{pro}}$ with its inverse retraction event $\mathcal{T}_{\mathrm{ret}}$, involving a cell α and no third party cells (in other words: no cell-cell contacts are made or broken), will not yield a net energy cost or gain; cf. **Equation S14a**. To account for the dissipative nature of cell-substrate contacts, we proceed similarly as when we have considered the disspative nature of cell-cell contacts. We introduce dissipation in substrate adhesion by leaving the Hamiltonian unaltered for protrusion events but adding a penalty for retraction events:

$$\Delta\mathcal{H}(\mathcal{T}_{\mathrm{ret}}) \rightarrow \Delta\mathcal{H}(\mathcal{T}_{\mathrm{ret}}) + D. \tag{S21}$$

Therefore, a cell that adheres to the substrate at some grid point has to pay a cost D to retract from it. In other words, we assume that a fixed amount of energy D is dissipated once the adhesive bonds between a cell and the substrate break.

To keep its overall size across translations, the cell has to gain and lose equal amounts of hexagons, with $\Delta\epsilon$ as the maximal energy gained by a single gain-and-loss in the absence of dissipation. In the presence of dissipation however, the cell has to pay at least a cost of $(\epsilon_0 - \Delta\epsilon/2) + D$ to detach at an arbitrary location, resulting in $\Delta\epsilon - D$ as the maximal energy gained by a single gain-and-loss in the presence of dissipation. Thus, while for $D = 0$ there is no impact of substrate dissipation on cell motility, it will at the latest for $D = \Delta\epsilon$ completely inhibit (directed) cell migration. Therefore, we study substrate dissipation in the range $D \in [0, \Delta\epsilon]$.

Cell domain update routine

Having discussed the implementation concerning the two basic types of elementary events, namely protrusion events $\mathcal{T}_{\mathrm{pro}}$ and retraction events $\mathcal{T}_{\mathrm{ret}}$, as well as the two subtypes of regular retraction events and rupture events $\mathcal{T}_{\mathrm{rup}}$, we can now summarize the cell domain update routine, point 3.5 in section 'Monte-Carlo scheme'. To this end, and in accordance with our previous notation, we use the cell indices α and β to denote source and target cell, and $\mathbf{x}_s$ and $\mathbf{x}_t$ to denote source and target grid site. Moreover, equal signs "$=$" in the following listing are to be interpreted as assignment operators, where the value of the variable on the right hand side of the operator is assigned to the variable on the left hand side. With these preliminary remarks in mind, the cell update routine can be summarized as follows:

- If the accepted elementary event is a protrusion event:
  1. Set $\epsilon(\mathbf{x}_t) = \epsilon(\mathbf{x}_s)$ and $F(\mathbf{x}_t) = F(\mathbf{x}_s)$.
  2. $\mathcal{D}^{(\alpha)} \rightarrow \mathcal{D}^{(\alpha)} \cup \{\mathbf{x}_t\}$.
  3. $\mathcal{D}^{(\beta)} \rightarrow \mathcal{D}^{(\beta)} \setminus \{\mathbf{x}_t\}$.
  4. Distribute regulatory factors according to **Equation S12a**.
- If the accepted elementary event is a regular retraction event:
  1. Set $\epsilon(\mathbf{x}_s) = \epsilon(\mathbf{x}_t)$ and $F(\mathbf{x}_s) = F(\mathbf{x}_t)$.
  2. Set $\mathcal{D}^{(\alpha)} \rightarrow \mathcal{D}^{(\alpha)} \setminus \{\mathbf{x}_s\}$
  3. Set $\mathcal{D}^{(\beta)} \rightarrow \mathcal{D}^{(\beta)} \cup \{\mathbf{x}_s\}$
  4. Distribute regulatory factors according to **Equation S12b**.
- If the accepted elementary event is a rupture event:
  1. Set $\epsilon(\mathbf{x}_s) = 0$ and $F(\mathbf{x}_s) = 0$.
  2. Set $\mathcal{D}^{(\alpha)} \rightarrow \mathcal{D}^{(\alpha)} \setminus \{\mathbf{x}_s\}$

3. Distribute regulatory factors according to *Equation S12c*.

Cell proliferation and mitosis

While cell proliferation and mitosis play no role in the experimental setup of rotating cell clusters, cell growth and division are observed experimentally in a setup where a sheet of cells expands into free space after removal of a stencil. Therefore, it is essential to include proliferation of cells in the numerical model. How this is done is described in this section.

We distinguish between two phases in the cell cycle, an *interphase* during which cells roughly double in volume and *mitosis*, the process of cell division. Even though a further partitioning of the interphase was considered in previous work (*Li and Lowengrub, 2014*), we do not expect that such a distinction is relevant for our results. In our computational framework cell growth may be implemented by progressively changing any cellular parameter that affects the cell's equilibrium size. The two possible, largely equivalent choices are a successive reduction of the area coupling constant $\kappa_A^{(\alpha)}$ or an increase of the average cell polarization $\epsilon_0^{(\alpha)}$. We here employ the first method. We assume that individual cells grow exponentially (*Barber et al., 2017*) over a well-defined period T_g. Additional variability in cell cycle length can be achieved by introducing an additional refractory phase with exponentially distributed waiting times and the average waiting time T_r, which we set to $T_r = 0$ in this work. Moreover, we assume that the migratory behavior of a cell should not change significantly as it grows. However, as the cell grows in size by a factor of 2, it also increases its perimeter and the corresponding energy cost for adding new membrane segments roughly by a factor of $\sqrt{2}$. Therefore, as we do not scale the polarization field ϵ and the resulting energy gains for protrusions during cell growth, we mitigate the increased cost for ruffling the membrane by reducing the perimeter stiffness by a factor of $\sqrt{2}$. The quantitative viability of this approach is further discussed in section 'Single cell size'.

To prevent tissue overgrowth, cell proliferation is generally contact inhibited in healthy cells: When the tissue approaches a state where each cell has formed adhesive contacts with the substrate and is completely surrounded by neighbours, cells stop proliferating. In addition, it has been proposed that the pressure or local density in the tissue has a negative impact on the local growth rate (*Shraiman, 2005*; *Ranft et al., 2010*). To account for these phenomena in the model, we complement the two cell cycle periods interphase and mitosis by a quiescent cell state during which cell growth is halted. The parameters κ_A and κ_P are, therefore, kept constant for a quiescent cell; we denote the corresponding values as $\kappa_{A/0}$ and $\kappa_{P/0}$. There are many possible ways to implement contact inhibition in our computational model. For example, it could be implemented by allowing a quiescent cell to enter the cell cycle triggered by low local cell density, or when a sufficiently large fraction of its membrane length is not in contact with neighbour cells but exposed to free space. In our model it proves numerically advantageous to make a quiescent cell enter the interphase when its area succeeds a certain reference area. We choose this area threshold as $A_T = r A_{ref}$, where the factor $r = \mathcal{O}(1)$ relates the threshold size to the equilibrium cell size A_{ref} reached by a free, solitary cell with constant polarization field $\epsilon = \epsilon_0$. Cells living in a densely packed environment will not exceed the area threshold due to the pressure exerted on them by neighboring cells and can, therefore, not grow. Conversely, cells exposed to free space are more likely to reach this threshold and proliferate. Finally, a growing cell in interphase becomes mitotic after the growth time T_g has passed, at which point cell size has roughly doubled with respect to the size in the quiescent period. We assume that cell migration and mitosis are processes that exclude each other. Hence, the positive feedback leading to persistent cell migration is switched off for mitotic cells and the polarization field relaxes to the neutral state ϵ_0 according to *Equation S13c*.

There appears to be no universal set of rules which determine the orientation of the cleavage plane along which cells divide (*Minc and Piel, 2012*). Rather, for epithelial tissues there are a variety of factors which include local cell geometry and the direction of stress in the tissue (*Gibson and Gibson, 2009*). Though it is in principle possible to implement any given rule in our computational model, in its present version the axis along which a cell divides

is chosen as a random direction through the geometric center of the cell. In case of irregular cell shapes, a separation of the cellular domain into more than two connected components can occur. To prevent violation of topological constraints, in this case the two largest components are considered as descendant cells and the residual grid sites are filled by substrate.

We explicitly account for the finite duration of the mitotic phase T_d by keeping the cells in a mitotic state for the aforementioned time period, until the final instantaneous splitting of the cellular domains. After cell division, persistent cell migration of the daughter cells is enabled again. The descendent cells will subsequently re-enter the growing phase if their area exceeds the defined threshold, as mentioned above.

The following list summarizes the steps motivated and explained in the previous paragraphs. These additional steps are performed in a simulation that includes cell proliferation:

1. Assign a state variable $s^{(\alpha)}$ to each cell which encodes the current phase in the cell cycle:

$$s^{(\alpha)} = \begin{cases} 0, & \text{quiescent phase} \\ 1, & \text{refractory phase} \\ 2, & \text{interphase} \\ 3, & \text{mitotic phase} \end{cases} \tag{S22}$$

2. Compute the equilibrium size $A_{\text{ref}} = (\epsilon_0 - 2\pi\sqrt{3}\kappa_P)/(\sqrt{3}\kappa_A)$ of a free, solitary cell with fixed polarization field $\epsilon = \epsilon_0$, which spreads on the substrate used in the simulation.

3. At the beginning of the simulation, $t = 0$, all cells are in the quiescent state, $s^{(\alpha)}(0) = 0$, and have the following area and perimeter coupling constants, respectively: $\kappa_A^{(\alpha)}(0) = \kappa_{A/0}$ and $\kappa_P^{(\alpha)}(0) = \kappa_{P/0}$.

4. After the completion of each Monte Carlo time step t, perform one of the following changes for each cell:

- Switch from quiescent to refractory state:

$$s^{(\alpha)}(t) = 0 \;\wedge\; A^{(\alpha)}(t) > A_{\text{T}}$$
$$\Rightarrow s^{(\alpha)}(t+1) = 1. \tag{S23}$$

- Switch from refractory state to growing state with probability $p = 1 - \exp(-1/T_r)$:

$$s^{(\alpha)}(t) = 1$$
$$\Rightarrow s^{(\alpha)}(t+1) = \begin{cases} 2, & (p), \\ 1, & (1\text{-}p), \end{cases} \tag{S24}$$

where the terms in the brackets denote the respective probability.

- Exponential growth in interphase over a period of T_g:

$$s^{(\alpha)}(t) = 2$$
$$\Rightarrow \kappa_A^{(\alpha)}(t+1) = \kappa_A^{(\alpha)}(t) \cdot (1/2)^{1/T_g}$$
$$\Rightarrow \kappa_P^{(\alpha)}(t+1) = \kappa_P^{(\alpha)}(t) \cdot (1/2)^{1/(2T_g)}. \tag{S25}$$

- Switch from interphase to mitosis:

$$s^{(\alpha)}(\tau) = 2 \text{ for all } \tau \in [t - T_g,\, t]$$
$$\Rightarrow s^{(\alpha)}(t+1) = 3. \tag{S26}$$

- During cell division, cell motility is switched off and the polarization field relaxes to the neutral state according to **Equation S13c**.
- Perform cell division, reset area and perimeter stiffness and exit mitotic phase:

$$s^{(\alpha)}(\tau) = 3 \text{ for all } \tau \in [t - T_d, \, t]$$
$$\Rightarrow \text{ divide cell } \alpha \text{ into cells } (\alpha, \beta)$$
$$\Rightarrow \kappa_A^{(\alpha,\beta)}(t+1) = \kappa_{A/0}$$
$$\Rightarrow \kappa_P^{(\alpha,\beta)}(t+1) = \kappa_{P/0}$$
$$\Rightarrow s^{(\alpha,\beta)}(t+1) = 0. \tag{S27}$$

- Cell motility is restored after cell division.
- If none of the above rules apply, then do not perform any changes.

Numerical computation of stress in a tissue

In the section describing the numerical results on tissue expansion, the stress distribution in the tissue is shown in the kymographs **Figure 5(C,G)** and **Figure 6(C,G)**. Hereafter we explain how the stress tensor for each cell in the tissue can be computed from the forces acting on the cell's membrane segments in the Monte Carlo simulation. The mean value of the stress tensor in a deformed body can be calculated numerically from the formula

$$\bar{\sigma}_{ij}^{(\alpha)} = \frac{\ell}{2A^{(\alpha)}} \sum_{\mathbf{x}_k \in \mathcal{B}^{(\alpha)}} \left(f_k^i \tilde{x}_k^j + f_k^j \tilde{x}_k^i \right), \tag{S28}$$

which is a discretized version of the surface integral in **Landau et al. (1986)**. Here, $\mathbf{f}_k$ is the force acting on the membrane element $\mathbf{x}_k$ of cell α, $\tilde{\mathbf{x}}_k = \mathbf{x}_k - \mathbf{x}_{\mathrm{com}}^{(\alpha)}$ is the position of the element with respect to the center of mass $\mathbf{x}_{\mathrm{com}}^{(\alpha)}$ of the cell, and the superscripts i and j are Cartesian indices. The forces $\mathbf{f}_k$ can be computed from the energy differences of all possible protrusion and retraction events originating from $\mathbf{x}_k$,

$$\mathbf{f}_k = -\sum_{\mathbf{x}_l \in \mathcal{N}_k} \frac{\Delta \mathcal{H}(\mathcal{T}_{\mathrm{pro}})}{\|\mathbf{x}_l - \mathbf{x}_k\|} \frac{\mathbf{x}_l - \mathbf{x}_k}{\|\mathbf{x}_l - \mathbf{x}_k\|}$$
$$- \sum_{\mathbf{x}_l \in \mathcal{N}_k} {}^{\#} \frac{\Delta \mathcal{H}(\mathcal{T}_{\mathrm{ret}})}{\|\mathbf{x}_k - \mathbf{x}_l\|} \frac{\mathbf{x}_k - \mathbf{x}_l}{\|\mathbf{x}_k - \mathbf{x}_l\|}, \tag{S29}$$

where the number sign indicates a sum over substrate grid sites only, i.e. grid sites with $c(\mathbf{x}_l) < 0$, and where $\Delta \mathcal{H} \equiv \mathcal{H}_{\mathrm{cont}} + \mathcal{H}_{\mathrm{adh}} + \mathcal{H}_{\mathrm{cyto}}$.

Numerical computation of the cell shape

We use two complementary measures for the cell shape. The first is a simple measure for the deviation of an object from a circle (we refer to this as *cell extension*):

$$K = 1 - \frac{4\pi A}{P^2}. \tag{S30}$$

It becomes zero if the object is a circle and becomes 1 if the object is a line. The second measure for the cell shape is obtained from a principle components analysis of the cell shape. Specifically, we compute the covariance matrix of the point cloud representing the cell domain $\mathcal{D}^{(\alpha)}$:

$$\left(\mathrm{Cov}(\mathcal{D}^{(\alpha)}) \right)_{ij} = \frac{\sum_{\mathbf{x}_k \in \mathcal{D}^{(\alpha)}} \tilde{x}_k^i \tilde{x}_k^j}{\sum_{\mathbf{x}_k \in \mathcal{D}^{(\alpha)}} 1}, \tag{S31}$$

where $\tilde{\mathbf{x}}_k = \mathbf{x}_k - \mathbf{x}_{\mathrm{com}}^{(\alpha)}$ denotes the coordinates of element $\mathbf{x}_k$ of cell α, relative to the cell's

center of mass $\mathbf{x}_{\mathrm{com},i}^{(\alpha)}$; the superscipts i and j are Cartesian indices. Then, we compute the two eigenvalues l_+^2 (larger eigenvalue) and l_-^2 (smaller eigenvalue) of the covariance matrix, which determine the variance of the point distributions along the two principal axes of the cell. Finally, the aspect ratio of the cell is given by l_+/l_-.

Cell Biology | Physics of Living Systems

Appendix 2

Parameter screening in silico

In this section we provide additional analysis of the model parameters beyond what is already shown in the main text.

We explore all three rotational phases $\mathcal{R}_1$, $\mathcal{R}_2$ and $\mathcal{R}_3$ within confinements of varying size and constant cell density. In the $\mathcal{R}_1$-phase, the cell clusters rotate slowly and frequently reorient their direction of rotation. With increasing cell count, the cell clusters cease to rotate. In the highly coordinated $\mathcal{R}_2$ and $\mathcal{R}_3$-phases, we find scale-free behavior such that there is always a macroscopic rotation of the whole cell population regardless of the cell count and corresponding confinement size.

We also explore the parameter space of the tissue simulations. There, we find that an increased cell-cell dissipation ΔB impairs monolayer growth, while at the same time increasing front roughness. Similarly, an increased cell-substrate dissipation D also impairs monolayer growth. In contrast, increasing the maximum cell polarity $\Delta\epsilon$ improves monolayer growth and also increases front roughness. We thus find that the speed of monolayer expansion depends on whether it is dominated by cell migration or cell proliferation, with the former improving monolayer growth through a better exploration of the cell-free area.

Single cell size

To rationalize our choice of the cell growth algorithm (see section 'Cell proliferation and mitosis'), we have explored the shape and motility of differently sized solitary cells. To this end, we have varied the area stiffness parameter κ_A for different values of perimeter stiffness κ_P, while keeping all other parameters constant. We find that the area occupied by the motile cell increases linearly with $1/\kappa_A$ (*Appendix 2—figure 1A*). In particular, the cell area can be approximated quite well by the area of an immotile and equilibrated cell with uniform $\epsilon = \epsilon_0$ (fit not shown):

$$A = \frac{\epsilon_0 - 2\pi\sqrt{3}\kappa_P}{\sqrt{3}\kappa_A} \propto 1/\kappa_A. \qquad \text{(S32)}$$

Appendix 2—figure 1. Role of area stiffness κ_A for cell size and motility. (**A**) The cell area increases linearly with $1/\kappa_A$. The aspect ratio (**B**), speed (**C**) and persistence (**D**) of the cell decrease with increasing cell size. In the simulations, the area elasticity was varied in the interval $\kappa_A \in [0.09, 0.18]$, and the membrane elasticity was chosen from $\kappa_P \in \{0.054, 0.057, 0.060, 0.063, 0.066\}$. Fixed parameters: average cell polarization field $\epsilon_0 = 225$; maximum cell polarity $\Delta\epsilon = 50$; signaling radius $R = 5$; cytoskeletal update rate $\mu = 0.1$; cell-substrate dissipation $D = 0$; cell-substrate adhesion penalty $\varphi = 0$.

Furthermore, we find that with increasing size, and all other parameters constant, cells become rounder, slower, and less persistent (*Appendix 2—figure 1B-D*). To intuitively explain this phenomenology, let us compare a cell of size A_{ref} with a cell of size $r A_{\text{ref}}$, where $r \in [1, \ 2]$, with the respective area stiffnesses κ_A and κ_A/r. While the smaller cell has a perimeter P_{ref}, neglecting geometric effects the larger cell has a larger perimeter of approximately $\sqrt{r}\,P_{\text{ref}}$. Hence, the larger cell has to pay a larger energy cost (roughly by a factor $\sqrt{r}$) to ruffle its

membrane by adding segments and therefore increasing its perimeter. Meanwhile, both the energy gain from the polarization field ϵ and the energy cost for increasing the cell area (as $A\kappa_A = $ cst.) are the same for both cells. Due to the increased energy cost for adding membrane segments, larger cells finds find it more difficult to polarize, and are therefore rounder, slower and less persistent.

To offset this increased energy cost for adding membrane segments to the cell, one can scale the perimeter stiffness of the larger cell to $\kappa_P/\sqrt{r}$, such that $P\kappa_P \approx$ cst. We would then predict that the ratio κ_P^2/κ_A is constant for differently sized cells of similar shape, speed and persistence time. The same relation can also be obtained by realizing that different amounts of grid sites occupied by two otherwise identical cells (in terms of their corresponding Hamiltonian) simply stem from a different discretization of said cells, which is controlled by the parameter κ_A. Interestingly, we observe such a data collapse for the aspect ratio l_+/l_- and the velocity v of the cells onto two respective master curves depending on the ratio κ_P^2/κ_A (*Appendix 2—figure 1B,C*). While the proposed data collapse for the persistence time of directed migration of a cell (*Appendix 2—figure 1D*) is somewhat unsatisfactory, this may be owed to the following effect: by keeping R constant we have actually varied the ratio between the area that the signaling molecules typically explore due to diffusion and the area of the cell, R^2/A. Finally, we speculate that all observed quantities collapse unto respective master curves $f(\Delta\epsilon\sqrt{\kappa_A}/\kappa_P) \cdot g(R\sqrt{\kappa_A})$.

Single cell shape and dynamics depend on substrate dissipation

We have also studied the effect of cell-substrate dissipation (see section 'Rupture of substrate contacts') on cell morphology and motility. We have varied the substrate dissipation D for different values of maximum cell polarity $\Delta\epsilon$ and cell perimeter stiffness κ_P; however, we were not able to achieve a data collapse in D (*Figure 2—figure supplement 1*). We observe that with increasing cell-substrate dissipation, cells become round and cease migrating. This can be illustrated as follows: Consider a situation where the cell conquers a new hexagon at its prospective leading edge. Because the cell on average tends to constrain its area and perimeter while migrating, it consequently needs to lose a different hexagon at its prospective trailing edge. However, this retraction at the trailing edge is energetically penalized and thus cell displacement from its initial position and the positive feedback leading to cell polarization are effectively inhibited. With increasing cell-substrate dissipation, retraction events are further penalized and the cell 'sticks' to the substrate at its trailing edge, preventing persistent motion of the cell. Additionally, to further illustrate the correlation between cell shape and cell migration, we have replotted the values of *Figure 2—figure supplement 1A-C and E-G* (*Figure 2—figure supplement 1D and H*, respectively). Here and in the main text, we find that only cells with an aspect ratio larger than 2 are motile (*Figure 2F*, *Figure 2—figure supplement 1D, H*; white regions).

Cells in circular confinement

In this section we report on additional parameter studies of the dynamics of cells enclosed in a circular confinement (*Figure 4—figure supplement 1*, *Figure 4—figure supplement 2* and *Figure 4—figure supplement 3*). Specifically, we investigate how the radius of circular confinement affects the synchronized rotation of the cell population. We performed simulations with a densely populated circular confinement and varied the confinement radius, while keeping the cell density constant. The parameters are chosen such that a population consisting of 4 cells (cf. main text, *Figure 4*) would rotate in the $\mathcal{R}_1$, $\mathcal{R}_2$ or $\mathcal{R}_3$-phase, respectively. We studied the mean angular velocity

$$\omega(t) = \hat{\mathbf{e}}_z \cdot \left\langle \frac{\hat{\mathbf{v}}_\alpha(t) \times \tilde{\mathbf{R}}_\alpha(t)}{\|\tilde{\mathbf{R}}_\alpha(t)\|^2} \right\rangle_\mathcal{C}, \tag{S33}$$

averaged over the set $\mathcal{C} = \{\alpha \mid \text{is not substrate}\}$ of all cells in confinement, where $\tilde{\mathbf{v}}_\alpha(t) = \mathbf{v}_\alpha(t) - \langle \mathbf{v}_\alpha(t) \rangle_\mathcal{C}$ and $\tilde{\mathbf{R}}_\alpha(t) = \mathbf{R}_\alpha(t) - \langle \mathbf{R}_\alpha(t) \rangle_\mathcal{C}$ are the velocity and position of cell α relative to the cell cluster, respectively.

In the lowly polarizable $\mathcal{R}_1$-phase, small cell populations rotate in a highly synchronized way, and rotation is maximized for populations of 7 cells per confinement (*Figure 4—figure supplement 1A*). As can be inferred from the time traces and snapshots (*Figure 4—figure supplement 1B, C*), cells in small populations all synchronously move in the same direction at a given time and randomly switch between clockwise and counter-clockwise rotation; the switching rate decreases with increasing size of the cell population. Upon increasing the cell count and concomitantly the confinement size, global rotation of the cell population gradually vanishes (*Figure 4—figure supplement 1A*).

Unlike in the $\mathcal{R}_1$-phase, we observe that in the highly polarizable $\mathcal{R}_2$ and $\mathcal{R}_3$-phases populations of all sizes rotate in a highly synchronized way (*Figure 4—figure supplement 2A* and *Figure 4—figure supplement 3A*). There, the dependence of $\langle |\omega| \rangle$ on the population size N can be fitted by a power law of the form $\langle |\omega| \rangle \propto N^{-1/2} \propto r_0^{-1}$. This inverse proportionality between the average angular velocity and the confinement size r_0 implies total rotational order, with every cell moving at a constant velocity $|\mathbf{v}_{\text{rot}}| \approx 0.008$ ($\mathbf{v}_{\text{rot}} \perp \tilde{\mathbf{R}}$). Furthermore, in the $\mathcal{R}_2$, and $\mathcal{R}_3$-phases we have only scarcely observed switching of the rotational direction of cell clusters; e.g. for 4-cell clusters in the $\mathcal{R}_3$-phase.

Interestingly, fluctuations in the angular velocity (σ_ω) change in a highly non-monotonic fashion with the cell count and concomitantly the confinement size. Certain cell counts exhibit especially high fluctuations of the mean angular velocity (e.g. 5 cells in the $\mathcal{R}_1$-phase, see *Figure 4—figure supplement 1A*; 3 or 10 cells in the $\mathcal{R}_2$-phase, see *Figure 4—figure supplement 2A*; 3 cells in the $\mathcal{R}_3$-phase, see *Figure 4—figure supplement 3A*). This can likely be attributed to frustration of the cells in the population center (*Segerer et al., 2015*); cf. 10 cells in *Figure 4—figure supplement 2C*.

Velocity and roughness of spreading tissue

We have studied the velocity and roughness of spreading tissue, while varying cell-cell dissipation ΔB, cell-substrate dissipation D and maximum cell polarity $\Delta\epsilon$.

First, let us introduce the observables that we are interested in. Let $X_{>/<}$ be the sets of x-coordinates of the left and right outermost edges of the cell sheet. Our *in silico* setup is axially symmetric with respect to the y-axis. This initial symmetry persists, as the cell fronts advance towards the cell-free area with the same average speed. Hence, it is not needed to consider the two cell fronts separately, and we can instead consider the set of *unsigned* front positions $X := \text{abs}(X_{>/<})$. Then, we define the average front position as $x_{\text{F}} := \mathbb{E}(X)$ and the front roughness as $\sigma_{\text{F}}^2 := \text{Var}(X)$. In particular, we study the total growth of the tissue over the course of 500 MCS, which is captured by the maximal position of the front, $\max(x_{\text{F}})$, as well as the maximal roughness of the front $\max(\sigma_{\text{F}})$. We have chosen our parameters such that a cell takes a total amount of 200 MCS to divide, provided that it exceeds the threshold size of a solitary reference cell A_{ref}. Because the first daughter cells may only appear after 200 MCS have passed, we exclude this initial period from the measurements of the maximal front position and roughness, respectively. Additionally, we provide some exemplary time traces of the front evolution (Figure 5-figure supplement B,D,F).

First, we investigated how the monolayer expansion and front roughness depend on cell-substrate dissipation, ΔB (*Figure 5—figure supplement 1A, B*). Our simulations show that the cell sheet expands slower with increasing cell-cell dissipation ΔB (*Figure 5—figure supplement 1A, B*), because the dissipation penalizes cells sliding past each other. At the same time, the cell sheet also becomes slightly rougher with increasing cell-cell dissipation ΔB (inset of *Figure 5—figure supplement 1A*).

We also investigated how the monolayer expansion and front roughness depend on cell-substrate dissipation, D (*Figure 5—figure supplement 1C, D*). Before we turn to the monolayer, let us recall the observed single-cell behavior in the previous section (see section 'Single cell shape and dynamics depend on substrate dissipation'): for high enough cell-substrate dissipation D (typically of the same order of magnitude as the maximum cell polarity

$\Delta\epsilon$) cell migration is switched off (**Figure 2—figure supplement 1**). Extrapolating the single-cell results, we expect that the same holds also for collectives of cells and that cell migration does not play a role for high cell-substrate dissipation. Indeed, with increasing cell-substrate dissipation, the monolayer expands slower, until this effect appears to saturate at a threshold value $D^\star \approx 5$ (**Figure 5—figure supplement 1C, D**). Following this line of argument, monolayer growth is slowed down if we suppress cell migration and thus move the cell monolayer towards a proliferation-dominated mode of expansion.

What about the inverse? Is the monolayer growth increased if we enhance cell migration and thus move the cell monolayer towards a migration-dominated mode of expansion? To test this hypothesis, we have analyzed how the monolayer growth and front roughness depend on the maximum cell polarity $\Delta\epsilon$. As predicted, monolayer growth increases with the maximum cell polarity $\Delta\epsilon$ (**Figure 5—figure supplement 1E, F**), because an increased amount of cells exceed the threshold size to switch to mitosis (cf. the stretching of bulk cells in the monolayer in **Figure 5B**). Additionally, we also find that the front roughness increases with increasing maximum cell polarity $\Delta\epsilon$.
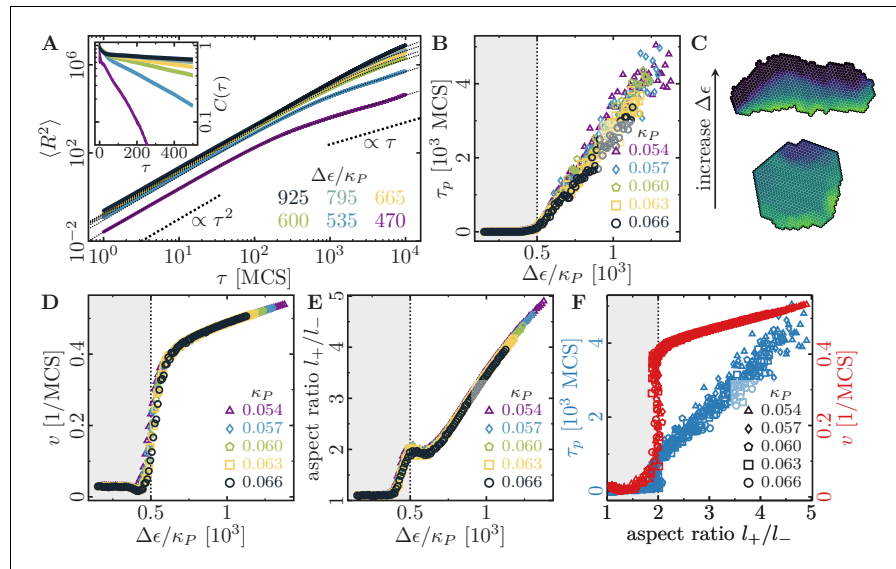
Reprint of published manuscript

Figures and figure supplements

Bridging the gap between single-cell migration and collective dynamics
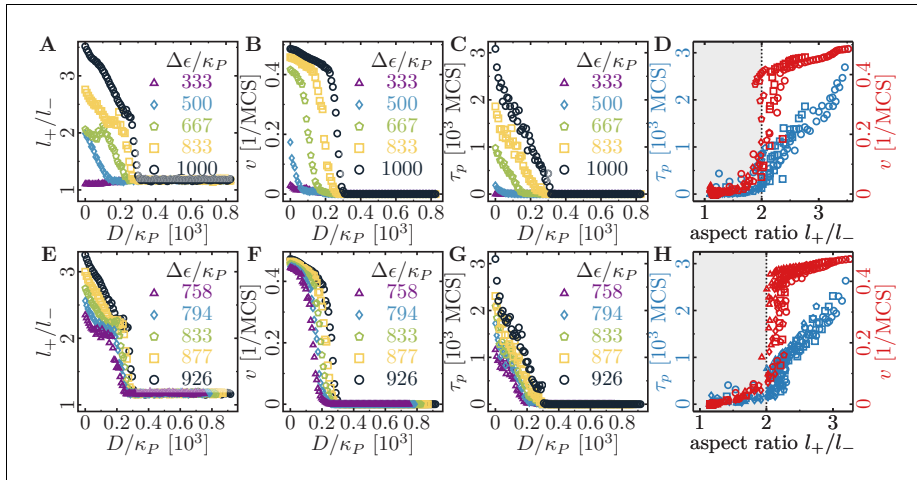
Florian Thüroff *et al*

Figure 1. Illustration of the computational model with the pertinent simulation steps. (**A**) Illustration of a small cell cohort that adheres to a surface ((x, y)-plane). The polarization field, ϵ, is defined on the contact surface with the adhesion plane. The magnitude of the polarization field, which is indicated by the colorbar in Figure (**C**), encodes the local strength of cell-substrate adhesions and emulates the local mass of force-generating (pushing) cytoskeletal structures. Cell-cell adhesions are indicated in red. (**B**) Cytoskeletal structures respond to external mechanical stimuli through reaction networks involving different feedback loops. We greatly simplify these complex processes into two prototypic feedback loops, which break detailed balance and drive cell migration, as follows. The polarization field induces membrane protrusions and inhibits retractions. In turn, protrusions increase the polarization field (positive feedback) and therefore the likelihood of further protrusive activity, while retractions decrease the polarization field (negative feedback). In the absence of mechanochemical signals, the polarization field approaches its rest state. (**C**) Zoom-in to a common boundary shared between the substrate contact areas of three cells (bounded by the red lines), each represented by a contiguous set of occupied grid sites (hexagons). *Top left:* The upper right corner of the lower left cell (source cell) initiates a protrusion event against a neighboring element in the cell to its right (target cell), as indicated by the arrow, in an attempt to displace it. The success of each such attempted elementary event depends on the balance between contractile forces, cytoskeletal forces, and cell adhesion. *Top right:* If the protrusion event is successful, then the levels of regulatory factors are increased (decreased) in integer steps, at all lattice sites inside the source (target) cell that lie within a radius R of the accepted protrusion event (as indicated by the plus and minus signs). *Bottom right:* During the course of one MCS, different levels of regulatory factors accumulate locally within each cell, with positive levels of regulatory factors (green plus signs) promoting a build-up of cytoskeletal structures, negative levels of regulatory factors (red minus signs) causing degradation of cytoskeletal structures, and neutral levels of regulatory factors (white zero signs) causing relaxation towards a resting state, as indicated in the *lower left image*. The color code indicates local levels of cytoskeletal structures, ϵ.
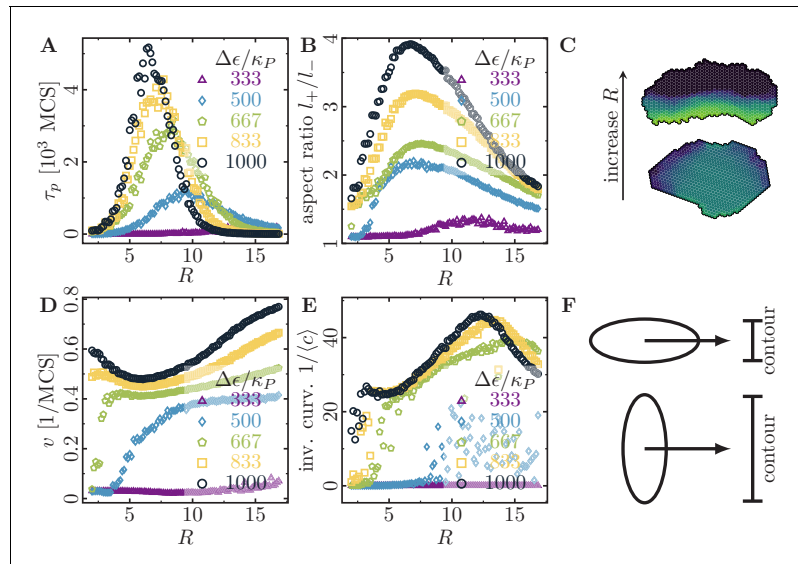
Figure 2. Cell shape and persistence of migration as a function of cell polarizability. (**A**) Mean-squared displacement (MSD) for single-cell movements at different maximum cell polarity $\Delta\epsilon$ (stiffness parameters $\kappa_P = 0.060$, $\kappa_A = 0.18$; average polarization field $\epsilon_0 = 225$; signaling radius $R = 5$; cell-substrate dissipation $D = 0$; cell-substrate adhesion penalty $\varphi = 0$; cytoskeletal update rate $\mu = 0.1$; 100 independent simulations for each set of parameters). Single cells perform a persistent random walk, i.e. they move ballistically (MSD $\propto \tau^2$) for $\tau \ll \tau_p$, and diffusively (MSD $\propto \tau$) for $\tau \gg \tau_p$. *Inset:* Normalized velocity auto-correlation function for the same parameters as in the main figure. (**B**) Persistence time of directed cell migration plotted as a function of maximum cell polarity $\Delta\epsilon$, and perimeter stiffness κ_P (area stiffness $\kappa_A = 0.18$; average polarization field $\epsilon_0 = 225$; signaling radius $R = 5$; cell-substrate dissipation $D = 0$; cell-substrate adhesion penalty $\varphi = 0$; cytoskeletal update rate $\mu = 0.1$; 100 independent simulations for each set of parameters). The persistence time of the random walk increases with increasing cytoskeletal polarity and decreasing perimeter elasticity. (**C**) Cytoskeletal polarity also controls cell shapes, with crescent cell shapes (long persistence times) being observed at large cytoskeletal polartities, and round cell shapes (short persistence times) at small cytoskeletal polarities. Color code: cell polarization; cf. color bar in *Figure 1C*. (**D**) Single cell speed plotted as a function of maximum cell polarity $\Delta\epsilon$, and perimeter stiffness κ_P. (**E**) Single cell aspect ratio plotted as a function of maximum cell polarity $\Delta\epsilon$, and perimeter stiffness κ_P. (**F**) Speed and persistence time of single cells are correlated with the cell aspect ratio.
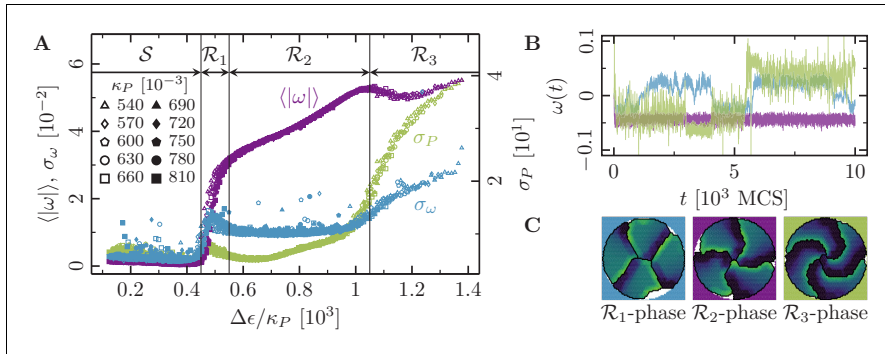
Figure 2—figure supplement 1. Role of substrate dissipation for cell shape and motility. (**A–D**) Role of substrate dissipation for cells of varying maximum cell polarity $\Delta\epsilon$. The aspect ratio l_+/l_- (**A**), the speed v (**B**), and the persistence time τ_p (**C**) as a function of substrate dissipation D for a series of values for $\Delta\epsilon/\kappa_P$ indicated in the graphs. (**D**) Cell persistence and cell speed are correlated with the aspect ratio of the cell. Only cells with an aspect ratio larger than 2 are motile. In the simulations, the substrate dissipation was varied in the interval $D \in [0, 50]$, and the maximum cell polarity $\Delta\epsilon \in \{20, 30, 40, 50, 60\}$. Fixed parameters: average polarization field $\epsilon_0 = 225$; area elasticity $\kappa_A = 0.18$; membrane elasticity $\kappa_P = 0.060$; cytoskeletal update rate $\mu = 0.1$; cell-substrate adhesion penalty $\varphi = 0$; 100 independent simulations for each set of parameters. (**E–F**) Role of substrate dissipation for cells of varying membrane stiffness κ_P. The aspect ratio l_+/l_- (**E**), the speed v (**F**), and the persistence time τ_p (**G**) as a function of substrate dissipation D for a series of values for $\Delta\epsilon/\kappa_P$ indicated in the graphs. (**H**) Cell persistence and cell speed are correlated with the aspect ratio of the cell. Only cells with an aspect ratio larger than 2 are motile. In the simulations, the substrate dissipation was varied in the interval $D \in [0, 50]$, and the membrane elasticity $\kappa_P \in \{0.054, 0.057, 0.060, 0.063, 0.066\}$. Fixed parameters: average polarization field $\epsilon_0 = 225$; area elasticity $\kappa_A = 0.18$; maximum cell polarity $\Delta\epsilon = 50$; cytoskeletal update rate $\mu = 0.1$; cell-substrate adhesion penalty $\varphi = 0$; 100 independent simulations for each set of parameters.
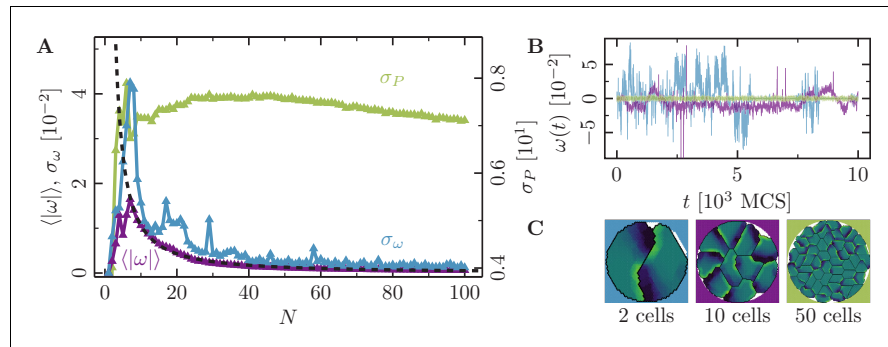
Figure 3. Migratory behavior of single cells as a function of the cell's signaling radius R at different values for the maximal cytoskeletal polarity $\Delta\epsilon$. (Stiffness parameters $\kappa_P = 0.060$, $\kappa_A = 0.18$; average polarization field $\epsilon_0 = 225$; cell-substrate dissipation $D = 0$; cell-substrate adhesion penalty $\varphi = 0$; cytoskeletal update rate $\mu = 0.1$; 100 independent simulations for each set of parameters). (A) The persistence times of directed migration of single cells exhibit a pronounced maximum at an optimal signaling radius, which depends on cell polarizability. (B) The shapes of single cells exhibit a pronounced maximal elongation at an optimal signaling radius, which depends on cell polarizability. (C) The signaling radius critically determines the synchronicity of internal cytoskeletal remodeling processes. Small signaling radii frequently lead to transient formation of mutually independent lamellipodia at different positions around the cell perimeter, thereby interrupting persistent motion (reducing persistence times of directed migration). Large signaling radii lead to structurally stable front-rear polarization profiles across the entire cell body (long persistence times of directed migration). Color code: cell polarization; cf. color bar in *Figure 1C*. (D) The speed of single cells does not drop to zero even when their persistence time of directed migration vanishes. This indicates single cell rotations. (E) The inverse curvature of the cell trajectories as a function of the signaling radius. (F) Depending on whether a cell migrates along its long axis (top) or short axis (bottom), it has to move a different projected contour length. If each protrusion takes roughly the same amount of time, then migration along the long axis (top; cell has to move a smaller projected contour length) allows for greater cell speeds than migration along the short axis (bottom; cell has to move a larger projected contour length).
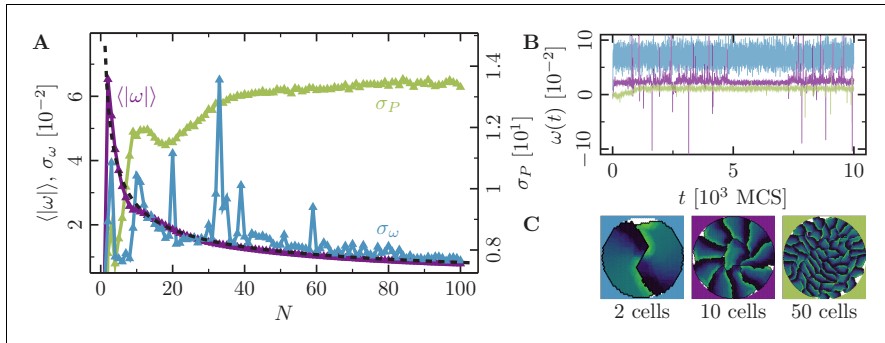
Figure 4. Phases of collective motion. (4-cell systems; confinement radius $r_0 = 30.6$; area stiffness $\kappa_A = 0.18$; average polarization field $\epsilon_0 = 225$; signaling radius $R = 5$; cytoskeletal update rate $\mu = 0.1$; cell-cell adhesion $B = 0$; cell-cell dissipation $\Delta B = 12$; cell-substrate dissipation $D = 0$; cell-substrate adhesion penalty $\varphi = 0$ $(r < r_0)$, $\varphi \to -\infty$ $(r > r_0)$; 100 independent simulations for each set of parameters). (A) Characteristic observables of collective cell rotation at different values of the cell perimeter stiffness parameter κ_P: mean $(\langle|\omega|\rangle)$ and standard deviation (σ_ω) of the magnitude of the cell cluster's angular velocity, and the standard deviation of the cell perimeter (σ_P). The statistics of collective cell motion depends only on the ratio of maximum cell polarity, $\Delta\epsilon$, to cell contractility, κ_P (specific polarizability). (B) Representative angular trajectories and (C) cell shapes (color code represents cell polarization; cf. *Figure 1C*) for the different parameter regimes as described in the main text. The cellular dynamics in the different parameter regimes are shown in *Figure 4—video 1*, *Figure 4—video 2* and *Figure 4—video 3*.

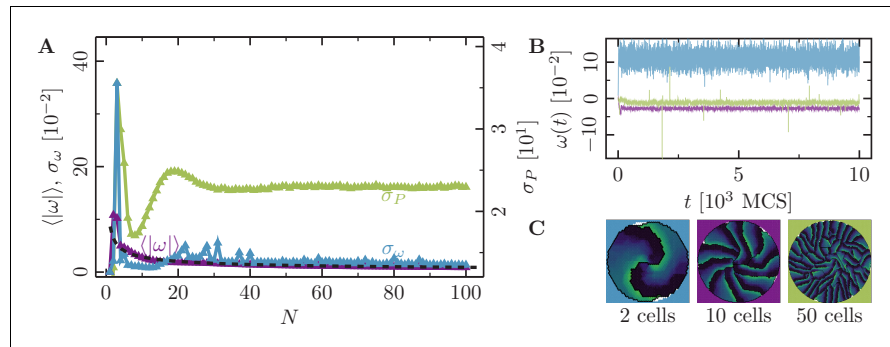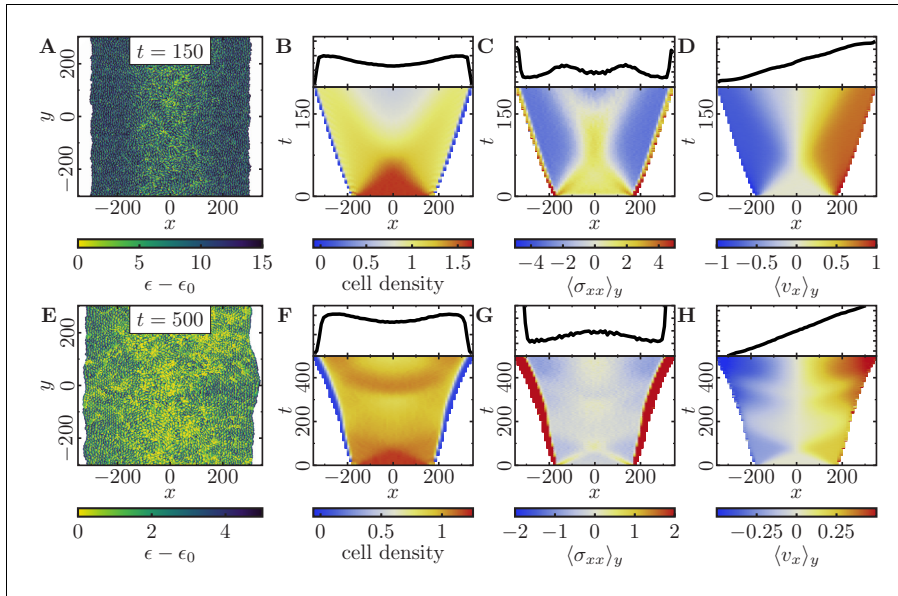**Figure 4—figure supplement 1.** Collective motion for varying number of cells at low polarizability. (N-cell systems; confinement radius $r_0 = \sqrt{234\,N}$; stiffness parameters $\kappa_P = 0.060$, $\kappa_A = 0.18$; average polarization field $\epsilon_0 = 225$; maximum cell polarity $\Delta\epsilon = 28$; signaling radius $R = 5$; cytoskeletal update rate $\mu = 0.1$; cell-cell adhesion $B = 0$; cell-cell dissipation $\Delta B = 12$; cell-substrate dissipation $D = 0$; cell-substrate adhesion penalty $\varphi = 0$ ($r<r_0$), $\varphi \to -\infty$ ($r>r_0$); 100 independent simulations for each set of parameters). For this choice of parameters 4-cell populations rotate in the $\mathcal{R}_1$-phase. We observe a similar behavior here: the cell clusters rotate slowly and reorient frequently. (A) Characteristic observables of collective cell rotation at different values of the cell perimeter stiffness parameter κ_P: mean ($\langle|\omega|\rangle$) and standard deviation (σ_ω) of the angular velocity magnitude of cell motion, and the standard deviation of the cell perimeter (σ_P). The black line corresponds to a power-law fit of the form $\langle|\omega|\rangle \propto N^{-k/2} \propto r_0^{-k}$ with the fitted exponent $k \approx 8/3$. (B) Representative angular trajectories and (C) cell shapes (color code represents cell polarization; cf. *Figure 1*) for the different parameter regimes as described in the main text. .
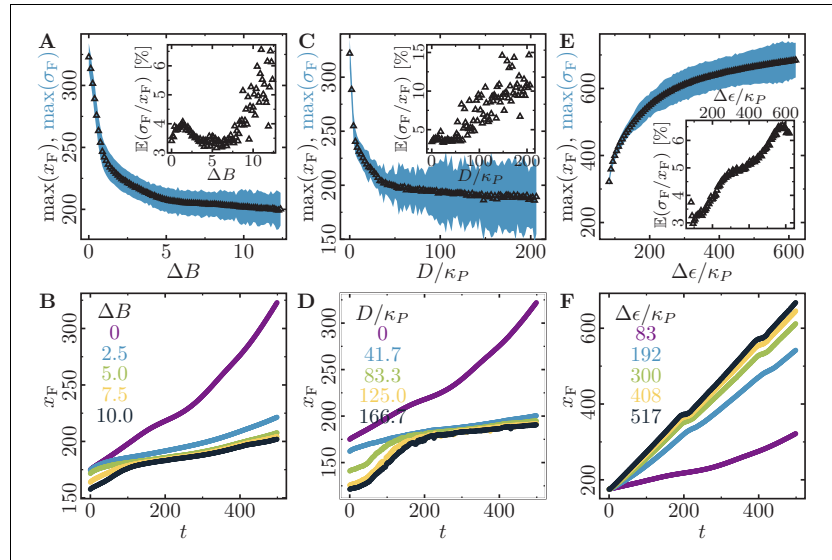
Figure 4—figure supplement 2. Collective motion for varying number of cells at intermediate polarizability. (N-cell systems; confinement radius $r_0 = \sqrt{234\,N}$; stiffness parameters $\kappa_P = 0.060$, $\kappa_A = 0.18$; average polarization field $\epsilon_0 = 225$; maximum cell polarity $\Delta\epsilon = 50$; signaling radius $R = 5$; cytoskeletal update rate $\mu = 0.1$; cell-cell adhesion $B = 0$; cell-cell dissipation $\Delta B = 12$; cell-substrate dissipation $D = 0$; cell-substrate adhesion penalty $\varphi = 0$ ($r<r_0$), $\varphi \to -\infty$ ($r>r_0$); 100 independent simulations for each set of parameters). For this choice of parameters 4-cell populations rotate in the $\mathcal{R}_2$-phase. We observe a similar behavior here: highly correlated rotations with no changes in rotational direction. (A) Characteristic observables of collective cell rotation at different values of the cell perimeter stiffness parameter κ_P: mean ($\langle|\omega|\rangle$) and standard deviation (σ_ω) of the angular velocity magnitude of cell motion, and the standard deviation of the cell perimeter (σ_P). The black line corresponds to a power-law fit of the form $\langle|\omega|\rangle \propto N^{-1/2} \propto r_0^{-1}$. (B) Representative angular trajectories and (C) cell shapes (color code represents cell polarization; cf. *Figure 1*) for the different parameter regimes as described in the main text. .

Figure 4—figure supplement 3. Collective motion for varying number of cells at high polarizability. (*N*-cell systems; confinement radius $r_0 = \sqrt{234\,N}$; stiffness parameters $\kappa_P = 0.060$, $\kappa_A = 0.18$; average polarization field $\epsilon_0 = 225$; maximum cell polarity $\Delta\epsilon = 70$; signaling radius $R = 5$; cytoskeletal update rate $\mu = 0.1$; cell-cell adhesion $B = 0$; cell-cell dissipation $\Delta B = 12$; cell-substrate dissipation $D = 0$; cell-substrate adhesion penalty $\varphi = 0$ ($r<r_0$), $\varphi \to -\infty$ ($r>r_0$); 100 independent simulations for each set of parameters). For this choice of parameters 4-cell populations rotate in the $\mathcal{R}_3$-phase. We observe a similar behavior here: highly correlated rotations. (**A**) Characteristic observables of collective cell rotation at different values of the cell perimeter stiffness parameter κ_P: mean ($\langle|\omega|\rangle$) and standard deviation (σ_ω) of the angular velocity magnitude of cell motion, and the standard deviation of the cell perimeter (σ_P). The black line corresponds to a power-law fit of the form $\langle|\omega|\rangle \propto N^{-1/2} \propto r_0^{-1}$. (**B**) Representative angular trajectories and (**C**) cell shapes (color code represents cell polarization; cf. **Figure 1**) for the different parameter regimes as described in the main text.
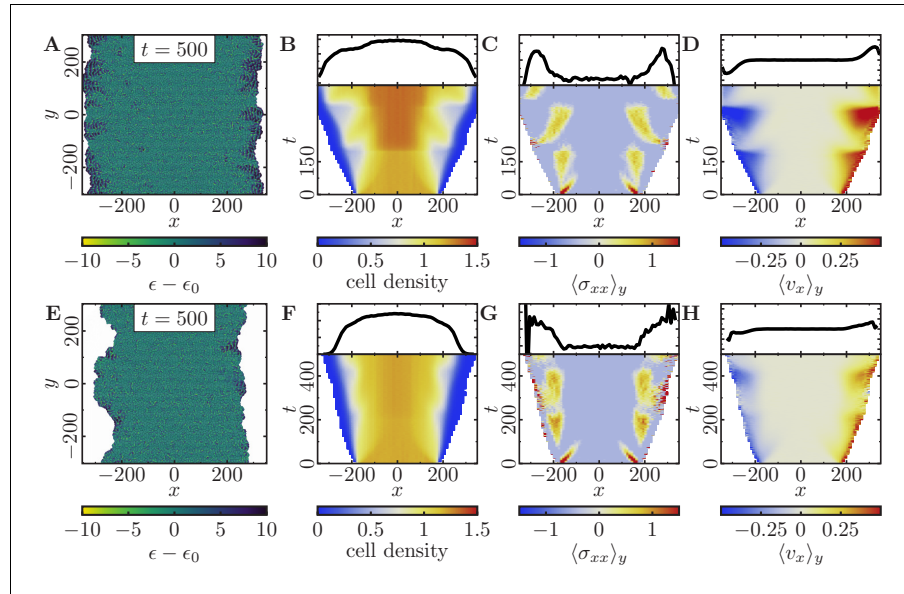
Figure 5. Expansion of a confluent epithelial cell sheet after removal of boundaries positioned at $x = \pm175$ for two different parameter settings. (Stiffness parameters $\kappa_P = 0.12$, $\kappa_A = 0.18$; average polarization field $\epsilon_0 = 35$; signaling radius $R = 2$; cytoskeletal update rate $\mu = 0.1$; cell-cell adhesion $B = 12$; cell-cell dissipation $\Delta B = 0$; cell-substrate dissipation $D = 0$; cell-substrate adhesion penalty $\varphi = 0$; 100 independent simulations for each set of parameters). (A–D) Tissue expansion for a migration-dominated setup without explicit cell growth and mitosis. (3300-cell system; maximum cell polarity $\Delta\epsilon = 30$). (E–H) Tissue expansion at low density and cell polarizability for a cell sheet comprised of dividing cells. (Initially a 2500-cell system; maximum cell polarity $\Delta\epsilon = 10$; growth time $T_g = 180$; division time $T_d = 20$; size threshold for cell growth $A_T = 1\,A_{ref}$, where A_{ref} is the size of a solitary cell in equilibrium). (A, E) Snapshots of the polarization field ϵ; cf. *Figure 5—video 1* and *Figure 5—video 2*. (B, F) Kymographs showing the cell density averaged over the y-direction and (*top*) final snapshots of the cell density profiles. (C, G) Kymographs showing the component σ_{xx} of the stress tensor averaged over the y-direction and (*top*) final snapshots of the stress profiles. (D, H) Kymographs showing the component v_x of the cell velocities averaged over the y-direction and (*top*) final snapshot of the velocity profiles.
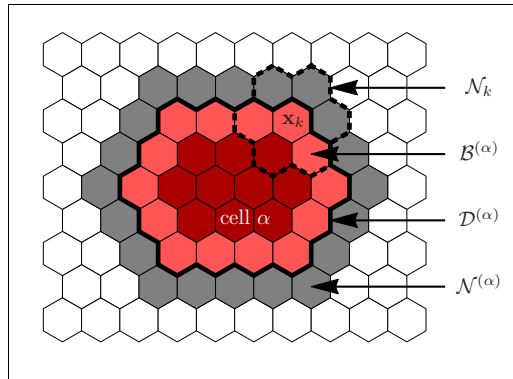
Figure 5—figure supplement 1. Monolayer expansion depends on dissipation and cell polarizability. Cell monolayer expansion depends on the cell-cell dissipation, cell-substrate dissipation, and maximum cell polarity. (Initially a 2500-cell system; stiffness parameters $\kappa_P = 0.12$, $\kappa_A = 0.18$; average polarization field $\epsilon_0 = 35$; maximum cell polarity $\Delta\epsilon = 10$; signalling radius $R = 2$; cytoskeletal update rate $\mu = 0.1$; cell-cell adhesion $B = 12$; cell-substrate adhesion penalty $\varphi = 0$; growth time $T_g = 180$; division time $T_d = 20$; size threshold for cell growth $A_T = 1\,A_{\mathrm{ref}}$, where A_{ref} is the size of a solitary cell in equilibrium; 100 independent simulations for each set of parameters). (A,B) Cell monolayer expansion depends on the cell-cell dissipation ΔB (maximum cell polarity $\Delta\epsilon = 10$; cell-substrate dissipation $D = 0$). (A) Maximal monolayer extension and roughness (we exclude an initial time interval of 200 MCS because it takes at least that long for first daughter cells to appear). *Inset*: Relative roughness of the spreading monolayer relative to its size. (B) Time traces for selected values of ΔB. (C,D) Cell monolayer expansion depends on the cell-substrate dissipation D (maximum cell polarity $\Delta\epsilon = 10$; cell-cell dissipation $\Delta B = 0$). (C) Maximal monolayer extension and roughness (we exclude an initial time interval of 200 MCS because it takes at least that long for first daughter cells to appear). (D) Time traces for selected values of D. (E,F) Cell monolayer expansion depends on the maximum cell polarity $\Delta\epsilon$ (cell-cell dissipation $\Delta B = 0$; cell-substrate dissipation $D = 0$). (E) Maximal monolayer extension and roughness (we exclude an initial time interval of 200 MCS because it takes at least that long for first daughter cells to appear). (F) Time traces for selected values of $\Delta\epsilon/\kappa_P$. .
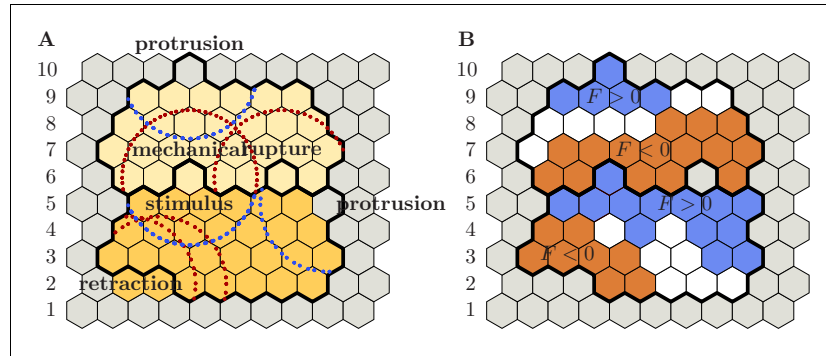
Figure 6. Expansion of a confluent epithelial cell sheet after removal of boundaries positioned at $x = \pm 175$ for two different parameter settings that produce rough tissue fronts. (Initially a 2500-cell system; stiffness parameters $\kappa_P = 0.10$, $\kappa_A = 0.18$; average polarization field $\epsilon_0 = 35$; maximum cell polarity $\Delta\epsilon = 20$; signaling radius $R = 5$; cytoskeletal update rate $\mu = 0.1$; cell-cell adhesion $B = 5$; cell-cell dissipation $\Delta B = 10$; cell-substrate dissipation $D = 0$; cell-substrate adhesion penalty $\varphi = 0$; growth time $T_g = 180$; division time $T_d = 20$; 100 independent simulations for each set of parameters). (A–D) Tissue expansion at low density and cell polarizability for a cell sheet comprised of quickly dividing cells. (Size threshold for cell growth $A_T = 1.05 A_{ref}$, where A_{ref} is the size of a solitary cell in equilibrium). (E–H) Tissue expansion at low density and cell polarizability for a cell sheet comprised of slowly dividing cells. (Size threshold for cell growth $A_T = 1.10 A_{ref}$, where A_{ref} is the size of a solitary cell in equilibrium). (A, E) Snapshots of the polarization field ϵ; cf. *Figure 6—video 1* and *Figure 6—video 2*. (B, F) Kymographs showing the cell density averaged over the y-direction and (*top*) final snapshots of the cell density profiles. (C, G) Kymographs showing the component σ_{xx} of the stress tensor averaged over the y-direction and (*top*) final snapshots of the stress profiles. (D, H) Kymographs showing the component v_x of the cell velocities averaged over the y-direction and (*top*) final snapshot of the velocity profiles.
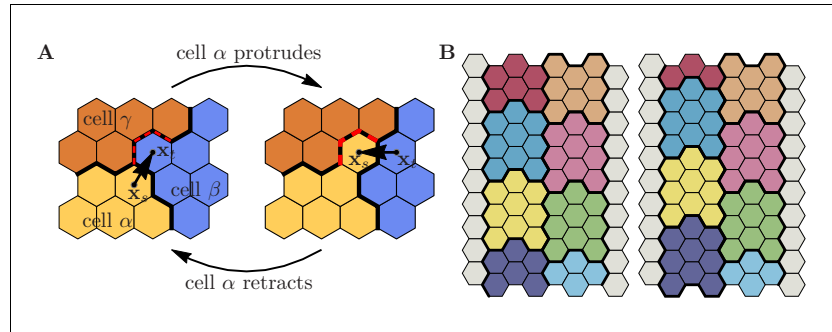
Appendix 1—figure 1. Illustration of the various sets defining a cell and its environment. Grid sites occupied by cell α, i.e. its domain $\mathcal{D}^{(\alpha)}$, are indicated in red colors. The cell's membrane sites, $\mathcal{B}^{(\alpha)}$, are indicated by the lighter red color, the cell's immediate neighborhood, $\mathcal{N}^{(\alpha)}$, is indicated in gray. Elementary events involving cell α always involve one grid site in $\mathcal{B}^{(\alpha)}$ and one grid site in $\mathcal{N}^{(\alpha)}$. For the hexagonal lattices used in this work, each grid site $\mathbf{x}_k$ is surrounded by 6 nearest neighbors which we collectively denote by $\mathcal{N}_k$.
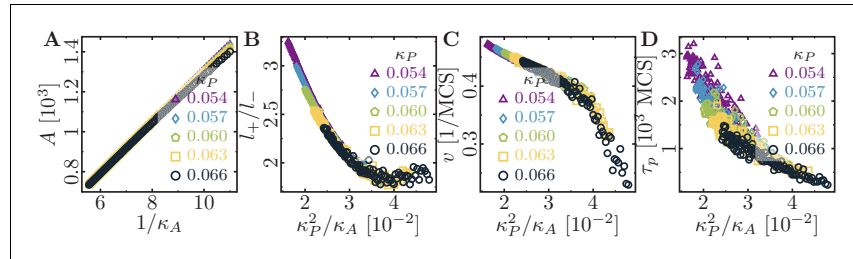
Appendix 1—figure 2. Distribution of regulatory factors on the basis of accepted elementary events. For ease of reference, grid rows have been numbered from 1 to 10. *Left* (**A**): Solid black lines indicate cells' membrane positions *after* acceptance of the respective elementary event; colors indicate cellular domains *before* the respective elementary event has been accepted (gray: substrate; shades of yellow: cells). Blue and red circular arcs (of radius R) delineate areas of local increase or decrease in the level of regulatory factors, respectively. The following elementary events are depicted: (i) lower cell retracts (two grid sites in row 2); (ii) lower cell protrudes (row 5); (iii) upper cell protrudes (row 10). In addition, the following elementary events occur across the cell-cell boundary: (iv) retraction of upper cell leads to rupture of cell-cell contacts (row 6, right event); (v) either the lower cell protrudes and pushes the upper cell or the upper cell retracts and pulls on the lower cell (row 6, left event). Specifically, event (v) entails mechanical signaling between the upper and lower cell and, therefore, affects the distribution of regulatory factors in both cells. *Right* (**B**): Identical copy of the left image (**A**). Colors indicate local levels of regulatory factors F (blue: F is positive; white: F is zero; red: F is negative; gray: substrate site). Note, in particular, that a substrate grid site has been inserted where cell rupture occurred (row 6, right grid site). The following cases can be distinguished: (i) Grid site $\mathbf{x}_k$ lies in the zone of influence of only positive (blue circles) or negative (red circles) chemical feedback, in which case the level of regulatory factors is positive or negative, respectively (e.g. red grid sites in row 2, or blue grid sites in row 5). (ii) Grid site $\mathbf{x}_k$ lies outside of any zone of influence, in which case the level regulatory factors is zero (e.g. white grid sites in row 2). (iii) Grid site $\mathbf{x}_k$ lies in the zone of influence of equally many positive and negative feedbacks, in which case the level of regulatory factors remains zero (e.g. fourth grid site in row 4). (iv) Grid site $\mathbf{x}_k$ lies in a zone of predominantly positive or negative feedback, in which case the level of regulatory factors is positive or negative, respectively (e.g. third grid site in row 4). Recall that only the sign of F is of significance to update the cells' polarization field; cf. *Equation S13*.

Appendix 1—figure 3. Cell-cell adhesion. (**A**) Adhesive energy contribution in a cyclic process, where a protrusion of source cell α against target cell β is followed by the inverse retraction event. Both events involve a third party cell γ, leading to net energy dissipation after the cyclic process has been completed. *Protrusion*: (i) Three pre-existing cell-cell contacts between β and γ are torn apart (red dashed contacts); (ii) three new contacts between α and γ are formed; (iii) the contact length between source cell α and target cell β increases by one unit of length. This implies $\Delta\mathcal{H}_{\rm adh}(\mathcal{T}_{\rm pro}) = \ell\,(3B'_{\beta,\gamma} - 3B_{\alpha,\gamma} - B_{\alpha,\beta})$. *Retraction*: (i) Three pre-existing cell-cell contacts between α and γ are torn apart (red dashed contacts); (ii) three new contacts between β and γ are formed; (iii) the contact length between source cell α and target cell β decreases by one unit of length. This implies $\Delta\mathcal{H}_{\rm adh}(\mathcal{T}_{\rm ret}) = \ell\,(3B'_{\alpha,\gamma} - 3B_{\beta,\gamma} + B_{\alpha,\beta})$. Altogether, this leads to

$\Delta\mathcal{H}_{\rm adh}^{(\rm cycl)} = \Delta\mathcal{H}_{\rm adh}(\mathcal{T}_{\rm pro}) + \Delta\mathcal{H}_{\rm adh}(\mathcal{T}_{\rm ret}) = \ell\,(3(\Delta B)_{\alpha,\gamma} + 3(\Delta B)_{\beta,\gamma}) \geq 0$, i.e. a (non-negative) dissipative contribution, whose magnitude depends on the dissipation matrix $(\Delta B)_{\alpha,\beta} = B'_{\alpha,\beta} - B_{\alpha,\beta} \geq 0$. (**B**) Shear viscosity due to cell-cell adhesion. Consider two rows of adhesive cells sliding past each other as indicated in the figure (left row of cells moves up by one grid site; colors indicate different cells). The associated adhesion energy change (per cell) reads $\Delta\mathcal{H}_{\rm adh}/n_c = 2\,(B' - B) \geq 0$, where n_c denotes the number of cells sliding past each other, and where we assumed cells of like type, i.e. $B_{\alpha,\beta} \equiv B$ and $B'_{\alpha,\beta} \equiv B'$ ($\alpha \neq \beta$). The condition $B'>B$, *Equation S15e*, thus implies positive friction associated with cellular shear flows, whose magnitude is proportional to the number of cells sliding past each other. Note that this shear viscosity vanishes for $B' = B$, i.e. for zero dissipation matrix.

Appendix 2—figure 1. Role of area stiffness κ_A for cell size and motility. (A) The cell area increases linearly with $1/\kappa_A$. The aspect ratio (B), speed (C) and persistence (D) of the cell decrease with increasing cell size. In the simulations, the area elasticity was varied in the interval $\kappa_A \in [0.09,\ 0.18]$, and the membrane elasticity was chosen from $\kappa_P \in \{0.054, 0.057, 0.060, 0.063, 0.066\}$. Fixed parameters: average cell polarization field $\epsilon_0 = 225$; maximum cell polarity $\Delta\epsilon = 50$; signaling radius $R = 5$; cytoskeletal update rate $\mu = 0.1$; cell-substrate dissipation $D = 0$; cell-substrate adhesion penalty $\varphi = 0$.

III.2 CELL MIGRATION AND SHAPE IN SOFT ENVIRONMENTS

In Section III.1 "Collective Cell Dynamics in Rigid Environments", we have developed a *Cellular Potts* model that describes the migration of cells. So far, we have assumed that the substrate on which the cells migrate is rigid (that is, not deformable). Now, we relax this assumption, while building on the discussion in Section III.1 "Collective Cell Dynamics in Rigid Environments". To that end, we further generalize the discrete *Cellular Potts* model (Graner and Glazier, 1992; Segerer et al., 2015; F. Thüroff et al., 2019), now aimed at describing the migration of polar cells in soft environments. We refer to pages 273–285 for a preprint of the main text and to pages 287–324 for the Supplementary Material. The following serves as an introduction into the project and a summary of its main results, for the convenience of the reader.

A note about the notation.   To be consistent with the rest of the thesis, we denote the mechanical rigidity coefficients with k instead of κ, because the latter is reserved for curvatures in this thesis. We use G for the shear modulus instead of μ, because the latter is reserved for chemical potentials in this thesis. We denote the cytoskeletal update rate with r_ϵ instead of μ, because the latter is reserved for chemical potentials in this thesis. To be consistent with the rest of the thesis, we denote the traction forces with $\boldsymbol{f}_{tr}$ instead of $\boldsymbol{T}$. Finally, as in Section III.1 "Collective Cell Dynamics in Rigid Environments", we discuss our model in terms of the Helmholtz free energy of a spatially extended cell.

### III.2.1 STARTING POINT OF THE PROJECT

General Scope and Relevance.   As we have discussed in Section III.1 "Collective Cell Dynamics in Rigid Environments", cell migration plays a crucial role for many processes that occur in development, homeostasis and disease. To propel themselves, cells make use of their cytoskeleton, a complex machinery that converts biochemical fuel into mechanical work. This mechanical work shows itself not only in the form of visible propulsion, but also via measurable traction forces (Schwarz and Soiné, 2015) that indicate how cells actively pull on their surroundings (Schwarz and S. A. Safran, 2013). In turn, cells also detect mechanical signals from their environment, by making use of mechanochemical connectors such as integrins (Charras and Sahai, 2014; De Pascalis and Etienne-Manneville, 2017; Van Helvert et al., 2018), linked to different biochemical regulatory networks (Lauffenburger and Horwitz, 1996; Schwartz and Shattil, 2000; Parsons et al., 2010; Ridley, 2001; Ridley et al., 2003; Ridley, 2015;

Hodge and Ridley, 2016; Lawson and Ridley, 2018). Examples of mechanical signals that cells respond to include not only external stresses applied via the environment (Bischofs and Schwarz, 2003; Rens and R. M. H. Merks, 2017), but also cellular sensing of the environment's mechanical properties (Lo et al., 2000; Isenberg et al., 2009; Zemel et al., 2010a; Zemel et al., 2010b; Vincent et al., 2013; Sunyer et al., 2016; Hadden et al., 2017; Lachowski et al., 2017; Hakim and Silberzan, 2017). This directly brings us to our research question.

Research Question and Hypothesis.   How do the mechanical properties of a soft deformable substrate alter cell behavior? One possibility for cells to sense their environment is on the microscopic level of focal adhesions, through load-dependent binding and unbinding of integrins, and molecular clutch mechanisms (Mitchison and Kirschner, 1988; Chan and Odde, 2008; Elosegui-Artola, Bazellières, et al., 2014; Elosegui-Artola, Oria, et al., 2016; Sunyer et al., 2016; Bennett et al., 2018; Sens, 2020), and also reinforcement of adhesions in response to stress (Bershadsky et al., 2006). Here, however, we focus on purely mesoscopic and even more generic effects, without a need to go into microscopic details. In particular, we invoke purely geometric effects, as described in Section I.3 "A Foundation for Patterns in Adapting Organisms", which are the most basic and inescapable type of interaction. Cells pull on the substrate that they adhere to, and thereby induce strains. To do so, the cell cytoskeleton must also be coupled to the substrate through adhesions. The resulting strains imply a change of integrin density on the cell side and a change of fibronectin density on the substrate side. We hypothesize that these basic effects are sufficient for a rudimentary form of cellular substrate sensing.

III.2.2 TECHNICAL SUMMARY

Traction force generation.   In our model, the cellular dynamics are driven by (i) two competing contributions that we encapsulate into an effective free energy functional, and (ii) one out-of-equilibrium reaction. The first contribution to the free energy functional, F_{el}, see Equation (III.1), favors the rounding up of a cell into a spherical shape due to homogeneous actomyosin contractility, thereby detaching the cell from the substrate. This is counteracted by the second contribution to the free energy functional, F_{ad}, see Equation (III.6), which represents (i) an effective adhesion energy between the cell and the substrate, as well as (ii) the ability of the cell to generate active stresses. We have to distinguish between these two contributions when we determine substrate deformations, lest a cell will exert no traction after reaching stationary state (mechanical equilibrium) as in (Rens and Edelstein-Keshet, 2019).
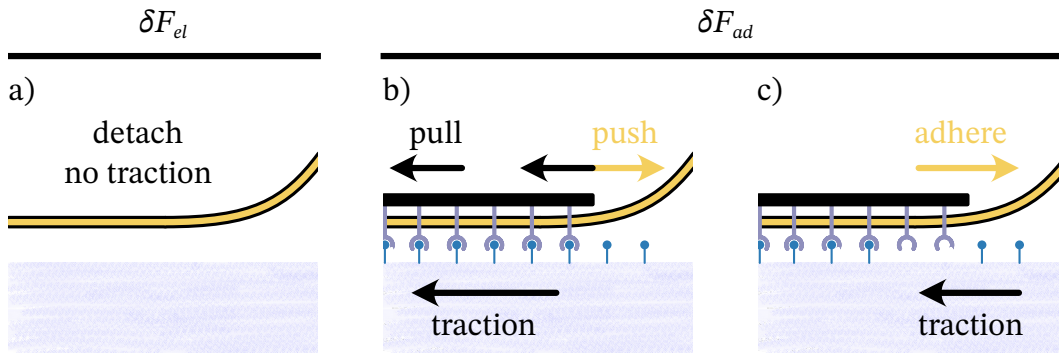
Figure III.1: Contributions of different intracellular processes to traction force generation. a) Detachment of cells from the substrate, in the absence of adhesions or friction, does not lead to traction forces. b) Actin polymerization induces pushing forces on the membrane, while actomyosin contractility pulls the actin filaments into the cell body (retrograde flow). Both processes induce traction forces, transmitted to the substrate via integrin molecules. c) Locomotion due to gradients in adhesion strength alone also leads to effective traction forces. By virtue of Onsager's theory (Balian, 2007), cellular adhesions pull the substrate towards the cell.

Now, suppose that the cell makes an attempt to extend a protrusion from position x to a new position $x + \delta x$, or to do the opposite process of a retraction from $x + \delta x$ to x. While doing so, the cell will perform a total work of

$$\delta W = -\delta F = -\delta F_{el} - \delta F_{ad} \,. \tag{III.11}$$

We now discuss how the two contributions to the total work enter the traction forces that the cell exerts on the substrate. The first term, $-\delta F_{el}$, corresponds to the work performed by cell elasticity and homogeneous cell contractility, ultimately driving cell detachment from the substrate. These processes occur even in total absence of a coupling to the substrate, when there is neither friction nor adhesion. Therefore, the term $-\delta F_{el}$ does not contribute to the traction that the cell exerts on the substrate (Fig. III.1a). The situation is completely different for the second term, $-\delta F_{ad}$, which models the presence of adhesions. Then, as the cytoskeleton exerts pushing forces on the membrane due to actin polymerization and is pulled back by actomyosin contractility (Pollard and Borisy, 2003; Mogilner, 2009; Mogilner and Keren, 2009; Murrell et al., 2015), adhesions transmit these forces to the substrate as traction (Fig. III.1b). An analogous situation occurs if we leave aside all of these cytoskeletal processes and only consider an effective substrate adhesion, such as in our model. Then, the cell is effectively pulled outwards by the gradient in adhesiveness (which is a chemical potential), and conversely the substrate is pulled inwards (Fig. III.1c).

Taking all of these arguments together, the traction forces that our *in silico* cell exerts during a single protrusion or retraction are given by

$$\boldsymbol{f}_{tr} = -\frac{|\delta F_{ad}|}{\|\delta \boldsymbol{x}\|^2} \delta \boldsymbol{x}\,. \tag{III.12}$$

Next, we describe how the traction forces that arise from many protrusions and retractions induce deformations of the substrate.

Substrate deformation. We model the deformable substrate as a bead-spring network, where the beads represent the locations $\boldsymbol{x}_i$ where a cell can adhere. We denote the deflection of each bead from its initial position with $\boldsymbol{u}_i$. Each bead is connected to its neighbors, $\boldsymbol{x}_j \in \mathcal{N}_i$, via springs with stiffness k. Furthermore, each bead experiences a viscous friction ζ when it is dragged through the embedding fluid. We consider two model networks, an "overstretched" network with a Poisson ratio of $\nu_{2D} = -1$ and an "understretched" network with a Poisson ratio of $\nu_{2D} = 1/3$. In our "overstretched" network, the dynamics of the beads are determined by the following force-balance equation:

$$\zeta \, \partial_t \boldsymbol{x}_i = \boldsymbol{f}_{tr} + k \sum_{\boldsymbol{x}_j \in \mathcal{N}_i} \left[\boldsymbol{x}_j - \boldsymbol{x}_i \right], \tag{III.13a}$$

which corresponds to a network of loaded springs. In this "overstretched" case, our bead-spring network approximates a homogeneous two-dimensional elastic medium with elastic shear modulus $G = \sqrt{3}\,k$. In our "understretched" network, the dynamics of the beads are determined by the following force-balance equation:

$$\zeta \, \partial_t \boldsymbol{x}_i = \boldsymbol{f}_{tr} + k \sum_{\boldsymbol{x}_j \in \mathcal{N}_i} \left[\hat{\boldsymbol{e}}_{ij} \cdot \left(\boldsymbol{u}_j - \boldsymbol{u}_i \right) \right] \hat{\boldsymbol{e}}_{ij}\,, \tag{III.13b}$$

which corresponds to a network of linearized springs with small deflections (Yucht et al., 2013). Here, $\hat{\boldsymbol{e}}_{ij}$ is the unit vector that points from the bead at position $\boldsymbol{x}_i$ to the bead at position $\boldsymbol{x}_j$. In this "understretched" case, our bead-spring network approximates a homogeneous two-dimensional elastic medium with elastic shear modulus $G = (\sqrt{3}/4)\,k$. For both substrate models, we observe almost identical cell behavior, which underlines the robustness of the geometric effects that we study.

Finally, note that our model is agnostic as to whether we describe a migrating cell or the motion of an active droplet on an elastic surface. Within our framework, both descriptions are fully analogous (Fig. III.1b,c).

Cellular sensing of substrate deformations. In our model, a cell can directly sense substrate deformations via changes in the effective surface density of substrate adhesions, $\rho(\boldsymbol{x})$, by virtue of Eq. (III.6).
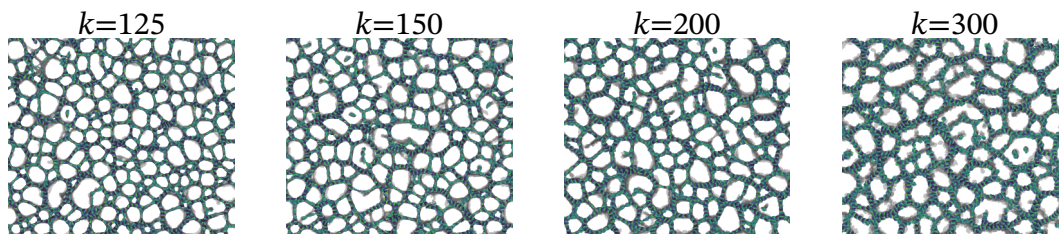
Figure III.2: Cells form networks when placed on a compliant substrate. Model parameters: 1000 cells; average cell polarization field $\epsilon_0 = 75$; cell polarizability $\Delta\epsilon = 25$, signaling radius $R = 5$; cytoskeletal update rate $r_\epsilon = 0.1$; cell stiffness parameters $k_A = 0.2$ and $k_P = 0.15$; effective temperature $k_B T = 10$; substrate viscous friction $\zeta = 500$; substrate stiffness as indicated above the snapshots. Substrate modeled as "understretched" network.

III.2.3 SUMMARY OF THE MAIN RESULTS

From migrating force monopoles to isotropic force dipoles to anisotropic force dipoles. Depending on the mechanical properties of the substrate, we find that a cell behaves more like a persistently migrating force monopole, a self-trapping isotropic force dipole, or an elongating anisotropic force dipole. In particular, a cell behaves like a migrating force monopole on very stiff or very viscous substrates. In contrast, on soft substrates that deform quickly compared to the cell dynamics, we find that the cell traps itself by creating an island of high substrate density and, therefore, high adhesiveness. In that case, the cell rounds up and behaves like an isotropic force dipole. When we further reduce substrate stiffness, the cell elongates drastically and therefore resembles an anisotropic force dipole. These qualitative differences in phenomenology arise purely as a consequence of mechanical interactions and geometric effects, and do not rely on a control of gene expression or metabolism through extracellular matrix rigidity (Bissell and Barcellos-Hoff, 1987; C. M. Nelson and Bissell, 2006; Ge et al., 2021; Pandamooz et al., 2020; Jang et al., 2021).

Addendum: Formation of cellular networks. In our model, cells induce substrate deformations and at the same time also detect these substrate deformations. This suggests that cells can engage in long-ranged mechanical communication through the elastic substrate (Reinhart-King et al., 2008; Winer et al., 2009; Sopher et al., 2018; van Oers et al., 2014). Therefore, we test if and how cells will self-organize through such long-ranged communication. We find that cells form networks when placed on soft substrates, where each cell behaves like an anisotropic force dipole (Fig. III.2). These networks resemble the formation of vasculature *in vitro* during angiogenesis, in so-called tube-formation

assays (Vailhé et al., 2001). Interestingly, tube formation was shown to strongly depend on the mechanical properties of the substrate (Saunders and Hammer, 2010; Rüdiger et al., 2020), which is consistent with substrate-mediated mechanical interactions.

Our *in silico* results can be explained as follows. Because the cells behave like anisotropic force dipoles, they will align with external tensile stress fields, which includes the stress generated by other cells (Bischofs and Schwarz, 2003; Bischofs, S. A. Safran, et al., 2004). Therefore, many such anisotropic force dipoles will typically align into stringlike structures (Bischofs and Schwarz, 2003; Bischofs, S. A. Safran, et al., 2004), and can also form ringlike structures (Bischofs and Schwarz, 2006). In our two-dimensional geometry, we hypothesize that this effect, together with cell elongation, leads to cell networks.

Model limitations.   The same limitations as in Section III.1 "Collective Cell Dynamics in Rigid Environments" apply. In addition, one should be wary of mesh deterioration as a consequence of very low substrate stiffness or very large traction stresses, which can show itself via inverted mesh tiles.

III.2.4 MANUSCRIPT M4

TITLE:

MORPHOLOGY AND MOTILITY OF ENDOTHELIAL CELLS ON SOFT SUBSTRATES

AUTHORS:

Andriy Goychuk, David B. Brückner, Andrew W. Holle, Joachim P. Spatz, Chase P. Broedersz and Erwin Frey

Morphology and Motility of Endothelial Cells on Soft Substrates

Andriy Goychuk,[1] David B. Brückner,[1] Andrew W. Holle,[2,3]
Joachim P. Spatz,[4,5] Chase P. Broedersz,[1,6] and Erwin Frey[1]

[1] *Arnold Sommerfeld Center for Theoretical Physics and Center for NanoScience, Department of Physics,*
Ludwig-Maximilians-Universität München, Theresienstr. 37, D-80333 Munich, Germany
[2] *Mechanobiology Institute, National University of Singapore, Singapore, Republic of Singapore*
[3] *Department of Biomedical Engineering, National University of Singapore, Singapore, Republic of Singapore*
[4] *Department of Cellular Biophysics, Max-Planck-Institute for Medical Research, D-69120 Heidelberg, Germany*
[5] *Department of Biophysical Chemistry, University of Heidelberg, D-69120 Heidelberg, Germany*
[6] *Department of Physics and Astronomy, Vrije Universiteit Amsterdam, Amsterdam, The Netherlands*

Recent experiments suggest that the interplay between cells and the mechanics of their environment gives rise to a diversity of morphological and migrational phenotypes. Here, we develop a cellular Potts model of polarizing cells that migrate on a two-dimensional viscoelastic substrate. To constrain the model parameters and test our predictions, we compare our model with experiments on endothelial cells plated on polyacrylamide hydrogels. Our analysis reveals that the morphology and motility of cells may be determined by an intricate interplay between asymmetric cellular traction forces (polarization) and the resulting substrate deformation gradients. Specifically, as the surface density field of adhesive ligands transforms in an affine manner with the substrate, we predict that cells perform self-haptotaxis by following ligand density gradients.

Cells possess an intricate mechanochemical machinery that allows them to survey their surroundings. Specific biomolecules, so-called integrins, form adhesion complexes that serve as an interface between the intracellular actomyosin cytoskeleton and the extracellular matrix [1–3]. These adhesion complexes act as multipurpose tools by transmitting cytoskeletal forces to the extracellular matrix in the form of traction. Furthermore, adhesion complexes enable the cell to detect and react to extracellular stimuli [4, 5], triggering intracellular signaling cascades that coordinate the organization of the actomyosin cytoskeleton [6–8]. By using these mechanisms in concert, cells can sense and migrate in response to the mechanical properties of the substrate to which they adhere [9–16]. Interestingly, the response of a cell to mechanical signals depends on the composition of the adhesion complexes and the substrate [17, 18]. Furthermore, when varying the mechanical properties of the substrate like its rigidity, different cell types show qualitatively distinct morphological and motile responses, as summarized in Table I. Most cells increase their persistence time of directed migration on stiffer substrates [19–22]. However, it seems that no such universal relationship exists for the cell speed. While some cells move faster on stiffer substrates [14, 19, 22–25], other cells show the opposing behavior and move slower [9, 20, 22, 26–28]. Even for a single cell type, the qualitative trend of the cell speed as a function of substrate stiffness may depend on the coating of the substrate [22]. Thus, it seems that the concept of a universal coupling between cell speed and persistence [29], successful in many different settings, ceases to hold in the context of varying substrate rigidity. What then are the common physical principles that lead to such diverse cell behaviors?

There is a broad range of different theoretical models that have led to important advances in understanding cell migration and traction force generation [16]. Particle-based approaches [30–38] are often successfully applied to single and collective cell motion, but are incapable of describing cell shape. To then model the spatiotemporal dynamics of both cell shape and migration, there are two different approaches. Phase-field models [39–44], for one, consider each cell as a smooth field with a diffuse interface, whose deterministic behavior is determined by a set of partial differential equations. In contrast, cellular Potts models (CPMs) treat each cell as a discrete set of points [45–56], where the stochastic cell dynamics are determined by a Monte Carlo scheme. On a conceptual level, both approaches can be understood as a description of the active wetting dynamics of droplets that move on a flat surface. We exploit this analogy between cells and liquid droplets to formulate a theoretical model [Fig. 2A]. Of note, a recent phase-field model has explicitly studied the wetting dynamics of a *vertical* cell cross-section [57]. In contrast, we focus on the *horizontal* contact area between a cell and the substrate that it adheres to.

Here, we study the spatiotemporal dynamics of actively polarizing cells, which adhere to flat viscoelastic substrates of varying mechanical properties [Fig. 2A]. To that end, we build on a recent generalization of the CPM that permits computationally efficient simulations of both single cells and large cell collectives [51, 54]. We complete the CPM [51, 54] by also accounting for the dynamics of the viscoelastic substrate to which the cells adhere. To constrain the model parameters, we use experimental measurements on human umbilical vein endothelial cells (HUVECs) plated on polyacrylamide gels. Our combined experimental and theoretical investigations suggest a minimal description of the cellular response to the physical properties of the substrate. Specifically, our model builds on a simple premise: (i) cellular traction forces induce strains, and (ii) strains are equivalent to changing the distance between material points. If a cell then migrates on the surface of an elastic medium,

TABLE I. An increase of substrate stiffness is accompanied by the following qualitative trends in cell migratory response (speed, persistence time of directed migration) and shape (aspect ratio).

Cell type	Cell line	Substrate, coating	Speed	Persistence		Aspect ratio	Source
				Time	Length		
glioma	U373-MG, U87-MG, U251-MG, SNB19, C6	PA, fibronectin	↗	—	—	↗	[23]
glioblastoma	JK2, WK1, RN1, PR1	PA, matrigel/laminin	↗	—	—	↗	[24]
	SJH1	PA, matrigel/laminin	→	—	—	→	[24]
hASCs	—	PA, fibronectin	↗	—	—	↗	[14]
fish keratocytes	—	PA & PDMS, fibronectin	↗	→	↗	↗	[25]
BALB/c fibroblasts	—	PA, n.a.	↗	↗	—	—	[19]
MSCs	—	PA, collagen	→	↗	—	—	[21]
VSMCs	—	PA, fibronectin	↗	↗	—	—	[22]
neutrophils	—	PA, fibronectin	↘	↗	—	—	[20]
AHD fibroblasts	—	PEG-based, fibronectin	↘	—	—	—	[27]
3T3 fibroblasts	—	PA, collagen	↘	—	—	—	[9]
3T3 fibroblasts	—	PA, collagen	↘	—	—	↘	[26]
rat fibroblasts	REF52 WT	PEG-based, fibronectin/vitronectin	↘	—	↗	→	[28]
VSMCs	—	PA, collagen	↘	↗	—	—	[22]

Glossary. hASCs: human adipose derived stem cells. **MSCs:** mesenchymal stem cells. **VSMCs:** vascular smooth muscle cells. **AHD fibroblasts:** adult human dermal fibroblasts. **PA:** polyacrylamide. **PEG:** polyethylene glycol. **PDMS:** polydimethylsiloxane

or in a dilute compressible matrix, then cellular traction forces will locally change the density of the substrate that the cell can adhere to. Therefore, cells generate substrate density gradients, which guide shape changes and cell migration (self-haptotaxis). This interaction with the substrate can in turn interfere with, and even override, internal feedback mechanisms that would under normal circumstances lead to cell polarization. These are generic geometric effects, and therefore do not depend on specific micromechanical mechanisms, such as a force-dependent (un)binding of adhesions or adhesion maturation.

RESULTS

Experimental observations

We started our investigation with several sets of experiments on human umbilical vein endothelial cells (HUVECs) and human foreskin fibroblasts (HFFs). All cells were plated on collagen-coated polyacrylamide gels, and analyzed as described in the Methods. Depending on the substrate stiffness, we observed distinct spatiotemporal cell dynamics. The behavior of HUVECs can be roughly grouped into three qualitative phenotypes [Fig. 1E, Supplemental Video 1]. At very low values of substrate stiffness, HUVECs elongate (that is, have a large aspect ratio) and do not form lamellipodia. In that case, HUVECs locally move at some slow speed in random directions but typically remain localized within a certain substrate area, without showing persistent motion. We refer to this phenotype as *elongation*. As one increases substrate stiffness, HUVECs first round up and increase their local speed,

but still remain localized, which we refer to as *rounding*. Only when further increasing substrate stiffness, do HUVECs begin to show persistent cell migration with formation of lamellipodia, which we refer to as *running*. Such migratory behavior can be described as a persistent random walk with ballistic motion on short timescales and diffusive motion on long timescales. In our experiments, we determined the persistence time of directed migration through an exponential fit of the normalized velocity autocorrelation function. Since the normalized velocity autocorrelation function decayed quickly, the persistence time of directed migration was mostly determined by the first 1–2 video frames. In line with our qualitative observations, we typically measured a larger persistence time of directed migration and also a larger cell speed on stiffer substrates [Fig. 1B,C]. Furthermore, HUVECs were typically elongated for small substrate stiffness, $E < 1\,\text{kPa}$, were typically round for $E \sim 2\,\text{kPa}$, and then elongated with increasing substrate stiffness for $E > 2\,\text{kPa}$ [Fig. 1A].

The behavior of HFFs is quite different. HFFs have trouble spreading on our softest substrates, leading to a small aspect ratio [Fig. 1A] and low motility [Fig. 1B,C]. Therefore, unlike HUVECs, HFFs do not elongate on very soft substrates, likely because they cannot adhere there. Above a substrate stiffness of $E > 0.5\,\text{kPa}$, we find that with increasing substrate stiffness HFFs become more elongated [Fig. 1A] and also exhibit a higher persistence time of directed migration [Fig. 1C]. However, in contrast to HUVECs, HFFs also become slower with increasing substrate stiffness [Fig. 1B]. These differences between HUVECs and HFFs are in good agreement with previous literature, as summarized in Table I and dis-

experimental results (HUVEC, HFF)
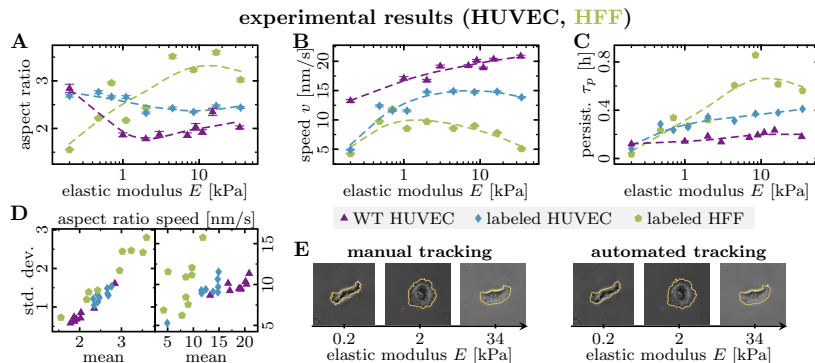
FIG. 1. **Cell dynamics in our experiments.** Depending on substrate stiffness, HUVECs show distinct behaviors, as shown in *E*: *elongation*, *rounding*, and *running*. (A) Wild-type HUVECs show the highest aspect ratio at very small substrate rigidity, indicating strong cell elongation. On substrates with intermediate rigidity, the wild-type HUVECs first round up, as shown by the minimum in aspect ratio. Then, as one further increases substrate stiffness, the wild-type HUVECs elongate again. For the HUVECs with labeled cell cores, this behavior is less clear. In contrast, HFFs elongate on the stiffest substrates, but remain round on soft substrates, likely because they cannot adhere there. Plot points correspond to mean values, with the error bars showing the respective error of the mean. Dashed lines are a guide to the eye. (B) Both wild-type and labeled HUVECs move faster on stiffer substrates than on soft substrates. Interestingly, labeled HUVECs are much slower than wild-type HUVECs, indicating some level of phototoxicity; we excluded a dataset with shorter measurement intervals because the cells did not spread at all. In contrast, HFFs exhibit their highest motility at intermediate values of substrate stiffness. Plot points correspond to mean values, with the error bars showing the respective error of the mean. Dashed lines are a guide to the eye. (C) All cell types (wild-type HUVECs, stained HUVECs and stained HFFs) show a higher persistence time of directed migration when plated on stiffer substrates. Plot points correspond to mean values, with the error bars showing the respective error of the mean. Dashed lines are a guide to the eye. (D) Because we perform averages over a very heterogeneous cell population, the standard deviation of the measurements is large. For both cell aspect ratio and cell speed, the standard deviation of the measurements correlates with the mean values and has similar magnitude. (E) Snapshots of wild-type HUVECs on a very soft substrate with $E = 0.2\,\mathrm{kPa}$, an intermediate substrate with $E = 2\,\mathrm{kPa}$ and a stiff substrate with $E = 34\,\mathrm{kPa}$. On the left side, we show an example of our manual tracking procedure. On the right side, we show the same cells but this time outlined with our automatic tracking procedure.

cussed in the introduction. Then, what could be the physical basis of these different observations?

In principle, because HUVECs and HFFs are different cell types, their disparate behavior could have its root in the intrinsic organization and regulation of their cytoskeleton. Here, however, our goal is not to describe the cell cytoskeleton and its regulation in full detail, including anisotropy on the microscopic level such as stress fibers. Instead, we map the process of cell migration to a surrogate problem: the wetting of elastic surfaces by active droplets. In doing so, we hope to uncover generic physical concepts that apply to vastly different model systems.

THEORETICAL MODEL

Generalized CPM

In the following, we take a reductionist theoretical approach to rationalize the diverse cell behaviors as a function of substrate stiffness. We only invoke basic phys-

ical concepts that should remain valid when increasing model complexity. To that end, we build on and extend a recently introduced generalization of the CPM [51, 54]. In this section, we first discuss the generic physical concepts that underlie the generalized CPM and allow it to successfully reproduce cellular behavior on rigid surfaces [51, 54, 56]. For a more detailed description, we refer to Ref. [54] and to Appendix A of the Supplementary Material. Then, in the next section, we complete the description by adding as a new feature the viscoelastic coupling between the cellular dynamics and substrate deformations. As we will discuss, the central point of our approach relies only on affine deformations of the geometry due to cellular traction forces.

From a geometrical perspective, we are interested in the spatiotemporal evolution of the contact area between a three-dimensional cell and a two-dimensional substrate [Fig. 2A]. We describe the spreading area (domain) of a cell as a simply connected set $\mathcal{D}$ of substrate adhesions sites, which the cell can form at discrete positions $\mathbf{x}_i(t)$. Each adhesion site is associated with a hexagonal tile of area $a(\mathbf{x}_i, t)$ whose reference configuration is defined by a honeycomb tessellation of the substrate [Fig. 2B].

Through affine deformations of the viscoelastic substrate, the individual positions of adhesion sites as well as the size and shape of the corresponding hexagonal tiles can change over time t. In analogy to the wetting behavior of active droplets, we interpret the locomotion and morphological dynamics of a cell as a competition between the formation of new adhesion sites (cell protrusion, droplet wetting) and the loss of adhesion (cell retraction, droplet dewetting). The morphology of a cell is then characterized by its spreading area $A(t)$, perimeter $P(t)$ and by the second moment of the spatial distribution of its adhesion sites (i.e., its aspect ratio). Similar to the original CPM [45], we assume that the shape of a cell is constrained by the elastic energy

$$\mathcal{H}_{\text{cont}} = \kappa_A A^2(t) + \kappa_P P^2(t),\qquad(1)$$

with two stiffness parameters κ_A and κ_P. The elastic energy, $\mathcal{H}_{\text{cont}}$, models cell membrane and cortex contractility, which in the absence of adhesion sites leads to cell rounding and detachment from the substrate (analogous to the dewetting behavior of a droplet). These tensile forces are counteracted by focal adhesion sites, where integrins link the cell cytoskeleton with the substrate, and by the outwardly directed forces that polymerizing cytoskeletal structures generate [58, 59]. In our model, we collect these contributions into a single spatially resolved *polarization field*, $\epsilon(\mathbf{x}_i, t) \in [\epsilon_0 - \Delta\epsilon/2, \epsilon_0 + \Delta\epsilon/2]$. Note that by choosing a scalar field, we assume that the cytoskeleton of the cell is locally isotropic. In analogy to the wetting behavior of active droplets, one can then interpret the polarization field as an effective local adhesion energy, with a total energetic contribution of [51, 54]:

$$\mathcal{H}_{\text{cyto}} = -\sum_{\mathbf{x}_i} \epsilon(\mathbf{x}_i, t).\qquad(2)$$

The total energy that is associated with the configuration of the cell, $\mathcal{H} = \mathcal{H}_{\text{cont}} + \mathcal{H}_{\text{cyto}}$, is gradually minimized by a Monte Carlo update scheme as a proxy for the cellular dynamics.

The cell is then driven out of equilibrium by locally up- or down-regulating the polarization field [51, 54]. The dynamics of the polarization field emulate the (dis)assembly of cytoskeletal structures via intracellular signaling cascades [6–8]. These signaling cascades involve regulatory cytoskeletal proteins that confer to the cell an ability to respond to extracellular stimuli [60, 61]. In the generalized CPM, these complex biochemical processes are accounted for in a simplified way via a nonlinear update rule with rate constant μ [51, 54]:

$$\partial_t \epsilon(\mathbf{x}_i, t) = \mu \left[\left(\epsilon_0 + \frac{\Delta\epsilon}{2} \operatorname{sgn} m(\mathbf{x}_i) \right) - \epsilon(\mathbf{x}_i, t) \right],\quad(3)$$

where $m(\mathbf{x}_i)$ is a bookkeeping field that tracks whether a given adhesion site received more stimuli from retraction or from protrusion events within a signaling radius R. Thus, the generalized CPM contains two prototypic feedback loops, where high (low) values of the polarization
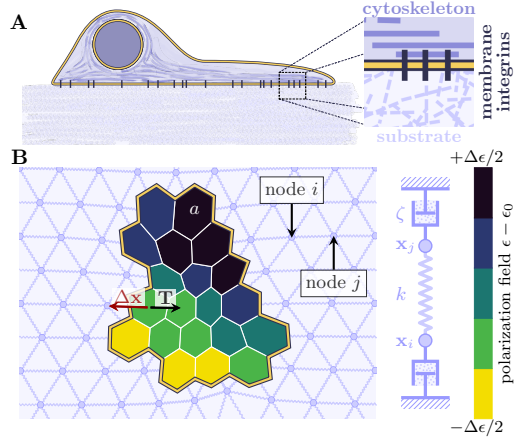

FIG. 2. **Sketch of the computational model.** The substrate is represented by beads at node positions $\mathbf{x}_i$, each connected to six nearest neighbors $\mathbf{x}_j \in \mathcal{N}_i$ via springs. A cell, with domain $\mathcal{D}$, is comprised of a set of hexagons with respective areas $a(\mathbf{x}_i, t)$ and local polarization field $\epsilon(\mathbf{x}_i, t) \in [\epsilon_0 - \Delta\epsilon/2, \epsilon_0 + \Delta\epsilon/2]$ (color scale). As the cell exerts traction forces $\mathbf{T}$ on the beads, it compresses the substrate beneath, while stretching the surrounding substrate. The cell protrudes or retracts over an effective distance $\|\Delta\mathbf{x}\|$ along the distance vector $\pm\Delta\mathbf{x}$, where $\Delta\mathbf{x} = \mathbf{x}_j - \mathbf{x}_i$.

field favor protrusions (retractions), which in turn lead to a further increase (decrease) of the polarization field in the vicinity [51, 54]. Returning to our active droplet analogy, Eq. (3) represents a conversion between molecular species that have different affinity for the surface, thereby providing the "fuel" necessary for active motion.

Cell-substrate coupling

Having discussed how the extended CPM emulates pertinent features of cellular dynamics [51, 54] and active droplets alike, we next turn towards the link between cell activity and substrate deformations. On the level of focal adhesions, cells can sense their environment via load-dependent binding and unbinding of integrins, which has led to a number of models based on the molecular clutch mechanism [13, 17, 62, 63]. In the present study, however, we do not explicitly invoke the load-dependent (un)binding of integrins. Instead, we investigate the implications of purely geometric effects, which occur due to deformations on the cell scale, for the cellular dynamics. To that end, we exploit the analogy between the generalized CPM [51, 54] and the wetting dynamics of active droplets, by interpreting the polarization field $\epsilon(\mathbf{x}_i, t)$ as an effective adhesion energy at discrete adhesion sites. We assume that the time-dependent position of each ad-

hesion site, $\mathbf{x}_i(t)$, is intrinsically coupled to the displacement of the substrate. Therefore, the hexagonal tile that corresponds to an adhesion site deforms in an affine way with the substrate [Fig. 2B]. Meanwhile, the effective adhesion energy in the co-moving frame of the adhesion site is only regulated by the nonlinear feedback loop, Eq. (3). In the continuum limit, the total effective adhesion energy can then be rewritten as a surface integral over the domain $\mathcal{D}$ of the cell:

$$\mathcal{H}_{\text{cyto}} = -\int_{\mathcal{D}} d^2\mathbf{x}\, \epsilon(\mathbf{x},t)\, \rho(\mathbf{x},t)\,, \qquad (4)$$

where $\rho(\mathbf{x},t) = 1/a(\mathbf{x},t)$ represents the local surface density of the substrate. In the context of the generalized CPM, one can understand Eq. (4) as the ability of a cell to exert isotropic stresses per set amount of integrin *times* the local integrin density. Specifically, $\rho(\mathbf{x},t)/\rho_0 = a_0/a(\mathbf{x},t)$ measures the compression or dilatation of a hexagonal tile with respect to its reference configuration a_0, and thus the relative change of integrin density. Thus, in our model the cell follows gradients of an effective chemical potential, which results in an effective motile force density $\boldsymbol{\nabla}[\epsilon(\mathbf{x},t)\,\rho(\mathbf{x},t)]$. This mechanism is conceptually similar to haptotaxis, where a cell is expected to follow externally imposed gradients of adhesiveness [64].

Traction force generation

In our model, we consider purely contractile contributions that homogeneously favor cell detachment from the substrate, Eq. (1), and the counteracting heterogeneously distributed effective adhesion energy, Eq. (2). These two contributions have to be treated separately when determining the corresponding traction forces that the cell exerts on the substrate. An attempt of the cell to protrude along the distance vector $+\Delta\mathbf{x}$ [Fig. 2B], or to retract along the distance vector $-\Delta\mathbf{x}$, corresponds to the virtual work $-\Delta\mathcal{H} = -\Delta\mathcal{H}_{\text{cont}} - \Delta\mathcal{H}_{\text{cyto}}$ that is required to change the cell configuration. From the individual contributions to this virtual work, we determine the effective forces that act on the cell boundary, and then connect them to the traction forces that the cell exerts on the substrate.

The virtual work that is associated with contractility of the cell, $-\Delta\mathcal{H}_{\text{cont}}$, is performed by the cytoskeleton even in the absence of adhesions, when there is pure slip between cell and substrate. Assuming frictionless slip, the corresponding traction forces should, on average, vanish. In our model, we implement this by balancing the effective contractile force that acts on a membrane segment, $\mathbf{F}_{\text{cont}}$, with traction forces that are homogeneously distributed across the whole cell spreading area. In other words, we assume that the cytoskeleton facilitates contractility by transmitting forces instantaneously throughout the cell [65]. Since there is no spatial heterogeneity of cell contractility in our model, Eq. (1), the total contractile force integrated over the cell boundary is zero. Therefore, the traction forces that are associated with cell detachment vanish on average,

$$\langle \mathbf{T}_{\text{cont}} \rangle_t = 0\,, \qquad (5)$$

while traction force fluctuations remain due to the stochastic nature of our model, see Appendix A of the Supplementary Material. Note that the model dynamics are the same even when explicitly setting the traction forces that are associated with cell detachment, $\mathbf{T}_{\text{cont}}$, to zero. Again making an analogy, this corresponds to a droplet that does not interact with the substrate at all, and therefore does not show wetting.

The situation is markedly different in the presence of engaged adhesions, i.e. when the cell "sticks" to the substrate. Then, the virtual work that is associated with spreading of the cell, $-\Delta\mathcal{H}_{\text{cyto}}$, is performed by the actin cytoskeleton, which locally exerts a force $\mathbf{F}_{\text{cyto}}$ on a membrane segment. Since the actin cytoskeleton is anchored to the substrate via focal adhesions [58, 59], the force that the cytoskeleton exerts on a membrane segment must be balanced by an equal and opposite traction force on the substrate, $\mathbf{T}_{\text{cyto}} = -\mathbf{F}_{\text{cyto}}$. Therefore, the traction forces that are associated with cell adhesion are non-zero:

$$\mathbf{T}_{\text{cyto}} = -\frac{|\Delta\mathcal{H}_{\text{cyto}}|}{\|\Delta\mathbf{x}\|^2}\,\Delta\mathbf{x}\,. \qquad (6)$$

Making the analogy to an active droplet, traction forces can then be interpreted in terms of Onsager's theory [66]. While "adhesion" favors substrate wetting, the corresponding chemical potential gradients at the same time also induce substrate fluxes towards the contact area between the droplet and the substrate, until these fluxes are stopped by elastic stresses.

Note that in equilibrium (i.e., when there are no feedback loops) the work that is associated with cell spreading exactly balances the work that is associated with cell contractility, $\Delta\mathcal{H}_{\text{cyto}} = -\Delta\mathcal{H}_{\text{cont}}$. Similar ideas were recently pursued [67], but did not distinguish between the work that is associated with forming new cell-substrate contacts (cell-substrate coupling is required) and the work that is performed by cell rounding due to contractility (no cell-substrate coupling is required). Therefore, in contrast to our approach, the method presented by [67] would predict vanishing traction forces in equilibrium, which is in contradiction to the balance of tensions that must hold at the cell-substrate interface.

Substrate deformation

In the course of spreading and migration, the cell exerts the total traction forces $\mathbf{T}(\mathbf{x}_i,t) = \mathbf{T}_{\text{cont}}(\mathbf{x}_i,t) + \mathbf{T}_{\text{cyto}}(\mathbf{x}_i,t)$ on the substrate. To close our description, we now discuss how one can determine the deformations of the substrate from the
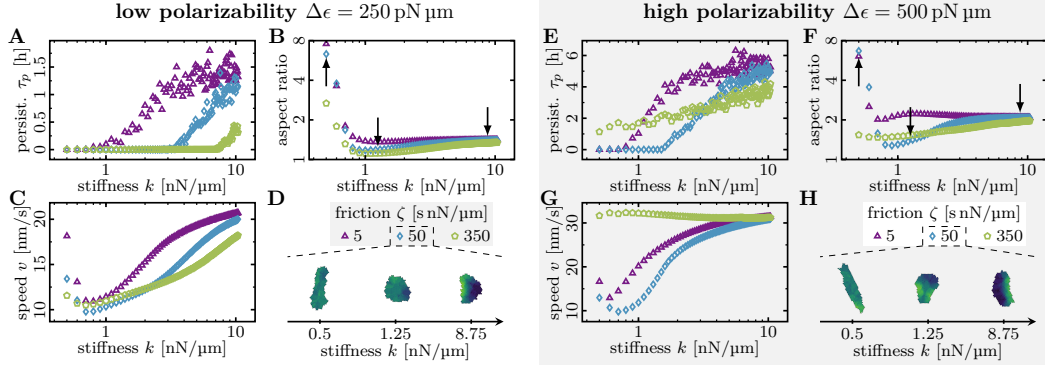
FIG. 3. **Characterization of cell migration and morphology**, both for low cell polarizability (A–D) and for high cell polarizability (E–H). (A, E) For all model parameters, the persistence time of directed migration increases with the substrate stiffness. This is consistent with all experiments that we have carried out, and with previous literature [Table I]. (B, F) The trend for the aspect ratio can depend on the model parameters. In most cases, the cells drastically elongate when placed on very soft substrates. This elongation is consistent with the shape of HUVECs on very soft substrates, and with the shape of HFFs on all substrates that they can adhere to. This trend is confirmed by simulations with a modified substrate model, see Fig. S3 in the Supplementary Material. In our modified model, further reducing substrate stiffness again leads to rounder cell shapes, see Fig. S3 in the Supplementary Material. (C, G) The cell speed shows a bi-phasic behavior. It typically increases as a function of the substrate stiffness for spring coefficients of $k > 1\,\mathrm{nN}\,\mathrm{\mu m}^{-1}$. Below this value, cells typically exhibit a larger instantaneous speed on the softer substrates, although they do not move persistently there, see A and E. (G) A special situation occurs for cells with a large polarizability that move on very viscous substrates with slow relaxation dynamics (green plot). Then, the cells can outrun the deformation field that they themselves create. For higher substrate stiffness, the substrate relaxes more quickly, with a typical timescale of ζ/k. In that case the substrate begins to "keep up" with the cell, and the overall cell speed decreases. (D, H) Snapshots of typical cell shapes in our simulations. On very soft substrates ($k = 0.5\,\mathrm{nN}\,\mathrm{\mu m}^{-1}$), the cell spontaneously breaks rotational symmetry and becomes an anisotropic force dipole. On substrates of intermediate stiffness ($k = 1.25\,\mathrm{nN}\,\mathrm{\mu m}^{-1}$), the cell remains round and trapped, and thus an isotropic force dipole. On very stiff substrates ($k = 8.75\,\mathrm{nN}\,\mathrm{\mu m}^{-1}$), the cell spontaneously breaks symmetry and behaves like a persistently migrating force monopole.

distribution of traction forces. We model the substrate as a discrete network of beads at positions $\mathbf{x}_i$, where a cell can form adhesions [Fig. 2B]. In addition to the traction forces, each bead is subject to viscous damping with viscous friction coefficient ζ, and is connected to nearby beads $\mathcal{N}_i$ via springs with stiffness k. Then, balance between all these forces determines the overdamped dynamics of each bead. In the main text, we focus on an overstretched network of beads that are connected by *loaded* springs:

$$\zeta\,\partial_t\mathbf{x}_i(t) = \mathbf{T}(\mathbf{x}_i, t) + k \sum_{\mathbf{x}_j \in \mathcal{N}_i} \left[\mathbf{x}_j(t) - \mathbf{x}_i(t)\right], \quad (7a)$$

which approximates a homogeneous two-dimensional elastic medium with elastic modulus $\mu_{\mathrm{el}} = \sqrt{3}k$ and two-dimensional Poisson ratio $\nu_{2D} = -1$ [cf. section A 4 d of the Supplementary Material]. In addition, in section A 4 c of the Supplementary Material, we also consider an understretched network of beads that are connected by linearized springs with small deflections $\mathbf{u}$ [68]:

$$\zeta\,\partial_t\mathbf{x}_i(t) = \mathbf{T}(\mathbf{x}_i, t) + k \sum_{\mathbf{x}_j \in \mathcal{N}_i} \left[\hat{\mathbf{e}}_{ij} \cdot \mathbf{u}_{ij}(t)\right]\hat{\mathbf{e}}_{ij}. \quad (7b)$$

Here, $\mathbf{u}_{ij} = \mathbf{u}_j - \mathbf{u}_i$ is the relative deflection of two beads, and $\hat{\mathbf{e}}_{ij}$ is the unit vector which connects two neighboring beads in the undeformed reference configuration. As we show in section A 4 d of the Supplementary Material, this model approximates a homogeneous two-dimensional elastic medium with elastic modulus $\mu_{\mathrm{el}} = (\sqrt{3}/4)k$ and two-dimensional Poisson ratio $\nu_{2D} = 1/3$. Interestingly, both substrate models show almost identical behavior despite their drastically different Poisson ratio [cf. Fig. S3 in the Supplementary Material], which shows the robustness of the theoretical concepts that we present here. Furthermore, because the substrate is softer in the "understretched" model, we observe that after elongating at very small substrate stiffness, cells round up again when further decreasing substrate rigidity [cf. Fig. S3 in the Supplementary Material]. We find that the cell speed shows a biphasic behavior, having a minimum at some intermediate value of substrate stiffness [cf. Fig. S3 in the Supplementary Material].

Instead of a discrete bead-spring network, one could also model the substrate as a continuum. However, even when considering the substrate as an incompressible three-dimensional medium, the *surface* of the substrate would remain compressible; see section A 4 e of the Sup-

plementary Material and [69]. Thus, we do not expect significant deviations from the present framework if one were to consider a continuum theory. Furthermore, modeling the substrate as a discrete bead-spring network has also the distinct advantage that one could directly connect our algorithm to nonlinear fiber networks [70] in later work.

Parameter estimation

Substrates like polyacrylamide and polyethylene glycol based hydrogels are widely regarded as almost ideally elastic materials [71, 72]. In addition to substrate stiffness, however, substrate viscosity may also affect cell migration. For example, correlations in the movement of epithelial sheets have been shown to increase with substrate viscosity [73], and a recent computational study has demonstrated the relevance of viscous substrate remodeling for cell spreading [74]. These studies suggest an intricate interplay between cell migration and both the elastic and viscous properties of the environment. It remains to be resolved, however, whether and how these cell-substrate interactions can reconcile the apparently contradictory migratory responses of various cell types on different substrates.

To compare the experimental results with our computational model, we chose the model parameters to ensure physiological values for the cell speed v, spreading area A and traction forces on the substrate, as we discuss in detail in section A 5 of the Supplementary Material. We determined the range of studied spring coefficients k to match the elastic properties of the substrate. Specifically, a spring coefficient of $k = 0.5\,\text{nN/µm}$ corresponds to a substrate modulus of $E \approx 0.6\,\text{kPa}$ for an overstretched bead-spring network or $E \approx 0.15\,\text{kPa}$ for an understretched bead-spring network. For the choice of the friction coefficient ζ, we distinguish between two representative cases, depending on the relative timescales for relaxation of the viscoelastic network ($\tau_R = \zeta/k$) and cell migration (τ_C). Since a lower bound for τ_C is given by the inverse update rate of internal cell polarization, $\tau_C \geq 1/\mu$, we expect viscous friction effects to become significant at $\zeta^* \approx 100\,\text{s}\,\text{nN/µm}$. This motivates our choice of the representative values $\zeta = 350\,\text{s}\,\text{nN/µm}$ and $\zeta = 50\,\text{s}\,\text{nN/µm}$ for what we henceforth call high and low substrate viscosity, respectively. While this estimate, of course, entirely neglects the persistence time of directed cell migration and the cell velocity, it suffices for setting a first qualitative threshold. A table of the parameter values of the CPM is given in section A 5 of the Supplementary Material.

Substrates with low viscous friction (quick relaxation dynamics)

Polyacrylamide gels are dominated by their elastic and not by their viscous properties [71]. Therefore, we first analyze the model dynamics for a situation where the viscous friction of the substrate is low, $\zeta = 50\,\text{s}\,\text{nN/µm}$, and thus smaller than the threshold value ζ^*. Under these conditions, we find the same phenomenology as in our experiments on HUVECs. In particular, as we discuss next, our model captures the distinct shapes and dynamics of cells across a broad range of substrate stiffness [Fig. 3D,H and Fig. S3D,H in the Supplementary Material].

Turning a cell from a force monopole... For small values of viscous friction, the relaxation of the substrate and its response to the traction forces of the cell occur on short timescales, $\tau_R = \zeta/k$, compared to the typical timescale of the cell dynamics, τ_C. This means that substrate deformations keep up with the motion of the cell, and that these deformations, depending on the substrate stiffness k, can become large enough to impair cell motion. When the substrate stiffness is high, substrate deformations remain small due to high elastic restoring forces [Fig. 4C, lower panel]. Therefore, the influence of the substrate on the cell behavior becomes negligible on very stiff substrates. Analogous to our previous study [54], where we have discussed cell migration on a completely rigid surface ($k \to \infty$), the cell polarizes strongly and has a long persistence time of directed migration. Furthermore, the cell's persistence time of directed migration increases with cell polarizability [54], and the cell has a typical keratocyte-like shape [Fig. 4C]. Conceptually, this means that the cell behaves like a migrating force monopole, which we refer to as the "running" state.

...to an isotropic force dipole... If one lowers substrate stiffness, k, then the substrate shows an increased compression at the position of the cell [Fig. 4B, lower panel], because the cell exerts traction against lower elastic restoring forces. Then, the cell can create an "island of adhesiveness", as indicated by a drastic increase in the surface density of the substrate [Fig. 4B, lower panel]. This effect will influence the cell dynamics as follows. We remind that the cell gradually maximizes its effective adhesion energy, cf. Eq. (4), and thus follows gradients in an effective chemical potential, $\nabla[\epsilon(\mathbf{x}, t)\,\rho(\mathbf{x}, t)]$. Therefore, the cell will respond to the compression or dilatation of the substrate, by migrating towards regions that have increased substrate density $\rho(\mathbf{x}, t)$. In the case of a small substrate rigidity, the cell creates an island of increased adhesiveness [Fig. 4B, lower panel], which penalizes all retractions that could move the cell away from this island. Even in the event that a cell should manage to move, it would be energetically advantageous to simply return to its previous position due to the local substrate density gradient; we refer to this effect as self-haptotaxis. Thus, the cell effectively sticks to the substrate at its trailing edge, which also inhibits protrusions due to a penalty incurred by the contractile terms, Eq. (1). Inhibiting both retractions and protrusions ultimately deprives the cell polarization mechanism of both positive and negative feedback signals, so that
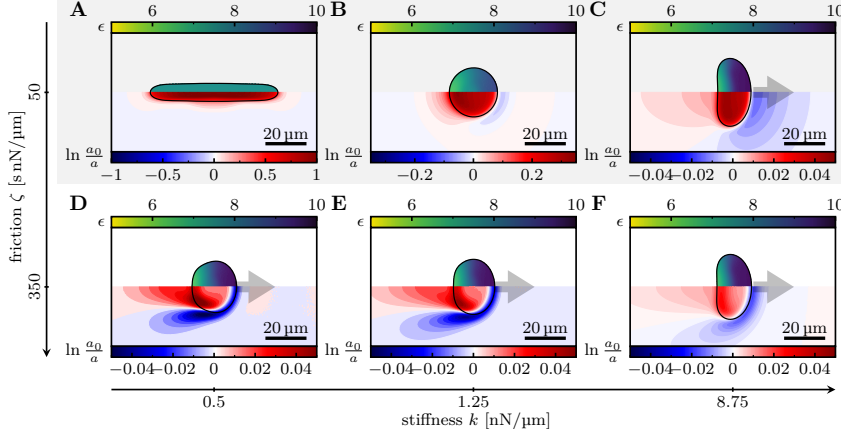
FIG. 4. **Cell polarization and substrate deformation.** Mirrored halves of a cell. The local polarization field, i.e. the effective adhesion energy *per substrate tile*, $\epsilon(x, y)$ [10^2 pN nm], is shown in the top half of each panel. The substrate density (number of substrate tiles per unit area), $\rho(x, -y)$, is shown in the bottom half of each panel. We obtain these quantities by transforming into the co-moving frame of each cell, orienting along the direction of the gradient of effective adhesion energy density, $\mathbf{g} \propto \nabla[\epsilon(\mathbf{x}, t) \rho(\mathbf{x}, t)]$, and then binning the respective data over all simulation times and for many cells. Note the differences in the scales of the substrate density ρ. Motile cells typically migrate along the gradient of effective adhesion energy. (A) An elongating cell, where the polarization field ϵ is homogeneous throughout the cell. At the cell tips, the value for the substrate density is elevated, thus increasing the effective adhesion energy density, $\epsilon \rho$. This effect balances the increased Laplace pressure at the cell tips, which originates from the large local curvature. The cell behaves like an effective anisotropic force dipole. (B) A self-trapping cell, which stays on an "adhesive island" that it generates itself by exerting traction forces on the substrate. The cell is round and approximately isotropic, thus behaving like an effective isotropic force dipole. (C) A polarized cell, which has a keratocyte-like shape and which migrates persistently. The cell behaves like a motile force monopole. (D-F) Strongly polarizable cells remain motile even on the softest substrates, because they can outrun the substrate deformations. On very soft substrates, see panel D, there is a lensing effect: because substrate density is lowest at the sides of the cell, the cell is quenched into a round shape but also remains on a straight path. This leads to a high cell velocity.

cell polarization is hampered and the cell stops performing a persistent random walk. Therefore, a cell effectively traps itself when placed on a soft substrate, which shows itself in the form of an oscillating velocity autocorrelation function [Fig. S7A in the Supplementary Material], and thus a vanishing persistence time of directed cell migration [Fig. 3A,E and Fig. S3A,E in the Supplementary Material]. When the cell traps itself, it turns into a round shape, and becomes approximately isotropic. Therefore, conceptually, a cell behaves like an isotropic force dipole when placed on a soft substrate, which we refer to as the "rounding" state. Interestingly, previous experiments on fish keratocytes [25] also showed a monotonic decrease in cell elongation when lowering substrate rigidity (they considered values >1.5 kPa), a behavior that is shared by other cell types [Table I]. We observe the same monotonic trend in experiments on HUVECs, which are plated on polyacrylamide gels of comparable rigidity (>1 kPa). Furthermore, in agreement with our simulations, we measure a decrease in both cell speed and persistence time of directed migration for HUVECs, when they are plated on substrates with a lower stiffness [Fig. 1B,C]. These results agree with a broad set of experiments [Table I].

. . . to an anisotropic force dipole. When further decreasing substrate stiffness, k, there is a dramatic change in cell shape. In particular, we observe that cells drastically elongate on very soft substrates [Fig. 4A]. This phenomenon is robust against changing parameters or the substrate model itself [Fig. 3B,F and Fig. S3B,F in the Supplementary Material]. Furthermore, we note that this breaking of rotational symmetry is mediated by the substrate alone, as the adhesion energy per substrate tile is homogeneous throughout the cell [Fig. 4A, top panel]. In particular, we find that the substrate density is increased at the tips of the elongated cell [Fig. 4A, bottom panel]. This observation indicates an increase in adhesion energy density, which balances an increased Laplace pressure at the cell tips (the tension is homogeneous along the cell boundary, but the cell tips have an increased curvature). Therefore, we conclude that in this case the cell effectively becomes an anisotropic force dipole. Interestingly, in our experiments, we also observe pronounced cell elongation on very soft substrates (rigidity less than 1 kPa), as indicated by Fig. 1A.

Substrates with high viscous friction (slow relaxation dynamics)

Next, we look at the effects of substrate viscosity on the migratory behavior of cells. If cells have a low polarizability ($\Delta\epsilon = 250\,\mathrm{pN\,\mu m}$) and therefore move slowly, then the qualitative behavior remains as before; the cells are not persistent enough to outrun the deformations of the substrate. However, for cells with a high polarizability ($\Delta\epsilon = 500\,\mathrm{pN\,\mu m}$), the situation is different. Then, upon raising the viscous friction coefficient ζ above the threshold value $\zeta^\star$, we find a considerable change in phenomenology [Fig. 3E–G]. Cells now only exhibit *running* states, with cell speed decreasing, and both persistence time of directed cell migration and cell elongation monotonically increasing with substrate stiffness. In particular, we note that the general trend for the cell speed as a function of substrate stiffness is *opposed* to that of cells that are placed on substrates with low viscous friction.

Furthermore, the persistence time of directed cell migration, τ_p, remains finite even for very soft substrates [Fig. 3E], which can be explained as follows. Because the response of the substrate is slow compared to the intracellular dynamics and to the cell motion, to a first approximation the cell behaves as if it were migrating on a completely rigid surface. Therefore, the cell can polarize even for low substrate stiffness [Fig. 4D]. Furthermore, the slow response of the substrate to cellular traction forces leads to a trail of increased substrate density behind the cell, and to a decrease in substrate density at the sides of the cell. This leads to a lensing effect, which decreases the probability that the cell will deviate from a straight path, and also explains why cell speed is enhanced at low substrate stiffness [Fig. 4D,E]. Because of this effect, the cell is also quenched from the sides into a round shape, thus making a reorientation of the cell less costly by reducing cell polarization. With increasing substrate stiffness, all of these effects are attenuated as substrate deformations become smaller. As a consequence, cell speed decreases and persistence time of directed migration increases, asymptotically approaching the corresponding values for low viscous friction of the substrate.

Qualitatively, the trend of a smaller cell velocity on stiffer substrates appears similar to measurements of fibroblast motility on polyethylene glycol-based hydrogels [28] and on polyacrylamide gels [26], as well as a number of other cell types [Table I], and our experiments on HFFs. However, we note that fibroblasts have typically a much more elongated shape [Fig. 1A] than HUVECs, which is different than the typically round cell shapes that our simulated cells exhibit on substrates with a high viscous friction. Instead, the elongated shape of fibroblasts rather resembles the situation where our simulated cells break rotational symmetry and drastically elongate on very soft substrates with low viscous friction [Fig. 4A]. Interestingly, one also observes that the instantaneous velocity of the simulated cells increases when further decreasing substrate stiffness [cf. Fig. 3C,G and Fig. S3C,G in the Supplementary Material]. But from these qualitative comparisons, it is difficult to make a conclusive statement which of these effects is most relevant for fibroblasts.

Cell persistence and polarizability

Finally, we aim to rationalize the qualitative behavior of the persistence time of directed cell migration and of the instantaneous cell speed. In [54], it was shown that the persistence time of directed cell migration increases if one considers cells that are more polarizable, as indicated by a larger value of the polarizability $\Delta\epsilon$. Here, however, deformations of the substrate can interfere with cell polarization, and therefore reduce cell persistence even if the polarizability is high. To account for these effects, we define the relative polarization as follows:

$$Z(\epsilon\,\rho) = \frac{\sqrt{\langle(\epsilon\rho)^2\rangle - \langle\epsilon\rho\rangle^2}}{\langle\epsilon\rho\rangle}\,, \qquad (8)$$

where $\langle\dots\rangle$ indicates an average along the boundary of the cell. The relative polarization, $Z(\epsilon\,\rho)$, is largest if the cell exhibits a strong polarization profile, while vanishing for small polarizations. We find that, for a cell with a given polarizability $\Delta\epsilon$, the relative polarization determines the persistence time of directed cell migration, regardless of the substrate properties [Fig. 5A].

Next, we turn to the cell speed. We have argued that in Fig. 4D and E, the substrate density having a minimum at the sides of the cell will lead to a lensing effect, thereby increasing cell speed by reducing the probability that the cell deviates from a straight path. By inversion of argument, this means that a cell should move slower if it makes more steps that do not align with its gradient of effective adhesion energy density, $\mathbf{g} \propto \boldsymbol{\nabla}[\epsilon(\mathbf{x}, t)\,\rho(\mathbf{x}, t)]$. To quantify this effect, we measure the width of the angular distribution of cell velocities, $\langle\mathrm{acos}(\hat{\mathbf{v}}\cdot\hat{\mathbf{g}})\rangle$. We find that, the narrower the angular distribution of cell velocities, the higher the average cell speed [Fig. 5B]. This can be explained by the simulated cell having a fixed "budget" for making protrusions or retractions, as the number of individual events per simulation step is conserved. Therefore, cell velocities are typically higher if there is a synergy between different events, for example if the cell protrudes at one point and then retracts at the opposite end.

DISCUSSION

We have seen that generic geometric effects, in the form of substrate compression and dilatation in response to traction stresses, can lead to a rich set of cell phenomenology. Though we cannot exclude gene regulation as a possible cause for distinct cellular responses
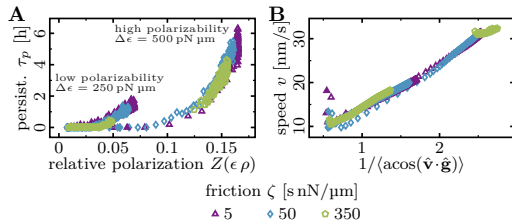
FIG. 5. **Rationalization of cell motility.** (A) The larger the relative polarization of the cell, the greater its persistence time of directed migration. This is a generalization of the results in [54], where it was shown that the persistence time of directed migration increases with cell polarizability. We need the additional measure of the relative polarization, because substrate deformations can interfere with cell polarization. (B) The narrower the angular distribution of cell velocities in a given time step, the greater the average cell speed. This is consistent with the cell having a fixed "budget" for making protrusions and retractions.

to substrate stiffness and viscosity, our study shows that variability in cell behaviors can also be explained simply in terms of the physical properties of the substrate and its interplay with cell polarization. This has potentially far-reaching consequences, as the mechanics of the physiological environment of cells varies depending on the tissue they are embedded in—and this not only determines cell migration [3] but also stem cell differentiation and fate [75, 76]. Based on our results, one may speculate that the typical shape of cells (e.g., elongated "neurons" at low stiffness, round "adipocytes" at intermediate stiffness, "keratocytes" at high stiffness) is not only predetermined by gene regulation, but strongly affected by mechanical crosstalk with the extracellular matrix.

Finally, we observe that the elastic properties of the substrate can determine whether a cell behaves like a migrating force monopole, an immobile isotropic force dipole, or an anisotropic force dipole. Interestingly, analytic work suggests that anisotropic force dipoles in elastic media can interact and align, mediated by deformations of the medium [77]. This raises the question whether cells that are not intrinsically anisotropic could potentially break rotational symmetry and align to external strains, or relative to other cells, if one explicitly accounts for the cell shape.

Author contributions A.G. and E.F. designed research. J.P.S. and A.W.H. designed experiments. A.W.H. performed experiments. A.G. implemented theoretical model and analyzed experiments. A.G., D.B.B, C.P.B. and E.F. interpreted experiments and model results. All authors wrote the paper.

Competing Interests The authors declare no competing interests.

EXPERIMENTAL METHODS

Cell culture

Human umbilical vein endothelial cells (HUVECs) were cultured in ready-to-use Endothelial Cell Growth Media (PromoCell) with $100\,$units/mL penicillin and $100\,\mu g$/mL streptomycin (Gibco). For live cell imaging, cells were plated at a density of approximately $2500\,$cells/cm^2, or $10\,000\,$cells/well.

Preparation of polyacrylamide substrate

For wild-type HUVECs, acrylamide solutions corresponding to $0.2\,$kPa, $1\,$kPa, $2\,$kPa, $3\,$kPa, $7\,$kPa, $15\,$kPa, $34\,$kPa and $100\,$kPa polyacrylamide hydrogels were prepared according to previous publications [78]. For stained HUVECs and HFFs, acrylamide solutions corresponding to $0.2\,$kPa, $0.48\,$kPa, $0.71\,$kPa, $1.10\,$kPa, $2.01\,$kPa, $4.47\,$kPa, $8.44\,$kPa, $16.70\,$kPa and $34.88\,$kPa polyacrylamide hydrogels were prepared according to previous publications [78]. Briefly, an acrylamide/bis-acrylamide solution (Bio-Rad) was degassed and mixed with 1/100 volume 10% ammonium persulfate and 1/1000 volume tetramethylethylenediamine (Sigma Aldrich). $20\,\mu L$ of solution was pipetted into a single well of an untreated 12 well glass bottom plate (In Vitro Scientific). A $12\,$mm glass coverslip chlorosilanized with dichlorodimethylsilane (Sigma Aldrich) was placed above the acrylamide solution. Upon polymerization, hydrogels were rinsed and functionalized with photoactivatable Sulfo-SANPAH (Thermo Fisher) before overnight conjugation with $100\,\mu g$/mL Collagen type I (Gibco). Prior to cell culture all hydrogels were UV sterilized.

Microscopy

Cells on hydrogels were maintained in a microscope-mounted incubator at $37\,°C$ and 5% CO_2. An AxioVert 200M with Axiovision software (Zeiss) and a PerkinElmer UltraVIEW ERS with Volocity software (PerkinElmer) were used to capture phase contrast images every ten minutes for a period of 48 h (wild-type HUVECs). Stained HUVECs were imaged once every ten minutes for a period of 24 h. Stained HFFs were imaged once every five minutes for a period of 24 h.

Cell shape and velocity analysis

Two different approaches were used to analyze the experimental data: (a) For unlabeled wild-type HUVECs, solitary cells were manually tracked and outlined in the bright-field images, using the software Fiji [79]. Cells were selected and measured at various times to mitigate fluctuations in cell shape. Each selected cell should satisfy four conditions: (i) no alignment with the cracks on the substrate, as this is a strong measurement bias to find elongated cells, (ii) no divisions at the time of measurement, as this is a strong measurement bias to find round cells, (iii) must be distinguishable from the background and neighboring cells. (iv) should not be in contact with neighboring cells. Analogously, the cell positions were also extracted manually from the phase contrast images, using the software Fiji [79] and the Plug-In MTrackJ [80]. (b) For labeled HUVECs and HFFs (SiR-DNA staining of cell cores), a neuronal network based on the U-Net architecture [81, 82] was used to automatically detect cell outlines in the bright-field images. At the same time, the cell cores were tracked based on the fluorescence images. Then, both sets of data were matched, so that each cell core was associated with exactly one cell outline. This procedure ensured that only solitary cells were analyzed. Manual cell segmentation and automatic cell segmentation yielded very similar cell outlines, as illustrated side-by-side in Fig. 1D where both procedures were performed for exemplary unlabeled wild-type HUVECs. However, there appears to be some phototoxicity associated with SiR-DNA staining of cell cores. We observe that stained HUVECs that were imaged once every 10 min move much slower than their wild-type counterparts [Fig. 1B], are at the same time more persistent [Fig. 1C] and show less variation in shape as a function of substrate stiffness [Fig. 1A]. We excluded data on stained HUVECs that were imaged once every 5 min, because a significant portion of these cells was immobile and rounded up after a few snapshots, indicating either cell death or an impeded ability to form focal adhesions.

[1] G. Charras and E. Sahai, Physical influences of the extracellular environment on cell migration, Nat. Rev. Mol. Cell Biol. **15**, 813 (2014).

[2] C. De Pascalis and S. Etienne-Manneville, Single and collective cell migration: the mechanics of adhesions, Mol. Biol. Cell **28**, 1833 (2017).

[3] S. Van Helvert, C. Storm, and P. Friedl, Mechanoreciprocity in cell migration, Nat. Cell Biol. **20**, 8 (2018).

[4] M. A. Schwartz and S. J. Shattil, Signaling networks linking integrins and rho family gtpases, Trends Biochem. Sci. **25**, 388 (2000).

[5] J. T. Parsons, A. R. Horwitz, and M. A. Schwartz, Cell adhesion: integrating cytoskeletal dynamics and cellular tension, Nat. Rev. Mol. Cell Biol. **11**, 633 (2010).

[6] D. A. Lauffenburger and A. F. Horwitz, Cell migration: A physically integrated molecular process, Cell **84**, 359 (1996).

[7] R. G. Hodge and A. J. Ridley, Regulating rho gtpases and their regulators, Nature Reviews Molecular Cell Biology **17**, 496 (2016).

[8] C. D. Lawson and A. J. Ridley, Rho gtpase signaling complexes in cell migration and invasion, Journal of Cell Biology **217**, 447 (2018).

[9] C.-M. Lo, H.-B. Wang, M. Dembo, and Y.-L. Wang, Cell movement is guided by the rigidity of the substrate, Biophys. J. **79**, 144 (2000).

[10] B. C. Isenberg, P. A. Dimilla, M. Walker, S. Kim, and J. Y. Wong, Vascular smooth muscle cell durotaxis depends on substrate stiffness gradient strength, Biophys. J. **97**, 1313 (2009).

[11] A. Zemel, F. Rehfeldt, A. E. X. Brown, D. E. Discher, and S. A. Safran, Optimal matrix rigidity for stress-fibre polarization in stem cells, Nat. Phys. **6**, 468 (2010).

[12] L. G. Vincent, Y. S. Choi, B. Alonso-Latorre, J. C. del Álamo, and A. J. Engler, Mesenchymal stem cell durotaxis depends on substrate stiffness gradient strength, Biotechnol. J. **8**, 472 (2013).

[13] R. Sunyer, V. Conte, J. Escribano, A. Elosegui-Artola, A. Labernadie, L. Valon, D. Navajas, J. M. García-Aznar, J. J. Muñoz, P. Roca-Cusachs, and X. Trepat, Collective cell durotaxis emerges from long-range intercellular force transmission, Science **353**, 1157 (2016).

[14] W. J. Hadden, J. L. Young, A. W. Holle, M. L. McFetridge, D. Y. Kim, P. Wijesinghe, H. Taylor-Weiner, J. H. Wen, A. R. Lee, K. Bieback, B.-N. Vo, D. D. Sampson, B. F. Kennedy, J. P. Spatz, A. J. Engler, and Y. S. Choi, Stem cell migration and mechanotransduction on linear stiffness gradient hydrogels, Proc. Natl. Acad. Sci. U.S.A. **114**, 5647 (2017).

[15] D. Lachowski, E. Cortes, D. Pink, A. Chronopoulos, S. A. Karim, J. P. Morton, and A. E. del Río Hernández, Substrate rigidity controls activation and durotaxis in pancreatic stellate cells, Sci. Rep. **7**, 2506 (2017).

[16] V. Hakim and P. Silberzan, Collective cell migration: a physics perspective, Rep. Prog. Phys. **80**, 076601 (2017).

[17] A. Elosegui-Artola, E. Bazellières, M. D. Allen, I. Andreu, R. Oria, R. Sunyer, J. J. Gomm, J. F. Marshall, J. L. Jones, X. Trepat, and P. Roca-Cusachs, Rigidity sensing and adaptation through regulation of integrin

types, Nat. Mater. **13**, 631 (2014).

[18] C. D. Hartman, B. C. Isenberg, S. G. Chua, and J. Y. Wong, Vascular smooth muscle cell durotaxis depends on extracellular matrix composition, Proc. Natl. Acad. Sci. U.S.A. **113**, 11190 (2016).

[19] D. House, M. L. Walker, W. Zheng, J. Y. Wong, and M. Betke, Tracking of cell populations to understand their spatio-temporal behavior in response to physical stimuli, in *2009 IEEE Computer Society Conference on Computer Vision and Pattern Recognition Workshops* (2009) pp. 186–193.

[20] P. W. Oakes, D. C. Patel, N. A. Morin, D. P. Zitterbart, B. Fabry, J. S. Reichner, and J. X. Tang, Neutrophil morphology and migration are affected by substrate elasticity, Blood **114**, 1387 (2009).

[21] M. Raab, J. Swift, P. C. D. P. Dingal, P. Shah, J.-W. Shin, and D. E. Discher, Crawling from soft to stiff matrix polarizes the cytoskeleton and phosphoregulates myosin-II heavy chain, J. Cell Biol. **199**, 669 (2012).

[22] A. P. Rickel, H. J. Sanyour, N. A. Leyda, and Z. Hong, Extracellular matrix proteins and substrate stiffness synergistically regulate vascular smooth muscle cell migration and cortical cytoskeleton organization, ACS Appl. Bio Mater. **3**, 2360 (2020).

[23] T. A. Ulrich, E. M. de Juan Pardo, and S. Kumar, The mechanical rigidity of the extracellular matrix regulates the structure, motility, and proliferation of glioma cells, Cancer Res. **69**, 4167 (2009).

[24] T. J. Grundy, E. De Leon, K. R. Griffin, B. W. Stringer, B. W. Day, B. Fabry, J. Cooper-White, and G. M. O'Neill, Differential response of patient-derived primary glioblastoma cells to environmental stiffness, Sci. Rep. **6**, 23353 (2016).

[25] M. Riaz, M. Versaevel, D. Mohammed, K. Glinel, and S. Gabriele, Persistence of fan-shaped keratocytes is a matrix-rigidity-dependent mechanism that requires $\alpha_5\beta_1$ integrin engagement, Sci. Rep. **6**, 34141 (2016).

[26] R. J. Pelham and Y.-l. Wang, Cell locomotion and focal adhesions are regulated by substrate flexibility, Proc. Natl. Acad. Sci. U.S.A. **94**, 13661 (1997).

[27] K. Ghosh, Z. Pan, E. Guan, S. Ge, Y. Liu, T. Nakamura, X.-D. Ren, M. Rafailovich, and R. A. F. Clark, Cell adaptation to a physiologically relevant ECM mimic with different viscoelastic properties, Biomaterials **28**, 671 (2007).

[28] D. Missirlis and J. P. Spatz, Combined effects of PEG hydrogel elasticity and cell-adhesive coating on fibroblast adhesion and persistent migration, Biomacromolecules **15**, 195 (2014).

[29] P. Maiuri, J.-F. Rupprecht, S. Wieser, V. Ruprecht, O. Bénichou, N. Carpi, M. Coppey, S. De Beco, N. Gov, C.-P. Heisenberg, C. Lage Crespo, F. Lautenschlaeger, M. Le Berre, A.-M. Lennon-Dumenil, M. Raab, H.-R. Thiam, M. Piel, M. Sixt, and R. Voituriez, Actin flows mediate a universal coupling between cell speed and cell persistence, Cell **161**, 374 (2015).

[30] T. Vicsek, A. Czirók, E. Ben-Jacob, I. Cohen, and O. Shochet, Novel type of phase transition in a system of self-driven particles, Phys. Rev. Lett. **75**, 1226 (1995).

[31] M. H. Zaman, R. D. Kamm, P. Matsudaira, and D. A. Lauffenburger, Computational model for cell migration in three-dimensional matrices, Biophys. J. **89**, 1389 (2005).

[32] N. Sepúlveda, L. Petitjean, O. Cochet, E. Grasland-Mongrain, P. Silberzan, and V. Hakim, Collective cell motion in an epithelial sheet can be quantitatively described by a stochastic interacting particle model, PLOS Comput. Biol. **9**, e1002944 (2013).

[33] E. L. Barnhart, K.-C. Lee, K. Keren, A. Mogilner, and J. A. Theriot, An adhesion-dependent switch between mechanisms that determine motile cell shape, PLOS Biol. **9**, e1001059 (2011).

[34] S. Garcia, E. Hannezo, J. Elgeti, J.-F. Joanny, P. Silberzan, and N. S. Gov, Physics of active jamming during collective cellular motion in a monolayer, Proc. Natl. Acad. Sci. U.S.A. **112**, 15314 (2015).

[35] O. Chepizhko, C. Giampietro, E. Mastrapasqua, M. Nourazar, M. Ascagni, M. Sugni, U. Fascio, L. Leggio, C. Malinverno, G. Scita, S. Santucci, M. J. Alava, S. Zapperi, and C. A. M. La Porta, Bursts of activity in collective cell migration, Proc. Natl. Acad. Sci. U.S.A. **113**, 11408 (2016).

[36] E. A. Novikova, M. Raab, D. E. Discher, and C. Storm, Persistence-driven durotaxis: Generic, directed motility in rigidity gradients, Phys. Rev. Lett. **118**, 078103 (2017).

[37] S. K. Schnyder, J. J. Molina, Y. Tanaka, and R. Yamamoto, Collective motion of cells crawling on a substrate: roles of cell shape and contact inhibition, Sci. Rep. **7**, 5163 (2017).

[38] M. Dietrich, H. Le Roy, D. B. Brückner, H. Engelke, R. Zantl, J. O. Rädler, and C. P. Broedersz, Guiding 3D cell migration in deformed synthetic hydrogel microstructures, Soft Matter **14**, 2816 (2018).

[39] D. Shao, W.-J. Rappel, and H. Levine, Computational model for cell morphodynamics, Phys. Rev. Lett. **105**, 108104 (2010).

[40] D. Shao, H. Levine, and W.-J. Rappel, Coupling actin flow, adhesion, and morphology in a computational cell motility model, Proc. Natl. Acad. Sci. U.S.A. **109**, 6851 (2012).

[41] F. Ziebert, S. Swaminathan, and I. S. Aranson, Model for self-polarization and motility of keratocyte fragments, J. R. Soc. Interface **9**, 1084 (2012).

[42] F. Ziebert and I. S. Aranson, Effects of adhesion dynamics and substrate compliance on the shape and motility of crawling cells, PLOS One **8**, e64511 (2013).

[43] B. A. Camley, Y. Zhao, B. Li, H. Levine, and W.-J. Rappel, Periodic migration in a physical model of cells on micropatterns, Phys. Rev. Lett. **111**, 158102 (2013).

[44] J. Löber, F. Ziebert, and I. S. Aranson, Modeling crawling cell movement on soft engineered substrates, Soft Matter **10**, 1365 (2014).

[45] F. Graner and J. A. Glazier, Simulation of biological cell sorting using a two-dimensional extended Potts model, Phys. Rev. Lett. **69**, 2013 (1992).

[46] A. Szabó, R. Ünnep, E. Méhes, W. O. Twal, W. S. Argraves, Y. Cao, and A. Czirók, Collective cell motion in endothelial monolayers, Phys. Biol. **7**, 046007 (2010).

[47] A. Szabó and R. M. Merks, Cellular Potts modeling of tumor growth, tumor invasion, and tumor evolution, Front. Oncol. **3**, 10.3389/fonc.2013.00087 (2013).

[48] P. J. Albert and U. S. Schwarz, Dynamics of cell shape and forces on micropatterned substrates predicted by a cellular Potts model, Biophys. J. **106**, 2340 (2014).

[49] R. F. M. van Oers, E. G. Rens, D. J. LaValley, C. A. Reinhart-King, and R. M. H. Merks, Mechanical cell-matrix feedback explains pairwise and collective endothe-

lial cell behavior in vitro, PLOS Comput. Biol. **10**, e1003774 (2014).

[50] I. Niculescu, J. Textor, and R. J. de Boer, Crawling and gliding: A computational model for shape-driven cell migration, PLOS Comput. Biol. **11**, e1004280 (2015).

[51] F. J. Segerer, F. Thüroff, A. Piera Alberola, E. Frey, and J. O. Rädler, Emergence and persistence of collective cell migration on small circular micropatterns, Phys. Rev. Lett. **114**, 228102 (2015).

[52] P. J. Albert and U. S. Schwarz, Dynamics of cell ensembles on adhesive micropatterns: Bridging the gap between single cell spreading and collective cell migration, PLOS Comput. Biol. **12**, e1004863 (2016).

[53] E. G. Rens and R. M. H. Merks, Cell contractility facilitates alignment of cells and tissues to static uniaxial stretch, Biophys. J. **112**, 755 (2017).

[54] F. Thüroff, A. Goychuk, M. Reiter, and E. Frey, Bridging the gap between single-cell migration and collective dynamics, eLife **8**, 10.7554/elife.46842 (2019).

[55] E. G. Rens and R. M. H. Merks, Cell shape and durotaxis explained from cell-extracellular matrix forces and focal adhesion dynamics, iScience **23**, 101488 (2020).

[56] F. Zhou, S. A. Schaffer, C. Schreiber, F. J. Segerer, A. Goychuk, E. Frey, and J. O. Rädler, Quasi-periodic migration of single cells on short microlanes, PLOS ONE **15**, e0230679 (2020).

[57] Y. Cao, R. Karmakar, E. Ghabache, E. Gutierrez, Y. Zhao, A. Groisman, H. Levine, B. A. Camley, and W.-J. Rappel, Cell motility dependence on adhesive wetting, Soft Matter **15**, 2043 (2019).

[58] T. D. Pollard and G. G. Borisy, Cellular motility driven by assembly and disassembly of actin filaments, Cell **112**, 453 (2003).

[59] A. Mogilner, Mathematics of cell motility: have we got its number?, Journal of Mathematical Biology **58**, 105 (2009).

[60] A. F. M. Marée, A. Jilkine, A. Dawes, V. A. Grieneisen, and L. Edelstein-Keshet, Polarization and movement of keratocytes: A multiscale modelling approach, Bull. Math. Biol. **68**, 1169 (2006).

[61] A. F. M. Marée, V. A. Grieneisen, and L. Edelstein-Keshet, How cells integrate complex stimuli: The effect of feedback from phosphoinositides and cell shape on cell polarization and motility, PLOS Comput. Biol. **8**, e1002402 (2012).

[62] C. E. Chan and D. J. Odde, Traction dynamics of filopodia on compliant substrates, Science **322**, 1687 (2008).

[63] P. Sens, Stick–slip model for actin-driven cell protrusions, cell polarization, and crawling, Proc. Natl. Acad. Sci. U.S.A. **117**, 24670 (2020).

[64] G. F. Oster, J. D. Murray, and A. K. Harris, Mechanical aspects of mesenchymal morphogenesis, J. Embryol. Exp. Morphol. **78**, 83 (1983).

[65] N. Wang, J. D. Tytell, and D. E. Ingber, Mechanotransduction at a distance: mechanically coupling the extracellular matrix with the nucleus, Nat. Rev. Mol. Cell Biol. **10**, 75 (2009).

[66] R. Balian, *From Microphysics to Macrophysics* (Springer, Berlin, 2007).

[67] E. G. Rens and L. Edelstein-Keshet, From energy to cellular forces in the cellular potts model: An algorithmic approach, PLOS Comput. Biol. **15**, e1007459 (2019).

[68] M. G. Yucht, M. Sheinman, and C. P. Broedersz, Dynamical behavior of disordered spring networks, Soft Matter **9**, 7000 (2013).

[69] L. D. Landau, L. P. Pitaevskii, A. M. Kosevich, and E. M. Lifshitz, *Theory of Elasticity*, third edition ed. (Butterworth-Heinemann, 1986).

[70] P. Ronceray, C. P. Broedersz, and M. Lenz, Fiber networks amplify active stress, Proc. Natl. Acad. Sci. U.S.A. , 201514208 (2016).

[71] D. Calvet, J. Y. Wong, and S. Giasson, Rheological monitoring of polyacrylamide gelation: Importance of crosslink density and temperature, Macromolecules **37**, 7762 (2004).

[72] G. P. Raeber, M. P. Lutolf, and J. A. Hubbell, Molecularly engineered PEG hydrogels: A novel model system for proteolytically mediated cell migration, Biophys. J. **89**, 1374 (2005).

[73] M. Murrell, R. Kamm, and P. Matsudaira, Substrate viscosity enhances correlation in epithelial sheet movement, Biophys. J. **101**, 297 (2011).

[74] O. Chaudhuri, L. Gu, M. Darnell, D. Klumpers, S. A. Bencherif, J. C. Weaver, N. Huebsch, and D. J. Mooney, Substrate stress relaxation regulates cell spreading, Nat. Commun. **6**, 6365 (2015).

[75] A. J. Engler, S. Sen, H. L. Sweeney, and D. E. Discher, Matrix elasticity directs stem cell lineage specification, Cell **126**, 677 (2006).

[76] M. Akhmanova, E. Osidak, S. Domogatsky, S. Rodin, and A. Domogatskaya, Physical, spatial, and molecular aspects of extracellular matrix of ¡i¿in vivo¡/i¿ niches and artificial scaffolds relevant to stem cells research, Stem Cells Int. **2015**, 167025 (2015).

[77] I. B. Bischofs and U. S. Schwarz, Cell organization in soft media due to active mechanosensing, Proceedings of the National Academy of Sciences of the United States of America **100**, 9274 (2003).

[78] J. R. Tse and A. J. Engler, Preparation of hydrogel substrates with tunable mechanical properties, Curr. Protoc. Cell Biol. **47**, 10161 (2010).

[79] J. Schindelin, I. Arganda-Carreras, E. Frise, V. Kaynig, M. Longair, T. Pietzsch, S. Preibisch, C. Rueden, S. Saalfeld, B. Schmid, J.-Y. Tinevez, D. J. White, V. Hartenstein, K. Eliceiri, P. Tomancak, and A. Cardona, Fiji: an open-source platform for biological-image analysis, Nat. Methods **9**, 676 (2012).

[80] E. Meijering, O. Dzyubachyk, and I. Smal, Methods for cell and particle tracking, in *Methods in Enzymology*, Vol. 504, edited by P. M. Conn (Academic Press, 2012) pp. 183–200.

[81] O. Ronneberger, P. Fischer, and T. Brox, U-Net: Convolutional networks for biomedical image segmentation, in *Medical Image Computing and Computer-Assisted Intervention (MICCAI)*, LNCS, Vol. 9351 (Springer, 2015) pp. 234–241, (available on arXiv:1505.04597 [cs.CV]).

[82] T. Falk, D. Mai, R. Bensch, O. Çiçek, A. Abdulkadir, Y. Marrakchi, A. Böhm, J. Deubner, Z. Jäckel, K. Seiwald, A. Dovzhenko, O. Tietz, C. Dal Bosco, S. Walsh, D. Saltukoglu, T. L. Tay, M. Prinz, K. Palme, M. Simons, I. Diester, T. Brox, and O. Ronneberger, U-Net: deep learning for cell counting, detection, and morphometry, Nat. Methods **16**, 67 (2019).

Morphology and Motility of Endothelial Cells on Soft Substrates
— Supplementary Material —

Andriy Goychuk,[1] David B. Brückner,[1] Andrew W. Holle,[2,3]

Joachim P. Spatz,[4,5] Chase P. Broedersz,[1,6] and Erwin Frey[1]

[1] *Arnold Sommerfeld Center for Theoretical Physics and Center for NanoScience,*

Department of Physics, Ludwig-Maximilian-University Munich,

Theresienstr. 37, D-80333 Munich, Germany

[2] *Mechanobiology Institute, National University of Singapore, Singapore, Republic of Singapore*

[3] *Department of Biomedical Engineering,*

National University of Singapore, Singapore, Republic of Singapore

[4] *Department of Cellular Biophysics, Max-Planck-Institute*

for Medical Research, D-69120 Heidelberg, Germany

[5] *Department of Biophysical Chemistry,*

University of Heidelberg, D-69120 Heidelberg, Germany

[6] *Department of Physics and Astronomy,*

Vrije Universiteit Amsterdam, Amsterdam, The Netherlands

2

CONTENTS

3

Appendix A: Computational Model

In the following sections, we complement the model description in the main text, by discussing the detailed numerical implementation and the technical aspects of our model. We start by introducing the necessary mathematical definitions for the substrate and the adhering cell. Then, we recapitulate the Cellular Potts model [1, 2], and extend this model by taking substrate deformations into account. As we proceed, we also discuss the limitations of our model assumptions and how these limitations could be addressed in future work.

1.   Mathematical Representation of the Substrate

a.   Spatial discretization of the substrate.   In our model, we simulate the spatiotemporal dynamics of the contact area between a cell and an underlying flat surface, which we also refer to as *substrate*. For this purpose, we tessellate the surface into N hexagonal *tiles* (or *grid sites*). To each of these hexagonal tiles, we assign a position vector $\mathbf{x}_i$. The hexagonal tiles form a space-filling triangular lattice $\mathcal{S}$, which we also refer to as *grid*:

$$\mathcal{S} = \left\{ \mathbf{x}_i(t) \right\}_{i=1,\ldots,N}. \tag{A1}$$

The substrate is an elastic deformable body. Therefore, the positions of the lattice vectors $\mathbf{x}_i$ (or *nodes*) are time-dependent. We model deformations of the substrate by deflections of the lattice nodes $\mathbf{x}_i(t)$ from their zero-strain reference configuration.

b.   Topological neighborhood of each node.   Each lattice node $\mathbf{x}_i$ is surrounded by six nearest neighbors, thus defining its neighborhood $\mathcal{N}_i$ by the following sequence:

$$\mathcal{N}_i = \left(\mathbf{x}_j(t) \,\Big|\, \text{node } \mathbf{x}_j(t) \text{ is nearest neighbor of node } \mathbf{x}_i(t) \right). \tag{A2}$$

This sequence has a (clockwise) cyclic order relative to the central node $\mathbf{x}_i$:

4
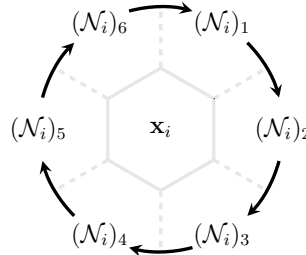
In the zero-strain reference configuration (i.e., at the beginning of our simulations, $t = 0$, or for an undeformable substrate), the distance between nearest neighbors is given by:

$$\|\mathbf{x}_j(0) - \mathbf{x}_i(0)\| = d_0 \iff \mathbf{x}_j \in \mathcal{N}_i \,. \tag{A3}$$

Thus, d_0 sets the spatial discretization in our simulations. When the substrate is deformed, the distance between neighboring lattice nodes must change accordingly.

In our simulations, we assume that the neighborhood of each lattice node remains (topologically) immutable, i.e., any two nearest neighbors remain nearest neighbors irrespective of the applied deformation. This limitation can only be lifted by frequently performing a (computationally expensive) Delaunay triangulation to re-mesh the whole simulation grid, and then computing the corresponding Voronoi tiles. As a side effect, re-meshing can typically introduce (topological) changes of neighborhood as well as change the number of vertices on each tile. These effects would require further generalization of our model implementation[1].

c.   **Hexagonal tessellation of the substrate.**   Each lattice node $\mathbf{x}_i$ corresponds to a hexagonal tile [Fig. S1], whose six vertices form the following sequence:

$$\mathcal{V}_i = \left(\mathbf{v}_j \,\Big|\, \mathbf{v}_j \text{ is a vertex of the hexagonal tile at the node } \mathbf{x}_i \right). \tag{A4}$$

Since the positions of all lattice nodes are time-dependent and move affinely with the deformations of the substrate, we also need to keep track of the shape of each hexagonal tile. To do so, we compute the positions of the vertices of each hexagonal tile, based on the time-dependent positions of the nodes. In particular, each vertex has three adjacent tiles that correspond to nodes $\mathbf{x}_i$. Therefore, we define the position of the vertex as the geometric center of these three adjacent nodes:

$$(\mathcal{V}_i)_k = \frac{1}{3} \Big[\mathbf{x}_i + (\mathcal{N}_i)_k + (\mathcal{N}_i)_{k-1} \Big] \,, \tag{A5}$$

where $(\mathcal{N}_i)_0 \equiv (\mathcal{N}_i)_6$. This definition ensures a (clockwise) cyclic order in the sequence of the vertices of a hexagon and can be graphically represented as follows:

---

[1] For example, the current implementation assumes that the contact area between a cell and the substrate is a simply connected set of grid sites.

5
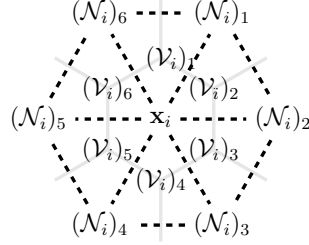
Similarly, we also define a sequence of edge vectors for each hexagonal tile,

$$\mathcal{E}_i = \left(\mathbf{e}_j \,\middle|\, \text{edge vector } \mathbf{e}_j \text{ borders the hexagonal tile at node } \mathbf{x}_i \right). \tag{A6}$$

Each edge vector $(\mathcal{E}_i)_k$ corresponds to the interface between the lattice node $\mathbf{x}_i$ and the lattice node $(\mathcal{N}_i)_k$, and can thus be defined via the vertex positions:

$$(\mathcal{E}_i)_k = (\mathcal{V}_i)_{k+1} - (\mathcal{V}_i)_k \,, \tag{A7}$$

where $(\mathcal{V}_i)_6 \equiv (\mathcal{V}_i)_0$. The corresponding edge lengths are given by $\|(\mathcal{E}_i)_k\|$.

We assume that the hexagons are at all times, which includes deformed configurations of the substrate, simple polygons. Then, the area $a(\mathbf{x}_i, t)$ of a hexagon spanned by the vertices $(\mathcal{V}_i)_k$ is given by Gauss's area formula:

$$a(\mathbf{x}_i, t) = \frac{1}{2} \left| \sum_{k=1}^{6} (\mathcal{V}_i)_k^x \left[(\mathcal{V}_i)_{k+1}^y - (\mathcal{V}_i)_{k-1}^y \right] \right| \,, \tag{A8}$$

where $(\mathcal{V}_i)_k^x$ and $(\mathcal{V}_i)_k^y$ refer to the x-coordinate and the y-coordinate of the vertex $(\mathcal{V}_i)_k$, respectively.

2. Mathematical Representation of a Cell

a. Domain and area of the cell. We represent the contact area between a cell and the underlying substrate (referred to as the *domain* of the cell) as a set $\mathcal{D}$ of simply connected hexagons [Fig. S1]:

$$\mathcal{D} = \left\{ \mathbf{x}_i \,\middle|\, \mathbf{x}_i \text{ is occupied by cell} \right\}. \tag{A9}$$

Thus, the area A of a cell is given by the sum of the individual areas of all hexagons in the cell domain (i.e., substrate tiles *occupied* by the cell):

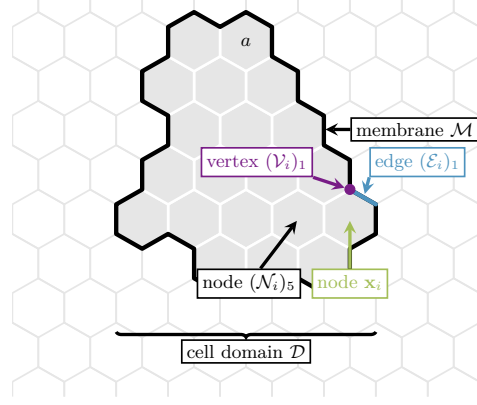$$A = \sum_{\mathbf{x}_i \in \mathcal{D}} a(\mathbf{x}_i, t) \,. \tag{A10}$$

FIG. S1. **Description of a cell and the substrate.** The substrate is tessellated into hexagons, which lie at node positions $\mathbf{x}_i$. Each vertex $(\mathcal{V}_i)_k$ of a hexagon is defined by the geometric center of the three adjacent nodes. The area $a(\mathbf{x}_i, t)$ of a hexagon is defined via Gauss's area formula. The cell domain is given by a morphologically connected set of hexagons $\mathbf{x}_i \in \mathcal{D}$. The cell membrane $\mathcal{M}$ is the set of membrane segments $(\mathcal{E}_i)_k$ that line the border of the cell domain.

b.   Membrane and perimeter of the cell.   We represent the cell membrane as the set of hexagon edges $(\mathcal{E}_i)_k$ that line the border of the cell domain $\mathcal{D}$ [Fig. S1]:

$$\mathcal{M} = \left\{ (\mathcal{E}_i)_k \left| \begin{array}{l} \mathbf{x}_i \in \mathcal{D}\,, \\ (\mathcal{N}_i)_k \notin \mathcal{D} \end{array} \right. \right\}. \tag{A11}$$

Thus, the perimeter P of the cell is given by the sum of the individual lengths of all line segments in the cell membrane:

$$P = \sum_{(\mathcal{E}_i)_k \in \mathcal{M}} \|(\mathcal{E}_i)_k\|\,. \tag{A12}$$

As we have mentioned above, the edge $(\mathcal{E}_i)_k$ defines the boundary between a hexagon $\mathbf{x}_i$ and its nearest neighbor $(\mathcal{N}_i)_k$. Thus, to close this section and to relate our present terminology to our previous work [1, 2], we also introduce the set of hexagons that line the inner side of the membrane (i.e., the "membrane grid sites"):

$$\mathcal{B} = \left\{ \mathbf{x}_i \left| (\mathcal{E}_i)_k \in \mathcal{M} \right. \right\}. \tag{A13}$$
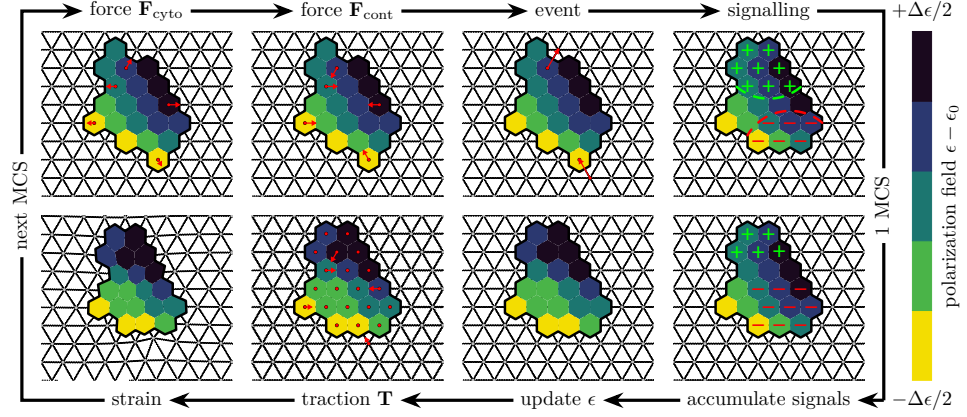
FIG. S2. **Overview of a single Monte Carlo Step.** When a cell attempts a protrusion or a retraction event, it makes a virtual (i.e., not yet realized) change in polarization energy $\mathcal{H}_{\mathrm{cyto}}$ and shape energy $\mathcal{H}_{\mathrm{cont}}$. These energy changes are related to effective protrusive $\mathbf{F}_{\mathrm{cyto}}$ and contractile $\mathbf{F}_{\mathrm{cont}}$ forces (illustrated in red for several simultaneously attempted events), acting on the boundary of the cell. An attempted event becomes accepted (i.e., the virtual change in cell state is actually realized) with a probability that we determine from the total energy difference $\Delta\mathcal{H} = \Delta\mathcal{H}_{\mathrm{cyto}} + \Delta\mathcal{H}_{\mathrm{cont}}$ [cf. Eq. (A21)]. Successful protrusions are then followed up by a secretion of internal signals within a radius R. Similarly, retractions lead to depletion of the mentioned internal signals. Over the course of a Monte Carlo Step, many such signals accumulate. Then, positive signaling increases the local cell polarization field ϵ, while negative signaling decreases the polarization field. Assuming force balance, the protrusive forces, $\mathbf{F}_{\mathrm{cyto}}$, and the contractile forces, $\mathbf{F}_{\mathrm{cont}}$, are related to effective traction forces $\mathbf{T}$ on the substrate, thus leading to substrate deformations.

Furthermore, we introduce the set of hexagons that line the outer side of the membrane (i.e., the "neighborhood of the cell"):

$$\mathcal{N} = \left\{ (\mathcal{N}_i)_k \,\middle|\, (\mathcal{E}_i)_k \in \mathcal{M} \right\}. \tag{A14}$$

8

3. Dynamics of the cell

For the reader's convenience, we briefly recapitulate the cell model that we use and generalize in the present study. The foundation of our model was previously laid by Refs. [1, 2]. Therefore, we refer to Refs. [1, 2] for a detailed discussion and a biological motivation of the core model for cell polarity and migration. We further extend this model, by explicitly accounting for the deformations of the substrate that the cell adheres to.

a. Metropolis algorithm. We carry out stochastic simulations with a discrete time stepping (*Monte Carlo Steps*). For a schematic overview over a single Monte Carlo Step, we refer to Fig. S2 and to the following discussion. During each Monte Carlo Step, the cell makes $K = |\mathcal{M}|$ individual protrusion or retraction attempts (*events*). Thus, on average, each membrane segment $(\mathcal{E}_i)_k \in \mathcal{M}$ has a chance to either protrude or retract in response to contractile and protrusive forces, respectively [cf. sections A 3 b "Contractility of the cellular membrane and cortex" and A 3 c "Actin network of the cell"]. In particular, we first select a random membrane segment $(\mathcal{E}_i)_k \in \mathcal{M}$ with a probability proportional to its length:

$$\mathrm{p}\big[(\mathcal{E}_i)_k\big] = \frac{\|(\mathcal{E}_i)_k\|}{P} \, . \tag{A15}$$

Then, we choose with equal probability whether the cell *attempts* to protrude or to retract along the direction perpendicular to the chosen membrane segment $(\mathcal{E}_i)_k$. Specifically, the membrane segment $(\mathcal{E}_i)_k$ lies at the interface between the tile $(\mathcal{N}_i)_k \in \mathcal{N}$ outside the cell boundary (*target tile*), and the tile $\mathbf{x}_i \in \mathcal{B}$ inside the cell boundary (*source tile*). If a protrusion event is *accepted*, $\mathcal{T}_{\mathrm{pro}}$, then the cell incorporates the target tile $(\mathcal{N}_i)_k$ into its domain:

$$\mathcal{T}_{\mathrm{pro}}\big[(\mathcal{E}_i)_k\big]: \quad \mathcal{D}_{\mathrm{old}} \to \mathcal{D}_{\mathrm{new}} = \mathcal{D}_{\mathrm{old}} \cup \{(\mathcal{N}_i)_k\} \, , \tag{A16}$$

and we update the set of its membrane segments $\mathcal{M}$ accordingly. In that case, the edge motion proceeds in the direction:

$$\Delta\mathbf{x}_{\mathrm{pro}}\big[(\mathcal{E}_i)_k\big] = (\mathcal{N}_i)_k - \mathbf{x}_i \, . \tag{A17}$$

Similarly, if a retraction event is *accepted* , $\mathcal{T}_{\mathrm{ret}}$, then the cell detaches from the source tile $\mathbf{x}_i$:

$$\mathcal{T}_{\mathrm{ret}}\big[(\mathcal{E}_i)_k\big]: \quad \mathcal{D}_{\mathrm{old}} \to \mathcal{D}_{\mathrm{new}} = \mathcal{D}_{\mathrm{old}} \backslash \{\mathbf{x}_i\} \, , \tag{A18}$$

and we update the set of its membrane segments $\mathcal{M}$ accordingly. Then, the edge motion proceeds in the direction:

$$\Delta\mathbf{x}_{\mathrm{ret}}\big[(\mathcal{E}_i)_k\big] = \mathbf{x}_i - (\mathcal{N}_i)_k = -\Delta\mathbf{x}_{\mathrm{pro}}\big[(\mathcal{E}_i)_k\big] . \tag{A19}$$

We associate each cell configuration $\mathcal{D}$ with an energy, which we describe by a Hamiltonian $\mathcal{H}[\mathcal{D}]$. If a protrusion or a retraction attempt is successful, then, as a consequence, the cell configuration $\mathcal{D}$ and the corresponding energy $\mathcal{H}[\mathcal{D}]$ will change. This change in energy can be either favorable (i.e., energy is released), or unfavorable (i.e., energy has to be expended). By inversion of argument, the motion of the cell will typically follow gradients in the chemical potential landscape, thus gradually minimizing its total energy. Here, our distinction between *attempted* and *accepted* events, either protrusions or retractions, becomes relevant. Specifically, we define an attempted event as a virtual change of the cell configuration, associated with the following virtual work

$$\Delta\mathcal{H}\big[\mathcal{T}_{\mathrm{pro/ret}}[(\mathcal{E}_i)_k]\big] = \mathcal{H}\big[\mathcal{D}_{\mathrm{new}}\big] - \mathcal{H}\big[\mathcal{D}_{\mathrm{old}}\big] . \tag{A20}$$

Such an attempted event becomes accepted (i.e., the virtual change of the cell configuration and the virtual work are actually realized) with a probability

$$p\big[\mathcal{T}_{\mathrm{pro/ret}}[(\mathcal{E}_i)_k]\big] = \min\big[\exp(-\Delta\mathcal{H}/k_{\mathrm{B}}T),\, 1\big] . \tag{A21}$$

Thus, events that are energetically favorable are likely to succeed, while events that are energetically costly are likely to be rejected. The effective temperature T is a measure for the fluctuations and activity of the cytoskeletal dynamics on a cellular scale. Thus, in Cellular Potts models, the effective temperature T does not correspond to the room temperature.

The Hamiltonian $\mathcal{H}$ consists of two competing contributions:

$$\mathcal{H}\big[\mathcal{D}\big] = \mathcal{H}_{\mathrm{cont}}\big[\mathcal{D}\big] + \mathcal{H}_{\mathrm{cyto}}\big[\mathcal{D}\big] . \tag{A22}$$

Here, the first term comes from cell contractility and the second, protrusive, term comes from the activity of the actin cytoskeleton network as well as substrate adhesions. In the following sections, we focus on these two contributions.

b.   Contractility of the cellular membrane and cortex.   The geometry of the cell is constrained by its elastic membrane and its contractile cytoskeleton [3–6]. Thus, as a first approximation, we assume that deformations of a cell's membrane and cortex are constrained by the following elastic energy [1, 2]:

$$\mathcal{H}_{\text{cont}}[\mathcal{D}] = \kappa_A A(t)^2 + \kappa_P P(t)^2 \,, \tag{A23}$$

similar as in the original Cellular Potts model [7]. Here, κ_A and κ_P denote the respective elastic coupling parameters corresponding to the area, $A(t)$, and perimeter, $P(t)$, of the cell. Analogous to our previous discussion, a change in cell morphology, represented by the cell configuration $\mathcal{D}$, due to a successful protrusion or retraction event $\mathcal{T}_{\text{pro/ret}}$ is accompanied by a change of shape energy:

$$\Delta\mathcal{H}_{\text{cont}}\big[\mathcal{T}_{\text{pro/ret}}[(\mathcal{E}_i)_k]\big] = \mathcal{H}_{\text{cont}}\big[\mathcal{D}_{\text{new}}\big] - \mathcal{H}_{\text{cont}}\big[\mathcal{D}_{\text{old}}\big]. \tag{A24}$$

In the case of a retraction, the contractile cell membrane and cortex will perform the work $-\Delta\mathcal{H}_{\text{cont}}\big[\mathcal{T}_{\text{ret}}[(\mathcal{E}_i)_k]\big]$. In the case of a protrusion, the work $-\Delta\mathcal{H}_{\text{cont}}\big[\mathcal{T}_{\text{pro}}[(\mathcal{E}_i)_k]\big] \approx \Delta\mathcal{H}_{\text{cont}}\big[\mathcal{T}_{\text{ret}}[(\mathcal{E}_i)_k]\big]$ has to be exercised to push against the contractile membrane and the cortex. Both cases are related to an effective contractile force on the membrane segment $(\mathcal{E}_i)_k$, which always points towards the inside of the cell [cf. Eq. (A19)]:

$$\mathbf{F}_{\text{cont}}\big[(\mathcal{E}_i)_k\big] = \frac{\big|\Delta\mathcal{H}_{\text{cont}}\big[\mathcal{T}_{\text{pro/ret}}[(\mathcal{E}_i)_k]\big]\big|}{\big\|\Delta\mathbf{x}_{\text{pro/ret}}\big[(\mathcal{E}_i)_k\big]\big\|} \, \frac{\Delta\mathbf{x}_{\text{ret}}\big[(\mathcal{E}_i)_k\big]}{\big\|\Delta\mathbf{x}_{\text{ret}}\big[(\mathcal{E}_i)_k\big]\big\|} \,. \tag{A25}$$

Here, the first term corresponds to the virtual work $-\Delta\mathcal{H}_{\text{cont}}$ that is performed over a virtual displacement $\Delta\mathbf{x}$, and the second term corresponds to the unit normal vector pointing towards the inside of the cell. Note that, unless the cellular contractile forces are counteracted by the pushing forces described in the following, the cell would detach from the underlying substrate, i.e., the contact area between the cell and the substrate would vanish.

c.   Actin network of the cell.   In addition to contractile forces due to myosin activity, the cellular actomyosin cytoskeleton also generates inhomogeneous pushing forces due to actin polymerization [8, 9]. These pushing cytoskeletal structures are locally anchored to the underlying substrate at focal adhesion sites [8, 9]. Since the actomyosin cytoskeleton is coupled to the underlying substrate via adhesions, any local substrate displacement corresponds to an identical displacement of the actomyosin cytoskeleton. In addition, each

hexagonal tile deforms affinely with the substrate, as described in section A 1 "Mathematical Representation of the Substrate". Thus, we expect that the local amount of actomyosin cytoskeleton per substrate tile will remain unaffected by a deformation of the underlying substrate.

Together, the pushing forces generated by cytoskeletal structures and the corresponding cell-substrate adhesions counteract the homogeneous contractile forces that are facilitated by cell cytoskeleton contractility. We encapsulate these physical interactions in a scalar *polarization field*, $\epsilon(\mathbf{x}_i, t) \in [\epsilon_0 - \Delta\epsilon/2, \epsilon_0 + \Delta\epsilon/2]$, which is akin to a spatially heterogeneous effective cell-substrate adhesion energy *per substrate tile* [1, 2]:

$$\mathcal{H}_{\mathrm{cyto}} = -\sum_{\mathbf{x}_i \in \mathcal{D}} \epsilon(\mathbf{x}_i, t) \,. \tag{A26}$$

The lower bound of the polarization field, $\epsilon_0 - \Delta\epsilon/2$, corresponds to a minimal adhesion energy so that cells do not detach from the substrate. In addition, the upper bound of the polarization field, $\epsilon_0 + \Delta\epsilon/2$, reflects a limited local availability of biomolecules such as integrins, myosin motors and actin filaments [2].

Analogous to our previous discussion, a change in cell morphology, represented by the cell configuration $\mathcal{D}$, due to a successful protrusion or retraction event $\mathcal{T}_{\mathrm{pro/ret}}$ is accompanied by a change of the effective cell-substrate adhesion energy:

$$\Delta\mathcal{H}_{\mathrm{cyto}}\big[\mathcal{T}_{\mathrm{pro/ret}}[(\mathcal{E}_i)_k]\big] = \mathcal{H}_{\mathrm{cyto}}\big[\mathcal{D}_{\mathrm{new}}\big] - \mathcal{H}_{\mathrm{cyto}}\big[\mathcal{D}_{\mathrm{old}}\big] \,. \tag{A27}$$

In particular, when retracting along the direction perpendicular to its membrane edge $(\mathcal{E}_i)_k$, a cell has to exercise work to detach from the substrate at node $\mathbf{x}_i$:

$$\Delta\mathcal{H}_{\mathrm{cyto}}\big[\mathcal{T}_{\mathrm{ret}}[(\mathcal{E}_i)_k]\big] = +\,\epsilon(\mathbf{x}_i, t) \,. \tag{A28}$$

Analogously, when protruding along the direction perpendicular to its membrane edge $(\mathcal{E}_i)_k$, the actomyosin cytoskeleton of the cell will perform work by creating a new adhesion to the substrate at the node $(\mathcal{N}_i)_k$:

$$\Delta\mathcal{H}_{\mathrm{cyto}}\big[\mathcal{T}_{\mathrm{pro}}[(\mathcal{E}_i)_k]\big] = -\,\epsilon(\mathbf{x}_i, t) \,. \tag{A29}$$

Here, we have assumed that a newly formed substrate contact at the target node $(\mathcal{N}_i)_k$ has the same effective adhesion energy as the pre-existing substrate contact at the source node

$\mathbf{x}_i$. Both retraction and protrusion attempts are related to an effective pushing force on the membrane segment $(\mathcal{E}_i)_k$, which always points towards the outside of the cell [cf. Eq. (A17)]:

$$\mathbf{F}_{\text{cyto}}\big[(\mathcal{E}_i)_k\big] = \frac{\big|\Delta\mathcal{H}_{\text{cyto}}\big[\mathcal{T}_{\text{pro/ret}}[(\mathcal{E}_i)_k]\big]\big|}{\big\|\Delta\mathbf{x}_{\text{pro/ret}}\big[(\mathcal{E}_i)_k\big]\big\|} \frac{\Delta\mathbf{x}_{\text{pro}}\big[(\mathcal{E}_i)_k\big]}{\big\|\Delta\mathbf{x}_{\text{pro}}\big[(\mathcal{E}_i)_k\big]\big\|} . \tag{A30}$$

The polarization field is dynamic and thus reflects the assembly and disassembly of cytoskeletal structures, which is mediated by intracellular signaling cascades [10–12]. These signaling cascades involve regulatory cytoskeletal proteins that enable the cell to respond to extracellular stimuli [13, 14].

d. Mechanochemical signaling. The actomyosin cytoskeleton of the cell, which drives cell migration, responds to mechanical stimuli via several signaling cascades and feedback loops that involve regulatory cytoskeletal proteins [10–12]. Here, we do not formulate a reaction-diffusion model that involves these different microscopic dynamics [13, 14]. Instead, as in our previous work [1, 2], we take a coarse-grained approach. Specifically, we assume that intracellular signaling cascades will typically up- or down-regulate the activity of the cellular actomyosin cytoskeleton within some finite radius R of a mechanical stimulus, i.e., near a protrusion or a retraction. Instead of accounting for the different signaling molecules individually, we introduce an integer bookkeeping field $m(\mathbf{x}_i)$ that has the role of propagating information from mechanical stimuli at the cell boundary across a distance R. This integer bookkeeping field $m(\mathbf{x}_i)$ can also take negative values, and resets after each Monte Carlo Step, thus reflecting quick degradation dynamics. We update the local integer bookkeeping field $m(\mathbf{x}_i)$ continuously over the course of each Monte Carlo Step, as follows. Specifically, we follow two distinct update rules for our two basic types of cellular activity, protrusion and retraction events [2].

In the case of a successful protrusion event $\mathcal{T}_{\text{pro}}[(\mathcal{E}_i)_k]$, which originates at the membrane segment $(\mathcal{E}_i)_k$ and incorporates the tile at node $(\mathcal{N}_i)_k$ into the cell, cf. Eq. (A16), we perform two operations. First, we copy the value of the bookkeeping field from the source tile to the target tile: $m((\mathcal{N}_i)_k) \rightarrow m(\mathbf{x}_i)$. Then, we increment the integer bookkeeping field for all tiles within a radius R of the target tile:

$$m(\mathbf{x}_j) \rightarrow \begin{cases} m(\mathbf{x}_j) + 1, & \|\mathbf{x}_j - (\mathcal{N}_i)_k\| < R \ \vee \ \mathbf{x}_j \in \mathcal{D} \\ m(\mathbf{x}_j), & \text{else.} \end{cases} \tag{A31}$$

In the case of a successful retraction event $\mathcal{T}_{\mathrm{ret}}[(\mathcal{E}_i)_k]$, which originates at the membrane segment $(\mathcal{E}_i)_k$ and removes the tile $\mathbf{x}_i$ from the cell, cf. Eq. (A18), we also perform two operations. First, we erase the value of the bookkeeping field from the target tile: $m(\mathbf{x}_i) \to 0$. Then, we decrement the integer bookkeeping field for all tiles within a radius R of the target tile:

$$m(\mathbf{x}_j) \to \begin{cases} m(\mathbf{x}_j) - 1, & \|\mathbf{x}_j - \mathbf{x}_i\| < R \vee \mathbf{x}_j \in \mathcal{D} \\ m(\mathbf{x}_j), & \text{else.} \end{cases} \tag{A32}$$

e. Mechanochemical feedback.   As we have discussed in section A 3 c "Actin network of the cell", cellular protrusions are driven by pushing forces that the actomyosin cytoskeleton generates. We model these effects with the scalar polarization field ϵ. This scalar polarization field acts like an effective adhesion energy, thus conferring pushing forces that counteract the contractile forces exerted by the cell cortex. In the absence of this effective adhesion energy, cell contractility would lead to cell retractions and ultimately to a detachment from the surface, as discussed in section A 3 b "Contractility of the cellular membrane and cortex". Thus, protrusion events are more likely to occur in regions with a high value of the polarization field ϵ, while retractions are more numerous in regions with a low value of the polarization field ϵ. These two elementary events, protrusions and retractions, correspond to mechanical stimuli at the cell boundary, initiating signaling cascades that propagate across a distance R into the cell. Throughout a single Monte Carlo Step, many protrusion and retraction events occur, and the corresponding signaling cascades overlap in space. As discussed in section A 3 d "Mechanochemical signaling", we represent these signaling cascades by an integer bookkeeping field $m(\mathbf{x}_j)$. The integer bookkeeping field $m(\mathbf{x}_j)$ thus informs us whether a tile $\mathbf{x}_j$ received more stimuli originating from protrusion events, or more stimuli from retraction events, within the signaling radius R. We assume that, at the end of a Monte Carlo Step with duration Δt, the actomyosin cytoskeleton is reinforced in regions of high protrusive activity, and disassembled in regions of low protrusive activity [2]:

$$\partial_t \epsilon(\mathbf{x}_i, t) = \frac{\epsilon(\mathbf{x}_i, t + \Delta t) - \epsilon(\mathbf{x}_i, t)}{\Delta t} = \mu \left[\left(\epsilon_0 + \frac{\Delta\epsilon}{2} \operatorname{sgn} m(\mathbf{x}_i) \right) - \epsilon(\mathbf{x}_i, t) \right] , \tag{A33}$$

14

where μ is the cytoskeletal update rate and sgn corresponds to the sign function:

$$\text{sgn}\, x = \begin{cases} 1, & x > 0, \\ 0, & x = 0, \\ -1, & x < 0. \end{cases} \quad (\text{A34})$$

The temporal evolution of the polarization field, given by Eq. (A33), ensures that the polarization field is bounded from below and from above: $\epsilon(\mathbf{x}_i, t) \in [\epsilon_0 - \Delta\epsilon/2, \epsilon_0 + \Delta\epsilon/2]$.

Finally, we would like to summarize that the Cellular Potts model in the present implementation contains two prototypical feedback loops [2]:

- High values of the polarization field favor protrusive activity, leading to an increase of the polarization field in the vicinity of protrusions.

- Low values of the polarization field favor retractive activity, leading to a decrease of the polarization field in the vicinity of retractions.

These two prototypic feedback loops break detailed balance and maintain macroscopic cell polarization throughout our simulations.

4. Dynamics of the deformable substrate

So far, we have focused on the spatiotemporal dynamics of a migrating cell alone. In this section, we discuss how the cell induces substrate deformations by generating traction forces.

a. **Cell traction forces.** The cell generates both contractile forces and protrusive forces, as discussed in sections A 3 b "Contractility of the cellular membrane and cortex" and A 3 c "Actin network of the cell". In the following, we first focus on contractile forces, and then proceed to discuss how protrusive forces transmit to the substrate via focal adhesions. In particular, contractile forces $\mathbf{F}_{\text{cont}}(\mathbf{x}_i, t)$ are independent of the cell's ability to adhere to the substrate via focal adhesions. Even if the cell cannot form adhesions at all, it will still generate contractile forces via its actomyosin cortex (in the form of cortical tension). These contractile forces will ultimately lead to a rounding up of the three-dimensional cell body, and to a disappearance of the two-dimensional cell-substrate contact area. In our model, the

contraction is homogeneous throughout the cell and, as a result, the integral of all contractile forces along the cell membrane $\mathcal{M}$, averaged over the time t, must vanish:

$$\sum_{(\mathcal{E}_i)_k \in \mathcal{M}} \mathrm{p}[(\mathcal{E}_i)_k] \, \mathbf{F}_{\mathrm{cont}}(\mathbf{x}_i, t) = 0 \,. \tag{A35}$$

This can also be interpreted as a consequence of global force balance, in the absence of traction. If there is a finite random force due to cellular contractility[2],

$$\sum_{\substack{\text{attempted} \\ \mathcal{T}_{\mathrm{pro/ret}}[(\mathcal{E}_i)_k]}} \mathbf{F}_{\mathrm{cont}}(\mathbf{x}_i, t) \neq 0 \,, \tag{A36}$$

then this random force must be balanced by equal and opposite traction forces on the substrate. We assume that the cytoskeleton facilitating this contractility transmits forces instantaneously throughout the cell. Then, the random net force is distributed homogeneously over all substrate tiles $\mathbf{x}_j \in \mathcal{D}$ that are occupied by the cell, and is balanced by the following equal and opposite homogeneous traction forces on the substrate:

$$\mathbf{x}_j \in \mathcal{D}: \quad \mathbf{T}_{\mathrm{cont}}(\mathbf{x}_j, t) = -\frac{1}{|\mathcal{D}|} \sum_{\substack{\text{attempted} \\ \mathcal{T}_{\mathrm{pro/ret}}[(\mathcal{E}_i)_k]}} \mathbf{F}_{\mathrm{cont}}(\mathbf{x}_i, t) \,. \tag{A37}$$

By taking the time average of Eq. (A37) and using Eq. (A35), we note that the contribution of contractile forces to the traction forces vanishes on average:

$$\left\langle \mathbf{T}_{\mathrm{cont}}(\mathbf{x}_j, t) \right\rangle_t = 0 \,. \tag{A38}$$

The situation is markedly different for the antagonist of cellular contractility, namely the *spatially heterogeneous* protrusive forces, $\mathbf{F}_{\mathrm{cyto}}(\mathbf{x}_i, t)$, that the actomyosin cytoskeleton of the cell generates. This cell cytoskeleton is *locally* anchored to the underlying substrate at focal adhesion sites [8, 9]. Thus, in contrast to cellular contractile forces, cellular protrusive forces rely on the ability of the cell to make focal adhesions, and the spatially heterogeneous protrusive forces must be *locally* balanced by equal and opposite traction forces

$$\mathbf{T}_{\mathrm{cyto}}(\mathbf{x}_i, t) = -\sum_{\substack{\text{attempted} \\ \mathcal{T}_{\mathrm{pro/ret}}[(\mathcal{E}_i)_k]}} \mathbf{F}_{\mathrm{cyto}}(\mathbf{x}_i, t) \,. \tag{A39}$$

---

[2] In the specific case of our Cellular Potts model, this corresponds to a situation where some membrane segments $(\mathcal{E}_i)_k \in \mathcal{M}$ are selected more often than other membrane segments, to perform a protrusion or retraction attempt during a Monte Carlo step.

If the cell cannot form adhesions to the underlying substrate at all, then it is not able to counteract the contractile forces originating from its actomyosin cortex. Then, as discussed in the previous paragraph, the cell would detach from the underlying substrate and round up its three-dimensional cell body. By taking the time average of Eq. (A39), we find

$$\left\langle \mathbf{T}_{\text{cyto}}(\mathbf{x}_i, t) \right\rangle_t = - \mathbf{F}_{\text{cyto}}(\mathbf{x}_i, t) . \tag{A40}$$

Thus, the contribution of protrusive forces to the traction force is finite on average.

The total traction forces, which stem from contractile and protrusive cellular forces, are then given by:

$$\mathbf{T}(\mathbf{x}_i, t) = \mathbf{T}_{\text{cont}}(\mathbf{x}_i, t) + \mathbf{T}_{\text{cyto}}(\mathbf{x}_i, t) . \tag{A41}$$

As discussed in section A 1 "Mathematical Representation of the Substrate", the substrate is defined by a triangular lattice with time-dependent nodes $\{\mathbf{x}_i(t)\}_{i=1,\dots,N}$. To describe the substrate deformations that arise as a consequence of cellular traction forces, we consider two different substrate models, as discussed in the following.

b. Overstretched substrate model. In our first approach, we model substrate elasticity by coupling any two neighboring nodes $\mathbf{x}_i$ and $\mathbf{x}_j \in \mathcal{N}_i$ via loaded (i.e., "overstretched") springs of zero rest length:

$$\zeta \, \partial_t \mathbf{x}_i(t) = \mathbf{T}(\mathbf{x}_i, t) + k \sum_{\mathbf{x}_j \in \mathcal{N}_i} \left[\mathbf{x}_j(t) - \mathbf{x}_i(t) \right] , \tag{A42}$$

where each node is subject to a viscous damping with friction ζ and a traction force $\mathbf{T}$. By assuming the rest length of the springs to be zero, we enforce a strictly linear response of the substrate to traction forces. In the absence of traction forces $\mathbf{T}$, periodic boundary conditions ensure that the lattice returns to its "rest state", i.e., its undeformed reference configuration. In this "rest state", any two neighboring nodes $\mathbf{x}_i$ and $\mathbf{x}_j \in \mathcal{N}_i$ are separated by their initial distance d_0, cf. Eq. (A3).

c. Understretched substrate model. For our second approach, we start with the force-deflection relationship (Hooke's law) of a spring that has a finite rest length l_0. This spring connects two neighboring nodes $\mathbf{x}_i$ and $\mathbf{x}_j \in \mathcal{N}_i$:

$$\mathbf{F}_{ij} = k \left[\|\mathbf{x}_j - \mathbf{x}_i\| - l_0 \right] \frac{\mathbf{x}_j - \mathbf{x}_i}{\|\mathbf{x}_j - \mathbf{x}_i\|} . \tag{A43}$$

17

By setting the rest length to zero, $l_0 \to 0$, one would recover Eq. (A42). In the following, however, we assume that the spring rest length is given by the initial distance between any two neighboring nodes, $l_0 = d_0$, cf. Eq. (A3). To proceed, we express the time-dependent position of each node, relative to its initial position, via the displacement $\mathbf{u}_i(t)$:

$$\mathbf{x}_i(t) = \mathbf{x}_i(0) + \mathbf{u}_i(t) \,. \tag{A44}$$

Furthermore, we also introduce the relative displacement of two neighboring nodes,

$$\mathbf{u}_{ij}(t) = \mathbf{u}_j(t) - \mathbf{u}_i(t) \,, \tag{A45}$$

and the unit vector which connects two neighboring nodes in the undeformed reference configuration,

$$\hat{\mathbf{e}}_{ij} = \frac{\mathbf{x}_j(0) - \mathbf{x}_i(0)}{d_0} \,. \tag{A46}$$

For sufficiently small deformation gradients, i.e., an "understretched" spring lattice, we can then use

$$\|\mathbf{x}_j - \mathbf{x}_i\|^2 \approx d_0^2 \left[1 + 2\,\frac{\hat{\mathbf{e}}_{ij} \cdot \mathbf{u}_{ij}(t)}{d_0} \right] \,, \tag{A47}$$

to linearize the force-deflection relationship in terms of the relative node displacements. Then, we finally obtain the following constitutive relation for the spatio-temporal evolution of each lattice node [15]:

$$\zeta\, \partial_t \mathbf{x}_i(t) = \mathbf{T}(\mathbf{x}_i, t) + k \sum_{\mathbf{x}_j \in \mathcal{N}_i} \left[\hat{\mathbf{e}}_{ij} \cdot \mathbf{u}_{ij}(t) \right] \hat{\mathbf{e}}_{ij} \,, \tag{A48}$$

where each node is subject to a viscous damping with friction ζ and a traction force $\mathbf{T}$.

d.   Comparison to continuum linear theory of elasticity.   Now, we discuss how our two lattice spring models of the substrate relate to a description within the continuum linear theory of elasticity. To that end, we apply a smooth deformation field $\mathbf{u}(\mathbf{x}, t)$ to an elastic body, whose infinitesimal strain tensor is given by [16]:

$$\boldsymbol{\varepsilon} = \frac{1}{2} \Big[(\boldsymbol{\nabla} \otimes \mathbf{u}) + (\boldsymbol{\nabla} \otimes \mathbf{u})^T \Big] \,, \tag{A49}$$

where $\otimes$ refers to an outer product. The corresponding elastic stress tensor is then given by [16]:

$$\boldsymbol{\sigma}_{\mathrm{el}} = 2\mu_{\mathrm{el}}\,\boldsymbol{\varepsilon} + \boldsymbol{I}\,\lambda_{\mathrm{el}}\,\mathrm{tr}\,\varepsilon \,, \tag{A50}$$

where μ_{el} refers to the shear modulus (first Lamé parameter), λ is the second Lamé parameter and $\boldsymbol{I}$ is the identity tensor. Assuming that the elastic body intersperses with a fluid that is stationary in the laboratory frame, the equation of motion for a parcel of the elastic body is then given by

$$\zeta_{\mathrm{fl}}\,\partial_t \mathbf{u}(\mathbf{x},t) = \mathbf{f}(\mathbf{x},t) + \mathbf{f}_{\mathrm{el}}(\mathbf{x},t)\,. \tag{A51}$$

Here, ζ_{fl} is the coefficient of friction between the elastic body and the fluid, $\mathbf{f}(\mathbf{x},t)$ is a *driving* force density, and $\mathbf{f}_{\mathrm{el}}(\mathbf{x},t) = \boldsymbol{\nabla} \cdot \boldsymbol{\sigma}_{\mathrm{el}}$ is the elastic body force:

$$\mathbf{f}_{\mathrm{el}}(\mathbf{x},t) = \mu_{\mathrm{el}}\Big[\Delta \mathbf{u}(\mathbf{x},t)\Big] + (\lambda_{\mathrm{el}} + \mu_{\mathrm{el}})\,\boldsymbol{\nabla}\Big[\boldsymbol{\nabla} \cdot \mathbf{u}(\mathbf{x},t)\Big]\,. \tag{A52}$$

The first term and the second term of Eq. (A51) are analogous to their counterparts in Eqs. (A42) and (A48), save for a difference in units between the variables. This difference arises from comparing a continuum theory to discrete theories (i.e., force density per surface area versus node force at a discrete point). What remains is to compare the terms representing an elastic coupling between different regions of the deforming body. To that end, we expand the relative node displacements $\mathbf{u}_{ij} = \mathbf{u}_j - \mathbf{u}_i$ between any two neighboring nodes $\mathbf{x}_i$ and $\mathbf{x}_j \in \mathcal{N}_i$ in terms of the smooth deformation field:

$$\mathbf{u}_{ij} = \sum_{n\in\{x,y\}} \partial_n \mathbf{u}\,d_0\,\hat{e}_{ij}^n + \frac{1}{2}\sum_{n,m\in\{x,y\}} \partial_n\partial_m \mathbf{u}\,d_0^2\,\hat{e}_{ij}^n\,\hat{e}_{ij}^m\,. \tag{A53}$$

Here, n and m represent Cartesian indices, and d_0 corresponds to the distance between two neighboring nodes in the undeformed reference configuration. Furthermore, $\hat{\mathbf{e}}_{ij} \equiv (\hat{e}_{ij}^x, \hat{e}_{ij}^y)$ refers to the unit vector that connects two neighboring nodes in the undeformed reference configuration, cf. Eq. (A46). To transform node forces into an effective surface force density, we use the typical size of a hexagonal tile, $a_0 = d_0^2\sqrt{3}/2$. In the continuum limit, $d_0 \to 0$, we find that the elastic coupling in Eq. (A42) corresponds to a vector Laplacian of the deformation field,

$$\frac{1}{a_0}\sum_{\mathbf{x}_i\in\mathcal{N}_i}\big[\mathbf{x}_j - \mathbf{x}_i\big] = \frac{1}{a_0}\sum_{\mathbf{x}_i\in\mathcal{N}_i}\mathbf{u}_{ij} \approx \sqrt{3}\,\Delta \mathbf{u}\,. \tag{A54}$$

Thus, the "overstretched" model represents an elastic sheet with shear modulus $\mu_{\mathrm{el}} = \sqrt{3}\,k$ and $\lambda_{\mathrm{el}} = -\mu_{\mathrm{el}}$, corresponding to a Poisson ration of $\nu_{2D} = -1$. In contrast, the elastic coupling in Eq. (A48) gives a more complicated expression in the continuum limit,

$$\frac{1}{a_0}\sum_{\mathbf{x}_i\in\mathcal{N}_i}\big[\hat{\mathbf{e}}_{ij}\cdot\mathbf{u}_{ij}(t)\big]\,\hat{\mathbf{e}}_{ij} \approx \frac{\sqrt{3}}{4}\big[\Delta\mathbf{u} + \boldsymbol{\nabla}(\boldsymbol{\nabla}\cdot\mathbf{u})\big]\,. \tag{A55}$$

Thus, the "understretched" model represents an elastic sheet with shear modulus $\mu_{\mathrm{el}} = (\sqrt{3}/4)\,k$ and $\lambda_{\mathrm{el}} = \mu_{\mathrm{el}}$, corresponding to a Poisson ratio of $\nu_{2D} = 1/3$. This simple analysis suggests that one can tune both the effective Poisson ratio and the effective shear modulus of a spring network, via a homogeneous stretching (increase d_0 relative to the spring rest length l_0) or compression (decrease d_0 relative to the spring rest length l_0) of the mesh. Then, the resulting effective model would become a linear superposition of Eqs. (A42) and (A48). In particular, we expect that under homogeneous stretch, the network stiffens and that, at the same time, the effective Poisson ratio can become negative, indicating an auxetic material. In contrast, we expect that under homogeneous compression, the network softens and that it, at the same, gradually becomes incompressible.

e. The substrate does not need to be a compressible material. Surprisingly, both the "overstretched" and the "understretched" model yield very similar cell phenomenology in our simulations, see Fig. S3. Both of these models consider a compressible two-dimensional substrate, i.e., a material with Poisson's ratio $\nu < 1/2$. Furthermore, as discussed in the main text, we find that the dynamics of the cell is significantly coupled to compression and dilatation of the substrate. Thus, one may wonder whether our results are also valid if one considers cell migration on an *incompressible* three-dimensional material, i.e. on a material with Poisson ratio $\nu = 1/2$. In the following, we show that two-dimensional compression or dilatation of the *surface* takes place even if the *bulk* of the material is incompressible. To that end, we consider a linearly elastic half space that is bounded at one side by a plane. This plane acts as the elastic substrate for cell migration. In Ref. [16], a solution for the surface deformation field of such a body, in response to a point force $\mathbf{F}\,\delta(\mathbf{x})$, was derived. For an incompressible substrate, $\nu = 1/2$, and zero normal force, $F_z = 0$, the solution reads [16]:

$$u_x(x, y, 0) = \frac{1}{\mu_{\mathrm{el}}} \frac{1}{4\pi r} \left[F_x + \frac{x}{r^2}(xF_x + yF_y) \right] \tag{A56a}$$

$$u_y(x, y, 0) = \frac{1}{\mu_{\mathrm{el}}} \frac{1}{4\pi r} \left[F_y + \frac{y}{r^2}(xF_x + yF_y) \right] \tag{A56b}$$

$$u_z(x, y, 0) = 0\,. \tag{A56c}$$

Thus, a linearly elastic incompressible half space admits surface compression and dilatation:

$$\boldsymbol{\nabla} \cdot \mathbf{u} = -\frac{1}{\mu_{\mathrm{el}}} \frac{xF_x + yF_y}{4\pi r^3} \neq 0\,. \tag{A57}$$
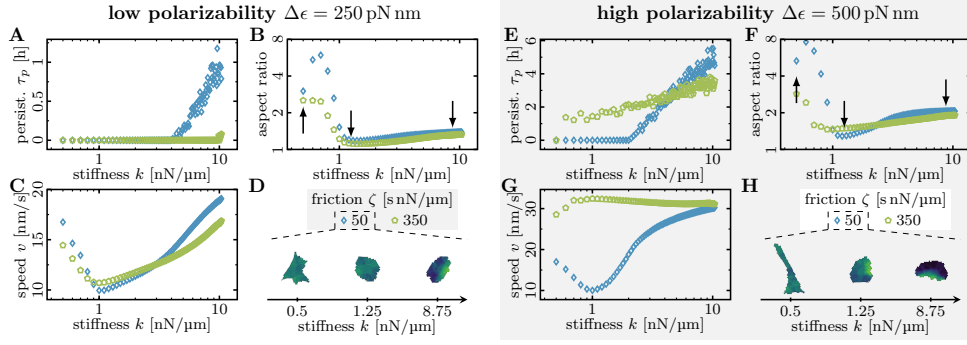
FIG. S3. **Model dynamics on an "understretched" substrate.** There is almost no difference to the dynamics of cells on an "overstretched" substrate, which we show in Fig. 3 of the main text. For very small substrate stiffness, the cells that are placed on the less viscous substrate ($\zeta = 50\,\mathrm{s\,nN\,\mu m^{-1}}$) become rounder again, while the cells on the more viscous substrate ($\zeta = 350\,\mathrm{s\,nN\,\mu m^{-1}}$) elongate (leftmost arrows in panels B and F). This difference to the "overstretched" substrate likely has its origin in the different elastic properties of our substrate models. An "understretched" substrate corresponds to a homogeneous elastic medium with four-fold smaller shear modulus than an "overstretched" substrate with the same spring coefficient.

We conclude that even an incompressible body can undergo changes in surface area.

5. Simulation parameters

In this section, we briefly discuss our choice of parameters. During the initialization of our simulations, we "pre-equilibrated" the cell by letting it grow on a non-deformable substrate for 1000 MCS. This "pre-equilibration" consists of seeding the cell at a single substrate tile and letting the cell grow until it reaches its final size. To that end, we switched off cell motility by deactivating the feedback mechanism [section A 3 e "Mechanochemical feedback"] and setting the polarization field to a fixed value $\epsilon = \epsilon_0$. Finally, we simulated single cells over the course of 10^4 Monte Carlo Steps, each divided into an adaptive amount of substrate update steps. To achieve a cell speed of approximately $20\,\mathrm{nm/s}$, we set the duration of a single Monte Carlo Step to $\Delta t = 20\,\mathrm{s}$. As initial distance between adjacent hexagons, we chose a lattice constant of $d_0 = 1.41\,\mu\mathrm{m}$. Hence, a cell that spreads over an

TABLE S.I. **Simulation parameters**

Parameter	Description	Value(s)
General		
$k_\mathrm{B}T$	effective temperature	$100\,\mathrm{pN\,\mu m}$
Δt	temporal discretization	$20\,\mathrm{s}$
d_0	spatial discretization	$1.41\,\mathrm{\mu m}$
Cell		
ϵ_0	average polarization	$750\,\mathrm{pN\,\mu m}$
$\Delta\epsilon$	polarization range	$500\,\mathrm{pN\,\mu m}$
κ_A	area stiffness	$0.5\,\mathrm{pN/\mu m^3}$
κ_P	perimeter stiffness	$0.75\,\mathrm{pN/\mu m}$
R	intracellular signalling radius	$7.07\,\mathrm{\mu m}$
μ	cytoskeletal update rate	$18/\mathrm{h}$
Substrate		
k	stiffness	0.5 to $10.4\,\mathrm{nN/\mu m}$
ζ	viscous friction	5 to $350\,\mathrm{s\,nN/\mu m}$

area of $400\,\mathrm{\mu m^2}$ will consist of roughly 2.3×10^2 hexagons. The substrate in our simulations is $283\,\mathrm{\mu m}$ long and $245\,\mathrm{\mu m}$ wide, with periodic boundary conditions.

The lower bound on the polarization field, $\epsilon_0 - \Delta\epsilon/2$, and the upper bound on the polarization field, $\epsilon_0 + \Delta\epsilon/2$, represent the ability of the cell to adhere to the substrate and to exert protrusive forces on the cell membrane. Thus, the cell polarization field also models the ability of the cell to generate traction on the substrate, cf. Eq. (A30). Human umbilical vein endothelial cells were measured to exert physiological traction stresses up to $600\,\mathrm{Pa}$ [17]. Furthermore, on average, similar traction stresses were measured in Ref. [18] for NIH 3T3 fibroblasts on a two-dimensional substrate (reaching up to several kPa), and for MDA-MB-231 cells in a three-dimensional environment [19]. To obtain sensible values for the traction forces, we set the average polarization field to $\epsilon = 750\,\mathrm{pN\,\mu m}$ and the polarizability to $\Delta\epsilon = 500\,\mathrm{pN\,\mu m}$. Specifically, given that the typical size of a substrate tile is $a_0 = d_0^2\sqrt{3}/2 = 1.73\,\mathrm{\mu m^2}$, cf. Table S.I, the typical traction stresses in our simulation, $(\epsilon/d_0)/a_0$, range from

200 Pa to 400 Pa. To obtain a cell size of approximately $400\,\mu m^2$ [20], for the area stiffness we chose a value of $\kappa_A = 0.5\,pN/\mu m^3$. To allow for significant fluctuations of the cell membrane and for a polarization of the cell, we chose a perimeter stiffness of $\kappa_P = 0.75\,pN/\mu m$. For the same reason, we also chose an effective temperature that is much larger than room temperature: $k_B T = 100\,pN\,\mu m$. For the remaining parameters, we set the signalling radius to $R = 7.07\,\mu m$ and the polarization update rate to $\mu = 18/h$.

We studied the substrate stiffness in the range of $0.5\,nN/\mu m$ to $10.4\,nN/\mu m$. For an "understretched" substrate with a thickness of $1.41\,\mu m$, this range of spring stiffnesses can be related to an effective elastic modulus ranging from $0.15\,kPa$ to $3.18\,kPa$. Finally, we studied the influence of the viscous friction of the substrate on the cell behavior within a range of $5\,s\,nN/\mu m$ to $350\,s\,nN/\mu m$. For each set of parameters, we performed 100 independent simulations.

6. Measurement of observables

a. Cell coordinates. The geometric center of the cell body is given by

$$\mathbf{x}_c(t) = \frac{\sum_{\mathbf{x}_i \in \mathcal{D}} a(\mathbf{x}_i, t)\,\mathbf{x}_i(t)}{\sum_{\mathbf{x}_i \in \mathcal{D}} a(\mathbf{x}_i, t)}\,. \tag{A58}$$

Analogously, we determine the "center of adhesion" by weighting each tile $\mathbf{x}_i$ with the value of its polarization field $\epsilon(\mathbf{x}_i)$:

$$\mathbf{x}_p(t) = \frac{\sum_{\mathbf{x}_i \in \mathcal{D}} \epsilon(\mathbf{x}_i, t)\,\mathbf{x}_i(t)}{\sum_{\mathbf{x}_i \in \mathcal{D}} \epsilon(\mathbf{x}_i, t)}\,. \tag{A59}$$

b. Cell velocity. The cell velocity is given by the displacement vector of the geometric center of the cell over the course of one Monte Carlo step, $\Delta t = 20\,s$:

$$\mathbf{v}(t) = \partial_t \mathbf{x}_c(t) = \frac{\mathbf{x}_c(t + \Delta t) - \mathbf{x}_c(t)}{\Delta t}\,. \tag{A60}$$

c. Cell polarization vector. We define "cell polarization" as the ability of the cell to choose a leading edge and a trailing edge, and thus its subsequent direction of migration. Furthermore, the cell will always migrate towards regions where the polarization field has a high value, i.e. where the cell adheres more strongly to the substrate and generates higher protrusive forces. Thus, "cell polarization" is concomitant with a shift of the "center of

adhesion", $\mathbf{x}_p(t)$, relative to the geometric center of the cell, $\mathbf{x}_c(t)$, towards the leading edge of the cell:

$$\mathbf{p}(t) = \mathbf{x}_p - \mathbf{x}_c \,. \tag{A61}$$

In the following, we refer to this quantity as the "cell polarization vector".

d. Cell adhesion gradient. We expect that the stochastic motion of the cell will gradually minimize the total energy $\mathcal{H}_{\text{cont}} + \mathcal{H}_{\text{cyto}}$, cf. Eqs. (A23) and (A26). On average, the energy associated with the shape of the cell, $\mathcal{H}_{\text{cont}}$, is invariant since area and perimeter of the cell are constant over time. The corresponding contractile forces are distributed homogeneously throughout the cell, as discussed in section A 3 b "Contractility of the cellular membrane and cortex". In contrast, the energy associated with the polarization field, $\mathcal{H}_{\text{cyto}}$, is highly dynamic and subject to feedback loops that break detailed balance, as discussed in section A 3 e "Mechanochemical feedback". Thus, cell motion is ultimately driven by the energy associated with the polarization field, cf. Eq. (A26), which we can reformulate as a surface integral over the domain $\mathcal{D}$ of the cell

$$\mathcal{H}_{\text{cyto}} = - \int_{\mathcal{D}} d^2\mathbf{x}\, \epsilon(\mathbf{x}, t)\, \rho(\mathbf{x}, t) \,. \tag{A62}$$

Here, $\rho(\mathbf{x}, t) = 1/a(\mathbf{x}, t)$ measures the local surface density of the substrate, i.e. nodes that the cell can adhere to. Furthermore, $\epsilon(\mathbf{x}, t)$ refers to the local polarization field, i.e. a local effective adhesion energy *per substrate tile*. Thus, we conclude that the cell follows gradients of an effective chemical potential, which results in an effective motile force density $\boldsymbol{\nabla}[\epsilon(\mathbf{x}, t)\, \rho(\mathbf{x}, t)]$. Intuitively, one may liken this motile force density to an "adhesion gradient". Consequently, we use Gauss' theorem to define the observable "adhesion gradient":

$$\mathbf{g} = \frac{1}{A} \oint ds\, \hat{\mathbf{n}}\, \epsilon(\mathbf{x}, t)\, \rho(\mathbf{x}, t) \,, \tag{A63}$$

where A refers to the area of the cell, ds is a line element along the boundary of the cell, and $\hat{\mathbf{n}}$ is the unit normal vector perpendicular to the cell boundary. Within our discretized description of the cell, the "adhesion gradient" is thus given by a sum over all elements $(\mathcal{E}_i)_k \in \mathcal{M}$ that line the cell boundary:

$$\mathbf{g} = \frac{\sum_{(\mathcal{E}_i)_k \in \mathcal{M}} \|(\mathcal{E}_i)_k\|\, \mathbf{n}[(\mathcal{E}_i)_k]\, \epsilon(\mathbf{x}_i, t)\, \rho(\mathbf{x}_i, t)}{\sum_{\mathbf{x}_i \in \mathcal{D}} a(\mathbf{x}_i, t)} \,. \tag{A64}$$

where $\mathbf{n}[(\mathcal{E}_i)_k] = \Delta\mathbf{x}_{\text{pro}}[(\mathcal{E}_i)_k]/\|\Delta\mathbf{x}_{\text{pro}}[(\mathcal{E}_i)_k]\|$ refers to the unit normal vector of the cell boundary, cf. Eq. (A17).

e. Cell shape. To determine the aspect ratio of the cell, we perform a principal components analysis of the cell-substrate contact area. Specifically, we consider the covariance matrix of the point cloud that represents the domain of the cell:

$$\text{Cov}(\mathcal{D}) = \frac{\sum_{\mathbf{x}_i \in \mathcal{D}} a(\mathbf{x}_i)\,(\mathbf{x}_i - \mathbf{x}_c) \otimes (\mathbf{x}_i - \mathbf{x}_c)}{\sum_{\mathbf{x}_i \in \mathcal{D}} a(\mathbf{x}_i)}\,, \tag{A65}$$

where $\otimes$ refers to an outer product and $\mathbf{x}_c$ is the geometric center of the cell. Then, the short and long axis of the cell are given by the two eigenvectors $\mathbf{n}_\pm$ of the covariance matrix $\text{Cov}(\mathcal{D})$, which correspond to a smaller and a larger eigenvalue $\lambda_\pm^2$, respectively:

$$\text{Cov}(\mathcal{D})\,\mathbf{n}_\pm = \lambda_\pm^2\,\mathbf{n}_\pm\,. \tag{A66}$$

The two eigenvalues of the covariance matrix, $\lambda_\pm^2$, measure the variance of the point distributions along the two principal axes of the cell. Thus, the aspect ratio of the cell is given by λ_+/λ_-.

f. Measuring two-dimensional spatial profiles in the co-moving frame. We define the co-moving frame of the cell as follows: its origin lies at the geometric center of the cell, and we parameterize it in polar coordinates relative to the direction of the effective "adhesion gradient" of the cell, $\mathbf{g}$. In the co-moving frame of the cell, the coordinates of some position on the substrate are then defined by $(\tilde{r}, \tilde{\theta}) \equiv \tilde{\mathbf{x}} = \mathbf{x} - \mathbf{x}_c$. To obtain the spatial profile of the typical substrate density field around the cell, we perform a radial and angular binning:

$$\rho(r, \theta) = \left\langle \frac{a_0}{a(\mathbf{x}_i)} \right\rangle_{\tilde{\mathbf{x}}_i \approx (r, \pm\theta)}. \tag{A67}$$

Analogously, we also perform a radial and angular binning to find the probability of encountering an occupied substrate tile at a given position,

$$\text{Prob}(r, \theta) = \frac{\sum_{\tilde{\mathbf{x}}_i \approx (r, \pm\theta)} \Theta(\epsilon(\mathbf{x}_i) - q)}{\sum_{\tilde{\mathbf{x}}_i \approx (r, \pm\theta)} 1}\,, \tag{A68}$$

where Θ is the Heaviside step function. Finally, the spatial profile of the typical polarization field around the cell center is also obtained by radial and angular binning:

$$\tilde{\epsilon}(r, \theta) = \left\langle \epsilon(\mathbf{x}_i) \right\rangle_{\tilde{\mathbf{x}}_i \approx (r, \pm\theta)}. \tag{A69}$$

Here, however, we must be aware that we have averaged over both occupied and free substrate tiles, although the polarization field is only defined on occupied tiles. Therefore, we

25

correct the spatial profile of the polarization field, by accounting for the probability of a substrate tile being occupied:

$$\epsilon(r, \theta) = \frac{\tilde{\epsilon}(r, \theta)}{\text{Prob}(r, \theta)} \, .$$

(A70)

Appendix B: Supplemental discussion

In our model, the cell can exhibit different migratory states, depending on the mechanical properties of the substrate: *running*, *rounding* and *elongation*. Complementary to the discussion in the main text, in the sections below we provide a more extensive explanation of the phenomenology.

1. Persistence time of directed migration

The persistence time of directed migration, τ_p, represents the typical time over which the cell decorrelates (in other words reorients) the direction in which it migrates. In Ref. [2], it was shown that the migration of a polarized cell in the Cellular Potts model [1, 2] can be described with a persistent random walk model. Specifically, the mean squared displacement of the cell,

$$\left\langle R(\tau)^2 \right\rangle = \left\langle \|\mathbf{x}_c(t+\tau) - \mathbf{x}_c(t)\|^2 \right\rangle, \tag{B1}$$

shows that the cell moves ballistically on short timescales and diffusively on long timescales. Here, the angular brackets $\langle \dots \rangle$ denote an average over the simulation time t and over 100 independent simulations. To obtain a numerical value for the persistence time of directed migration, τ_p, which measures the typical time of crossover from ballistic to diffusive motion, we fit the mean squared displacement with a persistent random walk model [21, 22]:

$$\left\langle R(\tau)^2 \right\rangle = 2v^2 \tau_p^2 \left[\tau/\tau_p + e^{-\tau/\tau_p} - 1 \right]. \tag{B2}$$

For this fitting procedure, we use the Nelder-Mead method with two fit parameters, v and τ_p, as implemented in the python package "lmfit" [23]. As another hallmark of a persistent random walk, the velocity autocorrelation function of the cell decays exponentially on sufficiently long timescales. This exponential decay also captures the persistence time of directed migration of the cell. In addition, as we discuss below, there are several measures that can be used to describe the behavior of the cell in our simulations.

a. Velocity autocorrelation function. First, we further investigate the normalized velocity autocorrelation function (VACF), which is defined by

$$C_v(\tau) = \left\langle \frac{\mathbf{v}(t+\tau)}{\|\mathbf{v}(t+\tau)\|} \cdot \frac{\mathbf{v}(t)}{\|\mathbf{v}(t)\|} \right\rangle. \tag{B3}$$

high polarizability $\Delta\epsilon = 500\,\mathrm{pN\,\mu m}$
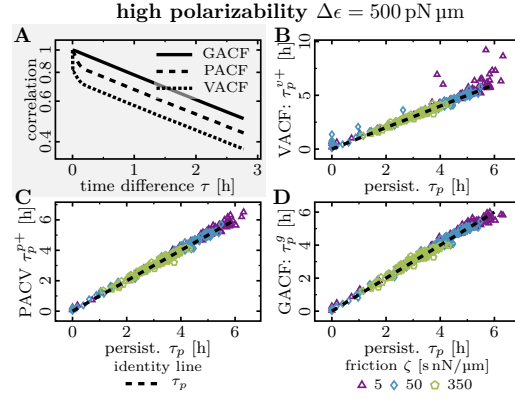
FIG. S4. **Correlation functions and measurement of persistence time of directed migration.** (A) Exemplary correlation functions of a cell that migrates on a stiff substrate, $k = 5\,\mathrm{nN/\mu m}$, with low viscous friction $\zeta = 50\,\mathrm{s\,nN/\mu m}$. The normalized velocity autocorrelation function (VACF), C_v, exhibits a sharp drop at $t = 0$, followed by a bi-exponential decay with a short and a long timescale. The sharp drop at $t = 0$ can be attributed to the "randomness" in the protrusion and retraction process (noise). In the normalized polarization vector autocorrelation function (PACF), C_p, noise is integrated out, and only the bi-exponential decay remains. The normalized gradient autocorrelation function (GACF), C_g, which measures the actual reorientation of the gradient of the polarization field, shows a mono-exponential decay (all shorter timescales are integrated out). (B-D) For all measured parameter sets, the timescales obtained by fitting the mean-squared displacement (MSD) to a persistent random walk model coincide with the (long) timescales of the VACF (panel B), the PACF (panel C) and the GACF (panel D). Thus, these are all equivalent measures for the persistence time of directed migration of the cell.

Here, the angular brackets $\langle \ldots \rangle$ denote an average over the simulation time t and over 100 independent simulations. Empirically, we find that the normalized velocity autocorrelation function is well described by a bi-exponentional decay [Fig. S4A]:

$$C_v(\tau) = a\,e^{-\tau/\tau_p^{v-}} + b\,e^{-\tau/\tau_p^{v+}} + (1 - a - b)\,\delta_{t,0}\,, \tag{B4}$$

which we fit to our simulated data using the Nelder-Mead method and four fit parameters, $\tau_p^{v+} > \tau_p^{v-}$ and $b > a$. The spike at $t = 0$ captures the rapid drop of the velocity autocorrelation function, C_v, from its initial value of 1 to a significantly smaller value of $a + b$, in the

very first time step. This initial drop comes from the stochasticity of our simulations, where protrusions and retractions are random events that are biased by the local polarization field, ϵ. In the following, we extract the information that the magnitude of this drop, which we refer to as "noise strength", contains about the cell dynamics in our simulations.

b. Cell speed and the stochasticity of events.   Before we proceed, we remind that the cell is more likely to protrude in regions that have a high value of the polarization field, ϵ, and is more likely to retract in regions with a low value of the polarization field. Therefore, we interpret the polarization field as an effective "adhesion energy" per individual substrate tile. We then measure the "adhesion gradient" of a cell, $\mathbf{g} = \langle \boldsymbol{\nabla}(\rho\,\epsilon) \rangle$, as discussed in detail in sections A 6 c "Cell polarization vector" and B 1 d "Orientation autocorrelation function". This "adhesion gradient" indicates the direction in which more protrusion events occur than retraction events.

On sufficiently long timescales (i.e., when many protrusion and retraction events occur), this bias becomes visible in a net translocation of the cell. Then, the cell shows a persistent random walk and a (bi-)exponentially decaying velocity autocorrelation function [Fig. S4A]. Therefore, we observe a long (dominant) timescale τ_p^{v+} that coincides with the persistence time of directed migration τ_p [Fig. S4B], and determines the long-term cell behavior. However, on short timescales, it becomes difficult to discern whether individual events are truly biased or, instead, actually random. Thus, we identify the initial drop in the velocity autocorrelation function, $1 - a - b$, as an effective "noise strength". This "noise strength" can be increased by either (a) decreasing the bias conferred by the polarization field, ϵ, or (b) increasing the effective temperature $k_{\mathrm{B}}T$ in our simulations, see Eq. (A21). A stronger random contribution to the processes of protrusion and retraction then directly leads to a broader cell velocity distribution around the effective adhesion gradient and thus to a lower cell speed.

One can illustrate these effects as follows: Consider a cell that has a pronounced profile in the polarization field, which acts as an effective adhesion energy per substrate tile. Then, in the low temperature limit ($\beta \to \infty$), the cell will *always* protrude at the location of the highest effective adhesion energy density and *always* retract at the location of the lowest effective adhesion energy density, thus leading to a narrow cell velocity distribution. In this case, because each individual protrusion and retraction event displaces the cell in the same
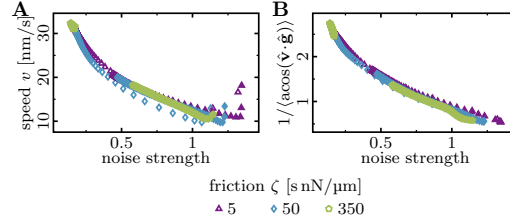
FIG. S5. **Stochasticity of the protrusion and retraction processes in our simulations.** (A) The cell speed decreases with increasing "noise strength", which encodes the stochasticity of the protrusion and retraction processes. We determine this "noise strength" from Eq. (B4). (B) A smaller "noise strength" corresponds to a narrower distribution of the cell velocities around the effective adhesion gradient of the cell. Filled symbols correspond to a low polarizability of the cell, $\Delta\epsilon = 250 \, \text{pN} \, \mu\text{m}$, while empty symbols correspond to a high polarizability of the cell, $\Delta\epsilon = 500 \, \text{pN} \, \mu\text{m}$. We find that all measurement points lie on the same curve.

direction and the total number of such events per Monte Carlo Step is limited, one observes a high cell translocation speed. Conversely, in the high temperature limit $(\beta \to 0)$, cell protrusions and retractions are completely unaffected by the spatial profile of the polarization field, leading to a uniform cell velocity distribution. In this case, because all individual protrusion and retraction events displace the cell in different directions and the total number of such events per Monte Carlo Step is limited, one observes a negligible cell translocation speed.

We conclude that the cell will migrate faster if one increases the bias for individual protrusion and retraction events to align with the effective adhesion gradient of the cell. One can measure this alignment via the width of the (symmetric) velocity distribution, around the direction of the effective adhesion gradient of the cell. Alternatively, one can also determine the overall randomness of the protrusion and retraction processes ("noise strength"), from Eq. (B4). For both measurements, we consistently find that the cell speed increases for narrower cell velocity distributions and for smaller "noise strength" [Fig. S5]. Thus, we find that the VACF contains valuable information about the dynamics of the cell. In general, however, a robust measurement of the current orientation of the cell requires an observable that is less sensitive to noise. Thus, we next set out to measure the current *polarization* of the cell.

c. Polarization autocorrelation function. So far, we have discussed the mean-squared displacement and the normalized velocity autocorrelation function of the cell. We have found that the normalized velocity autocorrelation function is very sensitive to noise, because it is tightly connected to the stochastic protrusion and retraction dynamics of the cell. To gain further insights into the process of cell repolarization, we now turn towards the dynamics of the polarization field. As discussed in section A 6 c "Cell polarization vector", we define a vector quantity that always points from the geometric center of the cell towards its "center of adhesion",

$$\mathbf{p}(t) = \mathbf{x}_p - \mathbf{x}_c \,, \tag{B5}$$

which we refer to as "cell polarization vector". The cell polarization vector is always oriented towards that side of the cell which has larger values of the polarization field ϵ. Furthermore, we remind that regions of the cell that have high values of the polarization field ϵ favor protrusive activity, while retractions occur most frequently in regions with low values of the polarization field. Thus, the "cell polarization vector" determines the cell's future direction of motion and its leading (protruding) edge. We measure the gradual reorientation of the cell polarization vector by computing the normalized polarization vector autocorrelation function (PACF):

$$C_p(\tau) = \left\langle \frac{\mathbf{p}(t+\tau)}{\|\mathbf{p}(t+\tau)\|} \cdot \frac{\mathbf{p}(t)}{\|\mathbf{p}(t)\|} \right\rangle \,. \tag{B6}$$

Here, the angular brackets $\langle \dots \rangle$ denote an average over the simulation time t and over 100 independent simulations. In contrast to the normalized velocity autocorrelation function, C_v, we do not observe a sharp drop at $t = 0$ in the normalized polarization vector autocorrelation function [Fig. S4A]. In addition, similarly to the normalized velocity autocorrelation function, we observe that the normalized polarization vector autocorrelation function, C_p, also exhibits a bi-exponential decay [Fig. S4A]:

$$C_p(\tau) = a \, e^{-\tau/\tau_p^{p-}} + (1-a) \, e^{-\tau/\tau_p^{p+}} \,, \tag{B7}$$

which we fit to our simulated data using the Nelder-Mead method and three fit parameters, $\tau_p^{p+} > \tau_p^{p-}$ and a. We now further illustrate the twofold relationship between the polarization vector $\mathbf{p}$ and the velocity vector $\mathbf{v}$, and their respective normalized autocorrelation functions C_p and C_v. On the one hand, the polarization vector $\mathbf{p}$ determines the *future* direction in which the cell will migrate. In particular, as discussed above, the cell will typically move its

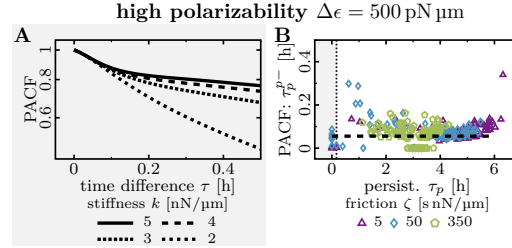**high polarizability** $\Delta\epsilon = 500\,\mathrm{pN}\,\mu\mathrm{m}$

FIG. S6. **Polarization vector autocorrelation function and its short timescale dynamics.** (A) Semi-logarithmic plot of several exemplary polarization vector autocorrelation functions for different substrate stiffness (as indicated by the legend). At short timescales, $\tau < 0.1\,\mathrm{h}$, all correlation functions decay identically. (B) The short timescale of the polarization vector autocorrelation function (PACF), τ_p^{p-}, corresponds to the typical timescale of cytoskeletal reorganization (dashed line). Consequently, the short timescale τ_p^{p-} is independent of the persistence time of directed migration, τ_p, for different values of substrate stiffness and viscous friction (as indicated by the legend).

geometric center towards its "center of adhesion". In addition to this bias due to the spatial distribution of the polarization field ϵ, each individual protrusion and retraction event is a stochastic process. These stochastic events serve as a source of noise for the instantaneous velocity vector $\mathbf{v}$, cf. section B 1 a "Velocity autocorrelation function" and Eq. (A21). On the other hand, the instantaneous velocity of the cell affects the polarization field ϵ and the corresponding polarization vector $\mathbf{p}$ via a dynamic feedback. Specifically, individual protrusion and retraction events induce signaling cascades that lead to a reorganization of the cell cytoskeleton (i.e., the landscape of the polarization field) on a typical timescale of $1/\mu \sim 0.06\,\mathrm{h}$, cf. section A 3 e "Mechanochemical feedback". We summarize these interactions graphically as follows:
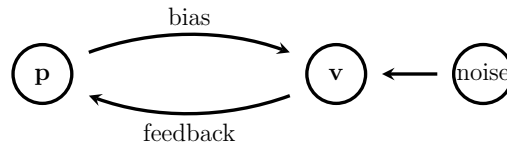
This allows us to rationalize the origin of the two different timescales, τ_p^{p-} and τ_p^{p+}, as follows. First, suppose that we decouple the instantaneous cell velocity $\mathbf{v}$ from the cell po-

larization vector $\mathbf{p}$ by removing the "bias" for migration, while keeping the "noise" and the "feedback" mechanisms intact. Then, the polarization vector $\mathbf{p}$ will follow the instantaneous cell velocity $\mathbf{v}$ with a typical timescale (i.e., memory) of $1/\mu \sim 0.06\,\text{h}$. In particular, the timescale $1/\mu$ represents a lower bound for the time that is required to reorganize the cell cytoskeleton, cf. section A 3 e "Mechanochemical feedback". In good agreement with this reasoning, we find that the short timescale corresponds to the timescale of cytoskeletal reorganization, $\tau_p^{p-} \approx 1/\mu$, for all persistently migrating cells [Fig. S6]. Finally, (re)activating the "bias" for migration will couple the instantaneous cell velocity $\mathbf{v}$ to the cell polarization vector $\mathbf{p}$ by introducing a memory. Then, the interplay between the strength of the "bias", the strength of the "noise", and the memory will lead to the emergence of a second timescale that reflects the persistence time of directed migration of the cell $\tau_p^{p+} = \tau_p$ [Fig. S4C]. If one gradually increases the "bias" or decreases the "noise", then the trajectory of the cell will gradually approach a straight line and the persistence time of directed migration will grow. In contrast, by decreasing the "bias" or increasing the "noise", one can reduce the persistence time of directed migration until it becomes indistinguishable from the (short) timescale of cytoskeletal reorganization, $\tau_p^{p-} \approx 1/\mu$. Thus, the timescale separation in the bi-exponential fit fails for very small persistence times, resulting in a large spread of the fitted values for the short timescale [Fig. S6B].

d. Orientation autocorrelation function.   So far, we have investigated the dynamics of the polarization field via the cell polarization vector $\mathbf{p}$, which corresponds to the distance vector between the geometric center of the cell and the cell's "center of adhesion", cf. sections A 6 c "Cell polarization vector" and B 1 c "Polarization autocorrelation function". Thus, the cell polarization vector $\mathbf{p}$ is affected both by changes in the geometric center of the cell and by changes in the "center of adhesion" of the cell. Furthermore, we have seen that the polarization vector $\mathbf{p}$, which determines the future direction of migration of the cell, exhibits two characteristic timescales τ_p^{p-} and τ_p^{p+}, cf. section B 1 c "Polarization autocorrelation function". The short timescale, τ_p^{p-}, corresponds to the timescale of cytoskeletal reorganization. The long timescale, τ_p^{p+}, faithfully captures the macroscopic migratory behavior of the cell, i.e., its persistence time of directed migration [Fig. S4C]. In the following, we discuss how one can robustly determine the instantaneous geometric orientation of the cell, which requires a measure that only exhibits the long timescale τ_p^{p+} while

integrating out the short timescale τ_p^{p-}. To do so, we can choose between several different procedures: (a) perform a sliding window average of the cell polarization vector $\mathbf{p}$, (b) track both principal axes of the cell via a principal components analysis [cf. section A 6 e "Cell shape"], or, as we see below, (c) determine the average *gradient* of the polarization field as a proxy for cell orientation. Our basic idea is that the average (macroscopic) gradient of the polarization field is tightly coupled to the cell orientation, and should move affinely with the cell geometry. In contrast, the microscopic intracellular dynamics are much faster than the macroscopic motion of the cell. We expect that the microscopic "noise" in the form of stochastic protrusions and retractions, which induces a short-timescale decay in the polarization vector autocorrelation function [cf. section B 1 c "Polarization autocorrelation function"], does not significantly affect the *average* gradient of the polarization field.

Thus, to measure the instantaneous orientation of the cell, we compute the average "adhesion gradient", $\langle \boldsymbol{\nabla}(\rho\,\epsilon) \rangle$, by making use of Gauss' theorem [section A 6 d "Cell adhesion gradient"]:

$$\mathbf{g} = \frac{1}{A} \oint ds\,\hat{\mathbf{n}}\left[\epsilon(\mathbf{x}, t)\,\rho(\mathbf{x}, t)\right]. \tag{B8}$$

Here, $\epsilon(\mathbf{x}, t)$ refers to the local polarization field, i.e., a local effective adhesion energy *per substrate tile*, and $\rho(\mathbf{x}, t)$ refers to the local substrate density. To verify whether the "adhesion gradient" exhibits only one timescale corresponding to the persistence time of directed migration, we compute the normalized gradient autocorrelation function (GACF) as follows:

$$C_g(\tau) = \left\langle \frac{\mathbf{g}(t + \tau)}{\|\mathbf{g}(t + \tau)\|} \cdot \frac{\mathbf{g}(t)}{\|\mathbf{g}(t)\|} \right\rangle. \tag{B9}$$

Here, the angular brackets $\langle \dots \rangle$ denote an average over the simulation time t and over 100 independent simulations. Empirically, we find that the normalized gradient autocorrelation function is well described by an exponential decay [Fig. S4A]:

$$C_g(\tau) = e^{-\tau/\tau_p^g}, \tag{B10}$$

which we fit to our simulated data using the Nelder-Mead method and one fit parameter, τ_p^g. As expected, we find that the typical time that is required for a reorientation of the "adhesion gradient" corresponds to the timescale of persistent cell migration [Fig. S4D]. Note that this approach for measuring cell orientation is limited to *polarized* cells. To measure the orientation of unpolarized cells, one must rely on a principal components analysis [cf. section A 6 e "Cell shape"], which, however, requires elongated cells.

To summarize, we have shown that the long-term behavior of the cell (i.e., its persistence time of directed migration) can be determined from the mean-squared displacement of the cell, the velocity autocorrelation function, polarization autocorrelation function, or the gradient autocorrelation function alike. Each approach gives quantitatively identical results in a consistent way [Fig. S4B-D]. Cell orientation can be robustly measured via the "adhesion gradient" [section A 6 d "Cell adhesion gradient"] or via a principal components analysis of the cell shape [section A 6 e "Cell shape"].

2. Cell Trapping

In this section, we briefly discuss which conditions the mechanical properties of the substrate have to meet, so that the cell stops performing a persistent random walk and becomes self-trapped. For quickly responding substrates, e.g., low substrate viscous friction, the normalized velocity autocorrelation function (VACF) oscillates if the substrate stiffness falls below a threshold value of $k^\star = 1.58\,\mathrm{nN/\mu m}$ [Fig. S7A]. Then, the mean-squared displacement of the cell also deviates from that of a persistent random walk model [Fig. S7B], and a typical persistence time of directed cell migration cannot be determined anymore. We identify this behavior, which leads to a decrease in overall cell motility, as cell trapping, or as cell *rounding* because of the corresponding cell shape.

To test our computational results, we measured the cell trajectories of wild-type HUVECs plated on polyacrylamide gels, as described in the Methods section of the main text. We have already seen in the main text that HUVECs move faster if their substrate is stiffer, in qualitative agreement with our model. We complement this by plotting the cell trajectories in Fig. S7E, which also show that cells are more motile on stiffer substrates. Furthermore, as Fig. S7C shows, there are anti-correlations in the VACF for $E < E^\star \approx 7\,\mathrm{kPa}$, which indicates cell trapping.

3. Cell Elongation on Soft Substrates Does Not Depend on Cell Polarizability

We have seen that cells can elongate drastically on very soft substrates that have a small value of viscous friction [cf. Fig. 3B,F in the main text and Fig. S3B,F]. This observation can be explained in the following way: Due to the inhibition of the positive feedback mechanism,
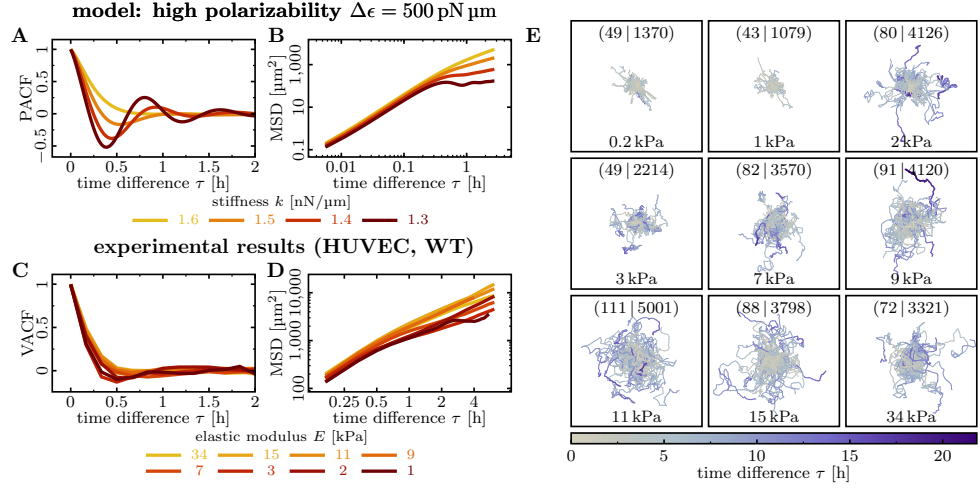
model: high polarizability $\Delta\epsilon = 500\,\mathrm{pN\,\mu m}$

A PACF

B MSD [μm^2]

stiffness k [nN/µm]
1.6   1.5   1.4   1.3

experimental results (HUVEC, WT)

C VACF

D MSD [μm^2]

elastic modulus E [kPa]
34   15   11   9
7   3   2   1

E

(49 | 1370)   (43 | 1079)   (80 | 4126)
0.2 kPa   1 kPa   24 kPa

(49 | 2214)   (82 | 3570)   (91 | 4120)
3 kPa   7 kPa   9 kPa

(111 | 5001)   (88 | 3798)   (72 | 3321)
11 kPa   15 kPa   34 kPa

time difference τ [h]

FIG. S7. **Persistent cell motion and self-trapping.** (A) Velocity autocorrelation function (VACF) of simulated cells, for different substrate stiffness (indicated by the legend). For $k < k^\star = 1.58\,\mathrm{nN/\mu m}$, we observe oscillations in the VACF. The frequency of these oscillations increases with substrate stiffness, k. (B) Mean-squared displacement, corresponding to the VACF shown in panel A. For $k < k^\star = 1.58\,\mathrm{nN/\mu m}$ we observe a saturation of the mean-squared displacement. Panels A and B strongly indicate cell trapping, where cells switch from the *running* to the *rounding* state. (C) Velocity autocorrelation function (VACF) of wild-type HUVECs plated on polyacrylamide gels of different stiffness (indicated by the legend). For $E < E^\star \approx 7\,\mathrm{kPa}$, we observe anti-correlations in the VACF ($C_v < 0$). *Note:* We excluded the data point at $0.2\,\mathrm{kPa}$, because the cells dramatically changed their mode of migration and ceased to form lamellipodia. Specifically, we observed that cells now migrated preferably along their long axis. (D) Mean-squared displacement of wild-type HUVECs plated on polyacrylamide gels, corresponding to the VACF shown in C. (E) Cell trajectories in the experiments. Substrate stiffness is indicated at the bottom of the panels. Number of measured trajectories N_T and measured data points N_P are indicated by $(N_T \,|\, N_P)$ at the top of the panels. Color code corresponds to the elapsed time in the respective trajectory (colorbar).

the cell is unpolarized. Hence, its behavior is dominated by the substrate density profile alone, and is indeed the same for cells of a wide range of different polarizabilities $\Delta\epsilon$ [Fig. S8],

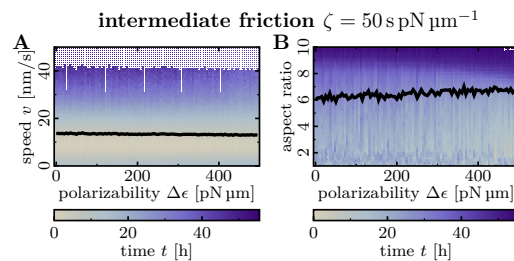**intermediate friction** $\zeta = 50\,\mathrm{s\,pN\,\mu m^{-1}}$

FIG. S8. **Cell extension.** The *elongation* state, which is characterized by (A) low cell speed and (B) strong cell elongation, is independent of the cell polarizability $\Delta\epsilon$. The color code represents the current elapsed time of a given cell trajectory in the simulation (color bar).

but identical average traction force. This particular substrate density profile is characterized by an increased substrate density at the short sides of the cell compared to the long sides of the cell. Hence, the cell has an increased protrusion activity at its short sides and subsequently stretches, as it tries to occupy areas of high substrate density. These effects do not depend on the polarizability of the cell, as the cell remains unpolarized.

[1] F. J. Segerer, F. Thüroff, A. Piera Alberola, E. Frey, and J. O. Rädler, Emergence and persistence of collective cell migration on small circular micropatterns, Phys. Rev. Lett. **114**, 228102 (2015).

[2] F. Thüroff, A. Goychuk, M. Reiter, and E. Frey, Bridging the gap between single-cell migration and collective dynamics, eLife **8**, 10.7554/elife.46842 (2019).

[3] S. Tojkander, G. Gateva, and P. Lappalainen, Actin stress fibers – assembly, dynamics and biological roles, J. Cell Sci. **125**, 1855 (2012).

[4] H. Herrmann, H. Bär, L. Kreplak, S. V. Strelkov, and U. Aebi, Intermediate filaments: from cell architecture to nanomechanics, Nat. Rev. Mol. Cell Biol. **8**, 562 (2007).

[5] C. Sultan, D. Stamenović, and D. E. Ingber, A computational tensegrity model predicts dynamic rheological behaviors in living cells, Ann. Biomed. Eng. **32**, 520 (2004).

[6] D. Tsuruta and J. C. R. Jones, The vimentin cytoskeleton regulates focal contact size and adhesion of endothelial cells subjected to shear stress, J. Cell Sci. **116**, 4977 (2003).

[7] F. Graner and J. A. Glazier, Simulation of biological cell sorting using a two-dimensional extended Potts model, Phys. Rev. Lett. **69**, 2013 (1992).

[8] T. D. Pollard and G. G. Borisy, Cellular motility driven by assembly and disassembly of actin filaments, Cell **112**, 453 (2003).

[9] A. Mogilner and K. Keren, The shape of motile cells, Curr. Biol. **19**, R762 (2009).

[10] D. A. Lauffenburger and A. F. Horwitz, Cell migration: A physically integrated molecular process, Cell **84**, 359 (1996).

[11] R. G. Hodge and A. J. Ridley, Regulating rho gtpases and their regulators, Nature Reviews Molecular Cell Biology **17**, 496 (2016).

[12] C. D. Lawson and A. J. Ridley, Rho gtpase signaling complexes in cell migration and invasion, Journal of Cell Biology **217**, 447 (2018).

[13] A. F. M. Marée, A. Jilkine, A. Dawes, V. A. Grieneisen, and L. Edelstein-Keshet, Polarization and movement of keratocytes: A multiscale modelling approach, Bull. Math. Biol. **68**, 1169 (2006).

[14] A. F. M. Marée, V. A. Grieneisen, and L. Edelstein-Keshet, How cells integrate complex stimuli: The effect of feedback from phosphoinositides and cell shape on cell polarization and motility, PLOS Comput. Biol. **8**, e1002402 (2012).

[15] M. G. Yucht, M. Sheinman, and C. P. Broedersz, Dynamical behavior of disordered spring networks, Soft Matter **9**, 7000 (2013).

[16] L. D. Landau, L. P. Pitaevskii, A. M. Kosevich, and E. M. Lifshitz, *Theory of Elasticity*, third edition ed. (Butterworth-Heinemann, 1986).

[17] T. Pompe, M. Kaufmann, M. Kasimir, S. Johne, S. Glorius, L. Renner, M. Bobeth, W. Pompe, and C. Werner, Friction-controlled traction force in cell adhesion, Biophys. J. **101**, 1863 (2011).

[18] C.-M. Lo, H.-B. Wang, M. Dembo, and Y.-L. Wang, Cell movement is guided by the rigidity of the substrate, Biophys. J. **79**, 144 (2000).

[19] Y. L. Han, P. Ronceray, G. Xu, A. Malandrino, R. D. Kamm, M. Lenz, C. P. Broedersz, and M. Guo, Cell contraction induces long-ranged stress stiffening in the extracellular matrix, Proc. Natl. Acad. Sci. U.S.A. **115**, 4075 (2018).

[20] M. Riaz, M. Versaevel, D. Mohammed, K. Glinel, and S. Gabriele, Persistence of fan-shaped keratocytes is a matrix-rigidity-dependent mechanism that requires $\alpha_5\beta_1$ integrin engagement, Sci. Rep. **6**, 34141 (2016).

38

[21] C. L. Stokes, D. A. Lauffenburger, and S. K. Williams, Migration of individual microvessel endothelial cells: stochastic model and parameter measurement, J. Cell Sci. **99**, 419 (1991).

[22] P. H. Wu, A. Giri, S. X. Sun, and D. Wirtz, Three-dimensional cell migration does not follow a random walk, Proc. Natl. Acad. Sci. U.S.A. **111**, 3949 (2014).

[23] M. Newville, T. Stensitzki, D. B. Allen, and A. Ingargiola, LMFIT: Non-linear least-square minimization and curve-fitting for Python (2014).

IV CELL ORGANIZATION AND MORPHOGENESIS

IV.1 COLLECTIVE CELL MIGRATION AFFECTS MORPHOGENESIS

In Chapter II "Between Protein Patterns and Mechanics", we have first focused on processes related to intracellular organization and pattern formation. Then, in Chapter III "From Cellular Dynamics to Self-Organization", we have switched gears a first time to focus on cell migration and the organization of cells. Now, we switch gears a second time and put the spotlight on a consequence of cellular organization: the morphogenesis of mammary glands. We refer to pages 341–362 for a reprint of the main text and to pages 363–394 for the Supplementary Material. The following serves as an introduction into the project and a summary of its main results, for the convenience of the reader.

Research Contribution. For this project, I developed the theory. In particular, I explained why the trace of the tension tensor is constant in the experiments of our collaborators, and then performed the linear stability analysis for the tube shape. Furthermore, I identified new and related research questions, as discussed in Section IV.2 "Between Morphogenesis and Hydrodynamic Flows".

A note about the notation. We use Y_s for the Young's modulus of the collagen cage instead of E_{cage}, because E is reserved for the nonlinear strain tensor in this thesis.

IV.1.1 STARTING POINT OF THE PROJECT

General Scope and Relevance. Cellular tissues undergo complex shape transformations during morphogenesis (Reece et al., 2014). These shape transformations are driven by the non-equilibrium activity of cells, which shape the growing tissue through collective motion (Lecaudey and Gilmour, 2006) and the generation of active mechanical stresses (Wozniak and Chen,

2009; Gross et al., 2017; Crest et al., 2017; Karzbrun et al., 2018; Petridou, Grigolon, et al., 2019; Münster et al., 2019). In that context, the embryogenesis of the fruit fly *Drosophila melanogaster* is a particularly well-studied example, showing dramatic shape changes during gastrulation (Streichan et al., 2018; Martin, 2020; Gheisari et al., 2020). Another prime example of morphogenesis relates to the formation of branched tubular structures in many organs such as blood vessels (Reece et al., 2014; Carlson, 2019). Some of these tubular organs form a closed network composed of tubular ducts, such as the blood circulatory system (Reece et al., 2014; Carlson, 2019; Wang et al., 2017), while other organs such as the mammary gland have a branched tubular structure that ends with spherical alveoli (Wang et al., 2017). This structure enables the mammary gland, for example, to store milk in the spherical alveoli during lactation (Reece et al., 2014; Carlson, 2019; Inman et al., 2015; Wang et al., 2017), which the mammal offspring then extracts during feeding. In the case of mammary glands, the shape transformation from a tubular geometry to alveoli (alveologenesis), occurs only during the lactation of an adult female mammal (Inman et al., 2015; Wang et al., 2017). This controlled shape transformation makes mammary glands an ideal system for studying epithelial gland morphogenesis (Linnemann et al., 2015; Rios et al., 2019).

Research Question and Hypothesis.   To study the dynamics of mammary gland morphogenesis, we employ a miniaturized and simplified version of the full organ, grown in a collagen gel inside a Petri dish (Linnemann et al., 2015). These *organoids* undergo a shape change from a tubular geometry to spherical alveoli, analogously to the full organ (Linnemann et al., 2015). Here, we ask: *What is the physical basis of this shape transformation?*

IV.1.2   SUMMARY OF THE MAIN RESULTS

Many tissues can be described as fluid-like active materials (Petridou, Grigolon, et al., 2019; Pérez-González et al., 2019; Tetley et al., 2019; He et al., 2014; Maître et al., 2012). The dynamics of such fluid-like tissues are determined by cortical cell tension, such as in the development of ducts (Chatterjee et al., 2019; Neumann et al., 2018) or gastrulation (Streichan et al., 2018). The data of our collaborators suggest this to also be the case for mammary gland organoids, because all tubular structures (organoid branches) quickly vanish by retracting towards the organoid body after enzymatic degradation of the extracellular collagen matrix. Therefore, we describe the cellular epithelium, which forms an interface between a passive fluid in the lumen and a passive elastic solid in the surroundings, as an active fluid-like material (Fig. IV.1a). The entire dynamics of the organoid are then driven by the (contractile) activity of cells.

The shape transformation from a tubular geometry to a spherical geometry in a tension-driven fluid reminds of the classical Rayleigh-Plateau instability, first described for passive isotropic fluids (Lord Rayleigh, 1878). The underlying mechanism of this shape instability is that surface tension "penalizes" surface area. Therefore, sufficiently long columns of fluid break up into droplets with a smaller surface-to-volume ratio. In a cell biological context such as ours, the column of fluid is typically surrounded by an elastic medium instead of air. In the experimental setup of our collaborators, the collagen gel is such an elastic medium. This elastic medium stabilizes the tubular shape as the reference configuration, leading to a competition between surface tension and elastic stresses. A shape transformation can then only happen if the surface tension overcomes the elastic stresses. In this context, one typically observes the formation of a necklace of pearls, hence coining the name of "pearling" instability (Bar-Ziv and Moses, 1994; Bar-Ziv, Tlusty, et al., 1999; Pullarkat et al., 2006). In the case of a negative tension, for example due to cell divisions, one can also observe buckling modes (Hannezo, Prost, et al., 2012; Dong et al., 2014). Because the organoid branch is under tension, as our collaborators demonstrated with matrix degradation and laser ablation experiments, we should rather observe a pearling instability.

But all instabilities that we described so far occur on a global scale: pearling as a long-wavelength instability and buckling as an instability with a defined wavelength. In contrast, experiments done by our collaborators demonstrate a well-defined *spatial localization*, where only the tips of the organoid branches transform into alveoli. The key to reconcile theory and experiment lies in the following observation: the shape transformation of tubular ducts to spherical alveoli is preceded by an onset of collective cell rotations, around the circumference of the tubular organoid branch. The existence of these collective rotations indicates that cells show characteristics of polar particles that self-propel through a motile force, analogous to our *Cellular Potts* model in Chapter III "From Cellular Dynamics to Self-Organization". As a consequence of this polar cell motility, the epithelium switches from collective oscillatory motion along the organoid branch axis to collective rotations along the organoid branch circumference, because the latter is the "least frustrated state". In this "least frustrated state", the cells minimize viscous shear and, at the same time, maintain constant polarization while migrating on a periodic path around the tube circumference. Such collective rotations typically also arise when polar matter is confined to circular geometries in two dimensions (Doxzen et al., 2013; Segerer et al., 2015; F. Thüroff et al., 2019), as described in Section III.1 "Collective Cell Dynamics in Rigid Environments". *Then, how does collective motion of cells affect tissue shape?*
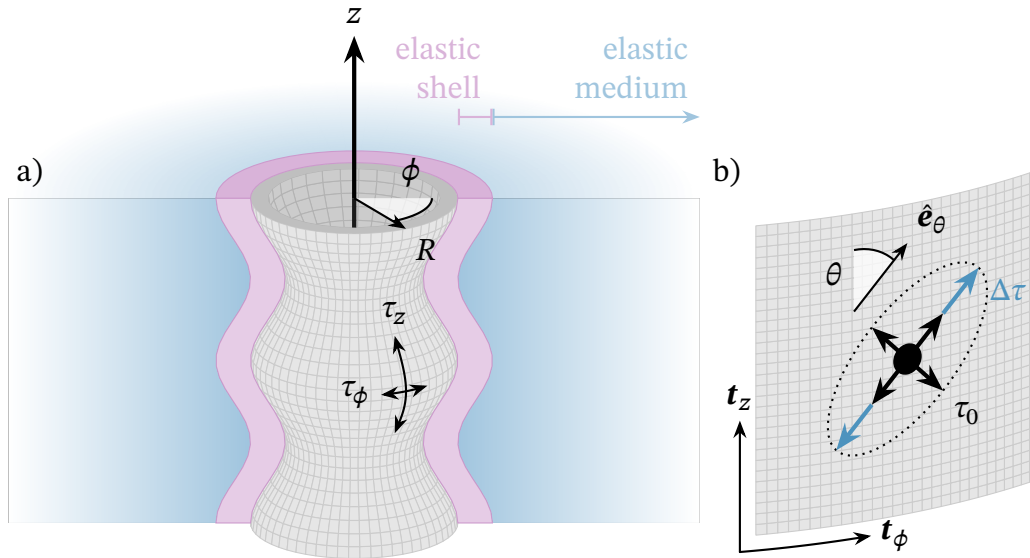
Figure IV.1: Schematic representation of the organoid branch geometry. a) The cell population forms a thin tubular shell (gray), whose lumen is filled by an aqueous solution under hydrostatic pressure p_0. The cellular tube is surrounded by a dense and rigid elastic shell (magenta): a collagen cage that the cells form via plastic remodeling of the extracellular matrix (Buchmann et al., 2021). Further away, the cellular tube is surrounded by a soft elastic medium (blue): the extracellular collagen matrix. b) Enlarged view of the cell population at the surface of the organoid branch. We consider each cell as a contractile force dipole with normalized orientation vector $\hat{\boldsymbol{e}}_\theta$. The cell cytoskeleton exerts contractile forces on the cell boundary. We decompose the corresponding cell tension tensor into two contributions: (i) isotropic contractile tension τ_0 (black arrows), and (ii) increased contractility ($\Delta\tau > 0$) or decreased contractility ($\Delta\tau < 0$) along the axis $\hat{\boldsymbol{e}}_\theta$. This figure is adapted from the reprint (Fernández et al., 2021) on pages 341–394.

Cell reorientation changes the tension field. In addition to being motile, cells typically show characteristics of anisotropic force dipoles, thus having a well-defined orientation along which they exert stronger tensile forces (Schwarz and S. A. Safran, 2002; Bischofs and Schwarz, 2003; Bischofs, S. A. Safran, et al., 2004; Schwarz and S. A. Safran, 2013). When switching from collective oscillatory motion along the organoid branch axis to collective rotations around the organoid branch circumference, cells must reorient. Through these reorientations, as we show in Section IV.1.3 "Technical Summary", the cells can *locally* increase circumferential tension at the expense of axial tension, while keeping the total tension constant. This effect then leads to a localized "budding" instability,

where spherical alveoli form at the tips of the organoid branches as an indirect consequence of cell motility. These generic effects, ultimately arising only from cell anisotropy and cell reorganization, could also play a role for the embryogenesis of the fruit fly *Drosophila melanogaster* (Streichan et al., 2018; Martin, 2020; Gheisari et al., 2020) or other organisms (Wozniak and Chen, 2009; Münster et al., 2019).

IV.1.3 TECHNICAL SUMMARY

Cell orientation and contractility lead to anisotropic tension.   Now, we explain in detail how cell orientation affects the tension tensor in a confluent tissue, such as on the surface of an organoid branch (Fig. IV.1b). To that end, we consider cells as anisotropic force dipoles (Schwarz and S. A. Safran, 2002; Bischofs and Schwarz, 2003; Bischofs, S. A. Safran, et al., 2004; Schwarz and S. A. Safran, 2013), where the anisotropy stems from the local orientation of the cells and their cytoskeleton[1]. For now, we choose the most general description of a confluent tissue that lies on an arbitrary two-dimensional surface in a three-dimensional Cartesian embedding. We use a curvilinear coordinate system, and the concepts of differential geometry that we have recapitulated in Section I.3 "A Foundation for Patterns in Adapting Organisms".

We place ourselves into the co-moving reference frame of some small parcel (infinitesimal surface element) of the confluent tissue, which is spanned by a local basis T with the two tangent vectors $t_1 \in T$ and $t_2 \in T$. These two tangent vectors are, in the most general case, not orthonormal; in the special case of a cylindrical geometry, the tangent vectors are orthogonal but not normalized. We define the orientation of each cell as a *normalized* vector that lies parallel to the surface:

$$\hat{e}_\theta := \sum_i \hat{e}_\theta^i \, t_i \,, \quad \text{with} \quad \hat{e}_\theta \cdot \hat{e}_\theta = \sum_{i,k} \hat{e}_\theta^i \, \hat{e}_\theta^k \, g_{ik} = 1 \,, \qquad \text{(IV.1)}$$

where we have used the definition of the metric tensor, Eq. (I.18). Due to orientational order in its cytoskeleton, a cell can exhibit increased or decreased contractility along its axis $\hat{e}_\theta$. Therefore, we split the tension tensor of each cell into two contributions: (i) an isotropic *base* tension τ_0 that preserves rotational symmetry in our local reference frame, and (ii) an additional anisotropic tension $\Delta\tau$ along the direction specified by the vector $\hat{e}_\theta$ that breaks rotational symmetry in our local reference frame. Taken together, we model cell contractility with

---

[1] In Eq. (III.4) of Section III.1 "Collective Cell Dynamics in Rigid Environments", we have constructed the tension tensor of a cellular cytoskeleton, with a given angular distribution of contractile (or extensile) fibers. The tension of the cell will be anisotropic if there is any orientational order in the cytoskeletal fibers.

the following cellular tension tensor:

$$\boldsymbol{\tau} = \tau_0 \boldsymbol{I} + \Delta\tau \, \hat{\boldsymbol{e}}_\theta \otimes \hat{\boldsymbol{e}}_\theta = \tau_0 \boldsymbol{I} + \Delta\tau \sum_{i,k} \hat{e}^i_\theta \, \hat{e}^k_\theta \, \boldsymbol{t}_i \otimes \boldsymbol{t}_k \,. \tag{IV.2}$$

The cell is an isotropic force dipole if $\Delta\tau = 0$, and is an anisotropic force dipole for any $\Delta\tau \neq 0$.

Before we go on to study the average tension tensor of a population of cells that have different orientations, we first ask: *Does the tension tensor of each individual cell have any special properties?* In fact, as we will see shortly, the trace of the tension tensor is a constant. To show this, we make use of orthonormalization, as introduced in Paragraph "Basis orthonormalization" (Section I.3.2). Specifically, we consider a transformation $\boldsymbol{O}$ that maps our non-orthonormal tangent basis $\boldsymbol{T}$ to an orthonormal tangent basis, $\boldsymbol{T}_\oplus = \boldsymbol{T} \cdot \boldsymbol{O}$, with orthonormal tangent vectors $\boldsymbol{t}_{\oplus,i} \in \boldsymbol{T}_\oplus$. Then, we express the identity mapping in terms of the orthonormal tangent vectors, $\boldsymbol{I} = \sum_l \boldsymbol{t}_{\oplus,l} \otimes \boldsymbol{t}_{\oplus,l}$. Multiplying the tension tensor, Eq. (IV.2), from left and right with the identity mapping, results in the following expression:

$$\begin{aligned}
\boldsymbol{\tau} = \tau_0 \boldsymbol{I} + \Delta\tau \sum_{i,k,l,m} \hat{e}^i_\theta \, \hat{e}^k_\theta \, (\boldsymbol{t}_i \cdot \boldsymbol{t}_{\oplus,l})(\boldsymbol{t}_k \cdot \boldsymbol{t}_{\oplus,m}) \, \boldsymbol{t}_{\oplus,l} \otimes \boldsymbol{t}_{\oplus,m} \\
= \tau_0 \boldsymbol{I} + \Delta\tau \sum_{i,k,l,m,n,p} \hat{e}^i_\theta \, \hat{e}^k_\theta \, (\boldsymbol{t}_i \cdot \boldsymbol{t}_n) \, O_{nl} \, (\boldsymbol{t}_k \cdot \boldsymbol{t}_p) \, O_{pm} \, \boldsymbol{t}_{\oplus,l} \otimes \boldsymbol{t}_{\oplus,m} \,. \tag{IV.3}
\end{aligned}$$

After taking the trace of the tension tensor, we then find:

$$\begin{aligned}
\operatorname{tr} \boldsymbol{\tau} = 2\tau_0 + \Delta\tau \sum_{i,k,l,n,p} \hat{e}^i_\theta \, \hat{e}^k_\theta \, g_{in} \, g_{kp} \, O_{nl} \, O_{pl} \\
= 2\tau_0 + \Delta\tau \sum_{i,k,n,p} \hat{e}^i_\theta \, \hat{e}^k_\theta \, g_{in} \, g_{kp} \, g^{-1}_{np} = 2\tau_0 + \Delta\tau \sum_{i,k} \hat{e}^i_\theta \, \hat{e}^k_\theta \, g_{ik} \,, \tag{IV.4}
\end{aligned}$$

where we have used the definition of the metric tensor, Eq. (I.18) and Eq. (I.26). Finally, by comparing Eq. (IV.4) with Eq. (IV.1), we find that the trace of the cellular tension tensor is constant:

$$\operatorname{tr} \boldsymbol{\tau} = 2\tau_0 + \Delta\tau \,, \tag{IV.5}$$

as we have claimed earlier. Next, we discuss how this property of the cellular tension tensor carries over to the tension tensor of a confluent tissue.

For this purpose, we now consider a population of cells in which the cells differ in their orientations $\hat{\boldsymbol{e}}_\theta$, but not in their contractile properties τ_0 and $\Delta\tau$. As an alternative way of representing cell orientation, we define a unique reference

EXAMPLE 10: ANISOTROPIC TENSION ON A CYLINDRICAL SURFACE

We construct a normalized orientation vector that lies on the surface of a cylindrical surface as follows:

$$\hat{\boldsymbol{e}}_\theta = \cos\theta\,\frac{\boldsymbol{t}_\phi}{\|\boldsymbol{t}_\phi\|} + \sin\theta\,\frac{\boldsymbol{t}_z}{\|\boldsymbol{t}_z\|} \equiv \begin{bmatrix} \cos\theta \\ \sin\theta \end{bmatrix},$$

where $\boldsymbol{t}_\phi$ is the circumferential tangent vector and $\boldsymbol{t}_z$ is the axial tangent vector. Then, the cellular tension tensor is given by:

$$\tau(\theta) = \begin{bmatrix} \tau_0 + \Delta\tau\,\cos^2\theta & \Delta\tau\,\cos\theta\,\sin\theta \\ \Delta\tau\,\cos\theta\,\sin\theta & \tau_0 + \Delta\tau\,\sin^2\theta \end{bmatrix} \equiv \begin{bmatrix} \tau_z & \ddots \\ \ddots & \tau_\phi \end{bmatrix}.$$

angle between the orientation vector and one of the two tangent vectors in our co-moving reference frame:

$$\theta := \cos^{-1}\left(\frac{\hat{\boldsymbol{e}}_\theta \cdot \boldsymbol{t}_1}{\|\boldsymbol{t}_1\|}\right) \times \begin{Bmatrix} +1, & \text{for } \hat{\boldsymbol{e}}_\theta \cdot \boldsymbol{t}_2 \geq 0 \\ -1, & \text{for } \hat{\boldsymbol{e}}_\theta \cdot \boldsymbol{t}_2 < 0 \end{Bmatrix}. \tag{IV.6}$$

Here, it is the conditional expression in the curly brackets that makes the angle unique. Then, each cell exerts an anisotropic tension $\tau(\theta)$, which only depends on the cell orientation angle θ. We statistically represent the occurrence of different cell orientations θ by the probability density function $P(\theta)$, which we refer to as *angular distribution of cell orientation*. The average tension tensor in the confluent tissue is then given by the following weighted average:

$$\bar{\tau} = \int_{-\pi}^{\pi} d\theta\, P(\theta)\,\tau(\theta), \tag{IV.7}$$

in analogy to the cortical tension of a single cell, Eq. (III.4). If there is order in the cell orientation, for example if all cells are oriented along one of the two tangent vectors, $P(\theta) = \delta(\theta)$, then the average tension in the tissue will be anisotropic. In contrast, if the cells are oriented randomly, $P(\theta) = 1/(2\pi)$, then the average tension in the tissue will be isotropic. However, one property of the tension tensor at the tissue level is independent of the specific angular distribution of cell orientation, and that is the trace:

$$\operatorname{tr}\bar{\tau} = 2\tau_0 + \Delta\tau. \tag{IV.8}$$

Here, we have first inserted the trace of the cellular tension tensor, Eq. (IV.5), into Eq. (IV.7) and then used that the angular distribution of cell orientation is

a normalized probability density function. Thus, the total tension in the confluent tissue, tr $\bar{\tau}$, is independent of the angular distribution of cell orientation. Our collaborators confirmed this property in experiments, where the sum of the axial and the circumferential tension remained constant, as discussed in the preprint on pages 341–394. Therefore, the predominant process underlying the changes in the tension field is a reorientation of cells and not a change in their tensile properties τ_0 and $\Delta\tau$. To summarize, we have found that the tissue can make trade-offs between, for example, axial and circumferential tension through a reorientation of cells.

From here on, we do not study the precise distribution of cell orientation. To simplify our notation, we omit the overline indicating the population average, $\tau \equiv \bar{\tau}$.

Cells perform work when deforming a surface.   After seeing how cell orientation can induce and control anisotropic tension at the tissue level, we next discuss possible consequences for tissue shape. We begin by deriving a generalization of the Laplace pressure, and then discuss conceptual differences between isotropic and anisotropic surface tension. As before, we choose the most general description of a confluent tissue that lies on an arbitrary two-dimensional surface in a three-dimensional Cartesian embedding.

We consider cells as active agents that perform work when they deform the surface. In the following, we explain in detail how the cells will then induce stresses on the surface. For this, suppose that the cells have introduced a slight deformation of the tissue, which we represent via a variation of the (nonlinear) strain tensor, $\delta\boldsymbol{E}$. As discussed in Paragraph "The strain as a variation of the metric" (Section I.3.5), introducing strain changes the distances between nearby material points (in other words, cells). For the tissue to then remain confluent and not rupture, the strain of individual cells must match the strain of the tissue. In turn, individual tensile cells perform work when they deform. Therefore, it follows that a tissue under tension $\boldsymbol{\tau}$ will also perform work when it deforms:

$$\delta W = -\oint dS\, \boldsymbol{\tau} : \delta\boldsymbol{E} = -\oint dS \left(\sum_{i,k} \tau^{ik}\, \boldsymbol{t}_i \otimes \boldsymbol{t}_k \right) : \left(\sum_{l,m} \delta E^{lm}\, \boldsymbol{t}_l \otimes \boldsymbol{t}_m \right)$$

$$:= -\oint dS \sum_{i,k,l,m} \tau^{ik}\, \delta E^{lm}\, (\boldsymbol{t}_i \cdot \boldsymbol{t}_l)(\boldsymbol{t}_k \cdot \boldsymbol{t}_m) = -\oint dS \sum_{i,k,l,m} \tau^{ik}\, \delta E^{lm}\, g_{il}\, g_{km}\,. \quad \text{(IV.9)}$$

Here, we have first defined the double dot product, "$:$", and then used the definition of the metric tensor, Eq. (I.18). Note that, after transforming to a local orthonormal coordinate system where $g_{ik} = \delta_{ik}$, Eq. (IV.9) becomes identical to an expression given by Landau, Pitaevskii, et al. (1986).

As an additional *a posteriori* motivation of Eq. (IV.9), one can also consider the following thought experiment. First, we "turn off" the cell activity, so that the cells reach a reference configuration that is in mechanical equilibrium. In this case, we can use elasticity theory to model the linear response of the cells to external stresses. Afterwards, we again "turn on" the cell activity. We represent the out-of-equilibrium characteristics of the cell via a new imaginary reference configuration, which is *slightly* distinct from the previous reference configuration. Then, each cell will behave like an (effectively) strained elastic body, and perform work while approaching this new imaginary reference configuration. Taking a closer look at the components of the tension tensor, one then finds:

$$-\frac{\delta W}{\delta E^{lm}} = \sum_{i,k} \tau^{ik} g_{il} g_{km}, \quad \text{and} \quad \tau^{ik} = -\sum_{l,m} \frac{\delta W}{\delta E^{lm}} g_{li}^{-1} g_{mk}^{-1}. \qquad \text{(IV.10)}$$

As before, after transforming to a local orthonormal coordinate system where $g_{ik} = \delta_{ik}$, one finds that Eq. (IV.10) becomes identical to an expression given by Landau, Pitaevskii, et al. (1986).

A generalization of Laplace pressure for anisotropic tension. Now, suppose that the surface moves by a small displacement δu along its unit normal vector, due to the contractility of cells. From our discussion in Paragraph "Variation of the boundary metric" (Section I.3.5), we know that such a *normal variation* will introduce a change in the surface strain, see Eq. (I.71):

$$\delta E = -T^{-T} \cdot h \cdot g^{-1} \cdot T^T \delta u = -T^{-T} \cdot h \cdot T^{-1} \delta u, \qquad \text{(IV.11)}$$

where h is the shape tensor of the surface. To proceed, we need to account for the dual basis T^{-1}. Therefore, we remind on the following representation for the basis T and choose an analogous representation for the dual basis T^{-1}:

$$T = \begin{bmatrix} t_1, t_2 \end{bmatrix}, \quad T^T = \begin{bmatrix} t_1^T \\ t_2^T \end{bmatrix}, \quad T^{-1} = \begin{bmatrix} t_1^{-T} \\ t_2^{-T} \end{bmatrix}, \quad \text{and} \quad T^{-T} = \begin{bmatrix} t_1^{-1}, t_2^{-1} \end{bmatrix}. \quad \text{(IV.12)}$$

Analogous to the discussion in Paragraph "Variation of the boundary shape" (Section I.3.5), we express the scalar product (inner product) through a formal matrix multiplication between a row vector s^T ($1 \times N$ matrix) and a column vector r ($N \times 1$ matrix), $s \cdot r \equiv s^T \cdot r$. Furthermore, we also represent the tensor product (outer product) as the formal matrix multiplication between a column vector s ($N \times 1$ matrix) and a row vector r^T ($1 \times N$ matrix), $s \otimes r \equiv s \cdot r^T$. When we express vectors via matrices, the symbol "·" identifies a matrix multiplication. Because this trick can cause a clash with the notation of an inner vector product, we

only use it in two places of the present thesis, and explicitly state where we do so. With these considerations, we can rewrite Eq. (IV.11) as follows:

$$\delta \boldsymbol{E} = -\delta u \sum_{i,k} h_{ik}\, \boldsymbol{t}_i^{-1} \otimes \boldsymbol{t}_k^{-1}\,. \tag{IV.13}$$

Thus, inserting Eq. (IV.13) into Eq. (IV.9), we find that the cellular tissue performs the following work when moving the surface by a small displacement δu along its unit normal vector:

$$\delta W = \oint dS \sum_{i,k} \tau^{ik}\, h_{ik}\, \delta u\,. \tag{IV.14}$$

Here, we have used $\boldsymbol{t}_i^T \cdot \boldsymbol{t}_k^{-1} = \delta_{ik}$, which follows from $\boldsymbol{T}^T \cdot \boldsymbol{T}^{-T} = \boldsymbol{I}$.

Finally, we have found a general expression for the Laplace pressure in the presence of an anisotropic surface tension:

$$\Delta p_\tau = \frac{\delta W}{\delta u} = \sum_{i,k} \tau^{ik}\, h_{ik}\,. \tag{IV.15}$$

With this, we conclude: *An anisotropic contractility of cells gives the cellular tissue additional control over the Laplace pressure, by reorienting cells without changing their contractile properties.* In contrast, in the special case of an isotropic surface tension, $\boldsymbol{\tau} = \tau_0\,\boldsymbol{I}$, the cellular tissue can only control the Laplace pressure via the contractile properties of the cells, as we discuss next. We can specialize Eq. (IV.15) to the case of an isotropic surface tension, but to do so we need to first determine the corresponding components of the isotropic tension tensor, τ^{ik}. To that end, we express the identity mapping in terms of the orthogonal tangent vectors,

$$\boldsymbol{I} = \sum_i \boldsymbol{t}_{\oplus,i} \otimes \boldsymbol{t}_{\oplus,i} = \sum_{i,k} g_{ik}^{-1}\, \boldsymbol{t}_i \otimes \boldsymbol{t}_k\,. \tag{IV.16}$$

Then, we find that the components of the tension tensor are given by $\tau^{ik} = \tau_0\, g_{ik}^{-1}$ in the case of isotropic surface tension. Only in this special case does the Laplace pressure take the following well-known form (S. Safran, 2003; D. Nelson et al., 2004):

$$\Delta p_\tau = \tau_0 \sum_{i,k} g_{ik}^{-1}\, h_{ik} = \tau_0\,\mathrm{tr}(\boldsymbol{h}\cdot\boldsymbol{g}^{-1}) = \tau_0\, H\,. \tag{IV.17}$$

Thus, if there is no anisotropy on a cellular level, then the Laplace pressure can only be regulated by cell contractility.

EXAMPLE 11: LAPLACE PRESSURE ON A CYLINDRICAL SURFACE

We consider a rotationally symmetric cylindrical surface with radius $R \equiv R(z)$. If the cylindrical surface has an axial tension τ_z and a (possibly different) circumferential tension τ_ϕ, then the generalized Laplace pressure is given by:

$$\Delta p_\tau = \tau_z \frac{\partial_z^2 R}{\sqrt{1 + (\partial_z R)^2}^3} - \frac{\tau_\phi}{R} \frac{1}{\sqrt{1 + (\partial_z R)^2}} = \tau_z \, \kappa_z + \tau_\phi \, \kappa_\phi \, ,$$

where κ_z is the axial curvature and κ_ϕ is the circumferential curvature of the surface. See also Example 10 for the definition of the tension tensor, and Example 5 on page 32 for a definition of the principal curvatures. One can envision the (anisotropic) surface tension as a meshwork of ropes. Each rope is either aligned along the axis or along the circumference of the cylinder. Axial tension is related to the mechanical work that is required to increase the (relative) length of the cylinder. Analogously, circumferential tension is related to the mechanical work that is required to increase the (relative) circumference of the cylinder.

Linear stability analysis for an organoid branch.   Having learned that an anisotropic cellular tissue can control the Laplace pressure by reorienting cells, we next investigate how this will affect tissue shape. To that end, we now specialize our general description to the rotationally symmetric cylindrical geometry of an organoid branch, whose surface is located at a distance $R \equiv R(z)$ from the centerline of the geometry (Fig. IV.1a). We consider rotationally symmetric deformations of the organoid branch surface, $R = R_0 + u$, where the deflection $u \equiv u(z)$ is much smaller than the initial radius of the surface, $u \ll R_0$.

The tubular organoid branch is filled by a passive viscous fluid in the lumen and enveloped by two passive elastic materials: a thin elastic shell (collagen cage) and an elastic medium (extracellular collagen matrix). At the interface between these passive materials, cells form an active confluent tissue (Fig. IV.1a). The anisotropic contractility of cells then confers a generalized Laplace pressure, Eq. (IV.15) and Example 11. This active stress is balanced by dynamic fluid stress and hydrostatic pressure in the lumen, as well as the elastic stresses of the thin elastic shell and the elastic medium. In Section IV.2.3 "Nonlinear Elasticity of the Collagen Cage", we determine the (nonlinear) elastic stresses that the elastic shell generates in response to deformations. In comparison, the elastic stresses that the elastic medium generates in response to deformations are negligible, because the elastic medium is much softer than the thin elastic
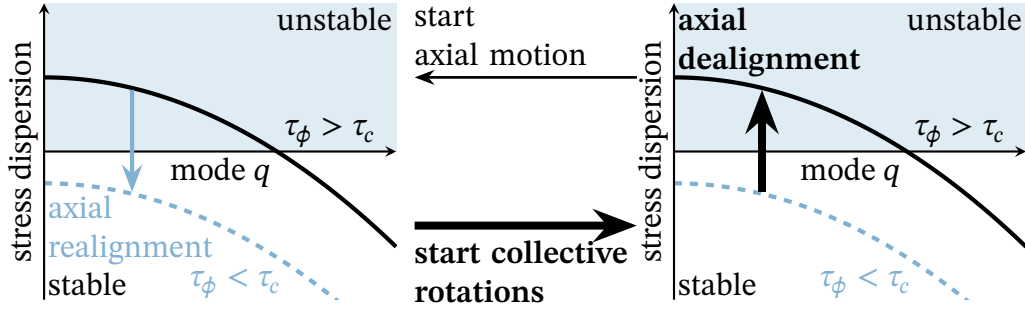
Figure IV.2: Stress dispersion relation as a function of the mode q. An onset of collective rotations (rightwards arrow) leads to cell reorientation and an increase of the circumferential surface tension at the expense of the axial surface tension. As a result, the stress dispersion relation shifts upwards (upwards arrow), leading to a band of unstable modes. The reverse process, a transition from collective rotations to axial motion (leftwards arrow), can in principle happen. Then, the tubular shell can stabilize again due to cellular realignment and a reduction of circumferential tension at the benefit of axial tension (downwards arrow). However, this reverse process is disfavored because collective rotations are the "least frustrated state". This figure is adapted from the reprint (Fernández et al., 2021) on pages 341–394.

shell, as discussed in the preprint on pages 341–394. Taking into account these contributions, the (linearized) balance equation of radial stresses at the surface of the organoid branch is then given by:

$$
\begin{aligned}
\sigma_{fl}^{rr} &= p_0 - \frac{\tau_\phi}{R_0 + u} + \tau_z\, \partial_z^2 u - Y_s\, h\, \frac{u}{R_0^2} - k_b \left[\frac{u}{R_0^4} + \partial_z^4 u \right] \\
&\approx p_0 - \frac{\tau_\phi}{R_0} + \left[\frac{\tau_\phi}{R_0^2} - \frac{Y_s\, h}{R_0^2} - \frac{k_b}{R_0^4} + \tau_z\, \partial_z^2 - k_b\, \partial_z^4 \right] u \,.
\end{aligned}
\tag{IV.18}
$$

Here, Y_s is the elastic modulus of the shell, which has thickness h, and k_b is the corresponding bending modulus. The radial stress balance equation, Eq. (IV.18), accounts for all stresses that act perpendicularly on our cylindrical surface. Therefore, there must also be an axial stress balance equation, accounting for all stresses that act parallel on our cylindrical surface. However, for now we content ourselves with studying only Eq. (IV.18), which, as we show in Section IV.2.5 "Cell Activity Drives Hydrodynamic Flows", contains all information that is necessary to determine whether the initial cylindrical shape of the organoid branch remains stable or not.

On the right-hand side of the radial stress-balance equation, Eq. (IV.18), we have collected the hydrostatic pressure, the generalized Laplace pressure,

and elastic stresses. The left-hand side of the radial stress-balance equation, Eq. (IV.18), corresponds to dynamic fluid stresses σ_{fl}^{rr}. We defer the explicit discussion of these dynamic viscous stresses to Section IV.2.5 "Cell Activity Drives Hydrodynamic Flows". However, even without doing so, we can already gain some insights. First, in the absence of a surface deflection, that is for $u = 0$, the dynamic fluid stresses must also vanish lest the reference configuration itself is ill-defined by being unstable. Therefore, the hydrostatic pressure is given by $p_0 = \tau_\phi/R_0$. To proceed, we now express both the viscous stresses and the deflection in terms of Fourier components[2]:

$$\sigma_{fl}^{rr} = \sum_q \Delta p_q \cos(q\,z)\,, \quad \text{and} \quad u = \sum_q u_q \cos(q\,z)\,. \qquad \text{(IV.19)}$$

Thus, we obtain the following dynamic stress dispersion relation near mechanical equilibrium (Fig. IV.2):

$$\Delta p_q = \left[\frac{\tau_\phi}{R_0^2} - \frac{Y_s\,h}{R_0^2} - \frac{k_b}{R_0^4} - \tau_z\,q^2 - k_b\,q^4 \right] u_q\,. \qquad \text{(IV.20)}$$

If the term in the square brackets of Eq. (IV.20) is positive, then deformations of the organoid branch will grow. This growth is ultimately driven by the hydrostatic pressure, although it does not appear in the stress dispersion relation, Eq. (IV.20), because the counteracting Laplace pressure *shrinks* for increasing organoid branch radius (Example 11). This effect also occurs for the $q = 0$ mode, thus indicating a long-wavelength instability according to the Cross-Hohenberg classification scheme (Cross and Hohenberg, 1993). In contrast, a positive axial tension τ_z stabilizes only short-wavelength modes by penalizing axial undulations of the cylindrical surface. Then, only the elastic shell can prevent the shape instability by penalizing stretching and bending[3]. Taken together, we find that a band of unstable modes will emerge if the circumferential tension is sufficiently high:

$$\tau_\phi > \tau_c = Y_s\,h + \frac{k_b}{R_0^2}\,. \qquad \text{(IV.21)}$$

Thus, we conclude: *The cellular tissue can control a shape transformation by reorienting cells, and therefore making trade-offs between the circumferential tension and the axial tension.*

We note that the mechanical driving stress on the right-hand side of Eq. (IV.20) is largest for the $q = 0$ mode, consistent with a long-wavelength

---

[2] We choose a cosine waveform, because, in principle, it permits a constant deflection u for the homogeneous $q = 0$ mode, without adding an additional constant offset.

[3] We assume that the elastic shell exhibits no bending stress in its cylindrical reference configuration. Therefore, the elastic shell has a spontaneous curvature of $c_\phi = -1/R_0$.

instability. However, as we show in Section IV.2.5 "Cell Activity Drives Hydrodynamic Flows", the homogeneous $q = 0$ mode is not the fastest-growing mode because it is actually prohibited by the incompressibility of the fluid in the lumen of the organoid branch. Finally, there is one open question that we will also address in Section IV.2.5 "Cell Activity Drives Hydrodynamic Flows": *How does the organoid branch, at the onset of its shape transformation, decide on the direction in which the instability occurs?*

IV.1.4 MANUSCRIPT M5

TITLE:

SURFACE TENSION INDUCED BUDDING DRIVES ALVEOLOGENESIS IN HUMAN MAMMARY GLAND ORGANOIDS

AUTHORS:

Pablo Fernández*, Benedikt Buchmann*, **Andriy Goychuk***, Lisa K. Engelbrecht, Marion Raich, Christina H. Scheel, Erwin Frey and Andreas R. Bausch

The asterisk symbol (*) indicates shared first authorship.

Surface tension induced budding drives alveologenesis in human mammary gland organoids.

Pablo A. Fernández,[1, *] Benedikt Buchmann,[1, *] Andriy Goychuk,[2, *] Lisa K. Engelbrecht,[3, †]

Marion K. Raich,[1] Christina H. Scheel,[3, ‡] Erwin Frey,[2, §] and Andreas R. Bausch[1, ¶]

[1]*Center for Protein Assemblies and Lehrstuhl für Biophysik E27,*

Technische Universität München, D-85747 Garching, Germany

[2]*Arnold Sommerfeld Center for Theoretical Physics and Center for NanoScience,*

Ludwig-Maximilians-Universität München, D-80333 Munich, Germany

[3]*Institute of Stem Cell Research, Helmholtz Center for Health and*

Environmental Research Munich, D-85764 Neuherberg, Germany

(Dated: July 18, 2021)

Organ development involves complex shape transformations driven by active mechanical stresses that sculpt the growing tissue [1, 2]. Epithelial gland morphogenesis is a prominent example where cylindrical branches transform into spherical alveoli during growth [3–5]. Here, we show that this shape transformation is induced by a local change from anisotropic to isotropic tension within the epithelial cell layer of developing human mammary gland organoids. By combining laser ablation with optical force inference and theoretical analysis, we demonstrate that the circumferential tension increases at the expense of axial tension, through a reorientation of cells that correlates with the onset of persistent collective rotation around the branch axis. This enables the tissue to locally control the onset of a generalized Rayleigh-Plateau instability leading to spherical tissue buds [6]. The interplay between cell motion, cell orientation, and tissue tension is a generic principle that may turn out to drive shape transformations in other cell tissues.

---

* P.F.,B.B., and A.G. contributed equally to this work.

† Present address: Center for Protein Assemblies and Lehrstuhl für Biophysik E27, Technische Universität München, D-85747 Garching, Germany

‡ christina.scheel@klinikum-bochum.de; Present address: Department of Dermatology, St. Josef Hospital, Ruhr-University Bochum, D-44791 Bochum, Germany

§ frey@lmu.de

¶ abausch@mytum.de

The transformation from tubular ducts into terminal spherical alveoli is ubiquitous in organ development of higher organisms [3]. The mammary gland is a unique example that relies on this shape change to undergo repeated postnatal cycles of expansion, alveologenesis and involution [7]. This self-organization of spherical structures is reminiscent of hydrodynamic instabilities driven by surface tension, first described by Lord Rayleigh and Joseph Plateau in passive isotropic fluids [6]. Specifically, a column of fluid always breaks up into droplets that have smaller surface-to-volume ratio. When the fluid column is not surrounded by air but by an elastic medium, then the shape instability only occurs if the surface tension can overcome the ensuing elastic stresses, resulting in pearling [8–10]. This is a compelling picture considering the fluid-like behaviour of tissues [1, 11–14] and the key role of cortical tension in duct development [15]. But classical pearling of isotropic fluids occurs on a global scale, as a long-wavelength instability without any defined spatial localization. In contrast, controlled development of the tissue requires spatially localized shape transformations that are regulated by cell activity. Since cells are able to move, orientate and generate forces, a plausible hypothesis is that these properties enable local changes in the tension field and that this is the mechanism to locally control fluid shape instabilities.

To understand the nature of such shape transformations, we exploit an organoid assay from primary cells which recapitulates the architecture of the human mammary gland, with its characteristic arrays of spherical alveoli [4, 16, 17]. In this assay, single primary human mammary epithelial cells are seeded into collagen I matrices and develop into highly branched organoids over a time period of two weeks (Fig. 1a). The resulting organoid morphology depends crucially on the adhesion of the elastic collagen matrix to the enclosing culture vessel [4]. In attached gels, branches stay cylindrical and their length continuously increases (Fig. 1a, lower row), while in floating gels, about 50% of the branches develop round alveoli at their ends (Fig. 1a, upper row, Supplementary Table 1). Starting around day 10, the average alveolus becomes spherical within 3-4 days (Fig. 1a).

To understand this shape transformation, we asked whether organoids behave like solids or fluids in the absence of the extracellular matrix (ECM). We found that enzymatic digestion of the collagen matrix leads to a dramatic loss of organoid structure: within minutes, cylindrical branches flow towards the organoid body (Fig. 1b, Supplementary Movie 1). Thus, organoids behave like fluids and crucially depend on the elasticity of the ECM for the stability of the branches. Observation of alveoli grown in fluorescent collagen revealed

that they are enveloped by a compacted collagen cage similar to the one around cylindrical branches (Fig. 1c, Supplementary Fig. 1) [17]. This suggests that the organoid deforms and compacts the surrounding collagen by exerting mechanical stresses above the plastic yield threshold, rather than by proteolysis and degradation [18–20]. To corroborate this hypothesis, we investigated the effect of inhibiting enzymatic ECM degradation by adding the metalloproteinase inhibitor Marimastat [17] right at the onset of alveologenesis. To quantify the degree of sphericity at the branch end we defined a "shape index" α (Fig. 1d; see also Supplementary Material B1). We found that addition of Marimastat has no effect on the formation of spherical alveoli, which proceeds at the normal rate despite a drastic inhibition of tubular branch growth (Fig. 1e,f, top row). To investigate the role of mechanical stresses, we increased cell contractility by addition of calyculin A. As a result, this leads to a faster formation of alveoli (Fig. 1e,f, middle row). Next, we sought to diminish epithelial tension by addition of the antibody HECD1 against E-cadherin. As a result, branches fail to become round and instead develop long, thin extensions (Fig. 1e,f, lower row). We conclude that alveologenesis involves a plastic deformation of the encasing ECM driven by epithelial contractility.

To determine the mechanical interaction between developing branches and the ECM, we performed UV laser ablation of the collagen network in close proximity to branch tips and alveoli (Fig. 1g). We found that straight, cylindrical branches react with a fast recoil towards the organoid body, indicating a catastrophic loss of the pulling tension generated by cell contractility [17]. In contrast, spherical alveoli exhibited a slight expansion towards the cut, revealing a compressive (negative) stress in the ECM.

Next, we applied laser ablation to the cells themselves. While the majority of cylindrical branches in floating gels is not stable but actually undergoing alveologenesis(Fig. 1a,f), branches in attached gels remain cylindrical. Therefore, we used branches in attached gels as a stable control. Immediately after ablation, the cell boundaries surrounding the cut move away with a fast recoil (see Supplementary Movie 2). We characterized the recoil response by an axial ϵ_z and circumferential strain ϵ_ϕ (Fig. 2b, Methods). The overall response $(\epsilon_z + \epsilon_\phi)/2$ is the same for all shapes and gel boundary conditions – indicating that spherical alveoli, branches undergoing alveologenesis, and stable cylindrical branches all maintain a similar contractile tonus (Fig. 2c). Next, we turned to the recoil strain difference $\epsilon_z - \epsilon_\phi$ to assess tension anisotropy. We found that branches in attached gels react with a

considerable axial bias (Fig. 2d, red squares). In floating gels, the response is less biased and decreases with increasing shape index, eventually becoming isotropic for spherical alveoli (Fig. 2d, blue circles). To confirm that the stresses leading to these responses originate from actomyosin activity, we ablated organoids after disruption of the actin network by addition of Cytochalasin D. The recoil response after laser ablation was significantly lower and no longer axially biased (Supplementary Fig. 2, Supplementary Movie 3).

Since cortical tension is mainly determined by the actin cortex located along cell boundaries [21, 22], we turned to confocal microscopy of the actin cytoskeleton and the cell boundaries. In straight cylindrical branches, we found that cells are highly elongated and aligned parallel to the branch axis; in contrast, in mature alveoli, cells are less elongated (Fig. 2e and f). We found that the distribution of boundary angles is strongly anisotropic in attached gels and becomes increasingly isotropic as the organoids develop into spheres in floating gels (Supplementary Fig. 3). To compute relative cortical tension from these images, we used the curvilinear boundaries force inference method (Fig. 2g) [23, 24]. We found that tension is axially biased in attached gels. This bias decreases in floating gels as the branches become rounder (Fig. 2h). These results quantitatively agree with our laser ablation experiments (Fig. 2d; see also Supplementary Fig. 5), indicating that the spatial arrangement of cell boundaries is linked to the anisotropy of cortical tension in mammary gland organoids.

Can we explain the observed constant mean recoil $\bar{\epsilon}$ from the arrangment of cell boundaries (Fig. 2c)? Considering each cell as force dipoles [25] oriented at an angle θ, relative to the branch axis, we decompose the cellular tension into an isotropic part τ_0 and an anisotropic part $\Delta\tau$ (see also Supplementary Material B2). For a distribution $P(\theta)$ of different cell orientation angles, the population-averaged tension tensor is then given by

$$\boldsymbol{\bar{\tau}} \equiv \begin{bmatrix} \bar{\tau}_z & \ddots \\ \ddots & \bar{\tau}_\phi \end{bmatrix} = \int_{-\pi}^{\pi} d\theta P(\theta) \begin{bmatrix} \tau_0 + \Delta\tau\cos^2(\theta) & \Delta\tau\cos(\theta)\sin(\theta) \\ \Delta\tau\cos(\theta)\sin(\theta) & \tau_0 + \Delta\tau\sin^2(\theta) \end{bmatrix} . \tag{1}$$

The trace of this surface tension tensor is constant, $\bar{\tau}_z + \bar{\tau}_\phi = 2\tau_0 + \Delta\tau$, and independent of the distribution of cell orientation, in agreement with our experiments. The tissue can therefore make trade-offs between axial and circumferential tension by reorienting the cells.

To directly observe the reorientations of the cells, we followed the time course of cell movements by staining cell nuclei. In cylindrical branches, cells collectively move parallel

to the branch axis in a back-and-forth manner (Fig. 3a). In contrast, we observed that mature spherical alveoli perform a persistent collective rotation around the branch axis lasting for at least 20 hours without direction reversal and no preferred chirality (Fig. 3b, see Supplementary Movie 4, Supplementary Fig. 6 and 7). Observation of branches at early stages of alveologenesis ($\alpha \simeq 0.3$) revealed that the rotational motion did not arise in a single step, but through transient bouts of localized rotation interspersed with phases of longitudinal translation (Fig. 3c, d). Whereas rotation broadly correlated with increasing sphericity of the branch end, longitudinal motion coincided with a partial recovery of the cylindrical shape; alveologenesis thus proceeded with superimposed oscillations (Fig. 3d, right and Supplementary Movie 5). Reasoning that strong cell-cell adhesion would explain the high spatial coherence of the motion, we live-imaged organoids treated with HECD1. We found that translation and rotation stop within 15-24 hours after antibody addition in 73% of the observed branches (n=15; see Supplementary Movie 6). Thus, longitudinal translation, rotation, and alveologenesis are all collective phenomena that require long-range force transmission via E-cadherin junctions, as previously described for a small number of human mammary epithelial cells spontaneously forming spherical aggregates [26] and other epithelial cell types in circular confinement [27].

To clarify the causal role of branch rotation in alveologenesis, we undertook a full characterization of the time course of branch shape, cell migration, and cortical tension. We used cell nuclei shapes as a proxy for cell tension and found a linear relation between the tension anisotropy inferred from cell boundaries and the anisotropy parameter χ characterizing the elongation and orientation of the nuclei (Fig. 3e). As a control measurement, we observed stable branches that remained cylindrical for at least 8 h with an average constant tension anisotropy $\chi \simeq 0.65$ and a predominantly axial motion (Fig. 3f, left). As we turned to the onset of the shape transformation, we defined an alveologenic event as an increase in shape index by at least 0.1 within 2 h, starting at onset time t_{AO} from a low value $\alpha < 0.1$ (see Supplementary Fig. 4). We found that already within the 2 hours before alveologenesis, these branches displayed a lower anisotropy parameter ($\chi \simeq 0.45$) and an increased rotational activity $|v_\phi|$ compared to the control (Fig. 3f). At the onset time t_{AO}, a robust decrease in nuclear anisotropy precedes the increase in shape index α by about 1 h (Fig. 3f, right, red traces; see also Supplementary Movies 7 and 8).This dynamic data quantitatively agrees with the laser ablation and force inference experiments, supporting our hypothesis of

151   a tension-driven shape transformation (Supplementary Fig. 5).

152   In general, polar matter such as motile cells aligns and forms collectively migrating groups

153 to minimize shear [28]. In a constrained cylindrical geometry like organoid branches, cells

154 can enter an axial translational motion that requires periodic cell repolarization (Fig. 4a).

155 To maintain this motion, cells have to remain axially aligned in the elastic ECM, which

156 could occur due to cellular sensing of fixed boundaries [25]. The longitudinal back-and-forth

157 movement of elongating branches (Fig. 3b, Supplementary Movie 4) can then be understood

158 from the generic tendency of planar epithelia to move along the principal stress direction [28].

159 In floating gels, the ECM cannot support high stresses and thus cells reorient freely (Fig. 4b).

160 Then, the state that minimizes shear corresponds to collective rotation, which runs without

161 cell repolarizations and also arises spontaneously in constrained planar epithelia [29, 30].

162 When the cells reorient, there is an increase of circumferential tension at the expense of

163 axial tension, cf. Eq. 1, which finally drives the formation of a stable spherical alveolus.

164   How can a shift from axially biased surface tension, $\tau_z - \tau_\phi > 0$, towards isotropic surface

165 tension, $\tau_z - \tau_\phi \approx 0$, induce a shape transformation as observed in our experiments? Con-

166 sider a cylindrical branch as a long, rotationally symmetric, fluid cylinder with radius R,

167 surrounded by an elastic shell with modulus E and thickness h that idealizes the collagen

168 cage. Since the cell layer of the organoid branch forms an interface between a fluid and the

169 ECM, there must be a stress balance between the viscous normal stresses due to fluid flow

170 (σ_{visc}^{rr}), the hydrostatic pressure p_0, the generalized Laplace pressure due to the circumfer-

171 ential tension τ_ϕ and the axial tension τ_z, as well as elastic stresses Δp_{el} due to the collagen

172 cage:

$$\sigma_{visc}^{rr} = p_0 - \frac{\tau_\phi}{R} + \tau_z \, \partial_z^2 R + \Delta p_{el} \qquad (2)$$

173 Thus, fluid flows and the corresponding viscous stresses arise whenever the right hand side

174 of Eq. 2 is unbalanced. Analysing the linear stability of the tubular branch with respect

175 to small deviations from its cylindrical shape, we find that a shape transformation appears

176 above a critical circumferential tension of $\tau_\phi > \tau_c = Eh$ (Fig. 4c, Supplementary Material

177 B4). In terms of the tension anisotropy, this criterion is equivalent to $\chi < \chi_c = 2 - 2 \, \tau_c/\bar{\tau}$; the

178 critical anisotropy parameter corresponding to the alveologenesis onset can be read off from

179 Fig. 3f to be $\chi_c \simeq 0.35$. Estimating that τ_c is of the order of 4–7 mN m^{-1} (Supplementary

180 Material B4), we finally obtain $\bar{\tau} \simeq 5$–8 mN m^{-1}, which is of the same order as the typi-

7

181 cal cortical tension of contractile cells, 0.3–4 mN m^{-1} [31], and organoids, 10 mN m^{-1} [32].
182 Thus, a redistribution of tension from the axial to the circumferential direction, resulting
183 from a simple reorientation of cells, cf. Eq. 1, is sufficient to trigger the shape transfor-
184 mation. Note that this remains a dynamic process with extensive cell motility: in early
185 phases of alveologenesis, the tension isotropification at the branch tip can be perturbed and
186 transiently reversed by the back-and-forth migration of the stalk cells, which actively drags
187 the branch towards the organoid centre and restores axial cell reorientation again (Supple-
188 mentary Movies 5 and 8, Supplementary Fig. 4b). Thus, the organoid shape change is not
189 monotonic. On long timescales, however, the spherical geometry is stabilized by collective
190 cell rotations and the plastic deformation of the surrounding ECM. Finally, once the alve-
191 olus is approximately spherical, the Laplace pressure $(\tau_\phi + \tau_z)/R$ decreases with increasing
192 radius; as a consequence, under a constant, osmotically balanced hydrostatic pressure differ-
193 ence p_0 and a plastic ECM response, isotropic alveoli keep growing. The presented results
194 show that the shape transformation underlying alveologenesis in human mammary gland
195 organoids can be understood as a budding instability triggered by a decrease in tension
196 anisotropy. This mechanism amounts to a global feedback loop: tissue shape and ECM
197 forces determine epithelial motion, which in turn influences the symmetry of the tension
198 tensor, which at the end feedbacks to the tissue shape via hydrodynamics (Fig. 4). The
199 mechanism presented here may turn out to be of general importance for complex shape
200 tranformations in organogenesis.

208 **Author contributions** P.A.F., C.H.S. and A.R.B. designed research; P.A.F., B.B, L.K.E.
209 and M.K.R. performed experiments and analysed the data; A.G., P.A.F. and E.F. per-
210 formed theoretical interpretation of experiments; P.A.F., A.G., E.F. and A.R.B. wrote the
211 paper; A.R.B., E.F. and C.H.S. supervised the project; all authors revised and edited the

8

²¹² manuscript.

²¹³ **Competing Interests**   The authors declare no competing interests.

²¹⁴ **Data availability**   Microscopy data that support the findings of this study have been
²¹⁵ deposited in Zenodo with the identifier https://doi.org/10.5281/zenodo.5076123. All other
²¹⁶ relevant data supporting the key findings of this study are available within the article and its
²¹⁷ Supplementary Information files or from the corresponding author upon reasonable request.
²¹⁸ Source data are provided with this paper.

²¹⁹ **Code availability**   Code used for analyzing the data of this study have been deposited in
²²⁰ Zenodo with the identifier https://doi.org/10.5281/zenodo.5076123.

Reprint of accepted manuscript

Fig. 1. **Morphology of human mammary gland organoids depends on the mechanical interaction with the ECM. a**, Primary cells from reduction mammoplasty are seeded in Collagen I gels and allowed to grow for up to 20 days. As a function of the attachment of the matrix, different morphologies are obtained. Scale bars: 100 µm. **b**, Organoids behave like liquids. After collagen hydrolysis by collagenase treatment, branches flow into the organoid body within a few minutes. Scale bar: 50 µm. **c**, Organoids grown in fluorescent collagen are completely surrounded by a layer of compacted collagen. Scale bar: 50 µm. **d**, To characterize branch shape we introduce the shape index α defined in terms of the axial and circumferential curvatures, $\kappa_z = \partial_z^2 R / \left[1 + (\partial_z R)^2 \right]^{\frac{3}{2}}$ and $\kappa_\phi = -R^{-1} / \left[1 + (\partial_z R)^2 \right]^{\frac{1}{2}}$ (see also Supplementary Material B1). To avoid the irregular shapes of the branch tip, the integration region was taken at a distance $a = 30$ µm from the tip. The upper bound $b = 100$ µm corresponds to the typical size of alveoli at days 12-14. **e**, Effect of several biochemical perturbations on the development of organoids grown in floating gels. Calyculin A increases contractility, Marimastat inhibits matrix metalloproteinases, and HECD1 antibody blocks cell–cell adhesion. **f**, Time evolution of average branch shape index α and overall organoid size (respectively for control, Marimastat, Calyculin A and HECD1: $n_{\mathrm{branches}} = 215, 95, 211, 119$; $n_{\mathrm{organoids}} = 33, 23, 28, 24$). The shaded regions correspond to $\pm$ S.E.. **g**, To determine the mechanical interaction between branch tip and ECM, we ablate a 30 µm high, 100 µm wide, 1 µm thick ECM region near the branch tip. Cylindrical branches recoil within 1 s away from the cut, revealing pulling tension (top); in contrast, round alveoli expand towards the cut, showing compressive ECM forces (bottom). The pink bar represents the ablated region (100 µm wide). Arrows: optical flow. Scale bar: 50 µm. Far right, recoil speed of the branch tip as a function of shape index.

Fig. 2. **Alveoli are under isotropic tension, cylindrical branches under axially biased tension. a**, We ablate a cylindrical region with a diameter of $10\,\mu$m and height of $30\,\mu$m, cutting through the ECM and the outer cell layer. From the recoil we estimate axial and circumferential elastic strains. Scale bar: $50\,\mu$m. **b**, Displacement field induced by the cut. We integrate the optical flow over an annular region to obtain recoil strains. **c**, Mean recoil $(\epsilon_z + \epsilon_\phi)/2$ as a function of shape index α, both in attached (n=16) and in floating gels (n=73). **d**, Recoil anisotropy $(\epsilon_z - \epsilon_\phi)$ as a function of shape index α for the same experiments as in c (p-Value: 8×10^{-4}). To compare with the force inference data (Fig. 2h) we scaled by the mean recoil averaged over the whole dataset, $\bar{\epsilon} = 0.017$. **e**, Confocal microscopy of actin and nuclei in a cylindrical branch and a spherical alveolus. Top: slice through the middle plane. Bottom: slice through the outer cell layer. **f**, Cell membrane stains. Scale bars: $50\,\mu$m. **g**, From the membrane segmentations we computed tensions using the curvilinear boundary force inference method. **h**, Inferred tension anisotropy $\tau_z - \tau_\phi$ as a function of shape index α, both in attached (n=10) as in floating gels (n=32) (p-Value: 2×10^{-7}). Note that we assume $\bar{\tau} = 1$.

Fig. 3.   **Alveoli undergo collective rotation. a**, Characteristic back-and-forth movement parallel to the axis in a cylindrical branch. Arrows show optical flow for a 20 min time step. Scale bar: $100\,\mu m$. Arrow: $30\,\mu m\,h^{-1}$. **b**, Spherical alveoli rotate for at least 20 h. Scale bar: $100\,\mu m$. **c**, Observation of cell dynamics during alveologenesis shows that rotation is spatially limited to the distal end, correlating with the location of the nascent alveolus. Notice the coexisting opposite rotation senses at time $t = 33$ h. Scale bar: $100\,\mu m$. Arrow: $30\,\mu m\,h^{-1}$ **d**, Mean circumferential velocity $v_\phi(z,t)$, mean axial velocity $v_z(z,t)$ and local radius $R(z,t)$ along the branch for the experiment shown in c. **e**, Nuclei elongation can be used to infer tension anisotropy. We defined a nuclear anisotropy parameter χ by averaging a function of the elongation b_i/a_i and angle θ_i over several nuclei located at the lower z-slices. This parameter may be positive, corresponding to elongated nuclei aligned parallel to the branch axis; zero, for isotropic distributions or round nuclei; and negative, for circumferential alignment. Comparing this parameter with the tensions obtained from force inference in double-stained branches, we found that χ is approximately equal to the anisotropy $(\tau_z - \tau_\phi)/\bar{\tau}$. **f** Sample-average shape index α, nuclear bias χ and absolute circumferential velocity $|v_\phi|$ as a function of time for two different scenarios: stable cylindrical branches where $\alpha < 0.1$ throughout (left, n=11), and alveologenic events aligned relative to the onset time t_{AO} $(n = 24)$.

12

Fig. 4. **A hydrodynamic model with anisotropic tension and ECM elasticity can explain the shape transition. a**, In attached gels, high ECM forces are balanced by anisotropic tension and cells move parallel to the branch axis. **b**, In floating gels, the onset of collective rotation is most likely a consequence of the decreased tension anisotropy, which is in agreement with flat epithelial dynamics [28]. The resulting surface shear aligns cells in the circumferential direction, increasing τ_ϕ at the expense of τ_z. **c**, Stability analysis for a fluid cylinder surrounded by an elastic shell. The cylindrical shape becomes unstable for $\tau_\phi > \tau_c \simeq Eh$, where E and h correspond to the elastic modulus and thickness of the collagen cage. Through cell reorientations, the tissue can increase circumferential tension at the expense of axial tension, thus taking the initially stable cylindrical organoid (red dot) into the unstable regime (black arrow).

13

METHODS

Cell culture. Organoids were prepared as described previously in Ref. [4]. Briefly, mammary gland tissue was obtained from healthy women undergoing reduction mammoplasty at the Nymphenburg Clinic for Plastic and Aesthetic Surgery, in accordance with the regulations of the ethics committee of the Ludwig-Maximilians-Universität München, Munich, Germany (proposal 397-12). The ductal tree was minced, enzymatically digested and cryopreserved. Prior to each experiment, cells were unfrozen and seeded in collagen gels. Cells were initially cultured in mammary epithelial cell growth medium (MECGM, PromoCell) supplemented with 1% pen/strep (Invitrogen), 0.5% FCS (Pan Biotech), 3 µM Y-27632 (Biomol) and 10 µM forskolin (Biomol). After 5 days, medium was changed to MECGM supplemented with 1% pen/strep and 10 µM forskolin. Organoids were prepared from 4 different donors (Supplementary Table 1).

3D collagen I gels. Organoids were grown in collagen I gels from rat tail (Corning). Freshly unfrozen single cell suspensions were mixed with MECGM medium, 11x Hepes, collagen solution and taken to pH 7.5 by addition of 1 M NaOH. Final collagen concentration was $1.3 \, \mathrm{mg \, ml^{-1}}$. The mixture was gently but thoroughly mixed before deposition in slides (ibidi). After polymerization for 1 h in the incubator at 37 °C, an equal volume of medium was added to the gel. Organoids were grown in a 3% oxygen atmosphere. For enzymatic digestion of the collagen matrix (Fig. 1c) we added to the gel an equal volume of medium containing 0.01 U/ml collagenase (Sigma). Within ~ 20 minutes the collagen fibers were no longer visible in the Hoffman contrast images and debris diffused freely, indicating complete hydrolysis of the matrix.

Biochemical perturbation. Organoids were grown under normal conditions for 9 days; at culture day 10, medium containing either 0.5 nM calyculin A (Gibco), 10 µM Marimastat (Santa Cruz Biotechnology) or HECD-1 at a ratio of 1:50 (abcam) was added. Fresh drug was replenished in a second medium change at day 12. Organoids were imaged by bright field Hoffman contrast microscopy. To determine organoid size, we manually drew ellipses tightly enclosing the structures and defined size as the mean of the elliptic axes.

14

Laser ablation. Laser ablation of collagen and organoids was performed with a custom setup based on the one described in Ref. [33]. Briefly, a pulsed 355 nm laser with 400 ps pulse duration and 25 mW average power (teem Photonics) was shone on the sample through a PL APO 40x 1.1 NA water immersion objective (Leica). Two galvanometric mirrors were used to tilt the beam and control the spot position in the focal plane. To cut along the Z direction, we simultaneously acquired three-dimensional stacks, displacing the sample with a piezo stage (ASI). Stack height along Z was 30 µm and the number of slices per stack was 10. To maximize acquisition rate, we used Micro-Manager's fast sequence mode [34], controlling the stage with the camera FIRE signal. Image exposure time was 50 ms, corresponding to a stack acquisition time of 0.5 s.

For organoid ablation experiments, the laser spot was displaced in a circular fashion, cutting a circle with a diameter of 10 µm and a height of 30 µm. We performed these experiments at culture days 14-15, both in floating as well as in attached gels. The cuts induced a fast recoil of the surrounding tissue. We determined the displacement field of the recoil by comparing slices at a given Z position in the initial, unperturbed configuration and 3 s after the cut. Specifically, we calculated the corresponding optical flow using the openCV implementation of the Farnebäck algorithm [35]. The axial and circumferential components of the displacement field were integrated over an annular region surrounding the cut to obtain the total displacement. The inner radius of the annular region was 15 µm, so chosen in order to avoid artifacts stemming from ablation bubbles. The outer radius of the annular region was determined by the branch width and was typically 30 µm. The data showed considerable scatter that seemed to be intrinsic variability in the rearrangement of cell boundaries after the cut, rather than noise in the image processing algorithm.

Confocal microscopy. The laser ablation setup was equipped with a spinning disc unit (Yokogawa), an sCMOS camera (Andor) and 488 nm, 561 nm and 638 nm lasers (Cobolt) for fluorescence confocal imaging, as well as an XYZ translation stage (ASI), a temperature control device and a gas incubation system to maintain 5% CO_2 and 3% O_2 (ibidi). Prior to the laser ablation experiments, organoid membranes were stained with 1X CellMask Deep Red (Invitrogen). For time-lapsed microscopy, cell nuclei were stained with 10 µM SiR-DNA (Spirochrome).

15

³⁴⁸ **Nuclear anisotropy parameter.** Organoids were stained with $10\,\mu M$ SiR-DNA and im-
³⁴⁹ aged by confocal microscopy using a HC FLUOTAR L 25X/0.95 W VISIR water immersion
³⁵⁰ objective (Leica). Since alveologenic events are rare, we devised a procedure that allowed
³⁵¹ for several days of continuous, simultaneous imaging of many structures (10–13) without
³⁵² evaporation of the water layer between slide and objective. Basically, we enclosed objective
³⁵³ and sample slide with a party balloon filled with $25\,mL$ of water. In this way we acquired
³⁵⁴ the images shown in Supplementary Movies 6–8. To calculate the anisotropy parameter
³⁵⁵ from the branch images, we manually drew ellipses around 5-15 nuclei located at low Z
³⁵⁶ slices using ImageJ. Ellipse parameters were exported and further processed using python
³⁵⁷ scripts. Rotation velocities were calculated by optical flow [35].

³⁵⁸

³⁵⁹ **Statistical analysis.** Data are presented as mean $\pm$ S.E.. To compare tension estimations
³⁶⁰ from branches with different shapes, data were pooled according to the shape index and
³⁶¹ compared with Student's t-test (two-tailed, unpaired). $P < 0.05$ was considered significant:
³⁶² *$P < 0.05$, **$P < 0.01$, ***$P < 0.001$.

³⁶³ [1] Petridou, N. I., Grigolon, S., Salbreux, G., Hannezo, E. & Heisenberg, C.-P. Fluidization-
³⁶⁴ mediated tissue spreading by mitotic cell rounding and non-canonical wnt signalling. *Nature*
³⁶⁵ *Cell Biology* **21**, 169–178 (2019).

³⁶⁶ [2] Karzbrun, E., Kshirsagar, A., Cohen, S. R., Hanna, J. H. & Reiner, O. Human brain organoids
³⁶⁷ on a chip reveal the physics of folding. *Nature Physics* **14**, 515–522 (2018).

³⁶⁸ [3] Wang, S., Sekiguchi, R., Daley, W. P. & Yamada, K. M. Patterned cell and matrix dynamics
³⁶⁹ in branching morphogenesis. *Journal of Cell Biology* **216**, 559–570 (2017).

³⁷⁰ [4] Linnemann, J. R. *et al.* Quantification of regenerative potential in primary human mammary
³⁷¹ epithelial cells. *Development* **142**, 3239–3251 (2015).

³⁷² [5] Rios, A. C. *et al.* Intraclonal plasticity in mammary tumors revealed through large-scale
³⁷³ single-cell resolution 3D imaging. *Cancer Cell* **35**, 618 – 632.e6 (2019).

³⁷⁴ [6] Rayleigh, L. On the instability of jets. *Proceedings of the London Mathematical Society* **s1-10**,
³⁷⁵ 4–13 (1878).

³⁷⁶ [7] Inman, J. L., Robertson, C., Mott, J. D. & Bissell, M. J. Mammary gland development: cell

16

377   fate specification, stem cells and the microenvironment. *Development* **142**, 1028–1042 (2015).

378 [8] Bar-Ziv, R., Tlusty, T., Moses, E., Safran, S. A. & Bershadsky, A. Pearling in cells: A clue to
379   understanding cell shape. *Proceedings of the National Academy of Sciences* **96**, 10140–10145
380   (1999).

381 [9] Bar-Ziv, R. & Moses, E. Instability and "pearling" states produced in tubular membranes by
382   competition of curvature and tension. *Phys. Rev. Lett.* **73**, 1392–1395 (1994). URL `https:`
383   `//link.aps.org/doi/10.1103/PhysRevLett.73.1392`.

384 [10] Dong, B., Hannezo, E. & Hayash, S. Balance between apical membrane growth and luminal
385   matrix resistance determines epithelial tubule shape. *Cell Reports* **7**, 941–950 (2014).

386 [11] Pérez-González, C. *et al.* Active wetting of epithelial tissues. *Nature Physics* **15**, 79–88 (2019).

387 [12] Tetley, R. J. *et al.* Tissue fluidity promotes epithelial wound healing. *Nature Physics* **15**,
388   1195–1203 (2019).

389 [13] He, B., Doubrovinski, K., Polyakov, O. & Wieschaus, E. Apical constriction drives tissue-scale
390   hydrodynamic flow to mediate cell elongation. *Nature* **508**, 392–396 (2014).

391 [14] Maître, J.-L. *et al.* Adhesion functions in cell sorting by mechanically coupling the cortices of
392   adhering cells. *Science* **338**, 253–256 (2012).

393 [15] Chatterjee, S. J., Halaoui, R., Deagle, R. C., Rejon, C. & McCaffrey, L. Numb regulates cell
394   tension required for mammary duct elongation. *Biology Open* **8** (2019).

395 [16] Parmar, H. & Cunha, G. R. Epithelial - stromal interactions in the mouse and human mam-
396   mary gland in vivo. *Endocrine-Related Cancer Endocr Relat Cancer* **11**, 437 – 458 (2004).

397 [17] Buchmann, B. *et al.* Mechanical plasticity of collagen directs invasive branching morphogenesis
398   in human mammary gland organoids. *Nature Communications* **12**, 2759 (2021).

399 [18] Alcaraz, J. *et al.* Collective epithelial cell invasion overcomes mechanical barriers of collagenous
400   extracellular matrix by a narrow tube-like geometry and mmp14-dependent local softening.
401   *Integr. Biol.* **3**, 1153–1166 (2011). URL `http://dx.doi.org/10.1039/C1IB00073J`.

402 [19] Wisdom, K. M. *et al.* Matrix mechanical plasticity regulates cancer cell migration through
403   confining microenvironments. *Nature Communications* **9**, 4144 (2018). URL `https://doi.`
404   `org/10.1038/s41467-018-06641-z`.

405 [20] Hall, M. S. *et al.* Fibrous nonlinear elasticity enables positive mechanical feed-
406   back between cells and ecms. *Proceedings of the National Academy of Sci-*
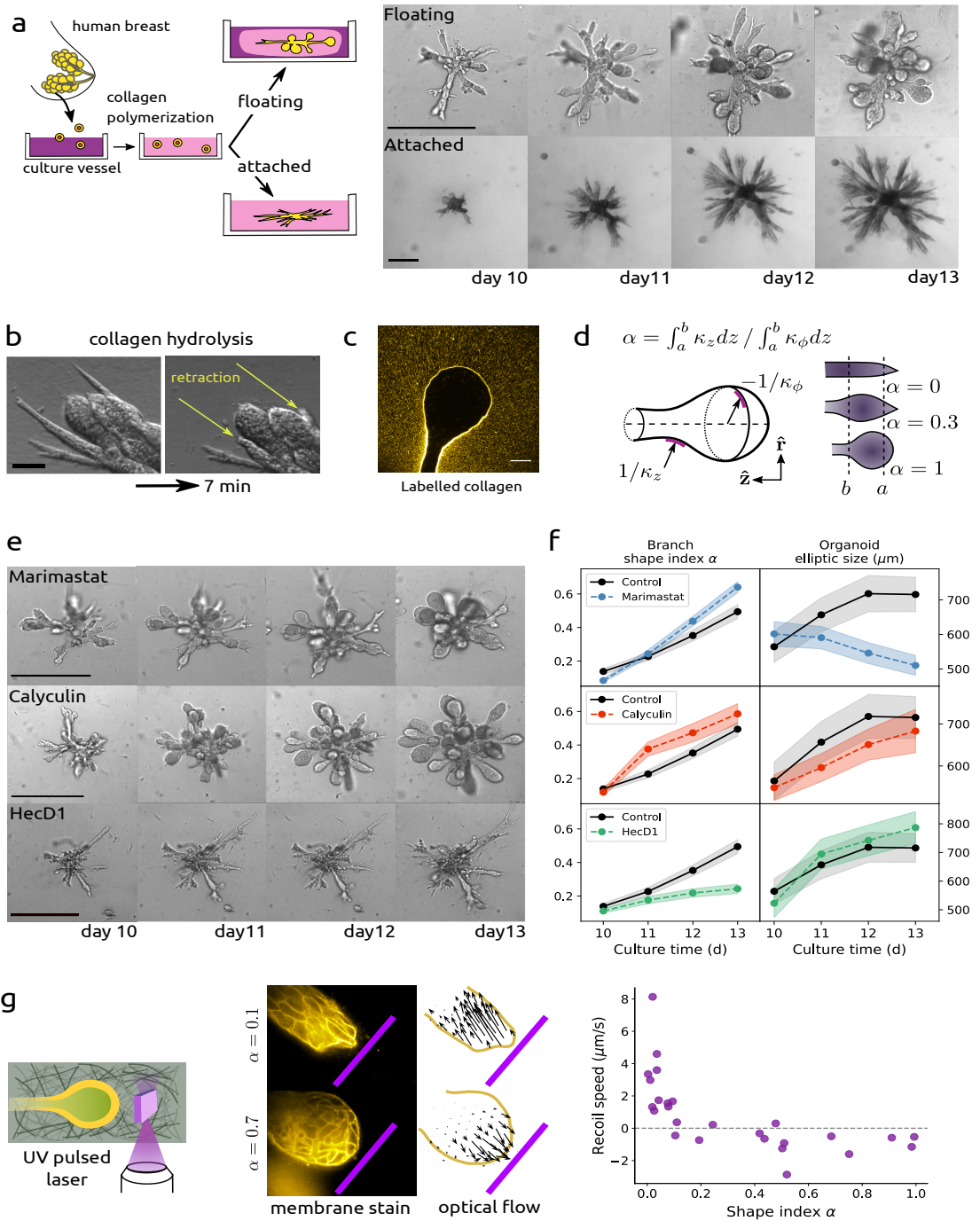407   *ences* **113**, 14043–14048 (2016). URL `https://www.pnas.org/content/113/49/14043`.

17

https://www.pnas.org/content/113/49/14043.full.pdf.

[21] Lecuit, T., Lenne, P.-F. & Munro, E. Force generation, transmission, and integration during cell and tissue morphogenesis. *Annual Review of Cell and Developmental Biology* **27**, 157–184 (2011).

[22] Brodland, G. W. *et al.* Video force microscopy reveals the mechanics of ventral furrow invagination in Drosophila. *Proceedings of the National Academy of Sciences* **107**, 22111–22116 (2010).

[23] Brodland, G. W. *et al.* CellFIT: A cellular force-inference toolkit using curvilinear cell boundaries. *PLOS ONE* **9**, 1–15 (2014).

[24] Kong, W. *et al.* Experimental validation of force inference in epithelia from cell to tissue scale. *Scientific Reports* **9**, 14647 (2019).

[25] Bischofs, I. B. & Schwarz, U. S. Cell organization in soft media due to active mechanosensing. *Proceedings of the National Academy of Sciences* **100**, 9274–9279 (2003). URL `https://www.pnas.org/content/100/16/9274`. https://www.pnas.org/content/100/16/9274.full.pdf.

[26] Tanner, K., Mori, H., Mroue, R., Bruni-Cardoso, A. & Bissell, M. J. Coherent angular motion in the establishment of multicellular architecture of glandular tissues. *Proceedings of the National Academy of Sciences* **109**, 1973–1978 (2012).

[27] Thüroff, F., Goychuk, A., Reiter, M. & Frey, E. Bridging the gap between single-cell migration and collective dynamics. *eLife* **8**, e46842 (2019). URL `https://doi.org/10.7554/eLife.46842`.

[28] Tambe, D. T. *et al.* Collective cell guidance by cooperative intercellular forces. *Nature Materials* **10**, 469–475 (2011). URL `https://doi.org/10.1038/nmat3025`.

[29] Jain, S. *et al.* The role of single-cell mechanical behaviour and polarity in driving collective cell migration. *Nature Physics* **16**, 802–809 (2020).

[30] Segerer, F. J., Thüroff, F., Piera Alberola, A., Frey, E. & Rädler, J. O. Emergence and persistence of collective cell migration on small circular micropatterns. *Phys. Rev. Lett.* **114**, 228102 (2015).

[31] Tinevez, J.-Y. *et al.* Role of cortical tension in bleb growth. *Proceedings of the National Academy of Sciences* **106**, 18581–18586 (2009).

[32] Villeneuve, C. *et al.* aPKCi triggers basal extrusion of luminal mammary epithelial cells by tuning contractility and vinculin localization at cell junctions. *Proceedings of the National*
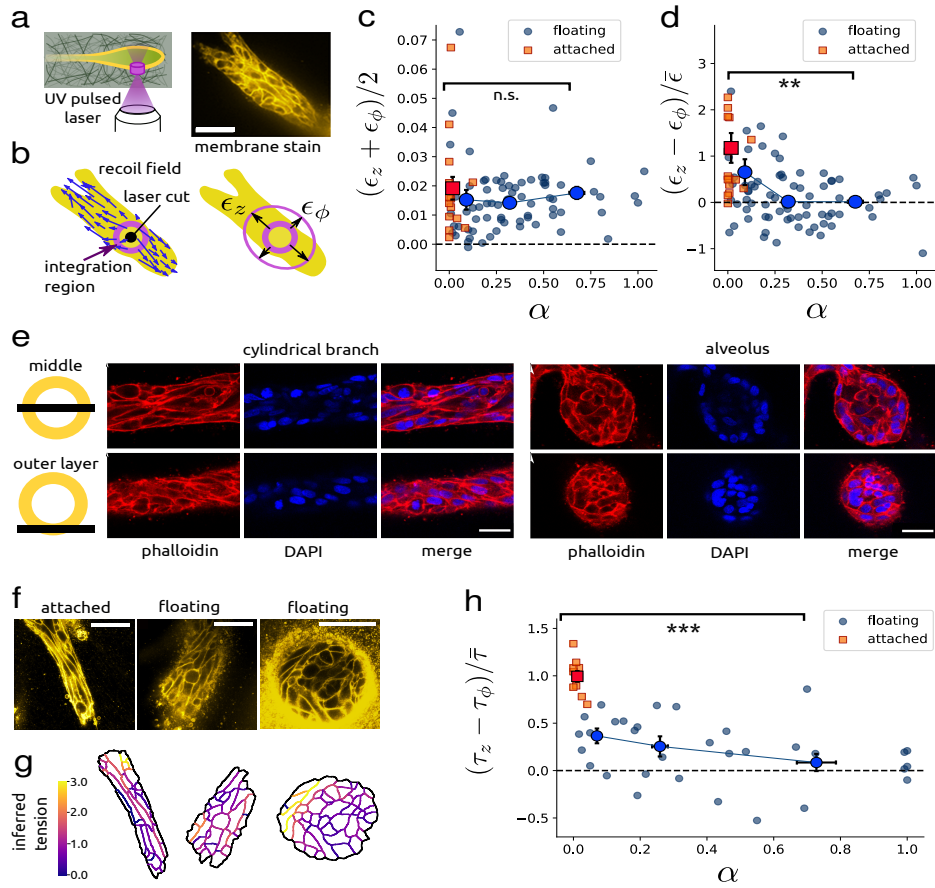
18

439   *Academy of Sciences of the United States of America* **116**, 24108–24114 (2019). URL `https:`

440   `//doi.org/10.1073/pnas.1906779116`.

441   [33] Colombelli, J., Grill, S. W. & Stelzer, E. H. K. Ultraviolet diffraction limited nanosurgery of

442   live biological tissues. *Review of Scientific Instruments* **75**, 472–478 (2004).

443   [34] Edelstein, A. *et al.* Advanced methods of microscope control using µManager software. *Journal*

444   *of Biological Methods* **1**, e10 (2014).

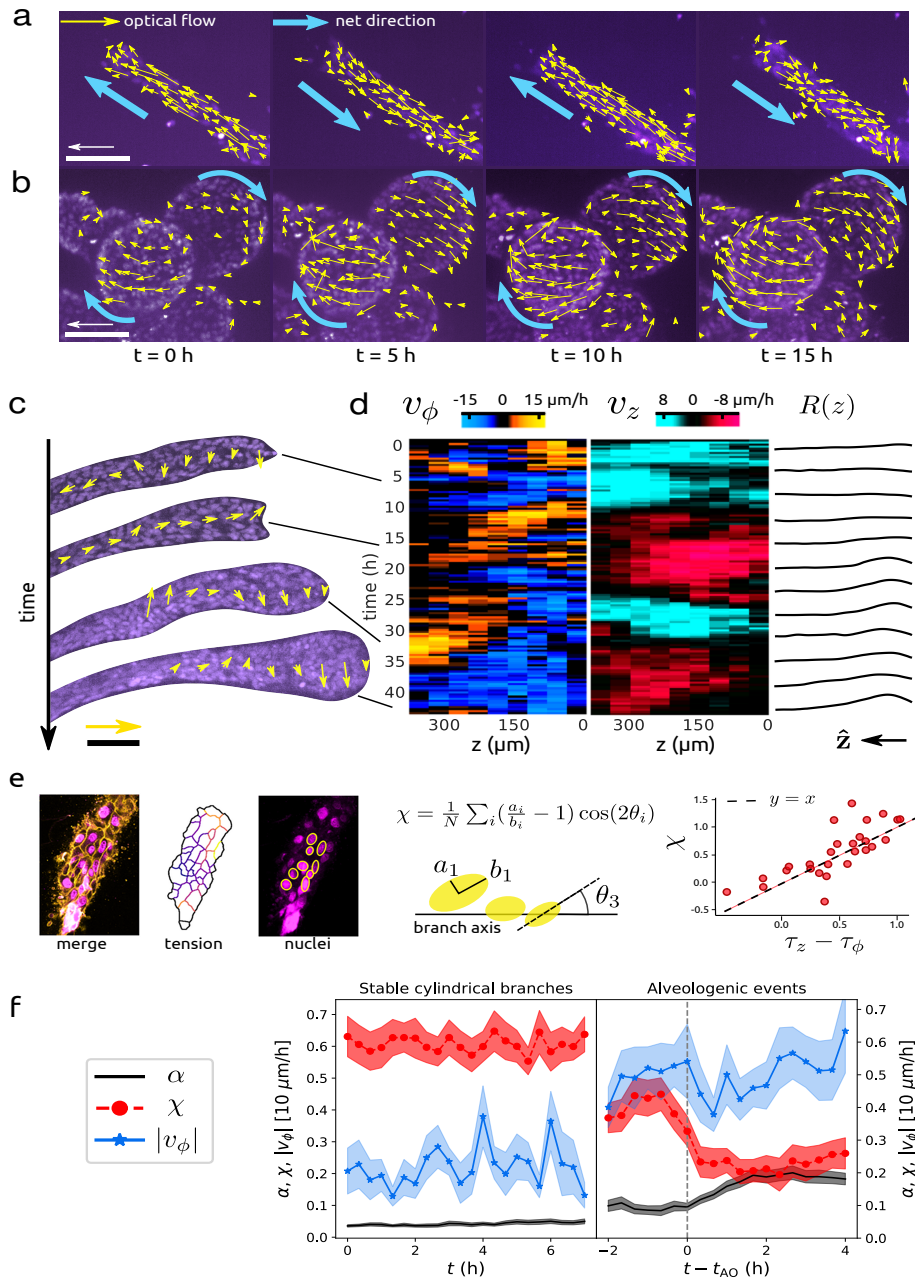445   [35] Bradski, G. The OpenCV Library. *Dr. Dobb's Journal of Software Tools* (2000).

a

attached gels:
high axial tension

τ_ϕ

τ_z

ECM invasion

longitudinal
oscillations

contractile remodelling

high ECM forces

collagen cage

b

floating gels:
decreased
tension anisotropy

τ_ϕ

τ_z

rigid body
rotation

shear
alignment

increased
circumferential
tension

τ_ϕ

τ_z

$\tau_\phi > \tau_c$

low ECM forces

geometrical
reinforcement
of rotation

budding instability

plastic ECM deformation

c

stable   unstable

τ_z/τ_c

isotropy

τ_ϕ/τ_c
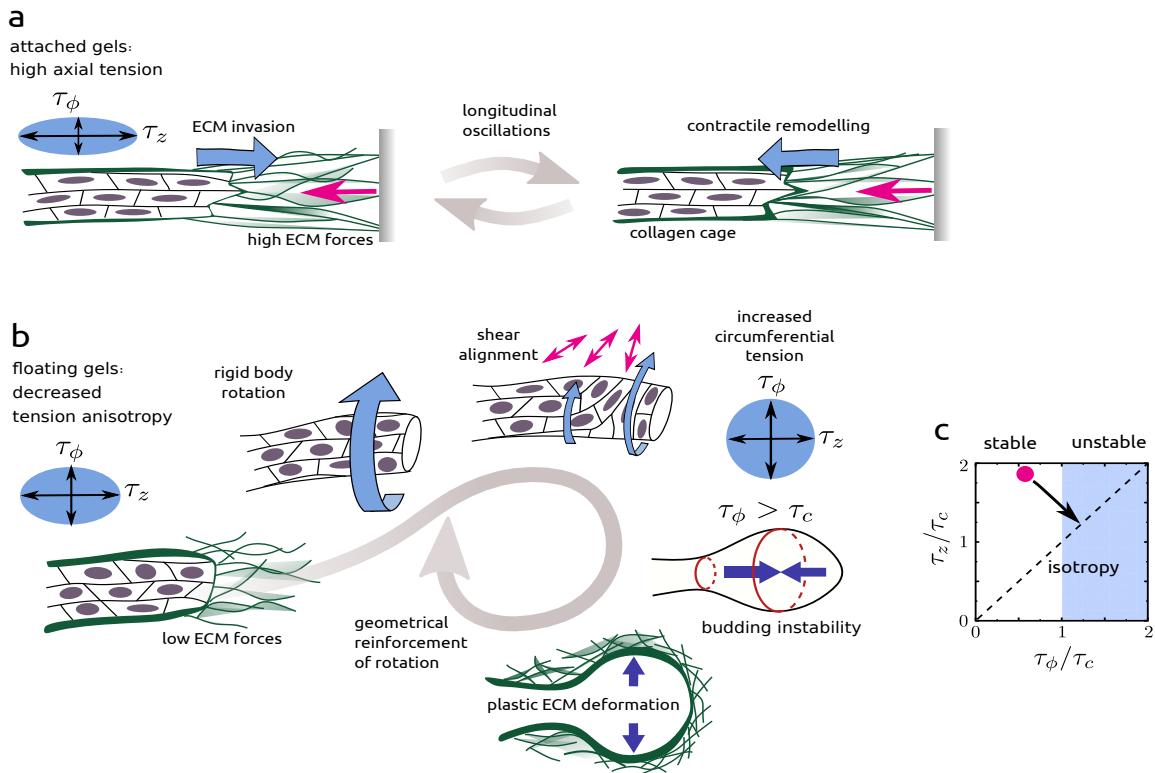
1

Appendix A: Supplementary Experimental Results

1. Movies

Supp. Movie 1 Cylindrical branches flow into the organoid body after hydrolysis of the collagen matrix.

Supp. Movie 2 Laser ablation of organoids for branches grown in the attached (left) and floating configuration (right).

Supp. Movie 3 Laser ablation in presence of Cytochalasin D.

Supp. Movie 4 Representative examples of cell dynamics over one day. All organoids stem from the same donor (M25) and were grown in floating gels. Notice that branch shape correlates strongly with the type of motion: axial translation in cylindrical branches, rotation in nascent and mature alveoli.

Supp. Movie 5 Long time observation of cell dynamics shows that alveologenesis and collective cell rotation are correlated (donor: M28).

Supp. Movie 6 Addition of HECD1 antibody against E–cadherin abolishes alveolar rotation within 15–25 hours (donor: M25).

Supp. Movie 7 Cell dynamics at 25X magnification. This experiment corresponds to Supplementary Fig. 4a (donor: M25).

Supp. Movie 8 Cell dynamics at 25X magnification. This experiment corresponds to Supplementary Fig. 4b (donor: M25).

2. Donors

Donor	Age (years)	Parity	Alveoli (%)	n
M20	67	2	30	80
M25	22	0	69	133
M26	34	2	60	78
M28	38	1	57	106

Table I. Age, parity, and frequency of alveoli occurrence at days 11-13 and number of branches analysed.

2

3. Collagen "cage"

Confocal microscopy of organoids grown in fluorescent collagen shows that organoid branches are surrounded by a thin, dense shell of collagen, which results from an irreversible compaction of the bulk collagen matrix due to active cell contractility. This "collagen cage" is thinner at the organoid branch tips and approaches a thickness of up to $h = 10\,\mu m$ towards the organoid body [1].

To determine whether the cage is also present around spherical alveoli, organoids were cultivated for two weeks in floating gels of collagen I conjugated with Atto 488. Confocal imaging of both cylindrical branches and spherical alveoli was done using a Leica SP8 confocal microscope and a 40X/1.1 water immersion objective. Subsequently, we measured the fluorescence intensity of the collagen network close to the tip of the branches and normalized on the maximum background. We found indeed a layer of strong fluorescence around spherical alveoli [Supplementary Fig. 1]. This suggests that the formation of the alveolus displaces the preexisting collagen cage, inducing a plastic strain of the surrounding ECM as the organoid surface pushes against it. As a corollary, a proteolytic mechanism for alveologenesis - one that would require the dissolution of the fluorescent collagen - seems unlikely.
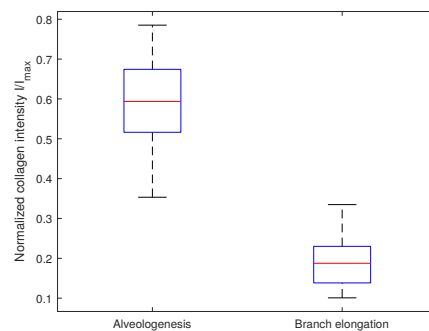
Supplementary Fig. 1. Intensity of the fluorescent collagen cage surrounding spherical alveoli ($n = 15$) and elongating cylindrical branches ($n = 12$)

### 4. Organoid ablation in the presence of Cytochalasin D

Laser ablation of organoid branches induces a fast recoil of the organoid tissue surrounding the cut. To confirm that this response is due to forces generated by the actomyosin system, we performed experiments in presence of Cytochalasin D (CD), which is known to disrupt actin organization [2]. We incubated organoids with CD at a concentration of $4\,\mu$M for $30\,$min, stained membranes with CellMask for $10\,$min, and replenished medium containing CD to perform ablation experiments. We found that the recoil response was no longer axially biased and the average strain was significantly lower in the presence of CD (Supplementary Fig. 2). This corroborates that the laser ablation experiments probe cortical tension and that the anisotropy of the response requires an intact actin cytoskeleton.
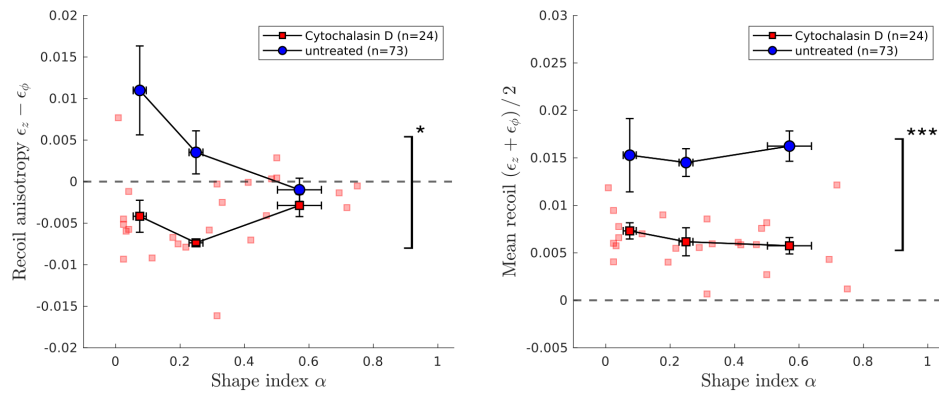
Supplementary Fig. 2. Recoil anisotropy $\epsilon_z - \epsilon_\phi$ and mean recoil $(\epsilon_z + \epsilon_\phi)/2$ as a function of index shape α in presence of Cytochalasin D (red squares). All organoids were grown in floating gels; control points are a replotting of the data shown in Fig. 2c,d (blue circles).

4

5. Cell boundary segmentation

Stained cell membranes were analysed with the Multicut segmentation tool included in the Ilastik software [3], which decomposes the image into closed regions without dangling edges. The respective boundaries of the cells were traced with a custom Python script. To characterize whether there is an orientational order in the cell population (i.e. a nematic order), we discretized the (smooth) cell boundaries into straight subsegments and computed the histogram of subsegment angles relative to the branch axis angle θ_0. We found that cell boundaries in attached gels are highly biased towards the branch axis, and become increasingly isotropic as the shape index increases (Supplementary Fig. 3). Branches with $\alpha = 0.3$ are already very close to an isotropic distribution of cell boundaries.
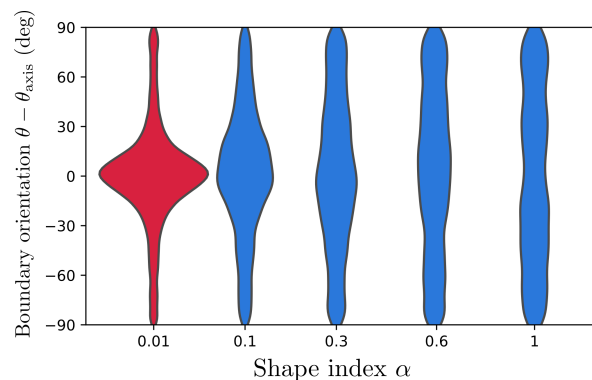
Supplementary Fig. 3. Distribution of cell boundary angles θ relative to the branch axis θ_0 (n=42 organoids) as a function of shape index α for attached (red) and floating gels (blue).

6. Force inference

From the segmented images we sought to estimate the surface tension tensor $\boldsymbol{\tau}$. To that end, we first computed the line tensions acting along individual cell boundaries using the method of force inference developed by Wayne Brodland et al. [4]. This elegant approach assumes a 2D vectorial force balance at every junction of boundaries, providing two scalar equations per junction for a number of unknown line tensions equal to that of boundaries. Arrangements of cells with high connectivity then give an overdetermined homogeneous system of equations. To avoid the trivial zero solution, the equation system is made hetero-

geneuos by adding an equation that imposes a mean line tension equal to 1. The full system
is solved by linear least squares. In this way, we obtained (relative) line tensions γ_i for each
cell boundary.

To obtain the surface tension tensor, we must integrate the contributions from each bound-
ary. Specifically, the mean stress tensor in a body can be obtained from the forces acting
along its boundary as follows [5]:

$$\bar{\boldsymbol{\tau}} = \frac{1}{2A} \oint dl \Big[\mathbf{f} \otimes \mathbf{x} + \big(\mathbf{f} \otimes \mathbf{x} \big)^T \Big], \tag{A1}$$

where $\mathbf{x}$ refers to the position vectors of each boundary point that is subject a force $\mathbf{f}\,dl$,
and A refers to the area of the body. Here, we used a computational scheme that, in
the end, reproduced an expression that is analogous to Eq. (A1). First, we divided each
boundary into subsegments of constant length $l = 1\,\mu\mathrm{m}$, where segment j of boundary i is
oriented in the direction θ_{ij} relative to the tube axis θ_0. Then, we summed the line tensions
of all subsegments that point along a given angle θ to obtain the total force distribution
$F(\theta) = \sum_{\theta_{ij}=\theta} \gamma_i$. The corresponding force vector is given by $F(\theta)\,\hat{\mathbf{e}}_\theta$, where $\hat{\mathbf{e}}_\theta = (\cos(\theta -$
$\theta_0), \sin(\theta - \theta_0))$ refers to the *unit* vector corresponding to the angle relative to the tube axis,
$\theta - \theta_0$. Then, the average tension tensor is proportional to

$$\boldsymbol{\tau} \propto \oint d\theta\, F(\theta)\, \hat{\mathbf{e}}_\theta \otimes \hat{\mathbf{e}}_\theta\,. \tag{A2}$$

Since the line tension is assumed to be constant along each boundary, the total force distri-
bution is symmetric with respect to $\theta \to \theta + \pi/2$. Thus, we calculated the *normalized* axial
stress component as follows:

$$\tau_z = \int_{\theta_0 - \pi/2}^{\theta_0 + \pi/2} d\theta\, F(\theta) \cos^2(\theta - \theta_0) \Big/ \int_{\theta_0 - \pi/2}^{\theta_0 + \pi/2} d\theta\, F(\theta)/2\,, \tag{A3}$$

where the normalization factor ensures that the stress is adimensional and equal to 1 for
a uniform stress distribution. Our choice of normalization is justified by the observation
that the mean recoil $(\epsilon_z + \epsilon_\phi)/2$ in our laser ablation experiments remained approximately
constant for all organoid shapes, cf. Supplementary Fig. 2. A similar equation holds for the

circumferential tension:

$$\tau_\phi = \int_{\theta_0-\pi/2}^{\theta_0+\pi/2} d\theta \, F(\theta) \sin^2(\theta - \theta_0) \bigg/ \int_{\theta_0-\pi/2}^{\theta_0+\pi/2} d\theta \, F(\theta)/2 \,. \tag{A4}$$

**7. Nuclear anisotropy parameter: an alternative measurement of cellular tension**

The shapes of nuclei closely follow the surrounding cell boundaries. We found that nuclei shape could be used to obtain an approximate estimate of the tension anisotropy $\tau_z - \tau_\phi$ determined by force inference, while offering the advantages of less phototoxicity and allowing for precise observation of cell movement. A similar approach was recently discussed and validated by Kong *et al* [6]. Following branch dynamics over 10–20 hours, we found that the nuclear anisotropy parameter χ is large and constant in stable cylindrical branches [Supplementary Fig. 4a]. It robustly decreases shortly before an alveologenic increase in shape index (main text, Fig. 3f), but it can also be seen to increase prior to a reversal of alveologenesis, as the branch resumes longitudinal motion towards the organoid body (Fig. 4b, $t = 10\,\text{h}$).
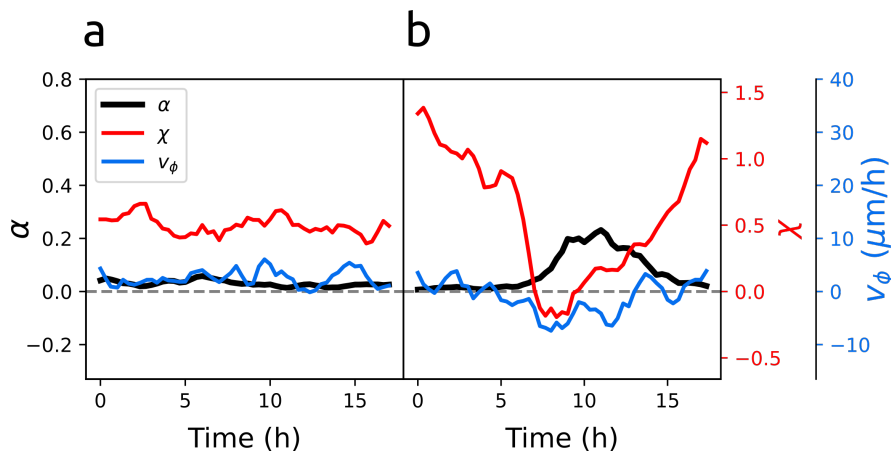
Supplementary Fig. 4. Shape index α, rotation velocity v_ϕ and nuclear anisotropy parameter χ as a function of time for two different experiments. **a,** Data corresponding to Supplementary Movie 7. **b,** Data corresponding to Supplementary Movie 8.

Plotting the replica-averaged nuclear anisotropy parameter as a function of the shape index, we could compare dynamic data with the results of (static) laser ablation and force

inference experiments [Supplementary Fig. 5]. We found a good agreement between all datasets, suggesting that the contrasting morphologies of organoids grown in attached and floating gels can be understood in terms of the same underlying physics.
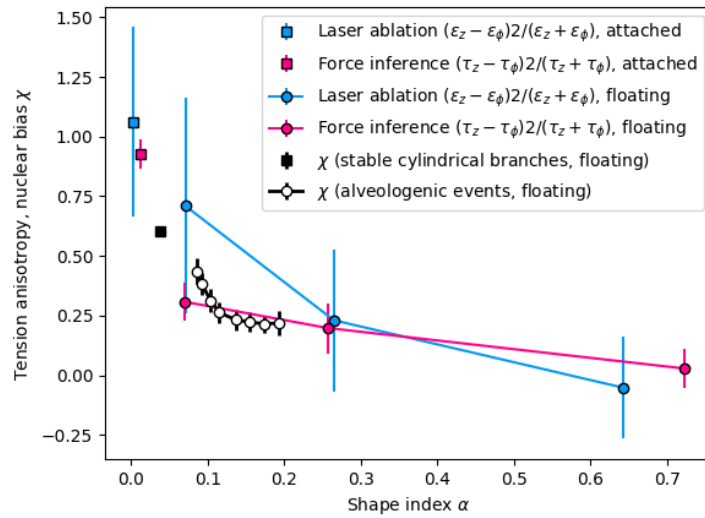

Supplementary Fig. 5. Comparison between laser ablation, force inference and nuclear anisotropy (dynamic) data. Laser ablation and force inference data are replotted from Figs. 2d,h; Nuclear anisotropy data from Fig. 3f.

8. Rotation of alveoli for several donors

The rotational motion of mammary gland organoid branches is largely determined by the branch shape, and the shape index α suffices to characterize this dependency. Branches undergoing translational motion have indexes below 0.3, whereas branches displaying persistent rotation for at least 5 hours have indexes above 0.2 [Supplementary Fig. 6].

To determine the generality of alveolar rotation, we counted the number of branches that showed a sustained rotation around their axis for at least 5 h. For the 4 donors under study, we found that 70%-80% of branches with $\alpha > 0.3$ rotated, whereas most cylindrical branches moved longitudinally (Supplementary Fig. 7).

8
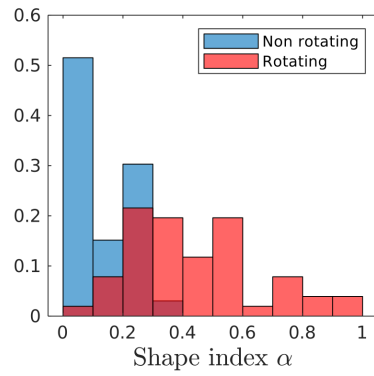
Supplementary Fig. 6. Histogram of shape index α for branches classified as either translating or rotating according to the dominant cell movement mode for 5 hours. Donor: M26.
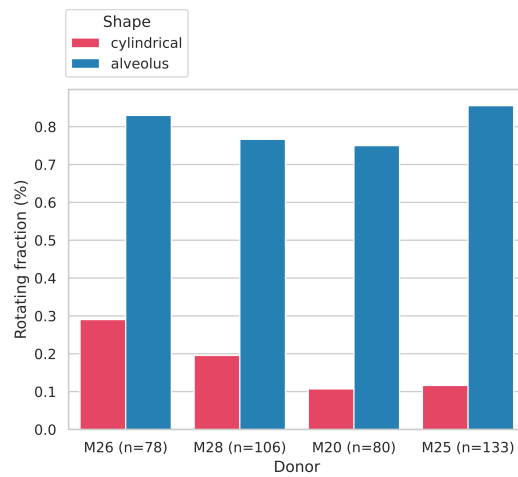
Supplementary Fig. 7. Frequency of rotation in cylindrical branches ($\alpha \leq 0.3$, red) and alveoli ($\alpha \geq 0.3$, blue) for all donors studied (see Supplementary Table 1 for branch sample size).

Appendix B: Supplementary Theoretical Discussion

In the following, we present and discuss in detail our mechanical model of organoid branches. We consider an organoid branch as a shell-like cylindrical tissue, where cell contractility confers an anisotropic surface tension. The lumen of the organoid branch is filled by a viscous fluid, while on the outside it is enveloped by an elastic collagen cage as well as an elastic extracellular matrix. Our theoretical analysis shows that the initial cylindrical shape of an organoid branch becomes unstable against long-wavelength perturbation modes when the circumferential component of the anisotropic surface tension exceeds a critical value. This critical circumferential tension is determined by the elastic properties of the collagen cage and the extracellular matrix. In contrast to the circumferential tension, the axial tension penalizes short-wavelength modes and thus only affects the wavelength of the fastest-growing mode, but not the onset of the shape instability itself.

After choosing a suitable (i.e. cylindrical) coordinate system, we discuss the mechanical stresses that act on organoid branches: active cell contractility, passive bending of the collagen cage and deformations of the extracellular matrix. Since viscous stresses asymptotically vanish if the dynamics of the organoid branch is sufficiently slow, the applied mechanical stresses determine whether a tubular shape is stable or not. To then find conditions under which a tubular conformation becomes mechanically unstable, we consider linear shape perturbations of a tubular shell that has a homogeneous initial radius and vanishing mechanical stress (mechanical steady state). Then, by expanding our theory beyond this linear regime and considering nonlinear contributions to the mechanical stress, we investigate how an organoid branch responds to an increase in surface tension.

1. Choice of coordinate system

We describe an organoid branch as a thin tubular shell that consist of contractile cells, and use a cylindrical coordinate system (r, z, ϕ), where the z-axis is aligned with the centerline of the tube, r measures the radial distance from the centerline, and ϕ is the azimuthal angle [Supplementary Fig. 8]. For the sake of simplicity, we restrict ourselves to a rotationally symmetric geometry, so that $\partial_\phi Q(z, \phi) \equiv \partial_\phi Q(z) = 0$ for any (scalar, vectorial or tensorial) quantity $Q(z, \phi)$.
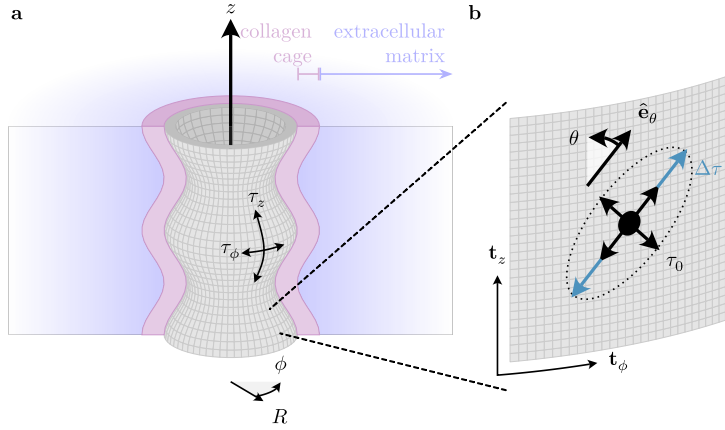
Supplementary Fig. 8. Schematic representation of the organoid branch geometry. **a)** The cell population forms a thin tubular shell (gray), whose lumen is filled by an aqueous solution under hydrostatic pressure p_0. On the outside, the cellular tube is surrounded by a dense and rigid collagen cage (magenta). Further away, the cellular tube is surrounded by a soft extracellular matrix (blue). **b)** Enlarged view of the cell population that forms the surface of the organoid branch. Each cell (within the local tangent plane) is oriented at an angle θ relative to the local axial tangent vector $\mathbf{t}_z$, with corresponding orientation vector $\hat{\mathbf{e}}_\theta$. We consider each cell as a contractile force dipole. To conceptually illustrate how such a contractile force dipole acts, one can envision an idealized cell with diameter d_0 and area A_0 (black circle). The cell cytoskeleton exerts contractile forces on the cell boundary, which we decompose into two contributions: (i) Isotropic contractile forces f_0 correspond to an isotropic tension $\tau_0 \equiv f_0 d_0/A_0$ (black arrows). (ii) In addition, the contractile cell breaks rotational symmetry in this local frame of reference by increasing contractility ($\Delta f > 0$) or decreasing contractility ($\Delta f < 0$) along its axis $\hat{\mathbf{e}}_\theta$. Therefore, in addition to the isotropic part of cell tension, there is also an anisotropic contribution $\Delta \tau \equiv \Delta f\, d_0/A_0$.

143   The tubular shell is located at a distance $r = R(z)$ from the centerline, where it forms an

144 interface between the viscous fluid in the lumen of the organoid branch and the extracellular

145 matrix outside of the organoid. We parameterize this interface by the two coordinates (z, ϕ)

146 and the corresponding position vector field

$$\mathbf{R}(z, \phi) = \begin{bmatrix} R(z)\, \cos \phi \\ R(z)\, \sin \phi \\ z \end{bmatrix} . \tag{B1}$$

147 The two (orthogonal but non-normalized) tangent vectors that span the surface of the tubu-

148   lar shell are given by

$$
\mathbf{t}_z =
\begin{bmatrix}
\partial_z R(z) \, \cos\phi \\
\partial_z R(z) \, \sin\phi \\
1
\end{bmatrix}, \quad \text{and} \quad
\mathbf{t}_\phi =
\begin{bmatrix}
-R(z) \, \sin\phi \\
R(z) \, \cos\phi \\
0
\end{bmatrix}.
\tag{B2}
$$

149   In the following, we usually omit the argument of the tube radius, $R(z) \equiv R$, to keep the

150   expressions concise. To measure arc distances on the surface of the tubular shell in terms of

151   the coordinates (z, ϕ), we use the metric tensor $g_{ij} = \mathbf{t}_i \cdot \mathbf{t}_j$ [7]:

$$
\mathbf{g} \equiv
\begin{bmatrix}
g_{\phi\phi} & g_{\phi z} \\
g_{\phi z} & g_{zz}
\end{bmatrix}
=
\begin{bmatrix}
R^2 & 0 \\
0 & 1 + (\partial_z R)^2
\end{bmatrix}.
\tag{B3}
$$

152   We complete the local coordinate system that spans the surface of the tubular shell by

153   introducing the (outward pointing) *unit* normal vector, $\hat{\mathbf{n}} = (\mathbf{t}_\phi \times \mathbf{t}_z)/\sqrt{\det \mathbf{g}}$, which lies

154   perpendicular to the surface:

$$
\hat{\mathbf{n}} = \frac{1}{[1 + (\partial_z R)^2]^{\frac{1}{2}}}
\begin{bmatrix}
\cos\phi \\
\sin\phi \\
-\partial_z R
\end{bmatrix}.
\tag{B4}
$$

155   Thus, to summarize, we have defined a local coordinate system on the surface of the tubular

156   shell, which is parameterized by the coordinates (z, ϕ) and spanned by the two tangent

157   vectors $(\mathbf{t}_z, \mathbf{t}_\phi)$ as well as the normal vector $\hat{\mathbf{n}}$.

158   Next, we determine the shape tensor, $h_{ij} = \hat{\mathbf{n}} \cdot \partial_i \mathbf{t}_j$, which describes the geometrical shape

159   of the tubular shell [7]. Specifically, one can directly read off the two principal curvatures of

160   the tubular shell from the following expression:

$$
\mathbf{h} \cdot \mathbf{g}^{-1} =
\begin{bmatrix}
-\dfrac{R^{-1}}{[1 + (\partial_z R)^2]^{\frac{1}{2}}} & 0 \\
0 & \dfrac{\partial_z^2 R}{[1 + (\partial_z R)^2]^{\frac{3}{2}}}
\end{bmatrix}
\equiv
\begin{bmatrix}
\kappa_\phi & 0 \\
0 & \kappa_z
\end{bmatrix}.
\tag{B5}
$$

161   As explained above, we view the organoid branch as a rotationally symmetric cylinder that

162   is parameterized by the distance $R(z)$ of its surface from the centerline. In the present work,

163   we always assume that deformation gradients are small, so that $\partial_z R \ll 1$. Then, the two

164 principal curvatures are simply given by

$$\kappa_\phi \approx -\frac{1}{R}, \quad \text{and} \quad \kappa_z \approx \partial_z^2 R, \tag{B6}$$

165 which are used in the remainder of the Supplementary Material. In the upcoming sections,
166 we will discuss the physical processes that can dynamically modify these local geometric
167 properties of the organoid branch.

168 **2. Active cell contractility induces anisotropic tension and Laplace pressure**

169 As discussed in section B 1 "Choice of coordinate system", we describe the organoid
170 branch as a thin tubular shell. At the surface of the organoid branch, contractile cells form
171 a thin confluent tissue. Furthermore, this surface defines an interface between the fluid
172 in the lumen of the organoid branch and the extracellular matrix outside of the organoid
173 branch [Supplementary Fig. 8]. Since the cells are the only active component of our system,
174 their activity determines the dynamics of the organoid branch. Specifically, nonequilibrium
175 cell contractility at the surface of the organoid branch confers an *active interfacial stress* in
176 the form of anisotropic surface tension, as we explain in the following.

177 **Link between cell orientation and tension anisotropy.** We consider cells as
178 anisotropic force dipoles [8, 9], where the anisotropy stems from the local orientation of
179 the cells and their cytoskeleton[1]. Before we characterize a population of many cells, we
180 first focus on describing a single cell. To that end, we consider the local reference frame
181 (tangent plane) that is spanned by the two (orthogonal but non-normalized) surface tangent
182 vectors $(\mathbf{t}_z, \mathbf{t}_\phi)$ and whose origin coincides with the position of the cell [Fig. 8b]. The cell is
183 oriented at an angle θ relative to the axial surface tangent vector $\mathbf{t}_z$, so that we represent
184 its orientation with the vector

$$\hat{\mathbf{e}}_\theta = \cos(\theta)\frac{\mathbf{t}_\phi}{\|\mathbf{t}_\phi\|} + \sin(\theta)\frac{\mathbf{t}_z}{\|\mathbf{t}_z\|} \equiv \begin{bmatrix} \cos(\theta) \\ \sin(\theta) \end{bmatrix}. \tag{B7}$$

185 Due to orientational order in its cytoskeleton, the cell can exert stronger (or weaker) tensile

---

[1] In section A 6 "Force inference", we have represented the average tension tensor of a cell as a boundary integral of the forces that act on the cell boundary. Here, we consider the body forces that act as a result of intracellular actomyosin contractility. In the co-moving reference frame of a non-deforming cell, both descriptions are equivalent because internal stresses must exactly balance externally applied stresses.

¹⁸⁶ forces along its axis $\hat{\mathbf{e}}_\theta$ than along the perpendicular axis. Therefore, we split the tension

¹⁸⁷ of a cell into two contributions: (i) an isotropic *base* tension τ_0 that preserves rotational

¹⁸⁸ symmetry in our local reference frame and (ii) an additional anisotropic tension $\Delta\tau$ along

¹⁸⁹ the direction specified by the vector $\hat{\mathbf{e}}_\theta$ that breaks rotational symmetry in our local reference

¹⁹⁰ frame. Taken together, we model cell contractility with the following cell tension tensor[2]:

$$\boldsymbol{\tau}(\theta) = \tau_0\, I_2 + \Delta\tau\, \hat{\mathbf{e}}_\theta \otimes \hat{\mathbf{e}}_\theta \,. \tag{B8}$$

¹⁹¹ The diagonal elements of the cell tension tensor then correspond to the axial τ_z and the

¹⁹² circumferential tension τ_ϕ, respectively:

$$\boldsymbol{\tau}(\theta) = \begin{bmatrix} \tau_0 + \Delta\tau\cos^2(\theta) & \Delta\tau\cos(\theta)\sin(\theta) \\ \Delta\tau\cos(\theta)\sin(\theta) & \tau_0 + \Delta\tau\sin^2(\theta) \end{bmatrix} \equiv \begin{bmatrix} \tau_z & \ddots \\ \ddots & \tau_\phi \end{bmatrix} . \tag{B9}$$

¹⁹³ Now consider a population of cells in which the cells differ in their orientations $\hat{\mathbf{e}}_\theta$ and

¹⁹⁴ exert an anisotropic tension $\boldsymbol{\tau}(\theta)$. We statistically represent the occurrence of different

¹⁹⁵ cell orientations θ by the probability density function $P(\theta)$, which we refer to as *angular*

¹⁹⁶ *distribution of cell orientations.* The average tension tensor in the confluent tissue is then

¹⁹⁷ given by the weighted average $\bar{\boldsymbol{\tau}} = \int_{-\pi}^{\pi} d\theta\, P(\theta)\, \boldsymbol{\tau}(\theta)$. Thus, the off-diagonal terms of the

¹⁹⁸ average tension tensor in the confluent tissue vanish for a symmetric angular distribution

¹⁹⁹ of cell orientations, $P(\theta) = P(-\theta)$. Furthermore, we note that the trace of the cell tension

²⁰⁰ tensor for each cell is independent of the cell's orientation, $\mathrm{tr}(\boldsymbol{\tau}) = \tau_z + \tau_\phi = 2\tau_0 + \Delta\tau$.

²⁰¹ Therefore, since the angular distribution of cell orientation is normalized, $\int_{-\pi}^{\pi} d\theta\, P(\theta) = 1$,

²⁰² the trace of the average tension tensor in the confluent tissue is constant,

$$\mathrm{tr}\, \bar{\boldsymbol{\tau}} = \bar{\tau}_z + \bar{\tau}_\phi = 2\tau_0 + \Delta\tau\,. \tag{B10}$$

²⁰³ In other words, the total tension in the confluent tissue, $\bar{\tau}_z + \bar{\tau}_\phi$, is independent of the angular

²⁰⁴ distribution of cell orientations. This explains our experimental finding that the sum of the

²⁰⁵ axial and the circumferential tension remains constant for all experiments.

²⁰⁶ If all cells are oriented in the same direction, e.g. along the centerline of the organoid

²⁰⁷ branch so that $P(\theta) = \delta(\theta)$, then the difference between the axial and the circumferential

---

[2] One can also rationalize this form by performing a boundary integral of the forces that act on the cell boundary, analogous to section A6 "Force inference".

208 tension is simply given by $\bar{\tau}_z - \bar{\tau}_\phi = \Delta\tau$. In contrast, if all cells are oriented randomly,

209 $P(\theta) = 1/(2\pi)$, then axial and circumferential tension are equal $\bar{\tau}_z = \bar{\tau}_\phi$. Thus, if the cells are

210 initially aligned with the axial surface tangent vector $\mathbf{t}_z$ (i.e. aligned with the centerline of the

211 tube) and subsequently *randomize* their orientation, then the circumferential tension in the

212 tissue will effectively increase at the expense of a decreasing axial tension. These theoretical

213 considerations imply that in our experiments the predominant process underlying tension

214 anisotropy is due to the reorientation of cells and not a change in their tensile properties τ_0

215 and $\Delta\tau$.

216 In the present section, we have investigated how the orientation of cells, treated as

217 anisotropic force dipoles, affects the average tension in a confluent tissue. From here on,

218 we will not describe the precise distribution of cell orientation. Instead, we simplify our de-

219 scription by considering only an axial tension τ_z and an independent circumferential tension

220 τ_ϕ on the surface of the tubular shell (i.e. the organoid branch); we also simplify notation

221 by omitting the overline indicating the population average.

222 **Tension anisotropy leads to generalized Laplace pressure.** Next, we discuss how

223 *anisotropic* surface tension couples to the organoid shape and how it is different from an

224 isotropic surface tension. We consider cells as active agents that perform work as they deform

225 the organoid branch (i.e. tubular shell). Instead of formally carrying out variational calculus

226 of surfaces, in this section we omit the corresponding surface integrals by considering the

227 dynamics of an (approximately homogeneous) infinitesimal surface patch with area A. In the

228 case of isotropic surface tension τ_{iso}, the cells perform the work $\delta W = -\tau_{iso}\,\delta A$ [10] as they

229 change the area of the surface patch on the tubular shell by δA. For a curved surface such as

230 the organoid branch, one can relate a change in surface area to a displacement of the surface

231 patch by a distance δu along its normal vector[3,4], $\delta A = -(\kappa_\phi + \kappa_z)\,\delta u\,A$ [7]. Thus, any

---

[3] This relation can be easily checked for spherical geometries (with radius R, azimuthal angle ϕ and polar angle ϑ), where a surface patch has area $A \equiv R^2\,d\vartheta\,d\cos\phi$. Then, radial movement of the surface patch by a distance δu changes its area by $\delta A = \partial_R A\,\delta u = 2R\,d\vartheta\,d\cos\phi\,\delta u$. Identifying the curvature of the sphere with $\kappa_\phi = \kappa_\vartheta = -1/R$, one then finds $\delta A = -(\kappa_\phi + \kappa_\vartheta)\,\delta u\,A$. One can perform an analogous calculation for straight tubular geometries.

[4] For general (i.e. undulating) tubular geometries, one has to determine how the surface area changes upon a deformation $\delta u(z)$ via variational calculus. The surface area of the cylinder is given by the functional $A[u] = 2\pi\int dz\sqrt{1 + (\partial_z u)^2}\,(R_0 + u)$. The variation of the surface area of the cylinder is then also a functional: $\delta A[u] = -2\pi\int dz\,(R_0 + u)\,(\kappa_\phi + \kappa_z)\,\delta u(z)$, where the curvatures are given by Eq. (B5). For sufficiently thin patches, one can then approximate their surface area as $2\pi\int dz\,(R_0 + u) \approx 2\pi dz\,(R_0 + u) \equiv A$, to arrive at the expression in the main text.
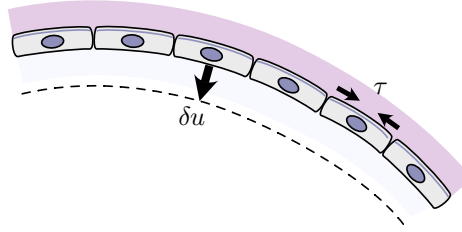
Supplementary Fig. 9. Illustration of a surface that moves by a distance δu, thereby decreasing its surface area from A (initial configuration, sketch) to $A + \delta A$ (dashed line), where $\delta A < 0$. The surface consists of contractile cells, which exert a tension τ that drives the dynamics.

232 surface patch that is curved towards its direction of motion, $(\kappa_\phi + \kappa_z)\,\delta u > 0$, will effectively

233 contract [Fig. 9]. This results in a cell-induced Laplace pressure $\Delta p_{iso} = \frac{\delta W}{A \delta u} = (\kappa_\phi + \kappa_z)\,\tau_{iso}$.

234 Note that this is a generalization of the expression for the Laplace pressure in a sphere,

236 $\Delta p_{iso} \sim 2\tau_{iso}/R$, to generic surfaces.

237   Unlike isotropic tension, *anisotropic* tension breaks rotational symmetry, so that one

238 must individually consider the (relative) length changes that occur in different directions as

239 the cells deform the organoid branch. Here, it helps to envision (anisotropic) surface tension

240 as a meshwork of ropes, which are aligned along the axis and along the circumference of

241 the tubular shell, respectively. Then, one may associate axial tension with the work that is

242 required for increasing the (relative) length of the tubular shell, and circumferential tension

243 with the work that is required for increasing the (relative) circumference of the tubular shell.

244 In summary, one then has:

$$\delta W = -\left(\tau_z\,\frac{\delta\ell_z}{\ell_z} + \tau_\phi\,\frac{\delta\ell_\phi}{\ell_\phi}\right) A\,, \tag{B11}$$

245 where ℓ_z and ℓ_ϕ refer to the arc lengths on the surface and $A = \ell_z\,\ell_\phi$ is the area of the

246 corresponding surface patch. Upon a displacement of the organoid surface by a distance δu

247 along its normal vector, the circumferential arc length ℓ_ϕ and the axial arc length ℓ_z change

16

as follows[5,6]:

$$\delta\ell_\phi = -\kappa_\phi\,\delta u\,\ell_\phi$$
$$\delta\ell_z = -\kappa_z\,\delta u\,\ell_z\,. \tag{B12}$$

With these considerations, the (generalized) Laplace pressure on the tubular shell, $\frac{\delta W}{A\delta u}$, is given by:

$$\Delta p_\tau = \tau_\phi\kappa_\phi + \tau_z\kappa_z\,. \tag{B13}$$

By explicitly inserting the expressions for the axial and the circumferential curvatures, Eq. (B6), we obtain:

$$\Delta p_\tau = -\frac{\tau_\phi}{R} + \tau_z\,\partial_z^2 R\,. \tag{B14}$$

The generalized Laplace pressure, Eq. (B14), must be balanced by stresses in the fluid (specifically, viscous stresses and hydrostatic pressure) as well as by elastic stresses in the extracellular matrix [discussed in sections A 3 "Collagen "cage"" and B 4 "Bulk extracellular matrix elasticity does not significantly affect tube stability"].

3. Collagen cage envelops organoids and confers mechanical stability

In this section, we discuss the elastic properties of the extracellular matrix, which puts constraints on the deformations of the thin tubular shell (i.e. the organoid branch). We base our model on the experimental determination of the density and thickness of the collagen cage that surrounds branches and alveoli, as discussed above (section A 3 "Collagen "cage""). This is built by the contractile activity of the cells in the organoid branches, which gives rise to complex mechanical properties. Furthermore, its mechanical properties currently cannot be separated from the mechanical properties of the surrounding collagen matrix and the mechanical properties of the cells. As a consequence, its elastic modulus is unknown and not readily accessible to experiments. In this section, we estimate the elastic modulus of the collagen cage.

Estimate for the rigidity of the collagen cage. From fluorescence intensity mea-

---

[5] This relation can be illustrated as follows. Any curved line segment can be understood as a circle segment with angle $d\phi$ and radius R. The arc length of this line segment is then given by $\ell_\phi = R\,d\phi$. Upon radial displacement by a distance δu, the arc length changes by $\delta\ell_\phi = \partial_R\ell_\phi\,\delta u = d\phi\,\delta u$. Identifying the curvature as $\kappa_\phi \equiv -1/R$, one then finds $\delta\ell_\phi = -\kappa_\phi\,\delta u\,\ell_\phi$.

[6] Note that from these relations one also finds $\delta A = \ell_z\delta\ell_\phi + \ell_\phi\delta\ell_z = -(\kappa_\phi + \kappa_z)\,\delta u\,A$, where $A \equiv \ell_\phi\ell_z$.

17

269 surements, we know that the collagen cage has a roughly 5-fold higher density than the

270 bulk collagen [1]. We now assume that the cage is structurally similar to bulk collagen, but

271 concentrated by a factor of 5. In general, the elastic modulus of collagen increases with

272 the concentration roughly in a power-law manner with an exponent in the range of 2.2–

273 2.6 [11, 12]. At our standard concentration of $\rho_{\text{bulk}} = 1.3\,\text{mg}\,\text{ml}^{-1}$, we measured the shear

274 modulus to be $\mu \simeq 7\,\text{Pa}$ (data not shown; see [12]). The corresponding elastic modulus

275 can be calculated from the shear modulus by using [5] $E = 2\,(1 + \nu)\,\mu$, where the Poisson

276 ratio can be approximated as $\nu = 0.5$ [13]. Taking a concentration-dependence exponent

277 of 2.2, we thus obtain a lower estimate of $E_{cage} = 0.72\,\text{kPa}$ for the elastic modulus of the

278 collagen cage. Instead taking a concentration-dependence exponent of 2.6, we obtain an

279 upper estimate of $E_{cage} = 1.38\,\text{kPa}$ for the elastic modulus of the collagen cage.

280 **Passive stretching of the collagen cage induces elastic stresses.** As discussed

281 in the previous paragraphs, organoid branches and alveoli are surrounded by a thin, dense

282 "collagen cage", which we model as a thin elastic shell. In the following, we first discuss how

283 much energy is stored in elastic deformations of the collagen cage, which includes bending

284 and stretching [14]. Then, we determine the corresponding elastic boundary stresses that act

285 on the surface of a deformed tubular shell. Since we account for the mechanical properties

286 of cells by treating them as contractile force dipoles, cf. section B 2 "Active cell contractility

287 induces anisotropic tension and Laplace pressure", we assume in the following that the elastic

288 response of the tubular shell is dominated by the elastic properties of the collagen cage and

289 not the cell sheet[7].

290 We begin by considering stretching (or compression) of the collagen cage. To parameterize

291 the corresponding deformation field $\mathbf{u}(z)$, we use a cylindrical coordinate system that is

292 spanned by the normalized basis vectors [cf. section B 4 "Bulk extracellular matrix elasticity

293 does not significantly affect tube stability"]:

$$\hat{\mathbf{b}}_r = \begin{bmatrix} \cos\phi \\ \sin\phi \\ 0 \end{bmatrix}, \quad \hat{\mathbf{b}}_z = \begin{bmatrix} 0 \\ 0 \\ 1 \end{bmatrix}, \quad \text{and} \quad \hat{\mathbf{b}}_\phi = \begin{bmatrix} \sin\phi \\ \cos\phi \\ 0 \end{bmatrix}. \tag{B15}$$

294 As we assume that the deformation gradients of the surface are small, $\partial_z R \ll 1$, the radial

---

[7] A more detailed approach would have to differentiate between the mechanical in-plane deformation of the collagen cage and the mechanical in-plane deformation of the cell sheet, because motile cells can move relative to the substrate that they adhere to.
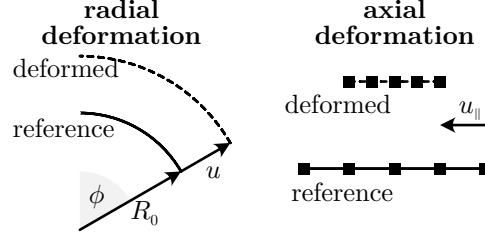
Supplementary Fig. 10. Illustration of radial deformations (left) and axial deformations (right). Any elastic body that is stretched or compressed exhibits elastic stresses that counteract these deformations.

basis vector coincides with the *unit* surface normal, $\hat{\mathbf{b}}_r \approx \hat{\mathbf{n}}$, and the axial basis vector coincides with the (in that case normalized) surface tangent vector, $\hat{\mathbf{b}}_z \approx \hat{\mathbf{t}}_z$, cf. section B 1 "Choice of coordinate system". We consider $u \equiv u(z)$ as the radial (or *normal*) component of the surface deformation field, which accounts for radial displacements of the surface. Such radial deformations change the radius of the tubular shell from R_0 in its cylindrical reference configuration to $R = R_0 + u$ in its deformed configuration. In addition, we also consider the axial (or *tangential*) component of the surface deformation field, $u_\parallel \equiv u_\parallel(z)$, which however has no effect on the shape of the tubular shell. To summarize, in our cylindrical geometry the surface deformation field is given by $\mathbf{u} = u\,\hat{\mathbf{b}}_r + u_\parallel\,\hat{\mathbf{b}}_z$

In the present work, we analyze the linear stability of the tubular shell and therefore consider only infinitesimal deformations of the collagen cage from its cylindrical reference configuration[8]. The corresponding linearized surface strain tensor is given by [5]:

$$\boldsymbol{\epsilon}_{lin} = \frac{1}{2}\left[\boldsymbol{\nabla}\otimes\mathbf{u} + (\boldsymbol{\nabla}\otimes\mathbf{u})^T\right] = \sum_{i,j\in\{\phi,z\}} \epsilon_{ij}\,\hat{\mathbf{b}}_i\otimes\hat{\mathbf{b}}_j\,, \tag{B16}$$

where the circumferential component $\epsilon_{\phi\phi}$ and the axial component ϵ_{zz} of the surface strain tensor are given by [Fig. 10]:

$$\epsilon_{\phi\phi} \approx \frac{u}{R_0}\,, \quad \text{and} \quad \epsilon_{zz} \approx \partial_z u_\parallel\,. \tag{B17}$$

Circumferential strain $\epsilon_{\phi\phi}$ corresponds to a change of the circumferential arc length ℓ_ϕ due

---

[8] For a nonlinear analysis, one would have to calculate the nonlinear (Green) strain tensor, $\boldsymbol{\epsilon}_g = \boldsymbol{\epsilon}_{lin} + \frac{1}{2}(\boldsymbol{\nabla}\otimes\mathbf{u})^T\cdot(\boldsymbol{\nabla}\otimes\mathbf{u})$, where $\boldsymbol{\epsilon}_{lin}$ refers to the linear part of the strain tensor (B16). Such an analysis was carried out by Hannezo et al. [15].

to an out-of-plane displacement u, cf. Eq. (B12) and Fig. 9. Axial strain corresponds to a compression or dilatation due to in-plane deformations. Neglecting in-plane shear strain $\epsilon_{z\phi}$, stretching of the tubular shell is associated with the following free energy density per surface area [14]:

$$f_s = \frac{E_{cage}\, h}{2\left(1-\nu^2\right)}\left[\epsilon_{\phi\phi}^2 + \epsilon_{zz}^2 + 2\nu\epsilon_{\phi\phi}\epsilon_{zz}\right],\tag{B18}$$

where $\nu \approx 0.5$ refers to the Poisson ratio of the collagen cage. The total energy that is stored in stretching of the collagen cage is given by $F_s[u, u_{\parallel}] = \int dS_0\, f_s$, and is thus a functional of the surface deformation field $(u, u_{\parallel})$. Here, $\int dS_0$ refers to a surface integral over the reference configuration of the collagen cage. In the cylindrical reference configuration, the (positive definite) stretching energy F_s vanishes and is therefore minimal. Consequently, any deformation of the collagen cage is accompanied by a finite energy cost so that a further deflection $(u, u_{\parallel}) \to (u + \delta u, u_{\parallel} + \delta u_{\parallel})$ costs an energy $\delta F_s = F_s[u + \delta u, u_{\parallel} + \delta u_{\parallel}] - F_s[u, u_{\parallel}]$. When external stresses are relieved, the collagen cage will gradually move back from the deformed configuration to its reference configuration by releasing the stored elastic stretching energy in the form of work. Thus, stretching of the collagen cage induces elastic stresses that drive movement towards the mechanical reference configuration. We distinguish between two possible (and independent) directions of movement, axial/tangential and radial/normal, which couple to the respective stress fields. Tangential movement by some infinitesimal distance $\delta u_{\parallel}$ is driven by a *shear stress* along the interface:

$$\begin{aligned}
\sigma_{cage}^{rz} &= -\frac{\delta F_s}{\delta u_{\parallel}} = -\frac{E_{cage}\, h}{2\left(1-\nu^2\right)}\frac{\delta}{\delta u_{\parallel}}\int dS_0 \left[\left(\frac{u}{R_0}\right)^2 + \left(\partial_z u_{\parallel}\right)^2 + 2\nu\left(\frac{u}{R_0}\right)\left(\partial_z u_{\parallel}\right)\right] \\
&= \partial_z\left[\frac{E_{cage}\, h}{1-\nu^2}\left(\epsilon_{zz} + \nu\epsilon_{\phi\phi}\right)\right].
\end{aligned}\tag{B19}$$

Here, the term in square brackets corresponds to the axial component of the elastic surface tension in response to deformations of the thin shell. Specifically, by identifying the axial tension with $\tau_{el,zz} \coloneqq \partial f_s / \partial \epsilon_{zz}$, cf. Eq. (B18), one finds that $\sigma_{cage}^{rz} = \partial_z \tau_{el,zz}$. Thus, Eq. (B19) illustrates that tangential shear stresses correspond to surface tension gradients, where regions with larger tension effectively pull on regions with lower tension.

These elastic shear stresses in the organoid branch are balanced by viscous stresses of the fluid that fills the organoid branch and by elastic stresses of the extracellular matrix. Since the cells are motile, they can move relative to the collagen cage. By extension of argument,

the collagen cage can *slip* against the cell sheet and the fluid in the lumen of the organoid branch, so that the tangential shear stresses induced by the collagen cage relax quickly compared to the normal stresses. Assuming such a timescale separation, the tangential shear stresses in the collagen cage will vanish on the timescales relevant for perpendicular motion of the interface[9]. Then, one finds from Eq. (B19) that $\epsilon_{zz} = C - \nu\epsilon_{\phi\phi}$, where C is some constant. With this adiabatic approximation, the free energy density (per surface area) that is stored in stretching deformations of the tubular shell simplifies to:

$$f_s^\star = \frac{E_{cage}\,h}{2}\left[\epsilon_{\phi\phi}^2 + \frac{C^2}{(1-\nu^2)}\right]. \tag{B20}$$

Since, by definition, both the free energy that is stored in deformations and the corresponding tensions vanish in the reference configuration, the constant $C = 0$ must also vanish. Just as tangential movement is driven by a *shear stress* along the interface, perpendicular motion of the surface by some infinitesimal distance δu is driven by a *normal stress* that acts on the surface:

$$\Delta p_s = -\frac{\delta F_s}{\delta u} \approx \partial_u f_s^\star = -\frac{1}{R_0}\left[E_{cage}\,h\,\frac{u}{R_0}\right]. \tag{B21}$$

The deformed radius of the tubular shell is given by $R = R_0 + u$ and the reference radius is given by R_0. The term in square brackets corresponds to the circumferential component of the elastic surface tension in response to deformations of the thin shell. Thus, Eq. (B21) can be understood as a Laplace pressure that is associated with tension due to elastic deformations.

Passive bending of the collagen cage is counteracted by elastic stresses. Next, we discuss the Helfrich free energy density per surface area that is stored in bending deformations of the collagen cage [16]:

$$f_b = \frac{1}{2}k_b\left[(\kappa_\phi - c_\phi)^2 + (\kappa_z - c_z)^2\right], \tag{B22}$$

where c_ϕ is the circumferential spontaneous curvature and c_z is the axial spontaneous curvature of the tubular shell. In the following, we assume that the tubular shape corresponds

---

[9] For a more general treatment, we would have to explicitly model the relaxation dynamics of the tangential shear stresses by considering the viscous properties of the collagen cage and/or the surrounding elastic medium.

to the mechanical reference configuration of the organoid branch, which therefore minimizes

the bending energy. Thus, we set the axial spontaneous curvature to $c_z = 0$ and the circumferential spontaneous curvature to $c_\phi = -1/R_0$. This is a plausible ansatz since the

collagen cage grows due to the contractility of the pre-existing organoid branch and persists

even after washing out the epithelial cells [1]. Nevertheless, one would have to modify this

assumption if the initial tubular shape corresponds to a pre-strained configuration, or if

the shell-like organoid branch itself also significantly contributes to the bending energy[10].

For small deformations u, the two principal curvatures of the tubular shell are in good approximation given by $\kappa_z = \partial_z^2 u$ and $\kappa_\phi = -1/R$, along the axis z and the circumference

ϕ respectively, cf. Eq. (B6). The free energy density (per surface area) that is stored in

deformations of the collagen cage is then given by:

$$f_b = \frac{1}{2} k_b \left[\left(\frac{1}{R} - \frac{1}{R_0} \right)^2 + (\partial_z^2 u)^2 \right] \approx \frac{1}{2} k_b \left[\frac{u^2}{R_0^4} + (\partial_z^2 u)^2 \right] , \qquad \text{(B23)}$$

for sufficiently small deformations of the tubular shell, $u \ll R_0$. The total bending energy

of the collagen cage is given by $F_b[u] = \int dS_0 \, f_b$, and is a functional of the radial component

of the surface deformation field, u. Here, as above, $\int dS_0$ refers to a surface integral over the

reference configuration of the collagen cage. In the cylindrical reference configuration, the

(positive definite) bending energy F_b vanishes and is therefore minimal. Consequently, any

deformation of the collagen cage is accompanied by a finite energy cost so that a further

deflection $u \to u + \delta u$ costs an energy $\delta F_b = F_b[u + \delta u] - F_b[u]$. When external stresses

are relieved, the collagen cage will gradually move back from the deformed configuration

to its reference configuration by releasing the stored elastic bending energy in the form of

work. Thus, bending deformations of the collagen cage induce elastic stresses that drive

movement towards the mechanical reference configuration. In principle, as above, we distinguish between two possible (and independent) directions of movement, axial/tangential and

radial/normal, which couple to the respective stress fields. However, since the free energy

that is stored in bending deformations does not depend on the axial component of the deformation field, $\delta F_b/\delta u_\parallel = 0$, the tangential shear stresses vanish. Note that there is a deeper

reason as to why there are no tangential shear stresses in response to bending. For tangen-

---

[10] Cell contractility can effectively lead to a spontaneous curvature of thin cell sheets due to an asymmetric
positioning of the cells' actomyosin cytoskeleton relative to the middle surface of the cell sheet [17]. If
the spontaneous curvature is induced by cell contractility, then it can also be influenced by the local
orientation of cells.

tial deformations, the material points of the thin shell only move along the surface, thus leaving its shape unchanged. Since the bending energy (B23) only depends on the shape of the thin shell, it follows that tangential deformations cannot induce bending stresses. This only leaves perpendicular motion of the surface by some infinitesimal distance δu, which is driven by a *normal stress* that acts on the surface:

$$\Delta p_b = -\frac{\delta F_b}{\delta u} = -k_b \left[\frac{u}{R_0^4} + \partial_z^4 u \right] , \tag{B24}$$

where the deformed radius of the tubular shell is given by $R = R_0 + u$ and the reference radius is given by R_0. Summing up the stresses that arise in response to stretching and bending of the collagen cage, Eq. (B21) and Eq. (B24),

$$\Delta p_{cage} = -E_{cage}\, h\, \frac{u}{R_0^2} - k_b \left[\frac{u}{R_0^4} + \partial_z^4 u \right] , \tag{B25}$$

yields the *normal* component of the total boundary stress due to elastic deformations. As our notation suggests, one can interpret the *normal* component of the boundary stresses as a pressure jump between the lumen of the organoid branch and the surrounding medium. This corresponds to an effective pushing stress (if positive) or pulling stress (if negative) on the interface from outside of the organoid branch.

Linear stability analysis. A cylindrical configuration of the thin tubular shell (i.e. the organoid branch) is stable whenever the combined effect of all elastic stresses and the active cellular tension *counteracts* any small shape perturbation. In this section, we use this argument to find conditions for which a cylindrical shape becomes linearly unstable. To that end, as we have done in the previous sections, we consider rotationally symmetric deformations of the tubular shell, $R = R_0 + u$, that are small compared to the equilibrium radius of the tube, $u \ll R_0$. At the organoid branch interface, there is a local balance between fluid stress, generalized Laplace pressure [Eq. (B14)] and the elastic stress induced by deformations of the collagen cage [Eq. (B25)]:

$$\begin{aligned}
\sigma_{visc}^{rr} &= p_0 - \frac{\tau_\phi}{R} + \tau_z \partial_z^2 u - E_{cage}\, h\, \frac{u}{R_0^2} - k_b \left[\frac{u}{R_0^4} + \partial_z^4 u \right] \\
&\approx p_0 - \frac{\tau_\phi}{R_0} + \left[\frac{\tau_\phi}{R_0^2} - \frac{E_{cage}\, h}{R_0^2} - \frac{k_b}{R_0^4} + \tau_z \partial_z^2 - k_b \partial_z^4 \right] u .
\end{aligned} \tag{B26}$$
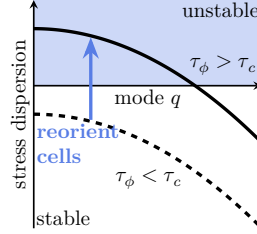
Supplementary Fig. 11. Stress dispersion relation as a function of the mode q. A reorientation of cells can increase the circumferential tension at the expense of the axial tension, thus shifting the stress dispersion relation upwards (blue arrow) and inducing a band of unstable modes.

The left-hand side of the stress-balance equation, Eq. (B26), corresponds to dynamic viscous stresses σ_{visc}^{rr} that vanish in steady state. Hence, only the right-hand side of the stress-balance equation (B26), where we have collected the hydrostatic pressure, the generalized Laplace pressure, and elastic stresses, determines the stability of the tubular shell. The stress-balance equation, Eq. (B26), must hold for any deformation of the tubular shell, including the reference configuration itself ($u = 0$). Therefore, the hydrostatic pressure is given by $p_0 = \tau_\phi/R_0$. Finally, we express the small deformations u in terms of Fourier components, $u = \sum_q u_q \cos(qz)$, and thus obtain the following stress dispersion relation near mechanical equilibrium [Fig. 11]:

$$\Delta p_q = \left[\frac{\tau_\phi}{R_0^2} - \frac{E_{cage}\,h}{R_0^2} - \frac{k_b}{R_0^4} - \tau_z q^2 - k_b q^4 \right] u_q \,. \tag{B27}$$

Since the last two terms of equation (B27) are stabilizing (positive axial tension τ_z and positive bending rigidity k_b), a band of unstable modes can only emerge if[11]:

$$\tau_\phi > \tau_c = E_{cage}\,h + \frac{k_b}{R_0^2} \,. \tag{B28}$$

These results indicate a long-wavelength instability according to the Cross/Hohenberg classification scheme [19]; specifically, the mechanical driving stress is largest for the $q = 0$ mode. However, note that here this will not be the fastest-growing mode, as homogeneous modes $q = 0$ are prohibited by the incompressibility of the fluid in the lumen of the organoid branch.

[11] The classical result for the pearling instability has an additional factor of 2/3 in the second term, because it considers a material with zero spontaneous curvature along both principal directions [18]. Then, the bending energy acts as an additional destabilizing term.

In general, increasing the circumferential tension will increase the mechanical driving stress [cf. right-hand side of the stress-balance equation (B26)], and will therefore speed up the pearling instability. Furthermore, we note that the pearling instability occurs when the circumferential tension and the corresponding Laplace pressure are sufficiently strong to overcome the stabilizing effects conferred by the elastic properties of the collagen cage [Eq. (B27)]. As the alveolus grows, the Laplace pressure will then decrease, while the hydrostatic pressure will remain approximately constant (if the alveolus is still connected to an organoid branch). Furthermore, the stress due to elastic bending of the collagen cage is much smaller than the stress due to elastic stretching, given that the former scales with the thickness of the collagen cage h and the latter scales with h^3. Therefore, for a spherical alveolus whose radius grows from R_0 to R at the tip of an organoid branch, we can make the following approximation:

$$\sigma_{visc}^{rr} = \Delta p = \frac{\tau_\phi}{R_0} - \frac{\tau_\phi}{R} - E_{cage}\, h\, \frac{R - R_0}{R_0^2} \, . \tag{B29}$$

The final equilibrium radius of the alveolus is then determined by the steady-state condition $\sigma_{visc}^{rr} = 0$ and is therefore given by

$$\frac{R}{R_0} = \frac{\tau_\phi}{E_{cage}\, h} \, . \tag{B30}$$

We conclude that the above theory predicts that an increase in surface tension will lead to larger alveoli that also form faster. These results hold on sufficiently short timescales, where the deformation of the extracellular matrix is elastic and fully reversible. On long timescales, if the stresses in the extracellular matrix are above the plastic yield threshold, then the reference radius R_0 will effectively increase due to plastic deformation of the extracellular matrix thus leading to a robust and continued growth of spherical alveoli as we have discussed in the main text.

Estimating the critical circumferential tension. We next estimate the magnitude of the critical tension. For a homogeneously elastic sheet with elastic modulus E_{cage}, Poisson ratio ν and thickness h, the bending modulus is given by [5] $k_b = E_{cage}\, h^3/[12(1 - \nu^2)]$. In section A 3 "Collagen "cage"", confocal microscopy data showed that the collagen cage has a typical thickness of $h \simeq 5\,\mu m$. Furthermore, we have estimated in section A 3 "Collagen

25

451 "cage"" that the elastic modulus of the collagen cage should lie in the range between $E_{cage} =$

452 $0.72\,\mathrm{kPa}$ and $E_{cage} = 1.38\,\mathrm{kPa}$. Furthermore, analogously to section A 3 "Collagen "cage"",

453 we assume that the collagen cage (which has a collagen concentration of roughly $6.5\,\mathrm{mg\,ml^{-1}}$)

454 is incompressible, such that $\nu = 1/2$ [20]. For a branch radius of $R_0 = 30\,\mu\mathrm{m}$, we find that

455 the critical circumferential tension τ_c of the organoid branch [Eq. (B28)] lies in the range

456 between $\tau_c = 3.6\,\mathrm{mN\,m^{-1}}$ and $\tau_c = 6.9\,\mathrm{mN\,m^{-1}}$. Values for the cortical tension of single

457 contractile cells have been measured via micropipette aspiration to be about $0.4\,\mathrm{mN\,m^{-1}}$

458 for L929 fibroblasts [21] and have similar values for chick fibroblasts [22], $4.1\,\mathrm{mN\,m^{-1}}$ for

459 Dictyostelium discoideum [23], and via traction force microscopy to reach up to $5\,\mathrm{mN\,m^{-1}}$ for

460 human microvascular endothelial cells [24] (HMEC-1). Furthermore, micropipette aspiration

461 of spheroids consisting of MCF-10A (human mammary epithelial) cells has yielded a value

462 of $10\,\mathrm{mN\,m^{-1}}$ [25] for the corresponding surface tension.

463 We conclude that the active tension induced by cellular contractility is strong enough

464 to trigger a pearling instability against the mechanical resistance of the collagen cage. In

465 addition, the active tension induced by cellular contractility is sufficiently small so that

466 an axial alignment of cells [cf. section B 2 "Active cell contractility induces anisotropic

467 tension and Laplace pressure"] could keep the circumferential component of the tension

468 tensor below the critical value, Eq. (B28). Finally, our cell tracking data show that collective

469 rotations of cells around the circumference of the organoid branch typically begin at the tips

470 of the organoid branches [cf. Fig. 3 in the main text]. This observation is rooted in the

471 fact that at the tips of the organoid branches, cells have to repolarize and either migrate

472 back or begin collectively migrating around the circumference (i.e. rotations); the latter

473 corresponds to the least frustrated state where cells can keep migrating with the least number

474 of changes in direction. Therefore, cell reorientation and an increase in circumferential

475 tension at the expense of axial tension also typically begin at the tips of the organoid

476 branches. Furthermore, note that Buchmann and Meixner et al. [1] have shown that the

477 collagen cage is thinner at the organoid branch tips and approaches a thickness of up to

478 $h = 10\,\mu\mathrm{m}$ towards the organoid body. In that case, the critical tension would increase

479 by a factor of at least 2 (relative to our estimated value, assuming that the collagen cage

480 has the same elastic modulus near the organoid body) towards the organoid body. These

481 two observations (preferred cell reorientation and thinner collagen cage) rationalize why the

482 pearling instability preferably occurs at the organoid branch tips.

4. Bulk extracellular matrix elasticity does not significantly affect tube stability

So far, we have assumed that a tubular configuration of the shell-like organoid branch is stabilized by a rigid collagen cage. In addition, the organoid branch is also surrounded by an elastic extracellular matrix. Thus, one may wonder whether a collagen cage is required, or if a homogeneous extracellular matrix itself would be sufficient to stabilize tubular shapes. In the following, we argue that a homogeneously elastic extracellular matrix is too soft to stabilize the cylindrical organoid branch against its own contractility.

To that end, we use linear elasticity theory. The extracellular collagen matrix is a three-dimensional body and thus requires a treatment in terms of three-dimensional bulk coordinates

$$\mathbf{r}(r, z, \phi) = \begin{bmatrix} r\cos\phi \\ r\sin\phi \\ z \end{bmatrix} , \tag{B31}$$

which match the surface coordinates at the interface of our tubular geometry [cf. section B 1 "Choice of coordinate system"]. The three (orthogonal but non-normalized) basis vectors that span the three-dimensional of our tubular geometry are then given by

$$\mathbf{b}_r = \begin{bmatrix} \cos\phi \\ \sin\phi \\ 0 \end{bmatrix} , \quad \mathbf{b}_z = \begin{bmatrix} 0 \\ 0 \\ 1 \end{bmatrix} , \quad \text{and} \quad \mathbf{b}_\phi = \begin{bmatrix} -r\sin\phi \\ r\cos\phi \\ 0 \end{bmatrix} . \tag{B32}$$

In the present section, we use contravariant notation to express vectors, $\mathbf{v} = v^i\,\mathbf{b}_i$, and tensors, $\boldsymbol{\sigma} = \sigma^{ij}\,\mathbf{b}_i \otimes \mathbf{b}_j$. Contravariant notation indicates that the components of any vector field, v^i, transform inversely in response to any basis transformation, so that the vector field $\mathbf{v}$ itself remains invariant. As before, we assume a rotational symmetry around the z-axis.

We associate the mechanical reference configuration of the organoid branch and of the extracellular matrix with the initial shape of the tubular shell. Then, we consider infinitesimal deviations from this reference configuration, which are parameterized by the deformation

field $\mathbf{u}$. The corresponding linearized strain tensor is given by [5]:

$$\boldsymbol{\epsilon}_{lin} = \frac{1}{2}\left[\boldsymbol{\nabla}\otimes\mathbf{u} + (\boldsymbol{\nabla}\otimes\mathbf{u})^T\right] = \sum_{i,j\in\{r,\phi,z\}}\epsilon^{ij}\,\mathbf{b}_i\otimes\mathbf{b}_j\,. \tag{B33}$$

In contrast to section A 3 "Collagen "cage"", as discussed above, we have here expressed the linearized strain tensor in contravariant notation. In our rotationally symmetric cylindrical coordinate system, the strain tensor is given by:

$$\boldsymbol{\epsilon}_{lin} \equiv \begin{bmatrix} \epsilon^{rr} & \epsilon^{rz} & \epsilon^{r\phi} \\ \epsilon^{zr} & \epsilon^{zz} & \epsilon^{z\phi} \\ \epsilon^{\phi r} & \epsilon^{\phi z} & \epsilon^{\phi\phi} \end{bmatrix} = \begin{bmatrix} \partial_r u^r & (\partial_z u^r + \partial_r u^z)/2 & \partial_r u^\phi/2 \\ (\partial_z u^r + \partial_r u^z)/2 & \partial_z u^z & \partial_z u^\phi/2 \\ \partial_r u^\phi/2 & \partial_z u^\phi/2 & u^r/r^3 \end{bmatrix}\,. \tag{B34}$$

The trace of the strain tensor in our cylindrical coordinate system,

$$\begin{aligned} \mathrm{tr}_g(\boldsymbol{\epsilon}_{lin}) &= \sum_{i\in\{r,\phi,z\}}\hat{\mathbf{b}}_i\cdot\boldsymbol{\epsilon}_{lin}\cdot\hat{\mathbf{b}}_i = \epsilon^{rr} + \epsilon^{zz} + r^2\epsilon^{\phi\phi} \\ &= \partial_z u^z + \frac{1}{r}\partial_r(r\,u^r) = \boldsymbol{\nabla}\cdot\mathbf{u}\,, \end{aligned} \tag{B35}$$

indicates volumetric changes (i.e. isotropic compression and dilatation) due to the deformation field u. Splitting the strain tensor into a pure shear component and a pure volumetric part, the linear elastic stress tensor is given by [5]:

$$\begin{aligned} \boldsymbol{\sigma}_{el} &= 2\mu\left[\boldsymbol{\epsilon}_{lin} - \frac{1}{3}\,\mathrm{tr}_g(\boldsymbol{\epsilon}_{lin})I_3\right] + \frac{2\mu}{3}\frac{1+\nu}{1-2\nu}\,\mathrm{tr}_g(\boldsymbol{\epsilon}_{lin})I_3 \\ &= 2\mu\left[\boldsymbol{\epsilon}_{lin} + \frac{\nu}{1-2\nu}\,\mathrm{tr}_g(\boldsymbol{\epsilon}_{lin})I_3\right]\,, \end{aligned} \tag{B36}$$

where I_3 refers to the identity matrix. A mechanical force balance in the bulk of the extracellular matrix implies that the body force that acts on an infinitesimal volume element vanishes [26]:

$$\mathbf{f} = \boldsymbol{\nabla}\cdot\boldsymbol{\sigma}_{lin} = \begin{bmatrix} \frac{1}{r}\partial_r(r\sigma_{el}^{rr}) + \partial_z\sigma_{el}^{rz} - r\sigma_{el}^{\phi\phi} \\ \frac{1}{r}\partial_r(r\sigma_{el}^{rz}) + \partial_z\sigma_{el}^{zz} \\ \frac{1}{r}\partial_r(r\sigma_{el}^{r\phi}) + \frac{2}{r}\sigma_{el}^{r\phi} + \partial_z\sigma_{el}^{z\phi} \end{bmatrix} = 0\,. \tag{B37}$$

The circumferential component of the body force vanishes in the absence of torques. Then, the remaining mechanical force balance equations in the bulk of the extracellular matrix are

given by:

$$\partial_z \left[\frac{1}{1-2\nu} \frac{1}{r} \partial_r(r\,u^r) + 2\frac{1-\nu}{1-2\nu} \partial_z u^z \right] + \frac{1}{r} \partial_r(r\,\partial_r u^z) = 0, \tag{B38a}$$

$$\partial_r \left[2\frac{1-\nu}{1-2\nu} \frac{1}{r} \partial_r(r\,u^r) + \frac{1}{1-2\nu} \partial_z u^z \right] + \partial_z^2 u^r = 0, \tag{B38b}$$

where u^r and u^z refer to the radial and axial deformation field, in contravariant notation, respectively. To solve these equations, we introduce the stress function Φ via an implicit definition:

$$u^r = -\partial_r \partial_z \Phi, \quad u^z = 2(1-\nu)\Delta\Phi - \partial_z^2 \Phi. \tag{B39}$$

By inserting Eq. (B39) into Eqs. (B38a) and (B38b), one finds that the stress function Φ must satisfy the biharmonic equation in cylindrical coordinates [26]:

$$\Delta^2 \Phi = 0. \tag{B40}$$

We are interested in undulations of the tubular organoid branch, and therefore decompose the deformation field of the extracellular matrix into Fourier modes: $u^r = \sum_q u_q^r(r)\cos(qz)$ and $u^z = \sum_q u_q^z(r)\sin(qz)$. Thus, we may also express the stress function in terms of Fourier modes: $\Phi = \sum_q \Phi_q(r)\sin(qz)$. The general real-valued solution to the biharmonic equation (B40) is then given by:

$$\Phi_q(r) = a_1 \left[Y_0(-iqr) + iI_0(qr) \right] + a_2 I_0(qr) + ia_3 r\left[I_1(qr) + Y_1(-iqr) \right] + a_4 rI_1(qr), \tag{B41}$$

where $I_k(x)$ refers to the modified Bessel function of the first kind and $Y_k(x)$ refers to the Bessel function of the second kind, respectively. As we consider the extracellular matrix as an elastic medium in the half-space $r \geq R$, we are only interested in real-valued solutions (u^r, u^z) that decay in the far field and approach zero as $r \to \infty$. This constraint fixes two of the four coefficients in Eq. (B41), $a_2 = 0$ and $a_4 = 0$, which correspond to solutions that would vanish at $r \to 0$ and diverge in the far field $r \to \infty$. The remaining two coefficients a_1 and a_3 can be determined by imposing boundary conditions on the deformation field. Here, we choose a general radial deformation, $u_q^r(R)$, and impose no-slip conditions on the axial
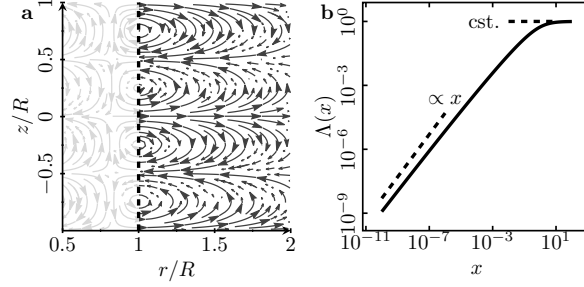
Supplementary Fig. 12. **a)** Exemplary deformation field around a tubular branch, for an incompressible extracellular matrix $\nu = 1/2$ and a Fourier mode $q = 2\pi/R$. The gray region indicates the wall of the organoid branch. **b)** Illustration of the function $\Lambda(x)$, which saturates (dashed line) for large arguments and grows (approximately) linearly for small arguments. Thus, the normal component of the elastic stress grows quadratically for small arguments qR and linearly for large arguments qR. For simplicity, we have assumed an incompressible material, $\nu = 1/2$.

deformation, $u_q^z(R) = 0$. Then, the stress function is given by the following expression:

$$\Phi_q(r) = \frac{u_q^r(R)}{q^2} \frac{K_0(qr)}{K_1(qR)} \left[1 + q\,\Theta(qR) \left(RB(qR) - \frac{r}{B(qr)} \right) \right], \tag{B42}$$

where we have defined

$$\Theta(x) \coloneqq \frac{B(x)}{x - B(x)\big[4(1-\nu) + xB(x)\big]}, \quad \text{and} \quad B(x) \coloneqq \frac{K_0(x)}{K_1(x)}, \tag{B43}$$

and where $K_k(x)$ refers to the modified Bessel function of the second kind. Using Eq. (B39), we readily obtain the full (rotationally symmetric) deformation field of the extracellular matrix. Then, we calculate the radial component of the elastic stress tensor, σ_{el}^{rr}, where μ refers to the shear modulus of the extracellular matrix [cf. Eq. (B36)]:

$$\sigma_{el}^{rr}(R) = -\frac{2\mu}{R} \sum_q \Big(1 + qR\Lambda(qR) \Big) u_q^r(R) \cos(qz), \tag{B44a}$$

$$\Lambda(x) \coloneqq -2(1-\nu)B(x)\Theta(x). \tag{B44b}$$

The above function $\Lambda(x)$ and the deformation field are depicted in Supplementary Fig. 12. For the no-slip boundary conditions that we have chosen here, the normal stress grows quadratically for small arguments $qR \ll 1$ and linearly for large arguments $qR \gg 1$.

Replacing the thin bendable collagen cage with an extended homogeneous extracellular matrix, the mechanical driving stress [cf. right-hand side of the stress-balance equation (B26)] on the shell-like organoid branch is given by

$$\Delta p_q = \left[\frac{\tau_\phi}{R_0^2} - \tau_z q^2 - \frac{2\mu}{R_0}\Big(1 + qR_0\,\Lambda(qR_0)\Big) \right] u_q \,. \tag{B45}$$

The first term (Laplace pressure due to circumferential tension) in the square brackets is destabilizing and does not depend on the wavelength. The second term (Laplace pressure due to axial tension) in the square brackets stabilizes short wavelengths. The third term in the square brackets (elastic stress) has a contribution that stabilizes long wavelengths ($q = 0$) and a contribution that stabilizes short wavelengths ($q > 0$). In particular, for the no-slip boundary conditions that we have chosen here, the function $\Lambda(x)$ grows monotonically as its argument x increases, cf. Supplementary Fig. 12b, with $x\Lambda(x) \propto x^2$ for small arguments. We conclude that a pearling-like instability at low wavelengths (i.e. for $q \to 0$) will only occur if the Laplace pressure due to circumferential tension can overcome the stabilizing effects conferred by the extracellular matrix:

$$\tau_\phi > 2\mu R_0 \tag{B46}$$

For a shear modulus of $\mu \approx 7\,\mathrm{Pa}$ this yields a critical surface tension of $0.4\,\mathrm{mN\,m^{-1}}$, which is far below the reference tension of $10\,\mathrm{mN\,m^{-1}}$ for the surface tension of spheroids consisting of MCF-10A (human mammary epithelial) cells [25]. Thus, we conclude that the homogeneous extracellular matrix alone is unlikely to stabilize a tubular geometry in our experiments, which further emphasizes the mechanical role of the collagen cage.

---

[1] Buchmann, B. *et al.* Mechanical plasticity of the ECM directs invasive branching morphogenesis in human mammary gland organoids. *To appear in Nat. Comm.* (2021). https://www.biorxiv.org/content/early/2019/11/29/860015.full.pdf.

[2] Schliwa, M. Action of cytochalasin D on cytoskeletal networks. *Journal of Cell Biology* **92**, 79–91 (1982).

[3] Berg, S. *et al.* ilastik: interactive machine learning for (bio)image analysis. *Nature Methods*

562   (2019).

563   [4] Brodland, G. W. *et al.* CellFIT: A cellular force-inference toolkit using curvilinear cell bound-
564   aries. *PLOS ONE* **9**, 1–15 (2014).

565   [5] Landau, L. *et al.* *Theory of Elasticity: Volume 7.* Course of theoretical physics (Elsevier
566   Science, 1986).

567   [6] Kong, W. *et al.* Experimental validation of force inference in epithelia from cell to tissue scale.
568   *Scientific Reports* **9**, 14647 (2019).

569   [7] Grinfeld, P. *Introduction to Tensor Analysis and the Calculus of Moving Surfaces* (Springer,
570   2013).

571   [8] Bischofs, I. B. & Schwarz, U. S. Cell organization in soft media due to active mechanosensing.
572   *Proceedings of the National Academy of Sciences* **100**, 9274–9279 (2003). URL `https://www.`
573   `pnas.org/content/100/16/9274`. https://www.pnas.org/content/100/16/9274.full.pdf.

574   [9] Bischofs, I. B., Safran, S. A. & Schwarz, U. S. Elastic interactions of active cells with soft
575   materials. *Phys. Rev. E* **69**, 021911 (2004). URL `https://link.aps.org/doi/10.1103/`
576   `PhysRevE.69.021911`.

577   [10] Safran, S. *Statistical Thermodynamics Of Surfaces, Interfaces, And Membranes* (CRC Press,
578   Boca Raton, 2003).

579   [11] Raub, C., Putnam, A., Tromberg, B. & George, S. Predicting bulk mechanical properties of
580   cellularized collagen gels using multiphoton microscopy. *Acta Biomaterialia* **6**, 4657 – 4665
581   (2010).

582   [12] Jansen, K. A. *et al.* The role of network architecture in collagen mechanics. *Biophysical*
583   *Journal* **114**, 2665–2678 (2018).

584   [13] Liu, B., Zhang, L. & Gao, H. Poisson ratio can play a crucial role in mechanical properties of
585   biocomposites. *Mechanics of Materials* **38**, 1128 – 1142 (2006).

586   [14] Timoshenko, S. P. & Gere, J. M. *Theory of Elastic Stability* (Dover Publications, 1961).

587   [15] Hannezo, E., Prost, J. & Joanny, J.-F. Mechanical instabilities of biological tubes. *Physical*
588   *Review Letters* **109**, 018101 (2012). URL `https://doi.org/10.1103/PhysRevLett.109.`
589   `018101`.

590   [16] Helfrich, W. Elastic properties of lipid bilayers: Theory and possible experiments.
591   *Zeitschrift für Naturforschung C* **28**, 693–703 (1973). URL `https://doi.org/10.1515/`
592   `znc-1973-11-1209`.

32

[17] Hannezo, E., Prost, J. & Joanny, J.-F. Theory of epithelial sheet morphology in three dimensions. *Proceedings of the National Academy of Sciences* **111**, 27–32 (2014).

[18] Bar-Ziv, R. & Moses, E. Instability and "pearling" states produced in tubular membranes by competition of curvature and tension. *Phys. Rev. Lett.* **73**, 1392–1395 (1994). URL `https://link.aps.org/doi/10.1103/PhysRevLett.73.1392`.

[19] Cross, M. C. & Hohenberg, P. C. Pattern formation outside of equilibrium. *Rev. Mod. Phys.* **65**, 851–1112 (1993). URL `https://link.aps.org/doi/10.1103/RevModPhys.65.851`.

[20] Castro, A. P. G. *et al.* Combined numerical and experimental biomechanical characterization of soft collagen hydrogel substrate. *J. Mater. Sci. Mater. Med.* **27**, 79 (2016).

[21] Tinevez, J.-Y. *et al.* Role of cortical tension in bleb growth. *Proceedings of the National Academy of Sciences* **106**, 18581–18586 (2009).

[22] Thoumine, O., Cardoso, O. & Meister, J.-J. Changes in the mechanical properties of fibroblasts during spreading: a micromanipulation study. *European Biophysics Journal* **28**, 222–234 (1999). URL `https://doi.org/10.1007/s002490050203`.

[23] Winklbauer, R. Cell adhesion strength from cortical tension - an integration of concepts. *J. Cell Sci.* **128**, 3687–3693 (2015).

[24] Bastounis, E. E., Ortega, F. E., Serrano, R. & Theriot, J. A. A multi-well format polyacrylamide-based assay for studying the effect of extracellular matrix stiffness on the bacterial infection of adherent cells. *JoVE* e57361 (2018). URL `https://www.jove.com/t/57361`.

[25] Villeneuve, C. *et al.* aPKCi triggers basal extrusion of luminal mammary epithelial cells by tuning contractility and vinculin localization at cell junctions. *Proceedings of the National Academy of Sciences of the United States of America* **116**, 24108–24114 (2019). URL `https://doi.org/10.1073/pnas.1906779116`.

[26] Amenzade, I. *Theory of Elasticity* (Mir, 1979).

IV.2 Between Morphogenesis and Hydrodynamic Flows

IV.2.1 Starting Point of the Project

Here, we discuss a very technical project, which aims at deepening our understanding of the tissue dynamics during alveologenesis, see Section IV.1 "Collective Cell Migration Affects Morphogenesis". To that end, we first investigate in Section IV.2.2 "Collective Cell Oscillations" the origin of oscillatory back-and-forth motion in tubular geometries, by introducing a greatly simplified model of polar motion in an elastic environment. Then, we go on to take a closer look at the different aspects of Section IV.1 "Collective Cell Migration Affects Morphogenesis":

(i) In Section IV.2.3 "Nonlinear Elasticity of the Collagen Cage", we generalize the description of the collagen cage by considering it as a nonlinear elastic material that can exhibit large strains. We apply these results in Section IV.2.6 "Tubular Shells as Pumps and Rectifiers", and have already taken them for granted in Section IV.1.3 "Technical Summary".

(ii) In Section IV.2.4 "Deformations of the Extracellular Matrix" we generalize the description of the extracellular matrix by allowing slip boundary conditions at the cellular surface of the organoid branch. We do not immediately apply these results, but they can prove useful in future work.

(iii) In Section IV.2.5 "Cell Activity Drives Hydrodynamic Flows", we derive the hydrodynamic flows in the lumen of an organoid branch. To that end, we solve the Stokes equations analytically, with stress boundary conditions at the cellular surface of the organoid branch. We find that cell influx into the tip of the organoid branch leads to an increase of hydraulic pressure, and thus expansion of the surface before the onset of the shape transformation. This effect biases the shape transformation, which occurs at the tip of the organoid branch, towards *growth*. The linear stability analysis in Section IV.1.3 "Technical Summary" alone does not give us this insight. Furthermore, we find that tubular shells can hydraulically bulge out due to cellular contractility alone. This could provide a minimal model for exocytosis via actin cortex contractility.

(iv) Finally, in Section IV.2.6 "Tubular Shells as Pumps and Rectifiers", we give an outlook to the nonlinear dynamics of fluid-filled tubular shells. Here, we find a hysteresis loop where, as a function of the hydrodynamic pressure, the tube switches between two stable branches of tube radii. This

hysteresis loop signifies a violation of time-reversal symmetry. Therefore, we hypothesize that tubular shells can act as mechanical rectifiers if one applies a temporally oscillating gradient of hydrodynamic pressure.

IV.2.2 COLLECTIVE CELL OSCILLATIONS

In this section, we propose and discuss a generic model that illustrates how periodic cell motion can naturally emerge from cell polarity. Conceptually, we build on Section IV.1 "Collective Cell Migration Affects Morphogenesis", where we have described each cell as an anisotropic force dipole whose local orientation is given by the unit vector $\hat{\boldsymbol{e}}_\theta$. The average surface tension tensor at the cellular surface of the organoid branch is then controlled by the distribution of cell orientation angles: aligned cells induce anisotropic tension at the tissue scale, while randomly oriented cells imply isotropic tension. If cells in one region, on average, pull harder than cells in a nearby region, then these tension gradients will drive cellular motion and fluid flows, as we will study in Section IV.2.5 "Cell Activity Drives Hydrodynamic Flows". Such tension gradients can be realized either by regulating the angular distribution of cell orientation or the tensile properties of the cells. As an example of the latter, mechanochemical signaling and tension regulation can lead to oscillatory motion in cell monolayers (Boocock et al., 2021). These tension-driven flows are a collective phenomenon, where cells communicate mechanochemically to act in concert, thus requiring a description of the cell population as a spatially extended confluent tissue. But single cells can also exhibit properties of active polar particles and migrate in the direction of their orientation vector $\hat{\boldsymbol{e}}_\theta$, see Section III.1 "Collective Cell Dynamics in Rigid Environments". Then, the cells effectively exhibit a motile net force by exerting traction on the substrate that they migrate on (Fig. IV.3). Therefore, the tension field in the cellular monolayer, which models the force-dipole nature of cells, is in general supplemented by an active (motile) force density field, which models the force-monopole nature of cells.

Analogous to how axial alignment of cells can lead to a tension anisotropy with increased axial tension, there is also an inverse effect where externally applied tension leads to cellular alignment (Bischofs and Schwarz, 2003; Bischofs, S. A. Safran, et al., 2004). This alignment is mediated by the extracellular matrix: cells have to perform less work (deforming the elastic extracellular matrix) to build up a force dipole that is aligned in parallel to an applied strain than to build up a force dipole with a perpendicular alignment (Bischofs and Schwarz, 2003; Bischofs, S. A. Safran, et al., 2004). Since parallel alignment of anisotropic force dipoles (like cells) with an external strain is energetically preferred over perpendicular alignment, the resulting torque will change the orientation of each cell. Similar effects follow if the cells are near a fixed boundary, which
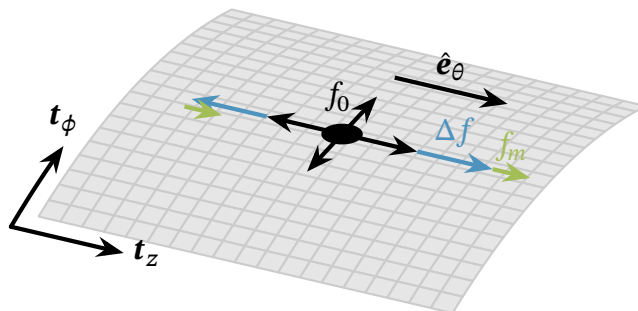
Figure IV.3: Idealized description of a cell with diameter d_0 and area A_0, whose orientation $\hat{e}_\theta$ aligns with the organoid branch axis z. The cell exhibits isotropic contractile forces f_0 that correspond to an isotropic tension $\tau_0 \simeq f_0 d_0/A_0$. Along one axis, the cell exhibits larger contractile forces ($\Delta f > 0$) or smaller contractile forces ($\Delta f < 0$) than along the perpendicular axis, leading to an anisotropic tension contribution of $\Delta\tau \simeq \Delta f d_0/A_0$. Finally, one side of the cell exhibits a larger traction on the substrate, f_m, compared to the opposing side (defined via the orientation vector $\hat{e}_\theta$). The motile force f_m does not contribute to the symmetric tension tensor, but rather acts as a body force of magnitude $2f_m$. Here, we assume that $\Delta f > 0$, so that the cell typically moves parallel to the axis along which it exhibits the largest tension.

(mathematically) acts like a mirror, thus coercing a cell to align with its own mirror image (Bischofs and Schwarz, 2003; Bischofs, S. A. Safran, et al., 2004). In the following, we consider two prototypical situations: (i) axial alignment of cells, and (ii) circumferential alignment of cells with respect to the organoid branch axis. We propose a conceptual model of self-polarizing motile cells, and discuss the implications of this model for cell migration in our two prototypical settings.

A minimal model of one-dimensional polar motion. Cells typically move by applying a motile force parallel to their orientation vector $\hat{e}_\theta$. The cells can regulate this motile force by (de)polarizing, and it can reach a value of up to $2f_m$ (Fig. IV.3). Then, the motile force vector that propels each cell is given by

$$\boldsymbol{f}_m = 2f_m \rho \, \hat{\boldsymbol{e}}_\theta \,, \tag{IV.22}$$

where ρ refers to the *cell polarization*. The cell self-polarizes with a rate k_ρ towards a "forward gear" saturation value of $\rho \to 1$, or towards a "reverse gear" saturation value of $\rho \to -1$. In addition, cell polarization is also affected by a positive feedback, with rate k_v, from the motion of the cell. This positive feedback allows the cell to integrate external mechanical signals. Consequently, the

cell polarization responds to externally applied forces that affect cell migration, and "remembers" their *history*—in other words, the cell polarization ρ acts as a memory kernel. Then, the temporal dynamics of the cell polarization is (to lowest order) governed by the following differential equation:

$$\partial_t \rho = k_\rho \left[1 - \rho^2\right]\rho + k_v \left[\boldsymbol{v} \cdot \hat{\boldsymbol{e}}_\theta\right], \tag{IV.23}$$

where $\boldsymbol{v}$ refers to the velocity of the cell. The external forces that affect cell migration depend on the cell orientation $\hat{\boldsymbol{e}}_\theta$. If the cells align along the circumference of the organoid branch, then one can assume that cell motion is mostly dominated by the motile force and a friction ξ with the collagen cage:

$$v_\phi = \frac{1}{\xi}\left[2 f_m \rho\right]. \tag{IV.24a}$$

Then, cells will preferably move along the circumference of the organoid branch, corresponding to organoid branch rotations. These collective rotations are a "least frustrated state", because there is no deterministic stimulus that could cause cells to change their direction of motion. Instead, as we observe in Section IV.1 "Collective Cell Migration Affects Morphogenesis", cell migration around the circumference of the organoid branch typically persists.

In contrast, if the cells align along the axis of the organoid branch, then any back-or-forth motion will lead to elastic deformations of the extracellular matrix (and the organoid branch), thereby inducing restoring forces. For now, we idealize these deformations with a single deflection u_z; in Paragraph "Addendum: Deformation gradients instead of a single deflection", we consider deformation gradients. Cell motion is then not only determined by the motile force $\boldsymbol{f}_m$, but is also affected by the elastic restoring forces in response to the deflection u_z. This results in the following equation for the axial velocity of a cell:

$$v_z = \frac{1}{\xi}\left[2 f_m \rho - Y u_z\right], \tag{IV.24b}$$

where Y is a spring coefficient that models the elastic properties of the extracellular matrix. In summary, the motion of cells that are aligned with the organoid branch axis is typically governed by the following set of differential equations:

$$\partial_t u_z = \frac{1}{\xi}\left[2 f_m \rho - Y u_z\right], \tag{IV.25a}$$

$$\partial_t \rho = k_\rho \left[1 - \rho^2\right]\rho + k_v \left[\partial_t u_z\right]. \tag{IV.25b}$$

To *nondimensionalize* these equations, we define $\tilde{t} := k_\rho t$, $\tilde{u}_z := k_v u_z$, $\tilde{f}_m := (2 f_m k_v)/(\xi k_\rho)$ and $\tilde{Y} := Y/(\xi k_\rho)$. Then, we arrive at the following set of *nondimensionalized* differential equations:

$$\partial_{\tilde{t}} \tilde{u}_z = \tilde{f}_m \rho - \tilde{Y} \tilde{u}_z, \tag{IV.26a}$$

$$\partial_{\tilde{t}} \rho = \left[1 - \rho^2\right]\rho + \tilde{f}_m \rho - \tilde{Y} \tilde{u}_z. \tag{IV.26b}$$
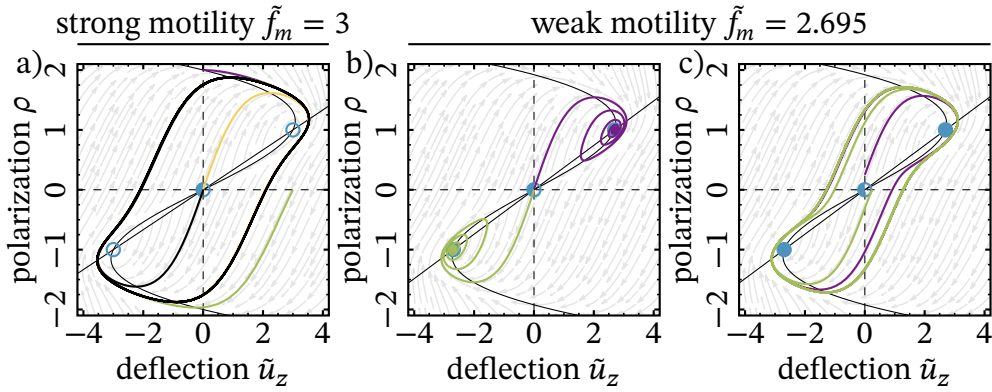
Figure IV.4: Cell migration dynamics along the organoid branch axis for different values of cell motility ($\tilde{f}_m$) and constant spring coefficient $\tilde{Y} = 1$. We realize different perturbations via the initial conditions. Filled circles indicate stable fixed points, empty circles indicate unstable fixed points, half-filled circles indicate saddle points. The gray arrows indicate the local phase space flow. Thin solid lines indicate nullclines. a) Large cell motility leads to a limit cycle in ($\tilde{u}_z, \rho$) phase space, which indicates oscillatory cell motion. This oscillatory motion is driven by two unstable fixed points (empty blue circles). b) Small cell motility typically leads to relaxation towards one of the stable fixed points (filled blue circles). c) For sufficiently large perturbations (which we idealize by choosing specific initial conditions), one may excite limit cycle oscillations of cells even when cell motility is smaller than the critical value of $\tilde{f}_c = \tilde{Y} + 2$. These limit cycle oscillations lie on a periodic orbit around two stable fixed points indicated by filled circles and a saddle point indicated by a half-filled circle.

In this model, axial cell motion is determined by the motile force $\tilde{f}_m$ scaled with the polarization ρ as well as an elastic restoring force with spring coefficient $\tilde{Y}$ and axial deflection $\tilde{u}_z$. In turn, the polarization ρ has nonlinear self-reinforcing dynamics and acts as a memory kernel for cell motion.

Linear stability analysis of our model. Our model has three fixed points. At the "unpolar" fixed point, the cell shows no polar motion, $(\tilde{u}_{z,0}, \rho_0) = (0, 0)$. At the two "polar" fixed points, the cell moves in a polar fashion and due to substrate slippage stays at a constant deflection, $(\tilde{u}_{z,\pm}, \rho_\pm) = (\pm \tilde{f}_m / \tilde{Y}, \pm 1)$. To further analyze the dynamics of our model, we consider small perturbations around these fixed points, $\tilde{u}_z = \tilde{u}_{z,i} + \delta \tilde{u}_z$ and $\rho = \rho_i + \delta \rho$, which yields the

following linear equation:

$$\partial_{\tilde{t}} \begin{bmatrix} \delta \tilde{u}_z \\ \delta \rho \end{bmatrix} = \begin{bmatrix} -\tilde{Y} & \tilde{f}_m \\ -\tilde{Y} & \tilde{f}_m + 1 - 3\rho_i^2 \end{bmatrix} \cdot \begin{bmatrix} \delta \tilde{u}_z \\ \delta \rho \end{bmatrix} = \boldsymbol{J}_i \cdot \begin{bmatrix} \delta \tilde{u}_z \\ \delta \rho \end{bmatrix}, \qquad \text{(IV.27)}$$

where the index $i \in \{0, \pm\}$ refers to the three fixed points.

At the "unpolar" fixed point, the determinant of the Jacobian is always negative, $\det \boldsymbol{J}_0 = -\tilde{Y}$. Therefore, the "unpolar" fixed point is a saddle point with one stable and one unstable direction in phase space (Strogatz, 2018). The dynamics in two-dimensional phase space typically evolve away from this saddle point, along the unstable direction in phase space. If the two "polar" fixed points are stable, then our system will approach one of these two states. However, if the two "polar" fixed points are unstable, then our system will orbit all three fixed points on a limit cycle (Strogatz, 2018).

To find a criterion for these limit cycle oscillations, we must take a closer look at the "polar" fixed points. The determinant of the Jacobian is always positive at the two "polar" fixed points, $\det \boldsymbol{J}_\pm = 2\tilde{Y}$, so they must be either stable or unstable. Then, the stability of these "polar" fixed points is determined by the trace of the Jacobian (Strogatz, 2018), $\text{tr} \, \boldsymbol{J}_\pm = \tilde{f}_m - 2 - \tilde{Y}$. We find that the two "polar" fixed points are unstable for sufficiently large motility of cells,

$$\tilde{f}_m > \tilde{f}_c = 2 + \tilde{Y}, \qquad \text{(IV.28)}$$

because the self-polarization and the motile force of the cells then overpower the elastic restoring force of the extracellular matrix. In this *motile* regime, we find a limit cycle, where the motility and self-polarization of cells lead to oscillatory motion (Fig. IV.4a). To observe such limit cycle oscillations, one requires only a small initial perturbation of the cell starting from the "unpolar" fixed point.

In contrast, if cell motility is small, $\tilde{f}_m < \tilde{f}_c$, then the two "polar" fixed points are stable. In that case, the cell can stay polarized at a constant deflection (Fig. IV.4b). However, even in this regime where cell motility is small, one can still excite oscillatory motion on a periodic orbit under certain conditions. First, cell motility must be sufficiently close to its critical value, $\tilde{f}_m \lesssim \tilde{f}_c$. In particular, the two "polar" fixed points have imaginary eigenvalues and thus correspond to spirals if:

$$2 + \tilde{Y} - \sqrt{8\tilde{Y}} < \tilde{f}_m < 2 + \tilde{Y} + \sqrt{8\tilde{Y}}. \qquad \text{(IV.29)}$$

Then, we observe that the cell relaxes to one of the two "polar" fixed points via dampened oscillations, thus permitting overshooting. If, in addition, the initial perturbation is sufficiently large, then we observe limit cycle oscillations (Fig. IV.4c).

Finally, since the stability of the "polar" fixed points is determined by $\tilde{f}_m - \tilde{Y}$, we can extrapolate these results to a change in (normalized) spring coefficient

$\tilde{Y}$ of the extracellular matrix. Then, we would expect that an increased stiffness of the extracellular matrix inhibits oscillatory motion of cells.

Addendum: Deformation gradients instead of a single deflection. So far, we have treated the elastic deformations of the extracellular matrix and the cellular tissue as a spring with stiffness $\tilde{Y}$ and deflection $\tilde{u}_z$. Next, we generalize this picture by accounting for the *strains* in the extracellular matrix and the cellular tissue. These strains correspond to the gradient of the deflection field, $\partial_z \tilde{u}_z$. To keep things simple, we stick to our nondimensionalized notation. Strains in our one-dimensional material lead to elastic stresses given by $\tilde{\tau} = \tilde{K} \partial_z \tilde{u}_z$, where $\tilde{K}$ is the elastic modulus of the material (Landau, Pitaevskii, et al., 1986). The elastic body force that acts on each volume element of our one-dimensional material is then given by the gradient of the stresses, $\partial_z \tilde{\tau}$. Taken together, our *nondimensionalized* differential equations take the following modified form:

$$\partial_{\tilde{t}} \tilde{u}_z = \tilde{f}_m \rho - \tilde{Y} \tilde{u}_z + \tilde{K} \partial_z^2 \tilde{u}_z \,, \tag{IV.30a}$$

$$\partial_{\tilde{t}} \rho = \left[1 - \rho^2\right] \rho + \tilde{f}_m \rho - \tilde{Y} \tilde{u}_z + \tilde{K} \partial_z^2 \tilde{u}_z \,. \tag{IV.30b}$$

We can analyze the dynamics of these equations by expanding the deflection field and the polarization field into Fourier series,

$$\tilde{u}_z = \tilde{u}_{hm} + \sum_q \tilde{u}_q \cos(q\,z)\,, \quad \text{and} \quad \rho = \rho_{hm} + \sum_q \rho_q \cos(q\,z)\,, \tag{IV.31}$$

respectively. If we need to account for a tissue in spatial confinement, and thus for longitudinal boundary conditions, then we would also need sine waveforms in the Fourier expansion. Here, however, we content ourselves with analyzing an infinitely long tissue, so that the cosine waveforms suffice. The springs with coefficients $\tilde{Y}$ localize the tissue and therefore play the role of an effective confinement.

Again, we perform a linear stability analysis around the *homogeneous* fixed points, $(\tilde{u}_{hm}, \rho_{hm}) \equiv (\tilde{u}_{z,i}, \rho_i)$, see Paragraph "Linear stability analysis of our model". We find that the Jacobian of our extended model has the same form as Eq. (IV.27). The only difference is that the spring coefficient now explicitly depends on the mode, $\tilde{Y} \rightarrow \tilde{Y} + q^2 \tilde{K}$:

$$\partial_{\tilde{t}} \begin{bmatrix} \tilde{u}_q \\ \rho_q \end{bmatrix} = \begin{bmatrix} -\tilde{Y} - q^2 \tilde{K} & \tilde{f}_m \\ -\tilde{Y} - q^2 \tilde{K} & \tilde{f}_m + 1 - 3\rho_i^2 \end{bmatrix} \cdot \begin{bmatrix} \tilde{u}_q \\ \rho_q \end{bmatrix} \,. \tag{IV.32}$$

Then, one will observe oscillations if the cell motility exceeds the (modified) critical value of $\tilde{f}_c = \tilde{Y} + q^2 \tilde{K} + 2$. Therefore, for sufficiently large cell motility $\tilde{f}_m$ there will be a band of unstable modes around the "polar" fixed points:

$$q < q_c = \sqrt{\frac{\tilde{f}_m - \tilde{Y} - 2}{\tilde{K}}} \,, \tag{IV.33}$$

which indicates an onset of density oscillations in the tissue.

Summary of the main results. To summarize, in this section we have discussed a conceptual model of polar cell motion under elastic constraints. We have found that polar cell motility can lead to oscillatory motion of cells along the axis of the organoid branch. We have first applied this model to a single cell that experiences an elastic restoring force towards its initial resting position. Then, we have generalized this model to a spatially extended population of cells that move in concert, and have found large-scale density oscillations if cell motility is large enough. Indeed, cell polarity was shown to lead to collective oscillatory motion of cells in confinement, in experiments as well as with vertex and phase field models (Petrolli et al., 2019; Peyret et al., 2019).

IV.2.3 NONLINEAR ELASTICITY OF THE COLLAGEN CAGE

As we have discussed in Section IV.1 "Collective Cell Migration Affects Morphogenesis", organoid branches and alveoli are enveloped by a thin elastic shell: a collagen cage that the cells form via plastic remodeling of the extracellular matrix (Buchmann et al., 2021). This collagen cage puts constraints on the deformations of an organoid branch, by providing mechanical rigidity. In the following, we derive the (nonlinear) elastic stresses that arise in response to deformations of this collagen cage. We have already used our results (in linearized form) in Section IV.1.3 "Technical Summary", and will, furthermore, apply them in Section IV.2.6 "Tubular Shells as Pumps and Rectifiers".

We split our discussion into two paragraphs, where we derive the elastic stresses due to (i) stretching, and (ii) bending of the cylindrical elastic shell. In both paragraphs, we proceed roughly as follows. First, we discuss how much free energy is stored in the respective type of elastic deformation (Timoshenko and Gere, 1961). Then, assuming that no work is dissipated into heat so that all elastic deformations are thermodynamically reversible processes, we derive how much work is required for increasing the strain of the elastic shell, and consequently how much work is released upon relaxing strain. From this mechanical work, we derive the corresponding surface tension on the tubular shell by using Eq. (IV.10). Finally, we connect the surface tension to the interfacial stresses that act on the organoid branch surface.

Elastic stresses in response to stretching. In the following, we consider a rotationally symmetric shell that consists of a material with Young's modulus Y_s and Poisson's ratio ν, with a total shell thickness of h. We express the free energy that is stored in elastic stretching of the shell in terms of the nonlinear Green-

Lagrange strain tensor, $\boldsymbol{E}$, as was also done by Hannezo, Prost, et al. (2012). An isotropic elastic shell with negligible surface shear strain, $E^{z\phi} \approx 0$, then stores the following free energy in stretching deformations[4] (Timoshenko and Gere, 1961):

$$F_s = \frac{Y_s\,h}{2\,(1-\nu^2)} \oint dS^\star \left[\left(E^{zz} g_{zz}\right)^2 + \left(E^{\phi\phi} g_{\phi\phi}\right)^2 + 2\nu\, E^{zz} g_{zz}\, E^{\phi\phi} g_{\phi\phi} \right]\,, \quad \text{(IV.34)}$$

where "$dS^\star$" indicates integration over a fixed surface area. When introducing additional strain to the elastic shell, one must then pay the price of increasing the free energy, F_s, by performing work. Consequently, when the elastic shell relieves strain, it will release stored free energy in the form of work:

$$-\,\delta W = \delta F_s = F_s\left[E^{zz} + \delta E^{zz}, E^{\phi\phi} + \delta E^{\phi\phi}\right] - F_s\left[E^{zz}, E^{\phi\phi}\right]\,. \quad \text{(IV.35)}$$

This leads to the following axial and circumferential tensions, see Eq. (IV.10):

$$\tau^{zz} = \frac{\delta F_s}{\delta E^{zz}}\left(g_{zz}^{-1}\right)^2 = \frac{Y_s\,h}{1-\nu^2}\left[E^{zz} + \nu\,E^{\phi\phi}\,g_{\phi\phi}\,g_{zz}^{-1}\right]\,, \quad \text{(IV.36)}$$

$$\tau^{\phi\phi} = \frac{\delta F_s}{\delta E^{\phi\phi}}\left(g_{\phi\phi}^{-1}\right)^2 = \frac{Y_s\,h}{1-\nu^2}\left[E^{\phi\phi} + \nu\,E^{zz}\,g_{zz}\,g_{\phi\phi}^{-1}\right]\,, \quad \text{(IV.37)}$$

given that the basis in our cylindrical coordinate system is orthogonal.

The surface divergence of the tension tensor yields a body force *per area* (Landau, Pitaevskii, et al., 1986), which acts parallel on the interface (surface) that the cells form in our cylindrical geometry. This means that the body force per area can be represented by a linear combination of the surface tangent vectors, and that it has to be balanced by tangential shear stresses at the interface. Because the cells migrate on the surface of the organoid branch, they will in general also move relative to the elastic shell (collagen cage). By extension of argument, the elastic shell can *slip* against the cell sheet and the fluid in the lumen of the organoid branch, so that the tangential shear stresses induced by the elastic shell relax quickly compared to the normal stresses. In the case of such a timescale separation, the tangential shear stresses in the elastic shell will vanish on the timescales relevant for perpendicular motion of the interface[5]. Then, the surface divergence of the tension tensor, see Eq. (I.53), must vanish:

$$\boldsymbol{\nabla} \cdot \boldsymbol{\tau} = \frac{Y_s\,h}{1-\nu^2}\,\frac{1}{\sqrt{g_{zz}g_{\phi\phi}}}\partial_z\left[\sqrt{g_{zz}g_{\phi\phi}}\,E^{zz} + \nu\,E^{\phi\phi}\,g_{\phi\phi}^{3/2}\,g_{zz}^{-1/2}\right]\boldsymbol{t}_z = 0\,, \quad \text{(IV.38)}$$

---

[4] In (Timoshenko and Gere, 1961), a *normalized* cylindrical basis was used. Here, we transformed into our *non-normalized* cylindrical basis, hence the occurrence of the metric.

[5] For a more general treatment, one would have to explicitly model the relaxation dynamics of the tangential shear stresses by considering the viscous properties of the elastic shell and the surrounding elastic medium.

where we have used $\partial_z \boldsymbol{t}_z = 0$ and the rotational symmetry of our coordinate system. For Eq. (IV.38) to hold, the term in the square brackets must be identical to some constant C. With this adiabatic approximation, the free energy density that is stored in stretching deformations of the tubular shell simplifies to:

$$F_s^\star = \frac{Y_s\, h}{2\,(1 - \nu^2)} \oint dS^\star \left[(1 - \nu^2)\left(E^{\phi\phi} g_{\phi\phi}\right)^2 + C^2\, \frac{g_{zz}}{g_{\phi\phi}} \right]. \tag{IV.39}$$

Since, by definition, both the free energy that is stored in deformations and the corresponding tensions vanish in the reference configuration, the constant must also vanish, $C = 0$. This results in the relation $E^{zz} = -\nu\, E^{\phi\phi}\, g_{\phi\phi}\, g_{zz}^{-1}$, which we insert into Eq. (IV.37) to find the following simplified expression for the circumferential tension:

$$\tau^{\phi\phi} = Y_s\, h\, E^{\phi\phi}. \tag{IV.40}$$

Now, all that is left is to determine the nonlinear circumferential strain, $E^{\phi\phi}$. To that end, we proceed analogously as we have done in Paragraph "The strain as a variation of the metric" (Section I.3.5), and consider the squared Euclidean distance between two points on the surface, at coordinates ϕ and $\phi + d\phi$, which is given by:

$$\|d\boldsymbol{x}\|^2 = d\phi\, R^2\, d\phi = d\phi\, \boldsymbol{t}_\phi \cdot \left(\frac{R^2}{R_0^2}\right) \cdot \boldsymbol{t}_\phi\, d\phi. \tag{IV.41}$$

This results in the following expression for the nonlinear circumferential strain (Hannezo, Prost, et al., 2012):

$$E^{\phi\phi} = \frac{1}{2}\, \frac{R^2 - R_0^2}{R_0^4}, \tag{IV.42}$$

where the additional powers in the denominator come from the contravariant notation. Taken together, stretching of the elastic shell induces the following Laplace pressure, see Eq. (IV.15):

$$\Delta p_s = -Y_s\, h\, \frac{R^2 - R_0^2}{2\, R_0^2}\, \frac{R}{R_0^2\, \sqrt{1 + (\partial_z R)^2}}. \tag{IV.43}$$

In Section IV.1.3 "Technical Summary", we have used a linearized version of Eq. (IV.43), by considering small deflections, $R = R_0 + u$, with $u \ll R_0$. Note that in the present chapter we typically assume that radial undulations of the tubular organoid branch are small, $\partial_z R \ll 1$, which allows us to leave out the squared root in Eq. (IV.43).

Elastic stresses in response to bending. Next, we discuss the Helfrich free energy that is stored in bending deformations of the elastic shell (Helfrich, 1973):

$$F_b = \frac{1}{2}k_b \oint dS^\star \left[(\kappa_\phi - c_\phi)^2 + (\kappa_z - c_z)^2 \right],$$ (IV.44)

with bending rigidity k_b. Here, c_ϕ is the circumferential spontaneous curvature and c_z is the axial spontaneous curvature of the elastic shell. In the following, we assume that a tubular shape with constant radius $R = R_0$ corresponds to the mechanical reference configuration of the elastic shell. For the mechanical reference configuration to minimize the bending energy[6], we set the axial spontaneous curvature to $c_z = 0$ and the circumferential spontaneous curvature to $c_\phi = -1/R_0$. In general, determining the variations of the two curvatures of the elastic shell requires a lengthy calculation. However, as mentioned before, in the present chapter we typically assume that radial undulations of the tubular organoid branch are small, $\partial_z R \ll 1$. This allows us to approximate the two curvatures of the elastic shell as follows:

$$\kappa_z = \partial_z^2 R, \quad \text{and} \quad \kappa_\phi = -\frac{1}{R}.$$ (IV.45)

The free energy that is stored in bending deformations of the elastic shell is then given by:

$$F_b = \frac{1}{2}k_b \oint dS^\star \left[\left(\frac{1}{R} - \frac{1}{R_0} \right)^2 + \left(\partial_z^2 R \right)^2 \right],$$ (IV.46)

a functional of only the elastic shell radius R. When bending the elastic shell, one must then pay the price of increasing the free energy, F_b, by performing work. Consequently, when the elastic shell relieves its bent state, it will release stored free energy in the form of work:

$$-\delta W = \delta F_b = F_b [R + \delta R] - F_b [R].$$ (IV.47)

This leads to the following interfacial stress due to bending:

$$\Delta p_b = -\frac{\delta F_b}{\delta R} = -\kappa_b \left[\frac{R - R_0}{R_0 \, R^3} + \partial_z^4 R \right].$$ (IV.48)

Note that there is no tangential shear stress in response to bending, because tangential deformations only move the material points along the surface of the elastic shell, thus leaving its shape unchanged. In Section IV.1.3 "Technical Summary", we have used a linearized version of Eq. (IV.48), by considering small deflections, $R = R_0 + u$, with $u \ll R_0$.

---

[6] This condition has to be modified if cellular activity alters the spontaneous curvature, for example due to an asymmetric positioning of the cells' actomyosin cytoskeleton relative to the middle surface of the cell sheet (Hannezo, Prost, et al., 2014). Note that if the spontaneous curvature is induced by cell contractility, then it can also be influenced by the local orientation of cells, thus adding an additional anisotropic contribution.

IV.2.4 DEFORMATIONS OF THE EXTRACELLULAR MATRIX

So far, we have discussed the nonlinear elastic properties of a thin elastic shell (collagen cage) that surrounds the organoid branch. Next, as we have done in the Supplementary Material of our preprint, on pages 363–394, we also consider the elastic stresses that arise from deformations of an elastic medium (extracellular collagen matrix), which surrounds the cylindrical collagen cage. In our preprint, we have assumed no-slip boundary conditions for the elastic medium at the surface of the organoid branch. We have then found that the elastic medium plays no significant stabilizing role for the shape of the organoid branch, because it is much softer than the elastic shell. Here, we generalize the description of the elastic medium by allowing slip boundary conditions at the cellular surface of the organoid branch, which forms an interface in our cylindrical geometry. Then, we show that the conclusions of our preprint are robust against such a change in boundary conditions. Along the way, we derive a relation between the boundary velocity and the boundary stresses, for the case where the elastic medium surrounds the tubular organoid branch, and also for the case where the elastic medium fills the tubular organoid branch. While we do not immediately apply these results, they can prove useful in future work.

The elastic medium requires a treatment in terms of three-dimensional bulk coordinates: the radial position r, the axial position z, and the azimuthal angle ϕ. These bulk coordinates match the surface coordinates at the interface of our tubular geometry, for $r \equiv R(z)$, see Example 2 on page 21. For the corresponding basis vectors that span the bulk volume of our geometry, $\boldsymbol{b}_i$, which are orthogonal but not normalized, we refer to Example 3 on page 24. As before, we assume a rotational symmetry around the centerline of our geometry, the z-axis.

The response matrix of a cylindrical elastic medium. We describe the elastic medium with linear elasticity theory. For the mechanical reference configuration of the elastic medium, we use a cylinder with homogeneous radius R_0, which agrees with the initial shape of the organoid branch. We parameterize the deformed mechanical configuration of the elastic medium by an infinitesimal deformation field $\boldsymbol{u}$, which deflects the material points, as discussed in Paragraph "Deformation field in the embedding" (Section I.3.5). Then, we determine the contravariant components of the linearized strain tensor (Landau, Pitaevskii, et al., 1986), as discussed in Paragraph "The strain as a variation of the metric" (Section I.3.5) and Example 9 on page 42:

$$
\begin{bmatrix} \varepsilon^{rr} & \varepsilon^{rz} & \varepsilon^{r\phi} \\ \varepsilon^{zr} & \varepsilon^{zz} & \varepsilon^{z\phi} \\ \varepsilon^{\phi r} & \varepsilon^{\phi z} & \varepsilon^{\phi\phi} \end{bmatrix} = \begin{bmatrix} \partial_r u^r & (\partial_z u^r + \partial_r u^z)/2 & \partial_r u^\phi/2 \\ (\partial_z u^r + \partial_r u^z)/2 & \partial_z u^z & \partial_z u^\phi/2 \\ \partial_r u^\phi/2 & \partial_z u^\phi/2 & u^r/r^3 \end{bmatrix} , \quad \text{(IV.49)}
$$

using the rotational symmetry of our coordinate system. The trace of the strain tensor in our cylindrical coordinate system, see Example 7 on page 37, is given by:

$$\text{tr}\,\varepsilon = \sum_{ik} \varepsilon^{ik}\, g_{ik}^{-1} = \varepsilon^{rr} + \varepsilon^{zz} + r^2 \varepsilon^{\phi\phi} = \frac{1}{r}\,\partial_r(r\,u^r) + \partial_z u^z = \boldsymbol{\nabla}\cdot\boldsymbol{u}\,, \qquad \text{(IV.50)}$$

and measures volumetric changes (that is, isotropic compression and dilation) of the elastic medium. After splitting the strain tensor into a pure shear part and a pure volumetric part, the linear elastic stress tensor is given by (Landau, Pitaevskii, et al., 1986):

$$\begin{aligned}\boldsymbol{\sigma}_{el} &= 2G\left[\varepsilon - \frac{1}{3}\boldsymbol{I}\,\text{tr}\,\varepsilon\right] + \frac{2G}{3}\frac{1+\nu}{1-2\nu}\boldsymbol{I}\,\text{tr}\,\varepsilon \\ &= 2G\left[\varepsilon + \frac{\nu}{1-2\nu}\boldsymbol{I}\,\text{tr}\,\varepsilon\right],\end{aligned} \qquad \text{(IV.51)}$$

where $\boldsymbol{I}$ refers to the identity mapping. The elastic properties of the medium are characterized by its shear modulus[7], G, and its Poisson ratio, ν. Note that the strain tensor and consequently also the elastic stress tensor are symmetric (Landau, Pitaevskii, et al., 1986), see Paragraph "The strain as a variation of the metric" (Section I.3.5).

The elastic medium is a passive material and only experiences deformations because the cellular tissue at the surface of the cylindrical organoid branch exerts active stresses. Therefore, the divergence of the stress tensor, $\boldsymbol{\nabla}\cdot\boldsymbol{\sigma}_{el}$, which measures the force that each parcel (infinitesimal volume element) of material experiences in the bulk volume, must vanish (Amenzade, 1979):

$$0 = f^r = \frac{1}{r}\,\partial_r\left(r\,\sigma_{el}^{rr}\right) + \partial_z\sigma_{el}^{rz} - r\,\sigma_{el}^{\phi\phi}\,, \qquad \text{(IV.52a)}$$

$$0 = f^z = \frac{1}{r}\,\partial_r\left(r\,\sigma_{el}^{rz}\right) + \partial_z\sigma_{el}^{zz}\,, \qquad \text{(IV.52b)}$$

$$0 = f^\phi = \frac{1}{r}\,\partial_r\left(r\,\sigma_{el}^{r\phi}\right) + \partial_z\sigma_{el}^{z\phi} + \frac{2}{r}\,\sigma_{el}^{r\phi}\,. \qquad \text{(IV.52c)}$$

Here, we have used that the elastic stress tensor is symmetric, see also Example 8 on page 39. The circumferential component of the bulk force density, f^ϕ, decouples from the axial and the radial deformations, and is therefore of no interest when no torque is applied. Therefore, the mechanical force balance in the elastic medium is described by the following two remaining equations (Amenzade,

---

[7] We use G for the shear modulus instead of μ, because the latter is reserved for chemical potentials in this thesis.

1979):

$$\partial_r\left[2\frac{1-\nu}{1-2\nu}\frac{1}{r}\partial_r(r\,u^r)+\frac{1}{1-2\nu}\partial_z u^z\right]+\partial_z^2 u^r=0\,, \tag{IV.53a}$$

$$\partial_z\left[\frac{1}{1-2\nu}\frac{1}{r}\partial_r(r\,u^r)+2\frac{1-\nu}{1-2\nu}\partial_z u^z\right]+\frac{1}{r}\partial_r(r\,\partial_r u^z)=0\,. \tag{IV.53b}$$

To solve these equations, we introduce the stress function, Φ, via an implicit definition (Landau, Pitaevskii, et al., 1986):

$$u^r =: -\partial_r\partial_z\Phi\,, \quad\text{and}\quad u^z =: 2(1-\nu)\,\boldsymbol{\nabla}^2\Phi-\partial_z^2\Phi\,, \tag{IV.54}$$

which can be interpreted as a pseudo-potential that represents the full deformation field. After inserting Eq. (IV.54) into Eq. (IV.53a) and Eq. (IV.53b), one finds that the stress function Φ must satisfy the biharmonic equation in cylindrical coordinates (Amenzade, 1979):

$$\boldsymbol{\nabla}^4\Phi=0\,. \tag{IV.55}$$

Next, we solve this biharmonic equation.

We are interested in undulations of the cellular surface of the organoid branch, which forms an interface in our cylindrical geometry. Therefore, we decompose the deformation field of the elastic medium, and thus also the stress function, into Fourier modes[8]:

$$\Phi=\sum_q\Phi_q(r)\,\sin(q\,z)\,, \quad\text{so that}$$

$$u^r=\sum_q u_q^r(r)\,\cos(q\,z) \quad\text{and}\quad u^z=\sum_q u_q^z(r)\,\sin(q\,z)\,. \tag{IV.56}$$

With this definition, the homogeneous $q=0$ mode corresponds to a uniform radial deflection of the interface, while $q\neq0$ modes correspond to shear deformations of the elastic medium. Note that all Fourier modes decouple for the equations of linear elasticity, and are thus independent of their *phase*. Therefore, we would obtain identical solutions if we were to shift our Fourier modes by some arbitrary phase.

The general real-valued solution to the biharmonic equation, Eq. (IV.55), is then given by:

$$\Phi_q(r)=a_1\left[Y_0(-i\,q\,r)+i\,I_0(q\,r)\right]+i\,a_2\,r\left[Y_1(-i\,q\,r)+I_1(q\,r)\right]$$
$$+a_3\,I_0(q\,r)+a_4\,r\,I_1(q\,r)\,, \tag{IV.57}$$

---

[8] We consider an infinitely long cylinder. For our analysis it thus does not make a difference if we choose cosine or sine waveforms in the Fourier expansion, as explained in the following.

where $I_k(x)$ refers to the modified Bessel function of the first kind and $Y_k(x)$ refers to the Bessel function of the second kind. Note that the first two terms, with coefficients a_1 and a_2, correspond to deformation fields that diverge at the centerline ($r \to 0$) and approach zero in the far field ($r \to \infty$). In contrast, the last two terms, with coefficients a_3 and a_4, correspond to deformation fields that diverge in the far field ($r \to \infty$) and remain finite at the centerline ($r \to 0$). Thus, there are two distinct solutions for the deformation field, one for an elastic medium in the half space $r > R$, and one for an elastic medium in the half space $r < R$. To proceed, we now also decompose the stress field into Fourier modes:

$$\sigma_{el}^{rr} = \sum_q \sigma_{el,q}^{rr} \cos(q\,z) \quad \text{and} \quad \sigma_{el}^{rz} = \sum_q \sigma_{el,q}^{rz} \sin(q\,z). \tag{IV.58}$$

Then, we find the following linear relationship between the deflection, $u_q^r(R)$ and $u_q^z(R)$, and the stress at the position of the interface:

$$\begin{bmatrix} \sigma_{el,q}^{rr}(R) \\ \sigma_{el,q}^{rz}(R) \end{bmatrix} = -\frac{2G}{R}\, \chi_{el}(q\,R) \cdot \begin{bmatrix} u_q^r(R) \\ u_q^z(R) \end{bmatrix}. \tag{IV.59}$$

Here, we have defined the following symmetric response matrix:

$$\chi_{el}(x) := \begin{bmatrix} 1 + \dfrac{2B^2(x)\,(1-\nu)}{B^2(x)+4B(x)\,(1-\nu)-x^2} & x - x\,\dfrac{2B(x)\,(1-\nu)}{B^2(x)+4B(x)\,(1-\nu)-x^2} \\ x - x\,\dfrac{2B(x)\,(1-\nu)}{B^2(x)+4B(x)\,(1-\nu)-x^2} & \dfrac{2(1-\nu)\,x^2}{B^2(x)+4B(x)\,(1-\nu)-x^2} \end{bmatrix}, \tag{IV.60}$$

with a placeholder function $B(x)$. Interestingly, the only difference between the near-field solution and the far-field solution lies in the definition of this placeholder function:

$$B_{near}(x) := -x\,\frac{I_0(x)}{I_1(x)}, \quad \text{and} \quad B_{far}(x) := x\,\frac{K_0(x)}{K_1(x)}, \tag{IV.61}$$

where $K_k(x)$ is the modified Bessel function of the second kind.

A worked example for the response of the elastic medium. Using our response matrix, Eq. (IV.60), we can now determine the elastic stresses that arise in response to deflections of the organoid branch surface. In the Supplementary Material of our preprint, on pages 341–394, we have assumed no-slip boundary conditions at the interface, so that $u_q^z(R) = 0$. Now, we instead consider an adiabatic relaxation of tangential shear stress in the extracellular collagen matrix (elastic medium that fills the half space $r > R$), as done for the collagen cage (elastic shell) in Section IV.2.3 "Nonlinear Elasticity of the Collagen Cage".

To proceed, we need to connect these interfacial stresses to the stresses in the elastic medium, which requires physical projections of the stress tensor (see
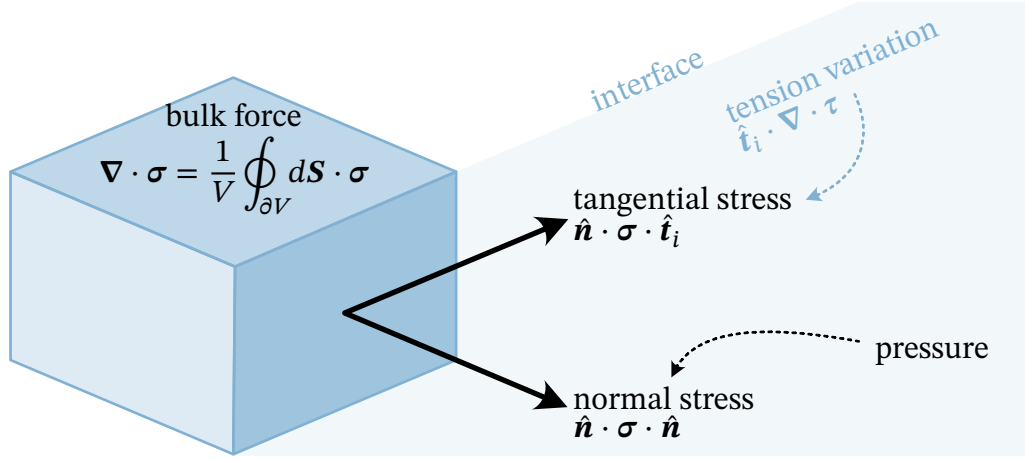
Figure IV.5: Sketch of a cuboid volume element. The average volume force that acts on the cuboid is given by the divergence of the stress tensor. The force that acts on one of the faces of the cuboid is given by a physical projection of the stress tensor with the normal vector of the face, $\hat{n} \cdot \sigma$. Then, the volume force can be understood as the integral of all surface forces (Gauss's theorem). Now, we connect one of the faces of the cuboid to an interface. From the other side of the interface, a pressure acts on the face, thus determining the normal component of the interfacial stress, $\hat{n} \cdot \sigma \cdot \hat{n}$. Finally, tension modulations at the interface lead to an average area force $\nabla \cdot \tau$, thus determining the tangential components of the interfacial stress, $\hat{n} \cdot \sigma \cdot \hat{t}_i$.

Fig. IV.5 for a geometric explanation). Here, we make these physical projections trivial by performing a *linearization of our geometry*. Specifically, as mentioned before, we consider a situation where the radial undulations of the tubular organoid branch are small, $\partial_z R \ll 1$. In that case, the unit normal vector of the interface points in the direction of the radial basis vector, $\hat{n} \propto b_r$, and the axial tangent vector of the interface points in the direction of the axial basis vector, $t_z \propto b_z$. Therefore, σ_{el}^{rr} is the normal stress at the interface, and σ_{el}^{rz} is the tangential shear stress at the interface. Using this simplification, we next investigate how the mechanical properties of the elastic medium will affect the organoid branch.

An adiabatic relaxation of the tangential shear stress implies $\sigma_{el}^{rz} = 0$ as boundary condition at the interface. Thus, after inverting Eq. (IV.59), we have:

$$\begin{bmatrix} u_q^r(R) \\ u_q^z(R) \end{bmatrix} = -\frac{R}{2G} \chi_{el}^{-1}(qR) \cdot \begin{bmatrix} \sigma_{el,q}^{rr}(R) \\ 0 \end{bmatrix}. \tag{IV.62}$$

For these boundary conditions, a typical deformation field is shown in Fig. IV.6a. We find that the restoring stress is minimal for the homogeneous $q = 0$ mode,
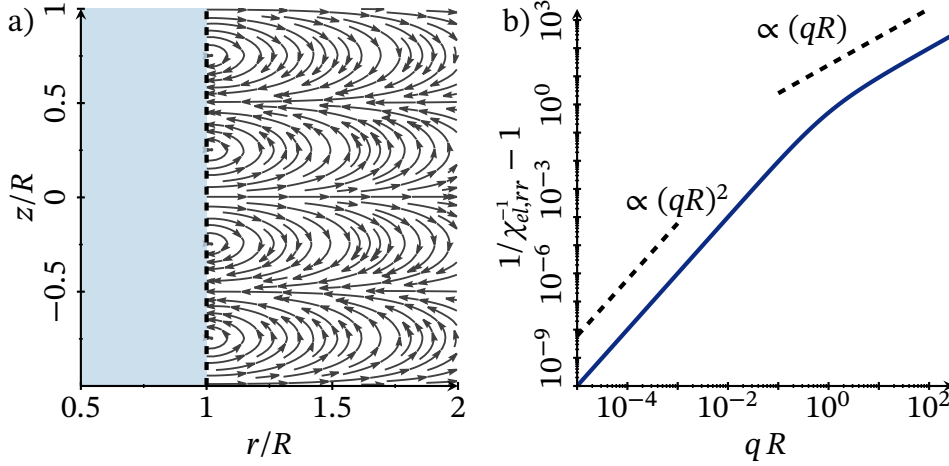
Figure IV.6: Response of an elastic medium, for slip boundary conditions at the surface of the cylindrical organoid branch (gray). a) A typical deformation field for an incompressible extracellular collagen matrix, $\nu = 1/2$, and a Fourier mode $q = 2\pi/R$. b) The restoring normal stress, $\sigma^{rr}_{el,q}(R)$ assuming an adiabatic relaxation of tangential shear stresses, $\sigma^{rz}_{el,q}(R) = 0$, typically grows with the Fourier mode q. One can understand this as the elastic material penalizing shear.

see Fig. IV.6b, with

$$\sigma^{rr}_{el,q}(R) = -\frac{2G}{R} \frac{1}{\chi^{-1}_{el,rr}(q\,R)} u^r_q(R) \leq -\frac{2G}{R} u^r_q(R) \,, \qquad \text{(IV.63)}$$

which is the same result as in our preprint. Because only the minimal restoring stress (in other words, least stabilizing) plays a role for the onset of a long-wavelength instability at $q = 0$, the conclusions that we made in our preprint are valid even for a change in boundary conditions. In particular, as we discuss in our preprint on pages 341–394, the extracellular collagen matrix (elastic medium) is roughly two orders of magnitude softer than the collagen cage (elastic shell). Therefore, we conclude that the elastic medium will not significantly affect the stability of the organoid branch.

IV.2.5 CELL ACTIVITY DRIVES HYDRODYNAMIC FLOWS

In this section, to describe the *dynamics* of organoid branch deformation, we derive a hydrodynamic theory. Before we proceed, we remind on the architecture of organoid branches, where cells form an active confluent tissue with a tubular shape (Fig. IV.1a). This confluent tissue lies at the interface between

different passive materials: a viscous fluid in the lumen, and two elastic solids in the surroundings consisting of a thin elastic shell (collagen cage) and an elastic medium[9] (extracellular collagen matrix). Therefore, we describe an organoid branch as a boundary-driven column of fluid, where cell activity induces hydrodynamic flows. This cell activity shows itself in the form of tension modulations and tension anisotropy. Of note, recent work has also investigated how anisotropic, but homogeneous, tension can affect the stability of columnar fluids (Bächer et al., 2021; Gräßel et al., 2021). Our first goal is to derive a relation between the boundary stresses and the boundary velocities, analogous to the relation between boundary stresses and boundary deflections in Section IV.2.4 "Deformations of the Extracellular Matrix". This will subsequently allow us to determine the dynamics of the organoid branch.

As before in Section IV.2.4 "Deformations of the Extracellular Matrix", the fluid in the lumen of the organoid branch requires a treatment in terms of three-dimensional bulk coordinates: the radial position r, the axial position z, and the azimuthal angle ϕ. These bulk coordinates match the surface coordinates at the interface of our tubular geometry, for $r \equiv R(z)$, see Example 2 on page 21. For the corresponding basis vectors that span the bulk volume of our geometry, $\boldsymbol{b}_i$, which are orthogonal but not normalized, we refer to Example 3 on page 24. Again, we assume a rotational symmetry around the centerline of our geometry, the z-axis.

The response matrix of a cylindrical fluid. We describe the fluid flow in the lumen of the organoid branch as follows. A velocity field, $\boldsymbol{v}$, moves the material points of the viscous fluid. The contravariant components of the linearized strain rate tensor (Landau and Lifshitz, 1987), which we discussed in Paragraph "The strain rate as gradual changes of the metric" (Section I.3.5), are then given by:

$$\begin{bmatrix} \dot{\varepsilon}^{rr} & \dot{\varepsilon}^{rz} & \dot{\varepsilon}^{r\phi} \\ \dot{\varepsilon}^{zr} & \dot{\varepsilon}^{zz} & \dot{\varepsilon}^{z\phi} \\ \dot{\varepsilon}^{\phi r} & \dot{\varepsilon}^{\phi z} & \dot{\varepsilon}^{\phi\phi} \end{bmatrix} = \begin{bmatrix} \partial_r v^r & (\partial_z v^r + \partial_r v^z)/2 & \partial_r v^\phi/2 \\ (\partial_z v^r + \partial_r v^z)/2 & \partial_z v^z & \partial_z v^\phi/2 \\ \partial_r v^\phi/2 & \partial_z v^\phi/2 & v^r/r^3 \end{bmatrix}, \quad \text{(IV.64)}$$

where we have used the rotational symmetry of our coordinate system; see also Eq. (IV.49) and Example 9 on page 42. The total stress in the fluid, which has viscosity η, consists of a viscous shear stress and a hydrodynamic pressure p (Landau and Lifshitz, 1987):

$$\boldsymbol{\sigma}_{fl} = \eta\,\dot{\boldsymbol{\varepsilon}} - p\,, \quad \text{(IV.65)}$$

One can understand the role of the hydrodynamic pressure by considering a hypothetical compressible fluid with viscosity η, vanishing shear modulus G, and

---

[9] We neglect the stresses in the elastic medium, because it is much softer than the elastic shell.

compression modulus K. Taking the limit of an infinitely large compression modulus, $K \to \infty$, then introduces the hydrodynamic pressure p as a *Lagrange multiplier* that substitutes the compressive stress, and enforces the incompressibility condition (Landau and Lifshitz, 1987):

$$\boldsymbol{\nabla} \cdot \boldsymbol{v} = \frac{1}{r} \partial_r(r\, v^r) + \partial_z v^z = 0 \,. \tag{IV.66}$$

For our hydrodynamic theory, we assume that the viscous fluid in the lumen of the organoid branch exhibits a creeping flow at low Reynolds number, and thus neglect the nonlinearity that would otherwise arise from momentum advection. Furthermore, we assume that the momentum relaxation dynamics are fast, so that we deal with a steady fluid flow that responds instantaneously to any external driving force. Because the fluid in the lumen of the organoid branch is only driven by interfacial stresses that the cells generate, it must be force-free in the bulk volume of the fluid. This leads us to the Stokes equation for the dynamics of the fluid (Landau and Lifshitz, 1987):

$$\boldsymbol{\nabla} \cdot \boldsymbol{\sigma}_{fl} = 0 \,. \tag{IV.67}$$

Together with the fluid incompressibility condition, Eq. (IV.66), we thus have a system of $d + 1$ equations and $d + 1$ unknowns, where d is the dimension of our geometry. Since our geometry is rotationally symmetric, we have $d = 2$ dimensions.

Explicitly calculating the divergence of the stress tensor, Eq. (IV.67), for our rotationally symmetric cylindrical coordinate system, see also Eq. (IV.52) and Example 8 on page 39, the mechanical force balance equations for the fluid in the lumen of the organoid branch are then given by (Landau and Lifshitz, 1987):

$$\eta\, \partial_z \Big[\partial_z v^r - \partial_r v^z \Big] - \partial_r p = \eta \left[\boldsymbol{\nabla}^2 - \frac{1}{r^2} \right] v^r - \partial_r p = 0 \,, \tag{IV.68a}$$

$$\frac{\eta}{r} \partial_r \Big[r \left(\partial_r v^z - \partial_z v^r \right) \Big] - \partial_z p = \eta \boldsymbol{\nabla}^2 v^z - \partial_z p = 0 \,. \tag{IV.68b}$$

In the above equations, $\partial_r v^z - \partial_z v^r$ can be understood as the vorticity of the flow field. As before in Section IV.2.4 "Deformations of the Extracellular Matrix", the circumferential component of the fluid force density decouples from the axial and the radial fluid flows. Therefore, it is of no interest when no torque is applied.

To now solve the Stokes equations in our cylindrical geometry, that is Eq. (IV.68a), Eq. (IV.68b) and Eq. (IV.66), we use a classical textbook technique by introducing the Stokes stream function (Landau and Lifshitz, 1987). The idea that underlies this technique is that one can eliminate the incompressibility

condition, Eq. (IV.66), by expressing the velocity field via derivatives of an implicitly defined scalar field Ψ, the so-called stream function (Landau and Lifshitz, 1987):

$$v^r =: \frac{1}{r}\,\partial_z\Psi\,, \quad \text{and} \quad v^z =: -\frac{1}{r}\,\partial_r\Psi\,. \tag{IV.69}$$

With this definition, we ensure that the incompressibility condition, Eq. (IV.66), is strictly fulfilled by all admissible solutions. After inserting Eq. (IV.69) into Eq. (IV.68a) and Eq. (IV.68b), one finds that the stream function must satisfy the following fourth order partial differential equation (Payne and Pell, 1960):

$$L_{-1}^2\Psi = 0\,, \quad \text{with differential operator} \quad L_{-1} = \boldsymbol{\nabla}^2 - \frac{2}{r}\partial_r\,. \tag{IV.70}$$

Using the Stokes stream function, we can also determine the pressure field. Specifically, by inserting the expression for the velocity field defined via the Stokes stream function, Eq. (IV.69), into the axial force balance equation, Eq. (IV.68b), one finds the following relation between the Stokes stream function and the pressure field:

$$\frac{\eta}{r}\,\partial_r\Big[L_{-1}\Psi\Big] + \partial_z p = 0\,, \tag{IV.71}$$

which defines the hydrodynamic pressure p up to a constant hydrostatic pressure p_0. As is generally the case for all force-free (that is, boundary-driven) Stokes flows, the hydrodynamic pressure satisfies the harmonic equation, here in cylindrical coordinates:

$$\boldsymbol{\nabla}^2 p = 0\,. \tag{IV.72}$$

Thus, we only need to determine the Stokes stream function to completely characterize the fluid flow in the lumen of the organoid branch.

As before in Section IV.2.4 "Deformations of the Extracellular Matrix", we are interested in undulations of the cellular surface of the organoid branch, which forms an interface in our cylindrical geometry. Therefore, we decompose the flow field of the viscous fluid, and thus also the Stokes stream function, into Fourier modes:

$$\Psi = \sum_q \Psi_q(r)\,\sin(q\,z)\,, \quad \text{so that}$$

$$v^r = \sum_q v_q^r(r)\,\cos(q\,z) \quad \text{and} \quad v^z = \sum_q v_q^z(r)\,\sin(q\,z)\,. \tag{IV.73}$$

With this definition, the homogeneous $q = 0$ mode corresponds to a uniform radial flow of the interface, while $q \neq 0$ modes correspond to shear flows of the fluid in the lumen of the organoid branch. Note that all Fourier modes decouple given that the Stokes equations are linear, and are thus independent of

their *phase*; therefore, we would obtain identical solutions if we were to shift our Fourier modes by some arbitrary phase. The general real-valued solution to Eq. (IV.70) is then given by:

$$\Psi_q(r) = r^2 \left[a_1 \left(Y_0(-i\,q\,r) + i\,I_0(q\,r) \right) + a_2 \left(Y_2(-i\,q\,r) - i\,I_2(q\,r) \right) \right.$$
$$\left. + a_3\,I_0(q\,r) + a_4\,I_2(q\,r) \right], \quad \text{(IV.74)}$$

where $I_k(x)$ refers to the modified Bessel function of the first kind and $Y_k(x)$ refers to the Bessel function of the second kind. Note that the first two terms, with coefficients a_1 and a_2, correspond to fluid flow fields that diverge at the centerline ($r \to 0$) and approach zero in the far field ($r \to \infty$). In contrast, the last two terms, with coefficients a_3 and a_4, correspond to fluid flow fields that diverge in the far field ($r \to \infty$) and remain finite at the centerline ($r \to 0$). Therefore, there are two distinct solutions for the fluid flow field: one for a viscous fluid in the half space $r > R$, and one for a viscous fluid in the half space $r < R$.

Analogous to Section IV.2.4 "Deformations of the Extracellular Matrix", we proceed by decomposing the stress field into Fourier modes:

$$\sigma_{fl}^{rr} = -p_0 + \sum_q \sigma_{fl,q}^{rr} \cos(q\,z), \quad \text{and} \quad \sigma_{fl}^{rz} = \sum_q \sigma_{fl,q}^{rz} \sin(q\,z). \quad \text{(IV.75)}$$

Then, we find the following linear relationship between the fluid flow, $v_q^r(R)$ and $v_q^z(R)$, and the stress at the position of the interface:

$$\begin{bmatrix} \sigma_{fl,q}^{rr}(R) \\ \sigma_{fl,q}^{rz}(R) \end{bmatrix} = -\frac{2\eta}{R} \chi_{fl}(q\,R) \cdot \begin{bmatrix} v_q^r(R) \\ v_q^z(R) \end{bmatrix}. \quad \text{(IV.76)}$$

Here, we have defined the following symmetric response matrix:

$$\chi_{fl}(x) := \begin{bmatrix} 1 + \dfrac{B^2(x)}{B^2(x)+2B(x)-x^2} & x - x\,\dfrac{B(x)}{B^2(x)+2B(x)-x^2} \\ x - x\,\dfrac{B(x)}{B^2(x)+2B(x)-x^2} & \dfrac{x^2}{B^2(x)+2B(x)-x^2} \end{bmatrix}, \quad \text{(IV.77)}$$

with a placeholder function $B(x)$. Interestingly, the only difference between the near-field solution and the far-field solution lies in the definition of this placeholder function:

$$B_{near}(x) := -x\,\frac{I_0(x)}{I_1(x)}, \quad \text{and} \quad B_{far}(x) := x\,\frac{K_0(x)}{K_1(x)}, \quad \text{(IV.78)}$$

where $I_k(x)$ refers to the modified Bessel function of the first kind and $K_k(x)$ refers to the modified Bessel function of the second kind. Finally, note that the

response matrix of the viscous fluid, Eq. (IV.77), is *exactly* the same as the response matrix of an incompressible elastic material, see Eq. (IV.60). With this, we have reached our first goal of deriving a relation between the viscous stresses at the interface and the corresponding interface velocity. If we know all the other stresses that act on the interface, then we can now determine its velocity by simply inverting the response matrix χ_{fl}.

Tension-driven fluid flow: Stress boundary conditions. Now that we have formulated a linear theory for the fluid response, we elucidate how active cell contractility can dictate the *dynamics* of the organoid branch. Specifically, we consider a baseline axial and an independent baseline circumferential tension, $\tau_{z,0}$ and $\tau_{\phi,0}$, which are superimposed by periodic modulations with amplitudes $\tau_z - \tau_{z,0}$ and $\gamma(\tau_\phi - \tau_{\phi,0})$, respectively. In that way, we account for a possible anisotropy of the tension modulations: $\gamma = -1$ keeps the trace of the tension tensor constant thus indicating modulations in cell orientation, $\gamma = 1$ indicates isotropic tension modulations, and $\gamma > 1$ indicates tension modulations mostly along the organoid branch axis. In analogy to the Fourier decomposition of all fluid flow descriptors in Paragraph "The response matrix of a cylindrical fluid", we treat the spatial heterogeneity of the active circumferential tension and the active axial tension by expanding them into Fourier modes:

$$\tau_\phi = \tau_{\phi,0} + \sum_q (\partial_q \tau)\, q\, \cos(qz)\,, \quad \text{and} \quad \tau_z = \tau_{z,0} + \sum_q \gamma\,(\partial_q \tau)\, q\, \cos(qz)\,. \quad \text{(IV.79)}$$

In addition, we have here also performed a Taylor expansion up to linear order to ensure that both tensions match their baseline values for the homogeneous $q = 0$ mode. As will become clear *a posteriori*, the specific phase of this Fourier expansion ensures matching Fourier modes between the viscous fluid stresses and the active stresses on the surface.

To proceed, we need to connect the interfacial stresses, which arise due to cell activity and elastic deformations of the thin shell, to the stresses in the viscous fluid. In a general setting, this requires physical projections of the stress tensor (see Fig. IV.5 for a geometric explanation). As before in Section IV.2.4 "Deformations of the Extracellular Matrix", we make these physical projections trivial by performing a *linearization of our geometry*. Specifically, as mentioned before, we consider a situation where the radial undulations of the tubular organoid branch are small, $\partial_z R \ll 1$. In that case, the unit normal vector of the interface points in the direction of the radial basis vector, $\hat{\boldsymbol{n}} \propto \boldsymbol{b}_r$, and the axial tangent vector of the interface points in the direction of the axial basis vector, $\boldsymbol{t}_z \propto \boldsymbol{b}_z$. Therefore, σ_{fl}^{rr} is the normal stress at the fluid interface, and σ_{fl}^{rz} is the tangential shear stress at the fluid interface. Note that the fluid only fills the lumen of the organoid branch, thus specializing to our near-field solution

with $B(x) \equiv B_{near}(x)$, see Eq. (IV.78). All normal stresses that apply at the fluid interface (that is, the fluid stress, the Laplace pressure due to active cell contractility, and all elastic stresses) must balance, leading to the following boundary condition:

$$\sigma_{fl}^{rr}(R) = -\frac{\tau_\phi}{R} + \tau_z\, \partial_z^2 R + \Delta p_s + \Delta p_b \,. \tag{IV.80}$$

Here, Δp_s is the elastic stress due to stretching of the thin shell, Eq. (IV.43), and Δp_b is the elastic stress due to bending of the thin shell, Eq. (IV.48). Analogously, all tangential shear stresses that apply at the fluid interface must also balance. These tangential shear stresses include: (i) the fluid stress, (ii) tension gradients that lead to a Marangoni effect, (iii) the motile force f_m that cells exert on the substrate (that is, the elastic shell), and (iv) a *slip friction* ξ because the cells (and thus the fluid) can slip against the elastic shell. With these considerations, the tangential shear stress boundary condition is given by:

$$\sigma_{fl}^{rz}(R) = \partial_z \tau_z + f_m - \xi\, v^z \,, \tag{IV.81}$$

The Marangoni effect can be illustrated as follows: if in region "1" cells contract more strongly than in an adjacent region "2", then the cells from region "2" will be pulled towards region "1", thus leading to flows. Note that we can also represent the motile force f_m as the gradient of a surface scalar field. Therefore, we absorb it into the modulations of the axial tension. This means that the case of $\gamma > 1$, see Eq. (IV.79), actually corresponds to axial oscillatory motion of the cells.

As we have done Section IV.1.3 "Technical Summary", we linearize Eq. (IV.80) by considering small radial deflections of the organoid branch surface, $R = R_0 + u$, with $u \ll R_0$. Furthermore, we insert all of our Fourier-expanded quantities into the boundary conditions, Eq. (IV.80) and Eq. (IV.81), and neglect mode coupling terms. By doing so, we arrive at the following linearized equations:
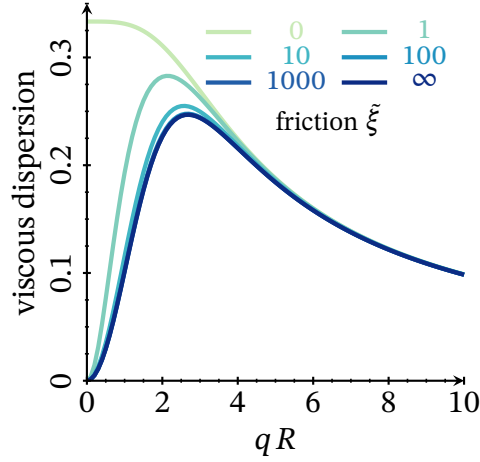
$$-p_0 + \sum_q \sigma_{fl,q}^{rr}(R) \cos(qz) = -\frac{\tau_{\phi,0}}{R_0} + \sum_q \left[\Delta p_q - \frac{(\partial_q \tau)\, q}{R_0}\right] \cos(qz), \tag{IV.82}$$

$$\sum_q \sigma_{fl,q}^{rz}(R) \sin(qz) = -\sum_q \left[\gamma\, (\partial_q \tau)\, q^2 + \xi\, v_q^z(R)\right] \sin(qz). \tag{IV.83}$$

Here, Δp_q is the same stress dispersion relation as in Section IV.1.3 "Technical Summary", see Eq. (IV.20):

$$\Delta p_q = \left[\frac{\tau_{\phi,0}}{R_0^2} - \frac{Y_s\, h}{R_0^2} - \frac{k_b}{R_0^4} - \tau_{z,0}\, q^2 - k_b\, q^4\right] u_q \,. \tag{IV.84}$$

Because the stress balance equations must hold for all Fourier modes and for all deflections, there is a balance between the hydrostatic pressure and the *baseline*

Figure IV.7: The viscous dispersion relation, together with the stress dispersion relation, determines the growth rate of a cylindrical boundary-driven fluid. The homogeneous $q = 0$ mode is hydrodynamically prohibited for any finite slip friction $\tilde{\xi}$. Note that vanishing slip friction $\tilde{\xi} = 0$ does not yield physical solutions in the case of a shape transformation, because it would require diverging axial flows to keep the incompressibility condition intact. The limit $\tilde{\xi} \to \infty$ corresponds to no-slip boundary conditions.

Laplace pressure, $p_0 = \tau_{\phi,0}/R_0$. Now, we can determine the interface velocity by using its relation to the interfacial fluid stress, Eq. (IV.76), and solving the resulting linear set of equations:

$$\begin{bmatrix} v_q^r(R_0) \\ v_q^z(R_0) \end{bmatrix} = -\frac{R_0}{2\eta} \begin{bmatrix} \chi_{fl,rr} & \chi_{fl,rz} \\ \chi_{fl,zr} & \chi_{fl,zz} - (\xi R_0)/(2\eta) \end{bmatrix}^{-1} \cdot \begin{bmatrix} \Delta p_q - (\partial_q \tau \, q)/R_0 \\ -\gamma \, \partial_q \tau \, q^2 \end{bmatrix} . \quad \text{(IV.85)}$$

With this, we have derived the dynamics of the organoid branch up to linear order. In the following, we study two limiting cases of these dynamics.

A first limiting case: Shape transformation due to cell reorientations. As our first limiting case, we consider a situation where the dynamics are entirely driven by the stress dispersion relation, Δp_q, neglecting any and all tension modulations. In that case, the radial growth rate is given by:

$$v_q^r(R_0) = \frac{R_0}{2\eta} \frac{\chi_{fl,zz} - \tilde{\xi}}{\chi_{fl,rz}^2 + \tilde{\xi} \, \chi_{fl,rr} - \chi_{fl,rr} \, \chi_{fl,zz}} \Delta p_q , \quad \text{(IV.86)}$$
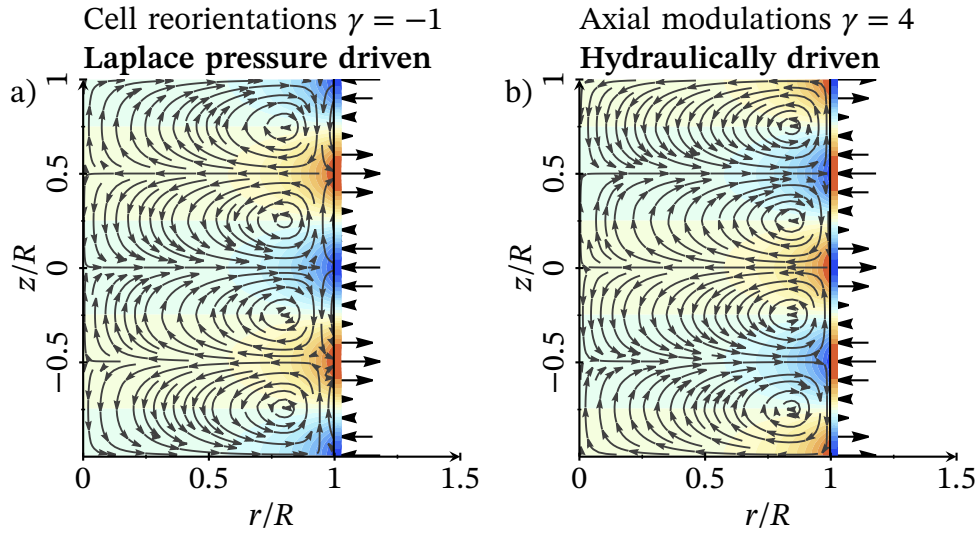
where we have defined $\tilde{\xi} := (\xi R_0)/(2\eta)$, and exploited the symmetry of the response matrix, Eq. (IV.77). Note that Eq. (IV.86) is solved by an exponential
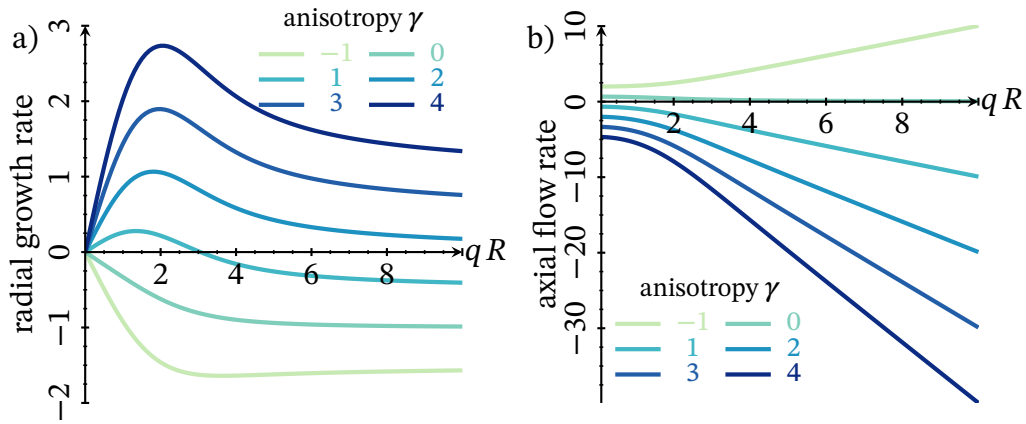
Figure IV.8: Response of the interface to tension modulations. a) Radial growth rate, $2\eta R_0 v_q^r/(\partial_q \tau)$. When applying a spatially varying surface tension, a viscous tubular fluid can actually *grow* in regions that have increased circumferential tension, and *shrink* in regions that have reduced circumferential surface tension. This is indicated by the positive sign of the radial growth rate. b) Axial flow rate, $2\eta R_0 v_q^z/(\partial_q \tau)$. We find that axial tension gradients induce tangential fluid flows at the organoid branch interface. If there are no gradients of axial tension ($\gamma = 0$), then the axial fluid flow is only determined by the distribution of the Laplace pressure.

growth law, because $v_q^r(R_0) = \dot{u}_q$ and $\Delta p_q \propto u_q$. We refer to the fraction in Eq. (IV.86) as "viscous dispersion relation". The viscous dispersion relation is strictly positive (Fig. IV.7), so that the stability of the tubular fluid is fully determined by the stress dispersion relation, Δp_q, in agreement with Section IV.1.3 "Technical Summary". Thus, the cellular tissue can control a shape transformation by reorienting cells and thereby making trade-offs between axial and circumferential tension. In the general case of finite slip friction, we find that the homogeneous $q = 0$ mode does not grow (Fig. IV.7), because homogeneous expansion is prohibited by fluid incompressibility. Therefore, the fastest-growing mode is *not* the $q = 0$ mode, although it has the greatest driving stress.

A second limiting case: Tension modulations.   As our second limiting case, we consider a situation where the dynamics are entirely driven by the tension modulations, because the deflection of the surface is still negligible $u_q \approx 0$. To show the greatest effect, we consider a situation where the slip friction is also negligible $\tilde{\xi} \approx 0$. Our general results remain the same as long as we choose any finite slip friction $\tilde{\xi} < \infty$. Then, the boundary velocity is given by the following

Cell reorientations $\gamma = -1$
Laplace pressure driven
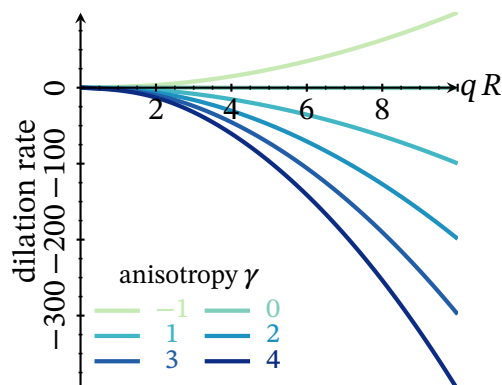
Axial modulations $\gamma = 4$
Hydraulically driven

Figure IV.9: Exemplary flow fields for tension modulations, shown for the Fourier mode $q = 2\pi/R$. Black line corresponds to the boundary of the organoid branch. The hydrodynamic pressure is shown left of the black line (a red color means high pressure, while a blue color means low pressure). Modulations of the Laplace pressure, $-\tau_\phi/R_0$, are shown right of the black line. Black arrows indicate in which direction the interface will move. Gray arrows indicate the fluid flow field. a) If the tension modulations conserve the trace of the tension tensor, then this corresponds to fluctuations in cell orientation. In this case, the interface is driven by the Laplace pressure. b) If the axial tension modulations are much greater than the circumferential tension modulations, then this indicates axial oscillatory motion of cells. In this case, the interface is driven by hydraulic pressure.

linear equation, see Eq. (IV.85):

$$\begin{bmatrix} v_q^r(R_0) \\ v_q^z(R_0) \end{bmatrix} = \frac{\partial_q \tau}{2\eta R_0} \begin{bmatrix} \chi_{fl,rr} & \chi_{fl,rz} \\ \chi_{fl,zr} & \chi_{fl,zz} \end{bmatrix}^{-1} \cdot \begin{bmatrix} q R_0 \\ \gamma (q R_0)^2 \end{bmatrix} . \tag{IV.87}$$

We find that a reorientation of cells without changes in cell contractility itself, $\gamma = -1$, leads to inwards motion of the interface in regions of high circumferential tension, because of the corresponding Laplace pressure (Fig. IV.8a, Fig. IV.9a). Interestingly, however, we also find that if the tension modulations occur preferentially along the axis of the cylindrical organoid branches, $\gamma > 1$, then the interface will expand in regions of high circumferential tension, and will contract in regions of low circumferential tension (Fig. IV.8a). The reason for this observation, which one would not expect from the Laplace pressure alone, is the Marangoni effect. Regions with high axial tension pull more

Figure IV.10: The dilation rate of a conserved material on the surface of the cylindrical organoid branch, for different anisotropic modulations of the surface tension. For tension modulations that are either isotropic or axially biased, $\gamma_\tau \geq 1$, we find that material is gradually accumulated in regions of increased circumferential tension. For anisotropic tension modulations that conserve the total tension, $\gamma_\tau = -1$, we find that material is gradually dilated in regions of increased circumferential tension.

cells towards them (Fig. IV.8b), thereby increasing hydrodynamic pressure in the fluid until it can overcome the Laplace pressure (Fig. IV.9b). Thus, the interface expands in precisely the regions that attract cells, which provides a first pointer, as to how organoid branches choose the direction in which the shape transformation occurs. First, cells flow towards the tip of an organoid branch, leading to a slight expansion because of the hydrodynamic pressure. Then, the cells reorient, begin collectively rotating, and the instability takes off. We discuss a second, even stronger, reason for organoid branch expansion at the onset of the shape transformation in Section IV.2.6 "Tubular Shells as Pumps and Rectifiers", which has its origin in nonlinear effects.

What if the tension modulations change upon movement of the interface? So far, we have assumed that the tension modulations are not affected by the movement of the interface. However, it is easy to imagine a situation where this is different: (i) tension might increase due to elastic stretching, or (ii) cells could actively adapt their tensile properties, or (iii) one considers an entirely different active material in the form of an actomyosin cortex, with isotropic tension that is proportional to the density of myosin motors (Salbreux et al., 2012; Chugh and Paluch, 2018). For that reason, it is interesting to study whether the interface of a columnar fluid will be dilated or compressed in regions of increased circumferential tension. To do so, we investigate the material derivative of an advected material; this means that we follow a parcel of the surface in the co-

moving frame. Now, we consider an arbitrary conserved density field, and study how the local density will change due to the motion of the interface:

$$\frac{1}{c}\left[\partial_t c + \boldsymbol{v}\cdot\boldsymbol{\nabla}c\right] = -\left[\partial_z v^z + \frac{v^r}{R_0}\right]$$

$$= -\frac{1}{R_0}\sum_q \left[v_q^z(R_0)\, q\, R_0 + v_q^r(R_0)\right]\cos(q\,z)\,. \quad \text{(IV.88)}$$

Here, $\boldsymbol{v}$ corresponds to the advection velocity, see Paragraph "Advection in the embedding" (Section I.3.5). We refer to the term in the square brackets, in the second line of Eq. (IV.88), as "dilation rate". If it is positive, then the material is dilated, while a negative value signifies enrichment.

We find that if the tension modulations originate from a reorientation of cells, $\gamma = -1$, then the material is further dilated in regions of increased circumferential tension (Fig. IV.10). If the material is elastic and increases its tension upon dilation, then this signifies a positive feedback loop that could play a role for tension-induced shape transformations. The situation is different if we have an isotropic material, with $\gamma = 1$, where the material is always further enriched in regions of high tension (Fig. IV.10). For elastic materials, this would counteract tension-driven instabilities. However, if we are dealing with an actomyosin cortex, where tension increases upon enrichment of myosin motors, then we have again the signature of a positive feedback loop that could lead to an instability. Similar advective instabilities have been studied theoretically for a flat actomyosin cortex (Bois et al., 2011).

IV.2.6 TUBULAR SHELLS AS PUMPS AND RECTIFIERS

So far, we have studied a linear theory, which in Section IV.2.5 "Cell Activity Drives Hydrodynamic Flows" allowed us to analytically determine the dynamics of a tubular boundary-driven fluid that is enveloped by a thin elastic shell, such as an organoid branch. In the following, we refer to this setup as "tube". Now, we aim to go beyond the restrictions of this linear theory, and give an outlook on elastic nonlinear effects that arise for such tubular systems. We do not consider geometric nonlinearity, and therefore still assume that radial undulations of the tubular organoid branch are small, $\partial_z R \ll 1$. Now, we revisit the normal stress balance equation, Eq. (IV.80), but this time keep all nonlinear elastic terms:

$$\sigma_{fl}^{rr} = -\left[\frac{\tau_\phi}{R} + Y_s\, h\, \frac{R^2 - R_0^2}{2\, R_0^2}\, \frac{R}{R_0^2} + \kappa_b \frac{R - R_0}{R_0\, R^3}\right] + \tau_z\, \partial_z^2 R - \kappa_b\, \partial_z^4 R\,. \quad \text{(IV.89)}$$

Note that for a homogeneous elastic shell with elastic modulus Y_s, Poisson's ratio ν and thickness h, the bending modulus is given by $k_b = Y_s\, h^3/[12(1-\nu^2)]$ (Landau, Pitaevskii, et al., 1986). As our model parameters, we choose estimated

values that proved sensible for organoid branches, as discussed in our preprint on pages 341–394 . In particular, the elastic shell is characterized by the Poisson ratio $\nu = 1/2$, the elastic modulus $Y_s = 0.72\,\text{kPa}$ and a thickness $h = 5\,\mu\text{m}$. In its reference configuration, the organoid branch has a radius of $R_0 = 30\,\mu\text{m}$. We will come back to the surface tension, τ_ϕ and τ_z, shortly.

Next, we split the radial fluid stress into a pure viscous shear part, $\sigma_{\underset{\scriptscriptstyle=}{}}^{rr} = 2\eta\,\partial_r v^r$, and the hydrodynamic pressure: $\sigma_{fl}^{rr} = \sigma_{\underset{\scriptscriptstyle=}{}}^{rr} - p$. Furthermore, the hydrodynamic pressure has a homogeneous reference contribution, determined by the Laplace pressure of the undeformed tube, and an inhomogeneous contribution: $p = \tau_\phi/R_0 + \Delta p_{ex}$. In the following, we refer to the inhomogeneous pressure contribution Δp_{ex} as "excess pressure". Taken together, our radial stress balance equation takes the following form:

$$\sigma_{\underset{\scriptscriptstyle=}{}}^{rr} = \Delta p_{ex} - \Delta p_{tube} + \tau_z\,\partial_z^2 R - \kappa_b\,\partial_z^4 R\,, \quad \text{where} \tag{IV.90a}$$

$$\Delta p_{tube} = -\tau_\phi\,\frac{R - R_0}{R_0\,R} + Y_s\,h\,\frac{R^2 - R_0^2}{2\,R_0^2}\,\frac{R}{R_0^2} + \kappa_b\,\frac{R - R_0}{R_0\,R^3}\,. \tag{IV.90b}$$

Now, we see that the viscous fluid in the lumen of the tube will respond with viscous flows if the right-hand side of Eq. (IV.90a) is out of balance. The last two terms on the right-hand side of Eq. (IV.90a) smooth out the tube shape, while the first two terms on the right-hand side of Eq. (IV.90a) define local attractors for the tube radius, R. In the following, we are interested in these local attractors that drive the deformations of the tube.

To that end, we first revisit our criterion for the stability of the initial cylindrical configuration of the tube. In particular, even for vanishing local excess pressure Δp_{ex}, the initial cylindrical shape of the tube becomes unstable if $\partial_R(\Delta p_{tube})|_{R_0} < 0$. As discussed in Section IV.1.3 "Technical Summary" and Section IV.2.5 "Cell Activity Drives Hydrodynamic Flows", this leads to a critical value for the circumferential tension, $\tau_\phi > \tau_c$, beyond which the initial cylindrical configuration becomes unstable. To gain more insight into the dynamics of this shape transformation, suppose that we start with a tube in its cylindrical reference shape, $R \approx R_0$, which in addition has a vanishing circumferential tension $\tau_\phi \approx 0$. When we slowly increase the circumferential tension, τ_ϕ, the tube remains cylindrical until a critical value, $\tau_\phi \gtrsim \tau_c$, beyond which we observe a *continuous* shape transformation (Fig. IV.11a) with a growing tube radius.

Stochastic pumping. In addition, we hypothesize that these dynamics could be even richer if the tube shape is subject to random fluctuations. What we have described just now is only the first of two distinct stable branches for the tube radius, separated by an unstable branch (Fig. IV.11a). Right at the critical point
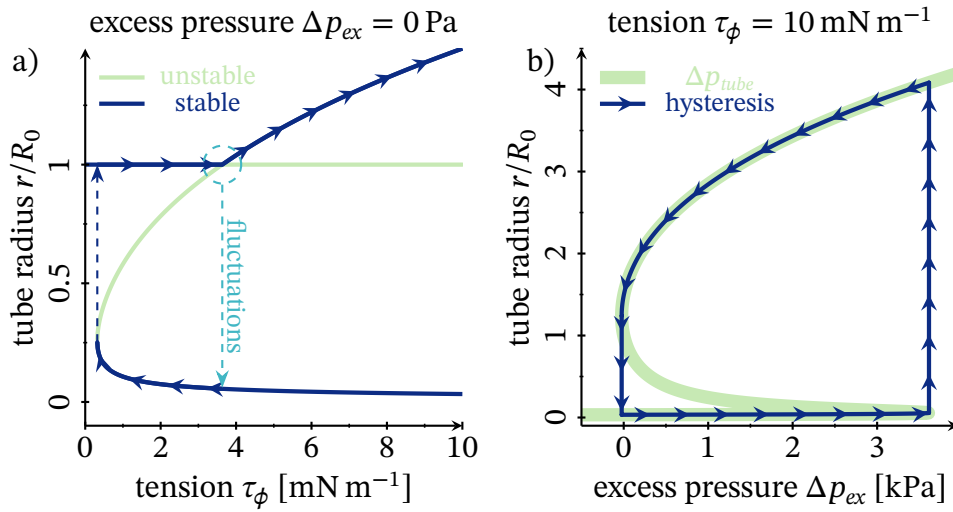
Figure IV.11: Local attractors of the tube radius as a function of different control parameters. a) Increasing circumferential tension, starting from the reference configuration $R = R_0$ and vanishing circumferential tension, leads to a continuous shape transformation at a critical value for the circumferential tension. The corresponding critical point is indicated by a dashed circle. At this critical point, shape fluctuations can lead to a discontinuous shape transformation in the form of a tube collapse. Cyclic modulation of the circumferential tension leads to a stochastic hysteresis loop. b) Cyclic modulation of the excess pressure leads to a deterministic hysteresis loop, thus breaking time-reversal symmetry.

for the onset of the continuous shape transformation, (R_0, τ_c), *only* the unstable branch touches the upper stable branch. Then, even infinitesimally small shape fluctuations can lead to a *discontinuous* contraction of the tube towards the lower stable branch. Now, suppose that the cells periodically modulate their active tension, reducing their contractility after the shape transformation has occurred. Then, we find that the lower stable branch *vanishes* after the circumferential tension falls below a second critical value (Fig. IV.11). This constitutes a hysteresis loop in the presence of shape fluctuations, which is driven by active cell tension. Given that this hysteresis loop breaks time-reversal symmetry, we hypothesize that it could lead to stochastic pumping of the fluid that fills the lumen of the tube.

Deterministic rectification. Finally, we consider a situation where the circumferential tension stays at a constant value of $\tau_\phi \approx \tau = 10\,\mathrm{mN\,m^{-1}}$, which was measured for spherical mammary gland organoids via micropipette aspira-

tion (Villeneuve et al., 2019). Now, we vary the excess pressure Δp_{ex} instead of the surface tension. Such a situation can be realized by applying a hydrodynamic pressure gradient along the length of the tube, and then temporally modulating the pressure at one of the two tube ends. From a pure Stokes fluid in a non-deformable tube, we would expect that there is no net transport in response to a pressure gradient that flips periodically, because the Stokes equations are time reversible (Purcell, 1977). However, the situation is already different if the wall of the tube is a thin deformable shell. In that case, we find a deterministic hysteresis loop of the tube radius, as a function of the excess pressure. For low pressure, the tube shape is stabilized by elastic bending, while for high pressure it is stabilized by elastic stretching (Fig. IV.11b). This hysteresis loop breaks time-reversal symmetry and in this case turns the tube into a mechanical rectifier, which can be illustrated as follows. Suppose that at one end of the tube, labeled "−" and termed "outlet", we keep the excess pressure constant, at a value where the tube has ballooned up to the upper stable branch. At the other end of the tube, labeled "+" and termed "inlet", we vary the excess pressure. If the excess pressure is much larger at the inlet than at the outlet, $p_+ \gg p_-$, then both ends of the tube lie on the same (upper) stable branch and forward flow is permitted. However, if the excess pressure is much smaller than the fixed pressure at the other side of the tube, $p_- \ll p_+$, then the tube at the inlet collapses to the lower stable branch and reverse flow is prohibited (Fig. IV.11b). To drop to the lower branch, the (relative) inlet pressure must fall below a value of $-24\,\mathrm{Pa}$ (Fig. IV.11b). Increasing the pressure at the inlet again, forward flow will then only be allowed if the (relative) inlet pressure exceeds a much larger value of $3.6\,\mathrm{kPa}$ (Fig. IV.11b). Thus, the thin shell acts like an elastic check valve, which is the hydrodynamic equivalent of an electrical rectifier.

Bibliography

References to Theses

B. Ramm, "Self-organization and molecular transport by a biological reaction-diffusion system", Thesis (Feb. 2020).

F. P. Thüroff, "Collective motion in active matter", Thesis (July 2014).

References to Books

B. Alberts, D. Bray, K. Hopkin, A. Johnson, J. Lewis, M. C. Raff, K. Roberts, and P. Walter, *Essential cell biology*, Fourth Edition (Garland Science, New York, 2014).

B. Alberts, A. Johnson, J. Lewis, D. Morgan, M. Raff, K. Roberts, and P. Walter, *Molecular biology of the cell*, Sixth Edition (Garland Science, New York, 2014).

Y. A. Amenzade, *Theory of elasticity* (Mir, Moscow, 1979).

R. Balian, *From microphysics to macrophysics: Methods and applications of statistical physics* (Springer, Berlin, 2007).

B. M. Carlson, *The human body: Linking structure and function* (Academic Press, London, 2019).

R. Courant and D. Hilbert, *Methods of mathematical physics: Partial differential equations* (Wiley, Weinheim, 2004).

P. G. de Gennes, *Scaling concepts in polymer physics* (Cornell University Press, Ithaca, 1979).

T. Frankel, *The geometry of physics: An introduction*, Third Edition (Cambridge University Press, Cambridge, 2011).

I. M. Gelfand and S. V. Fomin, *Calculus of variations* (Dover Publications, New York, 2000).

P. Grinfeld, *Introduction to tensor analysis and the calculus of moving surfaces* (Springer, New York, 2013).

I. P. Herman, *Physics of the human body*, Second Edition (Springer, Berlin, 2016).

E. Kreyszig, *Differential geometry* (University of Toronto Press, Toronto, 1959).

W. M. Lai, D. Rubin, and E. Krempl, *Introduction to continuum mechanics*, Fourth Edition (Butterworth-Heinemann, Burlington, 2010).

L. D. Landau and E. M. Lifshitz, *Statistical physics*, Third Edition, Course of Theoretical Physics (Butterworth-Heinemann, Oxford, 1980).

L. D. Landau and E. M. Lifshitz, *Fluid mechanics*, Second Edition, Course of Theoretical Physics (Butterworth-Heinemann, Oxford, 1987).

L. D. Landau, L. P. Pitaevskii, A. M. Kosevich, and E. M. Lifshitz, *Theory of elasticity*, Third Edition, Course of Theoretical Physics (Butterworth-Heinemann, Oxford, 1986).

L. P. Lebedev and M. J. Cloud, *Tensor analysis* (World Scientific, 2003).

R. Milo and R. Phillips, *Cell biology by the numbers* (Garland Science, New York, 2015).

C. M. Murea, *Stable numerical schemes for fluids, structures and their interactions* (Elsevier, Oxford, 2018).

D. Nelson, T. Piran, and S. Weinberg, *Statistical mechanics of membranes and surfaces*, Second Edition (World Scientific, 2004).

R. Phillips, J. Kondev, J. Theriot, and H. Garcia, *Physical biology of the cell*, Second Edition (Garland Science, New York, 2012).

R. Phillips, *The molecular switch: Signaling and allostery* (Princeton University Press, Princeton, 2020).

A. N. Pressley, *Elementary differential geometry*, Second Edition (Springer, London, 2010).

J. B. Reece, L. A. Urry, M. L. Cain, S. A. Wasserman, P. V. Minorsky, R. B. Jackson, and N. A. Campbell, *Biology*, Tenth Edition (Pearson, Boston, 2014).

S. Safran, *Statistical thermodynamics of surfaces, interfaces, and membranes* (CRC Press, Boca Raton, 2003).

A. C. Steven, W. Baumeister, L. N. Johnson, and R. N. Perham, *Molecular biology of assemblies and machines* (Garland Science, New York, 2016).

S. H. Strogatz, *Nonlinear dynamics and chaos: With applications to physics, biology, chemistry, and engineering*, Second Edition (CRC Press, Boca Raton, 2018).

S. Timoshenko and J. M. Gere, *Theory of elastic stability*, Second Edition (McGraw-Hill, New York, 1961).

L. W. Tu, *Differential geometry: Connections, curvature, and characteristic classes* (Springer, Cham, 2017).

REFERENCES TO REVIEW ARTICLES

S. Alt, P. Ganguly, and G. Salbreux, Philosophical Transactions of the Royal Society B: Biological Sciences **372**, 20150520 (2017).

A. Bershadsky, M. Kozlov, and B. Geiger, Current Opinion in Cell Biology **18**, 472 (2006).

M. J. Bissell and M. H. Barcellos-Hoff, Journal of Cell Science **Supplement 8**, 327 (1987).

G. Charras and E. Sahai, Nature Reviews Molecular Cell Biology **15**, 813 (2014).

P. Chugh and E. K. Paluch, Journal of Cell Science **131**, jcs186254 (2018).

M. C. Cross and P. C. Hohenberg, Reviews of Modern Physics **65**, 851 (1993).

C. De Pascalis and S. Etienne-Manneville, Molecular Biology of the Cell **28**, 1833 (2017).

M. Deserno, Chemistry and Physics of Lipids **185**, 11 (2015).

D. E. Discher, P. Janmey, and Y.-l. Wang, Science **310**, 1139 (2005).

P. Friedl, Y. Hegerfeldt, and M. Tusch, International Journal of Developmental Biology **48**, 441 (2004).

P. Friedl and D. Gilmour, Nature Reviews Molecular Cell Biology **10**, 445 (2009).

P. Friedl and B. Weigelin, Nature Immunology **9**, 960 (2008).

H. Ge, M. Tian, Q. Pei, F. Tan, and H. Pei, Frontiers in Oncology **11**, 631991 (2021).

E. Gheisari, M. Aakhte, and H.-A. J. Müller, Mechanisms of Development **163**, 103629 (2020).

N. W. Goehring and S. W. Grill, Trends in Cell Biology **23**, 72 (2013).

B. Goldstein and I. G. Macara, Developmental Cell **13**, 609 (2007).

R. Golestanian, Preprint deposited on arXiv (2019), arXiv:1909 . 03747 [cond-mat.soft].

N. S. Gov, Philosophical Transactions of the Royal Society B: Biological Sciences **373**, 20170115 (2018).

I. Goychuk, Beilstein Journal of Nanotechnology **7**, 328 (2016).

P. Gross, K. V. Kumar, and S. W. Grill, Annual Review of Biophysics **46**, 337 (2017).

A. Guckenberger and S. Gekle, Journal of Physics: Condensed Matter **29**, 203001 (2017).

V. Hakim and P. Silberzan, Reports on Progress in Physics **80**, 076601 (2017).

J. Halatek, F. Brauns, and E. Frey, Philosophical Transactions of the Royal Society B: Biological Sciences **373**, 20170107 (2018).

P. Hänggi, P. Talkner, and M. Borkovec, Reviews of Modern Physics **62**, 251 (1990).

E. Hannezo and C.-P. Heisenberg, Cell **178**, 12 (2019).

R. G. Hodge and A. J. Ridley, Nature Reviews Molecular Cell Biology **17**, 496 (2016).

T. Idema and D. J. Kraft, Current Opinion in Colloid & Interface Science **40**, 58 (2019).

P. Illien, R. Golestanian, and A. Sen, Chemical Society Reviews **46**, 5508 (2017).

J. L. Inman, C. Robertson, J. D. Mott, and M. J. Bissell, Development **142**, 1028 (2015).

I. K. Jarsch, F. Daste, and J. L. Gallop, Journal of Cell Biology **214**, 375 (2016).

D. I. Johnson, Microbiology and Molecular Biology Reviews **63**, 54 (1999).

R. D. Kamien, Reviews of Modern Physics **74**, 953 (2002).

R. Krishna and J. A. Wesselingh, Chemical Engineering Science **52**, 861 (1997).

P. Kunda and B. Baum, Trends in Cell Biology **19**, 174 (2009).

C. F. Lang and E. Munro, Development **144**, 3405 (2017).

D. A. Lauffenburger and A. F. Horwitz, Cell **84**, 359 (1996).

C. D. Lawson and A. J. Ridley, Journal of Cell Biology **217**, 447 (2018).

V. Lecaudey and D. Gilmour, Current Opinion in Cell Biology **18**, 102 (2006).

J. Lutkenhaus, Annual Review of Biochemistry **76**, 539 (2007).

S. Marbach and L. Bocquet, Chemical Society Reviews **48**, 3102 (2019).

D. Marenduzzo, K. Finan, and P. R. Cook, Journal of Cell Biology **175**, 681 (2006).

A. C. Martin, Genetics **214**, 543 (2020).

H. T. McMahon and E. Boucrot, Journal of Cell Science **128**, 1065 (2015).

C. Mim and V. M. Unger, Trends in Biochemical Sciences **37**, 526 (2012).

T. Mitchison and M. Kirschner, Neuron **1**, 761 (1988).

A. Mogilner, Journal of Mathematical Biology **58**, 105 (2009).

A. Mogilner and K. Keren, Current Biology **19**, R762 (2009).

M. Murrell, P. W. Oakes, M. Lenz, and M. L. Gardel, Nature Reviews Molecular Cell Biology **16**, 486 (2015).

C. M. Nelson and M. J. Bissell, Annual Review of Cell and Developmental Biology **22**, 287 (2006).

J. T. Parsons, A. R. Horwitz, and M. A. Schwartz, Nature Reviews Molecular Cell Biology **11**, 633 (2010).

N. I. Petridou, Z. Spiró, and C.-P. Heisenberg, Nature Cell Biology **19**, 581 (2017).

R. Phillips, T. Ursell, P. Wiggins, and P. Sens, Nature **459**, 379 (2009).

T. D. Pollard and G. G. Borisy, Cell **112**, 453 (2003).

W. A. Prinz and J. E. Hinshaw, Critical Reviews in Biochemistry and Molecular Biology **44**, 278 (2009).

B. Ramm, T. Heermann, and P. Schwille, Cellular and Molecular Life Sciences **76**, 4245 (2019).

A. J. Ridley, Journal of Cell Science **114**, 2713 (2001).

A. J. Ridley, Current Opinion in Cell Biology **36**, 103 (2015).

A. J. Ridley, M. A. Schwartz, K. Burridge, R. A. Firtel, M. H. Ginsberg, G. Borisy, J. T. Parsons, and A. R. Horwitz, Science **302**, 1704 (2003).

M. Rodrigues, N. Kosaric, C. A. Bonham, and G. C. Gurtner, Physiological Reviews **99**, 665 (2019).

L. J. Rothschild and R. L. Mancinelli, Nature **409**, 1092 (2001).

G. Salbreux, G. Charras, and E. Paluch, Trends in Cell Biology **22**, 536 (2012).

E. S. Schiffhauer and D. N. Robinson, Biophysical Journal **112**, 207 (2017).

M. A. Schwartz and S. J. Shattil, Trends in Biochemical Sciences **25**, 388 (2000).

U. S. Schwarz and S. A. Safran, Reviews of Modern Physics **85**, 1327 (2013).

U. S. Schwarz and J. R. D. Soiné, Biochimica et Biophysica Acta **1853**, 3095 (2015).

U. Seifert, Advances in Physics **46**, 13 (1997).

M. Simunovic, G. A. Voth, A. Callan-Jones, and P. Bassereau, Trends in Cell Biology **25**, 780 (2015).

C.-P. Spatarelu, H. Zhang, D. T. Nguyen, X. Han, R. Liu, Q. Guo, J. Notbohm, J. Fan, L. Liu, and Z. Chen, ACS Biomaterials Science & Engineering **5**, 3766 (2019).

M. I. Stefan and N. Le Novère, PLOS Computational Biology **9**, e1003106 (2013).

A. Szabó and R. M. Merks, Frontiers in Oncology **3**, 87 (2013).

M. Théry and M. Bornens, Current Opinion in Cell Biology **18**, 648 (2006).

B. Vailhé, D. Vittet, and J.-J. Feige, Laboratory Investigation **81**, 439 (2001).

J. van den Berg, A. J. Boersma, and B. Poolman, Nature Reviews Microbiology **15**, 309 (2017).

S. Van Helvert, C. Storm, and P. Friedl, Nature Cell Biology **20**, 8 (2018).

K. H. Vining and D. J. Mooney, Nature Reviews Molecular Cell Biology **18**, 728 (2017).

S. Wang, R. Sekiguchi, W. P. Daley, and K. M. Yamada, Journal of Cell Biology **216**, 559 (2017).

T. R. Weikl, Annual Review of Physical Chemistry **69**, 521 (2018).

M. A. Wozniak and C. S. Chen, Nature Reviews Molecular Cell Biology **10**, 34 (2009).

H. Yamaguchi, J. Wyckoff, and J. Condeelis, Current Opinion in Cell Biology **17**, 559 (2005).

H. Zhao, A. Pykäläinen, and P. Lappalainen, Current Opinion in Cell Biology **23**, 14 (2011).

J. Zimmerberg and M. M. Kozlov, Nature Reviews Molecular Cell Biology **7**, 9 (2006).

J. Zimmerberg and S. McLaughlin, Current Biology **14**, R250 (2004).

References to Research Articles

B. Abécassis, C. Cottin-Bizonne, C. Ybert, A. Ajdari, and L. Bocquet, Nature Materials **7**, 785 (2008).

T. Adeleke-Larodo, J. Agudo-Canalejo, and R. Golestanian, The Journal of Chemical Physics **150**, 115102 (2019).

J. Agudo-Canalejo, P. Illien, and R. Golestanian, Nano Letters **18**, 2711 (2018).

P. J. Albert and U. S. Schwarz, Biophysical Journal **106**, 2340 (2014).

P. J. Albert and U. S. Schwarz, PLOS Computational Biology **12**, e1004863 (2016).

J. L. Anderson, M. E. Lowell, and D. C. Prieve, Journal of Fluid Mechanics **117**, 107 (1982).

S. Arrhenius, Zeitschrift für Physikalische Chemie **4U**, 226 (1889).

S. Asakura and F. Oosawa, The Journal of Chemical Physics **22**, 1255 (1954).

C. Bächer, K. Gräßel, and S. Gekle, Journal of Fluid Mechanics **910**, A47 (2021).

S. Banerjee, K. J. C. Utuje, and M. C. Marchetti, Physical Review Letters **114**, 228101 (2015).

E. J. Banigan, M. A. Gelbart, Z. Gitai, N. S. Wingreen, and A. J. Liu, PLOS Computational Biology **7**, e1002145 (2011).

R. Bar-Ziv and E. Moses, Physical Review Letters **73**, 1392 (1994).

R. Bar-Ziv, T. Tlusty, E. Moses, S. A. Safran, and A. Bershadsky, Proceedings of the National Academy of Sciences of the United States of America **96**, 10140 (1999).

M. Basan, J. Elgeti, E. Hannezo, W.-J. Rappel, and H. Levine, Proceedings of the National Academy of Sciences of the United States of America **110**, 2452 (2013).

M. Bennett, M. Cantini, J. Reboud, J. M. Cooper, P. Roca-Cusachs, and M. Salmeron-Sanchez, Proceedings of the National Academy of Sciences of the United States of America **115**, 1192 (2018).

V. K. Bhatia, K. L. Madsen, P.-Y. Bolinger, A. Kunding, P. Hedegård, U. Gether, and D. Stamou, The EMBO Journal **28**, 3303 (2009).

I. B. Bischofs, S. A. Safran, and U. S. Schwarz, Physical Review E **69**, 021911 (2004).

I. B. Bischofs and U. S. Schwarz, Proceedings of the National Academy of Sciences of the United States of America **100**, 9274 (2003).

I. B. Bischofs and U. S. Schwarz, Acta Biomaterialia **2**, 253 (2006).

J. S. Bois, F. Jülicher, and S. W. Grill, Physical Review Letters **106**, 028103 (2011).

D. Boocock, N. Hino, N. Ruzickova, T. Hirashima, and E. Hannezo, Nature Physics **17**, 267 (2021).

F. Brinkmann, M. Mercker, T. Richter, and A. Marciniak-Czochra, PLOS Computational Biology **14**, e1006259 (2018).

D. B. Brückner, A. Fink, C. Schreiber, P. J. F. Röttgermann, J. O. Rädler, and C. P. Broedersz, Nature Physics **15**, 595 (2019).

B. Buchmann, L. K. Engelbrecht, P. Fernandez, F. P. Hutterer, M. K. Raich, C. H. Scheel, and A. R. Bausch, Nature Communications **12**, 2759 (2021).

B. A. Camley, Y. Zhang, Y. Zhao, B. Li, E. Ben-Jacob, H. Levine, and W.-J. Rappel, Proceedings of the National Academy of Sciences of the United States of America **111**, 14770 (2014).

B. A. Camley, Y. Zhao, B. Li, H. Levine, and W.-J. Rappel, Physical Review Letters **111**, 158102 (2013).

Y. Cao, R. Karmakar, E. Ghabache, E. Gutierrez, Y. Zhao, A. Groisman, H. Levine, B. A. Camley, and W.-J. Rappel, Soft Matter **15**, 2043 (2019).

R. Capovilla, J. Guven, and J. A. Santiago, Journal of Physics A **36**, 6281 (2003).

Y. Caspi and C. Dekker, eLife **5**, e19271 (2016).

C. E. Chan and D. J. Odde, Science **322**, 1687 (2008).

S. J. Chatterjee, R. Halaoui, R. C. Deagle, C. Rejon, and L. McCaffrey, Biology Open **8**, bio042341 (2019).

A. Cont, T. Rossy, Z. Al-Mayyah, and A. Persat, eLife **9**, e56533 (2020).

J. Crest, A. Diz-Muñoz, D.-Y. Chen, D. A. Fletcher, and D. Bilder, eLife **6**, e24958 (2017).

P. A. J. de Boer, R. E. Crossley, and L. I. Rothfield, Cell **56**, 641 (1989).

J. Denk, S. Kretschmer, J. Halatek, C. Hartl, P. Schwille, and E. Frey, Proceedings of the National Academy of Sciences of the United States of America **115**, 4553 (2018).

M. Dietrich, H. Le Roy, D. B. Brückner, H. Engelke, R. Zantl, J. O. Rädler, and C. P. Broedersz, Soft Matter **14**, 2816 (2018).

B. Dong, E. Hannezo, and S. Hayashi, Cell Reports **7**, 941 (2014).

K. Doxzen, S. R. K. Vedula, M. C. Leong, H. Hirata, N. S. Gov, A. J. Kabla, B. Ladoux, and C. T. Lim, Integrative Biology **5**, 1026 (2013).

A. Elosegui-Artola, E. Bazellières, M. D. Allen, I. Andreu, R. Oria, R. Sunyer, J. J. Gomm, J. F. Marshall, J. L. Jones, X. Trepat, and P. Roca-Cusachs, Nature Materials **13**, 631 (2014).

A. Elosegui-Artola, R. Oria, Y. Chen, A. Kosmalska, C. Pérez-González, N. Castro, C. Zhu, X. Trepat, and P. Roca-Cusachs, Nature Cell Biology **18**, 540 (2016).

K. Eroumé, A. Vasilevich, S. Vermeulen, J. de Boer, and A. Carlier, PLOS ONE **16**, e0248293 (2021).

C. Fei, S. Mao, J. Yan, R. Alert, H. A. Stone, B. L. Bassler, N. S. Wingreen, and A. Košmrlj, Proceedings of the National Academy of Sciences of the United States of America **117**, 7622 (2020).

P. Fernández, B. Buchmann, A. Goychuk, L. K. Engelbrecht, M. Raich, C. H. Scheel, E. Frey, and A. R. Bausch, Nature Physics, `10.1038/s41567-021-01336-7` (2021).

P. J. Flory, The Journal of Chemical Physics **10**, 51 (1942).

M. G. J. Ford, I. G. Mills, B. J. Peter, Y. Vallis, G. J. K. Praefcke, P. R. Evans, and H. T. McMahon, Nature **419**, 361 (2002).

M. Fu, H. G. Franquelim, S. Kretschmer, and P. Schwille, Angewandte Chemie International Edition **60**, 6496 (2021).

P. Glock, B. Ramm, T. Heermann, S. Kretschmer, J. Schweizer, J. Mücksch, G. Alagöz, and P. Schwille, ACS Synthetic Biology **8**, 148 (2019).

N. W. Goehring, P. K. Trong, J. S. Bois, D. Chowdhury, E. M. Nicola, A. A. Hyman, and S. W. Grill, Science **334**, 1137 (2011).

N. S. Gov and A. Gopinathan, Biophysical Journal **90**, 454 (2006).

A. Goychuk, D. B. Brückner, A. W. Holle, J. P. Spatz, C. P. Broedersz, and E. Frey, Preprint deposited on arXiv (2018), arXiv:1808.00314 [`physics.bio-ph`].

A. Goychuk and E. Frey, Physical Review Letters **123**, 178101 (2019).

F. Graner and J. A. Glazier, Physical Review Letters **69**, 2013 (1992).

K. Gräßel, C. Bächer, and S. Gekle, Journal of Fluid Mechanics **910**, A46 (2021).

W. J. Hadden, J. L. Young, A. W. Holle, M. L. McFetridge, D. Y. Kim, P. Wijesinghe, H. Taylor-Weiner, J. H. Wen, A. R. Lee, K. Bieback, B.-N. Vo, D. D. Sampson, B. F. Kennedy, J. P. Spatz, A. J. Engler, and Y. S. Choi, Proceedings of the National Academy of Sciences of the United States of America **114**, 5647 (2017).

J. Halatek and E. Frey, Cell Reports **1**, 741 (2012).

C. A. Hale, H. Meinhardt, and P. A. J. de Boer, The EMBO Journal **20**, 1563 (2001).

E. Hannezo, J. Prost, and J.-F. Joanny, Physical Review Letters **109**, 018101 (2012).

E. Hannezo, J. Prost, and J.-F. Joanny, Proceedings of the National Academy of Sciences of the United States of America **111**, 27 (2014).

C. A. Haselwandter and R. Phillips, Europhysics Letters **101**, 68002 (2013).

C. A. Haselwandter and N. S. Wingreen, PLOS Computational Biology **10**, e1003932 (2014).

B. He, K. Doubrovinski, O. Polyakov, and E. Wieschaus, Nature **508**, 392 (2014).

W. Helfrich, Zeitschrift für Naturforschung C **28**, 693 (1973).

A. V. Hill, Biochemical Journal **7**, 471 (1913).

Z. Hu and J. Lutkenhaus, Molecular Microbiology **34**, 82 (1999).

K. C. Huang, Y. Meir, and N. S. Wingreen, Proceedings of the National Academy of Sciences of the United States of America **100**, 12724 (2003).

M. L. Huggins, The Journal of Chemical Physics **9**, 440 (1941).

T. Idema, S. Semrau, C. Storm, and T. Schmidt, Physical Review Letters **104**, 198102 (2010).

B. C. Isenberg, P. A. Dimilla, M. Walker, S. Kim, and J. Y. Wong, Biophysical Journal **97**, 1313 (2009).

M. Jang, J. An, S. W. Oh, J. Y. Lim, J. Kim, J. K. Choi, J.-H. Cheong, and P. Kim, Nature Biomedical Engineering **5**, 114 (2021).

K. I. Jönsson, E. Rabbow, R. O. Schill, M. Harms-Ringdahl, and P. Rettberg, Current Biology **18**, R729 (2008).

A. J. Kabla, Journal of The Royal Society Interface **9**, 3268 (2012).

E. Karzbrun, A. Kshirsagar, S. R. Cohen, J. H. Hanna, and O. Reiner, Nature Physics **14**, 515 (2018).

A. R. Kay, Frontiers in Cell and Developmental Biology **5**, 41 (2017).

H. A. Kramers, Physica **7**, 284 (1940).

D. Lachowski, E. Cortes, D. Pink, A. Chronopoulos, S. A. Karim, J. P. Morton, and A. E. del Río Hernández, Scientific Reports **7**, 2506 (2017).

M. C. S. Lee, L. Orci, S. Hamamoto, E. Futai, M. Ravazzola, and R. Schekman, Cell **122**, 605 (2005).

J. R. Linnemann, H. Miura, L. K. Meixner, M. Irmler, U. J. Kloos, B. Hirschi, H. S. Bartsch, S. Sass, J. Beckers, F. J. Theis, C. Gabka, K. Sotlar, and C. H. Scheel, Development **142**, 3239 (2015).

T. Litschel, B. Ramm, R. Maas, M. Heymann, and P. Schwille, Angewandte Chemie International Edition **57**, 16286 (2018).

C.-M. Lo, H.-B. Wang, M. Dembo, and Y.-L. Wang, Biophysical Journal **79**, 144 (2000).

J. Löber, F. Ziebert, and I. S. Aranson, Scientific Reports **5**, 9172 (2015).

M. Loose, E. Fischer-Friedrich, C. Herold, K. Kruse, and P. Schwille, Nature Structural & Molecular Biology **18**, 577 (2011).

M. Loose, E. Fischer-Friedrich, J. Ries, K. Kruse, and P. Schwille, Science **320**, 789 (2008).

F. R. S. Lord Rayleigh, Proceedings of the London Mathematical Society **s1-10**, 4 (1878).

J.-L. Maître, H. Berthoumieux, S. F. G. Krens, G. Salbreux, F. Jülicher, E. Paluch, and C.-P. Heisenberg, Science **338**, 253 (2012).

A. F. M. Marée, V. A. Grieneisen, and L. Edelstein-Keshet, PLOS Computational Biology **8**, e1002402 (2012).

A. F. M. Marée, A. Jilkine, A. Dawes, V. A. Grieneisen, and L. Edelstein-Keshet, Bulletin of Mathematical Biology **68**, 1169 (2006).

J. C. Maxwell, Philosophical Transactions of the Royal Society of London **157**, 49 (1866).

L. Mesarec, W. Góźdź, V. K. Iglič, S. Kralj, and A. Iglič, Colloids and Surfaces B: Biointerfaces **141**, 132 (2016).

A. Mietke, V. Jemseena, K. V. Kumar, I. F. Sbalzarini, and F. Jülicher, Physical Review Letters **123**, 188101 (2019).

A. Mietke, F. Jülicher, and I. F. Sbalzarini, Proceedings of the National Academy of Sciences of the United States of America **116**, 29 (2019).

S. Münster, A. Jain, A. Mietke, A. Pavlopoulos, S. W. Grill, and P. Tomancak, Nature **568**, 395 (2019).

N. M. Neumann, M. C. Perrone, J. H. Veldhuis, R. J. Huebner, H. Zhan, P. N. Devreotes, G. W. Brodland, and A. J. Ewald, Developmental Cell **45**, 67 (2018).

I. Niculescu, J. Textor, and R. J. de Boer, PLOS Computational Biology **11**, e1004280 (2015).

A. D. Olinger, E. J. Spangler, P. B. S. Kumar, and M. Laradji, Faraday Discussions **186**, 265 (2016).

J. Palacci, B. Abécassis, C. Cottin-Bizonne, C. Ybert, and L. Bocquet, Physical Review Letters **104**, 138302 (2010).

S. Pandamooz, A. Jafari, M. S. Salehi, B. Jurek, A. Ahmadiani, A. Safari, S. Hassanajili, A. Borhani-Haghighi, M. Dianatpour, H. Niknejad, N. Azarpira, and L. Dargahi, Biotechnology and Bioengineering **117**, 305 (2020).

K.-T. Park, M. T. Villar, A. Artigues, and J. Lutkenhaus, Proceedings of the National Academy of Sciences of the United States of America **114**, 7497 (2017).

K.-T. Park, W. Wu, K. P. Battaile, S. Lovell, T. Holyoak, and J. Lutkenhaus, Cell **146**, 396 (2011).

J. S. Paustian, C. D. Angulo, R. Nery-Azevedo, N. Shi, A. I. Abdel-Fattah, and T. M. Squires, Langmuir **31**, 4402 (2015).

L. E. Payne and W. H. Pell, Journal of Fluid Mechanics **7**, 529 (1960).

C. Pérez-González, R. Alert, C. Blanch-Mercader, M. Gómez-González, T. Kolodziej, E. Bazellieres, J. Casademunt, and X. Trepat, Nature Physics **15**, 79 (2019).

B. J. Peter, H. M. Kent, I. G. Mills, Y. Vallis, P. J. G. Butler, P. R. Evans, and H. T. McMahon, Science **303**, 495 (2004).

N. I. Petridou, S. Grigolon, G. Salbreux, E. Hannezo, and C.-P. Heisenberg, Nature Cell Biology **21**, 169 (2019).

V. Petrolli, M. Le Goff, M. Tadrous, K. Martens, C. Allier, O. Mandula, L. Hervé, S. Henkes, R. Sknepnek, T. Boudou, G. Cappello, and M. Balland, Physical Review Letters **122**, 168101 (2019).

G. Peyret, R. Mueller, J. d'Alessandro, S. Begnaud, P. Marcq, R.-M. Mège, J. M. Yeomans, A. Doostmohammadi, and B. Ladoux, Biophysical Journal **117**, 464 (2019).

M. Poujade, E. Grasland-Mongrain, A. Hertzog, J. Jouanneau, P. Chavrier, B. Ladoux, A. Buguin, and P. Silberzan, Proceedings of the National Academy of Sciences of the United States of America **104**, 15988 (2007).

C. Prévost, H. Zhao, J. Manzi, E. Lemichez, P. Lappalainen, A. Callan-Jones, and P. Bassereau, Nature Communications **6**, 8529 (2015).

D. C. Prieve, J. L. Anderson, J. P. Ebel, and M. E. Lowell, Journal of Fluid Mechanics **148**, 247 (1984).

D. C. Prieve, S. M. Malone, A. S. Khair, R. F. Stout, and M. Y. Kanj, Proceedings of the National Academy of Sciences of the United States of America **116**, 18257 (2019).

P. A. Pullarkat, P. Dommersnes, P. Fernández, J.-F. Joanny, and A. Ott, Physical Review Letters **96**, 048104 (2006).

E. M. Purcell, American Journal of Physics **45**, 3 (1977).

B. Ramm, P. Glock, J. Mücksch, P. Blumhardt, D. A. García-Soriano, M. Heymann, and P. Schwille, Nature Communications **9**, 3942 (2018).

B. Ramm, A. Goychuk, A. Khmelinskaia, P. Blumhardt, H. Eto, K. A. Ganzinger, E. Frey, and P. Schwille, Nature Physics **17**, 850 (2021).

D. M. Raskin and P. A. J. de Boer, Proceedings of the National Academy of Sciences of the United States of America **96**, 4971 (1999).

P. Recho, A. Hallou, and E. Hannezo, Proceedings of the National Academy of Sciences of the United States of America **116**, 5344 (2019).

C. A. Reinhart-King, M. Dembo, and D. A. Hammer, Biophysical Journal **95**, 6044 (2008).

E. G. Rens and L. Edelstein-Keshet, PLOS Computational Biology **15**, e1007459 (2019).

E. G. Rens and R. M. H. Merks, Biophysical Journal **112**, 755 (2017).

A. C. Rios, B. D. Capaldo, F. Vaillant, B. Pal, R. van Ineveld, C. A. Dawson, Y. Chen, E. Nolan, N. Y. Fu, F. C. Jackling, S. Devi, D. Clouston, L. Whitehead, G. K. Smyth, S. N. Mueller, G. J. Lindeman, and J. E. Visvader, Cancer Cell **35**, 618 (2019).

D. Rüdiger, K. Kick, A. Goychuk, A. M. Vollmar, E. Frey, and S. Zahler, Cell Reports **32**, 108015 (2020).

R. L. Saunders and D. A. Hammer, Cellular and Molecular Bioengineering **3**, 60 (2010).

U. Schmidt, G. Guigas, and M. Weiss, Physical Review Letters **101**, 128104 (2008).

U. S. Schwarz and S. A. Safran, Physical Review Letters **88**, 048102 (2002).

Y. Schweitzer and M. M. Kozlov, PLOS Computational Biology **11**, e1004054 (2015).

R. P. Sear, Physical Review Letters **122**, 128101 (2019).

F. J. Segerer, F. Thüroff, A. Piera Alberola, E. Frey, and J. O. Rädler, Physical Review Letters **114**, 228102 (2015).

P. Sens, Proceedings of the National Academy of Sciences of the United States of America **117**, 24670 (2020).

N. Sepúlveda, L. Petitjean, O. Cochet, E. Grasland-Mongrain, P. Silberzan, and V. Hakim, PLOS Computational Biology **9**, e1002944 (2013).

D. Shao, H. Levine, and W.-J. Rappel, Proceedings of the National Academy of Sciences of the United States of America **109**, 6851 (2012).

D. Shao, W.-J. Rappel, and H. Levine, Physical Review Letters **105**, 108104 (2010).

N. Shi, R. Nery-Azevedo, A. I. Abdel-Fattah, and T. M. Squires, Physical Review Letters **117**, 258001 (2016).

Y.-L. Shih, L.-T. Huang, Y.-M. Tu, B.-F. Lee, Y.-C. Bau, C. Y. Hong, H.-l. Lee, Y.-P. Shih, M.-F. Hsu, Z.-X. Lu, J.-S. Chen, and L. Chao, Biophysical Journal **116**, 1469 (2019).

S. Shin, E. Um, B. Sabass, J. T. Ault, M. Rahimi, P. B. Warren, and H. A. Stone, Proceedings of the National Academy of Sciences of the United States of America **113**, 257 (2016).

R. Shlomovitz and N. S. Gov, Physical Biology **6**, 046017 (2009).

R. S. Sopher, H. Tokash, S. Natan, M. Sharabi, O. Shelah, O. Tchaicheeyan, and A. Lesman, Biophysical Journal **115**, 1357 (2018).

J. C. Stachowiak, E. M. Schmid, C. J. Ryan, H. S. Ann, D. Y. Sasaki, M. B. Sherman, P. L. Geissler, D. A. Fletcher, and C. C. Hayden, Nature Cell Biology **14**, 944 (2012).

J. Stefan, Sitzungsberichte der Mathematisch-Naturwissenschaftlichen Classe der Kaiserlichen Akademie der Wissenschaften Wien, 2te Abteilung **63**, 63 (1871).

S. J. Streichan, M. F. Lefebvre, N. Noll, E. F. Wieschaus, and B. I. Shraiman, eLife **7**, e27454 (2018).

R. Sunyer, V. Conte, J. Escribano, A. Elosegui-Artola, A. Labernadie, L. Valon, D. Navajas, J. M. García-Aznar, J. J. Muñoz, P. Roca-Cusachs, and X. Trepat, Science **353**, 1157 (2016).

A. Szabó, R. Ünnep, E. Méhes, W. O. Twal, W. S. Argraves, Y. Cao, and A. Czirók, Physical Biology **7**, 046007 (2010).

B. Szabó, G. J. Szöllösi, B. Gönci, Z. Jurányi, D. Selmeczi, and T. Vicsek, Physical Review E **74**, 061908 (2006).

V. Tarle, E. Gauquelin, S. R. K. Vedula, J. D'Alessandro, C. T. Lim, B. Ladoux, and N. S. Gov, Physical Biology **14**, 035001 (2017).

R. J. Tetley, M. F. Staddon, D. Heller, A. Hoppe, S. Banerjee, and Y. Mao, Nature Physics **15**, 1195 (2019).

D. Thalmeier, J. Halatek, and E. Frey, Proceedings of the National Academy of Sciences of the United States of America **113**, 548 (2016).

F. Thüroff, A. Goychuk, M. Reiter, and E. Frey, eLife **8**, e46842 (2019).

I. Tsafrir, Y. Caspi, M.-A. Guedeau-Boudeville, T. Arzi, and J. Stavans, Physical Review Letters **91**, 138102 (2003).

A. M. Turing, Philosophical Transactions of the Royal Society B: Biological Sciences **237**, 37 (1952).

A. Vahid, G. Dadunashvili, and T. Idema, bioRxiv, 336545 (2019).

A. Vahid and T. Idema, Physical Review Letters **117**, 138102 (2016).

A. Vahid, A. Šarić, and T. Idema, Soft Matter **13**, 4924 (2017).

C. van der Wel, A. Vahid, A. Šarić, T. Idema, D. Heinrich, and D. J. Kraft, Scientific Reports **6**, 32825 (2016).

R. F. M. van Oers, E. G. Rens, D. J. LaValley, C. A. Reinhart-King, and R. M. H. Merks, PLOS Computational Biology **10**, e1003774 (2014).

A. G. Vecchiarelli, M. Li, M. Mizuuchi, L. C. Hwang, Y. Seol, K. C. Neuman, and K. Mizuuchi, Proceedings of the National Academy of Sciences of the United States of America **113**, E1479 (2016).

T. Vicsek, A. Czirók, E. Ben-Jacob, I. Cohen, and O. Shochet, Physical Review Letters **75**, 1226 (1995).

C. Villeneuve, E. Lagoutte, L. de Plater, S. Mathieu, J.-B. Manneville, J.-L. Maître, P. Chavrier, and C. Rossé, Proceedings of the National Academy of Sciences of the United States of America **116**, 24108 (2019).

L. G. Vincent, Y. S. Choi, B. Alonso-Latorre, J. C. del Álamo, and A. J. Engler, Biotechnology Journal **8**, 472 (2013).

M. C. Wigbers, T. H. Tan, F. Brauns, J. Liu, S. Z. Swartz, E. Frey, and N. Fakhri, Nature Physics, `10.1038/s41567-021-01164-9` (2021).

J. P. Winer, S. Oake, and P. A. Janmey, PLOS ONE **4**, e6382 (2009).

F. Wu, B. G. C. van Schie, J. E. Keymer, and C. Dekker, Nature Nanotechnology **10**, 719 (2015).

F. Yuan, H. Alimohamadi, B. Bakka, A. N. Trementozzi, K. J. Day, N. L. Fawzi, P. Rangamani, and J. C. Stachowiak, Proceedings of the National Academy of Sciences of the United States of America **118**, e2017435118 (2021).

M. G. Yucht, M. Sheinman, and C. P. Broedersz, Soft Matter **9**, 7000 (2013).

A. Zemel, F. Rehfeldt, A. E. X. Brown, D. E. Discher, and S. A. Safran, Journal of Physics: Condensed Matter **22**, 194110 (2010).

A. Zemel, F. Rehfeldt, A. E. X. Brown, D. E. Discher, and S. A. Safran, Nature Physics **6**, 468 (2010).

O.-Y. Zhong-can and W. Helfrich, Physical Review A **39**, 5280 (1989).

C. Zhu, S. L. Das, and T. Baumgart, Biophysical Journal **102**, 1837 (2012).

F. Ziebert and I. S. Aranson, PLOS ONE **8**, e64511 (2013).

F. Ziebert, S. Swaminathan, and I. S. Aranson, Journal of The Royal Society Interface **9**, 1084 (2012).

K. Zieske and P. Schwille, eLife **3**, e03949 (2014).